

nature

TELEPHONE CONNECTIONS

AI and mobile-phone data help target COVID aid more effectively

Gas exchange

The race to turn carbon dioxide into useful products

Supply and demand

Fix the way vaccines are rolled out before the next pandemic

High tide

Increase in extreme storm surges linked to rising sea levels

Nature.2022.04.02

[Sat, 02 Apr 2022]

- [This Week](#)
- [News in Focus](#)
- [Opinion](#)
- [Work](#)
- [Research](#)
- [Amendments & Corrections](#)

This Week

- **[Afghanistan's girls' schools can — and must — stay open. There is no alternative](#)** [28 March 2022]
Editorial • The Taliban have broken a promise and betrayed a generation.
- **[Time is running out for COVID vaccine patent waivers](#)** [29 March 2022]
Editorial • The European Union needs to go further and faster in embracing a temporary waiver on COVID-19 intellectual property.
- **[Study conspiracy theories with compassion](#)** [29 March 2022]
World View • The societal forces that drive people to join a belief system matter more than the specifics of what they believe.
- **[Social-media reform is flying blind](#)** [28 March 2022]
World View • Redesigning social media to improve society requires a new platform for research.
- **[Mice eat less and explore more after intake of certain amino acids](#)** [21 March 2022]
Research Highlight • The response to ‘non-essential’ amino acids, which can be made in the body, might help animals to seek out more important nutrients.
- **[Where are Earth's oldest trees? Far from prying eyes](#)** [22 March 2022]
Research Highlight • A comprehensive tally identifies 30 trees more than 2 millennia old, almost all growing at high altitudes.
- **[The sulfurous dust that helped to do in the dinosaurs](#)** [21 March 2022]
Research Highlight • An asteroid strike kicked sulfur-infused dust so high that it contributed to catastrophic cooling 66 million years ago.
- **[Astronomy's carbon footprint is sky-high](#)** [21 March 2022]
Research Highlight • Among the most intensive sources are the Hubble Space Telescope and, on Earth, the Very Large Telescope.
- **[How spirulina could help make smoothies with a kick](#)** [21 March 2022]
Research Highlight • Scientists genetically engineer the widely consumed microorganism to produce protein-based pharmaceuticals.

- **Fluid dynamics rises to the challenge of yeast-free pizza** [22

March 2022]

Research Highlight • A toothsome pizza base is achieved by bubbling gas through balls of dough.

- **How boa constrictors squeeze and breathe at the same time**

[24 March 2022]

Research Highlight • A boa avoids suffocation by inflating its lungs with one part of its ribcage and wrapping prey with another.

- EDITORIAL
- 28 March 2022

Afghanistan's girls' schools can — and must — stay open. There is no alternative

The Taliban have broken a promise and betrayed a generation.



Excitement at the start of a new term ended in heartbreak as the Taliban leadership ordered thousands of secondary-school-age girls to return home.Credit: Ahmad Sahel Arman/AFP/Getty

We are girls. We are from Afghanistan. We are humans. Why shouldn't we go to school? What crime have we committed?" This tearful plea from a schoolgirl in Afghanistan was echoed by thousands of children last week, cruelly denied that most basic of human rights: the right to learn.

Before the Taliban retook all of Afghanistan last August, for the first time since 2001, it pledged that this time would be different: that unlike 20 years ago, girls and women would be attending educational institutions. That promise has been broken. At the start of the year, the country's education ministry announced that girls of secondary-school age would be permitted to go back to class. But tens of thousands, those over the age of 12, were sent home on 22 March, the start of the school year in the northern half of the country — a generation betrayed.

The earlier directive suggested that the ministry was satisfied that its requirements for reopening girls' schools had been met — namely that girls of secondary-school age be taught by female teachers, and in separate buildings to boys. But the ministry was overruled by the Taliban's top leadership. Girls' schools will stay shut until further notice, pending a new plan in keeping with "Sharia and Afghan tradition and culture", tweeted the state-run Bakhtar news agency. The top leadership's decision has confirmed what many researchers had previously warned about — that the idea that the Taliban has changed needs to be treated with caution, if not outright scepticism.

Researchers who study the Taliban's education policies say that official documents endorse the principle of education for all. Girls' schools have remained open in some areas because of pressure from parents, and also because the United Nation's children's charity UNICEF has negotiated agreements that permit it to run schools in parts of the country. In the capital, Kabul, there is evidence that girls are attending schools, and that universities are functioning (albeit without publicity).

But researchers also say that a divided Taliban leadership [cannot agree on how its policies should be implemented](#). One faction is completely opposed to girls' education and women's employment — in line with original Taliban ideology, under which girls and women were prevented from getting an education, going to work, running businesses or taking part in the country's

governance. Worse still, girls and women were killed for violating Taliban laws.

Others in the Taliban envisage a different future. Several generations of Afghans have grown up as refugees in Iran, Pakistan and the Gulf States, having fled after the Soviet Union invaded Afghanistan in 1979. Many have been to schools and universities abroad and acquired professional qualifications. Among their number are current Taliban leaders whose own daughters and sons are being educated, according to a [report last month from the Afghan Analysts Network](#), a non-profit policy-research organization.

Neighbours must speak out

This week's policy reversal will also have unsettled Afghanistan's neighbours, as well as those countries that have provided the Taliban with a degree of legitimacy. Iran and Pakistan are now home to several million Afghans — including thousands of students. Qatar helped broker talks between the Taliban and the United States, leading to last August's withdrawal of international forces from Afghanistan. There can be very few among these countries' policymakers who will have any truck with the idea that religion or 'tradition' prevents half of Afghanistan's population from being educated. But they have been silent for too long and now have a responsibility to make their views heard.

The UN (especially UNICEF) and other international donors are rightly outraged. But they need to tread carefully and must not withdraw humanitarian assistance, because that will punish people who are in desperate need through no fault of their own. The leaders of Afghanistan's neighbours — and their education and research policymakers — can and should apply more leverage, especially to the Taliban's top leadership.

In spite of the many injustices perpetuated by the previous Afghan government, it made significant strides in education and in gender equality. In 2020, nearly 10 million Afghan children (40% of them girls) were enrolled in schools, compared with less than one million (only boys) in 2001. Women made up one-quarter of Afghanistan's parliamentarians and some 150,000 women have held some form of public office. The tragedy for

Afghanistan's girls and women is that getting back to school, should it eventually happen, will not automatically mean regaining these lost rights.

More than a century ago, *Nature* backed the United Kingdom's education reformers in their campaign to remove barriers to women's education ([*Nature* 10, 395–396; 1874](#)). Two years ago, a UN target (part of the Sustainable Development Goals) to get all of the world's children into schools finally looked to be within reach. But the COVID-19 pandemic, and now the return of the Taliban in Afghanistan, have set the effort back. Afghanistan is once more the only country in the world where girls of secondary-school age are prevented by a national government from going to school.

Last week's scenes of girls being sent home, their hopes destroyed, remind us that the world can never take learning for granted. For the children's sake, and for Afghanistan's future, the education ministry's original policy must be allowed to stand — these events must never be allowed to happen again.

Nature 603, 763 (2022)

doi: <https://doi.org/10.1038/d41586-022-00877-y>

This article was downloaded by **calibre** from <https://www.nature.com/articles/d41586-022-00877-y>.

| [Section menu](#) | [Main menu](#) |

- EDITORIAL
- 29 March 2022

Time is running out for COVID vaccine patent waivers

The European Union needs to go further and faster in embracing a temporary waiver on COVID-19 intellectual property.



World Trade Organization director-general Ngozi Okonjo-Iweala has said her team members are ready to roll up their sleeves to reach an agreement on waiving intellectual property for COVID-19 vaccines. Credit: Dursun Aydemir/Anadolu/Bloomberg/Getty

Should more countries be making their own coronavirus vaccines, drugs and testing kits? Yes, without a shadow of doubt, [says an international campaign](#) led by India and South Africa, and backed by researchers, non-governmental organizations (NGOs) and publications including *Nature*. The campaign is

calling for temporary relief on COVID-19-related intellectual property (IP), including patents, for at least the duration of the pandemic.

More companies in more countries must be able to make vaccines without the threat of being sued by high-powered legal teams representing the pharmaceutical firms that dominate vaccine supply. By giving more companies the legal ability to reproduce COVID-19 vaccines and drugs, a waiver could help to increase supplies and pave the way for a more equitable distribution of life-saving technologies.

China and the United States, along with more than 100 other countries, are sympathetic to this idea. Until now, most European nations have been opposed. However, European Union member states finally seem to be warming to the principle that IP needs to be shared in a pandemic, and have agreed to accelerate the existing process for IP relief. This is not the breakthrough that is needed, because it does not give low-income countries the ability to produce and distribute vaccines freely, quickly and without completing time-consuming paperwork so that lives can be saved now. But it does represent a change in the EU's position.

The need to share COVID-19-related IP remains urgent. Two years into the pandemic, fewer than 15% of people in low-income countries have had at least one dose of a vaccine, whereas in some high-income countries, people are being offered fourth doses. This has happened, in part, because the governments of wealthy nations can offer vaccine makers large sums that poor countries cannot match. A number of companies are, in turn, making large profits, so have little incentive to change their business model. Last month, Pfizer, which, along with its partner BioNTech, has manufactured and distributed more than 3 billion mRNA vaccines, reported a net profit of almost US\$22 billion for 2021 — more than double the amount for 2020. According to data from the Center for Global Development, a think tank in Washington DC, richer nations have vaccinated people against COVID-19 at a rate faster than for any previous disease.

The EU has previously said that existing international rules allow countries to override IP in an emergency such as a pandemic, so there should be no need for extra relief. But these rules, known as compulsory licensing, are not

fit for a pandemic. During the past two years, no company has been granted a compulsory licence to make a COVID-19 vaccine.

Representatives of the EU, India, South Africa and the United States have been meeting at the World Trade Organization (WTO) in Geneva, Switzerland, to try to resolve the impasse. Earlier this month, they announced that the compulsory-licensing process can be accelerated. Under existing compulsory-licensing rules, a separate application has to be made for a waiver for each patent involved — and a single technology can involve dozens of patented processes. The group proposes that companies in low- and middle-income countries be allowed to make just one application per vaccine.

In February, Afrigen Biologics and Vaccines in Cape Town, South Africa, demonstrated that it has [the technical ability to reproduce Moderna's mRNA vaccine](#). If the proposal agreed at the WTO is endorsed by all members, Afrigen could, in theory, make one application to the South African government for permission to make and sell the vaccines at scale.

But researchers and IP experts say that the latest proposal still has a number of problems. First, pharmaceutical companies can seek to block compulsory-licence applications, which [Pfizer is already doing](#). Second, the proposal does not include access to forms of data that might be needed to make vaccines, but that are not covered in a patent. It also requires companies looking to reproduce a vaccine to draw up a list of all patents that must be waived — something that would take too long to be practical in a pandemic. Moreover, the EU does not have the backing of the United Kingdom and Switzerland, where several of the world's biggest pharmaceutical companies are based.

Identifying all of the IP that goes into specific technologies cannot be done quickly. A preliminary analysis by the World Intellectual Property Organization shows that [applications were made for 417 COVID-19 vaccine-related patents](#) between the start of 2020 and the end of September 2021. The analysis is preliminary because it takes an average of 18 months between an application being filed with a patent office and the application being published. There are many more patents still to come.

A faster solution would be to allow vaccines to be reproduced, legally, without the need to wait for a complete list of patents as a condition to getting started. Such a document could still be drawn up, but it should not be used to hold up vaccine development and manufacturing.

Agreements necessarily need compromise, especially when they involve finding a consensus between the WTO's 164 member countries and maintaining the support of more than 100 NGOs. But there's no benefit to a massive negotiation if the result is no extra COVID-19 drugs or vaccines. That's why one compromise might be to focus on vaccine IP alone, rather than on all COVID-19 interventions. This could provide the best chance of saving lives, protecting economies, stopping the rise of new variants and, ultimately, curbing this devastating pandemic.

Nature **603**, 764 (2022)

doi: <https://doi.org/10.1038/d41586-022-00878-x>

This article was downloaded by **calibre** from <https://www.nature.com/articles/d41586-022-00878-x>

| [Section menu](#) | [Main menu](#) |

- WORLD VIEW
- 29 March 2022

Study conspiracy theories with compassion



The societal forces that drive people to join a belief system matter more than the specifics of what they believe.

- [Elżbieta Drążkiewicz](#) 0

In 2019, a senior colleague warned me that my research focus was a niche area of a frivolous topic: conspiracy theories related to vaccine hesitancy among parents in Ireland.

My area is niche no longer. Motivated to end the pandemic, and to encourage vaccination and other health-promoting behaviours, many researchers new to the subject are asking how best to ‘confront’ or ‘fight’ conspiracy theories, and how to characterize people wary of medical technologies. But my field has worked for decades to push back on this

tendency to pathologize and ‘other’. Whether researchers are trying to understand beliefs around vaccination or theories surrounding NATO, Russia and bioweapons labs, such framing limits what can be learnt.

Conspiracy theories are more about values than about information. Debunking statements might occasionally be effective, but does little to tackle their root cause. When investigators ask only about knowledge, they tend to see only ignorance as the root of the problem.

Let me be clear: I am in no way arguing that conspiracy theories are harmless. It is precisely because they are so dangerous that it is crucial to understand their causes. It’s not enough to study individuals and their ideas: we must consider societal structures, and cultural and historical contexts that generate and propagate conspiratorial ideas.

First, some basics. Conspiracy theories do not exist in a vacuum. They amplify existing fears and ideas about people’s place in the world. Researchers should consider what rallying around such theories says about fears over global power struggles or scientific advances, or about indignation over the status quo or societal changes.

It is not useful simply to say, “People who feel powerless embrace conspiracy theories.” Researchers must learn why people feel this way. Often, it is because of mistreatment by other people or institutions. Women who have experienced oppressive reproductive regimes, such as that in Romania during the regime of Nicolae Ceaușescu, frequently opt out of immunization. People who get vaccinated generally do so not because of an understanding of immunology, but because of trust in — and access to — health-care systems.

Over the first months of the pandemic, I worked with anthropologist Elisa Sobo at San Diego State University in California to analyse social-media posts that touched on COVID-19 conspiracy theories in three countries (E. J. Sobo and E. Drażkiewicz in *Viral Loads* (eds L. Manderson *et al.*) Ch. 4; UCL Press, 2021). Although specific theories seemed similar (‘the government is hiding the truth about the disease’), the cultural reasoning differed. In the United States, conspiratorial tropes were framed as an attack on self-built prosperity. In Poland, they reflected concern that the state was

hiding its failures. In Ireland, the discourse hinged on fears tied to post-colonial memories of British rule and suspicion of foreign influence. To gain traction, conspiracy theories had to resonate with localized histories. To counter medical conspiracy theories, institutions must be aware of these histories and be ready to incorporate them (not just medical facts) in campaigns. ‘One size fits all’ explanations or strategies are not the best way to counter conspiracy theories.

Here’s an example from my research in Ireland ([E. Drażkiewicz Grodzicka](#) *J. Cult. Res.* **25**, 69–87; 2021). For decades, state and church ran ‘charity’ institutions in which ‘fallen women’ who became pregnant outside marriage were subjected to forced labour, illegal adoptions and, sometimes, unethical clinical trials. These Magdalene Laundries and similar places represent notorious welfare scandals. They made it easy to believe rumours that programmes to prevent a sexually transmitted disease with HPV vaccines actually caused harm.

Ireland’s low HPV vaccination rate was caused by a deficit not in knowledge, but in trust, and so the solution was not to debunk specific rumours, but to make health services more trustworthy. Ireland ran a ‘Protect our future’ campaign that emphasized the importance of trustworthy information, but its ultimate goal was to convince people that the government has nothing to hide, and clinicians’ main motivation is their duty of care. The vaccination rate went up from 56% in 2016–17 to 76% in 2019–20.

Another counterproductive tendency, in my view, is the quest to create a profile of ‘those people’ who engage with conspiracy theories, obsessing over characteristics that make them distinct — especially from the researcher. This othering is, in part, a legacy of a field that has frequently opted to study people drawn in by, say, fantastic stories of alien abductions rather than more-plausible beliefs such as corruption scandals. But much of this ‘us versus them’ framing has to do with researchers’ motivations. Many, myself included, want to defend democracy and science, so it is easy to define those who embrace conspiracy theories as a threat or enemy. But that deflects researchers’ attentions to individuals and their beliefs, and

stops them looking at the systems that push people towards conspiratorial circles.

I understand and share concerns that a more empathetic approach has risks. I've been accused of giving visibility to views that would be better dismissed. But it is important to examine the structures that make conspiracy theories appealing. A focus on individuals' perceived deficits diverts attention from the social realities — displacement, alienation, repression — that make false theories resonate.

Nature **603**, 765 (2022)

doi: <https://doi.org/10.1038/d41586-022-00879-w>

This article was downloaded by **calibre** from <https://www.nature.com/articles/d41586-022-00879-w>

| [Section menu](#) | [Main menu](#) |

- WORLD VIEW
- 28 March 2022

Social-media reform is flying blind



Redesigning social media to improve society requires a new platform for research.

- [Chris Bail](#) 0

As Russia continues its ruthless war in Ukraine, pundits are speculating what social-media platforms might have done years ago to undermine propaganda well before the attack. Amid accusations that social media fuels political violence — and even genocide — it is easy to forget that Facebook evolved from a site for university students to rate each other's physical attractiveness. Instagram was founded to facilitate alcohol-based gatherings. TikTok and YouTube were built to share funny videos.

The world's social-media platforms are now among the most important forums for discussing urgent social problems, such as Russia's invasion of Ukraine, COVID-19 and climate change. Techno-idealists continue to

promise that these platforms will bring the world together — despite mounting evidence that they are pulling us apart.

Efforts to regulate social media have largely stalled, perhaps because no one knows what something better would look like. If we could hit ‘reset’ and redesign our platforms from scratch, could we make them strengthen civil society?

Researchers have a hard time studying such questions. Most corporations want to ensure studies serve their business model and avoid controversy. They don’t share much data. And getting answers requires not just making observations, but doing experiments.

In 2017, I co-founded the Polarization Lab at Duke University in Durham, North Carolina. We have created a social-media platform for scientific research. On it, we can turn features on and off, and introduce new ones, to identify those that improve social cohesion. We have recruited thousands of people to interact with each other on these platforms, alongside bots that can simulate social-media users.

We hope our effort will help to evaluate some of the most basic premises of social media. For example, tech leaders have long measured success by the number of connections people have. Anthropologist Robin Dunbar has suggested that humans struggle to maintain meaningful relationships with more than 150 people. Experiments could encourage some social-media users to create deeper connections with a small group of users while allowing others to connect with anyone. Researchers could investigate the optimal number of connections in different situations, to work out how to optimize breadth of relationships without sacrificing depth.

A related question is whether social-media platforms should be customized for different societies or groups. Although today’s platforms seem to have largely negative effects on US and Western-Europe politics, the opposite might be true in emerging democracies ([P. Lorenz-Spreen et al. Preprint at https://doi.org/hmq2; 2021](https://doi.org/hmq2)). One study suggested that Facebook could reduce ethnic tensions in Bosnia–Herzegovina ([N. Asimovic et al. Proc. Natl Acad. Sci. USA 118, e2022819118; 2021](https://doi.org/10.1073/pnas.2022819118)), and social media has helped Ukraine to rally support around the world for its resistance.

The next question is what types of algorithm could encourage consensus and discourage hate, abuse and division. Most platforms order posts according to engagement. But this incentivizes extreme statements that generate controversy and create vicious cycles of incivility and outrage. Our laboratory's Bipartisanship Leaderboard ranks Twitter users by the number of likes their posts receive from both Republicans and Democrats. What would happen if news feeds were filled with content that diverse groups appreciate, instead of people preaching to the choir?

Yet another line of research concerns what would happen if social-media users had to be identifiable in real life. Anonymity can help people to avoid censorship in authoritarian regimes or to explore alternative viewpoints without peer pressure. How can we give people the freedom to explore ideas anonymously without enabling trolls or imposters?

Answers to such questions could inform regulators, entrepreneurs and any effort to make social media healthy for society. We cannot leave social-media companies to attain these answers themselves. These companies will always struggle to balance profits with improving human life — but they will respond to legislation, public opinion and individual behaviour. Facebook, which once seemed invincible, just announced its most dismal earnings report in years — and admitted it is struggling to compete with TikTok for users.

In the wake of the testimony to Congress of Frances Haugen — who blew the whistle on Facebook for failing to curb misinformation, mental health impacts, crime and more — public trust in tech companies is low. A social-media platform for scientific research could help them. Facebook can't suddenly make some users anonymous, but could test this feature in a carefully controlled setting. (Disclosure: we have received funding from social-media companies, but without restrictions on what we study or publish.)

Building a broader platform for scientific research on social media requires an unprecedented interdisciplinary effort that involves social scientists, computer scientists and many others in and outside industry. It also needs extensive funding — ideally from governments or specialized philanthropies. Perhaps a government agency to regulate social media

should be funded by tech corporations themselves, based on the model of the US Food and Drug Administration.

It's a tall order, but regulators and tech leaders are currently flying blind. Without evidence-based insights about how to innovate, pundits and policymakers will continue to speculate about how to fix a system that is beyond repair — while the rest of us suffer the consequences.

Nature **603**, 766 (2022)

doi: <https://doi.org/10.1038/d41586-022-00805-0>

This article was downloaded by **calibre** from <https://www.nature.com/articles/d41586-022-00805-0>

| [Section menu](#) | [Main menu](#) |

- RESEARCH HIGHLIGHT
- 21 March 2022

Mice eat less and explore more after intake of certain amino acids

The response to ‘non-essential’ amino acids, which can be made in the body, might help animals to seek out more important nutrients.

 Confocal light micrograph of orexin receptors (red), also known as hypocretins, in the brain.

Orexin receptors (red) dot brain neurons. Scientists have now uncovered the effects of non-essential amino acids acting on these neurons. Credit: C.J.Guerin, PhD, MRC Toxicology Unit/Science Photo Library

Consuming amino acids that can be made in the body leads mice to eat less and explore their surroundings more — an effect that might offer evolutionary benefits¹.

Access options

Subscribe to Nature+

Get immediate online access to the entire Nature family of 50+ journals

\$29.99

monthly

[Subscribe](#)

Subscribe to Journal

Get full journal access for 1 year

\$199.00

only \$3.90 per issue

[Subscribe](#)

All prices are NET prices.

VAT will be added later in the checkout.

Tax calculation will be finalised during checkout.

Buy article

Get time limited or full article access on ReadCube.

\$32.00

[Buy](#)

All prices are NET prices.

Additional access options:

- [Log in](#)
- [Learn about institutional subscriptions](#)

Nature **603**, 768 (2022)

doi: <https://doi.org/10.1038/d41586-022-00830-z>

References

1. Viskaitis, P. *et al.* *Curr. Biol.* <https://doi.org/10.1016/j.cub.2022.02.067> (2022)

| [Section menu](#) | [Main menu](#) |

- RESEARCH HIGHLIGHT
- 22 March 2022

Where are Earth's oldest trees? Far from prying eyes

A comprehensive tally identifies 30 trees more than 2 millennia old, almost all growing at high altitudes.

 Great Basin Bristlecone Pine (*Pinus longaeva*) ancient tree in the White Mountains of California, USA.

A bristlecone pine in California. The two oldest trees in the world are members of the species. Credit: Juan Carlos Munoz/Nature Picture Library

Ancient trees thrive where humans don't: on the remote, rocky slopes of high mountains. So shows an analysis of tens of thousands of trees¹.

Access options

Subscribe to Nature+

Get immediate online access to the entire Nature family of 50+ journals

\$29.99

monthly

[Subscribe](#)

Subscribe to Journal

Get full journal access for 1 year

\$199.00

only \$3.90 per issue

[Subscribe](#)

All prices are NET prices.

VAT will be added later in the checkout.

Tax calculation will be finalised during checkout.

Buy article

Get time limited or full article access on ReadCube.

\$32.00

[Buy](#)

All prices are NET prices.

Additional access options:

- [Log in](#)
- [Learn about institutional subscriptions](#)

Nature **603**, 768 (2022)

doi: <https://doi.org/10.1038/d41586-022-00832-x>

References

1. Liu, J. *et al.* *Conserv. Biol.* <https://doi.org/10.1111/cobi.13907> (2022).

This article was downloaded by **calibre** from <https://www.nature.com/articles/d41586-022-00832-x>

- RESEARCH HIGHLIGHT
- 21 March 2022

The sulfurous dust that helped to do in the dinosaurs

An asteroid strike kicked sulfur-infused dust so high that it contributed to catastrophic cooling 66 million years ago.

 Illustration of the last days of dinosaurs during the Cretaceous Period, caused by a giant asteroid impact at Chicxulub.

The extinction of the dinosaurs was triggered in part by high levels of sunlight-blocking sulfur in the atmosphere. Credit: Getty

The catastrophic Chicxulub asteroid impact 66 million years ago launched enormous quantities of sulfur into the stratosphere, rock chemistry suggests. This sulfur enhanced global cooling that contributed to the dinosaurs' demise¹.

Access options

Subscribe to Nature+

Get immediate online access to the entire Nature family of 50+ journals

\$29.99

monthly

[Subscribe](#)

Subscribe to Journal

Get full journal access for 1 year

\$199.00

only \$3.90 per issue

[Subscribe](#)

All prices are NET prices.

VAT will be added later in the checkout.

Tax calculation will be finalised during checkout.

Buy article

Get time limited or full article access on ReadCube.

\$32.00

[Buy](#)

All prices are NET prices.

Additional access options:

- [Log in](#)
- [Learn about institutional subscriptions](#)

Nature **603**, 768 (2022)

doi: [*https://doi.org/10.1038/d41586-022-00831-y*](https://doi.org/10.1038/d41586-022-00831-y)

References

1. Junium, C. K. *et al. Proc. Natl Acad. Sci. USA* **119**, e2119194119 (2022).

| [Section menu](#) | [Main menu](#) |

- RESEARCH HIGHLIGHT
- 21 March 2022

Astronomy's carbon footprint is sky-high

Among the most intensive sources are the Hubble Space Telescope and, on Earth, the Very Large Telescope.

The Very Large Telescope operated by the European Southern Observatory at Paranal, Antofagasta Region, Chile.

The Very Large Telescope on Cerro Paranal, Chile, has a corresponding very large carbon footprint. Credit: Insights/Universal Images Group via Getty

The first rough estimate of astronomy's total impact on Earth's climate suggests that, between them, space missions and ground-based observatories emit greenhouse gases equivalent to more than one million tonnes of carbon dioxide each year¹.

Access options

Subscribe to Nature+

Get immediate online access to the entire Nature family of 50+ journals

\$29.99

monthly

[Subscribe](#)

Subscribe to Journal

Get full journal access for 1 year

\$199.00

only \$3.90 per issue

[Subscribe](#)

All prices are NET prices.

VAT will be added later in the checkout.

Tax calculation will be finalised during checkout.

Buy article

Get time limited or full article access on ReadCube.

\$32.00

[Buy](#)

All prices are NET prices.

Additional access options:

- [Log in](#)
- [Learn about institutional subscriptions](#)

Nature **603**, 768 (2022)

doi: <https://doi.org/10.1038/d41586-022-00824-x>

References

1. Knöldlseder, J. *et al.* *Nature Astron.* <https://doi.org/10.1038/s41550-022-01612-3> (2022).

| [Section menu](#) | [Main menu](#) |

- RESEARCH HIGHLIGHT
- 21 March 2022

How spirulina could help make smoothies with a kick

Scientists genetically engineer the widely consumed microorganism to produce protein-based pharmaceuticals.

 Coloured scanning electron micrograph (SEM) of Spirulina powder.

Powdered spirulina (artificially coloured) could make for a nutritious and stable carrier for protein-based therapies. Credit: Anne Weston, EM STP, Francis Crick Inst./SPL

The blue-green alga spirulina, a popular dietary supplement, could help bioengineers to produce therapeutic proteins such as antibodies¹.

Access options

Subscribe to Nature+

Get immediate online access to the entire Nature family of 50+ journals

\$29.99

monthly

[Subscribe](#)

Subscribe to Journal

Get full journal access for 1 year

\$199.00

only \$3.90 per issue

[Subscribe](#)

All prices are NET prices.

VAT will be added later in the checkout.

Tax calculation will be finalised during checkout.

Buy article

Get time limited or full article access on ReadCube.

\$32.00

[Buy](#)

All prices are NET prices.

Additional access options:

- [Log in](#)
- [Learn about institutional subscriptions](#)

Nature **603**, 769 (2022)

doi: <https://doi.org/10.1038/d41586-022-00834-9>

References

1. Jester, B. W. *et al.* *Nature Biotechnol.* <https://doi.org/10.1038/s41587-022-01249-7> (2022).

This article was downloaded by **calibre** from <https://www.nature.com/articles/d41586-022-00834-9>

- RESEARCH HIGHLIGHT
- 22 March 2022

Fluid dynamics rises to the challenge of yeast-free pizza

A toothsome pizza base is achieved by bubbling gas through balls of dough.

Three photos of the results of the visual observation of the baking and foaming of the pizza dough.

Yeast-free pizza dough (left) that is infused with carbon dioxide (middle) and baked forms large pores (right; yellow outlines) similar to those in pizza dough made with conventional methods. Credit: P. Renato Avallone *et al/Physics of Fluids*

A physics-driven baking technique can produce a yeast-free pizza with the classic well-risen, porous base¹.

Access options

Subscribe to Nature+

Get immediate online access to the entire Nature family of 50+ journals

\$29.99

monthly

[Subscribe](#)

Subscribe to Journal

Get full journal access for 1 year

\$199.00

only \$3.90 per issue

[Subscribe](#)

All prices are NET prices.

VAT will be added later in the checkout.

Tax calculation will be finalised during checkout.

Buy article

Get time limited or full article access on ReadCube.

\$32.00

[Buy](#)

All prices are NET prices.

Additional access options:

- [Log in](#)
- [Learn about institutional subscriptions](#)

Nature **603**, 769 (2022)

doi: [*https://doi.org/10.1038/d41586-022-00829-6*](https://doi.org/10.1038/d41586-022-00829-6)

References

1. Avallone, P. R., Iaccarino, P., Grizzuti, N., Pasquino, R. & Di Maio, E. *Phys. Fluid.* **34**, 033109 (2022).

This article was downloaded by **calibre** from <https://www.nature.com/articles/d41586-022-00829-6>

- RESEARCH HIGHLIGHT
- 24 March 2022

How boa constrictors squeeze and breathe at the same time

A boa avoids suffocation by inflating its lungs with one part of its ribcage and wrapping prey with another.



Boa constrictors have such long ribcages that they can devote one section to breathing and another to digesting large food items. Credit: Lucas Bustamante/Nature Picture Library

Boa constrictors breathe by expanding and collapsing their ribcages, a technique that seems at odds with the snakes' habit of constricting and swallowing huge meals — both actions that constrain rib movement. Now scientists have explained this conundrum: boas can breathe with one part of their bodies while prey occupies another part¹.

Access options

Subscribe to Nature+

Get immediate online access to the entire Nature family of 50+ journals

\$29.99

monthly

[Subscribe](#)

Subscribe to Journal

Get full journal access for 1 year

\$199.00

only \$3.90 per issue

[Subscribe](#)

All prices are NET prices.

VAT will be added later in the checkout.

Tax calculation will be finalised during checkout.

Buy article

Get time limited or full article access on ReadCube.

\$32.00

[Buy](#)

All prices are NET prices.

Additional access options:

- [Log in](#)
- [Learn about institutional subscriptions](#)

Nature **603**, 769 (2022)

doi: [*https://doi.org/10.1038/d41586-022-00833-w*](https://doi.org/10.1038/d41586-022-00833-w)

References

1. Capano, J. G. *et al.* *J. Exp. Biol.* **225**, jeb243119 (2022).

| [Section menu](#) | [Main menu](#) |

News in Focus

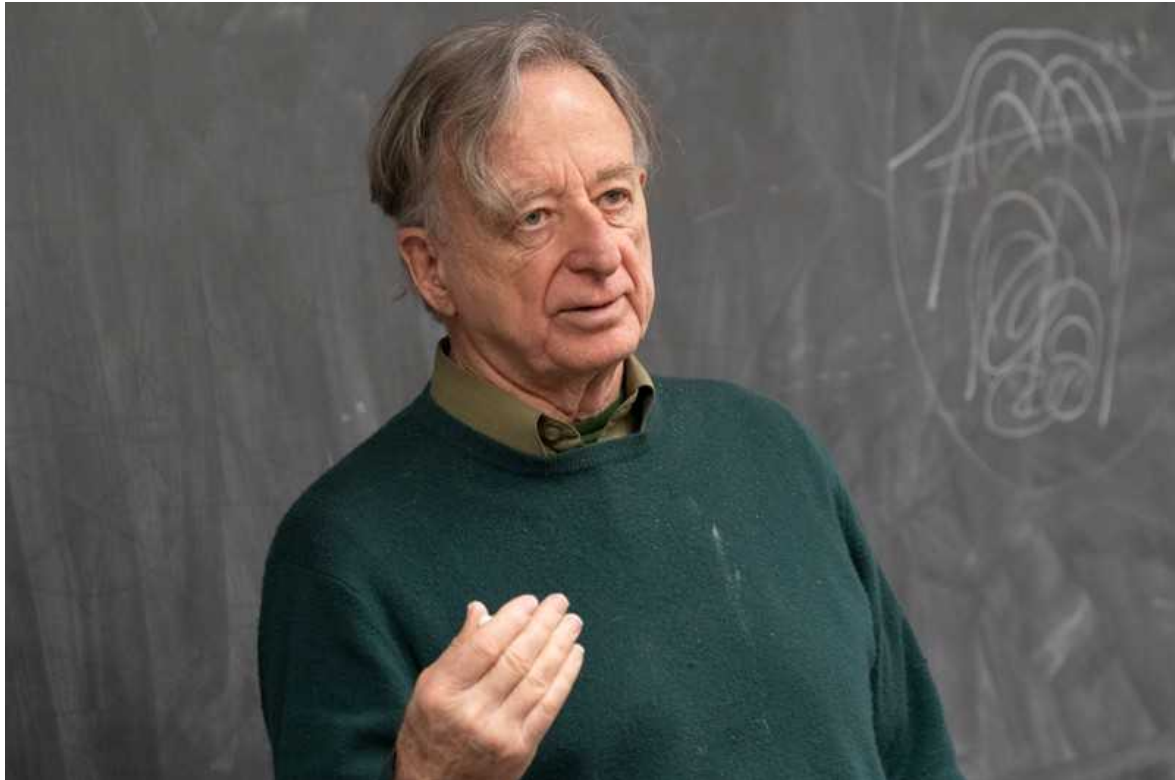
- **[Beautiful science, Omicron subvariant and a prestigious maths prize](#)** [30 March 2022]
News Round-Up • The latest science news, in brief.
- **[Scientists struggle to probe COVID's origins amid sparse data from China](#)** [17 March 2022]
News • Origin investigations typically take years, but some researchers say China is delaying the process for political reasons as international tensions rise.
- **[Where is Russia's cyberwar? Researchers decipher its strategy](#)** [17 March 2022]
News Explainer • Many analysts expected an unprecedented level of cyberattacks when Russia invaded Ukraine — which so far haven't materialized.
- **[Can brain scans reveal behaviour? Bombshell study says not yet](#)** [17 March 2022]
News • Most studies linking features in brain imaging to traits such as cognitive abilities are too small to be reliable, argues a controversial analysis.
- **[Morgue data hint at COVID's true toll in Africa](#)** [23 March 2022]
News • Around 90% of deceased people tested at a Lusaka facility during coronavirus surges were positive for SARS-CoV-2 infection, suggesting flaws in the idea of an 'African paradox'.
- **[Are 'COVID toes' actually caused by the coronavirus?](#)** [16 March 2022]
News • Study adds to evidence suggesting that SARS-CoV-2 infection doesn't cause an inflamed-toe condition called chilblains, but it doesn't close the door.
- **[The race to upcycle CO2 into fuels, concrete and more](#)** [29 March 2022]
News Feature • Companies are scrambling to turn the greenhouse gas into useful products — but will that slow climate change?
- **[The quest to prevent MS — and understand other post-viral diseases](#)** [30 March 2022]
News Feature • Some people develop multiple sclerosis after an infection. Could a vaccine prevent that — and what does it reveal about the long-term effects of viruses?

| [Next section](#) | [Main menu](#) | [Previous section](#) |

- NEWS ROUND-UP
- 30 March 2022

Beautiful science, Omicron subvariant and a prestigious maths prize

The latest science news, in brief.



Topologist Dennis Sullivan has won the 2022 Abel Prize. Credit: John Griffin/Stony Brook University/Abel Prize

Topology virtuoso wins Abel prize

US mathematician Dennis Sullivan (pictured) has [won one of the most prestigious awards in mathematics](#), for his contributions to topology — the study of qualitative properties of shapes — and related fields.

“Sullivan has repeatedly changed the landscape of topology by introducing new concepts, proving landmark theorems, answering old conjectures and formulating new problems that have driven the field forwards,” says the citation for the 2022 Abel Prize, which was announced by the Norwegian Academy of Science and Letters, based in Oslo, on 23 March. Throughout his career, Sullivan has moved from one area of mathematics to another and solved problems using a wide variety of tools, “like a true virtuoso”, the citation added. The prize is worth 7.5 million Norwegian kroner (US\$854,000).

Sullivan, who has positions at both Stony Brook University in New York and the City University of New York, says that the result he is proudest of is one he obtained in 1977, which distils the crucial properties of a space using a tool called rational homotopy ([D. Sullivan *Publ. Math IHES* 47, 269–331; 1977](#)). This became one of his most cited works and most widely applied techniques.

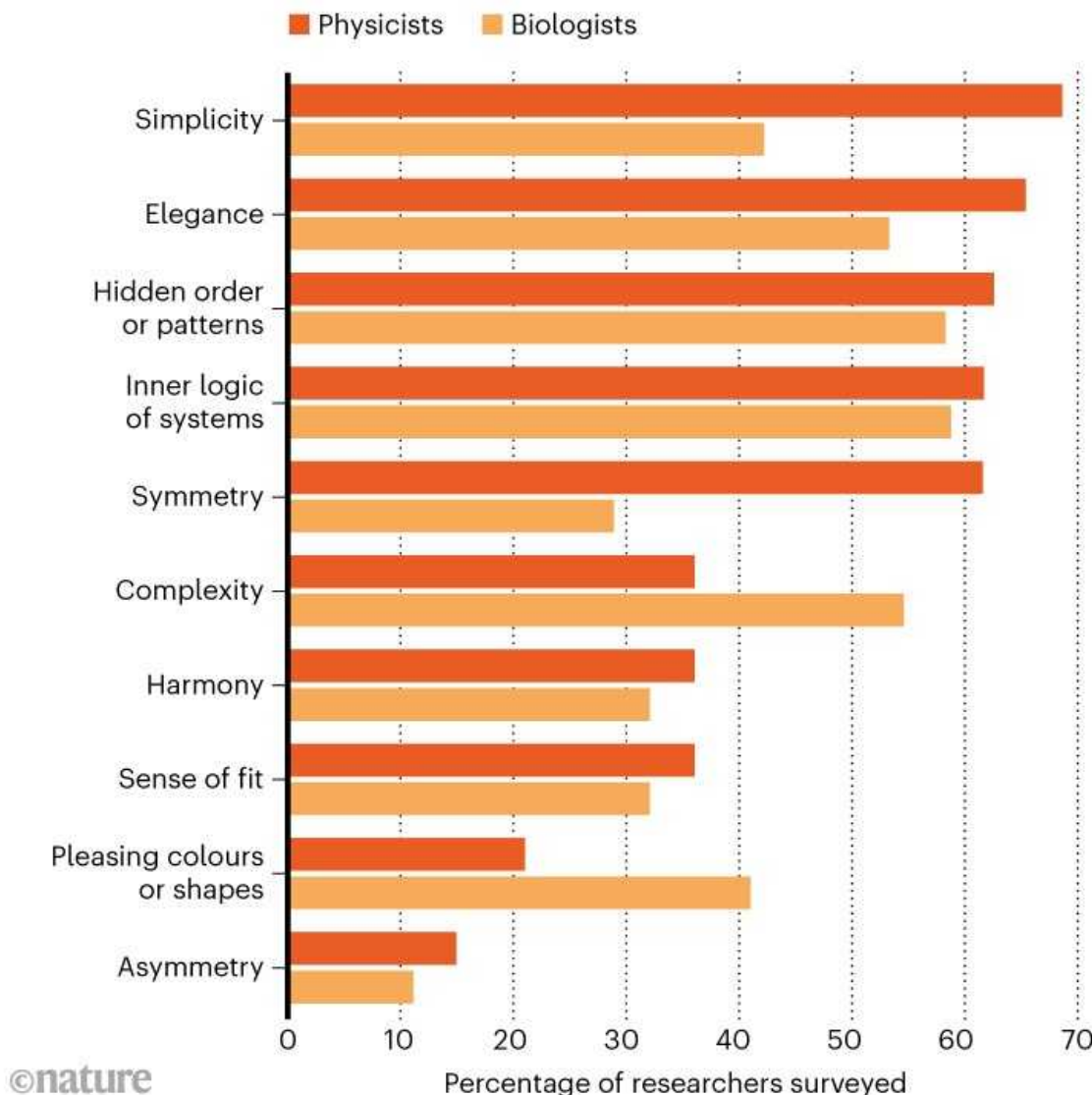
Beauty of science boosts researchers’ well-being

Scientists’ ability to experience wonder, awe and beauty in their work is associated with [higher levels of job satisfaction and better mental health](#), finds an international survey (see go.nature.com/36xuyos).

Brandon Vaidyanathan, a sociologist at the Catholic University of America in Washington DC, and his colleagues collected responses from more than 3,000 scientists — mainly biologists and physicists — in India, Italy, the United Kingdom and the United States. They asked participants about their job satisfaction and workplace culture, their experience of the COVID-19 pandemic and the role of aesthetics in science.

BEAUTIFUL SCIENCE

Three-quarters of researchers surveyed encounter beauty in the phenomena that they study. Biologists and physicists associate beauty with different aspects of their scientific work.



Source: Work and Well-Being in Science/The Catholic University of America.

The survey found that 75% of respondents encounter beauty in the phenomena that they study (see ‘Beautiful science’), and, for 62%, this had motivated them to pursue a scientific career. Half of those surveyed said that beauty helps them to persevere when they experience difficulty or failure,

and for 57%, beauty improves their scientific understanding. “When we experience scientific insight, it triggers the same operation in the brain as musical harmony, and we can take pleasure in this insight just like other art,” says Vaidyanathan.



Two doses of an mRNA vaccine such as that made by Pfizer–BioNTech provide similar protection against two subvariants of SARS-CoV-2. Credit: Allen J. Schaben/Los Angeles Times via Getty

Vaccines ward off Omicron subvariant

The Omicron subvariant BA.2 is replacing its sister version, BA.1, as the dominant form of SARS-CoV-2 in many nations. But a study published on 13 March shows that [mRNA vaccines offer similar protection against the two strains](#) — although protection against SARS-CoV-2 infection and symptomatic COVID-19 wanes within months of a third dose ([H. Chemaitelly, et al. Preprint at medRxiv https://doi.org/hnkw; 2022](#)). The study has not yet been peer reviewed.

Study co-author Laith Abu-Raddad, an infectious-diseases epidemiologist at Weill Cornell Medicine–Qatar in Doha, and his colleagues studied vaccine effectiveness using records and test results from Qatar’s health-care system. They found that Qatari residents with two doses of either the Pfizer–BioNTech or Moderna mRNA-based vaccine enjoyed several months of substantial protection against symptomatic disease caused by either BA.1 or BA.2. But protection waned to around 10% after only 4–6 months, meaning that the vaccines prevented only 10% of the cases that would have occurred if all of the individuals had been unvaccinated. A booster shot brought the protection against symptomatic infection by either subvariant back to 30–60%.

Nature **603**, 771 (2022)

doi: <https://doi.org/10.1038/d41586-022-00806-z>

This article was downloaded by **calibre** from <https://www.nature.com/articles/d41586-022-00806-z>

| [Section menu](#) | [Main menu](#) |

- NEWS
- 17 March 2022

Scientists struggle to probe COVID's origins amid sparse data from China

Origin investigations typically take years, but some researchers say China is delaying the process for political reasons as international tensions rise.

- [Amy Maxmen](#)



Researchers say that a next step in the COVID-19 origins hunt should be to study wildlife, such as foxes and raccoon dogs, on farms in China. Credit:

Biosphoto/Alamy

Scientists are anxious to obtain more data on the earliest days of the pandemic, following three tantalizing reports posted online in the past few weeks^{1,2,3}. Although not yet published in peer-reviewed journals, the preprints provide further evidence supporting the hypothesis that the coronavirus SARS-CoV-2 spread from animals to people who raised, butchered or bought them. But the reports don't reveal exactly what happened.

The World Health Organization's (WHO's) Scientific Advisory Group for the Origins of Novel Pathogens (SAGO) will soon put out a report specifying studies that are urgently needed, says Maria Van Kerkhove, an epidemiologist at the WHO. A principal ask in light of the new preprints is to collect and analyse samples from farmers and wildlife at farms that supplied the Huanan Seafood Wholesale Market in Wuhan — to which [many early COVID-19 cases were traced](#) and where coronavirus samples from January 2020 were concentrated — as well as from market vendors. The WHO made these suggestions a year ago, but the studies either haven't been conducted or haven't been published. The scientific community has grown frustrated with the wait as the world seeks answers to help prevent future pandemics.

Researchers in the United States, the United Kingdom and Australia who have worked closely with colleagues in China have told *Nature* that they're disappointed by the slow release of information from China about COVID-19's origins. "We are all trying to find out what the bloody hell happened, but we are hamstrung by the data available," says Edward Holmes, a virologist at the University of Sydney in Australia and a co-author of two of the latest preprints^{2,3}.

Some Chinese scientists say that they, too, would like to see more origin studies, but that the topic [is politically sensitive](#). In March 2020, [a directive](#) from the Chinese government — [highlighted by the Associated Press](#) — instructed researchers at universities, companies and medical institutions to have all studies on COVID-19 vetted by government research units and then published under the direction of public opinion teams. Those who don't follow procedures, the document warned, "shall be held accountable".

Investigations of an outbreak's origins usually take many years to reach a conclusion, if one is ever reached. But the scientific community fears that political barriers are holding this one up — and they're unsure of the best way to expedite matters. Van Kerkhove says that SAGO will continue to outline the most pertinent studies needed, and to offer help with analyses. Until these happen, she warns that gaps in knowledge will allow damaging and scientifically unsupported theories to flourish. "If we don't get the information we need," Van Kerkhove says, "then there's a space to fill, and people will fill that space with assumptions."

In a recent example, pundits and officials in the [United States](#) and [China](#) have linked unsupported allegations about COVID-19's origins to conspiracy theories about Ukrainian 'biolabs', says Yanzhong Huang, a specialist on China and global health at the Council on Foreign Relations in New York City. "All of these accusations poison the water and make an earnest search for answers to the origin of the pandemic even harder."

A focus on farms

Chinese authorities closed the Huanan market on 1 January 2020, after physicians in China reported that many of the people they were treating for a mysterious form of pneumonia had worked there or visited it soon before falling ill. Researchers in China leapt to investigate. On 22 January 2020, the Chinese Center for Disease Control and Prevention (CDC) reported that 33 of 585 swabs taken from around the market tested positive for SARS-CoV-2, and that these samples were concentrated in two aisles of stalls where wild animals were sold. "It is highly suspected that the current epidemic is related to the trade of wild animals," the report said.



In early 2021, an international research team visited the Huanan Seafood Wholesale Market in Wuhan, as part of an investigation into COVID-19's origins. Credit: Kyodo News via Getty

Investigators also collected samples from stray cats, mice and slabs of frozen and refrigerated seafood and meat, all of which tested negative for the virus. They continued to collect specimens for the next couple of months, but none seem to have been from wildlife sold at the Huanan market, or from farms that reared wildlife to be sold there for food, medicine or fur.

When an international team of researchers assembled by the WHO and the Chinese government set out to study the pandemic's origins in China in late January 2021, they asked about wildlife farms supplying Wuhan's markets. Chinese researchers handed the team a list of farms that included several in southern China. This is a region where a close relative of SARS-CoV-2 has

been found in bats⁴, notes Peter Daszak, one of the researchers on the team and president of EcoHealth Alliance, a scientific organization in New York City that has collaborated on coronavirus research with the Wuhan Institute of Virology. But the team didn't visit the farms, and Daszak was told that they hadn't been studied because the farms were shuttered following a ban on the consumption of wild animals in February 2020.

What's more, he says, when the team drafted a report on its investigation, some Chinese researchers and officials with China's foreign ministry wanted to change parts of it that discussed the sale of wild animals at the Huanan market. "We went into a room at 9:30 a.m. to talk about their changes — the rule was that any unpublished evidence had to be agreed upon," he says. "We were there until 4:30 a.m., arguing for almost 24 hours. Some people were sleeping, some had gone home."

The [final WHO report](#), posted in March 2021, was ambiguous over details on animals at the market — a departure from the clarity of the January 2020 notice from the Chinese CDC. The report said that "no illegal trade in wildlife has been found", and "no verified reports of live mammals being sold around 2019 were found". But it also referenced photographs of raccoon dogs and other live animals for sale at the Huanan market in 2014, which Holmes had submitted to the WHO team.

A few months after the report's release, conservation biologists in China published a paper in *Scientific Reports*⁵ documenting more than 47,000 animals — including 31 protected species — that had been sold at the Huanan market and others in Wuhan as recently as November 2019. The report noted that almost all of the animals were sold alive in cages, that butchering was usually done at the market, and that many of the traded species are known to host a range of infectious diseases. "I'm very disappointed that the [WHO] group didn't have access to that kind of information," Van Kerkhove says.

Seeking more details, the WHO report called for studies of wildlife farms. And it recommended that blood donations collected from people between September and December 2019, and stored at the Wuhan Blood Centre, should be analysed for antibodies against SARS-CoV-2. At [a press briefing in August 2021](#), Zeng Yixin, vice-minister of the National Health

Commission in Beijing, pledged to complete the studies outlined in the WHO report. At the same time, he fiercely rejected requests by the WHO director-general to further investigate the hypothesis that SARS-CoV-2 was released from the Wuhan Institute of Virology.

More than a year since the WHO's recommendations, studies from wildlife farms, the Wuhan Blood Centre and Wuhan laboratories have yet to materialize. Chinese researchers involved in the WHO investigation, as well as others at the Chinese CDC, did not respond to queries from *Nature* about the status of the studies and why they are slow to emerge.

Attitude shift

Ray Yip, an epidemiologist and former director of the Beijing branch of the US Centers for Disease Control and Prevention, says that China's approach to COVID-19 origin investigations shifted as anti-Chinese rhetoric mounted over the course of the pandemic. At first, there was former US president Donald Trump's insistence on using anti-Asian terms for the coronavirus. "I think there was a shift in China's attitude when they began to feel they were being humiliated or blamed for this pandemic, even though every new disease has to start somewhere," Yip says.

Then came the unsubstantiated allegations that COVID-19 was made in a Chinese lab. Former US secretary of state Mike Pompeo [said on Fox News](#) that "a pile of evidence a hundred feet high" supported that claim. But no strong evidence for an accidental or intentional leak of SARS-CoV-2 has been put forward, and [an investigation by US intelligence agencies](#) conducted last year found that SARS-CoV-2 was unlikely to have been genetically engineered. The lack of evidence hasn't curbed accusations, however. As a backlash, Yip says, China's foreign ministry has [promoted a baseless rumour](#) that the virus came from a US military laboratory.

This sort of defensiveness isn't limited to the lab-leak hypotheses, Huang says. He speculates that because tensions between China and the United States have grown, the Chinese government wants to avoid publicizing any data that might cause world leaders to blame China for the pandemic. And he suggests that China's government might be particularly sensitive about

the wildlife trade, which has been of significant cultural and economic value. Although China banned the trade and consumption of terrestrial wildlife in 2020, he and other researchers say that enforcement is difficult and demand remains high. According to a [Chinese Academy of Engineering report](#), the legal wildlife industry in China [was worth more than US\\$78 billion in 2016](#).

Nonetheless, Yip suggests that researchers in China might be quietly continuing to study COVID-19's origins, releasing reports only once they've gone through a lengthy review. For example, on 25 February, researchers at the Chinese CDC posted a preprint analysing the genetic sequences of samples that had tested positive for SARS-CoV-2 at the Huanan market two years earlier¹. But to the dismay of many virologists, the team didn't publish the sequences underlying the study.

Requests for data

Youngmee Jee, an infectious-diseases researcher and chief executive at the Pasteur Institute in South Korea, disagrees with those who say that China is withholding data on COVID-19's origins. She says that origin investigations usually take many years, and points out that Chinese researchers have already conducted a number of relevant studies. For example, a report published in *Cell* in February surveyed game animals across China for viral infections, and found 21 viruses that could be dangerous to humans — although none was SARS-CoV-2⁶.



The reservoir for the coronavirus SARS-CoV-2 might be revealed by sampling mammals in Southeast Asia, given that researchers found the closest-known relative of the virus in bats in Laos. Credit: Imagebroker/Shutterstock

In an e-mail to *Nature*, Shuo Su, a virologist at Nanjing Agricultural University in China, and a co-author of the *Cell* report, stresses that the study is not connected to COVID-19's origins. Another co-author of the report, Mang Shi, an evolutionary biologist at Sun Yat-sen University in Shenzhen, reiterates Su's point. He recommends that future origin investigations should survey bats and other mammals in Laos — where researchers [identified the closest-known relative](#) to SARS-CoV-2 in bats, a virus named BANAL-52 — as well as in the neighbouring province of Yunnan in southern China. “We should keep looking at animals in that area of Southeast Asia,” he says. “The exact country isn’t important.”

Shi adds that he would like to see the origin investigations move forwards — with science, not politics, leading the way. “I hope everything can be fair, and without so much finger-pointing and blaming,” he says.

Seeking to encourage the release of data, virologists outside China have sent e-mails to George Gao, the head of the Chinese CDC, and his colleagues, trying to convince them of the importance of sharing genetic sequences that could answer questions about the human or animal hosts of coronaviruses found at the Huanan market in early 2020. Taking a different tack, Jesse Bloom, a virologist at the Fred Hutchinson Cancer Research Center in Seattle, Washington, has collected signatures from scientists on a letter requesting such data. Bloom says he'll make his letter public if Chinese researchers don't comply with an initial private request.

As for the WHO, Van Kerkhove says that she is in contact with Gao, and that SAGO will continue to voice its recommendations for further studies, and to offer Chinese researchers help with data collection and analysis. In addition, the upcoming SAGO report will outline the types of origin studies that countries should conduct as soon as they're faced with new outbreaks of dangerous viruses.

Whatever the strategy, Huang fears that the COVID-19 origins probe is at an impasse. "Without cooperation from China," he says, "there isn't much that anyone can do."

Nature **603**, 773-775 (2022)

doi: <https://doi.org/10.1038/d41586-022-00732-0>

References

1. Gao, G. *et al.* Preprint at Research Square
<https://doi.org/10.21203/rs.3.rs-1370392/v1> (2022).
2. Worobey, M. *et al.* Preprint at Zenodo
<https://doi.org/10.5281/zenodo.6299600> (2022).
3. Pekar, J. E. *et al.* Preprint at Zenodo
<https://doi.org/10.5281/zenodo.6291628> (2022).
4. Zhou, P. *et al.* *Nature* **579**, 270–273 (2020).

5. Xiao, X., Newman, C., Buesching, C. D., Macdonald, D. W. & Zhou, Z.-M. *Sci. Rep.* **11**, 11898 (2021).
6. He, W.-T. *et al.* *Cell* <https://doi.org/10.1016/j.cell.2022.02.014> (2022).

This article was downloaded by **calibre** from <https://www.nature.com/articles/d41586-022-00732-0>

| [Section menu](#) | [Main menu](#) |

- NEWS EXPLAINER
- 17 March 2022
- Correction [18 March 2022](#)

Where is Russia's cyberwar? Researchers decipher its strategy

Many analysts expected an unprecedented level of cyberattacks when Russia invaded Ukraine — which so far haven't materialized.

- [Elizabeth Gibney](#)



Residents of Kyiv watch news on a laptop in a car park that is being used as a bombshelter.Credit: Chris McGrath/Getty

When [Russia invaded Ukraine last month](#), many security analysts were expecting a level of cyberwar never seen before, because of Russia's history of such aggression.

There has been low-level activity. Cyberattacks were under way in Ukraine even before Russian forces invaded on 24 February. Hours prior, a type of malware called a wiper circulated on Ukrainian government computing systems, corrupting data. Earlier that week, a massive distributed denial of service (DDoS) attack, widely attributed to Russia, had flooded Ukrainian bank websites with traffic, making them inaccessible.

Such assaults were unsurprising; Ukraine has faced a barrage of cyberattacks since conflict flared with Russia in 2014. But despite the slew of low-level cyberattacks, Ukraine's critical infrastructures — such as telephone, Internet, power and health-care systems — remain intact.

Nature spoke to researchers about the role of cyberwarfare in the conflict, and why it is surprising them.

Why did analysts expect cyberwarfare to play a significant part in Russia's invasion of Ukraine?

Russia has deployed cyberattacks in its most recent conflicts, including its invasions of Georgia in 2008 and Crimea in 2014. Since then, Ukraine has become a “training ground” for Russian cyberoperations, says Lauren Zabierek, a specialist in cybersecurity in international conflict at the Harvard Kennedy School in Cambridge, Massachusetts. In 2015 and 2016, Russia-attributed strikes disabled Ukraine’s power for hours, she says.

Russia has the capability to use cyberwarfare to disrupt enemy communications, organization and supplies, leading many to expect that it would deploy such tactics in this war, says Trey Herr, a cybersecurity-policy researcher at the Atlantic Council, a think-tank in Washington DC.

So why hasn't Russia used cyberwarfare, as expected?

One theory is that the decision to invade Ukraine was held at the highest level and didn’t trickle down the chain of command until it became too late to deploy significant cyberattacks, which can take months to organize, says Herr.

Cyberattacks might also be more suitable to skirmishes that fall short of physical war. Cyberweapons are cheaper than boots on the ground, but are still costly, says Mariarosaria Taddeo, a philosopher on the ethics of digital technologies at the Oxford Internet Institute, UK. Cyberattacks are a show of power, inflict damage without engaging in a conventional war and are difficult to attribute with certainty — but these advantages lose relevance once all-out war begins, she says.

If Russia thought it would take Ukraine quickly, preserving parts of Ukraine’s infrastructure, rather than destroying and having to rebuild them, might serve its interests, says Zhanna Malekos Smith, a systems engineer at the Center for Strategic and International Studies, a think-tank in

Washington DC. Russia could also have tapped into some networks, such as Ukraine's telecommunications system, as a source of intelligence, she adds.

Zabierek's leading hypothesis is that Russia is holding back to avoid escalation or spillover effects beyond Ukraine, which could prompt a response from the West. Cyberattacks can easily spread. In 2017, Russia-linked hackers launched NotPetya, malware targeting financial software used by businesses in Ukraine. But the malware's use of a common vulnerability allowed it to spread worldwide, destroying access to almost all records at companies such as the Danish shipping giant Maersk — and causing an estimated US\$10 billion in damages globally.

And on 24 February, an attack on the European satellite operator Viasat disrupted Internet access in Ukraine and disabled thousands of German wind turbines that used Viasat to communicate.



The city of Mariupol has experienced some of the most intense bombing in the war so far.Credit: Christopher Occhicone/Bloomberg via Getty

Could the cyberwar escalate?

Russia might be keeping its more aggressive cyberweapons in reserve, says Malekos Smith. If the ground war stalls and financial sanctions bite, Russia could increase cyberattacks, she says. It could ramp up its assault on Ukraine and target Western nations to inflict on them the same kind of chaos wrought by sanctions, for example by targeting companies and financial markets, she says.

Health-care systems and power networks could be vulnerable. In 2021, non-state hackers, possibly in Russia, used ransomware to shut down the US Colonial oil pipeline for days. “This is the kind of thing we can expect — an attack that’s enough to cripple infrastructure for a while and create disruption,” says Taddeo. On 12 February, before the invasion, the US Cyber Security and Infrastructure Agency warned organizations to prepare for cyber-attack.

How likely is that to happen?

Non-state actors who have joined both sides of the cyberconflict could trigger escalation. A Russian hacker group called Conti said it would retaliate against cyberthreats on the Russian government. Meanwhile, the international hacker collective Anonymous and an ‘IT army’ of civilians are pursuing Russian targets. And a pro-Ukrainian group calling itself the Belarusian Cyber-Partisans claimed to have hacked the train system in Belarus — which has supported Russia’s war — to prevent its government from moving Russian troops. However, that claim hasn’t been rigorously verified.

Many of these attacks include defacing or taking down Russian government websites — low-hanging fruit in the cyberworld. But they increase the chance that the cyberwar could escalate, says Taddeo. “Targeting the wrong item or doing an out-of-proportion of operation can be problematic and create extra friction,” she says. Herr agrees: vigilante groups might not calculate knock-on effects, and their actions could draw retaliation.

Meanwhile, an unforeseen effect of the West cutting energy, aviation and financial ties with Russia, is that the country might become more prepared to take risks because it would face fewer impacts of any resulting chaos, says Herr. “The downside for them of causing significant disruptive harm goes down,” he says.

What's the worst-case scenario?

So far, many analysts consider cyberattacks espionage or sabotage, rather than acts of war. Although Russia might want to cause damage to mirror the effects of sanctions, it is unlikely to cross the line that would provoke states' right to self-defence, says Malekos Smith. This could be any action that causes human casualties or massive physical destruction, for example by targeting a dam or nuclear power plant. “We haven’t seen it yet, and I hope we won’t see it,” says Taddeo.

If physical damage occurred, countries such as the United States have declared that they could respond with every means possible. The National Cyber Power Index by the Belfer Center, where Zabierek works, ranks Russia’s cybercapabilities below those of the United States, China and the United Kingdom. A cyberoperation could trigger Article 5 of the North Atlantic Trade Organization treaty, which states that an attack on one member nation is considered an attack on them all. If that happened, Russia would be outmatched on all fronts, says Zabierek.

Nature **603**, 775-776 (2022)

doi: <https://doi.org/10.1038/d41586-022-00753-9>

Updates & Corrections

- **Correction 18 March 2022:** Zhanna Malekos Smith's name was incorrectly spelled in an earlier version of this article.

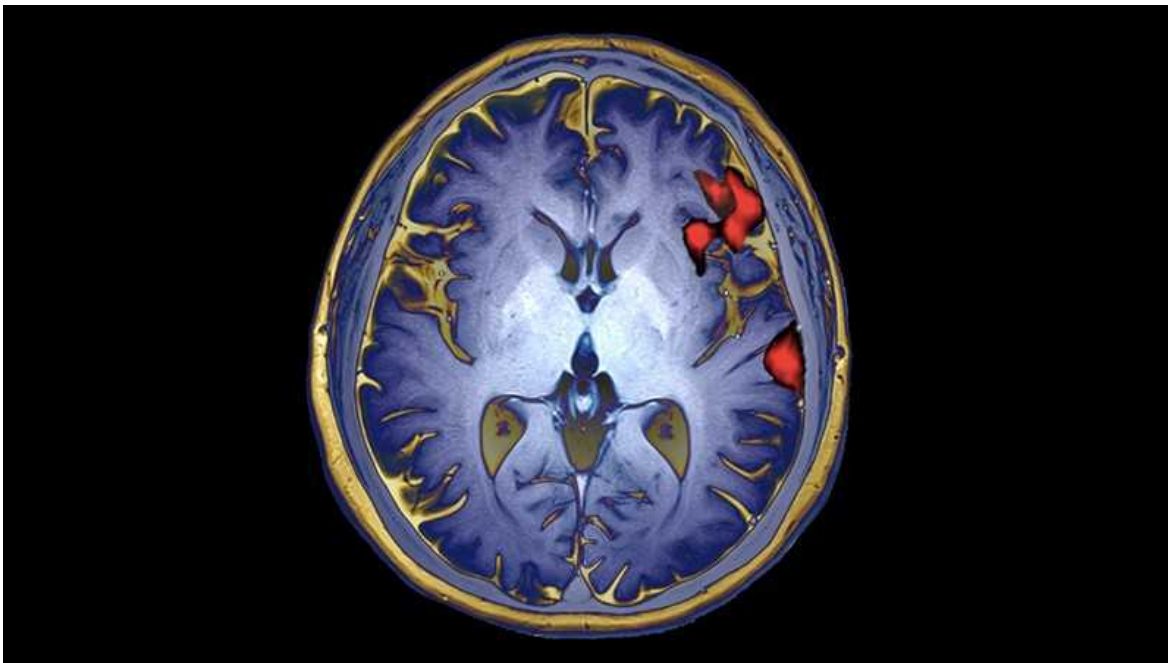
| [Section menu](#) | [Main menu](#) |

- NEWS
- 17 March 2022

Can brain scans reveal behaviour? Bombshell study says not yet

Most studies linking features in brain imaging to traits such as cognitive abilities are too small to be reliable, argues a controversial analysis.

- [Ewen Callaway](#)



A scan using functional magnetic resonance imaging, or fMRI, shows areas of the brain active during speech. Credit: Zephyr/Science Photo Library

In 2019, neuroscientist Scott Marek was asked to contribute [a paper](#) to a journal that focuses on child development. Previous studies had shown that differences in brain function between children were linked with performance in intelligence tests. So Marek decided to examine this trend in 2,000 kids.

Brain-imaging data sets had been swelling in size. To show that this growth was making studies more reliable, Marek, based at Washington University in St. Louis, Missouri (WashU), and his colleagues split the data in two and ran the same analysis on each subset, expecting the results to match. Instead, they found the opposite. “I was shocked. I thought it was going to look exactly the same in both sets,” says Marek. “I stared out of my apartment window in depression, taking in what it meant for the field.”

Now, in a bombshell 16 March *Nature* study¹, Marek and his colleagues show that even large brain-imaging studies, such as his, are still too small to reliably detect most links between brain function and behaviour.

As a result, the conclusions of most published ‘brain-wide association studies’ — typically involving dozens to hundreds of participants — might be wrong. Such studies link variations in brain structure and activity to differences in cognitive ability, mental health and other behavioural traits. For instance, numerous studies have identified brain anatomy or activity patterns that, the studies say, can distinguish people who have been diagnosed with depression from those who have not. Studies also often seek biomarkers for behavioural traits.

“There’s a lot of investigators who have committed their careers to doing the kind of science that this paper says is basically junk,” says Russell Poldrack, a cognitive neuroscientist at Stanford University in California, who was one of the paper’s peer reviewers. “It really forces a rethink.”

The authors emphasize that their critique applies only to the subset of research that seeks to explain differences in people’s behaviour through brain imaging. But some scientists think that the critique tars this field with too broad a brush. Smaller, more detailed studies of brain-behaviour links can produce robust findings, they say.

Weak correlations

After his botched replication, Marek set out to understand the reasons for the failure together with Nico Dosenbach, a neuroscientist at WashU, and their colleagues. That work resulted in the latest study, in which they analysed

magnetic resonance imaging (MRI) brain scans and behavioural data from 50,000 participants in several large brain-imaging efforts, such as the UK Biobank's collection of brain scans.

Some of these scans gauged aspects of brain structure, for instance the size of a particular region. Others used a method called functional MRI (fMRI) — the measurement of brain activity while people do a task, such as memory recall, or while at rest — to reveal how brain regions communicate.

The researchers then used subsets drawn from these large databases to simulate billions of smaller studies. These analyses looked for associations between MRI scans and various cognitive, behavioural and demographic traits, in samples ranging from 25 people to more than 32,000.

In simulated studies involving thousands of people, the researchers identified reliable correlations between brain structure and activity in particular regions and different behavioural traits — associations that they could replicate in different subsets of the data. However, these links tended to be much weaker than those typically reported by most other studies.

Researchers measure correlation strength using a metric called r , for which a value of 1 means a perfect correlation and 0 none at all. The strongest reliable correlations Marek and Dosenbach's team found had an r of 0.16, and the median was 0.01. In published studies, r values above 0.2 are not uncommon.

To understand this disconnect, the researchers simulated smaller studies and found that these identified much stronger associations, with high r values, but also that these findings did not replicate in other samples, large or small. Even associations identified in a study of 2,000 participants — large by current standards — had only a 25% chance of being replicated. More typical studies, with 500 or fewer participants, produced reliable associations around just 5% of the time.

Even larger studies

The study did not attempt to replicate other published brain-wide association studies. But it suggests that high r values common in the literature are

almost certainly a fluke, and not likely to be replicated. Factors that hinder reproducibility in other fields, such as the tendency to publish only statistically significant results with large effect sizes, means that these spurious brain-behaviour associations fill the literature, says Dosenbach. “People are only publishing things that have a strong enough effect size. You can find those, but those are the ones that are most wrong.”

To make such studies more reliable, brain-imaging studies need to get much bigger, Marek, Dosenbach and their colleagues argue. They point out that genetics research was plagued by false positives until researchers, and their funders, started looking for associations in very large numbers of people. The largest genome-wide association studies (GWAS) now involve millions of participants. The team coined the term brain-wide association study, or BWAS, to draw parallels with genetics.

For brain imaging, Marek says, “I don’t know if we need hundreds of thousands or millions. But thousands is a safe bet.”

“What the Marek paper suggests is that a lot of the time, if you don’t have these really large samples, you are most likely wrong or lucky in finding a good brain-behaviour correlation,” says Caterina Gratton, a cognitive neuroscientist at Northwestern University in Evanston, Illinois. The paper appeared as a preprint in 2020, and Gratton says she has sat on grant-review panels that have cited it when raising scepticism over relatively small BWAS studies. “This is an important paper for the field,” she adds.

But some researchers argue that smaller BWAS studies still have value. Peter Bandettini, a neuroscientist at the National Institute of Mental Health in Bethesda, Maryland, says that studies such as the ones Marek’s team simulated looked for correlations between crude measurements of behaviour or mental health (self-reported surveys, for example) and brain scans whose conditions might vary from participant to participant, diluting bona fide associations.

By selecting participants carefully and analysing brain-imaging data using sophisticated approaches, it might be possible to find associations between brain scans and behaviour that are stronger than those identified in the study, says Stephen Smith, a neuroscientist at the University of Oxford, UK who

leads the UK Biobank's brain imaging efforts. "I fear this paper may be overestimating unreliability."

Nature **603**, 777-778 (2022)

doi: <https://doi.org/10.1038/d41586-022-00767-3>

References

1. Marek, S. *et al.* *Nature* <https://doi.org/10.1038/s41586-022-04492-9> (2022).

This article was downloaded by **calibre** from <https://www.nature.com/articles/d41586-022-00767-3>

| [Section menu](#) | [Main menu](#) |

- NEWS
- 23 March 2022

Morgue data hint at COVID's true toll in Africa

Around 90% of deceased people tested at a Lusaka facility during coronavirus surges were positive for SARS-CoV-2 infection, suggesting flaws in the idea of an ‘African paradox’.

- [Freda Kreier](#)



A health-care worker in Lusaka is vaccinated against COVID-19.Credit: Xinhua/Shutterstock

Almost one-third of more than 1,000 bodies taken to a morgue in Lusaka in 2020 and 2021 tested positive for SARS-CoV-2, implying that many more people died of COVID-19 in Zambia's capital than official numbers suggest¹. Some scientists say that the findings further undermine the 'African paradox', a narrative that the pandemic was less severe in Africa than in other parts of the world.

This idea arose after health experts noticed that sub-Saharan nations were reporting [lower case numbers and fewer COVID-19 deaths than might be expected](#). But researchers say that the findings from Zambia could reflect a broader truth — that a deficit of testing and strained medical infrastructure have masked COVID-19's true toll on the continent. The findings have not yet been peer reviewed.

Ignoring the true extent of COVID-19 in Lusaka and beyond "is so wrong. People were ill. They've had their families destroyed," says co-author Christopher Gill, a global-health specialist at Boston University in Massachusetts. One of his colleagues in Zambia died of COVID-19 while working on the project.

"It's not hypothetical to me," says Gill.

Missing COVID cases

When SARS-CoV-2 began spreading globally, many health researchers worried that the virus would devastate sub-Saharan Africa. But the surprisingly low numbers of reported COVID-19 cases in the region led to the perception "that severe debilitation and deaths caused by COVID-19 were somehow less in Africa compared to other continents", says Yakubu Lawal, an endocrinologist at the Federal Medical Centre Azare in Nigeria.

Lawal and other scientists speculated² that the relative youth of Africa's population might have helped to spare the continent, but also suspected that official numbers were under-reported. The question was by how much.

Seeking answers, Gill and his colleagues in Zambia tested bodies in one of Lusaka's largest morgues for SARS-CoV-2 over several months in 2020 and

2021. Test positivity was 32% overall — and reached around 90% during the peak of the waves caused by the [Beta](#) and [Delta](#) variants. Moreover, only 10% of the people whose bodies were found to contain the virus after death had tested positive while still alive. Some had falsely tested negative, but most had never been tested at all.

Although Gill and his colleagues can't confirm that all of these people died of COVID-19, the results still stand in sharp contrast to official numbers. So far, there have been fewer than 4,000 confirmed COVID-19 deaths in Zambia, a country of around 19 million people. Separate findings published on 10 March suggest that Zambia's '[excess' deaths](#)' — those above what would usually be expected — from 1 January 2020 to the end of 2021 exceeded 80,000³.

The Lusaka numbers mesh with statistics from South Africa, where a 2021 study found that only 4–6% of SARS-CoV-2 infections in two communities were officially documented⁴. Further study of the same communities showed that 62% of study participants had been infected at least once from July 2020 to August 2021⁵. Co-author Cheryl Cohen, an epidemiologist at the University of the Witwatersrand in Johannesburg, South Africa, says that many of these infections were [asymptomatic](#), but that people with symptoms might also have gone undetected because of the cost and difficulty of getting tested.

Gill suspects that a major reason for the gap between his results and official counts is that most people in Zambia who die of COVID-19 do so outside medical care. Four out of five people tested in the study were never admitted to a hospital; the majority of unreported infections were in people living in Lusaka's lowest-income neighbourhoods.

“Nobody’s vaccinated. Nobody has masks. Nobody has access to the medical care they need,” says Gill. “We’re in a population that is already stressed and unhealthy, and then — bam! In comes COVID.”

Vast variation

But not everyone is convinced that the Lusaka findings invalidate the idea of the African paradox. In Ethiopia, for instance, “our experience is people get infected with the virus, are asymptomatic or have mild symptoms, and recover”, says Amare Abera Tareke, a physiologist at Wollo University in Dessie. “While it is difficult to ignore the current finding, we have to take it cautiously.”

Gill worries that the idea that Africa was spared the worst of the pandemic might have led people to take unnecessary risks or contributed to “the lack of urgency” in supplying African nations with vaccines.

“I suppose this could be unique to Lusaka,” he says, “But boy, you’d really have to try hard to explain why.”

Nature **603**, 778–779 (2022)

doi: <https://doi.org/10.1038/d41586-022-00842-9>

References

1. Gill, C. J. *et al.* Preprint at medRxiv
<https://doi.org/10.1101/2022.03.08.22272087> (2022).
2. Lawal, Y. *Int. J. Infect. Dis.* **102**, 118–122 (2021).
3. COVID-19 Excess Mortality Collaborators. *Lancet*
[https://doi.org/10.1016/S0140-6736\(21\)02796-3](https://doi.org/10.1016/S0140-6736(21)02796-3) (2022).
4. Kleynhans, J. *et al.* *Emerg. Infect. Dis.* **27**, 3020–3029 (2021).
5. Cohen, C. *et al.* *Lancet Infect. Dis.* [https://doi.org/10.1016/S1473-3099\(22\)00069-X](https://doi.org/10.1016/S1473-3099(22)00069-X) (2022).

This article was downloaded by **calibre** from <https://www.nature.com/articles/d41586-022-00842-9>

- NEWS
- 16 March 2022
- Correction [17 March 2022](#)

Are ‘COVID toes’ actually caused by the coronavirus?

Study adds to evidence suggesting that SARS-CoV-2 infection doesn’t cause an inflamed-toe condition called chilblains, but it doesn’t close the door.

- [Cassandra Willyard](#)



Researchers are debating whether ‘COVID toes’ are triggered by an infection with the coronavirus SARS-CoV-2. Credit: Cordelia Molloy/Science Photo Library

In March 2020, just as COVID-19 cases began to surge in Boston, Massachusetts, Esther Freeman noticed something peculiar — a deluge of

people with discoloured toes requesting appointments. Freeman, director of global health dermatology at Massachusetts General Hospital, had seen these kinds of toes before. The itchy red and purple patches are a classic sign of chilblains, a skin condition that typically appears in cold weather. But usually, she would see one or two cases each winter. “Suddenly, I was seeing 15, 20 patients a day,” she says. Intriguingly, the surge — seen by physicians around the globe — seemed to coincide with the rise of the COVID-19 pandemic.

Yet, when physicians examined people with what the media began calling ‘COVID toes’, most didn’t test positive for a coronavirus SARS-CoV-2 infection. Scientists were stumped, and have been looking for answers ever since.

The latest study, published on 25 February¹, is an immunological deep dive, examining 21 people who developed chilblains during the early months of the pandemic in Connecticut. Although the results don’t rule out a direct connection between COVID-19 and chilblains, the authors couldn’t find any immunological evidence of a past SARS-CoV-2 infection in 19 of those people. The report adds to the argument by some researchers that ‘COVID toe’ could have been caused by something unrelated to the virus. For instance, it might have arisen from people in lockdown “being at home, not wearing shoes and socks”, says Jeff Gehlhausen, a dermatologist and immunologist at Yale School of Medicine in New Haven, Connecticut, and first author of the study.

Still, the results raise “some very interesting questions that deserve further study”, says Freeman, who was not involved in the research. For instance, the study doesn’t exclude the possibility that people exposed to the virus could have fought it off using an innate immune response — a first-line defence that would not prompt the body to produce detectable antibodies and T cells against SARS-CoV-2. So for now, she adds, the mystery remains.

Toe talk

How chilblains arise isn't entirely clear. "We think of it as a cold-weather-related injury," says Patrick McCleskey, a dermatologist and researcher at Kaiser Permanente in Oakland, California. "We always see some amount of chilblains in the winter, and then it goes down in the summer." Researchers think that the cold probably leads to a restriction in blood flow, causing some cells to die and kicking off an inflammatory process. The purple or red patches that appear on toes (and sometimes fingers, ears or noses) can be itchy, tender or, in some cases, downright painful.

Most of the people in the latest study developed 'COVID toes' between April and May 2020, when COVID-19 cases surged in Connecticut. About one-third reported having some symptoms of COVID-19 before developing the condition, and one-third reported that they had been in contact with a person confirmed or suspected to have been infected with SARS-CoV-2.

The researchers used a variety of methods to look for antibodies and T cells specific for the coronavirus — signs of the body having what's called an adaptive immune response to a pathogen. These people were months past the onset of their chilblains, so their immune systems would have had plenty of time to respond to SARS-CoV-2 if they had been infected. But the team picked up signs of a past infection only in two people, one of whom had initially tested positive.

Many groups have tested people with chilblains for SARS-CoV-2 antibodies, but "nobody had looked really into this hypothesis about the T-cell response", Freeman says. "The team did a fantastic, really extraordinary job." But she emphasizes that the study is small — and therefore not necessarily generalizable — and that much larger epidemiological studies^{2,3} have shown a connection between chilblains and SARS-CoV-2.

Dermatologist Thierry Passeron, at Côte d'Azur University in Nice, France, still thinks COVID toes are triggered by the virus. His team found⁴ that people who developed chilblains during the pandemic showed evidence of a strong innate immune response. The researchers posit that many people with pandemic chilblains clear the virus in this way, so "very few develop antibodies", he says.

Unsolved mystery

Previous studies^{5,6} have examined whether people with chilblains had been infected with SARS-CoV-2 by taking tissue biopsies and staining the samples with a dye that identifies parts of the virus. Gehlhausen and colleagues tried the stain and found that it stuck to some of their tissue samples. But they also tested the stain on random tissue samples collected before the pandemic, when the virus was not in circulation, and found that it also marked some of those. “Our study suggests that there may be a lack of specificity in that staining,” Gehlhausen says.

With the link between COVID-19 and chilblains still in question, some researchers point to the lockdown theory — that people spent more time at home barefoot early in the pandemic and got cold feet, literally. Or perhaps all the media coverage of COVID toes led to more people than usual seeking medical attention for the problem.

For Freeman, “the case is not yet closed.” On one hand, she has seen patients who developed chilblains, justifiably, after walking in flip flops during a snowstorm. On the other hand, she has seen people who test positive for SARS-CoV-2 and then develop chilblains with no other obvious explanation.

The debate has become strangely polarizing, Gehlhausen says. But the hypotheses are not mutually exclusive. “It’s possible that all these things are true,” he says. “I am not on any team.”

It’s also possible the problem might be fading. “We’re still seeing patients with new chilblains, but it seems to be kind of back to the old background rate,” says Yale dermatologist William Damsky, an author on the paper.

In the end, the issue makes for an intriguing scientific debate, but the answer isn’t likely to alter how dermatologists treat patients, McCleskey says. Irrespective of whether a person had COVID-19, chilblains generally go away on their own in two or three weeks.

“Honestly, I think maybe we can chill out about chilblains,” he says.

Nature **603**, 779 (2022)

doi: <https://doi.org/10.1038/d41586-022-00707-1>

Updates & Corrections

- **Correction 17 March 2022:** An earlier version of this story showed an image of the foot of a person with severe COVID-19. However, this person did not have chilblains, they had a different condition affecting their toes.

References

1. Gehlhausen, J. R. *et al.* *Proc. Natl. Acad. Sci. USA* **119**, e2122090119 (2022).
2. Mascitti, H. *et al.* *Eur. J. Clin. Microbiol. Infect. Dis.* **40**, 2243–2248 (2021).
3. Visconti, A. *et al.* *Br. J. Dermatol.* **184**, 880–887 (2021).
4. Hubiche, T. *et al.* *JAMA Dermatol.* **157**, 202–206 (2021).
5. Ko, C. J. *et al.* *J. Cutan. Pathol.* **48**, 47–52 (2021).
6. Colmenero, I. *et al.* *Br. J. Dermatol.* **183**, 729–737 (2020).

This article was downloaded by **calibre** from <https://www.nature.com/articles/d41586-022-00707-1>

- NEWS FEATURE
- 29 March 2022

The race to upcycle CO₂ into fuels, concrete and more

Companies are scrambling to turn the greenhouse gas into useful products — but will that slow climate change?

- [Mark Peplow](#) ✉



Part of a chemical plant in Tongyezhen, China, that will recycle about 160,000 tonnes of CO₂ into fuel each year. Credit: Carbon Recycling International

Tongyezhen is a town with coal in its bones. In this part of China's Henan province, people have been mining coal and smelting metals for millennia. Today, Tongyezhen hosts a sprawling industrial park where huge ovens bake coal and limestone into coke and lime, both key ingredients for producing steel. Unsurprisingly, it is one of the smoggiest places in China.

It might seem an unlikely venue for a clean-technology milestone. But later this year, a chemical plant here is set to become the world's largest facility for recycling carbon dioxide into fuel. It will combine CO₂ from a lime kiln with excess hydrogen and CO₂ from a coking furnace to produce methanol, an industrial chemical used for fuel and to make plastics. Carbon Recycling International (CRI), the Reykjavik-based firm behind the operation, says that the Tongyezhen plant will recycle about 160,000 tonnes of CO₂ per year — equivalent to the emissions from tens of thousands of cars — that would otherwise go into the atmosphere.

It's an alluring idea: [industrial CO₂ emissions are warming the climate](#), and many countries are working on capturing the gas and storing it underground. But why not recycle it into products that are both virtuous and profitable? As long as the recycling process avoids creating more carbon emissions — by using renewable energy, or excess resources that would otherwise be wasted — it can reduce the CO₂ that industry pumps into the atmosphere and lower the demand for fossil fuels used in manufacturing. That's a double climate win, proponents say.

This kind of recycling (sometimes called upcycling) is an increasingly crowded field, as companies big and small race to market a bewildering array of products made from CO₂. Some are boutique items for the climate-conscious shopper — vodka or diamonds, for example — but most are staples of the global economy: fuels, polymers, other chemicals and building materials. More than 80 firms are working on new approaches to using CO₂, [noted a 2021 report by Lux Research](#), a market-research company in Boston, Massachusetts. The market for these products is tiny today, amounting to less than US\$1 billion — but Lux predicts that it will grow to \$70 billion by 2030, and could reach \$550 billion by 2040.

This activity is being driven by a fall in the cost of renewable energy, along with rising carbon taxes and other climate incentives that are persuading firms to avoid CO₂ emissions. At the same time, chemists have improved the efficiency of the underlying technologies.

But there are tough questions about whether CO₂ recycling genuinely benefits the climate. Many of the products made this way only briefly delay carbon's journey into the atmosphere — fuels are burnt, products made from chemicals degrade and the CO₂ consumed during their creation is released again. That will happen at Tongyezhen: much of the methanol produced is destined to be burnt as fuel in China's growing fleet of methanol-powered vehicles.

Meanwhile, some estimates suggest that the global market for recycled CO₂ products is unlikely to lock up more than a few per cent of the CO₂ that humans release into the atmosphere by burning fossil fuels, which totalled

36 billion tonnes last year. CRI's plant, for one, will convert the equivalent of a little over 2 minutes' worth of annual global CO₂ emissions. "We can avoid a lot of that, for a lot less money, than we can by turning CO₂ into stuff," says Niall Mac Dowell, an energy-systems engineer at Imperial College London.

"The assumption that we can fix this climate-change problem in an economically attractive and easy way — at best it's naive, and at worst it's actively disingenuous," he says. It's an argument that's heating up as CO₂ recycling goes mainstream.

Premium product

Using CO₂ as a chemical ingredient isn't a new idea. Roughly 200 million tonnes of CO₂ are used in a handful of processes each year, most of it reacted with ammonia to make urea for fertilizers. (Producing ammonia emits extra CO₂, and urea's carbon is quickly released after it is spread on a field, so there are no climate benefits.) The petroleum industry also injects CO₂ underground to help recover oil, but using that oil can generate more gas than is stored.

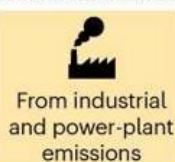
What's changing now is the sheer number of firms that are moving new CO₂-recycling methods towards the market and touting their climate benefits. Approaches range from co-opting biological processes to using electrochemical cells or catalysts (see 'Reusing carbon dioxide').

REUSING CARBON DIOXIDE

Companies are turning the greenhouse gas into many products. Some products lock CO₂ away for decades, but others are short-lived solutions, so the gas quickly ends up in the atmosphere.

Source

The CO₂ in some products comes from fossil-fuel-fed power plants. In others, it comes directly or indirectly (through plants) from the atmosphere.



From industrial and power-plant emissions



From the atmosphere

Capture

CO₂ can be pulled from waste streams or the air in several ways.

Micro-algae cultivation

Chemical carbon capture

Direct air capture

Trees and plants*

Reuse

Different products made with CO₂.

Syngas (CO+H₂) +H₂†

Catalyst-assisted electrochemical or chemical conversion

Injection into building materials (mineralization)

Direct use (no conversion)

Fermentation (by microbes)

Fuels (methanol, ethanol, methane)

Polymers (polyols)

Enrich air in greenhouses to increase plant yield

Injected underground to help recover oil

Feedstock chemicals (methanol, formic acid)

Building materials (concrete)

Lifetime

How long CO₂ is locked up in reused products.

Months to decades

Decades

Months to centuries

Days to years

Years to centuries

*Some crops can be converted into fuel. †Chemical conversion of CO₂ into fuels or feedstock chemicals often requires hydrogen (H₂) from industrial waste gases or from electrolysis of water.

Adapted from ref. 10

Many of the bigger players use catalysts that help to combine CO₂ with hydrogen to make fuels and commodity chemicals. Their main costs revolve around the energy needed to make hydrogen, capture streams of CO₂ and break this molecule's strong carbon–oxygen bonds to forge new molecules. That is why so many early plants are located where there are plentiful streams of high-purity waste CO₂, widely available spare hydrogen and heat (which powers the methanol production at Tongyezhen), or low-cost renewable electricity.

CRI, for instance, opened its first CO₂-to-methanol plant in 2012, next door to a geothermal power station in Iceland. There, boreholes tap into hot water and steam that come with unwanted CO₂. CRI's plant relies on Iceland's relatively low-carbon electricity grid to create 'green' hydrogen from water by electrolysis. Then the gases are combined, heated, pressurized and passed over a catalyst that eases the breaking of CO₂ bonds. Each year, the Iceland plant recycles 5,500 tonnes of CO₂.



CRI's first CO₂-to-methanol plant was built near a geothermal power station in Iceland.Credit: ARCTIC IMAGES/Alamy

“This is more expensive than producing conventional methanol, there is no doubt about it,” says Emeric Sarron, chief technology officer at CRI, who declines to say how much more expensive. “But companies that need to source renewable fuels are willing to pay a premium for it.” And the firm has customers: as well as the facility in Tongyezen, CRI is working on other full-size plants in China’s Jiangsu province and in northern Norway. Other consortia projects involving companies in Belgium, Sweden and Denmark will all recycle CO₂ to methanol for use as a chemical feedstock and shipping fuel, and aim to start operations between 2023 and 2025.

Electrochemical fuels

Rather than building such large, centralized projects, some start-ups think it will be cheaper and more efficient to convert CO₂ inside smaller, modular electrochemical cells. California-based start-up firm Twelve, for instance, aims by the end of this year to have an electrolyser system the size of a shipping container that uses electricity to process more than one tonne of CO₂ each day into syngas. This mixture of carbon monoxide and hydrogen is widely used to make other chemicals, including fuels. Twelve plans to offer CO₂ conversion as a service to firms wanting to reduce their emissions; it could charge per tonne converted, and sell its end products to cover costs. In July 2021, it raised \$57 million in venture-capital funding. “We definitely see ourselves being a player in greenhouse-gas emission reduction,” says Etosha Cave, the company’s co-founder and chief scientific officer.

Syngas is conventionally made by an energy-intensive process that crushes methane and water together at high temperatures and pressures. Twelve, by contrast, uses a modified commercial electrolyser, which normally splits water into hydrogen and oxygen. Adding a metal catalyst to one of the device’s electrodes (the cathode) enables it to simultaneously convert CO₂ into CO, so that the system produces syngas at room temperature. Twelve aims to use renewable electricity sources to run these CO₂-recycling units.



An electrochemical cell used by Twelve to turn CO₂ into chemicals and fuels.Credit: Twelve

Academic chemists have pressed the case for electrochemical recycling by making significant improvements to cathode catalysts. A key metric known as Faradaic efficiency — the proportion of electrons that go into producing CO rather than unwanted by-products — is now more than 90% in some cases¹. Chemists are also making headway on another front — improving the ability of catalysts to support a high electric-current density. This allows a given area of electrode to convert more CO₂ molecules. Nevertheless, many catalysts struggle to work for more than a few hundred hours before they start to degrade, says Jan Vaes, programme manager for sustainable chemistry at the Flemish Institute for Technological Research (VITO) near Antwerp, Belgium.

Electrochemists aren't only targeting syngas. Avantium, a renewables chemical company in Amsterdam, is using improved catalysts² to make formic acid, which can be converted into more-valuable chemicals. It is currently testing an electrochemical reactor at a fossil-fuel power plant in Germany.



An Avantium mobile container unit converts CO₂ from an industrial plant's carbon-capture unit into formic acid.Credit: Avantium

And some chemists are hoping to make more complex carbon molecules that could command higher prices. Larger molecules can be more troublesome to make this way — with more chemical bonds, there are more opportunities for electrons to be diverted into side products, reducing efficiency — but progress is being made. This year, for instance, electrical engineer and materials scientist Edward Sargent at the University of Toronto in Canada and his team unveiled an electrochemical system that converts CO₂ and water into ethylene oxide, which is widely used to make polymers. The team's catalyst achieved a record Faradaic efficiency of 35% for the conversion³.

Life-cycle arguments

Whether products recycled from industrial CO₂ emissions actually protect the climate is unclear — because the CO₂ they capture will still be released into the atmosphere if the molecules are burnt or broken down. Drawing CO₂ directly from the atmosphere could have clearer climate benefits, but capturing the gas from air is extremely expensive, as are products made that way.

Proponents argue that recycling industrial CO₂ into chemicals can reduce emissions in another way — by avoiding some fossil-fuel-based production. “Our process helps keep fossil fuels in the ground by tapping into existing streams of CO₂,” a spokesperson for Twelve told *Nature*.

The stringent way to examine this is through a life-cycle analysis (LCA) — a detailed accounting of the carbon involved in making and using a product, from the origins of its CO₂ to its final fate. Many CO₂-recycling firms say they have done these audits, but don’t publish them because they contain proprietary information.

One firm that has released LCAs is LanzaTech, headquartered in Skokie, Illinois. The company uses bioreactors filled with *Clostridium autoethanogenum* bacteria to ferment industrial CO₂, CO and hydrogen waste emissions into ethanol. Its chief executive, Jennifer Holmgren, notes that this kind of bioconversion can handle messy waste-gas streams, such as those from municipal waste gasifiers, better than chemical processes do. The firm’s reactor at a Shougang Group steel plant near Tianjin in China has been producing ethanol since 2018. A second plant began operating at a Chinese alloy plant last year, and commercial plants in Belgium and India are expected to come online by the end of this year.

On 8 March, LanzaTech announced that it would become publicly listed, a move that values the company at \$1.8 billion. This year, it reported that with genetic modifications, its bacteria could make larger molecules such as acetone and isopropanol, too⁴. Conventional production of acetone and isopropanol generates copious CO₂ emissions. By contrast, LanzaTech’s

LCA suggests that its route is carbon-negative — consuming much more carbon than it emits⁴. But this analysis did not include what would happen to the CO₂ when the products were used.

Holmgren thinks that CO₂-based products will save on emissions anyway, by displacing their conventionally made equivalents. But she concedes that it is hard to be certain this is true — CO₂-based products might simply add to the growing global consumption of fuels and other chemicals, rather than displace incumbent production. It's also tricky to pin down direct evidence for displacement in such a nascent market, adds Sarron.

“The problem is that people use displacement with the idea that the market will do it, somewhere around the globe,” says Andrea Ramírez Ramírez, who studies low-carbon systems and technologies at Delft University of Technology in the Netherlands. “But how do you monitor displacement? That’s very, very difficult.”

A greater availability of supposedly guilt-free CO₂-derived products might also lead to increased consumption of those resources, she adds. Anyone who is trying to limit their international flights, for instance, might fly more often if their airline boasts of its climate-friendly fuel. This ‘rebound effect’ has been observed for some energy-efficiency measures, Ramírez Ramírez says, although it hasn’t been studied for CO₂-based goods.

In her view, negative emissions⁵, such as those claimed by LanzaTech, “should mean real CO₂ removal from the atmosphere, that you can actually measure physically”.

Locking carbon down

To maximize climate benefits, it makes more sense to lock recycled CO₂ into products that last for decades. That’s where polymers come in. “You’re making products like insulation foam, mattresses, soft furnishings, that have quite a long lifetime,” says Charlotte Williams, a chemist at the University of Oxford, UK.

Williams develops catalysts that can incorporate CO₂ into polyols, which are used to make polyurethane foams. Polyols are usually made from expensive chemicals called epoxides, but her catalysts help CO₂ to take the place of some of these in the polymer chain. This traps CO₂ and reduces the consumption of epoxides — which themselves have a big carbon footprint.

Williams has founded a spin-off company, Econic Technologies. In September 2021, it signed a deal to build a pilot plant in India, and then retrofit an existing plant to incorporate waste CO₂ into polyols. Other companies are seasoning polymers with CO₂ in similar ways.

Despite this progress, projections suggest that using CO₂ as a polymer ingredient would lock up only around 10 million to 50 million tonnes of CO₂ per year by 2050⁶. So, is it really worth it? “I think it’s the wrong way of looking at the problem,” Williams says. “We have to make massive cuts in CO₂ emissions across the board, but we also have to invest in some technologies that can directly use it.”

The biggest opportunity to incorporate CO₂ into products lies in concrete and other building materials, says Runeel Daliah, a senior analyst at Lux Research, who is based in Amsterdam. The technology is proven and scalable, and could feed an enormous global demand for concrete, giving it the potential to dominate the CO₂-conversion market. “Concrete is really the only one where you have permanent sequestration of CO₂ in the product,” Daliah says.

One of the leaders in this sector is Canadian company CarbonCure in Halifax. Founded in 2012, it pumps waste CO₂ into fresh concrete to form nanoparticles of calcium carbonate. This improves the compressive strength of the concrete, so that less cement is needed⁷. Because cement-making accounts for most of concrete’s carbon emissions, the company says this could reduce the carbon footprint of every tonne of concrete by around 5% (or 6 kilograms of CO₂).



CarbonCure concrete is poured during a construction project. Pumping CO₂ into concrete locks up the gas for many years, or even centuries.Credit: CarbonCure Technologies

The company has installed more than 550 of its CO₂ injection units at concrete plants around the world, most of them in North America, which has avoided and mineralized 150,000 tonnes of CO₂ emissions so far. But with some 100,000 plants worldwide churning out roughly 33 billion tonnes of concrete per year, “we’re really just scratching the surface”, says Jennifer Wagner, CarbonCure’s president.

Ramírez Ramírez says that converting CO₂ into minerals offers a much clearer climate benefit than converting it into fuels. “In the life-cycle analysis, you can see the benefits are much larger, and I think much more robust.”

Carbon-removal incentives

When it comes to making fuels and other chemicals, most CO₂-derived products are currently more expensive than their conventional rivals, says Josh Schaidle, who led an analysis by the US National Renewable Energy Laboratory in Golden, Colorado, of 11 products made by CO₂ conversion⁸. Yet they could still have a strong business case, if they can take advantage of low-cost renewable electricity, as well as the tax breaks, subsidies and quotas that aim to wean the world off fossil resources.

In the European Union, for instance, a broad package of policy incentives under the banner of the European Green Deal aims to make the bloc climate neutral by 2050. Pending legislation specifies quotas for the use of CO₂-derived fuels in aviation. There will be reduced taxes on CO₂-based fuels, and the promise of plenty of innovation funding to help technologies to market.

In the United States, some companies say that a tax credit called 45Q is helping to encourage CO₂ conversion. It pays industries \$50 for every tonne of CO₂ they store permanently underground, or \$35 if they put the CO₂ to use. In China, there has been relatively little commercial activity in developing CO₂-conversion technologies⁹. But in 2021, key players in China's gigantic chemicals industry pledged to invest in CO₂-based chemical production, a move that could win financial support through the country's carbon-trading market, which launched last year.

The success of the CO₂-conversion businesses, however, could rest on LCAs and other measurements of carbon flows. The European Commission, for example, is developing a carbon-removal certification mechanism to provide a more rigorous framework for verifying whether a process is genuinely carbon negative.

So far, LCAs offer a rather downbeat assessment of most CO₂-conversion strategies. In a report¹⁰ published in February, environmental scientist Kiane de Kleijne at Radboud University in Nijmegen, the Netherlands, and her

colleagues scoured dozens of published LCAs to compare CO₂ conversion routes with conventional ways of making the same products. Then the researchers compared CO₂ savings from the recycling processes with the 2015 Paris agreement targets of halving global CO₂ emissions by 2030, and of achieving net zero emissions by 2050. “We found that very few of those routes are able to meet the criteria for Paris compatibility,” says de Kleijne. Routes that made the grade did so by storing CO₂ permanently — mixing the gas with slag from steel mills to make construction blocks, for example.

Climate-focused academics conducting LCAs often note that geological storage of CO₂ is better than conversion because it offers much greater reductions in emissions. That might be true, but it ignores a brutal economic reality, says Sarron. “Putting carbon back into the ground is expensive, and is not happening at a meaningful scale. The alternative to what we are doing today is not storage, it’s emission to the atmosphere.”

And if the global economy does eventually end its reliance on coal, oil and gas, industries of the future might need these CO₂-conversion processes to produce the polymers and other chemicals we depend on.

De Kleijne says that all too often, the academics performing LCAs and companies developing CO₂-conversion systems end up talking past each other on these issues.

But there is at least one point of broad agreement: that CO₂ recycling technologies should eventually draw as much of their feedstock as possible from the atmosphere, rather than from waste industrial gases. A project called Norsk e-Fuel in Oslo is taking a step in that direction with a pilot plant in Herøya, Norway, which aims to start turning CO₂-derived syngas into jet fuel. Some of the CO₂ will come directly from the air, snared by carbon-capture technology developed by Climeworks, a company that was spun off from the Swiss Federal Institute of Technology in Zurich in 2009.

That technology is now in operation at Climeworks’s first large-scale direct air-capture plant, which opened in September 2021 in Hellisheiði, Iceland. It will capture 4,000 tonnes of CO₂ a year to be pumped underground. It costs

\$600–800 to sequester one tonne of CO₂ in this way — hardly cheap — but the company says it can slash that to one-tenth of the cost as it scales up.

Even if there are limited climate benefits from converting today's fossil CO₂ emissions into products, some companies argue that it's important to develop the technology so that it is ready to feed off CO₂ from the air once direct air-capture technology matures. "I do think it's a valid argument," says Ramírez Ramírez. "But we need to be careful that it is part of a transition, that we eventually replace the fossil carbon with sustainable sources."

Nature **603**, 780–783 (2022)

doi: <https://doi.org/10.1038/d41586-022-00807-y>

References

1. Masel, R. I. *et al.* *Nature Nanotechnol.* **16**, 118–128 (2021).
2. Phillips, M. F., Gruter, G.-J. M., Koper, M. T. M. & Schouten, K. J. P. *ACS Sustain. Chem. Eng.* **8**, 15430–15444 (2020).
3. Li, Y. *et al.* *Nature Catal.* **5**, 185–192 (2022).
4. Liew, F. E. *et al.* *Nature Biotechnol.* **40**, 335–344 (2022).
5. Tanzer, S. E. & Ramírez, A. *Energy Environ. Sci.* **12**, 1210–1218 (2019).
6. Hepburn, C. *et al.* *Nature* **575**, 87–97 (2019).
7. Monkman, S. & MacDonald, M. J. *Cleaner Prod.* **167**, 365–375 (2017).
8. Huang, Z., Grim, R. G., Schaidle, J. A. & Tao, L. *Energy Environ. Sci.* **14**, 3664–3678 (2021).
9. Jiang, K. *et al.* *Renew. Sustain. Energy Rev.* **119**, 109061 (2020).

10. De Kleijne, K. *et al.* *One Earth* **5**, 168–185 (2022).

This article was downloaded by **calibre** from <https://www.nature.com/articles/d41586-022-00807-y>.

| [Section menu](#) | [Main menu](#) |

- NEWS FEATURE
- 30 March 2022

The quest to prevent MS — and understand other post-viral diseases

Some people develop multiple sclerosis after an infection. Could a vaccine prevent that — and what does it reveal about the long-term effects of viruses?

- [Asher Mullard](#) 0



A small number of people infected with Epstein-Barr virus (pictured) go on to develop multiple sclerosis years later. Credit: Dr Gopal Murti/SPL

In a sprawling facility in Silver Spring, Maryland, the US Department of Defense (DoD) has amassed a hoard of epidemiological treasure. Walk-in freezers each the size of a basketball court hold 72 million vials of blood serum meticulously tracked and sorted into cardboard boxes stacked nearly 4 metres high. Technicians pull on winter coats and gloves for 20-minute trips into these -30°C deep freezers. The vials they bring out hold untold riches.

For Alberto Ascherio, an epidemiologist at Harvard T.H. Chan Medical School in Boston, Massachusetts, the vials have yielded a rare gift in the quest to discover the cause of multiple sclerosis (MS), a disease in which the immune system attacks nerve cells.

Researchers have long suspected a link between MS and the Epstein–Barr virus (EBV), but it has been hard to establish a strong connection, partly because almost everyone gets an EBV infection at some point, most of them harmless. The samples in the DoD's freezers provided an unparalleled

chance to explore the link. After analysing data and samples collected from more than 10 million army, navy and air force service members since 1993, Ascherio found that EBV infection increases the risk of MS 32-fold¹.

“I’ve never seen anything so strong, so black and white,” says Ascherio. Smoking increases the risk of lung cancer 15–30-fold.

These results, combined with emerging mechanistic insight into how the virus triggers brain damage², are raising the prospect of treating and even preventing MS. A phase I trial of an EBV vaccine is under way, although it will be years, if not decades, before large trials can shed light on whether vaccines forestall MS.

These advances come at a time when researchers are more interested than ever in what happens months and years after a viral infection. Two years into the coronavirus pandemic, huge numbers of people face lasting symptoms after their initial infection with SARS-CoV-2. Concern over long COVID looms large for both the public and health officials, and funders have poured more than US\$1 billion dollars into understanding the biology of this nebulous post-viral condition.

The longer-running effort to understand the causes of MS highlights the problems and promise of untangling the complex relationships between infectious diseases and later chronic conditions. Progress with these investigations can seem slow, but Katherine Luzuriaga, a clinician-scientist specializing in childhood infectious diseases at UMass Chan Medical School in Worcester, Massachusetts, has faith in the steady march of science. “As scientific methods and technologies evolve,” she says, “I think we’re going to get a lot more insights into post-viral conditions.”

Mysterious origins

Researchers have been trying to prove for more than a century that various chronic diseases have roots in infection. Nobel-prizewinning microbiologist Barry Marshall went as far as drinking a slurry of *Helicobacter pylori* bacteria to show that they cause chronic stomach ulcers. Others have proposed that complex diseases from myalgic encephalomyelitis/chronic

fatigue syndrome to Alzheimer's disease are linked to certain pathogens, but irrefutable evidence is hard to come by. In some cases, that might be because multiple pathogens and factors are at play; in others, it could be because the relationships aren't real.

This year, the evidence that EBV can cause MS got a boost from two studies^{1,2}.

MS, a debilitating autoimmune disease, affects around 2.8 million people worldwide. As the immune system attacks nerves in the brain and spinal cord, stripping off their protective myelin sheathing, people with MS experience symptoms including fatigue, numbness, pain, loss of vision and depression. The symptoms worsen over time, and can lead to disability and shortened life expectancy. Drugs can slow the progress of disease, but don't completely prevent symptoms.

Several factors seem to make the immune system misfire and drive MS. The geographical distribution of cases and other data suggest that lack of sunshine and vitamin D have a role. Genetic factors raise the risk, at least a little bit. EBV, first discovered in 1964, has also been suspected since at least the 1970s.



A nurse visits a woman with multiple sclerosis at her home in the United Kingdom. Credit: Lindsey Parnaby/AFP/Getty

EBV is everywhere: more than 95% of adults are infected³. Most infections cause no symptoms, but EBV can trigger an illness called infectious mononucleosis. No one ever fully clears the virus from their body. Yet only a tiny proportion of people develop MS — 0.2% in the United Kingdom, for example. This creates a conundrum for researchers: how can you prove that a near-ubiquitous virus causes an autoimmune disease in an unlucky few?

Ascherio's epidemiological approach was to track the MS and EBV status of military recruits using medical records and the DoD's stored blood-serum samples. He and his team identified 955 individuals who were diagnosed with MS while in the military, they reported in *Science*¹. Just 35 of these people did not carry EBV at the start of their service, the team showed. All but one had contracted EBV by the time of their MS diagnosis — an infection rate of 97%. By contrast, the infection rate in controls, who did not develop MS, was 57%.

Then, the team measured levels of a protein called neurofilament light chain, a marker of neurodegeneration. After EBV infection, those individuals who went on to develop MS had higher levels of neurodegeneration than did people who did not develop the condition.

For Ascherio, this analysis proves that the virus drives the chronic disease, even if more work is needed to find out why only a fraction of infections result in MS. “We’ve all been brainwashed with the idea that association is not causation. OK, but then give me an alternative explanation for all the data,” he says.

One possible explanation is that a faltering immune system is an early sign of MS, and that viral invaders — including EBV — take advantage of the opportunity to infect. Ascherio failed to find any signs of other viral opportunists in the serum samples, helping to discount this hypothesis. But doubts persist in some quarters. Marshall’s critics raised similar arguments against his idea, suggesting that ulcers might create the environment for *H. pylori* infection, rather than the other way around.

Bill Robinson, chief of immunology and rheumatology at Stanford University in California, used to dismiss the EBV–MS hypothesis for this reason. “I was very sceptical that EBV was involved,” says Robinson. After spending five years using a battery of immunological techniques to study the antibodies that people with MS make, he has done a U-turn.

During EBV infections, immune-system cells known as B cells pump out antibodies against a protein made by the virus, called EBNA1. That protein happens to share some structural similarities with a protein in the central nervous system called GlialCAM. Over time, some of the B cells can start making antibodies that bind to both EBNA1 and GlialCAM. The result is a friendly fire attack on neurons. Some 20–25% of people with MS carry these trigger-happy antibodies, Robinson and his colleagues reported in *Nature*² this year.

“This changes everything. It’s been very hard to pin the tail on the donkey. Our work provides a mechanism,” says Robinson.

The combination of solid epidemiological data and mechanistic explanation is a compelling sales pitch for the post-viral theory, says Paul Lieberman, a molecular virologist at the Wistar Institute in Philadelphia, Pennsylvania. He was convinced even before the most recent data, but they “push the needle further”, he says. The surest way to convince the doubters would be to show that prevention or treatment of EBV wards off MS. “A clinical trial is definitely worth trying,” says Lieberman. “It’s not totally clear how to do that yet.”

Blocking EBV

A first step is to identify ways to keep EBV at bay. In January, Luzuriaga watched as a healthy volunteer walked into a sterile exam room to join a trial of one possible contender, a vaccine called mRNA-1189, made by biotechnology company Moderna in Cambridge, Massachusetts. Moderna hopes to build on the success of its mRNA COVID-19 vaccines by taking on EBV. mRNA-1189 encodes four EBV proteins that might teach the immune system to resist viral infection. Another Moderna vaccine candidate, mRNA-1195, has been designed to help the immune system to control EBV in people who already carry the virus. Two EBV vaccine candidates from the US National Institutes of Health are also approaching clinical trials.

“It’s tremendously exciting,” says Luzuriaga, the lead investigator on the mRNA-1189 trial.

The aim of the first trials will be to show that these vaccine candidates are safe, and can reduce the burden of infectious mononucleosis. Also known as mono, glandular fever and the kissing disease, this illness causes symptoms including extreme fatigue and fever, and affects 30–50% of people who contract EBV for the first time as teenagers or young adults⁴.



The freezers in the US Department of Defense Serum Repository hold tens of millions of blood samples from military recruits. Credit: Darrell Olson/AFHSD

Demonstrating that EBV vaccines have a benefit against MS will require much heavier lifting. Jeffrey Cohen, chief of the Laboratory of Infectious Diseases at the National Institute of Allergy and Infectious Diseases in Bethesda, Maryland, estimates that a trial would require tens of thousands of young-adult volunteers, followed for up to ten years. Because of the ubiquity of the virus, even screening for volunteers who haven't already had EBV would be a logistical headache.

A prevention trial that begins by vaccinating infants would make screening easier or unnecessary, says Ruth Dobson, a neurologist at Queen Mary University of London. But MS typically strikes between the ages of 20 and 40, so researchers would be waiting decades for the results. "I would have to have infinite money and infinite follow-up to do this trial," she says.

For Cohen, the most likely route to robust MS-prevention data is to wait for an EBV vaccine to be approved to prevent infectious mononucleosis, and then track whether recipients develop MS. On average, it takes around ten years for a vaccine to run the clinical-trial gauntlet. After approval,

observational data would take many more years to accumulate, but without the practical challenges of a prospective trial. Health authorities such as the US Food and Drug Administration (FDA) might need to mandate post-approval studies, he adds; otherwise, companies would have little incentive to collect the data. “That’s a really important lesson here.”

In the best case, EBV vaccines will provide long-lasting sterilizing immunity — blocking infection altogether. Vaccines against human papillomaviruses do this, and so prevent cervical cancer. But previous EBV vaccine candidates have not given that level of protection (the same is true for COVID-19 vaccines, which reduce the severity of illness but don’t necessarily prevent infection with SARS-CoV-2).

Partially protective EBV vaccines could still prevent MS, says Robinson, but their success will depend on how exactly the EBV infection triggers its downstream effects. Does a single bout set off post-viral problems, or do the levels and long-term persistence of the virus make a difference? For EBV–MS — and many other suspected post-viral conditions — these are open questions with big implications.

Antiviral adventure

If viral load and persistence matter, antiviral drugs are another good bet for preventing post-viral conditions. Antivirals that wipe out the hepatitis C virus, for instance, have helped to alleviate the burden of chronic liver disease that the virus can cause.

But for this to work, antivirals need to be great at their job. For now, nothing with enough power to kill EBV is ready for rigorous clinical trials. “We don’t have a real antiviral drug to target EBV-infected cells,” says Cohen. A few drugs slow the virus’s replication, he adds, but not enough to clear it from the body or change the clinical course of infectious mononucleosis.

This might be because the virus has two stages in its life cycle: a lytic phase, in which it replicates like mad; and a latent phase, in which it hides from the immune system. Latent viruses are notoriously challenging to kill: it is hard to jam up the viral machinery when the gears are barely turning.

“I certainly wouldn’t say it’s going to be easy,” says Lieberman, who is developing antivirals that target EBNA1 to take out the latent virus⁵. If the community can unpick the relative contributions of the two phases, and how the latent virus is reactivated, it could open new doors.

Another strategy is to destroy the virus’s breeding ground: the B cells. Atara Biotherapeutics in South San Francisco, California, is attempting this, with ATA188, a therapy made from immune T cells engineered to hunt and destroy B cells that harbour EBV.

A phase I/II trial is under way in people who already have progressive MS, in hopes of slowing the progression of disease. Preliminary results are due later this year. “If they see activity, that would mean game on,” says Robinson.

But neurological diseases are hard to treat once brain damage has set in. T-cell therapies might fare best when used earlier in the course of disease, but they are an emerging therapy with an uncertain safety profile — an unlikely candidate for a large-scale prevention trial.

Erin Longbrake, a neurologist at Yale University in New Haven, Connecticut, has thought about how to balance the need for early intervention with the side effects a treatment can bring. Her therapy of choice is the FDA-approved MS drug ocrelizumab, which kills B cells to reset the malfunctioning immune system. It was not designed as an antiviral, but by happy accident it knocks out at least some of the EBV reservoir. Because it broadly depletes the immune system, however, treated individuals are at high risk of other infections. It’s a high price to pay for someone without a disease.

So Longbrake has been looking for those with most to gain. A tiny subset of people have damaged areas in their brains similar to those caused by MS, but none of the accompanying symptoms. Such lesions are sometimes noticed incidentally on a brain scan. Nearly half of these people will develop MS within ten years of the discovery⁶.

“If you told me I had a 50:50 chance of having MS, I’d want to do something about that,” says Longbrake. A trial testing whether ocrelizumab

can slow the development of MS in 100 people with lesions is recruiting participants.

Researchers are also working to identify people at high risk of other post-viral complications to ease those clinical trials.

Be prepared

It could take decades before an EBV-directed intervention proves to be a way to stave off MS. And although long COVID has renewed broad interest in the lasting effects of infections, every suspected link between a virus and a disease has its own unique and lengthy research journey ahead. For Dobson, the keys to success are preparation and patience. Ascherio's epidemiological advances, for instance, were enabled by the decades of biological samples banked by the DoD — an expensive method that takes years to yield insights. "Biobanks are a really hard sell. And then everybody loves them once all the hard work has been done," says Dobson. Similar disease-agnostic resources — which have been collecting samples throughout the pandemic — will yield insights into the long-term effects of other viruses. Already, the UK Biobank has shown how the SARS-CoV-2 virus can affect brain structures⁷.

The long view is needed for clinical trials, too, she adds. Trials have to sign up the right people and find clear ways to measure success — easier for a condition such as MS, which doctors can diagnose and monitor with some precision, than for long COVID, which has no clear clinical definition. "If we don't start thinking about these trials now, we'll be in the same place 15 to 20 years from now."

Nature **603**, 784-786 (2022)

doi: <https://doi.org/10.1038/d41586-022-00808-x>

References

1. Bjornevik, K. *et al. Science* **375**, 296–301 (2022).

2. Lanz, T. V. *et al.* *Nature* **603**, 321–327 (2022).
3. Cohen, J. I. *Clin. Transl. Immunol.* **4**, e32 (2015).
4. Luzuriaga, K. & Sullivan, J. L. *N. Engl. J. Med.* **362**, 1993–2000 (2010).
5. Messick, T. E. *et al.* *Sci. Transl. Med.* **11**, eaau5612 (2019).
6. Lebrun-Frenay, C. *et al.* *Ann. Neurol.* **88**, 407–417 (2020).
7. Douaud, G. *et al.* *Nature* <https://doi.org/10.1038/s41586-022-04569-5> (2022).

This article was downloaded by **calibre** from <https://www.nature.com/articles/d41586-022-00808-x>

| [Section menu](#) | [Main menu](#) |

Opinion

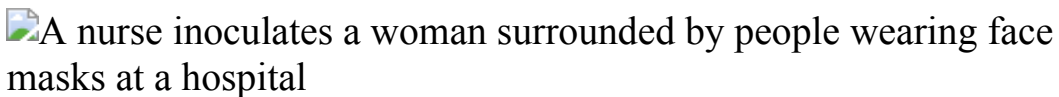
- **[Global vaccination must be swifter](#)** [28 March 2022]
Comment • Speeding up development of new vaccines won't help much in the next pandemic, unless world leaders work faster to roll out vaccination globally.
- **[Russia is weaponizing water in its invasion of Ukraine](#)** [29 March 2022]
Correspondence •
- **[Together, we must help refugee researchers to thrive](#)** [29 March 2022]
Correspondence •
- **[Open access: Brazilian scientists denied waivers and discounts](#)** [29 March 2022]
Correspondence •
- **[Chile's science ambitions — three notes of caution](#)** [29 March 2022]
Correspondence •

- COMMENT
- 28 March 2022

Global vaccination must be swifter

Speeding up development of new vaccines won't help much in the next pandemic, unless world leaders work faster to roll out vaccination globally.

- [Thomas J. Bollyky](#) ⁰,
- [Jennifer Nuzzo](#) ¹,
- [Noelle Huhn](#) ²,
- [Samantha Kiernan](#) ³ &
- [Emily Pond](#) ⁴



A woman in Dakar, Senegal, receives a COVID-19 vaccination in July 2021.
Credit: Zohra Bensemra/Reuters

Last September, more than 100 governments attending US President Joe Biden's virtual Global COVID-19 Summit committed to [vaccinating at least 70% of the population in every country by September 2022](#). Using national vaccination rates from mid-February, we estimate¹ that nearly 100 countries will fall short of that objective.

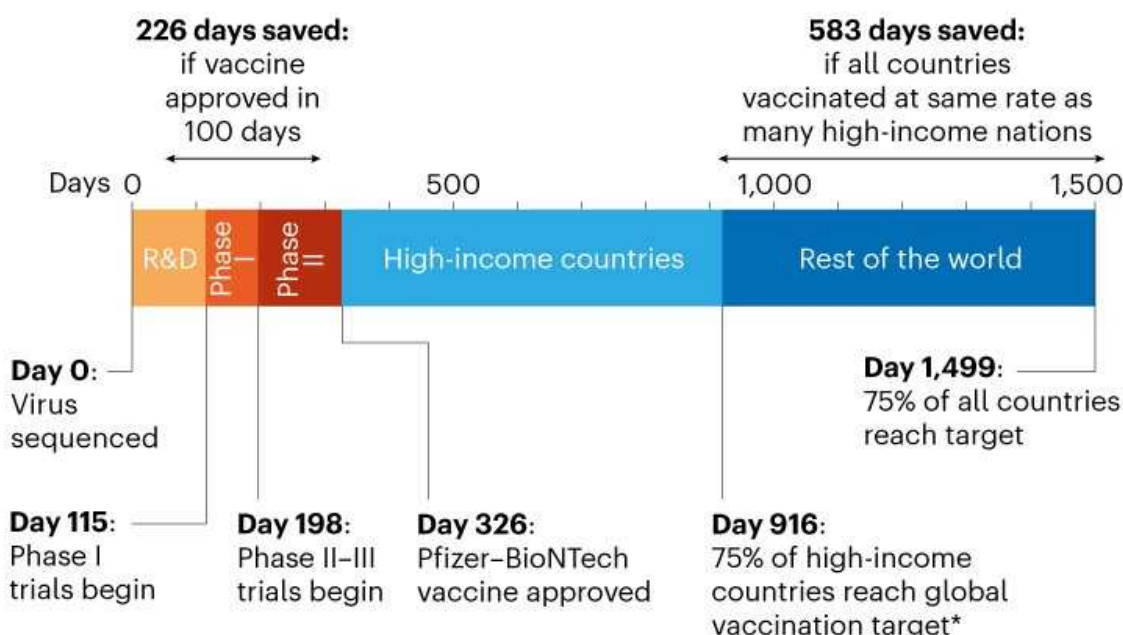
Those missing the target include four out of five African nations, and most countries in Central America and the Middle East. In low-income nations, only one in ten people is fully vaccinated. Seventeen high-income nations, including Poland and Oman, are not on track to reach this goal either. At its current pace, Slovakia will not vaccinate 70% of its population until May 2026.

In fact, at current vaccination rates, it will take until 15 July for 75% of high-income nations to fully vaccinate 70% of their populations. That's 590 days (more than 1.5 years) after the UK government first authorized a COVID-19 vaccine for general use (see 'Vaccinate the world faster next time'). Getting this proportion of people fully vaccinated in three-quarters of all countries will take almost double that time — 1,173 days, or more than three years¹.

These delays translate into millions of avoidable hospitalizations and deaths. They are mainly the result of inadequate global supplies of vaccine doses, and the challenges of planning, resourcing and implementing vast vaccination programmes in countries with already strained health systems.

VACCINATE THE WORLD FASTER NEXT TIME

Many more days could be saved through a more equitable global roll-out of vaccines than would be cut by shrinking the time for vaccine approval to 100 days.



*Target is for every country to vaccinate at least 70% of its population.

Timeline refers to Pfizer-BioNTech's COVID-19 vaccine, the first to be approved by a stringent national regulatory authority. Projections determined as of 16 February 2022, using the average rate of vaccination over the past 30 days for each country (see ref. 1 for methodology).

©nature

Source: T. J. Bollyky *et al.*

The US White House is convening another global COVID-19 summit in the near future. To limit further surges in hospitalizations and deaths in the current pandemic — and to prepare better for a potentially even deadlier one — attendees and world leaders must establish long-lasting adult-immunization infrastructure and vaccine-manufacturing capacity in their own countries. They must prioritize vulnerable groups for COVID-19 vaccination. And they must take steps to stem the spread of misinformation and disinformation around vaccination.

For many low- and middle-income countries, all this can be achieved only with adequate support from wealthy nations.

The 100-day goal

Over the past six months, the United Kingdom², the United States³ and the European Union (see go.nature.com/3jrxudk) have all launched various initiatives to boost vaccine production. These aim to reduce the research and development time needed to create vaccines against future pandemic threats to as little as 100 days from the publication of a virus's genetic sequence. Researchers are already trying to develop prototype vaccines for known pathogens in viral families deemed most likely to cause the next pandemic.

Such initiatives are crucial in preparing for future pandemics. On 2 December 2020, the UK Medicines and Healthcare products Regulatory Agency became the first stringent regulator to authorize a COVID-19 vaccine, namely that made by Pfizer and BioNTech. Developing vaccines in 100 days would have produced a publicly accessible vaccine 226 days sooner — a period in which 1.4 million COVID-19 deaths were recorded.

Yet, having faster ways to develop vaccines will not help unless world leaders also undertake the measures necessary to achieve much faster rates of vaccination globally.

As of February, COVAX, the multilateral COVID-19 vaccine initiative, had distributed 1.3 billion doses of vaccines to 144 countries and territories. But three-quarters of those doses were distributed in the past four months, almost two years into the pandemic. Millions of vaccine doses, donated through

COVAX and bilaterally, are going to waste because they are arriving in low- and middle-income countries too late for them to be used before they expire. The initial priority for COVAX was procuring and shipping vaccines, but many recipient governments lack resources to get the shots into arms. They do not have the workforce, information systems or cold-chain infrastructure and supply logistics to plan, finance and deploy massive and effective vaccination campaigns.

Forty-four of the African Union's 55 member states don't have enough fridges, freezers and other cold-storage infrastructure needed to distribute the Pfizer–BioNTech vaccine. This is according to a report last month by the Reuters news agency, which cited a January survey by the United Nations children's charity UNICEF (see go.nature.com/3jpiwpm). In fact, in February, the Africa Centres for Disease Control (Africa CDC) reportedly requested that vaccine donations be delayed or staggered because countries need more time and resources to deploy them. Meanwhile, COVAX has reportedly run out of money to help recipient countries with vaccine deployment, with no new funding sent since January⁴. Because of this and other challenges, 34% of the current supply of COVID-19 vaccines has yet to be administered across the African continent (see go.nature.com/3bgrhxy).

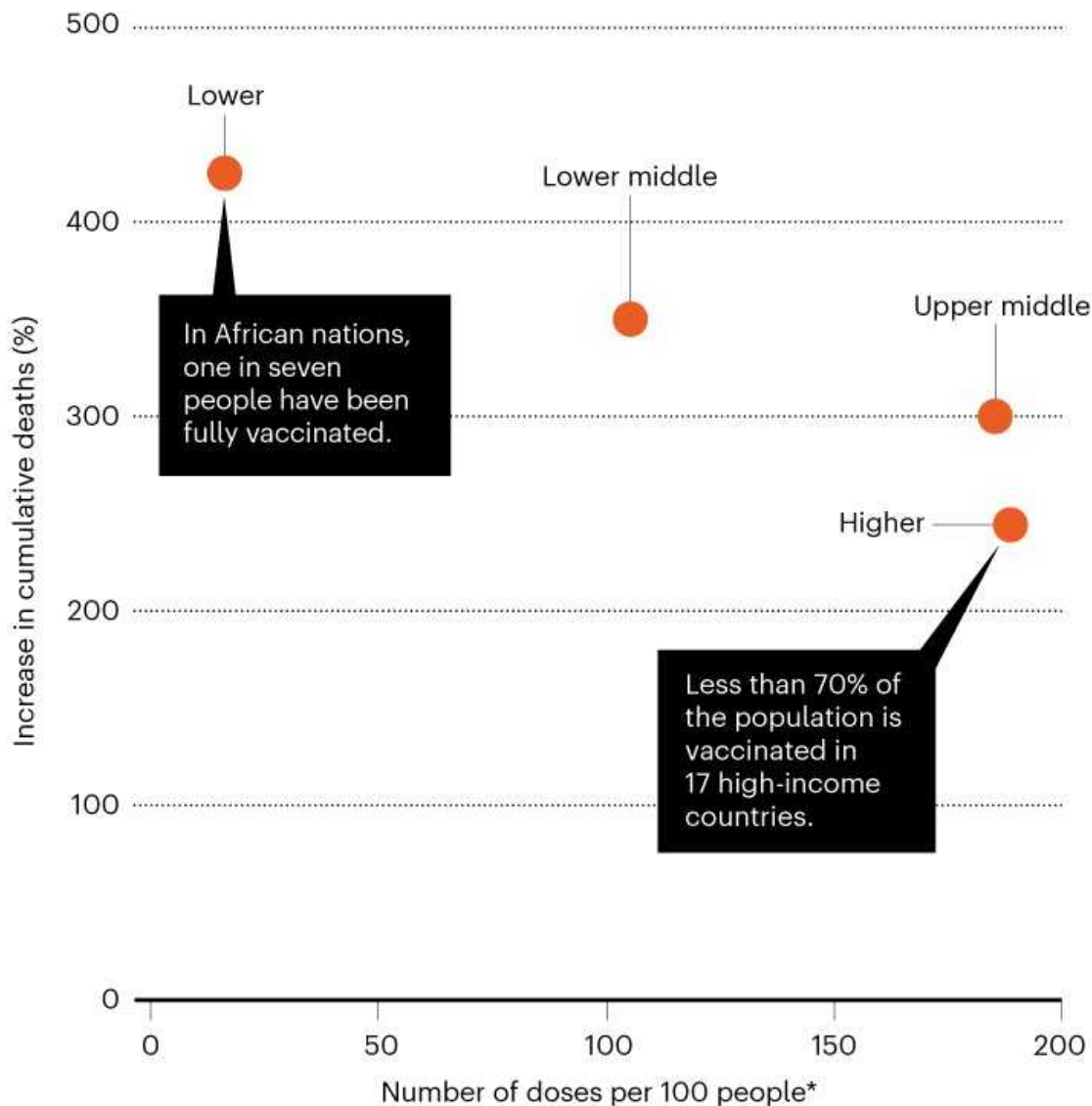
Such bottlenecks are compounded by a lack of consideration for the needs of low- and middle-income countries when it comes to vaccine authorization processes.

In wealthy nations, regulators such as the US Food and Drug Administration (FDA) and the European Union's European Medicines Agency have been slow to authorize vaccines that would be easier to administer in low-infrastructure settings. The protein-based vaccine made by Novavax, for example, might not be needed in wealthier countries where governments have purchased more than enough doses of other vaccines for their population. But Novavax does not require such cold storage as the Pfizer–BioNTech shot, and could be valuable in Africa. Likewise, the lack of FDA approval for the vaccine developed by the University of Oxford, UK, and AstraZeneca has reportedly undermined the willingness of other nations to take donations of this vaccine.

All these delays in vaccination have deadly consequences. In general, deaths from COVID-19 have been rising fastest in the countries and regions that have the lowest vaccination rates (see ‘Deadly delays’).

DEADLY DELAYS

Since 2 December 2020, deaths from COVID-19 have been rising fastest in the lowest-income countries — which also have the lowest vaccination rates.



*Doses administered per 100 people can be higher than 100 because of the two-dose regimen for most vaccines and the use of further booster shots.

©nature

Source: Our World In Data

Four priorities

Addressing the outstanding gaps in global vaccination coverage will require major investments across four domains — especially in the world's poorest regions.

Prioritizing vulnerable groups. That all nations have the same goal, of vaccinating 70% of their populations, remains important as a matter of global equity. But the public-health rationale behind this goal has shifted because stopping transmission of SARS-CoV-2 through a high vaccination rate alone is no longer feasible.

COVID-19 vaccines offer limited protection against infection by BA.1 and BA.2, the most common Omicron variants⁵. But vaccines still significantly reduce the probability that a person will be hospitalized or die as a result of infection. New York state reported that, in the latest Omicron wave, fully vaccinated individuals had a 90.1–95.9% lower chance of being hospitalized with COVID-19, compared with unvaccinated individuals (see go.nature.com/37tbshq).

Given this, prioritizing the most vulnerable groups for full vaccination is currently the best way to limit further waves of hospitalizations and deaths.

Indeed, the costs of not doing so were demonstrated by the recent surge in cases and deaths in Hong Kong. On average, 284 people were dying there each day between 6 and 13 March. That's a death rate of 38 per million people per day — the highest recorded globally in the pandemic⁶.

Although 65% of the population was fully vaccinated by 9 February, when Hong Kong's Omicron wave was escalating, only 33% of residents aged above 80 had received one dose — seemingly because of a mixture of complacency stemming from the region's zero-COVID policy, and insufficient effort by public-health officials to reach nursing homes.

Worldwide, a focus on getting as many shots in arms as possible and boosting population vaccination coverage has tended to leave high-risk individuals unprotected. In low-resource settings, the limited human resources and lack of patient-information systems makes it even harder for

health officials to identify and prioritize vulnerable and hard-to-reach individuals.

As we enter the third year of the pandemic, much more must be done in those settings to prioritize the most vulnerable — including health workers, those who are immunocompromised and older people, as well as disenfranchised populations.

To prioritize the vaccination of vulnerable groups, the World Health Organization (WHO), agencies such as UNICEF and the non-profit aid agency CARE, together with nations that provide aid, technical assistance and vaccines, could work with health officials in low- and middle-income countries. Over the past year, for example, the Ugandan government has worked with the US Centers for Disease Control and Prevention to establish centralized systems for tracking people by age and by medical and vaccination status, and to boost vaccine uptake in priority groups. This has been done in part through the use of clinics and infrastructure set up by the US President's Emergency Plan for AIDS Relief. In Mali, for example, more than 800 health workers were recruited and trained in the past year to conduct community surveys, to improve understanding of local attitudes towards COVID-19 vaccines, and to identify community-specific barriers to vaccinating vulnerable groups.

To be most effective, however, partnerships with local leaders and communication campaigns must be established in advance of a crisis. Investments to help to address the COVID-19 pandemic should result in lasting infrastructure that can be used to address future global health threats.



A community leader and health-care workers talk to schoolchildren in a remote part of the Peruvian Amazon about COVID-19. Credit: Sebastian Castaneda/Reuters

Adult immunization infrastructure. The infrastructure needed for COVID-19 vaccination is different from that for immunizing newborns and children, which global health programmes have supported for decades. For the latter, health-care workers and immunization initiatives can largely focus on providing information and shots in schools and paediatric clinics, or as part of prenatal care programmes. But in the case of COVID-19 vaccines, all age groups (usually above the age of five) must be reached across vastly diverse settings.

As such, the COVID-19 pandemic offers a rare opportunity to build on existing health systems to improve adult immunization infrastructure across low-income settings.

More people, from medical students to pharmacists, could be trained and mobilized to help with community outreach and vaccine administration in local clinics. Mobile vaccination clinics could be set up to reach people

where they live, work or socialize. In addition, community-specific education and messaging campaigns could be launched. In Zambia, for example, the US Agency for International Development (USAID) has supported health workers' door-to-door community outreach and COVID-19 vaccination events at stadiums and hair salons.

Building lasting adult immunization programmes in poorer nations would help to support any future need to provide boosters against COVID-19 variants, as well as bolster the response to a future pandemic and potential vaccination campaigns against other diseases, such as yellow fever and tuberculosis. Brazil, which has otherwise struggled in its pandemic response, achieved high rates of COVID-19 vaccination because of its well-established national immunization programme for children and adults, which is embedded in the primary health-care system.

Yet, to achieve all this, the United States, along with other governments and donors, must provide poorer countries with more financial and other support.

Just \$150 million of the \$3.5 billion that COVAX received in 2020 was for vaccine delivery (see go.nature.com/36jytcu). And according to Seth Berkley, chief executive of Gavi, the Vaccine Alliance, the international funding for getting shots into arms has run out. Last month, the White House asked the US Congress for \$5 billion to support global vaccination. This amount — which has yet to be provided — is roughly one-quarter of the \$19.5 billion that [USAID originally requested](#) to accelerate the uptake of COVID-19 vaccines globally.

Vaccine misinformation and disinformation. Globally, governments have underestimated the extent to which rampant disinformation impedes vaccination campaigns.

Targeted approaches, such as those involving community leaders discussing the benefits and risks of COVID-19 vaccination, can help to improve uptake in groups that have historical distrust in government interventions. In the United States, community-based vaccination efforts within the Navajo Nation helped to vaccinate adults at a rate that exceeded the US national average as of April last year (see go.nature.com/3irgecf). But evidence-based approaches with much broader reach will be crucial — both to address

this problem at scale in the COVID-19 pandemic, and to ensure that governments and health officials are better equipped to deal with misinformation and disinformation in a future pandemic.

Some governments, such as the United States, are better placed than others to combat vaccine misinformation and disinformation. A 2021 report by the non-profit Center for Countering Digital Hate (CCDH) determined that more than two-thirds of the COVID-19 misinformation and disinformation online could be attributed to 12 individuals on social media.⁷ Noting insufficient action by social-media companies to remove these people from their platforms, the CCDH has called on the US government to overhaul Section 230 of the US Communications Decency Act of 1996. This protects social-media companies from liability stemming from harms caused by content posted by users.

Until social-media firms or the US government take action to address disinformation at its source, social media will need to be continually monitored for untruths about vaccines, and evidence-based counter-narratives developed. Countries might need to do this for themselves, but given the common sources of vaccine falsehoods, a global monitoring effort could help.



A person with COVID-19 is taken to a hospital in Hong Kong in February 2022 as the region deals with a severe wave of infections. Credit: Emmanuel Serna/SOPA Images/LightRocket/Getty

The WHO, which warned of the existence of an ‘infodemic’ around COVID-19 as early as February 2020, might be able to help monitor and respond to some of the COVID-19 vaccine misinformation and disinformation that continue to arise. For instance, it could disseminate counter-information — in ways that capture enough people’s attention — to essentially drown out the false claims. But the WHO will need extra financial and technical resources to better fulfil this role.

Global capacity should also be expanded to monitor vaccine- and disease-related misinformation and disinformation; to understand what makes certain information spread so widely; and to develop and disseminate effective evidence-based counter-narratives.

Before the broad authorization of COVID-19 vaccines, the CCDH monitored anti-vaccination groups online and identified the ‘playbook’ these groups were planning to use to undermine vaccination efforts⁸.

Understanding the strategies of these groups is crucial to developing campaigns that debunk false information.

Regional vaccine manufacturing. Wealthy nations should provide greater financial and technical support to create vaccine-manufacturing hubs in underserved regions, to ensure earlier and more equitable global access to vaccines in future pandemics.

There have been welcome steps in this direction in Africa. The continent is the world's most underserved, importing 99% of the vaccines its populations use (see go.nature.com/36wcbre). Unsurprisingly, it also has the lowest COVID-19 vaccination rate in the world: just one in seven people there is fully vaccinated (see go.nature.com/38kusu4).

But in April 2021, Africa CDC launched Partnerships for African Vaccine Manufacturing (see go.nature.com/3wg2ysd). This framework aims to attract international investment, promote technology transfer, support local R&D and improve regional regulatory capacity. The aim is that, by 2040, 60% of all vaccines used on the continent will be produced there.

In recent months, the [US International Development Finance Corporation](#) (a development finance institution), the African Development Bank and the European Commission have [promised financial support for vaccine manufacturing in Africa](#).

What's more, in November 2020 the US-based company Johnson & Johnson signed a deal for ['fill-and-finish' manufacturing of its viral-vector COVID-19 vaccine in South Africa](#) (in which vials are filled with vaccine and packaged for distribution). Pfizer and BioNTech signed an agreement in July 2021 [to do the same for their vaccine](#). And in October 2021, the US-based biotechnology company Moderna announced [plans to build a production facility for 500 million annual doses](#) of messenger RNA (mRNA) vaccines in Africa, which it later indicated will be located in Kenya.

In addition to this, over the past year, the governments of around ten African nations — including Algeria, Egypt, Rwanda, Côte d'Ivoire, Ghana and Nigeria — have either [signed agreements to engage in manufacturing COVID-19 mRNA vaccines](#), or formally expressed an interest in doing so.

An emerging risk is that vaccine manufacturing efforts in Africa will become too heavily focused on a single platform — mRNA technology. The only approved mRNA vaccines so far are those for COVID-19; it is not yet clear whether mRNA vaccines will prove useful against diseases that must be tackled as a matter of routine in Africa, such as malaria and tuberculosis. Ultimately, however, decisions over the prioritization of manufacturing capacity and vaccine platforms are for governments in Africa and other underserved regions to make.

Also, so far, the partnerships involving the major COVID-19 vaccine manufacturers, such as Moderna, have sidestepped licensing their technology to third parties through the mRNA vaccine technology transfer hub. The hub was established by the WHO and other partners in June 2021 in Cape Town, South Africa, specifically to try to encourage licensing and the sharing of technology and technical know-how with local vaccine producers. However, Afrigen Biologics, a South African company, is working with the hub to develop a vaccine based on the Moderna vaccine.

The World Bank can help to support vaccine manufacturing in Africa and elsewhere by creating mechanisms to mobilize surge finance in future pandemics. It could also work with regional entities, such as the Africa CDC, to bolster pooled-procurement mechanisms such as the African Vaccine Acquisition Trust, a centralized vaccine-purchasing agent that acts on behalf of the African Union.

Governments should also [support efforts at the World Trade Organization](#) to limit or eliminate the use of export restrictions on vaccines and other essential medical supplies during pandemics.

Lastly, the governments of wealthy countries and the academic and philanthropic funders of vaccine research and development can include provisions in their licensing agreements and guidelines to require or encourage the [transfer of pandemic-relevant technology to qualified producers in underserved regions](#). Such funders can also work with recipient nations to provide training, perhaps through exchange programmes with vaccine manufacturers overseas, to help ensure that production meets international regulatory standards.

Many movies and novels about deadly disease outbreaks end the same way: with people lining up gratefully to receive a cure or vaccine that scientists have raced to discover. The response to COVID-19 has lost that plot. But is not too late to change the narrative and ensure that global vaccination efforts better match the remarkable achievement of vaccine science.

Nature **603**, 788-792 (2022)

doi: <https://doi.org/10.1038/d41586-022-00809-w>

References

1. Bollyky, T. J. *et al. Navigating the World That COVID-19 Made: A Strategy for Revamping the Pandemic Research and Development Preparedness and Response Ecosystem* (Johns Hopkins Center for Health Security, 2021).
2. Pandemic Preparedness Partnership. *100 Days Mission to Respond to Future Pandemic Threats*. (United Kingdom Cabinet Office, 2021)
3. US National Institute of Allergy and Infectious Diseases. *NIAID Pandemic Preparedness Plan December 2021* (NIAID, 2021).
4. Mancini, D. P. ‘Cash shortages mean Covax cannot accept new doses, says executive’. *Financial Times* (25 January 2022).
5. Andrews, N. *et al. N. Engl. J. Med.* <https://doi.org/10.1056/NEJMoa2119451> (2022).
6. Barnes, O., Burn-Murdoch, B., Riordan, P. & Lin, A. ’Hong Kong Omicron deaths expose limits of fraying zero-Covid policy’. *Financial Times* (14 March 2022).
7. Center for Countering Digital Hate. *The Disinformation Dozen* (CCDH, 2021).
8. Center for Countering Digital Hate. *The Anti-vax Playbook* (CCDH, 2020).

This article was downloaded by **calibre** from <https://www.nature.com/articles/d41586-022-00809-w>

| [Section menu](#) | [Main menu](#) |

- CORRESPONDENCE
- 29 March 2022

Russia is weaponizing water in its invasion of Ukraine

- [Hussam Hussein](#) 0

Water supplies are increasingly being targeted during armed conflicts. Since it invaded Ukraine last month, Russia has cut off the water supply to the besieged city of Mariupol to drive it to surrender. It has also destroyed a canal dam that Ukraine constructed in 2014 to control the water supply into Crimea after Russia annexed the peninsula.

Water resources and infrastructure have been attacked in other conflicts. In 2014, the Islamist terrorist group ISIS cut off water to Mosul in northern Iraq and threatened to use the dam there to flood Baghdad. Also in 2014, Syrian government forces targeted the country's ISIS-controlled water plant in Raqqa and, in 2016, they attacked the Fijeh Spring in the besieged Wadi Barada valley ([M. Daoudy *Int. Affairs* 96, 1347–1366; 2020](#)).

It is imperative that international humanitarian law be respected in relation to fresh-water supplies. The Geneva List of Principles on the Protection of Water Infrastructure sets out international rules for application during armed conflicts and makes valuable recommendations that go beyond existing law (see [go.nature.com/3nnznww](#)). Attempts to override these protective mechanisms should not be tolerated.

Nature **603**, 793 (2022)

doi: <https://doi.org/10.1038/d41586-022-00865-2>

This article was downloaded by **calibre** from <https://www.nature.com/articles/d41586-022-00865-2>

| [Section menu](#) | [Main menu](#) |

- CORRESPONDENCE
- 29 March 2022

Together, we must help refugee researchers to thrive

- [Peter Gluckman](#) 0

Many scientists and engineers fleeing armed conflicts remain in refugee camps or are underemployed in their new host countries (see [*Nature* 598, 527–529; 2021](#)) — a situation of renewed urgency since Russia’s invasion of Ukraine. Beyond meritorious efforts to support individuals, we need to work out how best to help displaced scholars to thrive.

Access options

Subscribe to Nature+

Get immediate online access to the entire Nature family of 50+ journals

\$29.99

monthly

[Subscribe](#)

Subscribe to Journal

Get full journal access for 1 year

\$199.00

only \$3.90 per issue

Subscribe

All prices are NET prices.
VAT will be added later in the checkout.
Tax calculation will be finalised during checkout.

Buy article

Get time limited or full article access on ReadCube.

\$32.00

Buy

All prices are NET prices.

Additional access options:

- [Log in](#)
- [Learn about institutional subscriptions](#)

Nature **603**, 793 (2022)

doi: <https://doi.org/10.1038/d41586-022-00863-4>

This article was downloaded by **calibre** from <https://www.nature.com/articles/d41586-022-00863-4>

| [Section menu](#) | [Main menu](#) |

- CORRESPONDENCE
- 29 March 2022

Open access: Brazilian scientists denied waivers and discounts

- [Alicia Kowaltowski](#)⁰,
- [Michel Naslavsky](#)¹ &
- [Mayana Zatz](#)²

A study comparing open-access versus paywalled publications finds less geographical diversity among authors who choose open access (see [Nature](#) <https://doi.org/gpkt87>; 2022). This does not surprise us in Brazil, where article-processing charges (APCs) typically correspond to many months, or even years, of a scientist's stipend. Yet we are not eligible for waivers or discounts under the open-access initiative Plan S (see go.nature.com/3d1qh), or for research-accessibility programmes such as Research4Life.

Both schemes support publications from low-income and lower-to-middle-income economies. Because Brazil is classed as an upper-middle-income economy, requests for APC waivers and discounts are generally turned down, in our experience. Many of us opt instead to publish behind paywalls. But that might not be possible after 2024, when Plan S transformative agreements will end and journals will transition to exclusively publishing open-access content.

If the open-access movement genuinely favours inclusion, authors in the global south must be able to publish papers as well as read them without barriers. Plan S and the principal editorial companies must consider the extraordinary differences in national scientific budgets and investment. They should offer upper-middle-income countries, such as Brazil, significant discounts or APC waivers upfront (see go.nature.com/3ipsh).

Nature **603**, 793 (2022)

doi: <https://doi.org/10.1038/d41586-022-00864-3>

This article was downloaded by **calibre** from <https://www.nature.com/articles/d41586-022-00864-3>

| [Section menu](#) | [Main menu](#) |

- CORRESPONDENCE
- 29 March 2022

Chile's science ambitions — three notes of caution

- [Pablo Astudillo](#) [ORCID: http://orcid.org/0000-0002-2472-8595](#) 9

I agree that Chile's new government offers fresh hope for the country's science (see [Nature 603, 560–561; 2022](#)). But, as an erstwhile advocate for the Ministry for Science, Technology, Knowledge and Innovation founded in 2018, I sound three notes of caution to help shape its policies for later this year.

Access options

Subscribe to Nature+

Get immediate online access to the entire Nature family of 50+ journals

\$29.99

monthly

[Subscribe](#)

Subscribe to Journal

Get full journal access for 1 year

\$199.00

only \$3.90 per issue

Subscribe

All prices are NET prices.
VAT will be added later in the checkout.
Tax calculation will be finalised during checkout.

Buy article

Get time limited or full article access on ReadCube.

\$32.00

Buy

All prices are NET prices.

Additional access options:

- [Log in](#)
- [Learn about institutional subscriptions](#)

Nature **603**, 793 (2022)

doi: <https://doi.org/10.1038/d41586-022-00862-5>

This article was downloaded by **calibre** from <https://www.nature.com/articles/d41586-022-00862-5>

Work

- **Science competitions can help to catapult your science into the real world** [28 February 2022]
Career Feature • Innovation challenges offer valuable lessons and resources for researcher-entrepreneurs.
- **Up for crabs: making a home for red-clawed crustaceans in Taiwan** [28 March 2022]
Where I Work • Chia-Hsuan Hsu's conservation efforts combine social science and ecological research.

- CAREER FEATURE
- 28 February 2022

Science competitions can help to catapult your science into the real world

Innovation challenges offer valuable lessons and resources for researcher-entrepreneurs.

- [Andy Tay](#) ⁰

[Find a new job](#)



Credit: Getty

Public and private institutions around the world are making use of science competitions to tap the brains of international talents. For the most high-profile contests, such as the ‘Feed the Next Billion’ challenge from the XPRIZE foundation and the Earthshot Prize, awards can run into millions of dollars — a life-changing amount for aspiring researcher-entrepreneurs.

Nature spoke to contest organizers, investors and winners about their take-home messages, tips for emerging victorious and ways to use competitions to get a head start in innovation and entrepreneurship.

LIANNA GENOVESE: The winner

Chief executive and founder of ImaginAble Solutions in Hamilton, Canada.

When I was a biomedical and mechanical engineering undergraduate student at McMaster University in Hamilton, Canada, I won the Canadian National James Dyson Award 2021 — which aims to inspire university-level students to solve societal problems using engineering designs. My winning idea was an assistive medical device that enables individuals with limited hand mobility to write, draw and use a touch-screen device. This project started in my first year after I met and was inspired by Elissa James — a talented painter with cerebral palsy. After we met, her condition had deteriorated to the point where she needed help to continue painting: so I started thinking about what device I could develop.

The Dyson competition pushed me to think hard about my designs. I knew that I was up against other talented inventors, and to have a chance of making a real-world impact (one of the judging criteria), my design had to be ergonomic. Over the past three years, the design of my device has gone through six iterations, and I have had multiple consultations with health-care professionals and people with limited hand mobility. From the first prototype, made of sponge, straws and pipe cleaners, I now have a product, named Guided Hands, on the market. We’ve sold 64 devices so far.

Winning the competition significantly enhanced the publicity of my start-up company. On the day the result was announced, there were more than 1,000 visitors to my company’s website, and over the next 3 months the traffic

remained high. I didn't have the expertise, time or money for lots of marketing, but as a winner I could now ride on Dyson's marketing effort and channel my own precious resources into building other aspects of my business, such as hiring staff and prototyping.

Most importantly, as the winner of a prestigious competition, I know that my innovation gained immediate credibility. I have health-care organizations from all around the world contacting me for collaboration and to test our product. The people we aim to reach and their caregivers are also more willing to try our product and give us feedback, which we can use to improve our design.

I would advise researcher-entrepreneurs to first apply for a patent to legally protect their ideas before entering science competitions. There is plenty of information about these competitions online: you can start by searching keywords that are specific to a field or subscribing to mailing lists of entrepreneurship societies to stay updated.

However, finding contests and entering them can distract from other aspects of having a start-up. Time is often short, especially when you're applying to take part in competitions: many require extra information and reports, which might take focus away from the day-to-day operations of a business. But overall, I'd say for me the time investment has been worth it.



Lianna Genovese won the Canadian National James Dyson Award in 2021. Credit: James Dyson Team

ULRICH BETZ: The business person

Vice-president of Innovation at Merck, Darmstadt, Germany.

The Merck Innovation Cup brings graduate students and postdocs from around the world into our pharmaceutical company for a week. They develop innovative ideas and business plans to solve unmet medical needs with support from experienced professionals. We've been running the competition since 2011. Once in the programme, the participants are selected on the basis of innovative ideas they submit, and then grouped in teams of five, and mentored by an alumnus of the challenge. The participants then decide which of the submitted ideas they wish to pursue over the week to win the grand prize of €20,000 (US\$22,700).

Joining competitions can be a useful way for researcher-entrepreneurs to learn what appeals to investors and companies — training that many academic researchers lack. We select winners on the basis of four criteria: innovativeness, probability of success, alignment with the company's focus

and the team's performance in pitching. Participants have told me they've become more confident working in science and business after taking part.

In my opinion, the best outcome of a science competition is the building of collaborative spirit and camaraderie. Unlike many competitions, in which organizers end their interactions with participants after the main event, the Merck Innovation Cup tries to maintain links after the competition. We continually connect with alumni on social media and invite them to alumni symposia. We sometimes also offer participants a chance to join us as paid consultants, or to be involved in our research projects as industry postdocs or academic collaborators when we wish to further develop the winning ideas in Merck.

Over the years, we have had alumni go on to become successful academic scientists, company managers and entrepreneurs. The networks that the participants create with each other during the competition are useful to tap into throughout their careers. Recently, I also learnt that a winning team from 2020 decided to create a bioelectronics start-up, INIA Biosciences, that aims to use ultrasound to interact with the immune system to relieve chronic inflammatory diseases.

More companies and foundations are seeing the advantages of science competitions and are organizing innovation challenges. The organizers benefit from recruiting talented people, gaining fresh ideas and promoting an image of innovativeness. The participants are rewarded with training, network building and prize money. In addition to the Innovation Cup, we also organize events such as the €1 million Future Insight Prize, which is given out annually to honour and enable scientists solving key challenges of humanity.

MARJOLEIN CROOIJMANS: The judge

*Chair of the International Genetically Engineered Machine (iGEM)
Entrepreneurship Program Innovation Community (EPIC), Cambridge,
Massachusetts and PhD Student at Leiden University, Leiden, Netherlands.*

iGEM is a science contest in which approximately 350 international teams compete annually using synthetic biology to solve societal challenges. I competed in 2018, and the positive experience motivated me to continue as a judge and mentor from 2019. iGEM teams identify problems unique to their region, such as rising sea levels in the Netherlands, or global problems such as antibiotic resistance, and come up with innovative solutions. The team I mentored was the overall winner for the ‘Overgraduate’ category in 2020. The researchers’ project, called Rapidemic, aimed to develop a point-of-care diagnostic tool for future infectious diseases.

iGEM has been successful in training researcher-entrepreneurs. There have been at least 175 start-ups based on iGEM projects, and we track these companies and publish updates on them in quarterly reports. Some of the more successful companies include Ginkgo Bioworks in Boston, Massachusetts, which produces industrially useful bacteria, and Opentrons, in New York City, which develops robots to automate biological experiments.

Many participants develop strong ownership of their ideas after iGEM and wish to see these ideas to fruition, but they might not get enough support from their academic institutions. That’s why two years ago, we started iGEM EPIC, which has an international committee of 21 members. After iGEM contests, if participants wish to further develop their ideas into start-ups, they can apply to EPIC, which aims to link participants with mentors from their local regions, as well as providing training programmes on how to write business proposals and pitches. Although we do not yet provide direct funding, we have an extensive network of entrepreneurs and business people, and we aim to provide connections to top-tier early-stage investors and accelerators around the world.

In my opinion, the most important reward from entering a science competition is gaining early insights into problems that our society will face in the future. Some of these problems are local challenges now but have the potential to eventually affect the entire world. Building and being part of a community of like-minded, talented people from around the world can help us to generate creative solutions.

HUICHAN ZHAO: The academic

Associate professor at Tsinghua University, Beijing, China.

I was one of 10 winners selected as a 2021 DAMO Academy Young Fellow out of 365 applicants. The award, which comes with a prize of 1 million yuan (roughly US\$158,000), is organized by Chinese technology giant Alibaba each year to promote scientific and technological innovation by encouraging young Chinese researchers to embark on socially impactful projects. The prize money can be used for various purposes, including laboratory renovations, hiring staff and embarking on research according to the needs of the award winner.

After receiving the prize, there was tremendous interest from investors and people in the industry to translate and bring my technology to market. My research is in the field of soft robotics — robots that have gentle, dexterous components, which have huge potential in areas such as rehabilitative medicine and manufacturing. Specifically, my lab is developing soft materials for use in prosthetics and artificial muscles.

For now, my preference is to continue working in the lab; I don't have concrete plans to commercialize my technology. Nevertheless, the enhanced visibility is great. I get to expand my networks beyond my typical academic circle. In the future, these connections will be helpful when my students and I consider entrepreneurship. And because the award comes from an internationally recognized company, this might attract more interest from talented collaborators and students abroad.

A piece of advice I have for people trying to win science competitions is to have a supportive network that includes people from your professional and social circles. For this award, I submitted two letters from my mentors, who are pioneers in my field. Their support probably convinced the selection committee of the potential impact of my research. I also practised my presentation to my family multiple times. This can be helpful because there are often non-experts on the award panel, and you should pitch your presentation at a level suitable for them.

Your family members will also be your strongest critics, which is useful. My family were not shy in telling me what part of my presentation was dry or where I needed to explain myself better.

TING YAN LECK: The investor

Partner at TRIVE Venture Capital, Singapore.

As an investor, there are a few key factors I look for before investing in an idea or start-up. The first is how well the product fits the market, taking into consideration who the specific user of an idea or technology is going to be, the challenges faced by that user and the advantages of the proposed technology over existing solutions. This is followed by an investigation of the market size, business strategy and pricing mechanism.

The technology itself is therefore only one of many considerations. Yet, when researcher-entrepreneurs pitch to investors, they often focus on how useful their technologies are, at the expense of other important points. I once listened to a pitch from a team of engineers about how their data server design could help to improve heat circulation and reduce server temperatures. But the team didn't know how purchasing of servers in data centres works, and how frequently data centres change their servers. The pitch was unsuccessful: they needed more awareness of how the product could work in the wider business context.

Science competitions are helpful because they typically force participants who want to succeed to consider commercial viability at an early stage of their business, before they seriously engage investors. This is how innovation begins — when a real problem is properly defined. I have volunteered as a judge, mentor and speaker at innovation challenges and have experienced first-hand that competitions can train researcher-entrepreneurs to become more creative and sharper in shaping narratives around their business ideas.

Start-ups should be aware that competition organizers might look out for different winning factors. In competitions organized by big companies with established marketing and sales teams, more attention is given to the core of

the technology, whereas in smaller scale competitions, the technology and business plans usually have equal weighting. Start-up founders must also balance participating in competitions and building their companies: there are advantages to participating, but each competition takes time away from the core business, which should remain the main goal.

Nature **603**, 957-959 (2022)

doi: <https://doi.org/10.1038/d41586-022-00581-x>

These interviews have been edited for length and clarity.

This article was downloaded by **calibre** from <https://www.nature.com/articles/d41586-022-00581-x>

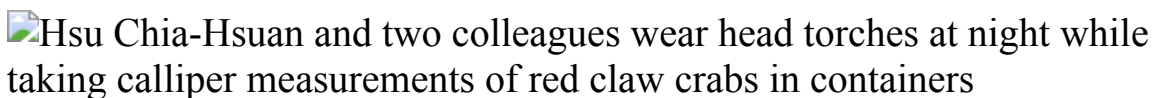
| [Section menu](#) | [Main menu](#) |

- WHERE I WORK
- 28 March 2022

Up for crabs: making a home for red-clawed crustaceans in Taiwan

Chia-Hsuan Hsu's conservation efforts combine social science and ecological research.

- [Flynn Murphy](#) ⁰



Chia-Hsuan Hsu is a postdoctoral researcher at the Graduate Institute of Environmental Education, National Taiwan Normal University. Credit: Ashley Pon for *Nature*

This picture was taken at night in the coastal community of Dakenggu in Yilan County, which is just southeast of Taipei in Taiwan. I'm on the left, working with two other researchers to measure the body size of a red-clawed crab (*Chiromantes haematocheir*).

An old man from the local community told me that years ago, during the breeding season, you could barely cross the road because of all the crabs. He said nobody knows where they all went. They're an important memory for the local people, and part of the culture here.

Habitat loss — especially resulting from the widespread use of concrete — seems to be driving the decline. I'm working with local people to create rocky microhabitats and artificial wetlands for the red-clawed crabs to live in. They're important scavengers — eating dead animals and other organic matter, breaking it down and playing a key part in the nutrient cycle.

Small organisms need our help — they can't stand up for themselves. But in Taiwan, a lot of people think a coastal villa is more important than a few crabs. Corporations want to build luxury developments in our national parks, and authorities often approve them. I've seen so many intact habitats destroyed or covered in concrete.

Crabs caught my interest because they were frequent visitors to my dormitory. National Sun Yat-sen University in Kaohsiung sits in a coastal buffer zone between a mountain and the ocean, and land hermit crabs (*Coenobita cavipes*) have to scurry through it on their way to breed.

After watching habitat after habitat destroyed by overdevelopment, I've realized that just doing the science is not enough. It doesn't matter how many papers you publish: you need to connect with people through education and communication. That's why I decided to do my PhD in social science. And it's why I believe conservation will be my life's work.

Nature **603**, 962 (2022)

doi: <https://doi.org/10.1038/d41586-022-00810-3>

This article was downloaded by **calibre** from <https://www.nature.com/articles/d41586-022-00810-3>

Research

- **[Bacteria swim faster when obstacles keep them in line](#)** [30 March 2022]
News & Views • Adding particles or polymers to a fluid can make bacteria swim straighter — and therefore faster — than they do through water, by inducing a torque that changes their body alignment.
- **[Mobile mantle could explain volcanic hotspot locations](#)** [30 March 2022]
News & Views • Ancient records of Earth's magnetic field seem to contradict a conceptual picture of how regions of volcanic activity form. Statistical modelling now reconciles these data with our understanding of mantle fluid dynamics.
- **[Mucus secretion blocked at its source in the lungs](#)** [23 March 2022]
News & Views • Higher than normal secretion of mucin, a molecular component of mucus, is a feature of many lung diseases. The development of a peptide that blocks mucin secretion in airway epithelial cells might lead to therapies.
- **[From the archive: fishy business in 1972 and 1922](#)** [29 March 2022]
News & Views • Snippets from Nature's past.
- **[Constrained human genes under scrutiny](#)** [23 March 2022]
News & Views Forum • A higher number of damaging variations in certain genes is associated with an increased likelihood that a man will be childless. A geneticist and an anthropologist discuss what can — and can't — be learnt from this finding.
- **[Critical advances and future opportunities in upcycling commodity polymers](#)** [30 March 2022]
Perspective • Methods for the transformation of plastics into materials with value, known as plastic waste upcycling, are outlined, and their advantages and challenges in terms of a sustainable plastics economy are discussed.
- **[A highly magnified star at redshift 6.2](#)** [30 March 2022]
Article • A massive star at a redshift of 6.2, corresponding to 900 million years after the Big Bang, is magnified greatly by lensing of the foreground galaxy cluster WH0137–08.
- **[The colloidal nature of complex fluids enhances bacterial motility](#)** [30 March 2022]

Article • Bacteria swimming in colloidal suspensions are shown to behave similarly to those in polymer solutions revealing a mechanism for motile behaviour in complex fluids.

- **Catalogue of flat-band stoichiometric materials** [30 March 2022]

Article • A catalogue of the naturally occurring three-dimensional stoichiometric materials with flat bands around the Fermi level provides a powerful search engine for future theoretical and experimental studies.

- **Orbital-resolved visualization of single-molecule photocurrent channels** [30 March 2022]

Article • Atomic-level imaging of photocurrents in a single molecule is achieved by combining a tunable laser with scanning tunnelling microscopy, revealing how photons turn into electric current via a photoexcited molecule.

- **Observing polymerization in 2D dynamic covalent polymers** [30 March 2022]

Article • In situ scanning tunnelling microscopy reveals the dynamic nature of the early stages of two-dimensional (2D) polymer formation and crystallization at the solid–liquid interface.

- **Trends in Europe storm surge extremes match the rate of sea-level rise** [30 March 2022]

Article • Analysis of tide gauge observations shows that, in contrast to the current assumption of stationary storm surge extremes in Europe, the surge contribution to changes in extreme sea levels since 1960 is similar to that of sea-level rise, influencing future coastal planning.

- **Assembly of the basal mantle structure beneath Africa** [30 March 2022]

Article • Reconstruction of one billion years of mantle flow shows that mobile basal mantle structures are just as consistent with the Earth’s volcanic history as are fixed mantle structures.

- **Subaqueous foraging among carnivorous dinosaurs** [23 March 2022]

Article • In extinct species including non-avian dinosaurs, bone density is shown to be a reliable indicator of aquatic behavioural adaptations, which emerged in spinosaurids during the Early Cretaceous.

- **Reduced reproductive success is associated with selective constraint on human genes** [23 March 2022]

Article • Human genetic variants that impair genes that are intolerant of damaging genetic variation are associated with lower reproductive success that is probably mediated by genetically associated cognitive and behavioural traits, particularly in males.

- **Machine learning and phone data can improve targeting of humanitarian aid** [16 March 2022]

Article • Machine-learning algorithms can take advantage of survey and mobile phone data to help to identify people most in need of aid, complementing traditional methods for targeting humanitarian assistance.

- **The development and evolution of inhibitory neurons in primate cerebrum** [23 March 2022]

Article • Evolutionary modelling shows that an initial set of inhibitory neurons serving olfactory bulbs may have been repurposed to diversify the taxonomy of interneurons found in the expanded striata and cortices in primates.

- **A multidimensional coding architecture of the vagal interoceptive system** [16 March 2022]

Article • Single-cell profiling of vagal sensory neurons from seven organs in mice and calcium-imaging-guided spatial transcriptomics reveal that interoceptive signals are coded through three distinct dimensions, allowing efficient processing of multiple signals in parallel using a combinatorial strategy.

- **A human brain vascular atlas reveals diverse mediators of Alzheimer's risk** [14 February 2022]

Article • A method called vessel isolation and nuclei extraction for sequencing (VINE-seq) produces a molecular map of vascular and perivascular cell types in the human brain and reveals their contributions to Alzheimer's disease risk.

- **Single-cell dissection of the human brain vasculature** [14 February 2022]

Article • A study describes single-cell characterization of the human cerebrovasculature, revealing human-specific transcriptomic signatures and providing insights into transcriptional changes associated with Huntington's disease.

- **Bacterial inhibition of Fas-mediated killing promotes neuroinvasion and persistence** [16 March 2022]

Article • Studies in a mouse model of neurolisteriosis show that the effector protein InlB produced by Listeria monocytogenes protects infected monocytes in the host from T cell-mediated cell death, and thereby increases bacterial neuroinvasion, persistence and transmission.

- **Human gut bacteria produce TH17-modulating bile acid metabolites** [16 March 2022]

Article • Bacterially produced bile acids inhibit TH17 cell function, which may be relevant to the pathophysiology of inflammatory disorders such as inflammatory bowel disease.

- **ACE2 binding is an ancestral and evolvable trait of sarbecoviruses** [03 February 2022]

Article • ACE2 binding is an ancestral, widespread trait of sarbecovirus receptor-binding domains, and many single mutations enable binding to different ACE2 receptors.

- **Memory B cell repertoire from triple vaccinees against diverse SARS-CoV-2 variants** [28 January 2022]
Article • Individual antibodies identified in the blood of people triple-vaccinated against SARS-CoV-2 predominantly bind spike protein and are highly effective at neutralizing SARS-CoV-2 variants, including Omicron (B.1.1.529).
- **A single-cell atlas of human and mouse white adipose tissue** [16 March 2022]
Article • A single-cell atlas of white adipose tissue from mouse and human reveals diverse cell types and similarities and differences across species and dietary conditions.
- **GD2-CAR T cell therapy for H3K27M-mutated diffuse midline gliomas** [07 February 2022]
Article • A phase I dose-escalation trial of GD2-CAR T cells in children and young adults with diffuse midline gliomas to assess the feasibility of manufacturing, safety and tolerability, and to preliminarily assess efficacy.
- **Nivolumab plus chemotherapy or ipilimumab in gastro-oesophageal cancer** [23 March 2022]
Article • Results in the CheckMate 649 phase 3 trial for first-line combined nivolumab and chemotherapy treatment continue to show clinically meaningful efficacy in gastric, gastro-oesophageal junction or oesophageal adenocarcinoma after 24 months, with no new safety signals.
- **Inhibition of calcium-triggered secretion by hydrocarbon-stapled peptides** [23 March 2022]
Article • Peptides that disrupt Ca²⁺-triggered membrane fusion may enable the therapeutic modulation of mucin secretory pathways.

- NEWS AND VIEWS
- 30 March 2022

Bacteria swim faster when obstacles keep them in line

Adding particles or polymers to a fluid can make bacteria swim straighter — and therefore faster — than they do through water, by inducing a torque that changes their body alignment.

- [Raphaël Jeanneret](#) ⁰ &
- [Marco Polin](#) ¹

It might come as a surprise that bacteria can swim tens of times their body length in a single second. This is equivalent to a human swimming 100 metres in less than 5 seconds. Even more surprising, however, is that bacteria sometimes swim even faster — not slower — than this when the fluid around them is filled with myriad obstacles that increase its viscosity. Such fluids are known as complex fluids, and they are found, for example, in our lungs and lining our stomach. [Writing in Nature](#), Kamdar *et al.*¹ show that the mysterious ability of bacteria to swim faster in complex fluids is actually the result of a remarkably simple effect: they swim straighter.

Access options

Subscribe to Nature+

Get immediate online access to the entire Nature family of 50+ journals

\$29.99

monthly

Subscribe

Subscribe to Journal

Get full journal access for 1 year

\$199.00

only \$3.90 per issue

Subscribe

All prices are NET prices.

VAT will be added later in the checkout.

Tax calculation will be finalised during checkout.

Buy article

Get time limited or full article access on ReadCube.

\$32.00

Buy

All prices are NET prices.

Additional access options:

- [Log in](#)
- [Learn about institutional subscriptions](#)

Nature **603**, 795–796 (2022)

doi: <https://doi.org/10.1038/d41586-022-00853-6>

References

1. Kamdar, S. *et al.* *Nature* **603**, 819–823 (2022).

2. Verdugo, P. *et al.* *Mar. Chem.* **92**, 67–85 (2004).
 3. Shoesmith, J. G. *J. Gen. Microbiol.* **22**, 528–585 (1960).
 4. Schneider, W. R. & Doetsch, R. N. *J. Bacteriol.* **117**, 696–701 (1974).
 5. Qu, Z. & Breuer, K. S. *Phys. Rev. Fluids* **5**, 073103 (2020).
 6. Patteson, A. E., Gopinath, A., Goulian, M. & Arratia, P. E. *Sci. Rep.* **5**, 15761 (2015).
 7. Spöring, I. *et al.* *PLoS Biol.* **16**, e2006989 (2018).
-

This article was downloaded by **calibre** from <https://www.nature.com/articles/d41586-022-00853-6>

| [Section menu](#) | [Main menu](#) |

- NEWS AND VIEWS
- 30 March 2022

Mobile mantle could explain volcanic hotspot locations

Ancient records of Earth's magnetic field seem to contradict a conceptual picture of how regions of volcanic activity form. Statistical modelling now reconciles these data with our understanding of mantle fluid dynamics.

- [Allen K. McNamara](#) 

The speed of seismic waves can reveal the temperature of structures under Earth's surface, with faster waves indicating cooler temperatures and slower waves, warmer ones. Unusually low wave speeds have been measured¹ beneath the African continent and the Pacific Ocean, and these regions are known as large low-shear-velocity provinces (LLSVPs). Palaeomagnetic data provide an ancient record of Earth's magnetic field, and have been interpreted as evidence that the LLSVPs have remained fixed in their current positions for several hundred million years^{2,3}. But this conclusion is at odds with our understanding of how mantle convects⁴. [Writing in Nature](#), Flament and colleagues⁵ report simulations showing that palaeomagnetic data cannot distinguish between fixed and mobile LLSVPs — a finding that reconciles these observations with mantle fluid dynamics.

Access options

Subscribe to Nature+

Get immediate online access to the entire Nature family of 50+ journals

\$29.99

monthly

[Subscribe](#)

Subscribe to Journal

Get full journal access for 1 year

\$199.00

only \$3.90 per issue

[Subscribe](#)

All prices are NET prices.

VAT will be added later in the checkout.

Tax calculation will be finalised during checkout.

Buy article

Get time limited or full article access on ReadCube.

\$32.00

[Buy](#)

All prices are NET prices.

Additional access options:

- [Log in](#)
- [Learn about institutional subscriptions](#)

Nature **603**, 796-797 (2022)

doi: <https://doi.org/10.1038/d41586-022-00854-5>

References

1. McNamara, A. K. *Tectonophysics* **760**, 199–220 (2019).
2. Torsvik, T. H., Burke, K., Steinberger, B., Webb, S. J. & Ashwal, L. D. *Nature* **466**, 352–355 (2010).
3. Torsvik, T. H., Smethurst, M. A., Burke, K. & Steinberger, B. *Earth Planet. Sci. Lett.* **267**, 444–452 (2008).
4. Bower, D. J., Gurnis, M. & Seton, M. *Geochem. Geophys. Geosyst.* **14**, 44–63 (2013).
5. Flament, N., Bodur, Ö. F., Williams, S. E. & Merdith, A. S. *Nature* **603**, 846–851 (2022).
6. Thorne, M. S., Garnero, E. J. & Grand, S. P. *Phys. Earth Planet. Inter.* **146**, 47–63 (2004).
7. Burke, K. & Torsvik, T. H. *Earth Planet. Sci. Lett.* **227**, 531–538 (2004).
8. Burke, K., Steinberger, B., Torsvik, T. H. & Smethurst, M. A. *Earth Planet. Sci. Lett.* **265**, 49–60 (2008).
9. Hofmann, A. W. & White, W. M. *Earth Planet. Sci. Lett.* **57**, 421–436 (1982).
10. Tackley, P. J. *Science* **288**, 2002–2007 (2000).
11. Zhao, C., Garnero, E. J., McNamara, A. K., Schmerr, N. & Carlson, R. W. *Earth Planet. Sci. Lett.* **426**, 143–153 (2015).

This article was downloaded by **calibre** from <https://www.nature.com/articles/d41586-022-00854-5>

- NEWS AND VIEWS
- 23 March 2022

Mucus secretion blocked at its source in the lungs

Higher than normal secretion of mucin, a molecular component of mucus, is a feature of many lung diseases. The development of a peptide that blocks mucin secretion in airway epithelial cells might lead to therapies.

- [Irina Gitlin](#)⁰ &
- [John V. Fahy](#)¹

Excessive production and secretion of mucins (the gel-forming protein components of mucus) contribute to the formation of mucus that causes blockade of the airways in many lung conditions¹. Mucins are produced by goblet cells (a type of epithelial cell that lines the airways) and by mucous cells in submucosal glands. They are packaged intracellularly in vesicles called secretory granules. Molecules that stimulate mucin secretion (termed mucin secretagogues), such as ATP, initiate a signalling cascade that results in calcium-ion-triggered fusion of the granule and cell membranes². The proteins that mediate this fusion include SNARE proteins, which are located mainly in the cell membrane, and a calcium-sensor protein called synaptotagmin-2 that is present in the granule membrane. [Writing in Nature](#), Lai *et al.*³ report that an engineered peptide disrupts the interaction of the SNARE complex with synaptotagmin-2, thereby blocking mucin secretion both *in vitro* and *in vivo*.

Access options

Subscribe to Nature+

Get immediate online access to the entire Nature family of 50+ journals

\$29.99

monthly

[Subscribe](#)

Subscribe to Journal

Get full journal access for 1 year

\$199.00

only \$3.90 per issue

[Subscribe](#)

All prices are NET prices.

VAT will be added later in the checkout.

Tax calculation will be finalised during checkout.

Buy article

Get time limited or full article access on ReadCube.

\$32.00

[Buy](#)

All prices are NET prices.

Additional access options:

- [Log in](#)
- [Learn about institutional subscriptions](#)

Nature **603**, 798-799 (2022)

References

1. Ridley, C. & Thornton, D. J. *Biochem. Soc. Trans.* **46**, 1099–1106 (2018).
2. Jaramillo, A. M., Azzegagh, Z., Tuvim, M. J. & Dickey, B. F. *Ann. Am. Thorac. Soc.* **15** (Suppl. 3), S164–S170 (2018).
3. Lai, Y. *et al.* *Nature* **603**, 949–956 (2022).
4. Boucher, R. C. *N. Engl. J. Med.* **380**, 1941–1953 (2019).
5. Fahy, J. V. & Dickey, B. F. *N. Engl. J. Med.* **363**, 2233–2247 (2010).
6. Yuan, S. *et al.* *Sci. Transl. Med.* **7**, 276ra27 (2015).
7. Yang, C. & Montgomery, M. *Cochrane Database Syst. Rev.* **3**, CD001127 (2021).
8. Fahy, J. V., Kim, K. W., Liu, J. & Boushey, H. A. *J. Allergy Clin. Immunol.* **95**, 843–852 (1995).
9. Bartoszewski, R., Matalon, S. & Collawn, J. F. *Am. J. Physiol. Lung Cell. Mol. Physiol.* **313**, L859–L872 (2017).
10. Lillehoj, E. P., Kato, K., Lu, W. & Kim, K. W. *Int. Rev. Cell Mol. Biol.* **303**, 139–202 (2013).
11. Castro, M. *et al.* *N. Engl. J. Med.* **378**, 2486–2496 (2018).
12. Woodruff, P. G. *et al.* *Am. J. Respir. Crit. Care Med.* **181**, 438–445 (2010).
13. Moiola, M., Memeo, M. G. & Quadrelli, P. *Molecules* **24**, 3654 (2019).
14. Verdine, G. L. & Hilinski, G. J. *Methods Enzymol.* **503**, 3–33 (2012).

This article was downloaded by **calibre** from <https://www.nature.com/articles/d41586-022-00700-8>

| [Section menu](#) | [Main menu](#) |

- NEWS AND VIEWS
- 29 March 2022

From the archive: fishy business in 1972 and 1922

Snippets from *Nature*'s past.

50 years ago

Access options

Subscribe to Nature+

Get immediate online access to the entire Nature family of 50+ journals

\$29.99

monthly

[Subscribe](#)

Subscribe to Journal

Get full journal access for 1 year

\$199.00

only \$3.90 per issue

[Subscribe](#)

All prices are NET prices.
VAT will be added later in the checkout.

Tax calculation will be finalised during checkout.

Buy article

Get time limited or full article access on ReadCube.

\$32.00

[Buy](#)

All prices are NET prices.

Additional access options:

- [Log in](#)
- [Learn about institutional subscriptions](#)

Nature **603**, 800 (2022)

doi: <https://doi.org/10.1038/d41586-022-00855-4>

This article was downloaded by **calibre** from <https://www.nature.com/articles/d41586-022-00855-4>

| [Section menu](#) | [Main menu](#) |

- NEWS & VIEWS FORUM
- 23 March 2022

Constrained human genes under scrutiny

A higher number of damaging variations in certain genes is associated with an increased likelihood that a man will be childless. A geneticist and an anthropologist discuss what can — and can't — be learnt from this finding.

- [Loic Yengo](#) ⁰ &
- [Heidi Colleran](#) ¹

THE PAPER IN BRIEF

- Some genes are constrained, which means that damaging variants of them are removed from the population by natural selection.
- [Writing in Nature](#), Gardner *et al.*¹ investigated the processes underlying this evolutionary process in humans.
- They report that having a high overall amount of damaging genetic variation in constrained genes is associated with childlessness in men.
- The association is linked to only 1% of the chance of childlessness between individuals, but to larger effects over many generations in a population.
- The findings are consistent with the hypothesis that having a greater burden of damaging genetic variation might affect a man's ability to find a mating partner.

LOIC YENGO: An evolving understanding of gene constraint

Loss-of-function (LoF) mutations inactivate genes completely. Some genes in a human population are able to ‘tolerate’ LoF mutations, whereas others, known as constrained genes, cannot — LoF variants in constrained genes tend to be lost over time through natural selection. As a result, fewer people would be expected to have LoF variants in a constrained gene than in an LoF-tolerant gene. A large study of human genetic variation carried out by Lek *et al.* in 2016 identified about 3,000 LoF-intolerant genes². Gardner and colleagues’ work might help us to understand how natural selection has constrained them.

It is thought that LoF mutations might affect reproductive fitness — that is, the number of offspring an individual produces. For example, these mutations might reduce the chance of a person living to reproductive age, cause infertility or affect a person’s ability to find a mate. About one-third of the 3,000 constrained genes identified in Lek and colleagues’ study have been linked to disorders associated with mortality before the individual reaches reproductive age and with reduced fertility (according to the Online Mendelian Inheritance in Man database; <https://omim.org>). But whether and how the other genes might affect reproductive fitness has been unclear.

To address this issue, Gardner and colleagues analysed rare protein-truncating mutations in the 3,000 genes in more than 300,000 unrelated individuals who are part of the UK Biobank — a database of genetic and health-related information for 500,000 volunteers in the United Kingdom. This cohort is made up largely of individuals between 39 and 73 years old, ensuring that most have, in principle, had the opportunity to reproduce. The authors quantified the overall association of all protein-truncating mutations and gene deletions with reproductive success. Their main finding is that, cumulatively, LoF variants in these 3,000 genes are associated with childlessness in men but not in women. Interestingly, this association is not mainly driven by reproductive dysfunction. Instead, men with a higher number of deleterious mutations in these genes are more likely than those

with fewer numbers to exhibit behavioural and cognitive traits that might reduce their likelihood of finding a partner.

One of the key implications of these findings is that cultural practices such as mate choice might have had a prominent role in the course of natural selection. The association between mutations constrained in our distant past and modern human behaviours could be a fundamental discovery, suggesting that traits associated with mate choice are the same today as they were thousands of generations ago.

But for studies such as those of Gardner *et al.* and Lek *et al.*, the sample size determines the evolutionary period that the study can tell us about. For example, larger samples are needed to track more-recent natural selection, because more-recent genetic changes will be present in fewer individuals³. And there is a near-sixfold difference in sample size between these two studies. This suggests that the evolutionary period over which the 3,000 genes became constrained might differ from the time over which natural selection has produced the genetic associations with reproductive fitness observed in the UK Biobank. This is a caveat that can weaken Gardner and colleagues' conclusions. But it could be addressed in the future by using a larger, updated list of constrained genes⁴.

Overall, Gardner and colleagues' findings seem to be consistent with Charles Darwin's still-debated theory of sexual selection⁵, which posits that reproductive fitness is partly driven by within-sex competition and mate-choice preferences between sexes. It is important to note, however, that the current associations involve only a limited number of (genetic) factors, which are not sufficient to explain all causes of childlessness. More evidence for the mechanisms underpinning Gardner and colleagues' findings is needed, through replication in other populations (and species), in which mate choice could be influenced by different cultural standards from those of ancestors of the contemporary UK population. This should improve our understanding of the mutational constraints that shape our evolution.

HEIDI COLLERAN: Mate choice beyond genetics

About 20% of people in the United Kingdom never have biological children⁶. Many interacting social, biological and demographic factors contribute to the dynamics of childlessness, whether or not a person is childless by choice. Gardner and colleagues' work highlights one element of this complexity, pointing to a possible connection between human behaviour and genetics as a component of childlessness.

The authors performed a battery of genetic-association analyses that indicate that men (but not women) who have a high number of rare damaging genetic variants are slightly less likely to have children than are those with fewer of these variants. A range of other associations exist, too, although the effects are small in all cases. For instance, both men and women with the highest number of variants are more likely to score lower in intelligence tests than are people with a lower number. They are less likely to have university degrees or high incomes, and are more likely to be socio-economically deprived or have mental-health conditions. The strongest correlation is related to being single: men with a high number of damaging variants were more likely than comparable women to be living alone at the time of data collection.

These results explain less than 1% of the variation in reproductive outcomes between individuals. But, compounded over many generations, the authors infer, this sex difference means that about 20% of the selective pressures that act on these genes as they evolve are attributable to sexual selection — that is, to female mate choice.

First, some crucial caveats. Causality cannot be inferred from any of Gardner and colleagues' results, given the associative nature of the analyses. And even men with the highest numbers of genetic variants have a 50% chance of reproducing, so these aren't 'genes for childlessness'. In addition, the authors have only a snapshot of each individual's relationship status at the time of recruitment to the UK Biobank, and no information about the type or length of their current or past relationships, or their partnership and reproductive preferences. Taken together, these factors would paint a more complex picture of each individual's life, making it harder to draw strong conclusions from these correlations.

Some demographic evidence corroborates Gardner and colleagues' findings: across 13 European countries, men with low incomes are more likely to be childless⁷. But broader demographic factors, which don't always affect men and women symmetrically, also play a part. There are typically more male children born than female. Men more often father children with multiple women than the reverse, and are regularly older than their reproductive partners. In declining populations, these differences can leave a larger proportion of men without partners⁸.

Unpicking many interrelated factors to tease out why men might forgo or miss out on having children is a huge challenge. For instance, poverty has adverse effects on both academic achievement and mental health^{9,10}. Broader social and cultural influences on partnership and reproductive preferences will surely outweigh the 1% of variance explainable by genetic differences.

In a simplified world, in which sexual selection alone determines the chances of having children, one possible assumption might be that men desire sex and reproduction, and that women choose mates who are wealthy and (in contemporary economies) well educated. Gardner and colleagues' work is centred around the genetic outcomes of such a potential scenario, but it is risky to interpret the findings too strongly. We must be careful not to reduce childlessness to a deviation from a presumed (hetero-)norm. To do so plays into problematic narratives about the 'childless' poor being lonely and unwanted, or the 'child-free' rich being selfish.

In fact, there are many more dimensions to mate choice. First, priorities vary between individuals and over time. Although some women might seek educated, neurotypical men to father their (increasingly few) desired children, evidence suggests that, in the United Kingdom, more women currently prioritize kindness and supportiveness (see go.nature.com/3hnvxlv). Second, individuals don't always freely choose their reproductive partners. Arranged marriages, still common today, were historically widespread. Darwin's own marriage didn't clearly follow straightforward sexual-selection criteria: his cousin (and sister-in-law) Emma Wedgwood accepted his proposal largely because of a mutual goal of family consolidation¹¹. The cross-cultural variation in human mating and

marriage practices is vast — inferring human universals from just one population would therefore be premature.

Although the genetics here have little predictive power on an individual level, a key message is that the ways in which we socially construct and organize our biological reproduction — which are at the heart of human social life — might have important genetic legacies at the population level and over many generations. A better understanding of the co-evolution of reproduction, culture and genetics is now crucial¹².

Nature **603**, 799–801 (2022)

doi: <https://doi.org/10.1038/d41586-022-00693-4>

References

1. Gardner, E. J. *et al.* *Nature* **603**, 858–863 (2022).
2. Lek, M. *et al.* *Nature* **536**, 285–291 (2016).
3. Field, Y. *et al.* *Science* **354**, 760–764 (2016).
4. Karczewski, K. J. *et al.* *Nature* **581**, 434–443 (2020).
5. Jones, A. G. & Ratterman, N. L. *Proc. Natl Acad. Sci. USA* **106**, 10001–10008 (2009).
6. Kreyenfeld, M. & Konietzka, D. (eds) in *Childlessness in Europe: Contexts, Causes, and Consequences* 57 (Springer, 2017).
7. Barthold, J., Myrskylä, M. & Jones, O. R. *Evol. Hum. Behav.* **33**, 628–638 (2012).
8. Kravdal, Ø. *Eur. J. Popul.* **37**, 1023–1041 (2021).
9. Murali, V. & Oyeboye, F. *Adv. Psychiat. Treat.* **10**, 216–224 (2004).

10. Blanden, J., Gregg, P. & Machin, S. in *Intergenerational Mobility in Europe and North America* 11 (Institute for Social and Economic Research, 2005).
11. Kuper, A. in *Incest and Influence: The Private Life of Bourgeois England* 3 (Harvard Univ. Press, 2009).
12. Colleran, H. in *Human Evolutionary Demography* (eds Burger, O., Lee, R. & Sear, R.) (Open Book, in the press).

This article was downloaded by **calibre** from <https://www.nature.com/articles/d41586-022-00693-4>

| [Section menu](#) | [Main menu](#) |

- Perspective
- [Published: 30 March 2022](#)

Critical advances and future opportunities in upcycling commodity polymers

- [Coralie Jehanno^{1,6}](#),
- [Jill W. Alty](#) [ORCID: orcid.org/0000-0002-9780-1343²](#),
- [Martijn Roosen³](#),
- [Steven De Meester](#) ³,
- [Andrew P. Dove](#) [ORCID: orcid.org/0000-0001-8208-9309⁴](#),
- [Eugene Y.-X. Chen](#) [ORCID: orcid.org/0000-0001-7512-3484⁵](#),
- [Frank A. Leibfarth](#) [ORCID: orcid.org/0000-0001-7737-0331²](#) &
- [Haritz Sardon](#) [ORCID: orcid.org/0000-0002-6268-0916¹](#)

[Nature](#) volume 603, pages 803–814 (2022)

- 2117 Accesses
- 68 Altmetric
- [Metrics details](#)

Subjects

- [Polymer synthesis](#)
- [Sustainability](#)

Abstract

The vast majority of commodity plastics do not degrade and therefore they permanently pollute the environment. At present, less than 20% of post-consumer plastic waste in developed countries is recycled, predominately for energy recovery or repurposing as lower-value materials by mechanical recycling. Chemical recycling offers an opportunity to revert plastics back to monomers for repolymerization to virgin materials without altering the properties of the material or the economic value of the polymer. For plastic waste that is either cost prohibitive or infeasible to mechanically or chemically recycle, the nascent field of chemical upcycling promises to use chemical or engineering approaches to place plastic waste at the beginning of a new value chain. Here state-of-the-art methods are highlighted for upcycling plastic waste into value-added performance materials, fine chemicals and specialty polymers. By identifying common conceptual approaches, we critically discuss how the advantages and challenges of each approach contribute to the goal of realizing a sustainable plastics economy.

This is a preview of subscription content

Access options

Subscribe to Nature+

Get immediate online access to the entire Nature family of 50+ journals

\$29.99

monthly

[Subscribe](#)

Subscribe to Journal

Get full journal access for 1 year

\$199.00

only \$3.90 per issue

Subscribe

All prices are NET prices.

VAT will be added later in the checkout.

Tax calculation will be finalised during checkout.

Buy article

Get time limited or full article access on ReadCube.

\$32.00

[Buy](#)

All prices are NET prices.

Additional access options:

- [Log in](#)
- [Learn about institutional subscriptions](#)

Fig. 1: Upcycling in the life cycle of plastics and plastic waste.



Fig. 2: Treatment of plastic waste through polymer-to-polymer transformations employing depolymerization–repolymerization methods.

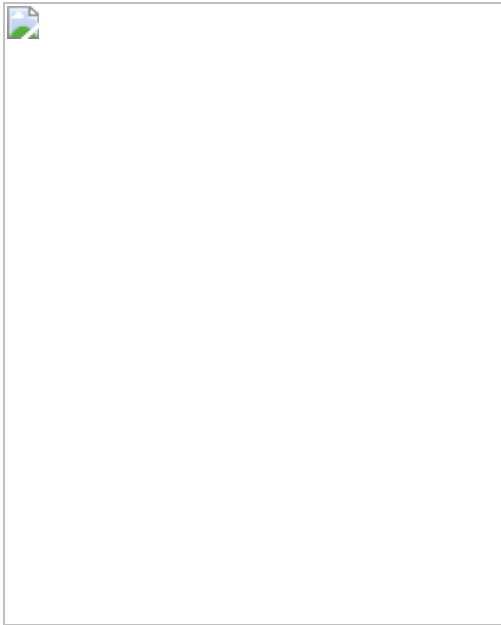


Fig. 3: Treatment of plastic waste through polymer-to-molecule transformations.



Fig. 4: Treatment of waste plastics through polymer-to-material transformations.

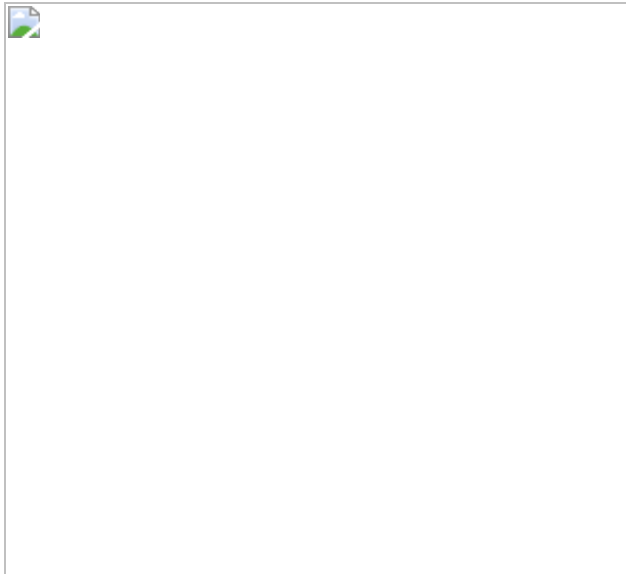
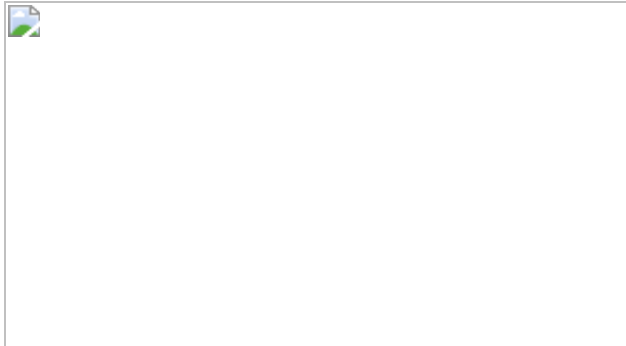


Fig. 5: Carbon footprint calculations for three upcycling cases.



References

1. Plastics—The Facts 2019 (PlasticsEurope, 2019).
2. Vollmer, I. et al. Beyond mechanical recycling: giving new life to plastic waste. *Angew. Chem. Int. Ed.* **59**, 2–24 (2020). **A Review on the different recycling technologies suitable for the reuse or the valorization of plastic wastes in a circular economy perspective.**
3. Lazarevic, D., Aoustin, E., Buclet, N. & Brandt, N. Plastic waste management in the context of a European recycling society: comparing results and uncertainties in a life cycle perspective. *Resour. Conserv. Recycl.* **55**, 246–259 (2010).

4. Antelava, A. et al. Plastic solid waste (PSW) in the context of life cycle assessment (LCA) and sustainable management. *Environ. Manage.* **64**, 230–244 (2019).
5. National overview: facts and figures on materials, wastes and recycling. US EPA <https://www.epa.gov/facts-and-figures-about-materials-waste-and-recycling/national-overview-facts-and-figures-materials> (2017).
6. What a Waste?: A Global Review of Solid Waste Management (World Bank, 2012);
<https://documents.worldbank.org/en/publication/documents-reports/documentdetail/302341468126264791/What-a-waste-a-global-review-of-solid-waste-management>.
7. Ügdüler, S., Van Geem, K. M., Roosen, M., Delbeke, E. I. P. & De Meester, S. Challenges and opportunities of solvent-based additive extraction methods for plastic recycling. *Waste Manage.* **104**, 148–182 (2020).
8. Tournier, V. et al. An engineered PET depolymerase to break down and recycle plastic bottles. *Nature* **580**, 216–219 (2020).
9. Ellis, L. D. et al. Tandem heterogeneous catalysis for polyethylene depolymerization via an olefin-intermediate process. *ACS Sustain. Chem. Eng.* **9**, 623–628 (2021).
10. Ellen MacArthur Foundation. The new plastic economy - catalysing action. <https://ellenmacarthurfoundation.org/the-new-plastics-economy-catalysing-action> (2018).
11. Hong, M. & Y.-X. Chen, E. Chemically recyclable polymers: a circular economy approach to sustainability. *Green Chem.* **19**, 3692–3706 (2017).
12. Schneiderman, D. K. & Hillmyer, M. A. 50th anniversary perspective: there is a great future in sustainable polymers. *Macromolecules* **50**, 3733–3749 (2017). **A Perspective summarizing the most important**

topics for moving to more sustainable polymers: renewable monomers and degradable polymers, the development of chemical recycling strategies, new classes of reprocessable thermosets and the design of advanced catalysts.

13. Rahimi, A. & García, J. M. Chemical recycling of waste plastics for new materials production. *Nat. Rev. Chem.* **1**, 0046 (2017).
14. Jehanno, C., Pérez-Madrigal, M. M., Demarteau, J., Sardon, H. & Dove, A. P. Organocatalysis for depolymerisation. *Polym. Chem.* **10**, 172–186 (2018).
15. Coates, G. W. & Getzler, Y. D. Y. L. Chemical recycling to monomer for an ideal, circular polymer economy. *Nat. Rev. Mater.* **5**, 501–516 (2020). **A Review and point of view on the ideal design for chemical recycling to monomer considering thermodynamic and processing issues.**
16. Ellis, L. D. et al. Chemical and biological catalysis for plastics recycling and upcycling. *Nat. Catal.* **4**, 539–556 (2021).
17. Pauli, G. & Hartkemeyer, J. F. *UpCycling* (Chronik Verlag im Bertelsmann LEXIKON Verlag, 1999).
18. Eriksen, M. K., Damgaard, A., Boldrin, A. & Astrup, T. F. Quality assessment and circularity potential of recovery systems for household plastic waste. *J. Ind. Ecol.* **23**, 156–168 (2019).
19. Vadenbo, C., Hellweg, S. & Astrup, T. F. Let's be clear(er) about substitution: a reporting framework to account for product displacement in life cycle assessment. *J. Ind. Ecol.* **21**, 1078–1089 (2017).
20. Geyer, B., Röhner, S., Lorenz, G. & Kandelbauer, A. Designing oligomeric ethylene terephthalate building blocks by chemical recycling of polyethylene terephthalate. *J. Appl. Polym. Sci.* **131**, 39786–39798 (2014).

21. Kathalewar, M. et al. Chemical recycling of PET using neopentyl glycol: reaction kinetics and preparation of polyurethane coatings. *Prog. Org. Coat.* **76**, 147–156 (2013).
22. Roy, P. K., Mathur, R., Kumar, D. & Rajagopal, C. Tertiary recycling of poly(ethylene terephthalate) wastes for production of polyurethane–polyisocyanurate foams. *J. Environ. Chem. Eng.* **1**, 1062–1069 (2013).
23. Rorrer, N. A. et al. Combining reclaimed PET with bio-based monomers enables plastics upcycling. *Joule* **3**, 1006–1027 (2019).
Recyclates from PET and bio-derived monomers recombined into fibreglass reinforced plastic resulting into an upcycled material with a lower production of energy and greenhouse gas emissions.
24. Kim, J. G. Chemical recycling of poly(bisphenol A carbonate). *Polym. Chem.* **11**, 1830–4849 (2020).
25. Jones, G. O., Yuen, A., Wojtecki, R. J., Hedrick, J. L. & García, J. M. Computational and experimental investigations of one-step conversion of poly(carbonate)s into value-added poly(aryl ether sulfone)s. *Proc. Natl Acad. Sci. USA* **113**, 7722–7726 (2016).
26. Pang, C. et al. Sustainable polycarbonates from a citric acid-based rigid diol and recycled BPA-PC: from synthesis to properties. *ACS Sustain. Chem. Eng.* **6**, 17059–17067 (2018). **The synthesis of innovative amorphous polycarbonates based on a bicyclic diol from naturally occurring citric acid derivatives and recyclates of BPA-PC wastes through melt polycondensation.**
27. Saito, K. et al. From plastic waste to polymer electrolytes for batteries through chemical upcycling of polycarbonate. *J. Mater. Chem. A* **8**, 13921–13926 (2020).
28. Wu, C.-H., Chen, L.-Y., Jeng, R.-J. & Dai, S. A. 100% atom-economy efficiency of recycling polycarbonate into versatile intermediates. *ACS Sustain. Chem. Eng.* **6**, 8964–8975 (2018).

29. Sohn, Y. J. et al. Recent advances in sustainable plastic upcycling and biopolymers. *Biotechnol. J.* **15**, 1900489 (2020).
30. Kenny, S. T. et al. Development of a bioprocess to convert PET derived terephthalic acid and biodiesel derived glycerol to medium chain length polyhydroxyalkanoate. *Appl. Microbiol. Biotechnol.* **95**, 623–633 (2012).
31. Kenny, S. T. et al. Up-cycling of PET (polyethylene terephthalate) to the biodegradable plastic PHA (polyhydroxyalkanoate). *Environ. Sci. Technol.* **42**, 7696–7701 (2008).
32. Tiso, T. et al. Towards bio-upcycling of polyethylene terephthalate. *Metab. Eng.* **66**, 167–178 (2021).
33. Ward, P. G., Goff, M., Donner, M., Kaminsky, W. & O'Connor, K. E. A two step chemo-biotechnological conversion of polystyrene to a biodegradable thermoplastic. *Environ. Sci. Technol.* **40**, 2433–2437 (2006).
34. Wei, R. et al. Possibilities and limitations of biotechnological plastic degradation and recycling. *Nat. Catal.* **3**, 867–871 (2020).
35. Geyer, R., Jambeck, J. R. & Law, K. L. Production, use, and fate of all plastics ever made. *Sci. Adv.* **3**, e1700782 (2017).
36. Williamson, J. B., Lewis, S. E., Johnson, R. R. III, Manning, I. M. & Leibfarth, F. A. C–H functionalization of commodity polymers. *Angew. Chem. Int. Ed.* **58**, 8654–8668 (2019).
37. Kondo, Y. et al. Rhodium-catalyzed, regiospecific functionalization of polyolefins in the melt. *J. Am. Chem. Soc.* **124**, 1164–1165 (2002).
38. Bae, C. et al. Regiospecific side-chain functionalization of linear low-density polyethylene with polar groups. *Angew. Chem. Int. Ed.* **44**, 6410–6413 (2005).

39. Bae, C. et al. Catalytic hydroxylation of polypropylenes. *J. Am. Chem. Soc.* **127**, 767–776 (2005).
40. Williamson, J. B., Czaplyski, W. L., Alexanian, E. J. & Leibfarth, F. A. Regioselective C–H xanthylation as a platform for polyolefin functionalization. *Angew. Chem. Int. Ed.* **57**, 6261–6265 (2018).
41. Williamson, J. B. et al. Chemo- and regioselective functionalization of isotactic polypropylene: a mechanistic and structure–property study. *J. Am. Chem. Soc.* **141**, 12815–12823 (2019).
42. Plummer, C., Li, L. & Chen, Y. The post-modification of polyolefins with emerging synthetic methods. *Polym. Chem.* **11**, 6862–6872 (2020).
43. Fakezas, T. J. et al. Diversification of aliphatic C–H bonds in small molecules and polyolefins through radical chain transfer. *Science* **375**, 545–550 (2022).
44. Chen, L. et al. Selective, catalytic oxidations of C–H bonds in polyethylenes produce functional materials with enhanced adhesion. *Chem* **7**, 137–145 (2021). **Selective functionalization of polyethylene through ruthenium-catalysed oxidation of C–H bonds for the synthesis of processable and adhesive materials.**
45. Röttger, M. et al. High-performance vitrimers from commodity thermoplastics through dioxaborolane metathesis. *Science* **356**, 62–65 (2017).
46. Easterling, C. P., Kubo, T., Orr, Z. M., Fanucci, G. E. & Sumerlin, B. S. Synthetic upcycling of polyacrylates through organocatalyzed post-polymerization modification. *Chem. Sci.* **8**, 7705–7709 (2017).
47. Lewis, S. E., Wilhelmy, B. E. & Leibfarth, F. A. Organocatalytic C–H fluoroalkylation of commodity polymers. *Polym. Chem.* <https://doi.org/10.1039/C9PY01884K> (2020).

48. Lewis, S. E., Wilhelmy, B. E. & Leibfarth, F. A. Upcycling aromatic polymers through C–H fluoroalkylation. *Chem. Sci.* **10**, 6270–6277 (2019).
49. Sharma, P., Lochab, B., Kumar, D. & Roy, P. K. Sustainable bis-benzoxazines from cardanol and PET-derived terephthalamides. *ACS Sustain. Chem. Eng.* **4**, 1085–1093 (2016).
50. Tan, J. P. K. et al. Upcycling poly(ethylene terephthalate) refuse to advanced therapeutics for the treatment of nosocomial and mycobacterial infections. *Macromolecules* **52**, 7878–7885 (2019).
51. Fukushima, K. et al. Supramolecular high-aspect ratio assemblies with strong antifungal activity. *Nat. Commun.* **4**, 2861 (2013).
52. Fukushima, K. et al. Advanced chemical recycling of poly(ethylene terephthalate) through organocatalytic aminolysis. *Polym. Chem.* **4**, 1610–1616 (2013).
53. Fukushima, K. et al. Broad-spectrum antimicrobial supramolecular assemblies with distinctive size and shape. *ACS Nano* **6**, 9191–9199 (2012).
54. Demarteau, J., O’Harra, K. E., Bara, J. E. & Sardon, H. Valorization of plastic wastes for the synthesis of imidazolium-based self-supported elastomeric ionenes. *ChemSusChem* **13**, 3122–3126 (2020).
55. Kammakakam, I., O’Harra, K. E., Dennis, G. P., Jackson, E. M. & Bara, J. E. Self-healing imidazolium-based ionene-polyamide membranes: an experimental study on physical and gas transport properties. *Polym. Int.* **68**, 1123–1129 (2019).
56. Iannone, F. et al. Ionic liquids/ZnO nanoparticles as recyclable catalyst for polycarbonate depolymerization. *J. Mol. Catal. A* **426**, 107–116 (2017).
57. Do, T., Baral, E. R. & Kim, J. G. Chemical recycling of poly(bisphenol A carbonate): 1,5,7-triazabicyclo[4.4.0]-dec-5-ene catalyzed

alcoholysis for highly efficient bisphenol A and organic carbonate recovery. *Polymer* **143**, 106–114 (2018).

58. Jehanno, C. et al. Synthesis of functionalized cyclic carbonates through commodity polymer upcycling. *ACS Macro Lett.* **9**, 443–447 (2020). **Selective upcycling of BPA-PC wastes into functionalized six-member cyclic carbonates through an organocatalysed-mediated depolymerization.**
59. Tempelaar, S., Mespouille, L., Coulembier, O., Dubois, P. & P. Dove, A. Synthesis and post-polymerisation modifications of aliphatic poly(carbonate)s prepared by ring-opening polymerisation. *Chem. Soc. Rev.* **42**, 1312–1336 (2013).
60. Sardon, H. et al. Synthesis of polyurethanes using organocatalysis: a perspective. *Macromolecules* **48**, 3153–3165 (2015).
61. Westhues, S., Idel, J. & Klankermayer, J. Molecular catalyst systems as key enablers for tailored polyesters and polycarbonate recycling concepts. *Sci. Adv.* **4**, eaat9669 (2018). **Catalytic depolymerization of polyesters and polycarbonates through a ruthenium catalyst-mediated hydrogenolysis, paving the way to innovative and sustainable recycling strategies.**
62. Monsigny, L., Berthet, J.-C. & Cantat, T. Depolymerization of waste plastics to monomers and chemicals using a hydrosilylation strategy facilitated by Brookhart’s iridium(III) catalyst. *ACS Sustain. Chem. Eng.* **6**, 10481–10488 (2018).
63. Zhang, F. et al. Polyethylene upcycling to long-chain alkyl aromatics by tandem hydrogenolysis/aromatization. *Science* **370**, 437–441 (2020).
64. Yoshida, S. et al. A bacterium that degrades and assimilates poly(ethylene terephthalate). *Science* **351**, 1196–1199 (2016).
65. Kim, H. T. et al. Biological valorization of poly(ethylene terephthalate) monomers for upcycling waste PET. *ACS Sustain. Chem. Eng.* **7**,

19396–19406 (2019).

66. *Additive Manufacturing Market Size: Industry Report, 2020–2025* <https://www.knowledge-sourcing.com/report/additive-manufacturing-market> (Knowledge Sourcing Intelligence LLP, 2021).
67. Bäckström, E., Odelius, K. & Hakkarainen, M. Trash to treasure: microwave-assisted conversion of polyethylene to functional chemicals. *Ind. Eng. Chem. Res.* **56**, 14814–14821 (2017).
68. Bäckström, E., Odelius, K. & Hakkarainen, M. Designed from recycled: turning polyethylene waste to covalently attached polylactide plasticizers. *ACS Sustain. Chem. Eng.* **7**, 11004–11013 (2019).
Microwave-assisted oxidative degradation of LDPE waste into functional chemicals (glutaric, succinic and adipic acids) for the subsequent synthesis of PLA plasticizer.
69. Mouawia, A., Nourry, A., Gaumont, A.-C., Pilard, J.-F. & Dez, I. Controlled metathetic depolymerization of natural rubber in ionic liquids: from waste tires to telechelic polyisoprene oligomers. *ACS Sustain. Chem. Eng.* **5**, 696–700 (2017).
70. Zhang, J., Yan, B., Wan, S. & Kong, Q. Converting polyethylene waste into large scale one-dimensional Fe₃O₄@C composites by a facile one-pot process. *Ind. Eng. Chem. Res.* **52**, 5708–5712 (2013).
71. Gong, J. et al. Upcycling waste polypropylene into graphene flakes on organically modified montmorillonite. *Ind. Eng. Chem. Res.* **53**, 4173–4181 (2014).
72. Yang, R.-X., Chuang, K.-H. & Wey, M.-Y. Effects of nickel species on Ni/Al₂O₃ catalysts in carbon nanotube and hydrogen production by waste plastic gasification: bench- and pilot-scale tests. *Energy Fuels* **29**, 8178–8187 (2015).
73. Zhao, D., Wang, X., Miller, J. B. & Huber, G. W. The chemistry and kinetics of polyethylene pyrolysis: a process to produce fuels and chemicals. *ChemSusChem* **13**, 1764–1774 (2020).

74. Zhuo, C. & Levendis, Y. A. Upcycling waste plastics into carbon nanomaterials: a review. *J. Appl. Polym. Sci.* <https://doi.org/10.1002/app.39931> (2014).
75. Gong, J., Chen, X. & Tang, T. Recent progress in controlled carbonization of (waste) polymers. *Prog. Polym. Sci.* **94**, 1–32 (2019).
76. Gong, J. et al. Converting mixed plastics into mesoporous hollow carbon spheres with controllable diameter. *Appl. Catal. B* **152–153**, 289–299 (2014).
77. Villagómez-Salas, S., Manikandan, P., Acuña Guzmán, S. F. & Pol, V. G. Amorphous carbon chips Li-ion battery anodes produced through polyethylene waste upcycling. *ACS Omega* **3**, 17520–17527 (2018).
78. Kim, P. J., Fontecha, H. D., Kim, K. & Pol, V. G. Toward high-performance lithium–sulfur batteries: upcycling of LDPE plastic into sulfonated carbon scaffold via microwave-promoted sulfonation. *ACS Appl. Mater. Interfaces* **10**, 14827–14834 (2018). **Preparation of highly porous sulfonated materials from microwave-promoted sulfonation of LDPE wastes.**
79. Mohamed, H. H., Alsanea, A. A., Alomair, N. A., Akhtar, S. & Bahnemann, D. W. ZnO@ porous graphite nanocomposite from waste for superior photocatalytic activity. *Environ. Sci. Pollut. Res.* **26**, 12288–12301 (2019).
80. Ko, S., Kwon, Y. J., Lee, J. U. & Jeon, Y.-P. Preparation of synthetic graphite from waste PET plastic. *J. Ind. Eng. Chem.* **83**, 449–458 (2019).
81. Koning, C., Van Duin, M., Pagnoulle, C. & Jerome, R. Strategies for compatibilization of polymer blends. *Prog. Polym. Sci.* **23**, 707–757 (1998).
82. Feldman, D. Polyblend compatibilization. *J. Macromol. Sci. A* **42**, 587–605 (2005).

83. Nechifor, M., Tanasă, F., Teacă, C.-A. & Zănoagă, M. Compatibilization strategies toward new polymer materials from re-/up-cycled plastics. *Int. J. Polym. Anal. Charact.* **23**, 740–757 (2018).
84. Santana, R. M. C. & Manrich, S. Studies on morphology and mechanical properties of PP/HIPS blends from postconsumer plastic waste. *J. Appl. Polym. Sci.* **87**, 747–751 (2003).
85. Equiza, N., Yave, W., Quijada, R. & Yazdani-Pedram, M. Use of SEBS/EPR and SBR/EPR as binary compatibilizers for PE/PP/PS/HIPS blends: a work oriented to the recycling of thermoplastic wastes. *Macromol. Mater. Eng.* **292**, 1001–1011 (2007).
86. Pracella, M., Rolla, L., Chionna, D. & Galeski, A. Compatibilization and properties of poly(ethylene terephthalate)/polyethylene blends based on recycled materials. *Macromol. Chem. Phys.* **203**, 1473–1485 (2002).
87. Pawlak, A., Morawiec, J., Pazzagli, F., Pracella, M. & Galeski, A. Recycling of postconsumer poly(ethylene terephthalate) and high-density polyethylene by compatibilized blending. *J. Appl. Polym. Sci.* **86**, 1473–1485 (2002).
88. Ragaert, K., Delva, L. & Van Geem, K. Mechanical and chemical recycling of solid plastic waste. *Waste Manage.* **69**, 24–58 (2017).
89. Eagan, J. M. et al. Combining polyethylene and polypropylene: enhanced performance with PE/iPP multiblock polymers. *Science* **355**, 814–816 (2017).
90. Xu, J. et al. Compatibilization of isotactic polypropylene (iPP) and high-density polyethylene (HDPE) with iPP–PE multiblock copolymers. *Macromolecules* **51**, 8585–8596 (2018).
91. Washiyama, J., Kramer, E. J. & Hui, C. Y. Fracture mechanisms of polymer interfaces reinforced with block copolymers: transition from chain pullout to crazing. *Macromolecules* **26**, 2928–2934 (1993).

92. Galloway, J. A., Jeon, H. K., Bell, J. R. & Macosko, C. W. Block copolymer compatibilization of cocontinuous polymer blends. *Polymer* **46**, 183–191 (2005).
93. Macosko, C. W., Jeon, H. K. & Hoye, T. R. Reactions at polymer–polymer interfaces for blend compatibilization. *Prog. Polym. Sci.* **30**, 939–947 (2005).
94. Sundararaj, U. & Macosko, C. W. Drop breakup and coalescence in polymer blends: the effects of concentration and compatibilization. *Macromolecules* **28**, 2647–2657 (1995).
95. Saleem, M. & Baker, W. E. In situ reactive compatibilization in polymer blends: effects of functional group concentrations. *J. Appl. Polym. Sci.* **39**, 655–678 (1990).
96. Hettema, R., Pasman, J. & Janssen, L. P. B. M. Reactive extrusion of recycled bottle waste material. *Polym. Eng. Sci.* **42**, 665–680 (2002).
97. Hlavatá, D., Kruliš, Z., Horák, Z., Lednický, F. & Hromádková, J. The role of lubricants in reactive compatibilization of polyolefin blends. *Macromol. Symp.* **176**, 93–106 (2001).
98. Ghose, A., Pizzol, M. & McLaren, S. J. Consequential LCA modelling of building refurbishment in New Zealand—an evaluation of resource and waste management scenarios. *J. Clean. Prod.* **165**, 119–133 (2017).
99. Buyle, M., Galle, W., Debacker, W. & Audenaert, A. Sustainability assessment of circular building alternatives: consequential LCA and LCC for internal wall assemblies as a case study in a Belgian context. *J. Clean. Prod.* **218**, 141–156 (2019).
100. Prosmans, E. J. & Sacchi, R. New environmental supplier selection criteria for circular supply chains: lessons from a consequential LCA study on waste recovery. *J. Clean. Prod.* **172**, 2782–2792 (2018).

101. Civancik-Uslu, D. et al. Moving from linear to circular household plastic packaging in Belgium: prospective life cycle assessment of mechanical and thermochemical recycling. *Resour. Conserv. Recycl.* **171**, 105633 (2021).
102. De Meester, S., Nachtergaele, P., Debaveye, S., Vos, P. & Dewulf, J. Using material flow analysis and life cycle assessment in decision support: a case study on WEEE valorization in Belgium. *Resour. Conserv. Recycl.* **142**, 1–9 (2019).
103. Moraga, G. et al. Circular economy indicators: What do they measure? *Resour. Conserv. Recycl.* **146**, 452–461 (2019).
104. Britt, P. et al. *Report of the Basic Energy Sciences Roundtable on Chemical Upcycling of Polymers* (2019).
105. Plastic upcycling. *Nat. Catal.* **2**, 945–946 (2019).
106. Shi, C. et al. Design principles for intrinsically circular polymers with tunable properties. *Chem.* **7**, 2896–2912 (2021)
107. Liu, X., Hong, M., Falivene, L., Cavallo, L. & Chen, E. Y.-X. Closed-loop polymer upcycling by installing property-enhancing comonomer sequences and recyclability. *Macromolecules* **52**, 4570–4578 (2019).
108. Christensen, P. R., Scheuermann, A. M., Loeffler, K. E. & Helms, B. A. Closed-loop recycling of plastics enabled by dynamic covalent diketoenamine bonds. *Nat. Chem.* **11**, 442 (2019).
109. *Science to Enable Sustainable Plastics*
https://www.rsc.org/globalassets/22-new-perspectives/sustainability/progressive-plastics/c19_tl_sustainability_cs3_whitepaper_a4_web_final.pdf
(Royal Society of Chemistry, 2020).
110. Anastas, P. T. & Warner, J. C. In *Green Chemistry: Theory and Practice* 30 (Univ. Press, 1998).

111. Anastas, P. T. & Zimmerman, J. B. Design through the 12 principles of green engineering. *Environ. Sci. Technol.* **37**, 94A–101A (2003).
112. Nicholson, S. R., Rorrer, N. A., Carpenter, A. C. & Beckham, G. T. Manufacturing energy and greenhouse gas emissions associated with plastics consumption. *Joule* **5**, 673–686 (2021).

Acknowledgements

C.J. and H.S. thank the Spanish Ministry for the excellence Grant POLYCE and the Basque University for the EHUrOPE grant. F.A.L. and J.W.A. acknowledge support from the Air Force Office of Scientific Research award number 17RT0487 under the Young Investigator Program. S.D.M. and M.R. acknowledge support from VLAIO and the Catalisti Moonshot programme through the PREFER project (The plastics refinery: No more waste - HBC20202609) and the European Regional Development Fund (ERDF) via the PSYCHE project (Interreg France-Wallonie-Vlaanderen) with co-financing from the provinces of East-Flanders and West-Flanders. E.Y.-X.C. acknowledges support from the BOTTLE Consortium funded by the US Department of Energy, Office of Energy Efficiency and Renewable Energy, Advanced Manufacturing Office and Bioenergy Technologies Office under contract number DE-AC36-08GO28308 with the National Renewable Energy Laboratory, operated by Alliance for Sustainable Energy. A.P.D. acknowledges the financial support from the University of Birmingham.

Author information

Affiliations

1. POLYMAT, University of the Basque Country UPV/EHU, Donostia–San Sebastian, Spain

Coralie Jehanno & Haritz Sardon

2. Department of Chemistry, University of North Carolina at Chapel Hill,
Chapel Hill, NC, USA

Jill W. Alty & Frank A. Leibfarth

3. Laboratory for Circular Process Engineering, Ghent University,
Kortrijk, Belgium

Martijn Roosen & Steven De Meester

4. School of Chemistry, University of Birmingham, Birmingham, UK

Andrew P. Dove

5. Department of Chemistry, Colorado State University, Fort Collins, CO,
USA

Eugene Y.-X. Chen

6. POLYKEY, Donostia-San Sebastian, Spain

Coralie Jehanno

Contributions

C.J. and J.W.A. wrote the initial manuscript under the supervision of and with contributions from H.S. and F.A.L. S.D.M. and M.R. performed the calculations for the quantification of carbon footprint and wrote the ‘Quantifying the sustainability of upcycling’ section. All authors have contributed to the discussion of the content and have revised and edited the manuscript. C.J. realized the figures.

Corresponding authors

Correspondence to [Steven De Meester](#), [Frank A. Leibfarth](#) or [Haritz Sardon](#).

Ethics declarations

Competing interests

The authors declare no competing interests.

Peer review

Peer review information

Nature thanks Edward Kosior, Tomonori Saito and the other, anonymous, reviewer(s) for their contribution to the peer review of this work.

Additional information

Publisher's note Springer Nature remains neutral with regard to jurisdictional claims in published maps and institutional affiliations.

Supplementary information

Supplementary Information

This file contains Supplementary Information, including Supplementary Figs. 1–6, Tables 1–3 and references.

Rights and permissions

Reprints and Permissions

About this article

Cite this article

Jehanno, C., Alty, J.W., Roosen, M. *et al.* Critical advances and future opportunities in upcycling commodity polymers. *Nature* **603**, 803–814 (2022). <https://doi.org/10.1038/s41586-021-04350-0>

- Received: 04 March 2020
- Accepted: 14 December 2021
- Published: 30 March 2022
- Issue Date: 31 March 2022
- DOI: <https://doi.org/10.1038/s41586-021-04350-0>

Share this article

Anyone you share the following link with will be able to read this content:

[Get shareable link](#)

Sorry, a shareable link is not currently available for this article.

[Copy to clipboard](#)

Provided by the Springer Nature SharedIt content-sharing initiative

This article was downloaded by **calibre** from <https://www.nature.com/articles/s41586-021-04350-0>

| [Section menu](#) | [Main menu](#) |

- Article
- [Published: 30 March 2022](#)

A highly magnified star at redshift 6.2

- [Brian Welch](#) [ORCID: orcid.org/0000-0003-1815-0114¹](#),
- [Dan Coe^{1,2,3}](#),
- [Jose M. Diego](#) [ORCID: orcid.org/0000-0001-9065-3926⁴](#),
- [Adi Zitrin⁵](#),
- [Erik Zackrisson⁶](#),
- [Paola Dimauro⁷](#),
- [Yolanda Jiménez-Teja⁸](#),
- [Patrick Kelly⁹](#),
- [Guillaume Mahler](#) [ORCID: orcid.org/0000-0003-3266-2001^{10,11,12}](#),
- [Masamune Oguri](#) [ORCID: orcid.org/0000-0003-3484-399X^{13,14,15}](#),
- [F. X. Timmes^{16,17}](#),
- [Rogier Windhorst¹⁶](#),
- [Michael Florian¹⁸](#),
- [S. E. de Mink^{19,20,21}](#),
- [Roberto J. Avila²](#),
- [Jay Anderson²](#),
- [Larry Bradley²](#),
- [Keren Sharon](#) [ORCID: orcid.org/0000-0002-7559-0864¹⁰](#),
- [Anton Vikaeus⁶](#),
- [Stephan McCandliss¹](#),
- [Maruša Bradač²²](#),
- [Jane Rigby²³](#),
- [Brenda Frye¹⁸](#),
- [Sune Toft](#) [ORCID: orcid.org/0000-0003-3631-7176^{24,25}](#),

- [Victoria Strait](#)^{22,24,25},
- [Michele Trenti](#)^{26,27},
- [Sonija Sharma](#)²³,
- [Felipe Andrade-Santos](#)^{21,28} &
- [Tom Broadhurst](#)^{29,30,31}

[*Nature*](#) volume **603**, pages 815–818 (2022)

- 7734 Accesses
- 2923 Altmetric
- [Metrics details](#)

Subjects

- [Galaxies and clusters](#)
- [Stars](#)

Abstract

Galaxy clusters magnify background objects through strong gravitational lensing. Typical magnifications for lensed galaxies are factors of a few but can also be as high as tens or hundreds, stretching galaxies into giant arcs^{1,2}. Individual stars can attain even higher magnifications given fortuitous alignment with the lensing cluster. Recently, several individual stars at redshifts between approximately 1 and 1.5 have been discovered, magnified by factors of thousands, temporarily boosted by microlensing^{3,4,5,6}. Here we report observations of a more distant and persistent magnified star at a redshift of 6.2 ± 0.1 , 900 million years after the Big Bang. This star is magnified by a factor of thousands by the foreground galaxy cluster lens WHL0137–08 (redshift 0.566), as estimated by four independent lens models. Unlike previous lensed stars, the magnification and observed brightness (AB magnitude, 27.2) have remained roughly constant over 3.5 years of imaging and follow-up. The delensed absolute UV magnitude, -10 ± 2 , is consistent with a star of mass

greater than 50 times the mass of the Sun. Confirmation and spectral classification are forthcoming from approved observations with the James Webb Space Telescope.

This is a preview of subscription content

Access options

Subscribe to Nature+

Get immediate online access to the entire Nature family of 50+ journals

\$29.99

monthly

[Subscribe](#)

Subscribe to Journal

Get full journal access for 1 year

\$199.00

only \$3.90 per issue

[Subscribe](#)

All prices are NET prices.

VAT will be added later in the checkout.

Tax calculation will be finalised during checkout.

Buy article

Get time limited or full article access on ReadCube.

\$32.00

[Buy](#)

All prices are NET prices.

Additional access options:

- [Log in](#)
- [Learn about institutional subscriptions](#)

Fig. 1: Labelled colour image of WHL0137-zD1.



Fig. 2: Strong lensing critical curves.

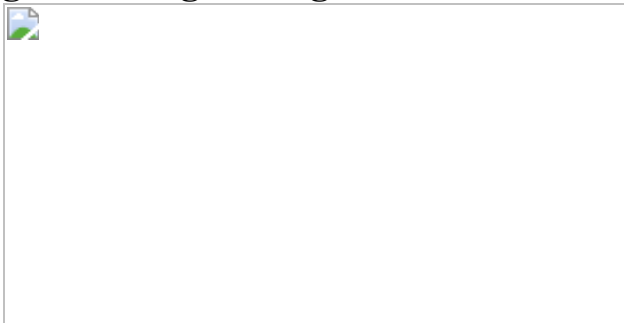
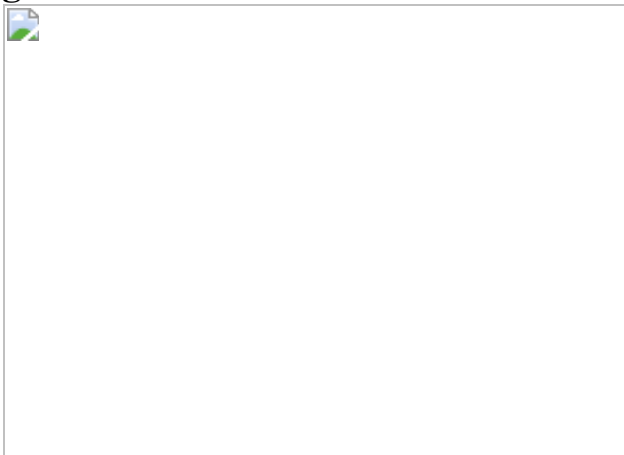


Fig. 3: Lensed star constraints on the H–R diagram.



Data availability

All HST image data used in this analysis are publicly available on the Mikulski Archive for Space Telescopes (MAST), and can be found through <https://doi.org/10.17909/T9SP45> (RELICS) and <https://doi.org/10.17909/t9-ztav-b843> (HST GO 15842).

References

1. Rivera-Thorsen, T. E. et al. The Sunburst Arc: direct Lyman α escape observed in the brightest known lensed galaxy. *Astron. Astrophys.* **608**, L4 (2017).
2. Johnson, T. L. et al. Star formation at $z=2.481$ in the lensed galaxy SDSS J1110+6459: star formation down to 30 pm scales. *Astrophys. J. Lett.* **843**, L21 (2017).
3. Kelly, P. L. et al. Extreme magnification of an individual star at redshift 1.5 by a galaxy-cluster lens. *Nat. Astron.* **2**, 334–342 (2018).
4. Rodney, S. A. et al. Two peculiar fast transients in a strongly lensed host galaxy. *Nat. Astron.* **2**, 324–333 (2018).
5. Chen, W. et al. Searching for highly magnified stars at cosmological distances: discovery of a redshift 0.94 supergiant in archival images of the galaxy cluster MACS J0416.1-2403. *Astrophys. J.* **881**, 8 (2019).
6. Kaurov, A. A., Dai, L., Venumadhav, T., Miralda-Escudé, J. & Frye, B. Highly magnified stars in lensing clusters: new evidence in a galaxy lensed by MACS J0416.1-2403. *Astrophys. J.* **881**, 58 (2019).
7. Coe, D. et al. RELICS: Reionization Lensing Cluster Survey. *Astrophys. J.* **884**, 85 (2019).
8. Salmon, B. et al. RELICS: The Reionization Lensing Cluster Survey and the brightest high- z galaxies. *Astrophys. J.* **889**, 189 (2020).

9. Rivera-Thorsen, T. E. et al. Gravitational lensing reveals ionizing ultraviolet photons escaping from a distant galaxy. *Science* **366**, 738–741 (2019).
10. Zitrin, A. et al. Hubble Space Telescope combined strong and weak lensing analysis of the CLASH sample: mass and magnification models and systematic uncertainties. *Astrophys. J.* **801**, 44 (2015).
11. Zitrin, A. et al. New multiply-lensed galaxies identified in ACS/NIC3 observations of Cl0024+1654 using an improved mass model. *Mon. Not. R. Astron. Soc.* **395**, 1319–1332 (2009).
12. Broadhurst, T. et al. Strong-lensing analysis of A1689 from Deep Advanced Camera images. *Astrophys. J.* **621**, 53–88 (2005).
13. Jullo, E. & Kneib, J. P. Multiscale cluster lens mass mapping – I. Strong lensing modelling. *Mon. Not. R. Astron. Soc.* **395**, 1319–1332 (2009).
14. Jullo, E. et al. A Bayesian approach to strong lensing modelling of galaxy clusters. *New J. Phys.* **9**, 447 (2007).
15. Oguri, M. The mass distribution of SDSS J1004+4112 revisited. *Publ. Astron. Soc. Jpn* **62**, 1017–1024 (2010).
16. Diego, J. M., Tegmark, M., Protopapas, P. & Sandvik, H. B. Combined reconstruction of weak and strong lensing data with WSLAP. *Mon. Mot. R. Astron. Soc.* **375**, 958–970 (2007).
17. Diego, J. M., Protopapas, P., Sandvik, H. B. & Tegmark, M. Non-parametric inversion of strong lensing systems. *Mon. Not. R. Astron. Soc.* **360**, 477–491 (2005).
18. Diego, J. M. The Universe at extreme magnification. *Astron. Astrophys.* **625**, A84 (2019).
19. Meneghetti, M. et al. The Frontier Fields lens modelling comparison project. *Mon. Mot. R. Astron. Soc.* **472**, 3177–3216 (2017).

20. Venumadhav, T., Dai, L. & Miralda-Escudé, J. Microlensing of extremely magnified stars near caustics of galaxy clusters. *Astrophys. J.* **850**, 49 (2017).
21. Diego, J. M. et al. Dark matter under the microscope: constraining compact dark matter with caustic crossing events. *Astrophys. J.* **857**, 25 (2018).
22. Dai, L. Statistical microlensing towards magnified high-redshift star clusters. *Mon. Mot. R. Astron. Soc.* **501**, 5538–5553 (2021).
23. Portegies Zwart, S. F., McMillan, S. L. W. & Gieles, M. Young massive star clusters. *Annu. Rev. Astron. Astrophys.* **48**, 431–493 (2010).
24. Figer, D. F., McLean, I. S. & Morris, M. Massive stars in the quintuplet cluster. *Astrophys. J.* **514**, 202–220 (1999).
25. Bouwens, R. J. et al. Very low-luminosity galaxies in the early universe have observed sizes similar to single star cluster complexes. Preprint at <https://arxiv.org/abs/1711.02090> (2017).
26. Vanzella, E. et al. Massive star cluster formation under the microscope at $z = 6$. *Mon. Not. R. Astron. Soc.* **483**, 3618–3635 (2019).
27. Behrendt, M., Schartmann, M. & Burkert, A. The possible hierarchical scales of observed clumps in high-redshift disc galaxies. *Mon. Not. R. Astron. Soc.* **488**, 306–323 (2019).
28. Sana, H. et al. Binary interaction dominates the evolution of massive stars. *Science* **337**, 444–446 (2012).
29. Sana, H. et al. Southern massive stars at high angular resolution: observational campaign and companion detection. *Astrophys. J. Suppl. Ser.* **215**, 15 (2014).
30. Moe, M. & Di Stefano, R. Mind your Ps and Qs: the interrelation between period (P) and mass-ratio (Q) distributions of binary stars.

Astrophys. J. Suppl. Ser. **230**, 15 (2017).

31. Szécsi, D., Agrawal, P., Wünsch, R. & Langer, N. Bonn Optimized Stellar Tracks (BoOST). Simulated populations of massive and very massive stars for astrophysical applications. *Astron. Astrophys.* **628**, A125 (2022).
32. Shimizu, I., Inoue, A. K., Okamoto, T. & Yoshida, N. Nebular line emission from $z > 7$ galaxies in a cosmological simulation: rest-frame UV to optical lines. *Mon. Not. R. Astron. Soc.* **461**, 3563–3575 (2016).
33. Wen, Z. L., Han, J. L. & Liu, F. S. A catalog of 132,684 clusters of galaxies identified from Sloan Digital Sky Survey III. *Astrophys. J. Suppl. Ser.* **199**, 34 (2012).
34. Wen, Z. L. & Han, J. L. Calibration of the optical mass proxy for clusters of galaxies and an update of the WHL12 cluster catalog. *Astrophys. J.* **807**, 178 (2015).
35. Alam, S. et al. The eleventh and twelfth data releases of the Sloan Digital Sky Survey: final data from SDSS-III. *Astrophys. J. Suppl. Ser.* **219**, 12 (2015).
36. Planck Collaboration. Planck 2015 results: XXVII. The second Planck catalogue of Sunyaev–Zeldovich sources. *Astron. Astrophys.* **594**, A27 (2016).
37. Sunyaev, R. A. & Zeldovich, Y. B. Small-scale fluctuations of relic radiation. *Astrophys. Space Sci.* **7**, 3–19 (1970).
38. Strait, V. et al. RELICS: properties of $z \geq 5.5$ galaxies inferred from Spitzer and Hubble imaging, including a candidate $z \sim 6.8$ strong [O iii] emitter. *Astrophys. J.* **910**, 135 (2021).
39. Bertin, E. & Arnouts, S. SExtractor: software for source extraction. *Astron. Astrophys. Suppl. Ser.* **117**, 393–404 (1996).

40. Beintez, N. Bayesian photometric redshift estimation. *Astrophys. J.* **536**, 571–583 (2000).
41. Coe, D. et al. Galaxies in the Hubble Ultra Deep Field. I. Detection, multiband photometry, photometric redshifts, and morphology. *Astron. J.* **132**, 926–959 (2006).
42. Carnall, A. C., McLure, R. J., Dunlop, J. S. & Davé, R. Inferring the star formation histories of massive quiescent galaxies with BAGPIPES: evidence for multiple quenching mechanisms. *Mon. Not. R. Astron. Soc.* **480**, 4379–4401 (2018).
43. Eldridge, J. J. et al. Binary Population and Spectral Synthesis version 2.1: construction, observational verification, and new results. *Publ. Astron. Soc. Aust.* **34**, e058 (2017).
44. Ferland, G. J. et al. The 2017 release of Cloudy. *Rev. Mex. Astron. Astr.* **53**, 385–438 (2017).
45. Salpeter, E. E. The luminosity function and stellar evolution. *Astrophys. J.* **121**, 161–167 (1955).
46. Calzetti, D. et al. The dust content and opacity of actively star-forming galaxies. *Astrophys. J.* **533**, 682–695 (2000).
47. Ellis, R. S. et al. The homogeneity of spheroidal populations in distant clusters. *Astrophys. J.* **483**, 582–596 (1997).
48. Stanford, S. A., Eisenhardt, P. R. & Dickinson, M. The evolution of early-type galaxies in distant clusters. *Astrophys. J.* **492**, 461–479 (1998).
49. Hastings, W. K. Monte Carlo sampling methods using Markov chains and their applications. *Biometrika* **57**, 97–109 (1970).
50. Limousin, M., Kneib, J.-P. & Natarajan, P. Constraining the mass distribution of galaxies using galaxy–galaxy lensing in clusters and in the field. *Mon. Not. R. Astron. Soc.* **356**, 309–322 (2005).

51. Eliasdóttir, Á. et al. Where is the matter in the Merging Cluster Abell 2218? Preprint at <https://arxiv.org/abs/0710.5636> (2007).
52. Navarro, J. F., Frenk, C. S. & White, S. D. M. The structure of cold dark matter halos. *Astrophys. J.* **462**, 563–575 (1996).
53. Johnson, T. L. et al. Star formation at $z=2.481$ in the lensed galaxy SDSS J1110+6459. I. Lens modeling and source reconstruction. *Astrophys. J.* **843**, 78 (2017).
54. Dai, L. & Pascale, M. New approximation of magnification statistics for random microlensing of magnified sources. Preprint at <https://arxiv.org/abs/2104.12009> (2021).
55. Jiménez-Teja, Y. et al. RELICS: ICL analysis of the $z=0.566$ merging cluster WHL J013719.8–08284. *Astrophys. J.* **922**, 268 (2021).
56. Kriek, M. et al. An ultra-deep near-infrared spectrum of a compact quiescent galaxy at $z=2.2$. *Astrophys. J.* **700**, 221–231 (2009).
57. Bruzual, G. & Charlot, S. Stellar population synthesis at the resolution of 2003. *Mon. Not. R. Astron. Soc.* **344**, 1000–1028 (2003).
58. Chabrier, G. Galactic stellar and substellar initial mass function. *Publ. Astron. Soc. Pacif.* **115**, 763–795 (2003).
59. Spera, M., Mapelli, M. & Bressan, A. The mass spectrum of compact remnants from the PARSEC stellar evolution tracks. *Mon. Not. R. Astron. Soc.* **451**, 4086–4103 (2015).
60. Oguri, M., Diego, J. M., Kaiser, N., Kelly, P. L. & Broadhurst, T. Understanding caustic crossings in giant arcs: characteristic scales, event rates, and constraints on compact dark matter. *Phys. Rev. D* **97**, 023518 (2018).
61. Windhorst, R. A. et al. On the observability of individual population III stars and their stellar-mass black hole accretion disks through cluster caustic transits. *Astrophys. J. Suppl. Ser.* **234**, 41 (2018).

62. Lejeune, T. H., Cuisinier, F. & Buser, R. Standard stellar library for evolutionary synthesis. I. Calibration of theoretical spectra. *Astron. Astrophys. Suppl. Ser.* **125**, 229–246 (1997).
63. Calzetti, D. et al. The brightest young star clusters in NGC 5253. *Astrophys. J.* **811**, 75 (2015).
64. Sanyal, D., Grassitelli, L., Langer, N. & Bestenlehner, J. M. Massive main-sequence stars evolving at the Eddington limit. *Astron. Astrophys.* **580**, A20 (2015).
65. El-Badry, K., Rix, H.-W., Tian, H., Duchêne, G. & Moe, M. Discovery of an equal-mass ‘twin’ binary population reaching 1000+ au separations. *Mon. Not. R. Astron. Soc.* **489**, 5822–5857 (2019).
66. Leitherer, C. et al. Starburst99: synthesis models for galaxies with active star formation. *Astrophys. J. Suppl. Ser.* **123**, 3–40 (1999).
67. Kroupa, P. On the variation of the initial mass function. *Mon. Not. R. Astron. Soc.* **322**, 231–246 (2001).
68. da Silva, R. L., Fumagalli, M. & Krumholz, M. SLUG—Stochastically Lighting Up Galaxies. I. Methods and validating tests. *Astrophys. J.* **745**, 145 (2012).
69. Krumholz, M. R., Fumagalli, M., da Silva, R. L., Rendahl, T. & Parra, J. SLUG – stochastically lighting up galaxies – III. A suite of tools for simulated photometry, spectroscopy, and Bayesian inference with stochastic stellar populations. *Mon. Not. R. Astron. Soc.* **452**, 1447–1467 (2015).
70. Madau, P. & Dickinson, M. Cosmic star-formation history. *Annu. Rev. Astron. Astrophys.* **52**, 415–486 (2014).
71. Kehrig, C. et al. The extended He ii λ 4686 emission in the extremely metal-poor galaxy SBS 0335 - 052E seen with MUSE. *Mon. Not. R. Astron. Soc.* **480**, 1081–1095 (2018).

72. Sarmento, R., Scannapieco, E. & Cohen, S. Following the cosmic evolution of pristine gas. II. The search for pop III–bright galaxies. *Astrophys. J.* **854**, 75 (2018).
73. Sarmento, R., Scannapieco, E. & Côté, B. Following the cosmic evolution of pristine gas. III. The observational consequences of the unknown properties of population III stars. *Astrophys. J.* **871**, 206 (2019).
74. Trenti, M., Stiavelli, M. & Shull, J. M. Metal-free gas supply at the edge of reionization: late-epoch population III star formation. *Astrophys. J.* **700**, 1672–1679 (2009).
75. Vanzella, E. et al. Candidate population III stellar complex at $z = 6.629$ in the MUSE Deep Lensed Field. *Mon. Not. R. Astron. Soc.* **494**, L81–L85 (2020).
76. Abbott, R. et al. GW190521: a binary black hole merger with a total mass of $150M_{\odot}$. *Phys. Rev. Lett.* **125**, 101102 (2020).
77. Farrell, E. et al. Is GW190521 the merger of black holes from the first stellar generations? *Mon. Not. R. Astron. Soc. Lett.* **502**, L40–L44 (2020).
78. Kinugawa, T., Nakamura, T. & Nakano, H. Formation of binary black holes similar to GW190521 with a total mass of $\sim 150M_{\odot}$ from population III binary star evolution. *Mon. Not. R. Astron. Soc. Lett.* **501**, L49–L53 (2020).
79. Zdziarski, A. A. & Gierliński, M. Radiative processes, spectral states and variability of black-hole binaries. *Prog. Theor. Phys. Suppl.* **155**, 99–119 (2004).
80. Holwerda, B. W. et al. Milky Way red dwarfs in the BoRG Survey; galactic scale-height and the distribution of dwarf stars in WFC3 imaging. *Astrophys. J.* **788**, 77 (2014).

81. Burgasser, A. J. & Splat Development Team. The SpeX Prism Library Analysis Toolkit (SPLAT): a data curation model. In *Proc. Intl Workshop on Stellar Spectral Libraries (IWSSL 2017)* (eds Coelho, P. et al.) 7–12 (Astronomical Society of India, 2017).
82. Hainline, K. N., Shapley, A. E., Greene, J. E. & Steidel, C. C. The rest-frame ultraviolet spectra of UV-selected active galactic nuclei at $z \sim 2$ –3. *Astrophys. J.* **733**, 31 (2011).

Acknowledgements

The RELICS Hubble Treasury Program (GO 14096) and follow-up programme (GO 15842) consist of observations obtained by the NASA/ESA Hubble Space Telescope (HST). Data from these HST programmes were obtained from the Mikulski Archive for Space Telescopes (MAST), operated by the Space Telescope Science Institute (STScI). Both HST and STScI are operated by the Association of Universities for Research in Astronomy, Inc. (AURA), under NASA contract NAS 5-26555. The HST Advanced Camera for Surveys (ACS) was developed under NASA contract NAS 5-32864. J.M.D. acknowledges the support of project PGC2018-101814-B-100 (MCIU/AEI/MINECO/FEDER, UE) and María de Maeztu, ref. MDM-2017-0765. A.Z. acknowledges support from the Ministry of Science and Technology, Israel. R.W. acknowledges support from NASA JWST Interdisciplinary Scientist grants NAG5-12460, NNX14AN10G and 80NSSC18K0200 from GSFC. E.Z. and A.V. acknowledge funding from the Swedish National Space Board. M.O. acknowledges support from World Premier International Research Center Initiative, MEXT, Japan, and JSPS KAKENHI grant numbers JP20H00181, JP20H05856, JP18K03693. G.M. received funding from the European Union’s Horizon 2020 research and innovation programme under the Marie Skłodowska-Curie grant agreement no. MARACAS – DLV-896778. P.K. acknowledges support from NSF AST-1908823. Y.J.-T. acknowledges financial support from the European Union’s Horizon 2020 research and innovation programme under the Marie Skłodowska-Curie grant agreement no. 898633, and from the State Agency for Research of the Spanish MCIU through the ‘Center of Excellence Severo Ochoa’ award to the Instituto de

Astrofísica de Andalucía (SEV-2017-0709). The Cosmic DAWN Center is funded by the Danish National Research Foundation under grant no. 140.

Author information

Affiliations

1. Center for Astrophysical Sciences, Department of Physics and Astronomy, The Johns Hopkins University, Baltimore, MD, USA
Brian Welch, Dan Coe & Stephan McCandliss
2. Space Telescope Science Institute (STScI), Baltimore, MD, USA
Dan Coe, Roberto J. Avila, Jay Anderson & Larry Bradley
3. Association of Universities for Research in Astronomy (AURA) for the European Space Agency (ESA), STScI, Baltimore, MD, USA
Dan Coe
4. Instituto de Física de Cantabria (CSIC-UC), Santander, Spain
Jose M. Diego
5. Physics Department, Ben-Gurion University of the Negev, Be'er-Sheva, Israel
Adi Zitrin
6. Observational Astrophysics, Department of Physics and Astronomy, Uppsala University, Uppsala, Sweden
Erik Zackrisson & Anton Vikaeus
7. Observatório Nacional, Ministério da Ciencia, Tecnologia, Inovaçaoe Comunicações, Rio de Janeiro, Brazil

Paola Dimauro

8. Instituto de Astrofísica de Andalucía, Granada, Spain

Yolanda Jiménez-Teja

9. School of Physics and Astronomy, University of Minnesota,
Minneapolis, MN, USA

Patrick Kelly

10. Department of Astronomy, University of Michigan, Ann Arbor, MI,
USA

Guillaume Mahler & Keren Sharon

11. Institute for Computational Cosmology, Durham University, Durham,
UK

Guillaume Mahler

12. Centre for Extragalactic Astronomy, Durham University, Durham, UK

Guillaume Mahler

13. Research Center for the Early Universe, University of Tokyo, Tokyo,
Japan

Masamune Oguri

14. Center for Frontier Science, Chiba University, Chiba, Japan

Masamune Oguri

15. Kavli Institute for the Physics and Mathematics of the Universe (Kavli
IPMU, WPI), University of Tokyo, Chiba, Japan

Masamune Oguri

16. School of Earth and Space Exploration, Arizona State University,
Tempe, AZ, USA

F. X. Timmes & Rogier Windhorst

17. Joint Institute for Nuclear Astrophysics – Center for the Evolution of
the Elements, Tempe, AZ, USA

F. X. Timmes

18. Department of Astronomy, Steward Observatory, University of
Arizona, Tucson, AZ, USA

Michael Florian & Brenda Frye

19. Max-Planck-Institut für Astrophysik, Garching, Germany

S. E. de Mink

20. GRAPPA, Anton Pannekoek Institute for Astronomy, University of
Amsterdam, Amsterdam, The Netherlands

S. E. de Mink

21. Center for Astrophysics | Harvard & Smithsonian, Cambridge, MA,
USA

S. E. de Mink & Felipe Andrade-Santos

22. Department of Physics, University of California, Davis, Davis, CA,
USA

Maruša Bradač & Victoria Strait

23. Observational Cosmology Lab, NASA Goddard Space Flight Center,
Greenbelt, MD, USA

Jane Rigby & Soniya Sharma

24. Cosmic Dawn Center (DAWN), Copenhagen, Denmark

Sune Toft & Victoria Strait

25. Niels Bohr Institute, University of Copenhagen, Copenhagen, Denmark

Sune Toft & Victoria Strait

26. School of Physics, University of Melbourne, Parkville, Victoria, Australia

Michele Trenti

27. ARC Centre of Excellence for All-Sky Astrophysics in 3 Dimensions, University of Melbourne, Parkville, Victoria, Australia

Michele Trenti

28. Clay Center Observatory, Dexter Southfield, Brookline, MA, USA

Felipe Andrade-Santos

29. Department of Theoretical Physics, University of the Basque Country UPV/EHU, Bilbao, Spain

Tom Broadhurst

30. Donostia International Physics Center (DIPC), Donostia, Spain

Tom Broadhurst

31. IKERBASQUE, Basque Foundation for Science, Bilbao, Spain

Tom Broadhurst

Contributions

B.W. identified the star, led the lens modelling and size constraint analysis, and wrote the majority of the manuscript. D.C. proposed and carried out observations, measured photometry and redshifts, and helped analyse size and magnification constraints. J.M.D. performed and analysed microlensing simulations, and contributed to lens model analysis. A.Z., G.M., M.O. and K.S. contributed to the lens model analyses. E.Z. calculated stellar constraints based on observed magnitude and magnification. P.D. and Y.J.-T. calculated stellar surface mass densities used in microlensing analysis. P.K. and R.W. helped compare results and methods to previous lensed star detections and theoretical predictions. F.X.T., S.E.d.M. and A.V. contributed to stellar constraint analysis and interpretation. R.J.A. reduced the HST images. M.B. and V.S. obtained and analysed Spitzer data. All authors contributed to the scientific interpretation of the results and to aspects of the analysis and writing.

Corresponding author

Correspondence to [Brian Welch](#).

Ethics declarations

Competing interests

The authors declare no competing interests.

Peer review

Peer review information

Nature thanks the anonymous reviewers for their contribution to the peer review of this work. Peer reviewer reports are available.

Additional information

Publisher's note Springer Nature remains neutral with regard to jurisdictional claims in published maps and institutional affiliations.

Extended data figures and tables

Extended Data Fig. 1 Photometry of the Sunrise Arc and Earendel.

a, HST photometry with 1σ error bars, SED fit, and redshift probability distribution for the Sunrise Arc using the photometric fitting code BAGPIPES. The arc shows a clear Lyman break feature, and has a photometric redshift $z = 6.24 \pm 0.10$ (68% CL). **b**, HST photometry for the full arc (black), clumps 1.1a/b (green/blue), and Earendel (red), with associated 1σ error bars. BPZ yields a photometric redshift of $z_{\text{phot}} = 6.20 \pm 0.05$ (inset; 68% CL), similar to the BAGPIPES result. Clumps 1.1a/b have similar photometry, strengthening the conclusion that they are multiple images. Note both BPZ and BAGPIPES find significant likelihood only between $5.95 < z < 6.55$ for the Sunrise Arc.

Extended Data Fig. 2 Lensed star variability across observations.

Earendel has remained consistently bright across 3.5 years of HST imaging. The figure shows WFC3/IR images of the lensed star (circled in green) across four epochs. **a, b**, Epoch 1 (**a**) and epoch 2 (**b**), taken as part of RELICS; they are a sum of the infrared imaging in four filters F105W + F125W + F140W + F160W from each epoch (one orbit each). **c, d**, Follow-up F110W imaging taken in epoch 3 (**c**) and epoch 4 (**d**). One orbit is shown in each, in a more efficient filter than those used for the previous epochs. **e**, Plot of the original RELICS photometry (blue) compared to the follow-up photometry (orange), each with 1σ error bars. The blue band is the weighted average of the original RELICS infrared fluxes (35 ± 9 nJy, 68% CL), and the orange band is the new F110W flux (49 ± 4 nJy, 68% CL).

Extended Data Fig. 3 Strong lens modelling constraints for WHL0137–08.

a, HST composite image of WHL0137–08, a massive galaxy cluster at $z = 0.566$ that lenses the Sunrise Arc. Multiple images of the two lensed galaxies used in the lens modelling are marked in cyan and labelled in zoomed outsets. Cluster member galaxies circled in magenta are those freely optimized in both the LTM and Lenstool lens models. Critical curves are shown for the best-fit LTM model. The dashed orange curve is at $z = 3.1$, the same photometric redshift as multiple image system 2 (shown in **b**), and the solid red curve is at $z = 6.2$, the photometric redshift of the Sunrise Arc (system 1, shown in **c**). The lensed star Earendel lies directly between 1.1a and 1.1b. Note that 1.1c appears fainter than its counter-images 1.1a/b, owing to its lower magnification and that all of these images are unresolved. The galaxies labelled A–E are described in Methods section ‘Lens modelling’. BCG, brightest cluster galaxy.

Extended Data Fig. 4 Size and separation upper limit measurements.

Earendel’s image is spatially unresolved. We manipulate this image, separating it in two or stretching it in place to put upper limits on its magnified radius $R < 0.055''$ and distance $2\xi < 0.11''$ between two unresolved images. These constraints allow us to calculate constraints on the intrinsic radius r , distance D to the critical curve, and magnification μ for each lens model. Here we show a zoomed region of the arc around Earendel in a $10\times$ super-sampled reconstruction of our HST WFC3/IR F110W image based on eight drizzled exposures. The distances and radius labelled in the diagram are exaggerated for visibility.

Extended Data Fig. 5 Diffuse cluster light measurements.

Stellar surface mass density calculations are performed in the vicinity of the lensed star, within the green boxes shown. The arc and star are masked to avoid contamination, but nearby cluster galaxies are included. This figure

shows the HST F110W band image, which is used to define the extent of the lensed arc.

Extended Data Fig. 6 Flux variations expected from microlensing simulations.

Microlensing is only expected to vary the total magnification by a factor of 2–3 over time, consistent with the observed steady flux over 3.5 years. **a**, The simulated microcaustic network arising from stars and stellar remnants within the lensing cluster. The cluster caustic is the extreme magnification horizontal region near the middle of the image, with individual cusps from microlenses still visible beyond the cluster caustic. We estimate Earendel will move relative to the microlens network at $\sim 1,000 \text{ km s}^{-1}$ in some unknown direction. **b**, Predicted magnification fluctuations over time arising from this motion in the $1M_\odot \text{ pc}^{-2}$ case (blue) and the $10M_\odot \text{ pc}^{-2}$ case (purple), assuming that the relative motion is at an angle of 45° . Grey bands highlight a factor of 2 (dark) and a factor of 4 (light) change in magnification. **c**, The likelihood of magnification variations between two observations separated by different times, again for both the $1M_\odot$ and $10M_\odot \text{ pc}^{-2}$ cases. Note the ‘more is less’ microlensing effect that reduces variability in the observed images when the density of microlenses increases.

Extended Data Fig. 7 H–R diagrams with stellar tracks at multiple metallicities.

a–d, A star’s metallicity will affect its evolution, so to probe this effect we show here our luminosity constraints compared to stellar tracks from BoOST at metallicities of $1Z_\odot$ (**a**), $0.1Z_\odot$ (**b**), $0.02Z_\odot$ (**c**) and $0.004Z_\odot$ (**d**). The $0.1Z_\odot$ case is also shown in Fig. 3, and these plots are similar, including the green region allowed by our analysis. Although the tracks do exhibit some notable differences, the resulting mass estimates do not change significantly given the current large uncertainties.

Extended Data Fig. 8 Stellar evolution tracks versus time.

Here we show the total magnification required to lens stars to Earendel's apparent magnitude as a function of time on stellar evolution tracks (BoOST $0.1Z_{\odot}$, as plotted in the H–R diagram Fig. 3). This required magnification changes over the lifetime of each star as it varies in luminosity or temperature, changing the flux observed in the F110W filter. We find that stars at $\sim 100M_{\odot}$ and above spend the most time (~ 2 Myr) in the green region that reproduces Earendel's observed flux, given our magnification estimates. But considering that lower-mass stars are more numerous, we conclude that masses of roughly $(50\text{--}100)M_{\odot}$ are most likely if Earendel is a single star.

Extended Data Table 1 Hubble imaging of WHL0137–08 in nine filters and photometry measured for the Sunrise Arc and Earendel
Extended Data Table 2 Stellar surface mass densities from two possible IMFs

Supplementary information

Peer Review File

Rights and permissions

Reprints and Permissions

About this article

Cite this article

Welch, B., Coe, D., Diego, J.M. *et al.* A highly magnified star at redshift 6.2. *Nature* **603**, 815–818 (2022). <https://doi.org/10.1038/s41586-022-04449-y>

- Received: 28 July 2021
- Accepted: 20 January 2022

- Published: 30 March 2022
- Issue Date: 31 March 2022
- DOI: <https://doi.org/10.1038/s41586-022-04449-y>

Share this article

Anyone you share the following link with will be able to read this content:

[Get shareable link](#)

Sorry, a shareable link is not currently available for this article.

[Copy to clipboard](#)

Provided by the Springer Nature SharedIt content-sharing initiative

This article was downloaded by **calibre** from <https://www.nature.com/articles/s41586-022-04449-y>.

| [Section menu](#) | [Main menu](#) |

- Article
- [Published: 30 March 2022](#)

The colloidal nature of complex fluids enhances bacterial motility

- [Shashank Kamdar](#) [ORCID: orcid.org/0000-0003-2455-692X¹](#),
- [Seunghwan Shin¹](#),
- [Premkumar Leishangthem²](#),
- [Lorraine F. Francis](#) [ORCID: orcid.org/0000-0003-2516-2957¹](#),
- [Xinliang Xu](#) [ORCID: orcid.org/0000-0003-4940-3612^{2,3}](#) &
- [Xiang Cheng](#) [ORCID: orcid.org/0000-0002-2759-764X¹](#)

[Nature](#) volume 603, pages 819–823 (2022)

- 2628 Accesses
- 94 Altmetric
- [Metrics details](#)

Subjects

- [Cellular motility](#)
- [Colloids](#)

Abstract

The natural habitats of microorganisms in the human microbiome, ocean and soil ecosystems are full of colloids and macromolecules. Such environments exhibit non-Newtonian flow properties, drastically affecting the locomotion of microorganisms^{1,2,3,4,5}. Although the low-Reynolds-

number hydrodynamics of swimming flagellated bacteria in simple Newtonian fluids has been well developed^{6,7,8,9}, our understanding of bacterial motility in complex non-Newtonian fluids is less mature^{10,11}. Even after six decades of research, fundamental questions about the nature and origin of bacterial motility enhancement in polymer solutions are still under debate^{12,13,14,15,16,17,18,19,20,21,22,23}. Here we show that flagellated bacteria in dilute colloidal suspensions display quantitatively similar motile behaviours to those in dilute polymer solutions, in particular a universal particle-size-dependent motility enhancement up to 80% accompanied by a strong suppression of bacterial wobbling^{18,24}. By virtue of the hard-sphere nature of colloids, whose size and volume fraction we vary across experiments, our results shed light on the long-standing controversy over bacterial motility enhancement in complex fluids and suggest that polymer dynamics may not be essential for capturing the phenomenon^{12,13,14,15,16,17,18,19,20,21,22,23}. A physical model that incorporates the colloidal nature of complex fluids quantitatively explains bacterial wobbling dynamics and mobility enhancement in both colloidal and polymeric fluids. Our findings contribute to the understanding of motile behaviours of bacteria in complex fluids, which are relevant for a wide range of microbiological processes²⁵ and for engineering bacterial swimming in complex environments^{26,27}.

This is a preview of subscription content

Access options

Subscribe to Nature+

Get immediate online access to the entire Nature family of 50+ journals

\$29.99

monthly

[Subscribe](#)

Subscribe to Journal

Get full journal access for 1 year

\$199.00

only \$3.90 per issue

[Subscribe](#)

All prices are NET prices.

VAT will be added later in the checkout.

Tax calculation will be finalised during checkout.

Buy article

Get time limited or full article access on ReadCube.

\$32.00

[Buy](#)

All prices are NET prices.

Additional access options:

- [Log in](#)
- [Learn about institutional subscriptions](#)

Fig. 1: Bacterial swimming in colloidal suspensions.

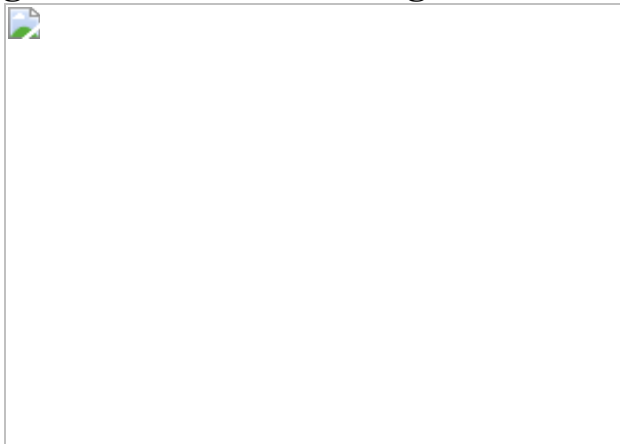


Fig. 2: Size-dependent bacterial motility enhancement.

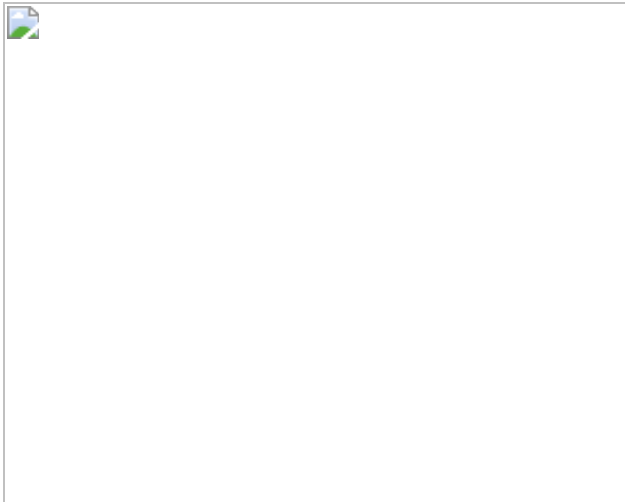


Fig. 3: Anticorrelation between the swimming speed and wobble angle of bacteria.

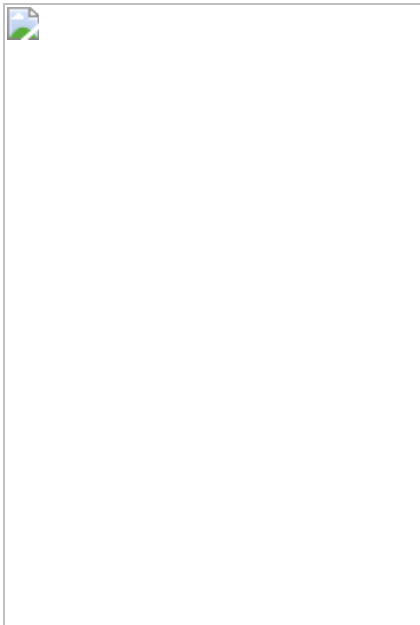
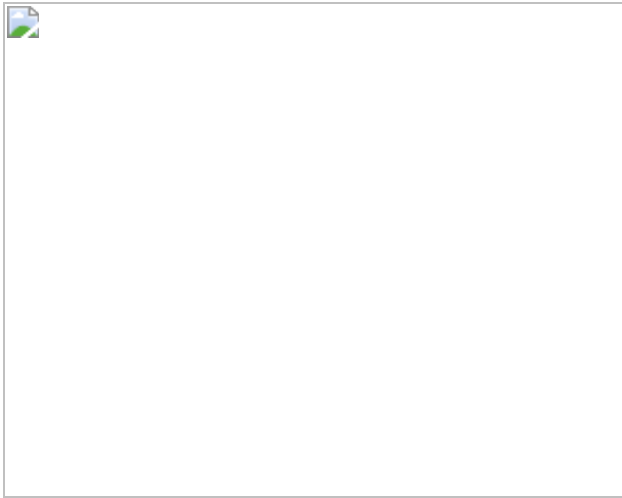


Fig. 4: Enhanced motility of bacteria near a colloid.



Data availability

All data needed to evaluate the conclusions herein are available from the University of Minnesota Data Repository: <https://doi.org/10.13020/nfr5-te36>.

Code availability

The codes used for tracking bacterial swimming speeds and wobble angles are available from the University of Minnesota Data Repository: <https://doi.org/10.13020/nfr5-te36>.

References

1. Celli, J. P. et al. *Helicobacter pylori* moves through mucus by reducing mucin viscoelasticity. *Proc. Natl Acad. Sci. USA* **106**, 14321–14326 (2009).
2. Suarez, S. S. & Pacey, A. A. Sperm transport in the female reproductive tract. *Hum. Reprod. Update* **12**, 23–37 (2006).
3. Wells, M. L. & Goldberg, E. D. Occurrence of small colloids in sea water. *Nature* **353**, 342–344 (1991).

4. Verdugo, P. et al. The oceanic gel phase: a bridge in the DOM–POM continuum. *Mar. Chem.* **92**, 67–85 (2004).
5. Azam, F. & Malfatti, F. Microbial structuring of marine ecosystems. *Nat. Rev. Microbiol.* **5**, 782–791 (2007).
6. Lauga, E. & Powers, T. R. The hydrodynamics of swimming microorganisms. *Rep. Prog. Phys.* **72**, 096601 (2009).
7. Childress, S. *Mechanics of Swimming and Flying* (Cambridge Univ. Press, 1981).
8. Berg, H. C. *E. coli in Motion* (Springer, 2004).
9. Lauga, E. Bacterial hydrodynamics. *Annu. Rev. Fluid Mech.* **48**, 105–130 (2016).
10. Elfring, G. J. & Lauga, E. in *Complex Fluids in Biological Systems* (ed. Spagnolie, S.) 283–317 (Springer, 2015).
11. Patteson, A. E., Gopinath, A. & Arratia, P. E. Active colloids in complex fluids. *Curr. Opin. Colloid Interf. Sci.* **21**, 86–96 (2016).
12. Shoesmith, J. G. The measurement of bacterial motility. *Microbiology* **22**, 528–535 (1960).
13. Schneider, W. R. & Doetsch, R. N. Effect of viscosity on bacterial motility. *J. Bacteriol.* **117**, 696–701 (1974).
14. Berg, H. C. & Turner, L. Movement of microorganisms in viscous environments. *Nature* **278**, 349–351 (1979).
15. Magariyama, Y. & Kudo, S. A mathematical explanation of an increase in bacterial swimming speed with viscosity in linear-polymer solutions. *Biophys. J.* **83**, 733–739 (2002).
16. Martinez, V. A. et al. Flagellated bacterial motility in polymer solutions. *Proc. Natl Acad. Sci. USA* **111**, 17771–17776 (2014).

17. Zhang, Y., Li, G. & Ardekani, A. M. Reduced viscosity for flagella moving in a solution of long polymer chains. *Phys. Rev. Fluids* **3**, 023101 (2018).
18. Patteson, A. E., Gopinath, A., Goulian, M. & Arratia, P. E. Running and tumbling with *E. coli* in polymeric solutions. *Sci. Rep.* **5**, 15761 (2015).
19. Qu, Z., Temel, F. Z., Henderikx, R. & Breuer, K. S. Changes in the flagellar bundling time account for variations in swimming behavior of flagellated bacteria in viscous media. *Proc. Natl Acad. Sci. USA* **115**, 1707–1712 (2018).
20. Qu, Z. & Breuer, K. S. Effects of shear-thinning viscosity and viscoelastic stresses on flagellated bacteria motility. *Phys. Rev. Fluids* **5**, 073103 (2020).
21. Zöttl, A. & Yeomans, J. M. Enhanced bacterial swimming speeds in macromolecular polymer solutions. *Nat. Phys.* **15**, 554–558 (2019).
22. Binagia, J. P., Phoa, A., Housiadas, K. D. & Shaqfeh, E. S. G. Swimming with swirl in a viscoelastic fluid. *J. Fluid Mech.* **900**, A4 (2020).
23. Man, Y. & Lauga, E. Phase-separation models for swimming enhancement in complex fluids. *Phys. Rev. E* **92**, 023004 (2015).
24. Hyon, Y., Marcos, Powers, T. R., Stocker, R. & Fu, H. C. The wiggling trajectories of bacteria. *J. Fluid Mech.* **705**, 58–76 (2012).
25. Hibbing, M. E., Fuqua, C., Parsek, M. R. & Peterson, S. B. Bacterial competition: surviving and thriving in the microbial jungle. *Nat. Rev. Microbiol.* **8**, 15–25 (2010).
26. Nelson, B. J., Kaliakatsos, I. K. & Abbott, J. J. Microrobots for minimally invasive medicine. *Annu. Rev. Biomed. Eng.* **12**, 55–85 (2010).

27. Bechinger, C. et al. Active particles in complex and crowded environments. *Rev. Mod. Phys.* **88**, 045006 (2016).
28. Peng, Y., Liu, Z. & Cheng, X. Imaging the emergence of bacterial turbulence: phase diagram and transition kinetics. *Sci. Adv.* **7**, eabd1240 (2021).
29. Liu, Z., Zeng, W., Ma, X. & Cheng, X. Density fluctuations and energy spectra of 3D bacterial suspensions. *Soft Matter* **17**, 10806–10817 (2021).
30. Lauga, E., DiLuzio, W. R., Whitesides, G. M. & Stone, H. A. Swimming in circles: motion of bacteria near solid boundaries. *Biophys. J.* **90**, 400–412 (2006).
31. Hiemenz, P. C. & Lodge, T. *Polymer Chemistry* 2nd edn (CRC Press, 2007).
32. Darnton, N. C., Turner, L., Rojevsky, S. & Berg, H. C. On torque and tumbling in swimming *Escherichia coli*. *J. Bacteriol.* **189**, 1756–1764 (2007).
33. Macosko, C. W. *Rheology: Principles, Measurements, and Applications* (VCH, 1994).
34. Jeffrey, D. J. & Onishi, Y. Calculation of the resistance and mobility functions for two unequal rigid spheres in low-Reynolds-number flow. *J. Fluid Mech.* **139**, 261–290 (1984).
35. Zhang, B. K., Leishangthem, P. K., Ding, Y. & Xu, X. L. An effective and efficient model of the near-field hydrodynamic interactions for active suspensions of bacteria. *Proc. Natl Acad. Sci. USA* **118**, e2100145118 (2021).
36. Li, G., Tam, L.-K. & Tang, J. X. Amplified effect of Brownian motion in bacterial near-surface swimming. *Proc. Natl Acad. Sci. USA* **105**, 18355–18359 (2008).

37. Block, S. M., Blair, D. F. & Berg, H. C. Compliance of bacterial flagella measured with optical tweezers. *Nature* **338**, 514–518 (1989).
38. Berg, H. C. & Brown, D. A. Chemotaxis in *Escherichia coli* analysed by three-dimensional tracking. *Nature* **239**, 500–504 (1972).
39. Crenshaw, H. C. A new look at locomotion in microorganisms: rotating and translating. *Am. Zool.* **36**, 608–618 (1996).
40. Rossi, M., Cicconofri, G., Beran, A., Noselli, G. & DeSimone, A. Kinematics of flagellar swimming in *Euglena gracilis*: helical trajectories and flagellar shapes. *Proc. Natl Acad. Sci. USA* **114**, 13085–13090 (2017).
41. Cortese, D. & Wan, K. Y. Control of helical navigation by three-dimensional flagellar beating. *Phys. Rev. Lett.* **126**, 088003 (2021).
42. Shimogonya, Y. et al. Torque-induced precession of bacterial flagella. *Sci. Rep.* **5**, 18488 (2015).
43. Poon, W. C. K., Weeks, E. R. & Royall, C. P. On measuring colloidal volume fractions. *Soft Matter* **8**, 21–30 (2012).
44. Crocker, J. C. & Grier, D. G. Methods of digital video microscopy for colloidal studies. *J. Colloid Interf. Sci.* **179**, 298–310 (1996).

Acknowledgements

We thank P. Agrawal, S. Ghosh, Y. Kim, Z. Liu, R. Patel and G. Pradipta for help with experiments and data analysis and S. Guo, P. Kolliopoulos, E. Lauga, Y. Man and Z. Qu for fruitful discussions. We would also like to acknowledge the late Professor Howard Berg, who answered our questions on *E. coli* mutant strains. This research is supported by the IPRIME program of University of Minnesota, and by the US National Science Foundation CBET-1702352 and 2028652. X.X. acknowledges the financial support from National Natural Science Foundation of China no. 11974038 and no. U1930402. Portions of this work were conducted in the Minnesota

Nano Center, which is supported by the US National Science Foundation through the National Nano Coordinated Infrastructure Network (NNCI) under award number ECCS-2025124.

Author information

Affiliations

1. Department of Chemical Engineering and Materials Science,
University of Minnesota, Minneapolis, MN, USA

Shashank Kamdar, Seunghwan Shin, Lorraine F. Francis & Xiang Cheng

2. Complex Systems Division, Beijing Computational Science Research Center, Beijing, China

Premkumar Leishangthem & Xinliang Xu

3. Department of Physics, Beijing Normal University, Beijing, China

Xinliang Xu

Contributions

S.K., L.F.F. and X.C. designed the research. S.K. performed the experiments. S.K., S.S., L.F.F. and X.C. discussed and analysed the experimental data. X.X. proposed the model and conducted the analytical calculations with input from X.C. P.L. and X.X. performed the simulation of Extended Data Fig. 7. X.C. conceived the project. L.F.F., X.X. and X.C. supervised the project. S.K. and X.C. co-wrote the manuscript. All authors discussed and commented on the manuscript.

Corresponding authors

Correspondence to [Xinliang Xu](#) or [Xiang Cheng](#).

Ethics declarations

Competing interests

The authors declare no competing interests.

Peer review

Peer review information

Nature thanks Paulo Arratia and the other, anonymous, reviewer(s) for their contribution to the peer review of this work. Peer reviewer reports are available.

Additional information

Publisher's note Springer Nature remains neutral with regard to jurisdictional claims in published maps and institutional affiliations.

Extended data figures and tables

Extended Data Fig. 1 Experimental methods.

a, The average swimming speed of bacteria V as a function of time after a bacterial suspension is injected into a PDMS microchannel. V is normalized by the average speed at time $t = 0$. The vertical dashed line indicates the maximum measurement time of our experiments of 15 min. **b**, Comparison of the average swimming speed of bacteria V in suspensions of Ficoll 400 of increasing concentrations c from our experiments with that from a previous study. V is normalized by the average swimming speed in the pure buffer V_0 . c is the weight percentage concentration. Blue circles are from our experiments, whereas orange diamonds are from ref. [16](#). **c**, Determination of the intrinsic viscosity of dilute solutions of carboxymethyl cellulose (CMC) of average molecular weight 700,000. The viscosities of

the solutions η as a function of polymer concentrations c are extracted from ref. [18](#). η_s is the solvent viscosity. c is in unit of g/ml. The slope of the linear fit gives $[\eta] = 56,344.1 \text{ ml/g}$.

Extended Data Fig. 2 The rotational diffusivity (a), the mean run time (b) and mean tumble time (c) of bacteria in dilute colloidal suspensions of increasing concentrations.

Black circles are for suspensions of colloids of radius $R = 500 \text{ nm}$, whereas red squares are for colloids of $R = 200 \text{ nm}$. The results are quantitatively similar to those reported in Figs. [3d](#), [4a–c](#) of ref. [18](#).

Extended Data Fig. 3 Anticorrelation between bacterial wobbling and motility enhancement.

a, The swimming speed versus the wobble angle of individual bacteria in pure buffer (black squares) and in a suspension of colloids of radius $R = 500 \text{ nm}$ and volume fraction $\phi = 4\%$ (blue triangles). The data are obtained by averaging the swimming speed of many bacteria binned over a small range of wobble angles. The raw data for each individual bacteria in the 4% colloidal suspension are also shown as the background (grey triangles). For clarity, we do not show the data of individual bacteria in buffer, which show a similar degree of scattering. $V_0 = 13 \mu\text{m/s}$ and $\theta_0 = 45^\circ$ are the average swimming speed and the average wobble angle of bacteria in buffer, respectively. As a comparison, the average swimming speed versus the average wobble of bacteria in polymer solutions of different concentrations from ref. [18](#) is also shown (red discs). **b**, A violin plot showing the probability distribution of the wobble angle of bacteria in buffer and in the 4% colloidal suspension. The interquartile range (IQR) gives the difference between the 75th and 25th percentiles of the data. **a** shows that at a given wobble angle, the swimming speed of a bacterium is nearly constant, independent whether it swims in buffer or in colloidal suspensions. **b** shows that the average swimming speed of bacteria increases in colloidal suspensions, because there are more weakly-wobbling bacteria in the suspensions.

Extended Data Fig. 4 Model description and prediction.

a, A schematic showing the 3D helical trajectory of a bacterium. The 2D projection of the 3D trajectory manifests as bacterial wobbling under optical microscopy. The pitch P and the radius R_w of the trajectory are indicated. The velocity of the bacterium tangential to the helical trajectory V_b and the swimming velocity of the bacterium measured in experiments V are also shown. The schematic is not to scale. R_w is comparable to the size of bacteria and much smaller than P for real trajectories (see Extended Data Fig. 5a). The detailed 3D configuration of a bacterium w.r.t. its trajectory is shown in Extended Data Fig. 6. **b**, A schematic showing the motion of a bacterium in our model. The angular velocity of the bacterial body ω_b and the flagellar bundle ω_t , as well as the angular velocity of the entire bacterium as a rigid body, ω_{cm} , are shown. ω_b , ω_t and ω_{cm} are in the same plane, which we define as the ω plane. The misaligned angle between ω_b and ω_t , α , and the angle of ω_{cm} with respect to the negative z direction, β , are also shown. The wobble angle $\theta = \beta - \alpha$. The coordinate system used in our model is defined at the upper right corner. **c**, Wobble angle θ as a function of the misaligned angle α . A maximum wobble angle $\theta_{max} = 44.5^\circ$ reaches when $\alpha_{max} = 22.8^\circ$. **d**, The anticorrelation between the normalized bacterial swimming speed V/V_0 and the wobble angle θ . Symbols are from our experiments and the solid line is our model prediction. Figure 3b shows the same results using the normalized wobble angle. In the model, we set $V = 1.8 V_0$ at $\theta = 24^\circ$ based on experimental observation. Inset: V/V_0 versus the misaligned angle α from our model.

Extended Data Fig. 5 Pitch and radius of bacterial helical trajectories.

a, The pitch P and the radius R_w of bacterial helical trajectories as a function of the wobble angle θ . See the definition of P and R_w in Extended Data Fig. 4a. P is shown to the left axis and R_w is shown to the right axis. The limiting pitch of 64 μm can be reached in our model. In comparison, the limiting pitch predicted by the previous minimal model of bacterial

wobbling is $4 \mu\text{m}$ for bacteria with single flagellar bundle²⁴. **b**, Probability distribution function (PDF) of the pitch of bacterial helical trajectories.

Black squares are experimental data extracted from Fig. 2a of ref. 24. The red solid line is our model prediction.

Extended Data Fig. 6 Schematics showing the 3D configuration of a swimming bacterium and its helical trajectory.

a, The top view of the configuration. The left-handed helical trajectory encloses a cylindrical space of radius R_w (the grey region). The angular velocity of the body and the flagellar bundle ω_b and ω_t are shown. The velocity of the bacterium tangential to the helical trajectory V_b is indicated. Note that ω_b and V_b tilt above the paper (the solid arrows), whereas ω_t tilts into the paper (the dashed arrow). The average swimming speed of bacteria measured in experiments V is normal to and points out of the paper. The ω plane is normal to the paper as indicated by the purple dashed line. The cross-section of the plane with the helical cylinder has a rectangular shape with the width $w < R_w$. The viewpoint of **b** is indicated at the lower right corner. **b**, The side view of the ω plane. The axis of the helical trajectory is indicated by the vertical dashed line, which is in front of the ω plane above the paper. The projection of V_b along the direction of $-\omega_{cm}$ gives V , whereas the projection of V_b along the direction of the bacterial flagellar bundle ($-\omega_t$) gives V_b^z . The angles α , β and θ are the same as those defined in Extended Data Fig. 4b. The coordinate defined in Extended Data Fig. 4b is reproduced on the lower right. As colloids are depleted from the cylindrical space due to the long-range hydrodynamics (Extended Data Fig. 7), colloids that exert torque on the bacterium via the short-range lubrication interaction are outside the cylindrical space. The effect breaks the symmetric role of colloids around the bacterium, which preferably reduces α and therefore suppresses bacterial wobbling.

Extended Data Fig. 7 Depletion of colloids from the cylindrical space enclosed by the helical trajectory of a wobbling bacteria.

The radius of colloids is 100 nm (top row), 500 nm (middle row) and 1.5 μm (bottom row). Whereas the 100 nm and 500 nm colloids are free, the large 1.5 μm colloids are pinned in the lab frame to match the condition of the optical tweezer experiments. The small discs indicate the initial positions of colloids when the bacterium is far away from the colloids, where the distance between the bacterium and the colloids along the axis of the helical trajectory $-\omega_{cm}$ is $l_{bc} \equiv |(\mathbf{r}_b - \mathbf{r}_c) \cdot \omega_{cm}| / |\omega_{cm}| = 6.5 \mu\text{m}$. Here, \mathbf{r}_b and \mathbf{r}_c are the centre of bacterial body and the centre of the colloids, respectively. The large discs indicate the positions of the corresponding colloids when $l_{bc} = 0$. The lines connecting the small and large discs represent the projection of the 3D trajectories of colloids on the plane normal to $-\omega_{cm}$ in the reference frame of the bacterium, where the bacterial body sits at the origin (0, 0) and orientates in the ω plane indicated by the black dashed lines. The large black circles mark the boundary of the cylindrical space. The radius R_w and the pitch P of the helical trajectory of the bacterium are 1.3 μm and 6.5 μm , respectively. The radius of bacterial body is 1 μm . All the colloids initially located inside the cylindrical space are depleted out of the space as the bacterium approaches the colloids. The results are obtained from numerical simulations with hydrodynamics interactions³⁵, where the interaction between one single colloid and one wobbling bacterium is simulated in each simulation run.

Extended Data Fig. 8 The volume fraction at which the motility enhancement peaks, ϕ_{max} :

$\langle\langle \varphi_{max} \rangle\rangle$ as a function of the radius of colloids or the hydrodynamic radius of polymer coils R . R is normalized by the characteristic radius of bacterial body $r_b = 1 \mu\text{m}$. Except for the datum from ref. 19, all the $\langle\langle \varphi_{max} \rangle\rangle$ are in the dilute regime.

Supplementary information

Supplementary Information

Supplementary text presenting a summary of our experimental finding and a detailed description and derivation of our model.

Peer Review File

41586_2022_4509_MOESM3_ESM.mp4

Supplementary Video **The swimming of a bacterium near a colloid held in an optical trap**. The radius of the colloid is 1.5 μm . The data points on the right show the swimming speed of bacteria (red squares) and the orientation of the bacterium with respect to the local tangential direction of the bacterial trajectory (black squares). Playing at 0.5 \times speed, the video shows the simultaneous increase of bacterial swimming speed and reduction of bacterial wobbling when the bacterium swims near to the colloid (the green region).

Rights and permissions

Reprints and Permissions

About this article

Cite this article

Kamdar, S., Shin, S., Leishangthem, P. *et al.* The colloidal nature of complex fluids enhances bacterial motility. *Nature* **603**, 819–823 (2022). <https://doi.org/10.1038/s41586-022-04509-3>

- Received: 03 May 2021
- Accepted: 03 February 2022
- Published: 30 March 2022
- Issue Date: 31 March 2022

- DOI: <https://doi.org/10.1038/s41586-022-04509-3>

Share this article

Anyone you share the following link with will be able to read this content:

[Get shareable link](#)

Sorry, a shareable link is not currently available for this article.

[Copy to clipboard](#)

Provided by the Springer Nature SharedIt content-sharing initiative

[**Bacteria swim faster when obstacles keep them in line**](#)

- Raphaël Jeanneret
- Marco Polin

News & Views 30 Mar 2022

This article was downloaded by **calibre** from <https://www.nature.com/articles/s41586-022-04509-3>

| [Section menu](#) | [Main menu](#) |

- Article
- [Published: 30 March 2022](#)

Catalogue of flat-band stoichiometric materials

- [Nicolas Regnault](#) [ORCID: orcid.org/0000-0002-0210-2428](#)^{1,2 na1},
- [Yuanfeng Xu](#) [ORCID: orcid.org/0000-0002-1390-2308](#)^{3 na1},
- [Ming-Rui Li](#) [ORCID: orcid.org/0000-0001-5453-1948](#)^{4 na1},
- [Da-Shuai Ma](#)^{5 na1},
- [Milena Jovanovic](#)⁶,
- [Ali Yazdani](#) [ORCID: orcid.org/0000-0003-4996-8904](#)¹,
- [Stuart S. P. Parkin](#) [ORCID: orcid.org/0000-0003-4702-6139](#)³,
- [Claudia Felser](#) [ORCID: orcid.org/0000-0002-8200-2063](#)⁷,
- [Leslie M. Schoop](#) [ORCID: orcid.org/0000-0003-3459-4241](#)⁶,
- [N. Phuan Ong](#) [ORCID: orcid.org/0000-0001-7166-1058](#)¹,
- [Robert J. Cava](#)⁶,
- [Luis Elcoro](#) [ORCID: orcid.org/0000-0002-5427-0984](#)^{8 na1},
- [Zhi-Da Song](#) [ORCID: orcid.org/0000-0002-4987-5962](#)^{1 na1} &
- [B. Andrei Bernevig](#) [ORCID: orcid.org/0000-0001-6337-4024](#)^{1,9,10 na1}

[Nature](#) volume **603**, pages 824–828 (2022)

- 1839 Accesses
- 61 Altmetric
- [Metrics details](#)

Subjects

- [Electronic properties and materials](#)
- [Topological insulators](#)

Abstract

Topological electronic flattened bands near or at the Fermi level are a promising route towards unconventional superconductivity and correlated insulating states. However, the related experiments are mostly limited to engineered materials, such as moiré systems^{1,2,3}. Here we present a catalogue of the naturally occurring three-dimensional stoichiometric materials with flat bands around the Fermi level. We consider 55,206 materials from the Inorganic Crystal Structure Database catalogued using the Topological Quantum Chemistry website^{4,5}, which provides their structural parameters, space group, band structure, density of states and topological characterization. We combine several direct signatures and properties of band flatness with a high-throughput analysis of all crystal structures. In particular, we identify materials hosting line-graph or bipartite sublattices—in either two or three dimensions—that probably lead to flat bands. From this trove of information, we create the Materials Flatband Database website, a powerful search engine for future theoretical and experimental studies. We use the database to extract a curated list of 2,379 high-quality flat-band materials, from which we identify 345 promising candidates that potentially host flat bands with charge centres that are not strongly localized on the atomic sites. We showcase five representative materials and provide a theoretical explanation for the origin of their flat bands close to the Fermi energy using the *S*-matrix method introduced in a parallel work⁶.

This is a preview of subscription content

Access options

Subscribe to Nature+

Get immediate online access to the entire Nature family of 50+ journals

\$29.99

monthly

[Subscribe](#)

Subscribe to Journal

Get full journal access for 1 year

\$199.00

only \$3.90 per issue

[Subscribe](#)

All prices are NET prices.

VAT will be added later in the checkout.

Tax calculation will be finalised during checkout.

Buy article

Get time limited or full article access on ReadCube.

\$32.00

[Buy](#)

All prices are NET prices.

Additional access options:

- [Log in](#)
- [Learn about institutional subscriptions](#)

Fig. 1: An illustration of the three possible types of flat band.

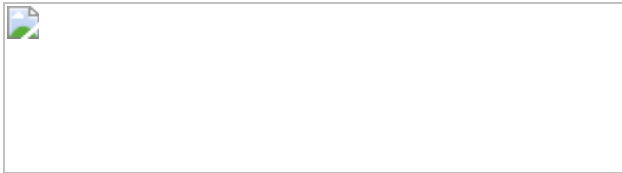
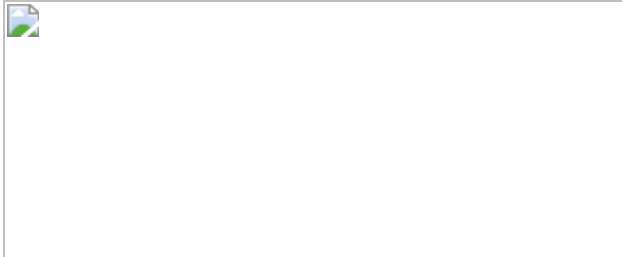


Fig. 2: Crystal and band structures of the representative flat-band materials.



Data availability

All data are available in the [Supplementary Information](#) and through our public website, the Materials Flatband Database (<https://www.topologicalquantumchemistry.fr/flatbands>).

References

1. Bistritzer, R. & MacDonald, A. H. Moiré bands in twisted double-layer graphene. *Proc. Natl Acad. Sci. USA* **108**, 12233–12237 (2011).
2. Cao, Y. et al. Unconventional superconductivity in magic-angle graphene superlattices. *Nature* **556**, 43–50 (2018).
3. Cao, Y. et al. Correlated insulator behaviour at half-filling in magic-angle graphene superlattices. *Nature* **556**, 80–84 (2018).
4. Vergniory, M. G. et al. A complete catalogue of high-quality topological materials. *Nature* **566**, 480–485 (2019).
5. Vergniory, M. G. et al. All topological bands of all stoichiometric materials. Preprint at <https://arxiv.org/abs/2105.09954> (2021).

6. Călugăru, D. et al. General construction and topological classification of crystalline flat bands. *Nat. Phys.* **18**, 185–189 (2022).
7. Kumar, P., Peotta, S., Takasu, Y., Takahashi, Y. & Törmä, P. Flat-band-induced non-Fermi-liquid behavior of multicomponent fermions. *Phys. Rev. A* **103**, L031301 (2021).
8. Tsui, D. C., Stormer, H. L. & Gossard, A. C. Two-dimensional magnetotransport in the extreme quantum limit. *Phys. Rev. Lett.* **48**, 1559–1562 (1982).
9. Laughlin, R. B. Anomalous quantum Hall effect: an incompressible quantum fluid with fractionally charged excitations. *Phys. Rev. Lett.* **50**, 1395–1398 (1983).
10. Moore, G. & Read, N. Nonabelions in the fractional quantum Hall effect. *Nucl. Phys. B* **360**, 362–396 (1991).
11. Drozdov, A., Eremets, M., Troyan, I., Ksenofontov, V. & Shylin, S. I. Conventional superconductivity at 203 kelvin at high pressures in the sulfur hydride system. *Nature* **525**, 73–76 (2015).
12. Drozdov, A. et al. Superconductivity at 250 K in lanthanum hydride under high pressures. *Nature* **569**, 528–531 (2019).
13. Tang, E., Mei, J.-W. & Wen, X.-G. High-temperature fractional quantum Hall states. *Phys. Rev. Lett.* **106**, 236802 (2011).
14. Neupert, T., Santos, L., Chamon, C. & Mudry, C. Fractional quantum Hall states at zero magnetic field. *Phys. Rev. Lett.* **106**, 236804 (2011).
15. Sheng, D., Gu, Z.-C., Sun, K. & Sheng, L. Fractional quantum Hall effect in the absence of Landau levels. *Nat. Commun.* **2**, 389 (2011).
16. Regnault, N. & Bernevig, B. A. Fractional Chern insulator. *Phys. Rev. X* **1**, 021014 (2011).
17. Balents, L., Dean, C. R., Efetov, D. K. & Young, A. F. Superconductivity and strong correlations in moiré flat bands. *Nat.*

Phys. **16**, 725–733 (2020).

18. Peri, V., Song, Z.-D., Bernevig, B. A. & Huber, S. D. Fragile topology and flat-band superconductivity in the strong-coupling regime. *Phys. Rev. Lett.* **126**, 027002 (2021).
19. Rhim, J.-W., Kim, K. & Yang, B.-J. Quantum distance and anomalous Landau levels of flat bands. *Nature* **584**, 59–63 (2020).
20. Xie, F., Song, Z., Lian, B. & Bernevig, B. A. Topology-bounded superfluid weight in twisted bilayer graphene. *Phys. Rev. Lett.* **124**, 167002 (2020).
21. Peotta, S. & Törmä, P. Superfluidity in topologically nontrivial flat bands. *Nat. Commun.* **6**, 8944 (2015).
22. Bradlyn, B. et al. Topological quantum chemistry. *Nature* **547**, 298–305 (2017).
23. Y. Xu et al. Filling-enforced obstructed atomic insulators. Preprint at <https://arxiv.org/abs/2106.10276> (2021).
24. Mielke, A. Exact ground states for the Hubbard model on the kagome lattice. *J. Phys. A* **25**, 4335–4345 (1992).
25. Tasaki, H. From Nagaoka’s ferromagnetism to flat-band ferromagnetism and beyond: an introduction to ferromagnetism in the Hubbard model. *Prog. Theor. Phys.* **99**, 489–548 (1998).
26. Bergman, D. L., Wu, C. & Balents, L. Band touching from real-space topology in frustrated hopping models. *Phys. Rev. B* **78**, 125104 (2008).
27. Liu, Z., Liu, F. & Wu, Y.-S. Exotic electronic states in the world of flat bands: from theory to material. *Chin. Phys. B* **23**, 077308 (2014).
28. Ma, D.-S. et al. Spin-orbit-induced topological flat bands in line and split graphs of bipartite lattices. *Phys. Rev. Lett.* **125**, 266403 (2020).

29. Chiu, C. S., Ma, D.-S., Song, Z.-D., Bernevig, B. A. & Houck, A. A. Fragile topology in line-graph lattices with two, three, or four gapped flat bands. *Phys. Rev. Res.* **2**, 043414 (2020).
30. *Inorganic Crystal Structure Database (ICSD)* (Fachinformationszentrum Karlsruhe, 2015); <https://icsd.products.fiz-karlsruhe.de/>.
31. Hohenberg, P. & Kohn, W. Inhomogeneous electron gas. *Phys. Rev.* **136**, B864–B871 (1964).
32. Kohn, W. & Sham, L. J. Self-consistent equations including exchange and correlation effects. *Phys. Rev.* **140**, A1133–A1138 (1965).
33. Kresse, G. & Hafner, J. Ab initio molecular dynamics for open-shell transition metals. *Phys. Rev. B* **48**, 13115–13118 (1993).
34. Kresse, G. & Furthmüller, J. Efficiency of ab-initio total energy calculations for metals and semiconductors using a plane-wave basis set. *Comput. Mater. Sci.* **6**, 15–50 (1996).
35. Ivantchev, S., Kroumova, E., Madariaga, G., Pérez-Mato, J. M. & Aroyo, M. I. SUBGROUPGRAPH: a computer program for analysis of group–subgroup relations between space groups. *J. Appl. Crystallogr.* **33**, 1190–1191 (2000).
36. Ivantchev, S. et al. SUPERGROUPS—a computer program for the determination of the supergroups of the space groups. *J. Appl. Crystallogr.* **35**, 511–512 (2002).
37. Souza, I., Marzari, N. & Vanderbilt, D. Maximally localized Wannier functions for entangled energy bands. *Phys. Rev. B* **65**, 035109 (2001).

Acknowledgements

We thank X. Dai, D. Calugaru, A. Chew, M. Vergniory and C. Chiu for discussions. We acknowledge the computational resources Cobra/Draco in the Max Planck Computing and Data Facility (MPCDF) and Atlas in the

Donostia International Physics Center (DIPC). This research also used the resources of the National Energy Research Scientific Computing Center (NERSC), a US Department of Energy Office of Science User Facility operated under contract number DE-AC02-05CH11231. This work is part of a project that has received funding from the European Research Council (ERC) under the European Union’s Horizon 2020 research and innovation programme (grant agreement number 101020833). B.A.B. and N.R. were also supported by the US Department of Energy (grant number DE-SC0016239), and were partially supported by the National Science Foundation (EAGER grant number DMR 1643312), a Simons Investigator grant (number 404513), the Office of Naval Research (ONR grant number N00014-20-1-2303), the Packard Foundation, the Schmidt Fund for Innovative Research, the BSF Israel US foundation (grant number 2018226), the Gordon and Betty Moore Foundation through grant number GBMF8685 towards the Princeton theory programme, and a Guggenheim Fellowship from the John Simon Guggenheim Memorial Foundation. A.Y., N.P.O., R.J.C., L.M.S., B.A.B. and N.R. were supported by the NSF-MRSEC (grant number DMR-2011750). A.Y. was supported by NSF-DMR-1904442. B.A.B., L.M.S. and N.R. acknowledge financial support from the Schmidt DataX Fund at Princeton University made possible through a major gift from the Schmidt Futures Foundation. L.M.S. acknowledges financial support from the Packard and Sloan Foundation. B.A.B. received additional support from the Max Planck Society. L.E. was supported by the Government of the Basque Country (Project IT1301-19) and the Spanish Ministry of Science and Innovation (PID2019-106644GB-I00). C.F. was supported by the European Research Council (ERC) advanced grant number 742068 ‘TOP-MAT’, Deutsche Forschungsgemeinschaft (DFG) through SFB 1143, and the Würzburg-Dresden Cluster of Excellence on Complexity and Topology in Quantum Matter-ct.qmat (EXC 2147, project number 390858490). S.S.P.P. acknowledges funding by the Deutsche Forschungsgemeinschaft (DFG, German Research Foundation)—project number 314790414.

Author information

Author notes

1. These authors contributed equally: Nicolas Regnault, Yuanfeng Xu, Ming-Rui Li, Da-Shuai Ma, Luis Elcoro, Zhi-Da Song, B. Andrei Bernevig

Affiliations

1. Department of Physics, Princeton University, Princeton, NJ, USA

Nicolas Regnault, Ali Yazdani, N. Phuan Ong, Zhi-Da Song & B. Andrei Bernevig

2. Laboratoire de Physique de l'Ecole normale supérieure, ENS, Université PSL, CNRS, Sorbonne Université, Université Paris-Diderot, Sorbonne Paris Cité, Paris, France

Nicolas Regnault

3. Max Planck Institute of Microstructure Physics, Halle, Germany

Yuanfeng Xu & Stuart S. P. Parkin

4. Department of Physics, Tsinghua University, Beijing, China

Ming-Rui Li

5. Beijing Key Laboratory of Nanophotonics and Ultrafine Optoelectronic Systems, School of Physics, Beijing Institute of Technology, Beijing, China

Da-Shuai Ma

6. Department of Chemistry, Princeton University, Princeton, NJ, USA

Milena Jovanovic, Leslie M. Schoop & Robert J. Cava

7. Max Planck Institute for Chemical Physics of Solids, Dresden, Germany

Claudia Felser

8. Department of Condensed Matter Physics, University of the Basque Country UPV/EHU, Bilbao, Spain

Luis Elcoro

9. Donostia International Physics Center, Donostia-San Sebastian, Spain

B. Andrei Bernevig

10. IKERBASQUE, Basque Foundation for Science, Bilbao, Spain

B. Andrei Bernevig

Contributions

B.A.B. and N.R. conceived this work; N.R. and M.-R.L. performed the high-throughput calculations with the help from L.E. and Y.X.; Y.X., D.-S.M., Z.-D.S., M.-R.L., L.E. and N.R. worked out the theoretical explanations for the flat-band materials detailed in Supplementary Section F; the material lists in Supplementary Section H were manually selected by Y.X., M.-R.L., Z.-D.S., M.J. and N.R.; N.R. built the flat-band material database; D.-S.M. performed the ab initio ferromagnetic calculations advised by Y.X.; M.J., L.S. and C.F. helped curate the list of materials to find the most experimentally relevant. All authors discussed the results and wrote the main text and Methods; Y.X., Z.-D.S., M.-R.L., D.-S.M., M.J., L.E. and N.R. wrote the Supplementary Information.

Corresponding authors

Correspondence to [Nicolas Regnault](#), [Yuanfeng Xu](#) or [B. Andrei Bernevig](#).

Ethics declarations

Competing interests

The authors declare no competing interests.

Peer review

Peer review information

Nature thanks David Carpentier and the other, anonymous, reviewer(s) for their contribution to the peer review of this work. Peer reviewer reports are available.

Additional information

Publisher's note Springer Nature remains neutral with regard to jurisdictional claims in published maps and institutional affiliations.

Supplementary information

Supplementary Information

This file contains supplementary text, equations, tables, figures and references.

Peer Review File

Rights and permissions

Reprints and Permissions

About this article

Cite this article

Regnault, N., Xu, Y., Li, MR. *et al.* Catalogue of flat-band stoichiometric materials. *Nature* **603**, 824–828 (2022). <https://doi.org/10.1038/s41586-022-04519-1>

- Received: 08 June 2021
- Accepted: 04 February 2022
- Published: 30 March 2022
- Issue Date: 31 March 2022
- DOI: <https://doi.org/10.1038/s41586-022-04519-1>

Share this article

Anyone you share the following link with will be able to read this content:

[Get shareable link](#)

Sorry, a shareable link is not currently available for this article.

[Copy to clipboard](#)

Provided by the Springer Nature SharedIt content-sharing initiative

This article was downloaded by **calibre** from <https://www.nature.com/articles/s41586-022-04519-1>

| [Section menu](#) | [Main menu](#) |

- Article
- [Published: 30 March 2022](#)

Orbital-resolved visualization of single-molecule photocurrent channels

- [Miyabi Imai-Imada](#) [ORCID: orcid.org/0000-0001-9053-7888](#)¹,
- [Hiroshi Imada](#) [ORCID: orcid.org/0000-0001-8508-8563](#)^{1,2},
- [Kuniyuki Miwa](#) [ORCID: orcid.org/0000-0001-7311-0284](#)^{1,3},
- [Yusuke Tanaka](#) [ORCID: orcid.org/0000-0003-0405-616X](#)^{4,5},
- [Kensuke Kimura](#) [ORCID: orcid.org/0000-0003-1270-5289](#)¹,
- [Inhae Zoh](#) [ORCID: orcid.org/0000-0002-7958-340X](#)^{1,6},
- [Rafael B. Jaculbia](#) [ORCID: orcid.org/0000-0003-3156-2404](#)¹,
- [Hiroko Yoshino](#) [ORCID: orcid.org/0000-0002-2087-128X](#)¹,
- [Atsuya Muranaka](#) [ORCID: orcid.org/0000-0002-3246-6003](#)⁴,
- [Masanobu Uchiyama](#) [ORCID: orcid.org/0000-0001-6385-5944](#)^{4,5} &
- [Yousoo Kim](#) [ORCID: orcid.org/0000-0001-7730-0704](#)¹

[Nature](#) volume **603**, pages 829–834 (2022)

- 1785 Accesses
- 12 Altmetric
- [Metrics details](#)

Subjects

- [Excited states](#)
- [Light harvesting](#)

- [Scanning probe microscopy](#)

Abstract

Given its central role in utilizing light energy, photoinduced electron transfer (PET) from an excited molecule has been widely studied^{1,2,3,4,5,6}. However, even though microscopic photocurrent measurement methods^{7,8,9,10,11} have made it possible to correlate the efficiency of the process with local features, spatial resolution has been insufficient to resolve it at the molecular level. Recent work has, however, shown that single molecules can be efficiently excited and probed when combining a scanning tunnelling microscope (STM) with localized plasmon fields driven by a tunable laser^{12,13}. Here we use that approach to directly visualize with atomic-scale resolution the photocurrent channels through the molecular orbitals of a single free-base phthalocyanine (FBPc) molecule, by detecting electrons from its first excited state tunnelling through the STM tip. We find that the direction and the spatial distribution of the photocurrent depend sensitively on the bias voltage, and detect counter-flowing photocurrent channels even at a voltage where the averaged photocurrent is near zero. Moreover, we see evidence of competition between PET and photoluminescence¹², and find that we can control whether the excited molecule primarily relaxes through PET or photoluminescence by positioning the STM tip with three-dimensional, atomic precision. These observations suggest that specific photocurrent channels can be promoted or suppressed by tuning the coupling to excited-state molecular orbitals, and thus provide new perspectives for improving energy-conversion efficiencies by atomic-scale electronic and geometric engineering of molecular interfaces.

This is a preview of subscription content

Access options

Subscribe to Nature+

Get immediate online access to the entire Nature family of 50+ journals

\$29.99

monthly

[Subscribe](#)

Subscribe to Journal

Get full journal access for 1 year

\$199.00

only \$3.90 per issue

[Subscribe](#)

All prices are NET prices.

VAT will be added later in the checkout.

Tax calculation will be finalised during checkout.

Buy article

Get time limited or full article access on ReadCube.

\$32.00

[Buy](#)

All prices are NET prices.

Additional access options:

- [Log in](#)
- [Learn about institutional subscriptions](#)

Fig. 1: Atomic-scale measurement of photocurrent generation in a single molecule.

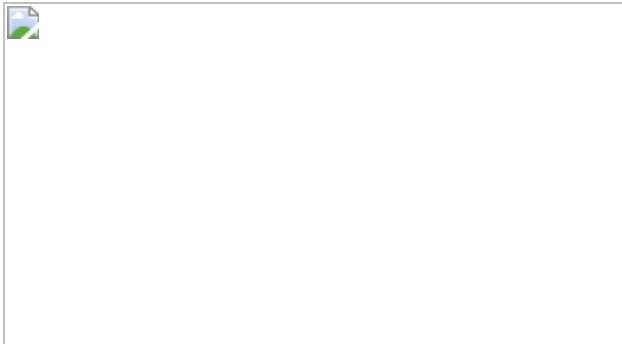


Fig. 2: Voltage dependence of photocurrent channels through a single molecule.

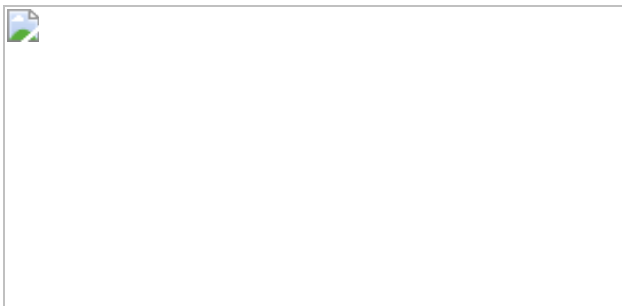


Fig. 3: Mechanism of photocurrent generation in an FBPc molecule.

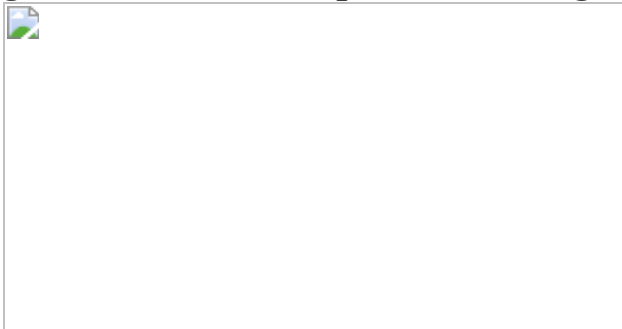
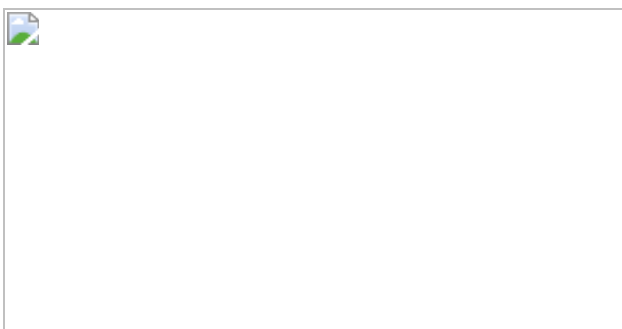


Fig. 4: Control of the quantum efficiencies of photoelectron energy conversion.



Data availability

All experimental data shown in Figs. 1–4, Extended Data Figs. 1–9 and Extended Data Tables 1, 2 can be found at Zenodo, <https://doi.org/10.5281/zenodo.5553643>, and are also available from the corresponding authors upon reasonable request.

Code availability

The code used to calculate the results shown in this work is available from the corresponding authors upon reasonable request.

References

1. Tokita, Y., Shimura, J., Nakajima, H., Goto, Y. & Watanabe, Y. Mechanism of intramolecular electron transfer in the photoexcited Zn-substituted cytochrome *c*: theoretical and experimental perspective. *J. Am. Chem. Soc.* **130**, 5302–5310 (2008).
2. Sariciftci, N. S., Smilowitz, L., Heeger, A. J. & Wudl, F. Photoinduced electron transfer from a conducting polymer to buckminsterfullerene. *Science* **258**, 1474–1476 (1992).
3. Murphy, C. J. et al. Long-range photoinduced electron transfer through a DNA helix. *Science* **262**, 1025–1029 (1993).
4. Lindstrom, C. D. & Zhu, X.-Y. Photoinduced electron transfer at molecule–metal interfaces. *Chem. Rev.* **106**, 4281–4300 (2006).
5. Ma, W., Ma, H., Peng, Y. Y., Tian, H. & Long, Y. T. An ultrasensitive photoelectrochemical platform for quantifying photoinduced electron-transfer properties of a single entity. *Nat. Protoc.* **14**, 2672–2690 (2019).
6. Jones, A. L., Jiang, J. & Schanze, K. S. Excitation-wavelength-dependent photoinduced electron transfer in a π -conjugated diblock oligomer. *J. Am. Chem. Soc.* **142**, 12658–12668 (2020).

7. O'Dea, J. R., Brown, L. M., Hoepker, N., Marohn, J. A. & Sadewasser, S. Scanning probe microscopy of solar cells: from inorganic thin films to organic photovoltaics. *MRS Bull.* **37**, 642–650 (2012).
8. Giridharagopal, R., Cox, P. A. & Ginger, D. S. Functional scanning probe imaging of nanostructured solar energy materials. *Acc. Chem. Res.* **49**, 1769–1776 (2016).
9. Gerster, D. et al. Photocurrent of a single photosynthetic protein. *Nat. Nanotechnol.* **7**, 673–676 (2012).
10. Takeuchi, O. et al. Microscopic description of the current–voltage characteristics of a bulk-heterojunction organic solar cell under illumination. *Appl. Phys. Express* **7**, 021602 (2014).
11. Coffey, D. C., Reid, O. G., Rodovsky, D. B., Bartholomew, G. P. & Ginger, D. S. Mapping local photocurrents in polymer/fullerene solar cells with photoconductive atomic force microscopy. *Nano Lett.* **7**, 738–744 (2007).
12. Imada, H. et al. Single-molecule laser nanospectroscopy with micro-electron volt energy resolution. *Science* **373**, 95–98 (2021).
13. Jaculbia, R. B. et al. Single-molecule resonance Raman effect in a plasmonic nanocavity. *Nat. Nanotechnol.* **15**, 105–110 (2020).
14. Wu, S. W., Ogawa, N. & Ho, W. Atomic-scale coupling of photons to single-molecule junctions. *Science* **312**, 1362–1365 (2006).
15. Zhu, S.-E. et al. Self-decoupled porphyrin with a tripodal anchor for molecular-scale electroluminescence. *J. Am. Chem. Soc.* **135**, 15794–15800 (2013).
16. Cocker, T. L., Peller, D., Yu, P., Repp, J. & Huber, R. Tracking the ultrafast motion of a single molecule by femtosecond orbital imaging. *Nature* **539**, 263–267 (2016).

17. Yoshioka, K. et al. Real-space coherent manipulation of electrons in a single tunnel junction by single-cycle terahertz electric fields. *Nat. Photonics* **10**, 762–765 (2016).
18. Garg, M. & Kern, K. Attosecond coherent manipulation of electrons in tunneling microscopy. *Science* **367**, 411–415 (2020).
19. Zhang, R. et al. Chemical mapping of a single molecule by plasmon-enhanced Raman scattering. *Nature* **498**, 82–86 (2013).
20. Zhang, Y. et al. Visualizing coherent intermolecular dipole–dipole coupling in real space. *Nature* **531**, 623–627 (2016).
21. Imada, H. et al. Real-space investigation of energy transfer in heterogeneous molecular dimers. *Nature* **538**, 364–367 (2016).
22. Doppagne, B. et al. Vibronic spectroscopy with submolecular resolution from STM-induced electroluminescence. *Phys. Rev. Lett.* **118**, 127401 (2017).
23. Kimura, K. et al. Selective triplet exciton formation in a single molecule. *Nature* **570**, 210–213 (2019).
24. Imada, H. et al. Single-molecule investigation of energy dynamics in a coupled plasmon–exciton system. *Phys. Rev. Lett.* **119**, 013901 (2017).
25. Murray, C. et al. Infrared and Raman spectroscopy of free-base and zinc phthalocyanines isolated in matrices. *Phys. Chem. Chem. Phys.* **12**, 10406–10422 (2010).
26. Murray, C. et al. Visible luminescence spectroscopy of free-base and zinc phthalocyanines isolated in cryogenic matrices. *Phys. Chem. Chem. Phys.* **13**, 17543–17554 (2011).
27. Imai-Imada, M. et al. Energy-level alignment of a single molecule on ultrathin insulating film. *Phys. Rev. B* **98**, 201403 (2018).
28. Doppagne, B. et al. Electrofluorochromism at the single-molecule level. *Science* **361**, 251–255 (2018).

29. Repp, J., Meyer, G., Stojković, S. M., Gourdon, A. & Joachim, C. Molecules on insulating films: scanning-tunneling microscopy imaging of individual molecular orbitals. *Phys. Rev. Lett.* **94**, 026803 (2005).
30. Ikeda, T., Iino, R. & Noji, H. Real-time fluorescence visualization of slow tautomerization of single free-base phthalocyanines under ambient conditions. *Chem. Commun.* **50**, 9443–9446 (2014).
31. Liljeroth, P., Repp, J. & Meyer, G. Current-induced hydrogen tautomerization and conductance switching of naphthalocyanine molecules. *Science* **317**, 1203–1206 (2007).
32. Doppagne, B. et al. Single-molecule tautomerization tracking through space- and time-resolved fluorescence spectroscopy. *Nat. Nanotechnol.* **15**, 207–211 (2020).
33. Böckmann, H. et al. Direct observation of photoinduced tautomerization in single molecules at a metal surface. *Nano Lett.* **16**, 1034–1041 (2016).
34. Miwa, K., Najarian, A. M., McCREERY, R. L. & Galperin, M. Hubbard nonequilibrium Green's function analysis of photocurrent in nitroazobenzene molecular junction. *J. Phys. Chem. Lett.* **10**, 1550–1557 (2019).
35. Miwa, K. et al. Many-body state description of single-molecule electroluminescence driven by a scanning tunneling microscope. *Nano Lett.* **19**, 2803–2811 (2019).
36. Yang, B. et al. Sub-nanometre resolution in single-molecule photoluminescence imaging. *Nat. Photonics* **14**, 693–699 (2020).
37. Qiu, X. H., Nazin, G. V. & Ho, W. vibrationally resolved fluorescence excited with submolecular precision. *Science* **299**, 542–546 (2003).
38. Kuhnke, K., Große, C., Merino, P. & Kern, K. Atomic-scale imaging and spectroscopy of electroluminescence at molecular interfaces.

Chem. Rev. **117**, 5174–5222 (2017).

39. Yang, B., Kazuma, E., Yokota, Y. & Kim, Y. Fabrication of sharp gold tips by three-electrode electrochemical etching with high controllability and reproducibility. *J. Phys. Chem. C* **122**, 16950–16955 (2018).
40. Miwa, K., Imada, H., Kawahara, S. & Kim, Y. Effects of molecule–insulator interaction on geometric property of a single phthalocyanine molecule adsorbed on an ultrathin NaCl film. *Phys. Rev. B* **93**, 165419 (2016).
41. Neuman, T., Esteban, R., Casanova, D., García-Vidal, F. J. & Aizpurua, J. Coupling of molecular emitters and plasmonic cavities beyond the point-dipole approximation. *Nano Lett.* **18**, 2358–2364 (2018).
42. Frisch, M. J. et al. Gaussian 16, revision C.01 (Gaussian, Inc., 2016); <https://gaussian.com>.
43. Dunning, T. H. Gaussian basis sets for use in correlated molecular calculations. I. The atoms boron through neon and hydrogen. *J. Chem. Phys.* **90**, 1007–1023 (1989).
44. Becke, A. D. Density-functional thermochemistry. III. The role of exact exchange. *J. Chem. Phys.* **98**, 5648–5652 (1993).
45. Henderson, T. M., Izmaylov, A. F., Scalmani, G. & Scuseria, G. E. Can short-range hybrids describe long-range-dependent properties? *J. Chem. Phys.* **131**, 044108 (2009).
46. Baer, R., Livshits, E. & Salzner, U. Tuned range-separated hybrids in density functional theory. *Annu. Rev. Phys. Chem.* **61**, 85–109 (2010).
47. Runge, E. & Gross, E. K. U. Density-functional theory for time-dependent systems. *Phys. Rev. Lett.* **52**, 997–1000 (1984).

48. Casida, M. E. Time-dependent density functional response theory for molecules. In *Recent Advances in Density Functional Methods: Part I* (ed. Chong, D. P.) 155–192 (World Scientific, 1995).
49. Hirata, S. & Head-Gordon, M. Time-dependent density functional theory within the Tamm–Dancoff approximation. *Chem. Phys. Lett.* **314**, 291–299 (1999).
50. Santoro, F., Improta, R., Lami, A., Bloino, J. & Barone, V. Effective method to compute Franck–Condon integrals for optical spectra of large molecules in solution. *J. Chem. Phys.* **126**, 084509 (2007).
51. Santoro, F., Lami, A., Improta, R. & Barone, V. Effective method to compute vibrationally resolved optical spectra of large molecules at finite temperature in the gas phase and in solution. *J. Chem. Phys.* **126**, 184102 (2007).
52. Santoro, F., Lami, A., Improta, R., Bloino, J. & Barone, V. Effective method for the computation of optical spectra of large molecules at finite temperature including the Duschinsky and Herzberg–Teller effect: the Q_x band of porphyrin as a case study. *J. Chem. Phys.* **128**, 224311 (2008).
53. Barone, V., Bloino, J., Biczysko, M. & Santoro, F. Fully integrated approach to compute vibrationally resolved optical spectra: from small molecules to macrosystems. *J. Chem. Theory Comput.* **5**, 540–554 (2009).
54. Scivetti, I. & Persson, M. Frontier molecular orbitals of a single molecule adsorbed on thin insulating films supported by a metal substrate: electron and hole attachment energies. *J. Phys. Condens. Matter* **29**, 355002 (2017).
55. Galperin, M. Photonics and spectroscopy in nanojunctions: a theoretical insight. *Chem. Soc. Rev.* **46**, 4000–4019 (2017).
56. Miwa, K., Chen, F. & Galperin, M. Towards noise simulation in interacting nonequilibrium systems strongly coupled to baths. *Sci. Rep.*

7, 9735 (2017).

57. Chen, F., Ochoa, M. A. & Galperin, M. Nonequilibrium diagrammatic technique for Hubbard Green functions. *J. Chem. Phys.* **146**, 92301 (2017).
58. Cohen, G. & Galperin, M. Green's function methods for single molecule junctions. *J. Chem. Phys.* **152**, 090901 (2020).
59. White, A. J., Ochoa, M. A. & Galperin, M. Nonequilibrium atomic limit for transport and optical response of molecular junctions. *J. Phys. Chem. C* **118**, 11159–11173 (2014).
60. Schulz, F. et al. Many-body transitions in a single molecule visualized by scanning tunnelling microscopy. *Nat. Phys.* **11**, 229–234 (2015).
61. Ervasti, M. M., Schulz, F., Liljeroth, P. & Harju, A. Single- and many-particle description of scanning tunneling spectroscopy. *J. Electron Spectros. Relat. Phenom.* **219**, 63–71 (2017).
62. Seldenthuis, J. S., van der Zant, H. S. J., Ratner, M. A. & Thijssen, J. M. Electroluminescence spectra in weakly coupled single-molecule junctions. *Phys. Rev. B* **81**, 205430 (2010).
63. Fatayer, S. et al. Reorganization energy upon charging a single molecule on an insulator measured by atomic force microscopy. *Nat. Nanotechnol.* **13**, 376–380 (2018).
64. Yu, P., Kocić, N., Repp, J., Siegert, B. & Donarini, A. Apparent reversal of molecular orbitals reveals entanglement. *Phys. Rev. Lett.* **119**, 56801 (2017).
65. Wu, S. W., Nazin, G. V., Chen, X., Qiu, X. H. & Ho, W. Control of relative tunneling rates in single molecule bipolar electron transport. *Phys. Rev. Lett.* **93**, 236802 (2004).
66. Novotny, L. A. & Hecht, B. *Principles of Nano-Optics* (Cambridge Univ. Press, 2012).

Acknowledgements

We thank B. Yang, E. Kazuma, Y. Hasegawa and Y. Shimizu for supporting the preparation of the Au tips. Some of the numerical calculations were carried out using the HOKUSAI system at RIKEN. All experiments were conducted at RIKEN in Japan. This work was financially supported in part by JST PRESTO (grant no. JPMJPR186225 (H.I.)) and by Japan Society for the Promotion of Science (JSPS) KAKENHI: grant nos JP 19K23591 (M.I.-I.), JP19H04681, JP 17H04796 (H.I.), JP 20K22488 (K.K.), JP 18K14153 (R.B.J.), JP 18H05257 (Y.K.), JP17H06173, JP17H05430 (M.U.), JP20H02728 (A.M.).

Author information

Affiliations

1. Surface and Interface Science Laboratory, RIKEN, Wako, Japan
Miyabi Imai-Imada, Hiroshi Imada, Kuniyuki Miwa, Kensuke Kimura, Inhae Zoh, Rafael B. Jaculbia, Hiroko Yoshino & Yousoo Kim
2. PRESTO, Japan Science and Technology Agency (JST), Kawaguchi, Japan
Hiroshi Imada
3. Institute for Molecular Science, Okazaki, Japan
Kuniyuki Miwa
4. Advanced Elements Chemistry Laboratory, RIKEN, Wako, Japan
Yusuke Tanaka, Atsuya Muranaka & Masanobu Uchiyama
5. Graduate School of Pharmaceutical Sciences, The University of Tokyo, Tokyo, Japan

Yusuke Tanaka & Masanobu Uchiyama

6. Department of Biophysics and Chemical Biology, Seoul National University, Seoul, Republic of Korea

Inhae Zoh

Contributions

M.I.-I, H.I. and Y.K. conceived the project and constructed the experimental set-up with the help of Y.K. M.I.-I., H.I., K.K., I.Z., R.B.J. and H.Y. performed the experiment using STM and analysed the data. Y.T., A.M. and M.U. synthesized and characterized the D₂Pc molecule. K.M. conducted the theoretical calculations. Y.K. directed the project. All authors discussed the results and wrote the manuscript.

Corresponding authors

Correspondence to [Hiroshi Imada](#) or [Yousoo Kim](#).

Ethics declarations

Competing interests

The authors declare no competing interests.

Peer review

Peer review information

Nature thanks Leo Gross, Christoph Lienau and the other, anonymous, reviewer(s) for their contribution to the peer review of this work.

Additional information

Publisher's note Springer Nature remains neutral with regard to jurisdictional claims in published maps and institutional affiliations.

Extended data figures and tables

Extended Data Fig. 1 Trace of tip–height variation under laser irradiation.

The laser power was 80 μW , and the energy was 1,816 meV. During the measurement, the tip was placed on the Ag(111) with the closed STM feedback loop.

Extended Data Fig. 2 Voltage dependence of dark-current images over a single molecule.

Current images over the FBPc molecule at -2.0 and 0.0 V (image size, 3.0 nm \times 3.0 nm). While the tip was scanning, the laser was turned off, and the STM feedback loop was open. The tip–molecule distance was maintained to be the same as the laser-on image in Fig. 2b. Shades of blue and red indicate current flow from the substrate to the tip and vice versa, respectively. The line profiles along the dashed lines are shown below the dark-current images. The red dots show the raw data at each pixel and the black line shows a smoothed profile by a moving average of five adjacent data points. At -2.0 V, the dark current slightly exceeds the margin of error around the centre of the molecule, whereas it does not at 0.0 V. The maximum absolute value of the detected current at -2.0 V was about 0.03 pA. Because this value was only 0.3% of the maximum detected current value under illumination (Fig. 2b), the contribution of the dark current to the photocurrent image in Fig. 2b is negligibly small.

Extended Data Fig. 3 Tautomerization reaction of an FBPc molecule under laser irradiation.

a, $Z(t)$ spectra were measured on a D₂Pc molecule on the NaCl(4ML)/Ag(111) with the STM feedback loop closed ($V_s = +1.0$ V, $I_t =$

3 pA). The black and blue spectra were measured under laser-off and laser-on conditions, respectively. The incident laser energy was tuned at the resonance of the S_0 - S_1 transition shown in Fig. 1d, with the power at 1 μ W. Both spectra were measured with the same tip placed at the same distance and angle from the centre of the molecule, and the Z values for both spectra refer to the identical position. **b**, The current images of a D₂Pc molecule ($V_s = +0.75$ V) under laser-on (left) and laser-off (right) conditions, respectively. The power of the laser was 2 μ W. **c**, The orientation of the molecule in the images shown in **b**. Under the laser-on condition, tautomerization reactions cause the molecular axes to rotate through 90°, whereas under laser-off condition it does not.

Extended Data Fig. 4 Molecular structure and the spatial distribution of frontier molecular orbitals.

Molecular structure of FBPc and the spatial distributions of the HOMO, LUMO and nearly degenerated LUMO+1 of FBPc in the gas phase as predicted by density functional theory (DFT) calculations. The orientation of molecule and the position of the arrows, which show the position 45° from the axes, correspond to those in Fig. 2b, d.

Extended Data Fig. 5 Voltage dependence of the photocurrent image in the transition range.

Photocurrent images over the FBpC molecule at -0.4, -0.3, -0.25, -0.2 and -0.1 V (Image size: 2.4 nm × 2.4 nm) acquired with the STM feedback loop open. The laser energy was set at the resonance of the S_0 - S_1 transition, with a power of 77 μ W. Shades of blue and red represent the current flow from the substrate to the tip and vice versa, respectively. The line profiles along the dashed line in each photocurrent image are shown below the respective images. The vertical dashed lines in the line profiles are for comparing the same tip positions. It is revealed that positions showing the local maximum of the positive photocurrent at -0.1 V correspond to where the negative photocurrent value shows a local minimum at -0.4 V. This result is indicative of the competition between the negative and positive photocurrent channels in the molecule.

Extended Data Fig. 6 Line profiles of photocurrent and photoluminescence signals.

a, Photocurrent image of an FBPc molecule on NaCl(4ML)/Ag(111) measured at $V_s = -2.0$ V and the STM tip position during the measurement in Fig. 4d,e (black circles). **b**, The line profile of the photocurrent along the dashed line in a (45° from the molecular axes). Photocurrent signals were measured at lateral tip positions ranging from 0.6 nm to 2.4 nm. The size of the photocurrent signal agrees well with the molecular size observed in the STM image, indicating that photocurrent generation occurs when the tip is placed on the molecule. **c**, The line profile of photoluminescence (PL) along the dashed line in a. Photoluminescence signals appear at all lateral tip positions between 0.0 nm and 3.0 nm. The intensity is minimal at the centre of the molecule (~1.5 nm), and increases with distance from the centre. The local maximum values appear at ~0.5 and ~2.6 nm, and the intensity further turns to decrease with distance. These tendencies correspond to the tip–position dependence of the coupling between the molecule and the localized plasmon which drives the molecular luminescence³⁶. Because the photoluminescence is driven by the localized plasmon, which is several nanometres long²⁴, photoluminescence can be observed even when the tip is outside the molecule. The STM tip positions during the measurement in Fig. 4d,e are shown by the arrows. Although both photocurrent and photoluminescence signals were observed on the molecule (at the position of the left arrow), only the photoluminescence signal was detected outside the molecule (at the right arrow). Using this difference, we investigated the influence of photocurrent generation on photoluminescence quenching (Fig. 4d,e).

Extended Data Fig. 7 Comparison of the populations of increasing electrons and decreasing photons.

The increase of electrons (red area in Fig. 4d) and the decrease of photons (blue area in Fig. 4d) are plotted against $Z_{\text{tip-mol}}$. The number of electrons was obtained from the detected photocurrent value divided by the elementary charge e . The number of quenched photons ($\langle I \rangle - \langle \rm{ph} \rangle \rangle^{\wedge} \langle \rm{quench} \rangle \rangle \rangle$) was obtained by the following

equation. $\langle I \rangle_{\rm ph}^{\rm quench} = \langle I \rangle_{\rm ph}^{\rm fit} - \langle I \rangle_{\rm ph}^{\rm det}$. Here, $\langle I \rangle_{\rm ph}^{\rm fit}$ is the number of the photons (counts per second) deduced by the fitting curve $I_{\rm ph} = 1.09 \times 10^5 \times \exp(-6.77Z_{\text{tip-mol}})$ for the $Z_{\text{tip-mol}}$ range between 1.1 nm and 0.55 nm shown in Fig. 4d. By extrapolating the fitted curve into the $Z_{\text{tip-mol}}$ value less than 0.53 nm, we estimated the expected photon intensity without the photoluminescence quenching in this region. η_{det} is the detection efficiency determined by the experimental set-up. By considering the collection solid angle of the lens, detection quantum efficiency of the detector, and the reflection, diffraction and transmission of the optics, η_{det} was estimated to be 4.9×10^{-4} for this measurement (see [Methods](#)). It was revealed that the number of electrons flowing as photocurrent and the number of quenched photons at each $Z_{\text{tip-mol}}$ were comparable. These results suggest that the observed photoluminescence quenching mainly originated from the photocurrent generation. The slightly large value of the quenched photons might come from another nonradiative recombination pathway or underestimation of η_{det} .

[Extended Data Fig. 8 Determination of the tip–molecule distance.](#)

a, The conductance (G) curve for the bare Ag(111) (black) and the linear fitting curve (red). The tip displacement Z refers to the initial tip position at $V_s = -2.5$ V and $I_t = 3$ pA. The G is normalized by the quantization conductance G_0 which is defined by $2e^2/h$ with the electron charge e and Planck's constant h . **b**, A schematic illustration of the various relevant distances in the photocurrent measurement.

[Extended Data Fig. 9 Simulation results of the \$I\$ – \$V\$ curve in the single-molecule junction under laser irradiation.](#)

a–f, Results are given for various values of electron–phonon coupling parameter λ .

Extended Data Table 1 Total energy E^{total} (summation of the electronic and zero-point vibrational energies) for each electronic state

**Extended Data Table 2 The correction **

({{\boldsymbol{E}}}_{{\boldsymbol{N}}})

{\boldsymbol{a}}^{\bf Img}) of the total energy for each molecular many-body state owing to the image-charge effects from the electrodes

Rights and permissions

[Reprints and Permissions](#)

About this article

Cite this article

Imai-Imada, M., Imada, H., Miwa, K. *et al.* Orbital-resolved visualization of single-molecule photocurrent channels. *Nature* **603**, 829–834 (2022).
<https://doi.org/10.1038/s41586-022-04401-0>

- Received: 16 March 2021
- Accepted: 03 January 2022
- Published: 30 March 2022
- Issue Date: 31 March 2022
- DOI: <https://doi.org/10.1038/s41586-022-04401-0>

Share this article

Anyone you share the following link with will be able to read this content:

[Get shareable link](#)

Sorry, a shareable link is not currently available for this article.

[Copy to clipboard](#)

Provided by the Springer Nature SharedIt content-sharing initiative

This article was downloaded by **calibre** from <https://www.nature.com/articles/s41586-022-04401-0>

| [Section menu](#) | [Main menu](#) |

- Article
- [Published: 30 March 2022](#)

Observing polymerization in 2D dynamic covalent polymers

- [Gaolei Zhan](#) ORCID: orcid.org/0000-0002-7935-7998¹ na1 nAff5,
- [Zhen-Feng Cai](#) ORCID: orcid.org/0000-0002-1659-4291¹ na1 nAff6,
- [Karol Strutyński](#) ORCID: orcid.org/0000-0001-8733-9012²,
- [Lihua Yu](#)¹,
- [Niklas Herrmann](#)¹,
- [Marta Martínez-Abadía](#)³,
- [Manuel Melle-Franco](#)²,
- [Aurelio Mateo-Alonso](#) ORCID: orcid.org/0000-0002-5316-2594^{3,4} &
- [Steven De Feyter](#) ORCID: orcid.org/0000-0002-0909-9292¹

[Nature](#) volume 603, pages 835–840 (2022)

- 4253 Accesses
- 96 Altmetric
- [Metrics details](#)

Subjects

- [Imaging techniques](#)
- [Organic molecules in materials science](#)
- [Polymerization mechanisms](#)

Abstract

The quality of crystalline two-dimensional (2D) polymers^{1,2,3,4,5,6} is intimately related to the elusive polymerization and crystallization processes. Understanding the mechanism of such processes at the (sub)molecular level is crucial to improve predictive synthesis and to tailor material properties for applications in catalysis^{7,8,9,10} and (opto)electronics^{11,12}, among others^{13,14,15,16,17,18}. We characterize a model boroxine 2D dynamic covalent polymer, by using *in situ* scanning tunnelling microscopy, to unveil both qualitative and quantitative details of the nucleation–elongation processes in real time and under ambient conditions. Sequential data analysis enables observation of the amorphous-to-crystalline transition, the time-dependent evolution of nuclei, the existence of ‘non-classical’ crystallization pathways and, importantly, the experimental determination of essential crystallization parameters with excellent accuracy, including critical nucleus size, nucleation rate and growth rate. The experimental data have been further rationalized by atomistic computer models, which, taken together, provide a detailed picture of the dynamic on-surface polymerization process. Furthermore, we show how 2D crystal growth can be affected by abnormal grain growth. This finding provides support for the use of abnormal grain growth (a typical phenomenon in metallic and ceramic systems) to convert a polycrystalline structure into a single crystal in organic and 2D material systems.

This is a preview of subscription content

Access options

Subscribe to Nature+

Get immediate online access to the entire Nature family of 50+ journals

\$29.99

monthly

[Subscribe](#)

[Subscribe to Journal](#)

Get full journal access for 1 year

\$199.00

only \$3.90 per issue

[Subscribe](#)

All prices are NET prices.

VAT will be added later in the checkout.

Tax calculation will be finalised during checkout.

[Buy article](#)

Get time limited or full article access on ReadCube.

\$32.00

[Buy](#)

All prices are NET prices.

Additional access options:

- [Log in](#)
- [Learn about institutional subscriptions](#)

Fig. 1: Disorder-to-order transition.

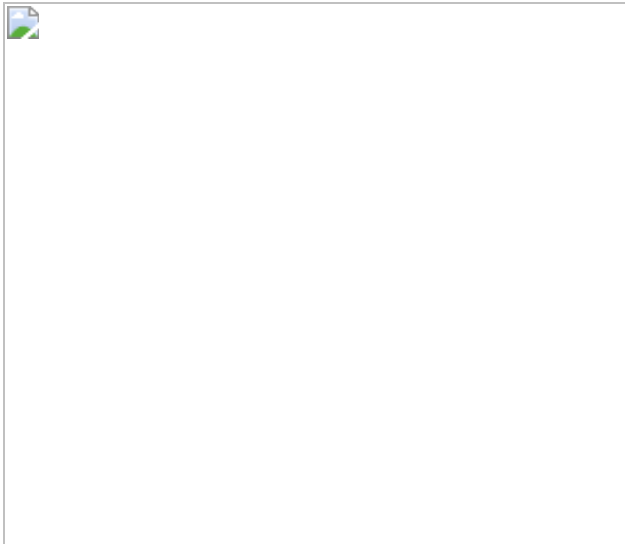


Fig. 2: Nucleation–elongation processes.

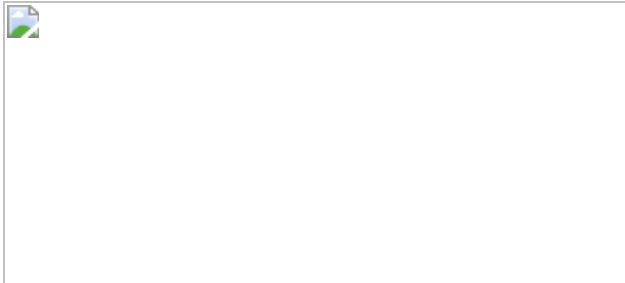
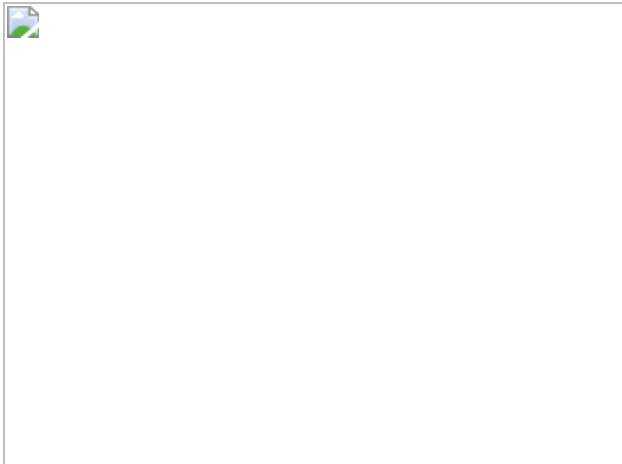


Fig. 3: Normal and abnormal 2D grain growth routes.



Fig. 4: Identification of grain boundaries and their kinetic movement.



Data availability

The main data supporting the findings of this study are available within the paper and its [Supplementary Information](#). Additional data are available from the corresponding authors upon reasonable request.

References

1. Wang, W. & Schlüter, A. D. Synthetic 2D polymers: a critical perspective and a look into the future. *Macromol. Rapid Commun.* **40**, 1800719 (2019).
2. Feng, X. & Schlüter, A. D. Towards macroscopic crystalline 2D polymers. *Angew. Chem. Int. Ed. Engl.* **57**, 13748–13763 (2018).
3. Servalli, M. & Schlüter, A. D. Synthetic two-dimensional polymers. *Annu. Rev. Mater. Res.* **47**, 361–389 (2017).
4. Payamyar, P., King, B. T., Öttinger, H. C. & Schlüter, A. D. Two-dimensional polymers: concepts and perspectives. *Chem. Commun.* **52**, 18–34 (2016).
5. Colson, J. W. & Dichtel, W. R. Rationally synthesized two-dimensional polymers. *Nat. Chem.* **5**, 453–465 (2013).

6. Sakamoto, J., van Heijst, J., Lukin, O. & Schlüter, A. D. Two-dimensional polymers: just a dream of synthetic chemists? *Angew. Chem. Int. Ed. Engl.* **48**, 1030–1069 (2009).
7. Wang, X. et al. Homochiral 2D porous covalent organic frameworks for heterogeneous asymmetric catalysis. *J. Am. Chem. Soc.* **138**, 12332–12335 (2016).
8. Lin, S. et al. Covalent organic frameworks comprising cobalt porphyrins for catalytic CO₂ reduction in water. *Science* **349**, 1208–1213 (2015).
9. Ding, S.-Y. et al. Construction of covalent organic framework for catalysis: Pd/COF-LZU1 in Suzuki–Miyaura coupling reaction. *J. Am. Chem. Soc.* **133**, 19816–19822 (2011).
10. Dong, R. et al. Large-area, free-standing, two-dimensional supramolecular polymer single-layer sheets for highly efficient electrocatalytic hydrogen evolution. *Angew. Chem. Int. Ed. Engl.* **54**, 12058–12063 (2015).
11. Dogru, M. et al. A photoconductive thienothiophene-based covalent organic framework showing charge transfer towards included fullerene. *Angew. Chem. Int. Ed. Engl.* **52**, 2920–2924 (2013).
12. Wan, S., Guo, J., Kim, J., Ihee, H. & Jiang, D. A belt-shaped, blue luminescent, and semiconducting covalent organic framework. *Angew. Chem. Int. Ed. Engl.* **47**, 8826–8830 (2008).
13. Li, X. et al. Tuneable near white-emissive two-dimensional covalent organic frameworks. *Nat. Commun.* **9**, 2335 (2018).
14. DeBlase, C. R., Silberstein, K. E., Truong, T.-T., Abruña, H. D. & Dichtel, W. R. β -Ketoenamine-linked covalent organic frameworks capable of pseudocapacitive energy storage. *J. Am. Chem. Soc.* **135**, 16821–16824 (2013).

15. Furukawa, H. & Yaghi, O. M. Storage of hydrogen, methane, and carbon dioxide in highly porous covalent organic frameworks for clean energy applications. *J. Am. Chem. Soc.* **131**, 8875–8883 (2009).
16. Côté, A. P. et al. Porous, crystalline, covalent organic frameworks. *Science* **310**, 1166–1170 (2005).
17. Liu, W. et al. A two-dimensional conjugated aromatic polymer via C–C coupling reaction. *Nat. Chem.* **9**, 563–570 (2017).
18. Bin, H. et al. 11.4% Efficiency non-fullerene polymer solar cells with trialkylsilyl substituted 2D-conjugated polymer as donor. *Nat. Commun.* **7**, 13651 (2016).
19. Liu, K. et al. On-water surface synthesis of crystalline, few-layer two-dimensional polymers assisted by surfactant monolayers. *Nat. Chem.* **11**, 994–1000 (2019).
20. Lange, R. Z., Hofer, G., Weber, T. & Schlüter, A. D. A two-dimensional polymer synthesized through topochemical [2 + 2]-cycloaddition on the multigram scale. *J. Am. Chem. Soc.* **139**, 2053–2059 (2017).
21. Kissel, P., Murray, D. J., Wulf Lange, W. J., Catalano, V. J. & King, B. T. A nanoporous two-dimensional polymer by single-crystal-to-single-crystal photopolymerization. *Nat. Chem.* **6**, 774–778 (2014).
22. Kory, M. J. et al. Gram-scale synthesis of two-dimensional polymer crystals and their structure analysis by X-ray diffraction. *Nat. Chem.* **6**, 779–784 (2014).
23. Schlüter, A. D. Mastering polymer chemistry in two dimensions. *Commun. Chem.* **3**, 12 (2020).
24. Grill, L. & Hecht, S. Covalent on-surface polymerization. *Nat. Chem.* **12**, 115–130 (2020).

25. Zhong, Y. et al. Wafer-scale synthesis of monolayer two-dimensional porphyrin polymers for hybrid superlattices. *Science* **366**, 1379–1384 (2019).
26. Kissel, P. et al. A two-dimensional polymer prepared by organic synthesis. *Nat. Chem.* **4**, 287–291 (2012).
27. Evans, A. M. et al. Seeded growth of single-crystal two-dimensional covalent organic frameworks. *Science* **361**, 52–57 (2018).
28. Evans, A. M. et al. Emissive single-crystalline boroxine-linked colloidal covalent organic frameworks. *J. Am. Chem. Soc.* **141**, 19728–19735 (2019).
29. Martínez-Abadía, M. & Mateo-Alonso, A. Structural approaches to control interlayer interactions in 2D covalent organic frameworks. *Adv. Mater.* **32**, 2002366 (2020).
30. Li, H. et al. Nucleation–elongation dynamics of two-dimensional covalent organic frameworks. *J. Am. Chem. Soc.* **142**, 1367–1374 (2020).
31. Li, H. et al. Nucleation and growth of covalent organic frameworks from solution: the example of COF-5. *J. Am. Chem. Soc.* **139**, 16310–16318 (2017).
32. Smith, B. J. & Dichtel, W. R. Mechanistic studies of two-dimensional covalent organic frameworks rapidly polymerized from initially homogenous conditions. *J. Am. Chem. Soc.* **136**, 8783–8789 (2014).
33. Liu, X.-H. et al. On-surface synthesis of single-layered two-dimensional covalent organic frameworks via solid–vapor interface reactions. *J. Am. Chem. Soc.* **135**, 10470–10474 (2013).
34. Liu, C., Yu, Y., Zhang, W., Zeng, Q. & Lei, S. Room-temperature synthesis of covalent organic frameworks with a boronic ester linkage at the liquid/solid interface. *Chem. Eur. J.* **22**, 18412–18418 (2016).

35. Grossmann, L. et al. On-surface photopolymerization of two-dimensional polymers ordered on the mesoscale. *Nat. Chem.* **13**, 730–736 (2021).
36. Schlüter, A. D., Weber, T. & Hofer, G. How to use X-ray diffraction to elucidate 2D polymerization propagation in single crystals. *Chem. Soc. Rev.* **49**, 5140–5158 (2020).
37. Crawford, A. G. et al. Synthesis of 2- and 2,7-functionalized pyrene derivatives: an application of selective C–H borylation. *Chem. Eur. J.* **18**, 5022–5035 (2012).
38. Wan, S., Guo, J., Kim, J., Ihee, H. & Jiang, D. A photoconductive covalent organic framework: self-condensed arene cubes composed of eclipsed 2D polypyrene sheets for photocurrent generation. *Angew. Chem. Int. Ed. Engl.* **48**, 5439–5442 (2009).
39. Medina, D. D. et al. Room temperature synthesis of covalent–organic framework films through vapor-assisted conversion. *J. Am. Chem. Soc.* **137**, 1016–1019 (2015).
40. Dienstmaier, J. F. et al. Isoreticular two-dimensional covalent organic frameworks synthesized by on-surface condensation of diboronic acids. *ACS Nano* **6**, 7234–7242 (2012).
41. Bilbao, N. et al. Anatomy of on-surface synthesized boroxine two-dimensional polymers. *ACS Nano* **14**, 2354–2365 (2020).
42. Sassi, M., Oison, V., Debierre, J.-M. & Humbel, S. Modelling the two-dimensional polymerization of 1,4-benzene diboronic acid on a Ag surface. *ChemPhysChem* **10**, 2480–2485 (2009).
43. Gasser, U., Weeks, E. R., Schofield, A., Pusey, P. N. & Weitz, D. A. Real-space imaging of nucleation and growth in colloidal crystallization. *Science* **292**, 258–262 (2001).
44. Cai, Z.-F. et al. Electric-field-mediated reversible transformation between supramolecular networks and covalent organic frameworks. *J.*

Am. Chem. Soc. **141**, 11404–11408 (2019).

45. Zhan, G., Cai, Z.-F., Martínez-Abadía, M., Mateo-Alonso, A. & De Feyter, S. Real-time molecular-scale imaging of dynamic network switching between covalent organic frameworks. *J. Am. Chem. Soc.* **142**, 5964–5968 (2020).
46. Li, D. et al. Direction-specific interactions control crystal growth by oriented attachment. *Science* **336**, 1014–1018 (2012).
47. De Yoreo, J. J. et al. Crystallization by particle attachment in synthetic, biogenic, and geologic environments. *Science* **349**, aaa6760 (2015).
48. Viswanathan, R. & Bauer, C. L. Kinetics of grain boundary migration in copper bicrystals with [001] rotation axes. *Acta Metall.* **21**, 1099–1109 (1973).
49. Sun, R. C. & Bauer, C. L. Tilt boundary migration in NaCl bicrystals. *Acta Metall.* **18**, 639–647 (1970).
50. Rollett, A. D., Srolovitz, D. J. & Anderson, M. P. Simulation and theory of abnormal grain growth—anisotropic grain boundary energies and mobilities. *Acta Metall.* **37**, 1227–1240 (1989).
51. Blum, V. et al. *Ab initio* molecular simulations with numeric atom-centered orbitals. *Comput. Phys. Commun.* **180**, 2175–2196 (2009).
52. Marek, A. et al. The ELPA library: scalable parallel eigenvalue solutions for electronic structure theory and computational science. *J. Phys. Condens. Matter* **26**, 213201 (2014).
53. Yu, V. W.-Z. et al. ELSI: a unified software interface for Kohn–Sham electronic structure solvers. *Comput. Phys. Commun.* **222**, 267–285 (2018).
54. Tkatchenko, A., DiStasio, R. A., Car, R. & Scheffler, M. Accurate and efficient method for many-body van der Waals interactions. *Phys. Rev. Lett.* **108**, 236402 (2012).

55. Ambrosetti, A., Reilly, A. M., DiStasio, R. A. Jr & Tkatchenko, A. Long-range correlation energy calculated from coupled atomic response functions. *J. Chem. Phys.* **140**, 18A508 (2014).
56. Bitzek, E., Koskinen, P., Gähler, F., Moseler, M. & Gumbsch, P. Structural relaxation made simple. *Phys. Rev. Lett.* **97**, 170201 (2006).
57. Hjorth Larsen, A. et al. The atomic simulation environment—a Python library for working with atoms. *J. Phys. Condens. Matter* **29**, 273002 (2017).
58. Jorgensen, W. L. & Tirado-Rives, J. The OPLS [optimized potentials for liquid simulations] potential functions for proteins, energy minimizations for crystals of cyclic peptides and crambin. *J. Am. Chem. Soc.* **110**, 1657–1666 (1988).
59. Jorgensen, W. L., Maxwell, D. S. & Tirado-Rives, J. Development and testing of the OPLS all-atom force field on conformational energetics and properties of organic liquids. *J. Am. Chem. Soc.* **118**, 11225–11236 (1996).
60. Hourahine, B. et al. DFTB plus, a software package for efficient approximate density functional theory based atomistic simulations. *J. Chem. Phys.* **152**, 124101 (2020).
61. Grimme, S., Bannwarth, C. & Shushkov, P. A robust and accurate tight-binding quantum chemical method for structures, vibrational frequencies, and noncovalent interactions of large molecular systems parametrized for all spd-block elements ($Z = 1\text{--}86$). *J. Chem. Theory Comput.* **13**, 1989–2009 (2017).
62. Rüger, R. et al. AMS v.2021.1 (SCM, Theoretical Chemistry, Vrije Universiteit, Amsterdam, the Netherlands, 2021); <http://www.scm.com>
63. Bannwarth, C. et al. Extended tight-binding quantum chemistry methods. *WIREs Comput. Mol. Sci.* **11**, e1493 (2021).

64. Spicher, S. & Grimme, S. Robust atomistic modeling of materials, organometallic, and biochemical systems. *Angew. Chem. Int. Ed. Engl.* **59**, 15665–15673 (2020).

Acknowledgements

We thank L. Verstraete and N. Bilbao for helpful discussions. We thank Y. Liao for helping with the preparation of the manuscript. We thank Y. Zhang for helping with data analysis. This work was supported by the Research Foundation - Flanders (FWO), in part by FWO under EOS 30489208, the Marie Skłodowska Curie ETN project ULTIMATE (GA-813036), and KU Leuven Internal Grant 3E180504, China Scholarship Council (201908350094), the Basque Foundation for Science (Ikerbasque), POLYMAT, the University of the Basque Country (Grupo de Investigación GIU17/054), Diputación Foral de Guipuzkoa, Gobierno Vasco (PIBA and BERC programmes), Gobierno de España (Ministerio de Economía y Competitividad CTQ2016-77970-R). Technical and human support provided by SGIker of UPV/EHU and European funding (ERDF and ESF) is acknowledged. This project has received funding from the European Research Council (ERC) under the European Union's Horizon 2020 research and innovation programme (grant agreement no. 722951). This project has received funding from the European Union's Horizon 2020 research and innovation programme under grant agreement no. 664878 and no. 899895. In addition, support through the project IF/00894/2015, the advanced computing CPC-A2/2524/2020 granting access to the Navigator cluster at LCA-UC and within the scope of the project CICECO-Aveiro Institute of Materials, UIDB/50011/2020 & UIDP/50011/2020 funded by national funds through the Portuguese Foundation for Science and Technology I.P./MCTES is gratefully acknowledged.

Author information

Author notes

1. Gaolei Zhan

Present address: Department of Chemistry, National University of Singapore, Singapore, Singapore

2. Zhen-Feng Cai

Present address: Department of Chemistry and Applied Biosciences, ETH Zurich, Zurich, Switzerland

3. These authors contributed equally: Gaolei Zhan, Zhen-Feng Cai

Affiliations

1. Department of Chemistry, Division of Molecular Imaging and Photonics, KU Leuven, Leuven, Belgium

Gaolei Zhan, Zhen-Feng Cai, Lihua Yu, Niklas Herrmann & Steven De Feyter

2. CICECO–Aveiro Institute of Materials, Department of Chemistry, University of Aveiro, Aveiro, Portugal

Karol Strutyński & Manuel Melle-Franco

3. POLYMAT, University of the Basque Country UPV/EHU, Donostia-San Sebastian, Spain

Marta Martínez-Abadía & Aurelio Mateo-Alonso

4. Ikerbasque, Basque Foundation for Science, Bilbao, Spain

Aurelio Mateo-Alonso

Contributions

G.Z., Z.-F.C. and S.D.F. conceived the idea and designed the experiments. G.Z., Z.-F.C., L.Y. and N.H. carried out the *in situ* STM experiments and analysed the data. K.S. and M.M.-F carried out the DFT and tight-binding calculation. M.M.-A. carried out the synthesis of the monomer. The text

was initially composed by G.Z., Z.-F.C., A.M.-A. and S.D.F., and all authors further contributed to the discussion of the experimental work and the final version of the manuscript.

Corresponding authors

Correspondence to [Zhen-Feng Cai](#) or [Steven De Feyter](#).

Ethics declarations

Competing interests

The authors declare no competing interests.

Peer review

Peer review information

Nature thanks Markus Lackinger and the other, anonymous, reviewer(s) for their contribution to the peer review of this work.

Additional information

Publisher's note Springer Nature remains neutral with regard to jurisdictional claims in published maps and institutional affiliations.

Supplementary information

[Supplementary Information](#)

Supplementary Text 1–4 and Figs. 1–30.

[Supplementary Data 1](#)

Statistical analysis of critical nucleation size for Fig. 2e.

[41586_2022_4409_MOESM3_ESM.mp4](#)

Supplementary Video 1 In situ STM showing the dynamic nucleation process at liquid–solid interface with a scan rate of 1.5 min per frame. The video shows the emergence and elongation of some 2DPs nuclei within the disordered area. The video also demonstrates the disappearance of on-surface generated 2DPs nuclei, implying the reversible boroxine chemistry on the HOPG surface. The video is played at $\times 180$ speed. Image size: 80 nm \times 80 nm.

[Supplementary Video 2 In situ STM showing the nucleation–elongation processes. The video is played at \$\times 180\$ speed. Image size: 150 nm \$\times\$ 150 nm.](#)

[Supplementary Video 3 In situ STM showing the restricted motion of 2DPs nuclei, with the presence of surface defect. The video is played at \$\times 180\$ speed. Image size: 60 nm \$\times\$ 60 nm.](#)

[Supplementary Video 4 In situ STM showing the slow kinetics during normal grain growth. The video is played at \$\times 180\$ speed. Image size: 60 nm \$\times\$ 60 nm.](#)

[41586_2022_4409_MOESM7_ESM.mp4](#)

Supplementary Video 5 In situ STM showing the preferential growth of some nuclei (S_2). During abnormal grain growth (AGG), S_2 grows at the expense of R_1 and S_1 . The video is played at $\times 180$ speed. Image size: 100 nm \times 100 nm.

[Supplementary Video 6 In situ STM showing the formation of a unidirectional domain \(\$S_2\$ \) by taking advantage of abnormal](#)

grain growth. The video is played at ×180 speed. Image size: 80 nm × 80 nm.

Rights and permissions

[Reprints and Permissions](#)

About this article

Cite this article

Zhan, G., Cai, ZF., Strutyński, K. *et al.* Observing polymerization in 2D dynamic covalent polymers. *Nature* **603**, 835–840 (2022).
<https://doi.org/10.1038/s41586-022-04409-6>

- Received: 01 September 2020
- Accepted: 06 January 2022
- Published: 30 March 2022
- Issue Date: 31 March 2022
- DOI: <https://doi.org/10.1038/s41586-022-04409-6>

Share this article

Anyone you share the following link with will be able to read this content:

[Get shareable link](#)

Sorry, a shareable link is not currently available for this article.

[Copy to clipboard](#)

Provided by the Springer Nature SharedIt content-sharing initiative

This article was downloaded by **calibre** from <https://www.nature.com/articles/s41586-022-04409-6>

| [Section menu](#) | [Main menu](#) |

- Article
- [Published: 30 March 2022](#)

Trends in Europe storm surge extremes match the rate of sea-level rise

- [Francisco M. Calafat](#) ORCID: [orcid.org/0000-0002-7474-135X¹](https://orcid.org/0000-0002-7474-135X),
- [Thomas Wahl](#) ORCID: [orcid.org/0000-0003-3643-5463^{2,3}](https://orcid.org/0000-0003-3643-5463),
- [Michael Getachew Tadesse^{2,3}](#) &
- [Sarah N. Sparrow](#) ORCID: [orcid.org/0000-0002-1802-6909⁴](https://orcid.org/0000-0002-1802-6909)

Nature volume 603, pages 841–845 (2022)

- 972 Accesses
- 281 Altmetric
- [Metrics details](#)

Subjects

- [Attribution](#)
- [Natural hazards](#)
- [Physical oceanography](#)

Abstract

Coastal communities across the world are already feeling the disastrous impacts of climate change through variations in extreme sea levels¹. These variations reflect the combined effect of sea-level rise and changes in storm

surge activity. Understanding the relative importance of these two factors in altering the likelihood of extreme events is crucial to the success of coastal adaptation measures. Existing analyses of tide gauge records^{2,3,4,5,6,7,8,9,10} agree that sea-level rise has been a considerable driver of trends in sea-level extremes since at least 1960. However, the contribution from changes in storminess remains unclear, owing to the difficulty of inferring this contribution from sparse data and the consequent inconclusive results that have accumulated in the literature^{11,12}. Here we analyse tide gauge observations using spatial Bayesian methods¹³ to show that, contrary to current thought, trends in surge extremes and sea-level rise both made comparable contributions to the overall change in extreme sea levels in Europe since 1960 . We determine that the trend pattern of surge extremes reflects the contributions from a dominant north–south dipole associated with internal climate variability and a single-sign positive pattern related to anthropogenic forcing. Our results demonstrate that both external and internal influences can considerably affect the likelihood of surge extremes over periods as long as 60 years, suggesting that the current coastal planning practice of assuming stationary surge extremes^{1,14} might be inadequate.

This is a preview of subscription content

Access options

Subscribe to Nature+

Get immediate online access to the entire Nature family of 50+ journals

\$29.99

monthly

[Subscribe](#)

Subscribe to Journal

Get full journal access for 1 year

\$199.00

only \$3.90 per issue

[Subscribe](#)

All prices are NET prices.

VAT will be added later in the checkout.

Tax calculation will be finalised during checkout.

Buy article

Get time limited or full article access on ReadCube.

\$32.00

[Buy](#)

All prices are NET prices.

Additional access options:

- [Log in](#)
- [Learn about institutional subscriptions](#)

Fig. 1: Historical trends in storm surge extremes.



Fig. 2: Temporal changes in return period.

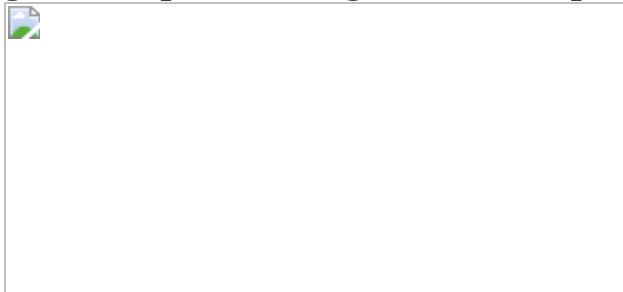


Fig. 3: Attribution of trends in surge extremes.



Data availability

The high-frequency tide gauge data used in this study for the period 1960–2013 are available from the Global Extreme Sea Level Analysis project (<https://www.gesla.org/>), whereas data for the period 2014–2018 are from the British Oceanographic Data Centre (https://www.bodc.ac.uk/data/hosted_data_systems/sea_level/uk_tide_gauge_network/) and the Copernicus Marine Environment Monitoring Service (https://resources.marine.copernicus.eu/product-detail/INSITU_GLO_NRT_OBSERVATIONS_013_030/). The ensemble of climate simulations is available from <https://doi.org/10.5285/0cea8d7aca57427fae92241348ae9b03> (baseline folder). The observed annual maxima from tide gauge records, the ensemble of surge simulations, as well as the Bayesian solutions from

BHM1 and BHM2 have been deposited in Zenodo (<https://doi.org/10.5281/zenodo.5749736>).

Code availability

The code that implements the BHM is available at Zenodo (<https://doi.org/10.5281/zenodo.5035438>).

References

1. Hinkel, J. et al. Coastal flood damage and adaptation costs under 21st century sea-level rise. *Proc. Natl Acad. Sci. USA* **111**, 3292–3297 (2014).
2. Zhang, K., Douglas, B. C. & Leatherman, S. P. Twentieth-century storm activity along the U.S. East Coast. *J. Clim.* **13**, 1748–1761 (2000).
3. Woodworth, P. L. & Blackman, D. L. Evidence for systematic changes in extreme high waters since the mid-1970s. *J. Clim.* **17**, 1190–1197 (2004).
4. Marcos, M., Tsimplis, M. N. & Shaw, A. G. P. Sea level extremes in southern Europe. *J. Geophys. Res. Oceans* **114**, C01007 (2009).
5. Haigh, I., Nicholls, R. & Wells, N. Assessing changes in extreme sea levels: application to the English Channel, 1900–2006. *Cont. Shelf Res.* **30**, 1042–1055 (2010).
6. Menéndez, M. & Woodworth, P. L. Changes in extreme high water levels based on a quasi-global tide-gauge data set. *J. Geophys. Res.* **115**, C10011 (2010).
7. Weisse, R. et al. Changing extreme sea levels along European coasts. *Coastal Eng.* **87**, 4–14 (2014).

8. Wahl, T. & Chambers, D. P. Evidence for multidecadal variability in US extreme sea level records. *J. Geophys. Res. Oceans* **120**, 1527–1544 (2015).
9. Marcos, M. & Woodworth, P. L. Spatiotemporal changes in extreme sea levels along the coasts of the North Atlantic and the Gulf of Mexico. *J. Geophys. Res. Oceans* **122**, 7031–7048 (2017).
10. Rohmer, J. & Le Cozannet, G. Dominance of the mean sea level in the high-percentile sea levels time evolution with respect to large-scale climate variability: a Bayesian statistical approach. *Environ. Res. Lett.* **14**, 014008 (2019).
11. Seneviratne, S. I. et al. In *Managing the Risks of Extreme Events and Disasters to Advance Climate Change Adaptation* (eds Field, C. B. et al.) 109–230 (Cambridge Univ. Press, 2012).
12. Intergovernmental Panel on Climate Change in *Climate Change 2013: The Physical Science Basis. Contribution of Working Group I to the Fifth Assessment Report of the Intergovernmental Panel on Climate Change* (eds Stocker, T. F. et al.) (Cambridge Univ. Press, 2013).
13. Calafat, F. M. & Marcos, M. Probabilistic reanalysis of storm surge extremes in Europe. *Proc. Natl Acad. Sci. USA* **117**, 1877–1883 (2020).
14. Luxford, F. & Faulkner, D. Recommendations for future research and practice on non-stationarity in UK flooding. FRS18087/REA/R2. *Environment Agency* https://assets.publishing.service.gov.uk/media/6038f813e90e07055685020c/Recommendations_for_future_research_and_practice_on_non-stationarity_in_UK_flooding_-_report_2_.pdf (2020).
15. Jevrejeva, S., Jackson, L. P., Grinsted, A., Lincke, D. & Marzeion, B. Flood damage costs under the sea level rise with warming of 1.5 °C and 2.0 °C. *Environ. Res. Lett.* **13**, 074014 (2018).

16. Kulp, S. A. & Strauss, B. H. New elevation data triple estimates of global vulnerability to sea-level rise and coastal flooding. *Nat. Commun.* **10**, 4844 (2019).
17. Tiggeloven, T. et al. Global-scale benefit–cost analysis of coastal flood adaptation to different flood risk drivers using structural measures. *Nat. Hazards Earth Syst. Sci.* **20**, 1025–1044 (2020).
18. Church, J. et al. in Climate Change 2013: The Physical Science Basis. Contribution of Working Group I to the Fifth Assessment Report of the Intergovernmental Panel on Climate Change (eds Stocker, T. F. et al.) Ch. 13, 1137–1216 (Cambridge Univ. Press, 2013).
19. Frederikse, T. et al. The causes of sea-level rise since 1900. *Nature* **584**, 393–397 (2020).
20. Marcos, M., Jordà, G., Gomis, D. & Pérez, B. Changes in storm surges in southern Europe from a regional model under climate change scenarios. *Glob. Planet. Change* **77**, 116–128 (2011).
21. Conte, D. & Lionello, P. Characteristics of large positive and negative surges in the Mediterranean Sea and their attenuation in future climate scenarios. *Glob. Planet. Change* **111**, 159–173 (2013).
22. Little, C. M. et al. Joint projections of US East Coast sea level and storm surge. *Nat. Clim. Change* **5**, 1114–1120 (2015).
23. Vousdoukas, M. I. et al. Projections of extreme storm surge levels along Europe. *Clim. Dyn.* **47**, 3171–3190 (2016).
24. Vousdoukas, M. I., Mentaschi, L., Voukouvalas, E., Verlaan, M. & Feyen, L. Extreme sea levels on the rise along Europe’s coasts. *Earth's Future* **5**, 304–323 (2017).
25. Howard, T., Palmer, M. D. & Bricheno, L. M. Contributions to 21st century projections of extreme sea-level change around the UK. *Environ. Res. Commun.* **1**, 095002 (2019).

26. Muis, S. et al. A high-resolution global dataset of extreme sea levels, tides, and storm surges, including future projections. *Front. Mar. Sci.* **7**, 263 (2020).
27. Greenland, S. et al. Statistical tests, *P* values, confidence intervals, and power: a guide to misinterpretations. *Eur. J. Epidemiol.* **31**, 337–350 (2016).
28. Button, K. et al. Power failure: why small sample size undermines the reliability of neuroscience. *Nat. Rev. Neurosci.* **14**, 365–376 (2013).
29. Coles, S. G. *An Introduction to Statistical Modelling of Extreme Values* 208 pp (Springer, 2001).
30. Schlather, M. Models for stationary max-stable random fields. *Extremes* **5**, 33–44 (2002).
31. McFadden, D. Modeling the choice of residential location. *Transp. Res. Rec.* **672**, 72–77 (1978).
32. Tadesse, M. G., Wahl, T. & Cid, A. Data-driven modeling of global storm surges. *Front. Mar. Sci.* **7**, 260 (2020).
33. Tadesse, M. G. & Wahl, T. A database of global storm surge reconstructions. *Sci. Data* **8**, 125 (2021).
34. Guillod, B. P. et al. A large set of potential past, present and future hydro-meteorological time series for the UK. *Hydrol. Earth Syst. Sci.* **22**, 611–634 (2018).
35. Stott, P. A. et al. Attribution of extreme weather and climate-related events. *Wiley Interdiscip. Rev. Clim. Change* **7**, 23–41 (2016).
36. Dangendorf, S., Arns, A., Pinto, J. G., Ludwig, P. & Jensen, J. The exceptional influence of storm ‘Xaver’ on design water levels in the German Bight. *Environ. Res. Lett.* **11**, 054001 (2016).
37. Zappa, G., Shaffrey, L. C., Hodges, K. I., Sansom, P. G. & Stephenson, D. B. A multimodel assessment of future projections of North Atlantic

- and European extratropical cyclones in the CMIP5 climate models. *J. Clim.* **26**, 5846–5862 (2013).
38. Feser, F. et al. Storminess over the North Atlantic and northwestern Europe—a review. *Q. J. R. Meteorol. Soc.* **141**, 350–382 (2015).
 39. Barcikowska, M. J. et al. Euro-Atlantic winter storminess and precipitation extremes under 1.5 °C vs. 2 °C warming scenarios. *Earth Syst. Dyn* **9**, 679–699 (2018).
 40. Vousdoukas, M. I. et al. Global probabilistic projections of extreme sea levels show intensification of coastal flood hazard. *Nat. Commun.* **9**, 2360 (2018).
 41. Woodworth, P. L. et al. Towards a global higher-frequency sea level dataset. *Geosci. Data J.* **3**, 50–59 (2017).
 42. Killick, R., Fearnhead, P. & Eckley, I. A. Optimal detection of changepoints with a linear computational cost. *J. Am. Stat. Assoc.* **107**, 1590–1598 (2012).
 43. Kalnay, et al. The NCEP/NCAR 40-year reanalysis project. *Bull. Am. Meteorol. Soc.* **77**, 437–470 (1996).
 44. Holgate, S. J. et al. New data systems and products at the Permanent Service for Mean Sea Level. *J. Coast. Res.* **29**, 493–504 (2013).
 45. Reich, B. J. & Shaby, B. A. A hierarchical max-stable spatial model for extreme precipitation. *Ann. Appl. Stat.* **6**, 1430–1451 (2012).
 46. Stephenson, A. G., Shaby, B. A., Reich, B. J. & Sullivan, A. L. Estimating spatially varying severity thresholds of a forest fire danger rating system using max-stable extreme-event modeling. *J. Appl. Meteorol. Climatol.* **54**, 395–407 (2015).
 47. Carpenter, B. et al. Stan: a probabilistic programming language. *J. Stat. Softw.* **76**, 1–32 (2017).

48. Guillod, B. P. et al. weather@home 2: validation of an improved global–regional climate modelling system. *Geosci. Model Dev.* **10**, 1849–1872 (2017).
49. Rayner, N. A. et al. Global analyses of sea surface temperature, sea ice, and night marine air temperature since the late nineteenth century. *J. Geophys. Res. Atmos.* **108**, 4407 (2003).
50. Taylor, K. E., Stouffer, R. J. & Meehl, G. A. An overview of CMIP5 and the experiment design. *Bull. Am. Meteorol. Soc.* **93**, 485–498 (2012).
51. Hersbach, et al. The ERA5 global reanalysis. *Q. J. R. Meteorol. Soc.* **146**, 1999–2049 (2020).

Acknowledgements

We acknowledge the GESLA project for assembling and making the tide gauge data available. F.M.C. was supported by the Natural Environment Research Council (NERC) National Capability funding. M.G.T. and T.W. were supported by the National Aeronautics and Space Administration (NASA) under the New (Early Career) Investigator Program (NIP) in Earth Science (grant number 80NSSC18K0743) and the NASA Sea Level Science Team (grant number 80NSSC20K1241). T.W. also acknowledges support from the National Science Foundation (under grant ICER-1854896). We acknowledge conversations with M. Marcos and also thank her for providing the tide gauge data (from the British Oceanographic Data Centre and the Copernicus Marine Environment Monitoring Service) for the period 2014–2018.

Author information

Affiliations

1. National Oceanography Centre, Liverpool, UK

Francisco M. Calafat

2. Department of Civil, Environmental and Construction Engineering,
University of Central Florida, Orlando, FL, USA

Thomas Wahl & Michael Getachew Tadesse

3. National Center for Integrated Coastal Research, University of Central
Florida, Orlando, FL, USA

Thomas Wahl & Michael Getachew Tadesse

4. Oxford e-Research Centre, Department of Engineering Science,
University of Oxford, Oxford, UK

Sarah N. Sparrow

Contributions

F.M.C. conceived and designed the study, with input from all authors. T.W. and M.G.T. produced the ensemble of surge simulations. S.N.S. provided the ensemble of climate simulations. F.M.C. performed the analyses and wrote the manuscript, with contributions from all authors.

Corresponding author

Correspondence to [Francisco M. Calafat](#).

Ethics declarations

Competing interests

The authors declare no competing interests.

Peer review

Peer review information

Nature thanks Nadia Bloemendaal, Jérémie Rohmer and the other, anonymous, reviewer for their contribution to the peer review of this work. Peer reviewer reports are available.

Additional information

Publisher's note Springer Nature remains neutral with regard to jurisdictional claims in published maps and institutional affiliations.

Extended data figures and tables

[Extended Data Fig. 1 Uncertainty of estimated \$\mu\$ trends at individual locations.](#)

Posterior standard deviations for the μ trends at tide gauge sites (**a**) and gridded locations (**b**). These standard deviations correspond to the μ trends shown in Fig. [1a, b](#).

[Extended Data Fig. 2 Tide gauge stations and spatial knots.](#)

Location of the tide gauge stations used in the analysis of extremes (red circles), along with the spatial knots used to construct the spatial residual process in the BHM (blue crosses).

[Extended Data Fig. 3 Amplitude of the anthropogenic fingerprint.](#)

Posterior (blue) and prior (red) distributions for the amplitude of the anthropogenic fingerprint (β_{ext}). The posterior has been estimated by fitting BHM2 to the tide gauge observations.

Extended Data Table 1 Scalar parameters of the BHM and prior distributions

Supplementary information

Supplementary Information

This file contains Supplementary Text and Supplementary Figures 1–4.

Peer Review File

Rights and permissions

Reprints and Permissions

About this article

Cite this article

Calafat, F.M., Wahl, T., Tadesse, M.G. *et al.* Trends in Europe storm surge extremes match the rate of sea-level rise. *Nature* **603**, 841–845 (2022). <https://doi.org/10.1038/s41586-022-04426-5>

- Received: 23 September 2021
- Accepted: 14 January 2022
- Published: 30 March 2022
- Issue Date: 31 March 2022
- DOI: <https://doi.org/10.1038/s41586-022-04426-5>

Share this article

Anyone you share the following link with will be able to read this content:

[Get shareable link](#)

Sorry, a shareable link is not currently available for this article.

[Copy to clipboard](#)

Provided by the Springer Nature SharedIt content-sharing initiative

Winding roads could make you a better navigator

- Shamini Bundell
- Nick Petrić Howe

Nature Podcast 30 Mar 2022

This article was downloaded by **calibre** from <https://www.nature.com/articles/s41586-022-04426-5>

| [Section menu](#) | [Main menu](#) |

- Article
- [Published: 30 March 2022](#)

Assembly of the basal mantle structure beneath Africa

- [Nicolas Flament](#) [ORCID: orcid.org/0000-0002-3237-0757¹](#),
- [Ömer F. Bodur](#) [ORCID: orcid.org/0000-0001-6836-0107¹](#),
- [Simon E. Williams](#) [ORCID: orcid.org/0000-0003-4670-8883²](#) &
- [Andrew S. Merdith](#) [ORCID: orcid.org/0000-0002-7564-8149³](#) nAff4

[Nature](#) volume **603**, pages 846–851 (2022)

- 858 Accesses
- 167 Altmetric
- [Metrics details](#)

Subjects

- [Geochemistry](#)
- [Geodynamics](#)
- [Seismology](#)
- [Tectonics](#)
- [Volcanology](#)

Abstract

Plate tectonics shapes Earth's surface, and is linked to motions within its deep interior^{1,2}. Cold oceanic lithosphere sinks into the mantle, and hot mantle plumes rise from the deep Earth, leading to volcanism^{3,4}. Volcanic

eruptions over the past 320 million years have been linked to two large structures at the base of the mantle presently under Africa and the Pacific Ocean^{5,6}. This has led to the hypothesis that these basal mantle structures have been stationary over geological time^{7,8}, in contrast to observations and models suggesting that tectonic plates^{9,10}, subduction zones^{11,12,13,14} and mantle plumes^{15,16} have been mobile, and that basal mantle structures are presently deforming^{17,18}. Here we reconstruct mantle flow from one billion years ago to the present day to show that the history of volcanism is statistically as consistent with mobile basal mantle structures as with fixed ones. In our reconstructions, cold lithosphere sank deep into the African hemisphere between 740 and 500 million years ago, and from 400 million years ago the structure beneath Africa progressively assembled, pushed by peri-Gondwana slabs, to become a coherent structure as recently as 60 million years ago. Our mantle flow models suggest that basal mantle structures are mobile, and aggregate and disperse over time, similarly to continents at Earth's surface⁹. Our models also predict the presence of continental material in the mantle beneath Africa, consistent with geochemical data^{19,20}.

This is a preview of subscription content

Access options

Subscribe to Nature+

Get immediate online access to the entire Nature family of 50+ journals

\$29.99

monthly

[Subscribe](#)

Subscribe to Journal

Get full journal access for 1 year

\$199.00

only \$3.90 per issue

[Subscribe](#)

All prices are NET prices.

VAT will be added later in the checkout.

Tax calculation will be finalised during checkout.

Buy article

Get time limited or full article access on ReadCube.

\$32.00

[Buy](#)

All prices are NET prices.

Additional access options:

- [Log in](#)
- [Learn about institutional subscriptions](#)

Fig. 1: Structure of the lower mantle and volcanic eruption locations from 320 Ma to the present day.



Fig. 2: Distributions of distances between basal mantle structures and reconstructed eruption locations.

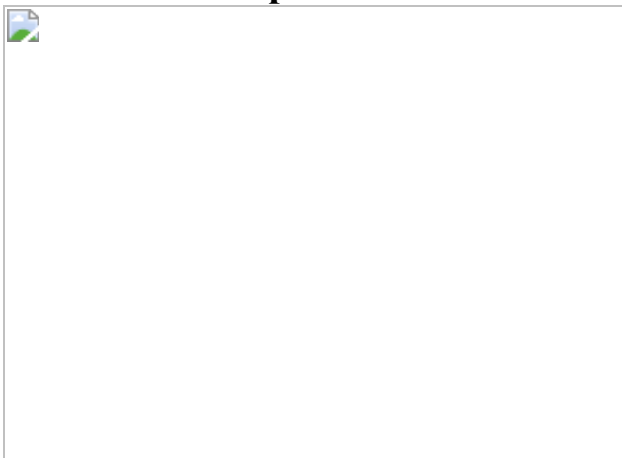


Fig. 3: Match of model basal mantle structures to volcanic eruption locations and tomographic models.

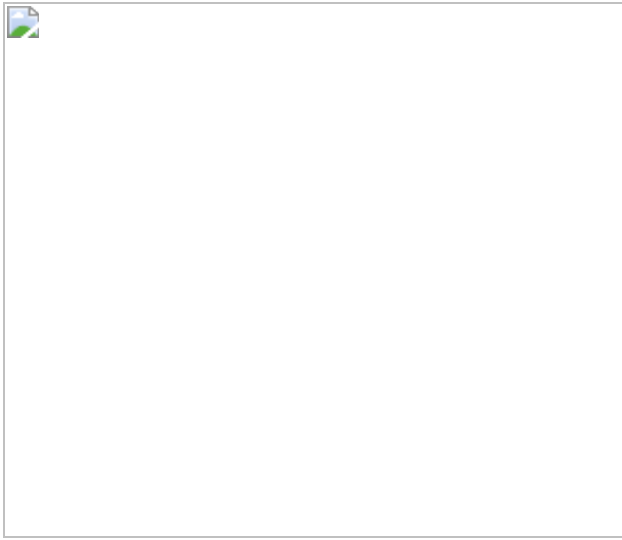
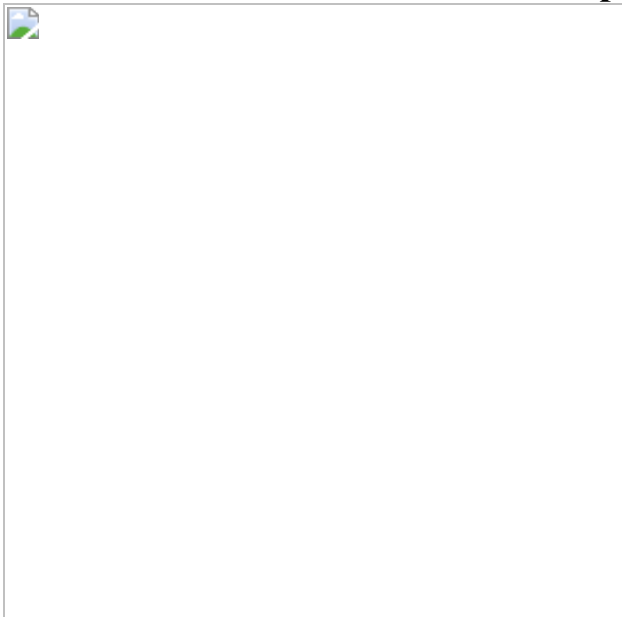


Fig. 4: Dynamic assembly of the African basal mantle structure and predicted continental crust in the deep Earth.



Data availability

Data generated for this study are available at <https://doi.org/10.5281/zenodo.6031641>. Source data are provided with this paper.

Code availability

The code used to compute the mantle flow models is available at <https://github.com/EarthByte/citcoms>. Figure 1 was created with the Generic Mapping Tools⁸² (GMT6) which is open-source software licensed under the GNU Lesser General Public License. Key Python scripts to compute the results shown in Figs. 2, 3 are available at <https://doi.org/10.5281/zenodo.6031641>. Figures 2, 3 were produced with the open-source Python library Matplotlib⁸³, and Fig. 4 was created with ParaView⁶⁷, which is shared openly under the 3-Clause BSD License.

References

1. Bunge, H.-P. et al. Time scales and heterogeneous structure in geodynamic Earth models. *Science* **280**, 91–95 (1998).
2. McNamara, A. K. & Zhong, S. Thermochemical structures beneath Africa and the Pacific Ocean. *Nature* **437**, 1136–1139 (2005).
3. Bercovici, D., Schubert, G. & Glatzmaier, G. A. Three-dimensional spherical models of convection in the Earth’s mantle. *Science* **244**, 950–955 (1989).
4. Campbell, I. H. Large igneous provinces and the mantle plume hypothesis. *Elements* **1**, 265–269 (2005).
5. Burke, K., Steinberger, B., Torsvik, T. H. & Smethurst, M. A. Plume generation zones at the margins of large low shear velocity provinces on the core–mantle boundary. *Earth Planet. Sci. Lett.* **265**, 49–60 (2008).
6. Torsvik, T. H., Burke, K., Steinberger, B., Webb, S. J. & Ashwal, L. D. Diamonds sampled by plumes from the core–mantle boundary. *Nature* **466**, 352–355 (2010).
7. Conrad, C. P., Steinberger, B. & Torsvik, T. H. Stability of active mantle upwelling revealed by net characteristics of plate tectonics. *Nature* **498**, 479–482 (2013).

8. Dziewonski, A. M., Lekic, V. & Romanowicz, B. A. Mantle anchor structure: an argument for bottom-up tectonics. *Earth Planet. Sci. Lett.* **299**, 69–79 (2010).
9. Irving, E. Drift of the major continental blocks since the Devonian. *Nature* **270**, 304–309 (1977).
10. Merdith, A. S. et al. Extending full-plate tectonic models into deep time: linking the neoproterozoic and the phanerozoic. *Earth-Sci. Rev.* **214**, 103477 (2021).
11. Moresi, L., Betts, P. G., Miller, M. S. & Cayley, R. A. Dynamics of continental accretion. *Nature* **508**, 245–248 (2014).
12. Domeier, M. & Torsvik, T. H. Plate tectonics in the late Paleozoic. *Geosci. Front.* **5**, 303–350 (2014).
13. Flament, N., Williams, S., Müller, R. D., Gurnis, M. & Bower, D. J. Correspondence: Reply to ‘Numerical modelling of the PERM anomaly and the Emeishan large igneous province’. *Nat. Commun.* **8**, 822 (2017).
14. Li, Z. X. et al. Decoding Earth’s rhythms: modulation of supercontinent cycles by longer superocean episodes. *Precambrian Res.* **323**, 1–5 (2019).
15. Tarduno, J., Bunge, H.-P., Sleep, N. & Hansen, U. The bent Hawaiian–Emperor hotspot track: inheriting the mantle wind. *Science* **324**, 50–53 (2009).
16. Hassan, R., Müller, R. D., Gurnis, M., Williams, S. E. & Flament, N. A rapid burst in hotspot motion through the interaction of tectonics and deep mantle flow. *Nature* **533**, 239–242 (2016).
17. Frost, D. A. & Rost, S. The P-wave boundary of the large-low shear velocity province beneath the Pacific. *Earth Planet. Sci. Lett.* **403**, 380–392 (2014).

18. Lynner, C. & Long, M. D. Lowermost mantle anisotropy and deformation along the boundary of the African LLSVP. *Geophys. Res. Lett.* **41**, 3447–3454 (2014).
19. Doucet, L. S. et al. Distinct formation history for deep-mantle domains reflected in geochemical differences. *Nat. Geosci.* **13**, 511–515 (2020).
20. Jackson, M., Becker, T. & Steinberger, B. Spatial characteristics of recycled and primordial reservoirs in the deep mantle. *Geochem. Geophys. Geosyst.* **22**, e2020GC009525 (2021).
21. Mégnin, C. & Romanowicz, B. A. The three-dimensional shear velocity structure of the mantle from the inversion of body, surface and higher-mode waveforms. *Geophys. J. Int.* **143**, 709–728 (2000).
22. Houser, C., Masters, G., Shearer, P. & Laske, G. Shear and compressional velocity models of the mantle from cluster analysis of long-period waveforms. *Geophys. J. Int.* **174**, 195–212 (2008).
23. Kustowski, B., Ekström, G. & Dziewoński, A. M. Anisotropic shear-wave velocity structure of the Earth’s mantle: a global model. *J. Geophys. Res. Solid Earth* **113**, B06306 (2008).
24. Simmons, N. A., Forte, A. M., Boschi, L. & Grand, S. P. GyPSuM: a joint tomographic model of mantle density and seismic wave speeds. *J. Geophys. Res. Solid Earth* **115**, B12310 (2010).
25. Ritsema, J., Deuss, A., van Heijst, H. J. & Woodhouse, J. H. S40RTS: a degree-40 shear-velocity model for the mantle from new Rayleigh wave dispersion, teleseismic traveltimes and normal-mode splitting function measurements. *Geophys. J. Int.* **184**, 1223–1236 (2011).
26. Auer, L., Boschi, L., Becker, T. W., Nissen-Meyer, T. & Giardini, D. Savani: a variable resolution whole-mantle model of anisotropic shear velocity variations based on multiple data sets. *J. Geophys. Res. Solid Earth* **119**, 3006–3034 (2014).

27. French, S. W. & Romanowicz, B. A. Whole-mantle radially anisotropic shear velocity structure from spectral-element waveform tomography. *Geophys. J. Int.* **199**, 1303–1327 (2014).
28. Davies, D., Goes, S. & Lau, H. C. P. In *The Earth's Heterogeneous Mantle* (eds Khan, A. & Deschamps, F.) 441–477 (Springer, 2015).
29. Garnero, E. J., McNamara, A. K. & Shim, S.-H. Continent-sized anomalous zones with low seismic velocity at the base of Earth's mantle. *Nat. Geosci.* **9**, 481–489 (2016).
30. Ni, S., Tan, E., Gurnis, M. & Helmberger, D. V. Sharp sides to the African superplume. *Science* **296**, 1850–1852 (2002).
31. Tkalčić, H., Young, M., Muir, J. B., Davies, D. R. & Mattesini, M. Strong, multi-scale heterogeneity in Earth's lowermost mantle. *Sci. Rep.* **5**, 18416 (2015).
32. Davaille, A. & Romanowicz, B. Deflating the LLSVPs: bundles of mantle thermochemical plumes rather than thick stagnant “piles”. *Tectonics* **39**, e2020TC006265 (2020).
33. Doubrovine, P. V., Steinberger, B. & Torsvik, T. H. A failure to reject: testing the correlation between large igneous provinces and deep mantle structures with EDF statistics. *Geochem. Geophys. Geosyst.* **17**, 1130–1163 (2016).
34. Austermann, J., Kaye, B. T., Mitrovica, J. X. & Huybers, P. A statistical analysis of the correlation between large igneous provinces and lower mantle seismic structure. *Geophys. J. Int.* **197**, 1–9 (2014).
35. Davies, D., Goes, S. & Sambridge, M. On the relationship between volcanic hotspot locations, the reconstructed eruption sites of large igneous provinces and deep mantle seismic structure. *Earth Planet. Sci. Lett.* **411**, 121–130 (2015).
36. Garnero, E. J. & McNamara, A. K. Structure and dynamics of Earth's lower mantle. *Science* **320**, 626–628 (2008).

37. Zhong, S. & Rudolph, M. L. On the temporal evolution of long-wavelength mantle structure of the Earth since the early Paleozoic. *Geochem. Geophys. Geosyst.* **16**, 1599–1615 (2015).
38. Flament, N., Williams, S., Müller, R., Gurnis, M. & Bower, D. J. Origin and evolution of the deep thermochemical structure beneath Eurasia. *Nat. Commun.* **8**, 14164 (2017).
39. Flament, N. Present-day dynamic topography and lower-mantle structure from palaeogeographically constrained mantle flow models. *Geophys. J. Int.* **216**, 2158–2182 (2019).
40. Johansson, L., Zahirovic, S. & Müller, R. D. The interplay between the eruption and weathering of large igneous provinces and the deep-time carbon cycle. *Geophys. Res. Lett.* **45**, 5380–5389 (2018).
41. Tappe, S., Smart, K., Torsvik, T., Massuyseau, M. & de Wit, M. Geodynamics of kimberlites on a cooling Earth: clues to plate tectonic evolution and deep volatile cycles. *Earth Planet. Sci. Lett.* **484**, 1–14 (2018).
42. Lekic, V., Cottaar, S., Dziewonski, A. & Romanowicz, B. A. Cluster analysis of global lower mantle tomography: a new class of structure and implications for chemical heterogeneity. *Earth Planet. Sci. Lett.* **357**, 68–77 (2012).
43. Kolmogorov, A. Sulla determinazione empirica di una lgge di distribuzione. *Giorn. Inst. Ital. Attuari* **4**, 83–91 (1933).
44. Matthews, K. J. et al. Global plate boundary evolution and kinematics since the late Paleozoic. *Global Planet. Change* **146**, 226–250 (2016).
45. Young, A. et al. Global kinematics of tectonic plates and subduction zones since the late Paleozoic Era. *Geosci. Front.* **10**, 989–1013 (2019).
46. Rudolph, M. L. & Zhong, S. History and dynamics of net rotation of the mantle and lithosphere. *Geochem. Geophys. Geosyst.* **15**, 3645–

3657 (2014).

47. Torsvik, T. H. et al. Deep mantle structure as a reference frame for movements in and on the Earth. *Proc. Natl Acad. Sci.* **111**, 8735–8740 (2014).
48. Lau, H. C. et al. Tidal tomography constrains Earth’s deep-mantle buoyancy. *Nature* **551**, 321–326 (2017).
49. Bower, D. J., Gurnis, M. & Seton, M. Lower mantle structure from paleogeographically constrained dynamic Earth models. *Geochem. Geophys. Geosyst.* **14**, 44–63 (2013).
50. Zhong, S., McNamara, A., Tan, E., Moresi, L. & Gurnis, M. A benchmark study on mantle convection in a 3-D spherical shell using CitcomS. *Geochem. Geophys. Geosyst.* **9**, Q10017 (2008).
51. Gurnis, M. et al. Plate tectonic reconstructions with continuously closing plates. *Comput. Geosci.* **38**, 35–42 (2012).
52. Bower, D. J., Gurnis, M. & Flament, N. Assimilating lithosphere and slab history in 4-D Earth models. *Phys. Earth Planet. Inter.* **238**, 8–22 (2015).
53. Stadler, G. et al. The dynamics of plate tectonics and mantle flow: from local to global scales. *Science* **329**, 1033–1038 (2010).
54. Coltice, N., Husson, L., Faccenna, C. & Arnould, M. What drives tectonic plates? *Sci. Adv.* **5**, eaax4295 (2019).
55. Flament, N. et al. Topographic asymmetry of the South Atlantic from global models of mantle flow and lithospheric stretching. *Earth Planet. Sci. Lett.* **387**, 107–119 (2014).
56. Chopelas, A. & Boehler, R. Thermal expansivity in the lower mantle. *Geophys. Res. Lett.* **19**, 1983–1986 (1992).
57. Tosi, N., Yuen, D. A., de Koker, N. & Wentzcovitch, R. M. Mantle dynamics with pressure- and temperature-dependent thermal

- expansivity and conductivity. *Phys. Earth Planet. Inter.* **217**, 48–58 (2013).
58. Hassan, R., Flament, N., Gurnis, M., Bower, D. J. & Müller, R. D. Provenance of plumes in global convection models. *Geochem. Geophys. Geosyst.* **16**, 1465–1489 (2015).
 59. Jaupart, C., Labrosse, S. & Mareschal, J. In Treatise on Geophysics. Volume 7: Mantle Dynamics 1st edn (ed. Bercovici, D.) 253–303 (Elsevier, 2007).
 60. Steinberger, B. & Calderwood, A. R. Models of large-scale viscous flow in the Earth’s mantle with constraints from mineral physics and surface observations. *Geophys. J. Int.* **167**, 1461–1481 (2006).
 61. Billen, M. I. Modeling the dynamics of subducting slabs. *Annu. Rev. Earth Planet. Sci.* **36**, 325–356 (2008).
 62. Williams, S., Wright, N. M., Cannon, J., Flament, N. & Müller, R. D. Reconstructing seafloor age distributions in lost ocean basins. *Geosci. Front.* **12**, 769–780 (2021).
 63. van der Meer, D. G., Spakman, W., van Hinsbergen, D. J., Amaru, M. L. & Torsvik, T. H. Towards absolute plate motions constrained by lower-mantle slab remnants. *Nat. Geosci.* **3**, 36–40 (2010).
 64. Hernlund, J. W. & Houiser, C. On the statistical distribution of seismic velocities in Earth’s deep mantle. *Earth Planet. Sci. Lett.* **265**, 423–437 (2008).
 65. Dziewonski, A. M. & Anderson, D. L. Preliminary reference Earth model. *Phys. Earth Planet. Inter.* **25**, 297–356 (1981).
 66. Ricard, Y., Richards, M., Lithgow-Bertelloni, C. & Le Stunff, Y. A geodynamic model of mantle density heterogeneity. *J. Geophys. Res.* **98**, 21895–21909 (1993).

67. Ahrens, J., Geveci, B. & Law, C. Paraview: an end-user tool for large data visualization. In *The Visualization Handbook* (eds Hansen, C. D. & Johnson, C. R.) 717–731 (Academic Press, 2005).
68. Müller, R. D. et al. Ocean basin evolution and global-scale plate reorganization events since Pangea breakup. *Annu. Rev. Earth Planet. Sci.* **44**, 107–138 (2016).
69. Torsvik, T. H. et al. Phanerozoic polar wander, palaeogeography and dynamics. *Earth Sci. Rev.* **114**, 325–368 (2012).
70. Torsvik, T. H., Müller, R. D., van der Voo, R., Steinberger, B. & Gaina, C. Global plate motion frames: toward a unified model. *Rev. Geophys.* **46**, RG3004 (2008).
71. Torsvik, T. H. & Voo, R. V. D. Refining Gondwana and Pangea palaeogeography: estimates of Phanerozoic non-dipole (octupole) fields. *Geophys. J. Int.* **151**, 771–794 (2002).
72. Merdith, A. S. et al. A full-plate global reconstruction of the Neoproterozoic. *Gondwana Res.* **50**, 84–134 (2017).
73. Domeier, M. A plate tectonic scenario for the Iapetus and Rheic oceans. *Gondwana Res.* **36**, 275–295 (2016).
74. Domeier, M. Early Paleozoic tectonics of Asia: towards a full-plate model. *Geosci. Front.* **9**, 789–862 (2018).
75. MacQueen, J. Some methods for classification and analysis of multivariate observations. In Proc. Fifth Berkeley Symp. Mathematical Statistics and Probability: Volume 1 (eds Le Cam, L. M. & Neyman, J.) 281–297 (Univ. California Press, 1967).
76. Bryan, S. E. & Ernst, R. E. Revised definition of large igneous provinces (LIPs). *Earth Sci. Rev.* **86**, 175–202 (2008).
77. Coffin, M. F. et al. Large igneous provinces and scientific ocean drilling: Status quo and a look ahead. *Oceanography* **19**, 150–160

(2006).

78. Ernst, R. E. Large Igneous Provinces (Cambridge Univ. Press, 2014).
79. Richards, M. A., Duncan, R. A. & Courtillot, V. E. Flood basalts and hot-spot tracks: plume heads and tails. *Science* **246**, 103–107 (1989).
80. Müller, R. D. et al. GPlates: building a virtual Earth through deep time. *Geochem. Geophys. Geosyst.* **19**, 2243–2261 (2018).
81. Knuth, D. E. Art of Computer Programming. Volume 2: Seminumerical Algorithms (Addison-Wesley, 2014).
82. Wessel, P., Smith, W. H., Scharroo, R., Luis, J. & Wobbe, F. Generic mapping tools: improved version released. *Eos* **94**, 409–410 (2013).
83. Hunter, J. D. Matplotlib: a 2D graphics environment. *IEEE Ann. Hist. Comput.* **9**, 90–95 (2007).

Acknowledgements

N.F. and Ö.F.B. were supported by Australian Research Council grant LP170100863 (industry partner: De Beers). S.E.W. was supported by National Natural Science Foundation of China grant 41972237 and by Australian Research Council grants DP180102280 and DP200100966. A.S.M. was supported by the Deep Carbon Observatory and the Richard Lounsbery Foundation. This research was supported by the Australian Government’s National Collaborative Research Infrastructure Strategy (NCRIS), with access to computational resources provided by the National Computational Infrastructure (NCI) through the National Computational Merit Allocation Scheme and through the University of Wollongong (UOW).

Author information

Author notes

1. Andrew S. Merdith

Present address: School of Earth and Environment, University of Leeds, Leeds, UK

Affiliations

1. GeoQuEST Research Centre, School of Earth, Atmospheric and Life Sciences, University of Wollongong, Wollongong, New South Wales, Australia

Nicolas Flament & Ömer F. Bodur

2. Department of Geology, Northwest University, Xi'an, China

Simon E. Williams

3. UnivLyon, Université Lyon 1, ENS de Lyon, CNRS, UMR 5276 LGL-TPE, Villeurbanne, France

Andrew S. Merdith

Contributions

N.F.: conceptualization, methodology, software, validation, formal analysis, investigation, writing of the original draft, and visualization. Ö.F.B.: methodology, software, formal analysis, review and editing of the paper, and visualization. S.E.W.: methodology, software, and review and editing of the paper. A.S.M.: resources and review and editing of the paper.

Corresponding author

Correspondence to [Nicolas Flament](#).

Ethics declarations

Competing interests

The authors declare no competing interests.

Peer review

Peer review information

Nature thanks Allen McNamara and the other, anonymous, reviewer(s) for their contribution to the peer review of this work. Peer reviewer reports are available.

Additional information

Publisher's note Springer Nature remains neutral with regard to jurisdictional claims in published maps and institutional affiliations.

Extended data figures and tables

[Extended Data Fig. 1 Temporal distribution of considered volcanic eruptions.](#)

Histograms showing the number of volcanic eruptions as a function of age. **a**, Back to 320 Ma. **b**, Back to 640 Ma. The number of volcanic eruptions over the considered period for each database is given in brackets.

Databases: J18 (ref. [40](#)) and T18 (ref. [41](#)).

[Extended Data Fig. 2 Location of volcanic eruptions from 320 Ma in different reconstructions.](#)

High-velocity (white) and low-velocity (grey) regions revealed by *k*-means cluster analysis between 1,000 km and 2,800 km depth for seismic tomographic model Savani^{[26](#)}, and location of volcanic eruptions (diamonds, J18, ref. [40](#)) and kimberlites (circles, T18, ref. [41](#)) reconstructed at their time of eruption and shown at present day using tectonic reconstruction M16 (ref. [44](#); **a**), tectonic reconstruction Y19 (ref. [45](#); **b**), tectonic reconstruction

M21 (ref. [10](#); **c**), and tectonic reconstruction M21-NNR without net rotation (no net rotation or ‘NNR’) (**d**). In **a–d**, the brown lines are present-day coastlines. Symbols are coloured by age. Robinson projection at Earth’s surface.

Extended Data Fig. 3 Spatial match of lower mantle structure between mantle flow and tomographic models with respect to tomographic model Savani, and distance to hot basal mantle structures from Savani.

a, Intersection of mantle structure revealed by *k*-means cluster analysis between 1,000 km and 2,800 km for tomographic model Savani^{[26](#)} and mantle flow model cases 1–9 as indicated. Orange (true positive) indicates high-temperature model regions and low-velocity tomographic regions, grey (true negative) indicates low-temperature model regions and high-velocity tomographic regions, green (false positive) indicates high-temperature model regions and high-velocity tomographic regions and blue (false negative) indicates low-temperature regions and low-velocity tomographic regions. **b**, As in **a** but for tomographic model Savani and other tomographic models as indicated. Orange (true positive) indicates low-velocity regions for both models, grey (true negative) indicates high-velocity regions for both models, green (false positive) indicates high-velocity regions for Savani and low-velocity regions for other models and blue (false negative) indicates low-velocity regions for Savani and high-velocity regions for other models. **c**, Angular distance (AD) to the edge or interior (as indicated) of LLSVPs (delineated by a red contour) as derived by *k*-means cluster analysis of tomographic model Savani between 1,000 km and 2,800 km depth. In **a** and **b**, the white lines indicate a value of five (solid) and a value of one (dotted) in a vote map for low-velocity regions in S-wave tomographic models^{[42](#)}. Present-day coastlines are shown in black in **a–c**. Robinson projection at Earth’s surface.

Extended Data Fig. 4 Distributions of distances between basal mantle structures and volcanic eruption locations.

Sample empirical distribution functions (EDFs; blue lines) showing the cumulative probability of minimum angular distances between volcanic eruption locations (J18 and T18) and the closest BMS for the last 320 Myr. Grey lines are a series of 1,000 random EDFs each consisting of points in random locations with the same temporal distribution as in the sample EDF. **a**, For S-wave tomographic models as indicated. **b**, For mantle flow models cases 1–22 as indicated.

Extended Data Fig. 5 Match between volcanic eruption locations, tomographic models and mantle flow models for different tectonic reconstructions.

a, Fractional area f_a of the surface of cluster maps covered by slow (in tomography) or hot (in flow models, averaged over 320 Myr) BMSs. **b**, Spatial match $\langle \overline{\{ \text{Acc} \}} \rangle$ between present-day BMSs for a given case and LLSVPs imaged by tomographic models. **c**, Time-averaged median of minimum angular distances $\langle \widetilde{\theta} \rangle$ between BMSs and volcanic eruption locations from 320 Ma. **d**, Fraction f_s of random EDFs compared to which the sample EDF passes a statistical test. In **a–d**, the first four rows show results for tomographic models (stationary LLSVPs) and different tectonic reconstructions as indicated, and the fifth and last row shows results for a series of mantle flow models (mobile BMSs) based on different tectonic reconstructions as indicated. NNR, no-net-rotation reference frame; MFM, mantle flow model. Tectonic reconstructions: M16, ref. [44](#); Y19, ref. [45](#); M21, ref. [10](#). The horizontal lines denote reference cases. The grey shadings in **a–c** highlight the range of results for tomographic models.

Source data

Extended Data Fig. 6 Match of model basal mantle structures to volcanic eruption locations and tomographic models: structure interiors and over 640 Myr.

a–d, Match to BMS interiors. **a**, Fractional area f_a of the surface of cluster maps covered by slow (in tomography) or hot (in flow models, averaged

over 320 Myr) BMSs. **b**, Spatial match $\langle \overline{\{ \text{Acc} \}} \rangle$ between present-day BMSs for a given case and LLSVPs imaged by tomographic models. **c**, Time-averaged median of minimum angular distances $\langle \widetilde{\theta} \rangle$ between BMSs and volcanic eruption locations from 320 Ma, considering distances to be zero within BMSs and positive outwards from their edges. **d**, Fraction f_s of random EDFs compared to which the sample EDF passes a statistical test. **e–h**, Match to BMS edges over 640 Myr. **e**, Fractional area f_a of the surface of cluster maps covered by hot (in flow models, averaged over 640 Myr) or slow (in tomography) BMSs. **f**, Same as **b**. **g**, Time-averaged median of minimum angular distances $\langle \widetilde{\theta} \rangle$ between BMSs and volcanic eruption locations from 640 Ma. **h**, Same as **d**. In **g**, **h**, open symbols denote results for reconstruction M21 as opposed to M21-NNR. In **a–h**, the first row shows results for a series of tomographic models (stationary LLSVPs), and subsequent rows show results for mantle flow models (mobile BMSs) across which parameters are varied as indicated. BL, basal layer; T1–T7, tomographic models 1–7; C1–C12, mantle flow model cases 1–12. The horizontal lines denote reference cases. The grey shadings in **a–c**, **e–g** highlight the range of results for tomographic models.

[Source data](#)

Extended Data Fig. 7 Match of model basal mantle structures to volcanic eruption locations and tomographic models: varying model parameters and African hemisphere.

a–d, Match for varied model parameters as indicated. **a**, Fractional area f_a of the surface of cluster maps covered by slow (in tomography) or hot (in flow models, averaged over 320 Myr) BMSs. **b**, Spatial match $\langle \overline{\{ \text{Acc} \}} \rangle$ between present-day BMSs for a given case and LLSVPs imaged by tomographic models. **c**, Time-averaged median of minimum angular distances $\langle \widetilde{\theta} \rangle$ between BMSs and volcanic eruption locations from 320 Ma. **d**, Fraction f_s of random EDFs compared to which the sample EDF passes a statistical test. **e–h**, Match in the African hemisphere. **e**, Same as **a** but for different model cases. **f**, Global spatial match $\langle \overline{\{ \text{Acc} \}} \rangle$ between present-day BMSs

for a given case and LLSVPs imaged by tomographic models. **g**, Time-averaged median of minimum angular distances $\langle \widetilde{\theta} \rangle$ between BMSs and volcanic eruption locations in the African hemisphere (within 10,000 km of a point located at 0° N, 11° E; ref. ⁴⁷) from 320 Ma. **h**, For points within the African hemisphere, fraction f_s of random EDFs compared to which the sample EDF passes a statistical test. In **a–h**, the first row shows results for a series of tomographic models (stationary LLSVPs), and subsequent rows show results for mantle flow models (mobile BMSs) across which parameters are varied as indicated. C1–C22, mantle flow model cases 1–22; T1–T7, tomographic models 1–7; ISD, initial slab depth; PCD, phase change depth; BL, basal layer. The horizontal lines denote reference cases. The grey shadings in **a–c**, **e–g** highlight the range of results for tomographic models.

[Source data](#)

[Extended Data Fig. 8 Snapshots of tectonic reconstruction and synthetic seafloor ages.](#)

a–f, Location of tectonic blocks for tectonic reconstruction M21-NNR¹⁰ in the no-net-rotation frame with synthetic seafloor ages⁶². Snapshots are shown at: 740 Ma (**a**), 550 Ma (**b**), 400 Ma (**c**), 250 Ma (**d**), 100 Ma (**e**), 0 Ma (**f**). The reconstructed subduction zones are shown as black lines with triangles on the overriding plate, reconstructed mid-oceanic ridges and transform faults are shown in light orange, reconstructed ancient continental interiors are shown as light grey polygons with a pattern fill, and present-day coastlines are shown in white in **f**. The colour scale indicates the palaeo-age of the ocean crust. WGB, west Gondwanan blocks; PTNM, Palaeo-Tethys northern margin; GWM, Gondwana western margin. Robinson projection at Earth's surface.

[Extended Data Fig. 9 Model initial temperature field and present-day temperature and viscosity.](#)

a, b, Initial temperature field for case 7 at 1,000 Ma. **a**, Temperature at 109 km depth. Reconstructed subduction zones are shown in red, mid-oceanic

ridges and transform faults in yellow, and continental blocks in grey. Robinson projection at Earth's surface. **b**, Temperature along an equatorial cross-section (green line in **a**). Numbers above the colour scale indicate non-dimensional temperature, and numbers below the colour scale indicate temperature in kelvin. **c**, **d**, Horizontally averaged present-day mantle temperature (**c**) and viscosity (**d**). The grey line in **d** is a viscosity profile adjusted to fit the geoid and post-glacial rebound⁶⁰.

Extended Data Table 1 Boundary conditions and parameters for mantle flow model cases

Supplementary information

Peer Review File

41586_2022_4538_MOESM2_ESM.mp4

Supplementary Video 1 Structure of the lower mantle and location of volcanic eruptions from 640 Ma to the present day. High-velocity (white) and low-velocity (grey) regions revealed by cluster analysis between 1,000 km and 2,800 km depth for 22 mantle flow model cases and seven tomographic models, and location of volcanic eruptions (diamonds, J18, ref. 40) and kimberlites (circles, T18, ref. 41) reconstructed from 640 Ma in 20-Myr increments. Results are shown starting 40 Myr into models starting after 600 Ma. Locations are shown for eruptions within 10 Myr of the considered age. The black lines indicate a value of (solid) and a value of one (dotted) in a vote map for low-velocity regions in S-wave tomographic models[42]. Symbols are coloured by age.

41586_2022_4538_MOESM3_ESM.mp4

Supplementary Video 2 Evolution of the spatial match of lower mantle structure between mantle flow and tomographic models with respect to tomographic model Savani from 640 Ma to the present day. Intersection of mantle structure revealed by *k*-means cluster analysis between 1,000 km and 2,800 km for tomographic model Savani[26] and 22 mantle flow model

cases and seven tomographic models mantle flow as indicated, since 640 Ma in 20-Myr increments. Results are shown starting 40 Myr into models starting after 600 Ma. Orange (true positive) indicates high-temperature (or low-velocity) regions and low-velocity tomographic regions, grey (true negative) indicates low-temperature (or high-velocity) regions and high-velocity tomographic regions, green (false positive) indicates high-temperature (or low-velocity) regions and high-velocity tomographic regions and blue (false negative) indicates low-temperature (or fast-velocity) regions and low-velocity tomographic regions. The white lines indicate a value of five (solid) and a value of one (dotted) in a vote map for low-velocity regions in S-wave tomographic models[42]. The time-dependent value of $\overline{\{ \text{rm} \{ \text{Acc} \} \}}$ is reported next to each panel.

[41586_2022_4538_MOESM4_ESM.mp4](#)

Supplementary Video 3 Evolution of mantle temperature in the African mantle domain from 740 Ma to the present day. Mantle structures 155 K colder than ambient mantle below 300 km depth (coloured by depth with cold colours), and mantle structures 310 K hotter than ambient mantle below 170 km depth (coloured by depth with warm colours) predicted by case 7, shown in 20-Myr increments since 740 Ma for the African mantle domain (the video is centred on the prime meridian, 0° longitude). Reconstructed plate boundaries are shown in cyan and the graticule spacing is 30°.

[Supplementary Video 4 Evolution of mantle temperature in the African mantle domain from 740 Ma to the present day. Same as Supplementary Video 3, but for case 4.](#)

[Supplementary Video 5 Evolution of mantle temperature in the African mantle domain from 740 Ma to the present day. Same as Supplementary Video 3, but for case 9.](#)

[41586_2022_4538_MOESM7_ESM.mp4](#)

Supplementary Video 6 Recycling of continental crust in the African mantle domain from 740 Ma to the present day. Mantle structures 310 K hotter than ambient mantle below 170 km depth (coloured by depth with warm colours), and mantle predicted to consist of at least 5% continental crust (below 170 km depth, coloured by depth with cold colours) shown in 20-Myr increments since 740 Ma for the African mantle domain (the video is centred on the prime meridian, 0° longitude). Reconstructed plate boundaries are shown in cyan and the graticule spacing is 30°.

[41586_2022_4538_MOESM8_ESM.mp4](#)

Supplementary Video 7 Recycling of continental crust in the Pacific mantle domain from 740 Ma to the present day. Mantle structures 310 K hotter than ambient mantle below 170 km depth (coloured by depth with warm colours), and mantle predicted to consist of at least 5% continental crust (below 170 km depth, coloured by depth with cold colours) shown in 20-Myr increments since 740 Ma for the Pacific mantle domain (the video is centred on the date line, 180° longitude). Reconstructed plate boundaries are shown in cyan and the graticule spacing is 30°.

Source data

[Source Data Fig. 3](#)

[Source Data Extended Data Fig. 5](#)

[Source Data Extended Data Fig. 6](#)

[Source Data Extended Data Fig. 7](#)

Rights and permissions

[Reprints and Permissions](#)

About this article

Cite this article

Flament, N., Bodur, Ö.F., Williams, S.E. *et al.* Assembly of the basal mantle structure beneath Africa. *Nature* **603**, 846–851 (2022).
<https://doi.org/10.1038/s41586-022-04538-y>

- Received: 22 April 2021
- Accepted: 09 February 2022
- Published: 30 March 2022
- Issue Date: 31 March 2022
- DOI: <https://doi.org/10.1038/s41586-022-04538-y>

Share this article

Anyone you share the following link with will be able to read this content:

[Get shareable link](#)

Sorry, a shareable link is not currently available for this article.

[Copy to clipboard](#)

Provided by the Springer Nature SharedIt content-sharing initiative

[Mobile mantle could explain volcanic hotspot locations](#)

- Allen K. McNamara

News & Views 30 Mar 2022

This article was downloaded by **calibre** from <https://www.nature.com/articles/s41586-022-04538-y>.

- Article
- [Published: 23 March 2022](#)

Subaqueous foraging among carnivorous dinosaurs

- [Matteo Fabbri](#) [ORCID: orcid.org/0000-0002-1257-1594¹](#),
- [Guillermo Navalón](#) [ORCID: orcid.org/0000-0002-2447-1275^{2,3,4}](#),
- [Roger B. J. Benson](#) [ORCID: orcid.org/0000-0001-8244-6177³](#),
- [Diego Pol](#) [ORCID: orcid.org/0000-0002-9690-7517⁵](#),
- [Jingmai O'Connor¹](#),
- [Bhart-Anjan S. Bhullar](#) [ORCID: orcid.org/0000-0002-0838-8068⁶](#),
- [Gregory M. Erickson⁷](#),
- [Mark A. Norell⁸](#),
- [Andrew Orkney](#) [ORCID: orcid.org/0000-0003-4972-2541³](#),
- [Matthew C. Lamanna](#) [ORCID: orcid.org/0000-0001-9845-0728⁹](#),
- [Samir Zouhri¹⁰](#),
- [Justine Becker¹¹](#),
- [Amanda Emke^{11,12}](#),
- [Cristiano Dal Sasso](#) [ORCID: orcid.org/0000-0001-6791-6601¹³](#),
- [Gabriele Bindellini](#) [ORCID: orcid.org/0000-0001-6359-3067^{13,14}](#),
- [Simone Maganuco^{13,15}](#),
- [Marco Auditore¹³](#) &
- [Nizar Ibrahim¹⁶](#)

[Nature](#) volume **603**, pages 852–857 (2022)

- 5664 Accesses
- 1339 Altmetric
- [Metrics details](#)

Subjects

- [Bone quality and biomechanics](#)
- [Palaeoecology](#)
- [Palaeontology](#)

Abstract

Secondary aquatic adaptations evolved independently more than 30 times from terrestrial vertebrate ancestors^{1,2}. For decades, non-avian dinosaurs were believed to be an exception to this pattern. Only a few species have been hypothesized to be partly or predominantly aquatic^{3,4,5,6,7,8,9,10,11}. However, these hypotheses remain controversial^{12,13}, largely owing to the difficulty of identifying unambiguous anatomical adaptations for aquatic habits in extinct animals. Here we demonstrate that the relationship between bone density and aquatic ecologies across extant amniotes provides a reliable inference of aquatic habits in extinct species. We use this approach to evaluate the distribution of aquatic adaptations among non-avian dinosaurs. We find strong support for aquatic habits in spinosaurids, associated with a marked increase in bone density, which precedes the evolution of more conspicuous anatomical modifications, a pattern also observed in other aquatic reptiles and mammals^{14,15,16}. Spinosaurids are revealed to be aquatic specialists with surprising ecological disparity, including subaqueous foraging behaviour in *Spinosaurus* and *Baryonyx*, and non-diving habits in *Suchomimus*. Adaptation to aquatic environments appeared in spinosaurids during the Early Cretaceous, following their divergence from other tetanuran theropods during the Early Jurassic¹⁷.

This is a preview of subscription content

Access options

Subscribe to Nature+

Get immediate online access to the entire Nature family of 50+ journals

\$29.99

monthly

[Subscribe](#)

Subscribe to Journal

Get full journal access for 1 year

\$199.00

only \$3.90 per issue

[Subscribe](#)

All prices are NET prices.

VAT will be added later in the checkout.

Tax calculation will be finalised during checkout.

Buy article

Get time limited or full article access on ReadCube.

\$32.00

[Buy](#)

All prices are NET prices.

Additional access options:

- [Log in](#)
- [Learn about institutional subscriptions](#)

Fig. 1: Osteohistology and ecological variation among amniotes, including the analysed spinosaurid taxa.

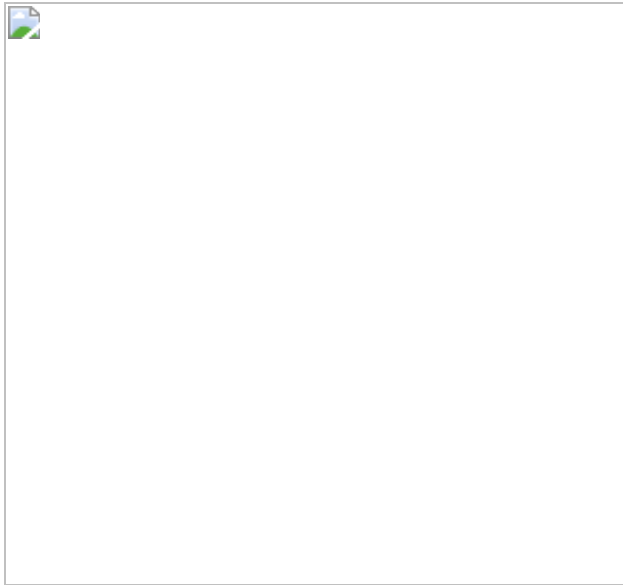


Fig. 2: Relationship between midshaft density of femur, diameter and major lifestyle among amniotes including Spinosauridae.

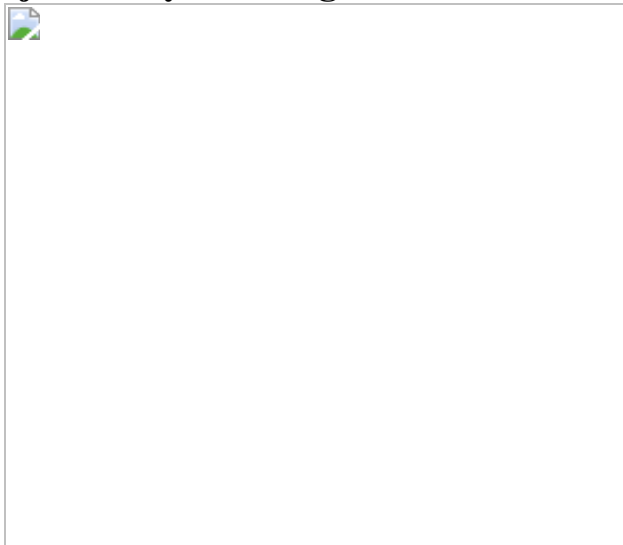
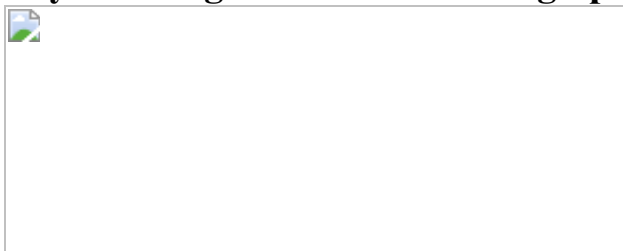


Fig. 3: Relationship between dorsal ribs density, diameter and major lifestyle among amniotes including Spinosauridae.



Data availability

All data described and used in this manuscript are freely available. The measurements and provenance information for fossil specimens can be found in the extended data figures and in the [Supplementary Dataset](#). The phylogenetic datasets and the R coding are available as [Supplementary Material](#). The CT scan datasets collected for this study are available in Morphosource (specific links for each taxon can be found in the [Supplementary Dataset](#)).

References

1. Kelley, N. P. & Pyenson, N. D. Evolutionary innovation and ecology in marine tetrapods from the Triassic to the Anthropocene. *Science* **348**, aaa3716 (2015).
2. Gutarra, S. & Rahman, I. A. The locomotion of extinct secondarily aquatic tetrapods. *Biol. Rev.* **97**, 67–98 (2022).
3. Owen, R. A description of a portion of the skeleton of the *Cetiosaurus*, a gigantic extinct saurian reptile occurring in the oolitic formations of different portions of England. *Proc. Geol. Soc. Lond.* **3**, 457–462 (1841).
4. Cope, E. On the characters of the skull in the Hadrosauridae. *Proc. Natl Acad. Nat. Sci. USA* **35**, 97–107 (1883).
5. Bidar, A., Demay, L. & Thomel, G. *Compsognathus corallestris*, une nouvelle espèce de dinosaure théropode du Portlandien de Canjuers (Sud-Est de la France). *Annales Muséum d'Histoire Naturelle de Nice* **1**, 9–40 (1972).
6. Norell, M. A., Makovicky, P. J. & Currie, P. J. The beaks of ostrich dinosaurs. *Nature* **412**, 873–874 (2001).
7. Tereschenko, V. S. Adaptive features of protoceratopoids (Ornithischia: Neoceratopsia). *Paleontol. J.* **42**, 273–286 (2008).

8. Lee, Y. N. et al. Resolving the long-standing enigmas of a giant ornithomimosaur *Deinocheirus mirificus*. *Nature* **515**, 257–260 (2014).
9. Ibrahim, N. et al. Semiaquatic adaptations in a giant predatory dinosaur. *Science* **345**, 1613–1616 (2014).
10. Cau, A. et al. Synchrotron scanning reveals amphibious ecomorphology in a new clade of bird-like dinosaurs. *Nature* **552**, 395–399 (2017).
11. Ibrahim, N. et al. Tail-propelled aquatic locomotion in a theropod dinosaur. *Nature* **581**, 67–70 (2020).
12. Henderson, D. M. A buoyancy, balance and stability challenge to the hypothesis of a semi-aquatic Spinosaurus Stromer, 1915 (Dinosauria: Theropoda). *PeerJ* **6**, e5409 (2018).
13. Hone, D. W. E. & Holtz, T. R. Jr Evaluating the ecology of *Spinosaurus*: shoreline generalist or aquatic pursuit specialist? *Palaeontol. Electronica* **24**, a03 (2021).
14. Thewissen, J. G., Cooper, L. N., Clementz, M. T., Bajpai, S. & Tiwari, B. N. Whales originated from aquatic artiodactyls in the Eocene epoch of India. *Nature* **450**, 1190–1194 (2007).
15. Houssaye, A. Bone histology of aquatic reptiles: what does it tell us about secondary adaptation to an aquatic life? *Biol. J. Linn. Soc.* **108**, 3–21 (2013).
16. Motani, R. et al. A basal ichthyosauriform with a short snout from the Lower Triassic of China. *Nature* **517**, 485–488 (2015).
17. Rauhut, O. W. & Pol, D. Probable basal allosauroid from the early Middle Jurassic Cañadón Asfalto Formation of Argentina highlights phylogenetic uncertainty in tetanuran theropod dinosaurs. *Sci. Rep.* **9**, 1–9 (2019).

18. You, H. L. et al. A nearly modern amphibious bird from the Early Cretaceous of northwestern China. *Science* **312**, 1640–1643 (2006).
19. Wilson, L. E. & Chin, K. Comparative osteohistology of *Hesperornis* with reference to pygoscelid penguins: the effects of climate and behaviour on avian bone microstructure. *R. Soc. Open Sci.* **1**, 140245 (2014).
20. Gatesy, S. M. & Dial, K. P. Locomotor modules and the evolution of avian flight. *Evolution* **50**, 331–340 (1996).
21. Amiot, R. et al. Oxygen isotope evidence for semi-aquatic habits among spinosaurid theropods. *Geology* **38**, 139–142 (2010).
22. Hassler, A. et al. Calcium isotopes offer clues on resource partitioning among Cretaceous predatory dinosaurs. *Proc. R. Soc. B* **285**, 20180197 (2018).
23. Larramendi, A., Paul, G. S. & Hsu, S. Y. A review and reappraisal of the specific gravities of present and past multicellular organisms, with an emphasis on tetrapods. *Anat. Rec.* **304**, 1833–1888 (2021).
24. Charig, A. J. & Milner, A. C. *Baryonyx*, a remarkable new theropod dinosaur. *Nature* **324**, 359–361 (1986).
25. Schoener, T. W. The newest synthesis: understanding the interplay of evolutionary and ecological dynamics. *Science* **331**, 426–429 (2011).
26. Houssaye, A. “Pachystostosis” in aquatic amniotes: a review. *Integr. Zool.* **4**, 325–340 (2009).
27. Houssaye, A., Sander, M. P. & Klein, N. Adaptive patterns in aquatic amniote bone microanatomy—more complex than previously thought. *Integr. Comp. Biol.* **56**, 1349–1369 (2016).
28. Quemeneur, S., De Buffrenil, V. & Laurin, M. Microanatomy of the amniote femur and inference of lifestyle in limbed vertebrates. *Biol. J. Linn. Soc.* **109**, 644–655 (2013).

29. Canoville, A., de Buffrénil, V. & Laurin, M. Microanatomical diversity of amniote ribs: an exploratory quantitative study. *Biol. J. Linn. Soc.* **118**, 706–733 (2016).
30. Amson, E., de Muizon, C., Laurin, M., Argot, C. & de Buffrénil, V. Gradual adaptation of bone structure to aquatic lifestyle in extinct sloths from Peru. *Proc. R. Soc. B* **281**, 20140192 (2014).
31. Grafen, A. The phylogenetic regression. *Philos. Trans. R. Soc. B* **326**, 119–157 (1989).
32. Liem, K. F. Adaptive significance of intra-and interspecific differences in the feeding repertoires of cichlid fishes. *Am. Zool.* **20**, 295–314 (1980).
33. Turner, A. H., Pol, D., Clarke, J. A., Erickson, G. M. & Norell, M. A. A basal dromaeosaurid and size evolution preceding avian flight. *Science* **317**, 1378–1381 (2007).
34. Voeten, D. F. et al. Wing bone geometry reveals active flight in *Archaeopteryx*. *Nat. Commun.* **9**, 1319 (2018).
35. Houssaye, A., Martin, F., Boisserie, J. R. & Lihoreau, F. Paleoecological inferences from long bone microanatomical specializations in Hippopotamoidea (Mammalia, Artiodactyla). *J. Mamm. Evol.* **28**, 847–870 (2021).
36. Amson, E. & Bibi, F. Differing effects of size and lifestyle on bone structure in mammals. *BMC Biol.* **19**, 87 (2021).
37. Malafaia, E. et al. A new spinosaurid theropod (Dinosauria: Megalosauroidea) from the upper Barremian of Vallibona, Spain: Implications for spinosaurid diversity in the Early Cretaceous of the Iberian Peninsula. *Cret. Res.* **106**, 104221 (2020).
38. Sereno, P. C. et al. A long-snouted predatory dinosaur from Africa and the evolution of spinosaurids. *Science* **282**, 1298–1302 (1998).

39. Aureliano, T. et al. Semi-aquatic adaptations in a spinosaur from the Lower Cretaceous of Brazil. *Cret. Res.* **90**, 283–295 (2018).
40. Barker, C. T. et al. New spinosaurids from the Wessex Formation (Early Cretaceous, UK) and the European origins of Spinosauridae. *Sci. Rep.* **11**, 19340 (2021).
41. Taquet, P. *Géologie et Paléontologie du Gisement de Gadoufaoua (Aptien du Niger)* (Éditions du Centre national de la Recherche Scientifique, 1976).
42. Rayfield, E. J., Milner, A. C., Xuan, V. B. & Young, P. G. Functional morphology of spinosaur ‘crocodile-mimic’ dinosaurs. *J. Vertebr. Paleontol.* **27**, 892–901 (2007).
43. Benson, R. B., Butler, R. J., Carrano, M. T. & O’Connor, P. M. Air-filled postcranial bones in theropod dinosaurs: physiological implications and the ‘reptile’–bird transition. *Biol. Rev.* **87**, 168–193 (2012).
44. Reid, R. E. H. Zonal “growth rings” in dinosaurs. *Mod. Geol.* **15**, 19–48 (1990).
45. Chinsamy, A. & Raath, M. A. Preparation of fossil bone for histological examination. *Palaeont. Afr.* **29**, 39–44 (1992).
46. Griffin, C. T. et al. Assessing ontogenetic maturity in extinct saurian reptiles. *Biol. Rev.* **96**, 470–525 (2021).
47. Carrano, M. T., Benson, R. B. & Sampson, S. D. The phylogeny of Tetanurae (Dinosauria: Theropoda). *J. Syst. Palaeontol.* **10**, 211–300 (2012).
48. Ibrahim, N. et al. Geology and paleontology of the Upper Cretaceous Kem Kem Group of eastern Morocco. *ZooKeys* **928**, 1–216 (2020).
49. Smyth, R. S., Ibrahim, N. & Martill, D. M. *Sigilmassasaurus* is *Spinosaurus*: a reappraisal of African spinosaurines. *Cret. Res.* **114**,

104520 (2020).

50. Goloboff, P. A., Farris, J. S. & Nixon, K. C. TNT, a free program for phylogenetic analysis. *Cladistics* **24**, 774–786 (2008).
51. Erickson, G. M. Assessing dinosaur growth patterns: a microscopic revolution. *Trends Ecol. Evol.* **20**, 677–684 (2005).
52. Hayashi, S. et al. Bone inner structure suggests increasing aquatic adaptations in Desmostyilia (Mammalia, Afrotheria). *PLoS ONE* **8**, e59146 (2013).
53. Straehl, F. R., Scheyer, T. M., Forasiepi, A. M., MacPhee, R. D. E. & Sánchez-Villagra, M. R. Evolutionary patterns of bone histology and bone compactness in xenarthran mammal long bones. *PLoS ONE* **8**, e69275 (2013).
54. Houssaye, A., Tafforeau, P., de Muizon, C. & Gingerich, P. D. Transition of Eocene whales from land to sea: evidence from bone microstructure. *PLoS ONE* **10**, e0118409 (2015).
55. Girondot, M. & Laurin, M. Bone profiler: a tool to quantify, model, and statistically compare bone-section compactness profiles. *J. Vertebr. Paleontol.* **23**, 458–461 (2003).
56. De Ricqlès, A. J., Padian, K., Horner, J. R., Lamm, E. T. & Myhrvold, N. Osteohistology of *Confuciusornis sanctus* (Theropoda: Aves). *Journ. Vertebr. Paleontol.* **23**, 373–386 (2003).
57. Maddison, W. P. Mesquite: a modular system for evolutionary analysis. *Evolution* **62**, 1103–1118 (2008).
58. Upham, N. S., Esselstyn, J. A. & Jetz, W. Inferring the mammal tree: species-level sets of phylogenies for questions in ecology, evolution, and conservation. *PLoS Biol.* **17**, e3000494 (2019).
59. Simoes, T. R. et al. The origin of squamates revealed by a Middle Triassic lizard from the Italian Alps. *Nature* **557**, 706–709 (2018).

60. Nesbitt, S. J. et al. The earliest bird-line archosaurs and the assembly of the dinosaur body plan. *Nature* **544**, 484–487 (2017).
61. Langer, M. C. et al. Untangling the dinosaur family tree. *Nature* **551**, E1–E3 (2017).
62. Brusatte, S. L., Lloyd, G. T., Wang, S. C. & Norell, M. A. Gradual assembly of avian body plan culminated in rapid rates of evolution across the dinosaur-bird transition. *Curr. Biol.* **24**, 2386–2392 (2014).
63. Prum, R. O. et al. A comprehensive phylogeny of birds (Aves) using targeted next-generation DNA sequencing. *Nature* **526**, 569–573 (2015).
64. Bapst, D. W. paleotree: an R package for paleontological and phylogenetic analyses of evolution. *Methods Ecol. Evol.* **3**, 803–807 (2012).
65. Schmitz, L. & Motani, R. Nocturnality in dinosaurs inferred from scleral ring and orbit morphology. *Science* **332**, 705–708 (2011).
66. Motani, R. & Schmitz, L. Phylogenetic versus functional signals in the evolution of form–function relationships in terrestrial vision. *Evolution* **65**, 2245–2257 (2011).

Acknowledgements

We acknowledge P. Barrett and S. Chapman for access to the holotype of *Baryonyx* at the Natural History Museum, London, J. Scannella for access to thin sections of *Tyrannosaurus* housed at the Museum of the Rockies, and M. Fox and J. Gauthier for access to *Poposaurus* at the Yale Peabody Museum. The Moroccan Ministry of Energy, Mines, and the Environment is thanked for providing fieldwork permits to N. I. Members of the 2015–2019 expedition seasons are thanked for their assistance in the field. We thank J. Choiniere, P. Falkingham, S. Nesbitt and the other, anonymous, reviewer for constructive comments that improved the manuscript. Funding was received from the European Union’s Horizon

2020 research and innovation program 2014–2018, starting grant (R. B. J. B., 677774); a National Geographic Society grant (N.I., CP-143R-170); a National Geographic Emerging Explorer Grant (N.I.); the Jurassic Foundation (M.F.); the Paleontological Society grant (M.F.), as well as the Explorers Club (grant awarded to M.F.). The Lokschuppen (Rosenheim, Germany) and J. Pfauntsch provided additional financial support for fieldwork led by N.I. in Morocco.

Author information

Affiliations

1. Negaunee Integrative Research Center, Field Museum of Natural History, Chicago, IL, USA

Matteo Fabbri & Jingmai O'Connor

2. Department of Earth Sciences, University of Cambridge, Cambridge, UK

Guillermo Navalón

3. Department of Earth Sciences, University of Oxford, Oxford, UK

Guillermo Navalón, Roger B. J. Benson & Andrew Orkney

4. Unidad de Paleontología, Departamento de Biología, Universidad Autónoma de Madrid, Madrid, Spain

Guillermo Navalón

5. CONICET, Museo Paleontológico Egidio Feruglio, Trelew, Argentina

Diego Pol

6. Department of Earth and Planetary Sciences and Peabody Museum of Natural History, Yale University, New Haven, CT, USA

Bhart-Anjan S. Bhullar

7. Department of Biological Science, Florida State University,
Tallahassee, FL, USA

Gregory M. Erickson

8. Division of Vertebrate Paleontology, American Museum of Natural History, New York, NY, USA

Mark A. Norell

9. Section of Vertebrate Paleontology, Carnegie Museum of Natural History, Pittsburgh, PA, USA

Matthew C. Lamanna

10. Department of Geology and Health and Environment Laboratory, Hassan II University of Casablanca, Casablanca, Morocco

Samir Zouhri

11. Department of Biology, University of Detroit Mercy, Detroit, MI, USA

Justine Becker & Amanda Emke

12. Department of Physician Assistant Studies, Wayne State University, Detroit, MI, USA

Amanda Emke

13. Sezione di Paleontologia dei Vertebrati, Museo di Storia Naturale di Milano, Milan, Italy

Cristiano Dal Sasso, Gabriele Bindellini, Simone Maganuco & Marco Auditore

14. Dipartimento di Scienze della Terra ‘A. Desio’, Università degli Studi di Milano, Milan, Italy

Gabriele Bindellini

15. Associazione Paleontologica Paleoartistica Italiana, Parma, Italy

Simone Maganuco

16. School of the Environment, Geography and Geosciences, University of Portsmouth, Portsmouth, UK

Nizar Ibrahim

Contributions

Conceptualization: M.F. Data collection and curation: all authors. Data quantification: M.F. Methodology: M.F., G.N. and R.B.J.B. Formal analysis: M.F., G.N. and R.B.J.B. Resources: all authors. Writing, original draft preparation: M.F. Writing, review and editing: all authors. Visualization: M.F. and G.N.; Supervision: M.F., G.N., R.B.J.B. and N.I. Funding acquisition: M.F., R.B.J.B. and N.I.

Corresponding authors

Correspondence to [Matteo Fabbri](#), [Guillermo Navalón](#) or [Roger B. J. Benson](#).

Ethics declarations

Competing interests

The authors declare no competing interests.

Peer review

Peer review information

Nature thanks Jonah Choiniere, Peter Falkingham, Sterling Nesbitt and the other, anonymous, reviewers for their contribution to the peer review of this work. Peer review reports are available.

Additional information

Publisher's note Springer Nature remains neutral with regard to jurisdictional claims in published maps and institutional affiliations.

Extended data figures and tables

[Extended Data Fig. 1 Comparative array of archosaurian femoral diaphysis included in the dataset.](#)

Numerical values represent the bone density quantified for each taxon. Asterisks indicate femoral diaphysis that were retro-deformed before quantification of bone density due to taphonomic deformation and/or fragmentation present in the fossil.

[Extended Data Fig. 2 Comparative array of non-avian and avian femoral diaphysis included in the dataset.](#)

Numerical values represent the bone density quantified for each taxon.

[Extended Data Fig. 3 Comparative array of avian and lepidosaur femoral diaphysis included in the dataset.](#)

Numerical values represent the bone density quantified for each taxon.

[Extended Data Fig. 4 Comparative array of amniote femoral diaphysis included in the dataset.](#)

Numerical values represent the bone density quantified for each taxon.

Extended Data Fig. 5 Comparative array of mammalian femoral diaphysis included in the dataset.

Numerical values represent the bone density quantified for each taxon.

Extended Data Fig. 6 Comparative array of archosaurian dorsal rib cross sections included in the dataset.

Numerical values represent the bone density quantified for each taxon.

Extended Data Fig. 7 Comparative array of amniote dorsal rib cross sections included in the dataset.

Numerical values represent the bone density quantified for each taxon.

Extended Data Fig. 8

Bone density and femur diameter phylogenetic distribution plotted on the informal consensus tree used for discriminant analyses representing the phylogenetic relationships of the taxa included in our study.

Extended Data Fig. 9

Bone density and dorsal rib diameter phylogenetic distribution plotted on the informal consensus tree used for discriminant analyses representing the phylogenetic relationships of the taxa included in our study.

Extended Data Fig. 10 Qualitative comparison of bone compactness in selected skeletal elements between osteosclerotic spinosaurids and other non-avian dinosaurs.

Baryonyx and *Spinosaurus* possess dense, compact bone throughout the postcranial skeleton, namely in the neural spines, ribs, scapula, ilium, pubis, ischium, femur, and fibula. Increased bone density is found in postcranial elements of *Spinosaurus* as well; a reduced medullary cavity is present in

the ribs, dorsal and caudal neural spines, manual phalanges, femur, tibia, and fibula. Abbreviations: bd=bone density.

Supplementary information

Supplementary Information

This file contains Supplementary Figs. 1–3 and Tables 1–10

Reporting Summary

Peer Review File

Supplementary Dataset

This folder contains the list of taxa analysed in this study; R coding; phylogenetic dataset from Malafaia et al. (2020) and phylogenetic dataset from Rauhut & Pol (2019)

Rights and permissions

Reprints and Permissions

About this article

Cite this article

Fabbri, M., Navalón, G., Benson, R.B.J. *et al.* Subaqueous foraging among carnivorous dinosaurs. *Nature* **603**, 852–857 (2022).

<https://doi.org/10.1038/s41586-022-04528-0>

- Received: 15 July 2021
- Accepted: 07 February 2022

- Published: 23 March 2022
- Issue Date: 31 March 2022
- DOI: <https://doi.org/10.1038/s41586-022-04528-0>

Share this article

Anyone you share the following link with will be able to read this content:

[Get shareable link](#)

Sorry, a shareable link is not currently available for this article.

[Copy to clipboard](#)

Provided by the Springer Nature SharedIt content-sharing initiative

This article was downloaded by **calibre** from <https://www.nature.com/articles/s41586-022-04528-0>

| [Section menu](#) | [Main menu](#) |

- Article
- [Published: 23 March 2022](#)

Reduced reproductive success is associated with selective constraint on human genes

- [Eugene J. Gardner^{1 nAff6}](#),
- [Matthew D. C. Neville](#) [ORCID: orcid.org/0000-0001-5816-7936¹](#),
- [Kaitlin E. Samocha](#) [ORCID: orcid.org/0000-0002-1704-3352¹](#),
- [Kieron Barclay^{2,3,4}](#),
- [Martin Kolk](#) [ORCID: orcid.org/0000-0002-7175-4040³](#),
- [Mari E. K. Niemi](#) [ORCID: orcid.org/0000-0003-0696-6175¹](#),
- [George Kirov⁵](#),
- [Hilary C. Martin](#) [ORCID: orcid.org/0000-0002-4454-9084¹](#) &
- [Matthew E. Hurles](#) [ORCID: orcid.org/0000-0002-2333-7015¹](#)

[Nature](#) volume 603, pages 858–863 (2022)

- 6674 Accesses
- 1 Citations
- 1066 Altmetric
- [Metrics details](#)

Subjects

- [Genetic association study](#)
- [Human behaviour](#)

- [Rare variants](#)
- [Sexual selection](#)

Abstract

Genome-wide sequencing of human populations has revealed substantial variation among genes in the intensity of purifying selection acting on damaging genetic variants¹. Although genes under the strongest selective constraint are highly enriched for associations with Mendelian disorders, most of these genes are not associated with disease and therefore the nature of the selection acting on them is not known². Here we show that genetic variants that damage these genes are associated with markedly reduced reproductive success, primarily owing to increased childlessness, with a stronger effect in males than in females. We present evidence that increased childlessness is probably mediated by genetically associated cognitive and behavioural traits, which may mean that male carriers are less likely to find reproductive partners. This reduction in reproductive success may account for 20% of purifying selection against heterozygous variants that ablate protein-coding genes. Although this genetic association may only account for a very minor fraction of the overall likelihood of being childless (less than 1%), especially when compared to more influential sociodemographic factors, it may influence how genes evolve over time.

This is a preview of subscription content

Access options

Subscribe to Nature+

Get immediate online access to the entire Nature family of 50+ journals

\$29.99

monthly

[Subscribe](#)

[Subscribe to Journal](#)

Get full journal access for 1 year

\$199.00

only \$3.90 per issue

[Subscribe](#)

All prices are NET prices.

VAT will be added later in the checkout.

Tax calculation will be finalised during checkout.

[Buy article](#)

Get time limited or full article access on ReadCube.

\$32.00

[Buy](#)

All prices are NET prices.

Additional access options:

- [Log in](#)
- [Learn about institutional subscriptions](#)

Fig. 1: Differences in male and female reproductive success as a function of cumulative rare deleterious genetic variation.

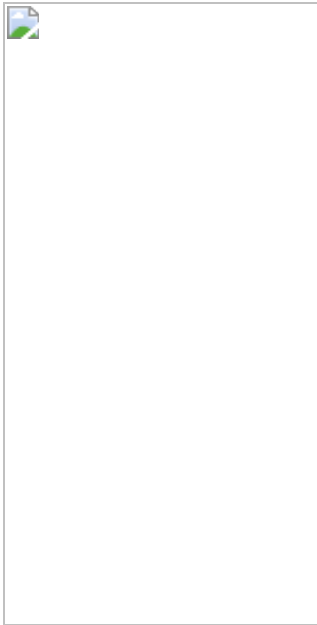


Fig. 2: Association of s_{het} burden with traits known to be associated with reproductive success.



Data availability

Raw data produced by this study are available as part of the UK Biobank data returns catalogue with application ID 44165:

<https://biobank.ndph.ox.ac.uk/ukb/docs.cgi?id=1>.

Code availability

Code used as part of this project to perform phenotype testing, CNV calling, variant quality control and to generate all main text figures, supplementary figures and supplementary tables is available on github: <https://github.com/HurlesGroupSanger/UKBBFertility>. All statistical analysis in this manuscript was performed using R v3.6.0.

References

1. Lek, M. et al. Analysis of protein-coding genetic variation in 60,706 humans. *Nature* **536**, 285–291 (2016).
2. Cassa, C. A. et al. Estimating the selective effects of heterozygous protein-truncating variants from human exome data. *Nat. Genet.* **49**, 806–810 (2017).
3. Collins, R. L. et al. A structural variation reference for medical and population genetics. *Nature* **581**, 444–451 (2020).
4. Weghorn, D. et al. Applicability of the mutation-selection balance model to population genetics of heterozygous protein-truncating variants in humans. *Mol. Biol. Evol.* **36**, 1701–1710 (2019).
5. Darwin, C. *The Descent of Man, and Selection in Relation to Sex* (A. L. Burt, 1874); <https://doi-org.ezp.lib.cam.ac.uk/10.5962/bhl.title.16749>
6. Ganna, A. et al. Ultra-rare disruptive and damaging mutations influence educational attainment in the general population. *Nat. Neurosci.* **19**, 1563–1565 (2016).
7. Männik, K. et al. Copy number variations and cognitive phenotypes in unselected populations. *JAMA* **313**, 2044–2054 (2015).
8. Huguet, G. et al. Measuring and estimating the effect sizes of copy number variants on general intelligence in community-based samples.

JAMA Psychiatry **75**, 447–457 (2018).

9. Ganna, A. et al. Quantifying the impact of rare and ultra-rare coding variation across the phenotypic spectrum. *Am. J. Hum. Genet.* **102**, 1204–1211 (2018).
10. Sudlow, C. et al. UK Biobank: an open access resource for identifying the causes of a wide range of complex diseases of middle and old age. *PLoS Med.* **12**, e1001779 (2015).
11. Szustakowski, J. D. et al. Advancing human genetics research and drug discovery through exome sequencing of the UK Biobank. *Nat. Genet.* **53**, 942–948 (2021).
12. Barthold, J. A., Myrskylä, M. & Jones, O. R. Childlessness drives the sex difference in the association between income and reproductive success of modern Europeans. *Evol. Hum. Behav.* **33**, 628–638 (2012).
13. Dudel, C. & Klüsener, S. Estimating men's fertility from vital registration data with missing values. *Popul. Stud.* **73**, 439–449 (2019).
14. Birth Summary Tables, England and Wales 2019 (Office of National Statistics, 2020).
15. Oud, M. S. et al. A systematic review and standardized clinical validity assessment of male infertility genes. *Hum. Reprod.* **34**, 932–941 (2019).
16. Bult, C. J. et al. Mouse Genome Database (MGD) 2019. *Nucleic Acids Res.* **47**, D801–D806 (2019).
17. Lopes, A. M. et al. Human spermatogenic failure purges deleterious mutation load from the autosomes and both sex chromosomes, including the gene DMRT1. *PLoS Genet.* **9**, e1003349 (2013).
18. Skjaerven, R., Wilcox, A. J. & Lie, R. T. A population-based study of survival and childbearing among female subjects with birth defects and

- the risk of recurrence in their children. *N. Engl. J. Med.* **340**, 1057–1062 (1999).
19. Lie, R. T., Wilcox, A. J. & Skjaerven, R. Survival and reproduction among males with birth defects and risk of recurrence in their children. *JAMA* **285**, 755–760 (2001).
 20. Power, R. A. et al. Fecundity of patients with schizophrenia, autism, bipolar disorder, depression, anorexia nervosa, or substance abuse vs their unaffected siblings. *JAMA Psychiatry* **70**, 22–30 (2013).
 21. Allen, M. S. The role of personality in sexual and reproductive health. *Curr. Dir. Psychol. Sci.* **28**, 581–586 (2019).
 22. Buss, D. M. et al. International preferences in selecting mates: a study of 37 cultures. *J. Cross. Cult. Psychol.* **21**, 5–47 (1990).
 23. Pawłowski, B. & Dunbar, R. I. Impact of market value on human mate choice decisions. *Proc. Biol. Sci.* **266**, 281–285 (1999).
 24. Buss, D. M. & Schmitt, D. P. Mate preferences and their behavioral manifestations. *Annu. Rev. Psychol.* **70**, 77–110 (2019).
 25. Fieder, M., Huber, S. & Bookstein, F. L. Socioeconomic status, marital status and childlessness in men and women: an analysis of census data from six countries. *J. Biosoc. Sci.* **43**, 619–635 (2011).
 26. Nettle, D. & Pollet, T. V. Natural selection on male wealth in humans. *Am. Nat.* **172**, 658–666 (2008).
 27. Miettinen, A., Rotkirch, A., Szalma, I., Donno, A. & Tanturri, M.-L. Increasing Childlessness in Europe: Time Trends and Country Differences Working Paper 33 (Family and Societies, 2015).
 28. Jalovaara, M. et al. Education, Gender, and Cohort Fertility in the Nordic Countries. *Eur. J. Popul.* **35**, 563–586 (2019).
 29. Fieder, M. & Huber, S. The effects of sex and childlessness on the association between status and reproductive output in modern society.

Evol. Hum. Behav. **28**, 392–398 (2007).

30. GTEx Consortium. The Genotype–Tissue Expression (GTEx) project. *Nat. Genet.* **45**, 580–585 (2013).
31. Trivers, R. in *Sexual Selection and the Descent of Man* (ed. Campbell, B.) (Aldine, 1972).
32. Bateman, A. J. Intra-sexual selection in *Drosophila*. *Heredity* **2**, 349–368 (1948).
33. Parker, G. A. & Pizzari, T. in *Current Perspectives on Sexual Selection* 119–163 (Springer, 2015).
34. Kolk, M. & Barclay, K. Cognitive ability and fertility among Swedish men born 1951–1967: evidence from military conscription registers. *Proc. Biol. Sci.* **286**, 20190359 (2019).
35. Kendall, K. M. et al. Cognitive performance among carriers of pathogenic copy number variants: analysis of 152,000 UK Biobank subjects. *Biol. Psychiatry* **82**, 103–110 (2017).
36. Davis, K. A. S. et al. Mental health in UK Biobank—development, implementation and results from an online questionnaire completed by 157,366 participants: a reanalysis. *BJPsych Open* **6**, e18 (2020).
37. Tyrrell, J. et al. Genetic predictors of participation in optional components of UK Biobank. *Nat. Commun.* **12**, 886 (2021).
38. Stefansson, H. et al. CNVs conferring risk of autism or schizophrenia affect cognition in controls. *Nature* **505**, 361–366 (2014).
39. Fry, A. et al. Comparison of sociodemographic and health-related characteristics of UK Biobank participants with those of the general population. *Am. J. Epidemiol.* **186**, 1026–1034 (2017).
40. Watanabe, K. et al. A global overview of pleiotropy and genetic architecture in complex traits. *Nat. Genet.* **51**, 1339–1348 (2019).

41. Barban, N. et al. Genome-wide analysis identifies 12 loci influencing human reproductive behavior. *Nat. Genet.* **48**, 1462–1472 (2016).
42. Verweij, R. M. et al. Sexual dimorphism in the genetic influence on human childlessness. *Eur. J. Hum. Genet.* **25**, 1067–1074 (2017).
43. Clark, D. W. et al. Associations of autozygosity with a broad range of human phenotypes. *Nat. Commun.* **10**, 4957 (2019).
44. Stanley, K. E. et al. Causal genetic variants in stillbirth. *N. Engl. J. Med.* **383**, 1107–1116 (2020).
45. Kaplanis, J. et al. Evidence for 28 genetic disorders discovered by combining healthcare and research data. *Nature* **586**, 757–762 (2020).
46. Girirajan, S. et al. Phenotypic heterogeneity of genomic disorders and rare copy-number variants. *N. Engl. J. Med.* **367**, 1321–1331 (2012).
47. Costain, G., Chow, E. W. C., Silversides, C. K. & Bassett, A. S. Sex differences in reproductive fitness contribute to preferential maternal transmission of 22q11.2 deletions. *J. Med. Genet.* **48**, 819–824 (2011).
48. De Rubeis, S. et al. Synaptic, transcriptional and chromatin genes disrupted in autism. *Nature* **515**, 209–215 (2014).
49. Berrington, A. in *Demographic Research Monographs* 57–76 (Springer, 2017).
50. Betzig, L. Means, variances, and ranges in reproductive success: comparative evidence. *Evol. Hum. Behav.* **33**, 309–317 (2012).
51. Bycroft, C. et al. The UK Biobank resource with deep phenotyping and genomic data. *Nature* **562**, 203–209 (2018).
52. Wang, K. et al. PennCNV: an integrated hidden Markov model designed for high-resolution copy number variation detection in whole-genome SNP genotyping data. *Genome Res.* **17**, 1665–1674 (2007).

53. Macé, A. et al. New quality measure for SNP array based CNV detection. *Bioinformatics* **32**, 3298–3305 (2016).
54. Liaw, A. & Wiener, M. Classification and regression by randomforest. *R News* **2**, 285 (2002).
55. Di Angelantonio, E. et al. Efficiency and safety of varying the frequency of whole blood donation (INTERVAL): a randomised trial of 45,000 donors. *Lancet* **390**, 2360–2371 (2017).
56. Fromer, M. et al. Discovery and statistical genotyping of copy-number variation from whole-exome sequencing depth. *Am. J. Hum. Genet.* **91**, 597–607 (2012).
57. Backenroth, D. et al. CANOES: detecting rare copy number variants from whole exome sequencing data. *Nucleic Acids Res.* **42**, e97 (2014).
58. Packer, J. S. et al. CLAMMS: a scalable algorithm for calling common and rare copy number variants from exome sequencing data. *Bioinformatics* **32**, 133–135 (2016).
59. Crawford, K. et al. Medical consequences of pathogenic CNVs in adults: analysis of the UK Biobank. *J. Med. Genet.* **56**, 131–138 (2019).
60. McLaren, W. et al. The Ensembl variant effect predictor. *Genome Biol.* **17**, 122 (2016).
61. Rentzsch, P., Schubach, M., Shendure, J. & Kircher, M. CADD-splice-improving genome-wide variant effect prediction using deep learning-derived splice scores. *Genome Med.* **13**, 31 (2021).
62. Karczewski, K. J. et al. The mutational constraint spectrum quantified from variation in 141,456 humans. *Nature* **581**, 434–443 (2020).
63. Samocha, K. E. et al. Regional missense constraint improves variant deleteriousness prediction. Preprint at <https://doi.org/10.1101/148353>

(2017).

64. Zhao, H. et al. CrossMap: a versatile tool for coordinate conversion between genome assemblies. *Bioinformatics* **30**, 1006–1007 (2014).
65. Kersey, P. J. et al. Ensembl Genomes 2016: more genomes, more complexity. *Nucleic Acids Res.* **44**, D574–D580 (2016).
66. Landrum, M. J. et al. ClinVar: improving access to variant interpretations and supporting evidence. *Nucleic Acids Res.* **46**, D1062–D1067 (2018).
67. Van Hout, C. V. et al. Exome sequencing and characterization of 49,960 individuals in the UK Biobank. *Nature* **586**, 749–756 (2020).
68. Nait Saada, J. et al. Identity-by-descent detection across 487,409 British samples reveals fine scale population structure and ultra-rare variant associations. *Nat. Commun.* **11**, 6130 (2020).
69. Virtanen, P. et al. SciPy 1.0: fundamental algorithms for scientific computing in Python. *Nat. Methods* **17**, 261–272 (2020).
70. Balduzzi, S., Rücker, G. & Schwarzer, G. How to perform a meta-analysis with R: a practical tutorial. *Evid. Based. Ment. Health* **22**, 153–160 (2019).
71. Population and Welfare Department. Multi-Generation Register 2016: A Description of Contents and Quality (Statistics Sweden, 2017).
72. Carlstedt, B. *Cognitive Abilities—Aspects of Structure, Process and Measurement*. Doctoral thesis, Univ. of Gothenburg (2000).
73. Hällsten, M. Inequality across three and four generations in egalitarian Sweden: 1st and 2nd cousin correlations in socio-economic outcomes. *Res. Soc. Stratif. Mobil.* **35**, 19–33 (2014).
74. Mårdberg, B. & Carlstedt, B. Swedish Enlistment Battery (SEB): construct validity and latent variable estimation of cognitive abilities

by the CAT-SEB. *Int. J. Sel.* **6**, 107–114 (1998).

75. Rönnlund, M., Carlstedt, B., Blomstedt, Y., Nilsson, L.-G. & Weinehall, L. Secular trends in cognitive test performance: Swedish conscript data 1970–1993. *Intelligence* **41**, 19–24 (2013).

Acknowledgements

We thank L. Parts, J. Kaplanis, M. Przeworski and G. Davey-Smith for useful discussions and advice on data analysis; M. Oud and J. Veltman for helpful discussions regarding infertility; G. Kalantzis and P. F. Palamara for assistance with correcting for recent ancestry; and the INTERVAL study for sharing genotyping and exome data that enabled us to refine our CNV filtering methodology. This work has been funded by core Wellcome funding to the Wellcome Sanger Institute (grant WT098051) and as part of a Medical Research Council (MRC) Centre Grant to the MRC Centre for Neuropsychiatric Genetics and Genomics (grant MR/L010305/1). K.B. is supported by a fellowship from the Bank of Sweden Tercentenary Foundation (Riksbankens Jubileumsfond). This work has been conducted using the UK Biobank Resource under application numbers 14421 (to G.K.) and 44165 (to H.C.M.).

Author information

Author notes

1. Eugene J. Gardner

Present address: Medical Research Council (MRC) Epidemiology Unit, University of Cambridge School of Clinical Medicine, Institute of Metabolic Science, Cambridge Biomedical Campus, Cambridge, UK

Affiliations

1. Wellcome Sanger Institute, Wellcome Genome Campus, Cambridge, Hinxton, UK

Eugene J. Gardner, Matthew D. C. Neville, Kaitlin E. Samocha, Mari E. K. Niemi, Hilary C. Martin & Matthew E. Hurles

2. Max Planck Institute for Demographic Research, Rostock, Germany

Kieron Barclay

3. Demography Unit, Department of Sociology, Stockholm University, Stockholm, Sweden

Kieron Barclay & Martin Kolk

4. Swedish Collegium for Advanced Study, Uppsala, Sweden

Kieron Barclay

5. Division of Psychological Medicine and Clinical Neurosciences, School of Medicine, Cardiff University, Cardiff, UK

George Kirov

Contributions

E.J.G., M.D.C.N. and K.E.S. assessed the contribution of rare genetic variation to the phenotypes and vital statistics presented in this manuscript. E.J.G. and G.K. performed CNV calling. E.J.G. and M.E.K.N. annotated and assessed SNV and indel variants from provided WES data. K.B., M.K., E.J.G. and M.E.H. curated and analysed Swedish IQ data. E.J.G., K.E.S., H.C.M. and M.E.H. designed experiments, oversaw the study and wrote the manuscript.

Corresponding author

Correspondence to [Matthew E. Hurles](#).

Ethics declarations

Competing interests

M.E.H. is a founder of, director of, consultant to, and holds shares in, Congenica Ltd and is a consultant to the AstraZeneca Centre for Genomics Research.

Peer review

Peer review information

Nature thanks Loic Yengo and the other, anonymous reviewers for their contribution to the peer review of this work. Peer review reports are available.

Additional information

Publisher's note Springer Nature remains neutral with regard to jurisdictional claims in published maps and institutional affiliations.

Extended data figures and tables

[Extended Data Fig. 1 Odds ratio estimates for the association of shet burden with having children for all variant classes.](#)

Identical plot to main text Fig. 1a, but with additional data for synonymous, missense, and duplication s_{het} scores, separated into females (violet) and males (jade). Asterisks indicate significance after Bonferroni correction for 20 tests ($P < 2.5 \times 10^{-3}$; [Methods](#)).

[Extended Data Fig. 2 Effect size estimate for the association of shet burden with number of children for individuals with](#)

children.

Shown are the effect size estimates for the association of s_{het} burden with number of children, separated into females (purple) and males (jade), but with all childless individuals in the UK Biobank removed. Like Main Text Fig. 1a, the regression used to generate the displayed result used the raw number of children, live births for females and children fathered for males, rather than a binary value for having children. Asterisks indicate significance after Bonferroni correction for 20 tests ($P < 2.5 \times 10^{-3}$; [Methods](#)).

Extended Data Fig. 3 Odds ratio estimate for s_{het} burden stratified by age group.

Shown are odds ratio estimates for the association of s_{het} burden with having children, stratified by participant age (y-axis) and separated into females (violet) and males (jade). Age range intervals are left-open. Dash of the line indicates whether the estimate comes from s_{het} burden calculated from deletions (long dash), PTVs (short dash), or from a fixed effects meta-analysis (no dash). Also shown for reference are the results for all individuals regardless of age (All Ages), which is identical to the result shown in main text Fig. 1b. Asterisks indicate significance after Bonferroni correction for 20 tests ($P < 2.5 \times 10^{-3}$; [Methods](#)).

Extended Data Fig. 4 Mediation of the relationship between s_{het} burden and childlessness by various disorders.

Plotted is the deletion and PTV meta-analysis $-\log_{10} P$ value for the association between s_{het} burden and having children, corrected by one of 1,294 ICD-10 codes from a combination of general practitioner, hospital episode records, and self-reported conditions (left) or hospital episode records alone (right) separately for males (top) and females (bottom). Remaining ICD-10 codes at different levels on the ICD-10 hierarchy not displayed here are plotted in Supplementary Figs. 8 and 9. Results are ordered first by ICD-10 chapter (x-axis) and then by increasing $-\log_{10} P$.

value (y-axis). The arrow for code Z37 indicates the point is below the scale of the y-axis with $-\log_{10} P$ value indicated in parentheses. Visual outliers are labelled and do not imply a significant change in the effect size of s_{het} on childlessness.

Extended Data Fig. 5 Mediation of the association between s_{het} burden and childlessness by various disorders.

Depicted are the results of our primary association between childlessness and individual s_{het} burden corrected for presence/absence of approximately 2,000 different disorders, diseases, and health factors queried from (A,B) hospital episode statistics and (C,D) complete health outcomes data as represented by the ICD-10 medical coding system separately for (A,C) males and (B,D) females (see main text methods). Shown on the x-axis is the $-\log_{10} p$ value for the association of s_{het} with having children, corrected for a given diagnostic code. On the y-axis is the $-\log_{10} p$ value for having a given medical code on likelihood of having children; p values are placed above or below $y = 0$ based on the direction of effect, with disorders which are associated with having children above and those associated with not having children below. Codes were chosen for labeling to highlight outliers and not based on any statistical criteria. Codes with points at the top or bottom of plots have $-\log_{10} p$ values ≥ 100 . Color of points and text is based on the ICD-10 chapter. Please note that text labels do not necessarily represent the full official name of a given ICD-10 code.

Extended Data Fig. 6 Association of eight relevant phenotypes/demographic measures with the likelihood of having children among UK Biobank participants.

Shown are the results of a logistic regression estimating the odds ratio for the relationship of (A) having a partner at home, (B) ever having had sex (C) completing university, (D) having a severe mental health disorder, (E) household income, (F) fluid intelligence, (G) Townsend deprivation index, and (H) engaging in same sex sexual behaviour with likelihood of having children, separated into females (violet) and males (jade). 95% confidence

intervals for all plots are included, but may be invisible at the resolution of the figure. Please note that the scales of the x-axis for plots (A) and (B) are different from plots (C-H) due to the relatively stronger association of these traits with having children.

Extended Data Fig. 7 Effect size estimates for the association between shet burden and Townsend Deprivation Index.

Shown are the effect size estimates for the association between s_{het} burden and Townsend Deprivation Index, separated into females (purple) and males (jade). Units are unnormalized Townsend Deprivation Indices for each individual in the UK Biobank. Asterisks indicate significance after Bonferroni correction for 20 tests ($p < 2.5 \times 10^{-3}$; [Methods](#)).

Extended Data Fig. 8 The role of individual phenotypes in the relationship between shet burden, childlessness, and fitness.

(A) Odds ratio estimates for the association of cumulative deleterious variation for a combined meta-analysis (deletions + PTVs) with childlessness (middle), corrected for a combination of whether or not a study participant has a mental health (MH) disorder, a partner at home, a university degree, infertility (as ascertained from Complete Health Outcomes Data; [Methods](#)), or ever had sex; traits included in each model are indicated as coloured boxes (males – jade, females – violet) on the y-axis. Stars within boxes indicate either nominal (*) or Bonferroni-corrected (**) significance level with childlessness for each covariate independently when correcting for PTV s_{het} burden. For all possible combinations of these traits, see Supplementary Fig. [17](#). As indicated by coloured boxes, all models include s_{het} burden and were run separately for males and females. The marginal bar plot to the right gives the proportion of the variance in childlessness explained by s_{het} burden as calculated for PTVs only, scaled to the model which only includes s_{het} burden (i.e. the model on the bottom of the plot). (B) Predicted reduction in overall fitness as a factor of individual s_{het} burden. Displayed is the expected reduction in fitness as a factor of increasing s_{het} burden, independently for each sex. Error is shown as the

lighter shaded area surrounding the trend line, and is based on the confidence intervals on the odds ratio as determined by our logistic regression model (Fig. 1b; [Methods](#)). The dashed line represents the theoretical reduction in fitness as predicted by s_{het} ⁴.

Extended Data Fig. 9 The association of s_{het} burden with childlessness.

Identical to Extended Data Fig. 8B, except in this instance, the y-axis represents predicted childlessness as a factor of individual s_{het} burden, rather than predicted reduction in fitness. Values at x = 0 represent actual mean childlessness among UK Biobank males (jade) and females (violet) with an s_{het} burden of 0.

Supplementary information

Supplementary Information

This file contains Supplementary Figs. 1–21, Supplementary Notes 1–3 and references.

Reporting Summary

Supplementary Table 1

Phenotypes assessed in this study.

Supplementary Table 2

Results from logistic models corrected for ICD-10 codings.

Supplementary Table 3

Covariates for training the CNV random forest QC model.

Supplementary Table 4

Catalogue of odds ratios and betas for associations reported in this manuscript.

Supplementary Table 5

Raw fertility statistics for all Swedish males born 1965–1967.

Supplementary Table 6

Values used for estimating contribution of mental health phenotypes to overall fitness.

Peer Review File

Rights and permissions

Reprints and Permissions

About this article

Cite this article

Gardner, E.J., Neville, M.D.C., Samocha, K.E. *et al.* Reduced reproductive success is associated with selective constraint on human genes. *Nature* **603**, 858–863 (2022). <https://doi.org/10.1038/s41586-022-04549-9>

- Received: 21 May 2020
- Accepted: 07 February 2022
- Published: 23 March 2022
- Issue Date: 31 March 2022

- DOI: <https://doi.org/10.1038/s41586-022-04549-9>

Share this article

Anyone you share the following link with will be able to read this content:

[Get shareable link](#)

Sorry, a shareable link is not currently available for this article.

[Copy to clipboard](#)

Provided by the Springer Nature SharedIt content-sharing initiative

Further reading

- [**Constrained human genes under scrutiny**](#)

- Loic Yengo
- Heidi Colleran

Nature (2022)

[**Constrained human genes under scrutiny**](#)

- Loic Yengo
- Heidi Colleran

News & Views Forum 23 Mar 2022

This article was downloaded by **calibre** from <https://www.nature.com/articles/s41586-022-04549-9>

- Article
- Open Access
- [Published: 16 March 2022](#)

Machine learning and phone data can improve targeting of humanitarian aid

- [Emily Aiken¹ nat](#),
- [Suzanne Bellue²](#),
- [Dean Karlan³](#),
- [Chris Udry⁴](#) &
- [Joshua E. Blumenstock](#) ORCID: [orcid.org/0000-0002-1813-7414¹ nat](https://orcid.org/0000-0002-1813-7414)

Nature volume 603, pages 864–870 (2022)

- 17k Accesses
- 433 Altmetric
- [Metrics details](#)

Subjects

- [Computer science](#)
- [Developing world](#)
- [Economics](#)
- [Policy](#)

Abstract

The COVID-19 pandemic has devastated many low- and middle-income countries, causing widespread food insecurity and a sharp decline in living standards¹. In response to this crisis, governments and humanitarian organizations worldwide have distributed social assistance to more than 1.5 billion people². Targeting is a central challenge in administering these programmes: it remains a difficult task to rapidly identify those with the greatest need given available data^{3,4}. Here we show that data from mobile phone networks can improve the targeting of humanitarian assistance.

Our approach uses traditional survey data to train machine-learning algorithms to recognize patterns of poverty in mobile phone data; the trained algorithms can then prioritize aid to the poorest mobile subscribers. We evaluate this approach by studying a flagship emergency cash transfer program in Togo, which used these algorithms to disburse millions of US dollars worth of COVID-19 relief aid. Our analysis compares outcomes—including exclusion errors, total social welfare and measures of fairness—under different targeting regimes. Relative to the geographic targeting options considered by the Government of Togo, the machine-learning approach reduces errors of exclusion by 4–21%. Relative to methods requiring a comprehensive social registry (a hypothetical exercise; no such registry exists in Togo), the machine-learning approach increases exclusion errors by 9–35%. These results highlight the potential for new data sources to complement traditional methods for targeting humanitarian assistance, particularly in crisis settings in which traditional data are missing or out of date.

[Download PDF](#)

Main

The COVID-19 pandemic has led to a sharp decline in living standards across the world, as policies designed to stop the spread of the disease have disrupted normal economic activity. Economically vulnerable households in low- and middle-income countries have been among the hardest hit, with more than 100 million individuals estimated to have transitioned into extreme poverty since the onset of the pandemic⁵.

To offset the most severe consequences of this sudden decline in income, governments and humanitarian organizations around the world have mobilized relief efforts. It has been estimated that more than 3,300 new social assistance programmes have been launched² since early 2020, providing more than US\$800 billion in cash transfer payments to over 1.5 billion people (roughly one fifth of the world's population).

The overwhelming majority of COVID-19 response efforts—and the majority of cash transfer programmes globally—provide targeted social assistance^{3,4}. In other words, specific criteria—typically a proxy for socioeconomic status—are used to determine potential eligibility. In most wealthy nations, governments rely on recent household income data to determine programme eligibility⁶. However, in low- and lower middle-income countries (LMICs), where economic activity is often informal and based on home-produced agriculture, governments typically do not observe income for the vast majority of the population³. Other potential sources of targeting data are often incomplete or out of date^{7,8}; for example, only half of the poorest countries have

completed a census in the past 10 years⁹. In such contexts, data gaps preclude governments from implementing well-targeted social assistance programmes^{10,11}.

Here we develop, implement and evaluate an approach to targeting social assistance based on machine-learning algorithms and non-traditional ‘big data’ from satellites and mobile phone networks. This approach leverages recent advances in machine learning that show that such data can help accurately estimate the wealth of small geographic regions^{12,13,14,15,16} and individual mobile subscribers^{17,18,19}. It also builds on a rich economics literature on the design of appropriate mechanisms for targeting social assistance^{3,20,21,22,23,24,25,26,27,28,29}. See [Supplementary Discussion](#), section 1 for a summary of previous work.

Humanitarian response to COVID-19 in Togo

Our results are based on the design and evaluation of Novissi, a flagship emergency social assistance programme carried out in Togo. The Government of Togo launched Novissi in April 2020, shortly after the first cases of COVID-19 appeared in the country. As economic lockdown orders forced many Togolese to stop working and led to widespread food insecurity (Supplementary Fig. 1), Novissi aimed to provide subsistence cash relief to those most affected (see <https://novissi.gouv.tg/>). Eligible beneficiaries received bi-weekly payments of roughly US\$10. In an effort to minimize in-person contact, Novissi enrolment and payments were implemented digitally: beneficiaries registered using their mobile phones and transfers were made via mobile money. Full details on the Novissi programme are provided in Methods, ‘The COVID-19 pandemic in Togo’.

When the government first launched Novissi, it did not have a traditional social registry that could be used to assess programme eligibility, and did not have the time or the resources to build such a registry in the middle of the pandemic. The most recent census, which was completed in 2011, did not contain information on household wealth or poverty; more recent national surveys on living standards only contacted a small fraction of all households ([Methods](#), ‘The COVID-19 pandemic in Togo’). Instead, eligibility for Novissi was determined on the basis of data contained in a national voter registry that had been updated in late 2019. Specifically, benefits were initially disbursed to individuals who met three criteria: (1) ‘self-targeted’²⁰ by dialling in to the Novissi platform and entering basic information from their mobile phone; (2) registered to vote in specific regions (the programme initially focused on the Greater Lomé region around the capital city); and (3) self-declared to work in an informal occupation in their voter registration. The decision to target informal occupations helped prioritize benefits to people who were forced to stop working at the onset of the crisis. However, this approach does not necessarily target benefits to the poorest households in the country (Supplementary Fig. 2).

Our research efforts focused on helping the government expand the Novissi programme from informal workers in Greater Lomé to poorer individuals in rural regions of the country, and were designed to meet the government's two stated policy objectives: first, to direct benefits to the poorest geographic regions of the country; and second, to prioritize benefits to the poorest mobile subscribers in those regions. (Individuals without access to a mobile phone could not receive Novissi payments, which were delivered digitally using mobile money; see [Methods](#), 'Programme exclusions' for details.) The approach we developed, which uses machine learning to analyse non-traditional data from satellites and mobile phone networks, has two distinct steps (Extended Data Fig. 1).

Targeting with mobile phone data

In the first step, we obtained public micro-estimates of the relative wealth of every 2.4 km by 2.4 km region in Togo, which were constructed by applying machine-learning algorithms to high-resolution satellite imagery¹⁶. These estimates provide an indication of the relative wealth of all the households in each small grid cell; we take the population-weighted average of these grid cells to estimate the average wealth of every canton, Togo's smallest administrative unit (see [Methods](#), 'Poverty maps').

In the second step, we estimated the average daily consumption of each mobile phone subscriber by applying machine-learning algorithms to mobile phone metadata provided by Togo's two mobile phone operators (see [Methods](#), 'Data privacy concerns'). Specifically, we conducted surveys with a large and representative sample of mobile phone subscribers, used the surveys to measure the wealth and/or consumption of each subscriber, and then matched the survey-based estimates to detailed metadata on each subscriber's history of phone use. This sample was used to train supervised machine-learning algorithms that predict wealth and consumption from phone use^{17,18,19} (Pearson's ρ ranges from 0.41–0.46; [Methods](#), 'Predicting poverty from phone data'). This second step is similar in spirit to a traditional proxy means test (PMT), with two main differences: we used a high-dimensional vector of mobile phone features instead of a low-dimensional vector of assets to estimate wealth; and we used machine-learning algorithms designed to maximize out-of-sample predictive power instead of the traditional linear regression that maximizes in-sample goodness of fit³⁰.

Evaluation of targeting accuracy

Our main analysis evaluates the performance of this new targeting approach that combines machine learning and mobile phone data—which we refer to more succinctly as the phone-based approach—by comparing targeting errors using this

approach to targeting errors under three counterfactual approaches: a geographic targeting approach that the government piloted in summer 2020 (in which all individuals are eligible within the poorest prefectures (Togo's admin-2 level), or poorest cantons (Togo's admin-3 level); occupation-based targeting (including Novissi's original approach to targeting informal workers, as well as an 'optimal' approach to targeting the poorest occupation categories in the country); and a parsimonious method based on phone data without machine learning (that uses total expenditures on calling and texting as a proxy for wealth).

We present results that compare the effectiveness of these different targeting mechanisms in two different scenarios. First, we evaluate the actual policy scenario faced by the government of Togo in September of 2020, which involved distributing cash to 60,000 beneficiaries in Togo's 100 poorest cantons. This first scenario is evaluated using data collected in a large phone survey we designed for this purpose and conducted in September 2020. The 'ground truth' measure of poverty in this first scenario is a PMT, as consumption data could not be feasibly collected in the phone survey. The PMT is based on a stepwise regression procedure, described in Supplementary Methods, section 3, which captures roughly 48% of the variation in consumption. Thus, for the first scenario focused on the rural Novissi programme, all targeting methods are evaluated with respect to this PMT. The phone-based machine-learning model is similarly trained using the PMT as ground truth. Second, we simulate and evaluate a more general and hypothetical policy scenario in which the government is interested in targeting the poorest individuals nationwide; this scenario is evaluated using national household survey data collected in person by the government in 2018 and 2019. The second simulation uses consumption as the ground truth measure of poverty. These data are described in the Methods section 'Data sources' and details on the evaluation are in the Methods section 'Targeting evaluations.'

In the first scenario focused on reaching the poorest people in the 100 poorest cantons, we find that the phone-based approach to targeting substantially reduces errors of exclusion (true poor who are mistakenly deemed ineligible) and errors of inclusion (non-poor who are mistakenly deemed eligible) relative to the other feasible approaches to targeting available to the government of Togo (Fig. 1a and Table 1, columns 3 to 6). We focus on the ability of each targeting method to reach the poorest 29% in each of the two survey datasets, as the rural expansion of Novissi only had sufficient funding to provide benefits to 29% of individuals in eligible geographies (Extended Data Tables 1, 2 evaluate performance using alternative poverty thresholds). Using a PMT as a measure of 'true' poverty status, phone-based targeting (area under the curve (AUC) = 0.70) outperforms the other feasible methods of targeting rural Novissi aid (for example, AUC = 0.59–0.64 for geographic blanket targeting). As a result, errors of exclusion (defined as 1 – Recall) are lower for the phone-based approach (53%) than for feasible alternatives (59%–78%).

Fig. 1: Comparing Novissi targeting to alternatives.

 figure 1



a, b, The performance of phone-based targeting (green) compared with alternative approaches that were feasible (red) and unfeasible (blue) in Togo in 2020. Targeting is evaluated for the actual rural Novissi programme (**a**), which focused on Togo's 100 poorest cantons (using a 2020 survey representative of mobile subscribers in the 100 cantons, where PMT is a ground truth for poverty since consumption data was not collected in the phone survey); and a hypothetical nationwide anti-poverty programme (using a national field survey conducted in 2018–2019, where consumption is a ground truth for poverty) (**b**). The darker bar in each pair indicates recall and precision (left axis), which is equivalent to $1 - \text{exclusion error}$; the lighter bar in each pair indicates area under the curve (right axis). The bar height represents the point estimate

from the full simulation; whiskers show s.d. produced from $n = 1,000$ bootstrap simulations. The figure highlights a subset of the results contained in Table 1.

Table 1 Performance of targeting mechanisms

Similarly, phone-based targeting outperforms most feasible methods when we simulate the targeting of a hypothetical national anti-poverty programme (Fig. 1b and Table 1, columns 7 to 10). Here, the phone-based approach is more effective at prioritizing the poor ($AUC = 0.73$) than geography-based alternatives ($AUC = 0.66\text{--}0.68$), and similarly leads to lower exclusion errors (50%) than most feasible alternatives (52%–76%). One exception in this hypothetical programme is occupation-based targeting: whereas the Novissi programme’s original criteria of targeting informal workers would not scale well to a national programme (76% exclusion errors), an alternative ‘optimal’ occupation-based approach that we develop (Methods, ‘Experimental design’)—which assigns all transfers to the poorest occupational category (agricultural workers)—slightly outperforms phone-based targeting (48% exclusion errors).

Together, the results in Table 1 indicate that the phone-based targeting approach was more effective in the actual rural Novissi programme than it would be in a hypothetical nationwide programme. Our analysis suggests that the benefits of phone-based targeting are greatest when the population under consideration is more homogeneous, and when there is less variation in other factors (such as place of residence) that are used in more traditional approaches to targeting (Methods, ‘Targeting methods and counterfactuals’). For instance, when we restrict the simulation of the hypothetical national programme to households in rural areas, the gains from phone-based targeting increase (Supplementary Table 1).

We also find that the performance benefits of phone-based targeting increase as programmes seek to target the most extreme poor. This increase can be seen by comparing Table 1, where targeting performance is measured by how many of the poorest 29% receive benefits, to Extended Data Table 1, which measures whether households below the extreme poverty line (US\$1.43 per capita daily consumption) receive benefits, and Extended Data Table 2, which measures whether households below the poverty line (US\$1.90 per capita daily consumption) receive benefits. Although all targeting methods perform better at targeting the extreme poor, the differential between the phone-based approach and other methods is greater when the consumption threshold is lower. (In this analysis, the wealth distribution of the underlying population is important: as more than half of the Togolese population is below the poverty line, the targeting methods are attempting to differentiate between different gradations of poverty. Just as precision increases as the target population grows—that is, from Table 1 to Extended Data Table 1 to Extended Data Table 2—results may differ in contexts where the target population is much smaller.)

The phone-based approach that we develop relies heavily on machine learning to construct a poverty score for each mobile subscriber, where eligibility is a complex function of how the subscriber uses their phone (Extended Data Table 3). We also consider an alternative approach that does not use machine learning, but instead simply targets mobile phone subscribers with the lowest mobile phone expenditures over the preceding months (Methods, ‘Parsimonious phone expenditure method’). We find that this ‘phone expenditure’ method ($AUC = 0.57$ for rural Novissi and 0.63 in for the hypothetical national programme; Table 1) performs substantially worse than the machine-learning-based model ($AUC = 0.70$ for rural Novissi and 0.73 for the hypothetical national programme). Although the phone expenditure model requires much less data and may be easier to implement, this parsimony increases targeting errors, and may also introduce scope for strategic ‘gaming’ if used repeatedly over time.

An important factor in the success of the machine-learning model is the fact that it was trained on representative survey data collected immediately before the programme’s expansion. Since an individual’s poverty status can change over time, and since the best phone-based predictors of wealth may also change, a model trained in one year or season may not perform well if applied in a different year or season. In Togo, we find that when the machine-learning model or the mobile phone data are roughly 18 months out of date, predictive accuracy decreases by 4–6% and precision drops by 10–14% (Extended Data Table 4 and Methods, ‘Temporal stability of results’). These losses are nearly as large as the gains that phone-based targeting provides over geographic targeting—a finding that underscores the importance of training the model with current and representative data.

We also compare the phone-based approach to alternative targeting approaches that require a recent and comprehensive social registry. Although the Government of Togo did not have such a registry, this comparison helps situate this method relative to other methods commonly used by development researchers and policymakers. These results, shown in Table 1, can only be simulated using the national in-person survey, since the phone survey did not collect consumption data. The results are more ambiguous: the phone-based approach ($AUC = 0.70\text{--}0.73$) is approximately as accurate as targeting using an asset-based wealth index ($AUC = 0.55\text{--}0.75$), but less accurate than using a poverty probability index ($AUC = 0.81$) or a perfectly calibrated PMT ($AUC = 0.85$) (see Methods, ‘Survey data’ for the differences between these indices). We note, however, that the performance of the ‘perfectly calibrated’ PMT may substantially overestimate the performance of a real-world PMT, which declines steadily over time since calibration^{27,29} (Methods, ‘Targeting methods and counterfactuals’).

Social welfare and fairness

Improvements in targeting performance translate to an increase in social welfare. Using the constant relative risk aversion (CRRA) utility function, we calculate aggregate welfare under the phone-based approach and each of the counterfactual targeting approaches. Under the CRRA assumptions, individual utility is a concave function of consumption. By assuming a fixed budget—which we fix at a size analogous to that of the Novissi rural aid programme, which had a budget of US\$4 million to distribute among 154,238 programme registrants—and equal transfer sizes to all beneficiaries, we simulate the distribution of benefits among eligible individuals at counterfactual targeting thresholds to construct social welfare curves for each targeting method. This social welfare analysis also allows us to identify the optimal beneficiary share and corresponding transfer size. Fig. 2 shows the utility curves for each of the targeting methods simulated, separately for the two populations. Note that phone-based targeting, geographic blanketing and an asset-based wealth index all achieve approximately the same maximum utility in the hypothetical national programme, but phone-based targeting dominates in the rural Novissi programme. Also note that all targeting methods outperform a universal basic income scheme if the beneficiary share and transfer size is well-calibrated.

Fig. 2: Welfare analysis of different targeting mechanisms.

 **figure 2**

Aggregate social welfare is calculated (assuming CRRA utility) under counterfactual targeting approaches. We assume a fixed budget of US\$4 million and a population of 154,238, with an equal transfer size for all beneficiaries. Utility curves for feasible targeting mechanisms are shown in solid lines; infeasible targeting mechanisms are shown in dashed lines. The horizontal dotted line indicates total social welfare for a universal basic income programme that provides (very small) transfers to the entire population; vertical dotted lines indicate the targeting threshold and associated transfer size that maximizes social welfare for each targeting mechanism. **a**, **b**, Targeting is evaluated for the Novissi anti-poverty programme in Togo's 100 poorest cantons (**a**) and a hypothetical nationwide anti-poverty programme (**b**).

These utilitarian welfare gains suggest that society as a whole will benefit from improved targeting, but do not imply that all subgroups of the population will benefit equally. Indeed, there is growing concern that algorithmic decision making can unfairly discriminate against vulnerable groups^{31,32,33}. To address these concerns in the context of the Novissi programme, we audit the fairness of each targeting method across a set of potentially sensitive characteristics, while noting that notions of fairness and parity are contested and often in tension³⁴. Figure 3a shows, as an example, that the phone-based approach does not cause women to be systematically more likely to be incorrectly excluded by the targeting mechanism from receiving benefits than men (see also [Methods](#), ‘Fairness’). Similarly, the phone-based approach does not create significant exclusion errors for specific ethnic groups (Fig. 3b), religions, age groups or types of household, though there are small differences in targeting accuracy between groups (Extended Data Fig. 2). We also compare the fairness of the phone-based approach to several other targeting approaches by evaluating each method’s demographic parity—that is, the extent to which each method under- or over-targets specific demographic subgroups relative to that group’s true poverty rate (Fig. 3c,d, Extended Data Fig. 3). Overall, we find that none of the targeting methods analysed naively achieves perfect parity across subgroups; a phenomenon referred to as ‘no fairness through unawareness’³⁵. The largest parity differences occur with geographic targeting methods.

Fig. 3: Fairness of targeting for different demographic subgroups.

 [figure 3](#)

a, b, Distributions of differences between ranking according to predicted wealth from the phone-based approach and ranking according to true wealth (using the 2018–2019

field survey; $n = 4,171$), disaggregated by gender (**a**) and ethnicity (**b**). Boxes show the 25th and 75th percentiles, whiskers show the minimum and maximum, and the centre line shows the median of the distribution. Left-skewed bars indicate groups that are consistently under-ranked; right-skewed bars indicate groups that are consistently over-ranked. **c, d**, Evaluation of demographic parity across subgroups by comparing the proportion of a subgroup targeted under counterfactual approaches to the proportion of the subgroup that falls into the poorest 29% of the population (using the 2018–2019 field survey; $n = 4,171$), disaggregated by gender (**c**) and ethnicity (**d**). Bubbles show the percentage point difference between the proportion of the subgroup that is targeted and the proportion that is poor according to ground-truth data. Large red bubbles indicate groups that are over-targeted; large blue bubbles indicate groups that are under-targeted.

Exclusions and limitations

This novel approach to targeting requires careful consideration of the ways in which individuals can be incorrectly excluded from receiving programme benefits (Methods, ‘Programme exclusions’). Our analysis highlights six main sources of exclusion errors for the expansion of Novissi (Table 2): (1) beneficiaries must have a SIM card and access to a mobile phone (field survey data from 2018–2019 indicate that 65% of adults and 85% of households have a phone; see also Supplementary Fig. 3); (2) they must have used their SIM card recently, in order to generate a poverty score (between 72% and 97% of programme registrants); (3) they must be a registered voter (roughly 87% of adults); (4) they must self-target and attempt to register (roughly 40% of eligible individuals attempted); (5) they must succeed in registering, which requires basic reading and digital literacy (72% succeed); and (6) they must be successfully identified as eligible by the machine-learning algorithm (47% recall; Table 1). Many of these sources of possible exclusion overlap; Extended Data Table 5 thus estimates, on the basis of the 2020 phone survey, the extent to which each successive step in registration creates additional exclusions. These results highlight the fact that algorithmic targeting errors are an important source of programme exclusion, but that real-world programmes also face structural and environmental constraints to inclusion.

Table 2 Sources of exclusion from rural Novissi benefits

More broadly, our analysis shows how non-traditional big data and machine learning can improve the targeting of humanitarian assistance. Beyond the gains in targeting performance, a key advantage of this approach is that it can be deployed quickly and responsively. In Togo, the government’s objective was to deliver benefits to the poorest people in the country, so our efforts focused on training a machine-learning model to target the poor. In other settings, such as following natural disasters, the people most impacted by adverse events may not be the poorest³⁶. With high-

frequency phone data available in near real-time, related techniques might be used to more dynamically prioritize the people with the greatest need. For example, it may be possible to train a machine-learning algorithm to identify people whose consumption fell by the greatest amount, based on changes in patterns of phone use following a crisis. Another possibility would be to simply use location information from mobile phone data to prioritize people who are likely to live in impacted regions (Methods, ‘Location-based targeting’).

It is important to emphasize that our phone-based approach is far from perfect, and may lead to important errors of both exclusion and inclusion. There are also practical limitations to this approach, for instance regarding data access and privacy^{[37,38,39,40,41,42,43](#)}; several such considerations are addressed in Supplementary Discussion, section 2. Moreover, our results do not imply that mobile-phone-based targeting should replace traditional approaches reliant on proxy means tests or community-based targeting. Rather, these methods provide a rapid and cost-effective supplement that may be most useful in crisis settings or in contexts where traditional data sources are incomplete or out of date. We believe that future work should explore how real-time data sources, such as the phone data used by Novissi, can be best combined with more traditional field-based measurements, so that these complementary data sources can be best integrated in the design of inclusive systems for social protection^{[19](#)}.

Methods

The COVID-19 pandemic in Togo

Togo is a small country with a population of roughly 8 million in West Africa. More than 50% of the population lives below the international poverty line. Shortly after the first COVID-19 cases were confirmed in Togo in early March 2020, the government imposed economic lockdown orders to prevent the spread of the disease. These lockdowns forced many Togolese to stop working, raising concerns about the potential for rising food insecurity (Supplementary Fig. 1).

On April 8, 2020, the government launched the Novissi programme (Novissi means solidarity in the Ewé language). According to the Togolese minister C. Lawson, Novissi “was built and designed in order to help those people who are the most vulnerable population and the most impacted by the anti-COVID measures”^{[46](#)}. Novissi was initially designed to provide benefits to informal workers in Greater Lomé, the large metropolitan area surrounding the capital city where the lockdown orders were initially focused. The rationale for targeting informal workers was that they were more likely to be vulnerable and more likely to be affected by the lockdown orders.

To determine eligibility for Novissi, the government relied upon a national voter registry that was updated in late 2019, in which individuals indicated their home location and occupation. At the time, the voter registry contained 3,633,898 entries, which the electoral commission reports is equivalent to 87% of the total adult population (see Table 2 for details).

Receiving Novissi benefits required that individuals register by dialing in to the Novissi unstructured supplementary service data (USSD) platform from a mobile phone. Thus, registration initially required (1) a valid and unique voter ID linked to an eligible occupation from an eligible location; (2) a valid SIM card, and (3) access to a mobile phone. A smartphone was not required for registration; the USSD platform was accessible from a basic phone. Since phone sharing is common in Togo, multiple SIM cards could be registered through a single phone (so long as each SIM was then linked to a valid voter ID). See ‘Programme exclusions’ for a discussion of the extent to which voter and phone requirement may have led to programme exclusions.

Eligible female beneficiaries were then paid 12,250 FCFA (US\$22.50) per month; men received 10,500 FCFA (US\$20) per month. The payments were disbursed in two bi-weekly installments, for three months, using existing mobile money infrastructure managed by the country’s two mobile network operators. The system was designed to be 100% digital, so that registration, eligibility determination and payment could all be accomplished without face-to-face contact. Novissi was promoted actively through radio advertisements and community leaders, and 4.4 million registration attempts were reported on the day the programme launched. In this first phase of Novissi, which focused on Greater Lomé, roughly 510,000 beneficiaries received payments.

During the summer of 2020, in response to localized outbreaks of COVID-19, the government piloted an expansion of Novissi based on geographic targeting. In this geographically targeted expansion, all individuals registered to vote in the Soudou canton were made eligible for Novissi benefits. The geographic targeting was determined primarily by public health considerations, and not by poverty rates. In total, roughly 5,800 beneficiaries were paid through this geographically targeted programme.

Our analysis focuses on a second phase of Novissi, which was initiated after the Novissi programme in Greater Lomé had terminated. Specifically, in partnership with the non-governmental organization GiveDirectly, the government wished to expand Novissi eligibility to the rural poor. The policy mandate from the government was to (1) prioritize benefits to people living in Togo’s 100 poorest cantons (of the 397 cantons nationally), where the number 100 was selected by the government in order to balance the desire to focus on the poorest villages, without focusing excessively on specific regions; and (2) prioritize the poorest individuals in those 100 cantons.

During the second phase of Novissi, registration and enrolment used several of the same steps described above: individuals were required to have a voter ID registered in one of the 100 poorest cantons, and they had to self-register using a mobile phone with a unique SIM card. However, the individual's occupation was not used to determine eligibility; instead, the estimated wealth of the individual, based on the machine-learning methods described in this paper, was used to limit eligibility to the estimated poorest subscribers in those 100 cantons.

Data sources

Survey data

Our core analysis relies heavily on two surveys conducted by Togo's Institut National de la Statistique et des Études Economiques et Démographiques (INSEED). The first survey, which is nationally representative, was conducted in the field in 2018 and 2019 ($n = 6,171$). The second survey was conducted over the phone in September 2020, and is representative of mobile network subscribers inferred to be living in rural cantons eligible for Novissi aid ($n = 8,915$). We use these two different survey datasets because neither dataset is sufficient by itself for the analysis we require: the 2020 survey did not collect consumption data, which is important for evaluating certain counterfactuals; the 2018–19 survey is representative only at the prefecture level, and only surveyed a small number of households in the 100 poorest cantons that were eligible for Novissi. (We had planned to conduct a large in-person survey in early 2021 that would provide the single point of focus for this paper, but were forced to postpone the survey indefinitely owing to a resurgence in COVID-19.)

2018–2019 field survey

Our first survey dataset was obtained from a nationally representative household survey. Specifically, 540 enumeration areas (EAs) were drawn at random from Togo's approximately 6,000 EAs, with weight proportional to the size of the EA in the last national census (conducted in 2011). Twelve households were then drawn at random from each of the selected EAs to be interviewed, for a total of 6,172 households. Surveys, which lasted about 3 h, were conducted in two waves, with the first wave between October and December 2018 and the second wave between April and June 2019. We removed one observation that is missing consumption expenditure and asset data, leaving 6,171 observations. Interviews took place with the head of household when possible, and alternatively with the most knowledgeable adult present. Answers were recorded by enumerators on tablets using SurveyCTO software.

As part of the survey's recontact protocol, phone numbers were requested from a representative of each household; 4,618 households (75%) of households are matched

to a phone number. The data do not include an identifier for which member of the household the phone number belongs to. A total of 4,171 households have phone numbers that contain at least one transaction in our mobile phone transaction logs in the three months prior to their survey date (90% of households with phone numbers), leading to a matched survey–mobile phone dataset with $n = 4,171$. Note that this matched dataset is not nationally representative or necessarily representative of mobile phone subscribers, as there is selection in which households and household members provide phone numbers.

2020 phone survey

Our second survey dataset is obtained from a phone survey conducted over two weeks in September 2020. The survey lasted approximately 40 min, and covered demographics, asset ownership and well-being. Answers were recorded by enumerators on tablets using SurveyCTO software. Phone numbers for the 2020 phone survey were drawn from mobile phone transaction logs and the sample is representative of subscribers inferred based on their mobile phone data to be living in rural cantons eligible for Novissi aid (see Supplementary Methods, section 4). Note that because the sample is drawn based on inferred location, not all interviewees necessarily reside in an aid-eligible canton. The survey includes a question on canton of residence, and 68% of observations report living in a Novissi-eligible canton.

Of the phone numbers drawn, 35% responded, consented to the survey, and completed the entire survey. In total, after removing low-quality surveys and those missing poverty outcomes, the dataset contains 8,915 observations corresponding to individual subscribers. We reweight the survey for nonresponse using the same mobile phone features and machine-learning methods described in ‘Predicting poverty from phone data’. Our sample weights consist of the inverse of the draw probability and the inverse of the predicted probability of response. More details on the content of the 2020 phone survey, the sampling procedure, and the reweighting procedure are available in Supplementary Methods, section 5.

Construction of poverty outcomes

We construct four poverty outcomes from the survey data: consumption expenditure (captured in the 2018–2019 field survey only), an asset-based wealth index, a poverty probability index (PPI), and a PMT.

Consumption expenditure

The consumption expenditure outcome is only available in the dataset from the 2018–2019 field survey. Disaggregated expenditures for more than 200 food and non-food

items are elicited in each household interview. The consumption aggregate is then adjusted for a price index calculated at the prefecture level. The final outcome measure is per capita adult equivalent household consumption expenditure, which we transform to US\$ per day.

Asset index

We calculate a principal component analysis (PCA) asset index for households in the 2018–2019 field survey and for the households associated with individuals interviewed in the 2020 phone survey. Asset indices are constructed with a PCA. The asset index is constructed from 24 underlying binary asset variables in the 2018–2019 field survey and 10 underlying binary asset variables in the 2020 phone survey. The asset indices for the two surveys are constructed independently, from different sets of assets, and therefore do not share a basis vector. The basis vector for each index is shown in Supplementary Table 2. The asset index explains 31.50% of the variance in asset ownership in the 2018–2019 field survey, and 53.45% of the variance in asset ownership in the 2020 phone survey. However, the variance explained in the two indices should not be directly compared since there are far fewer assets recorded in the 2020 phone survey than in the 2018–2019 field survey. We also note that the asset index for the 2020 phone survey dataset is dominated by variation in ownership of three assets (toilet, radio and motorcycle; see Supplementary Table 2) and is therefore considerably less smooth than the asset index in the 2018–2019 phone survey dataset.

PPI

We use the scorecard for the current PPI used by Innovations for Poverty Action (<https://www.povertyindex.org/country/togo>). The index is calibrated based on a nationally representative survey conducted by INSEED in 2015 ($n = 2,335$). ‘Poverty probability’ is scored based on ten household questions, including region of residence, education of adults and children, asset ownership, and consumption of sugar. We calculate the PPI only for households in the 2018–2019 field survey, as the data necessary for all components were not collected in the 2020 phone survey.

PMT

Using the data from the 2018–2019 field survey, we follow a stepwise forward selection process to select the 12 asset and demographic variables that are jointly most predictive of per capita household consumption (see Supplementary Fig. 4, Supplementary Methods, section 3 for details). We use these variables to construct a consistent PMT for the 2018–2019 field survey and the 2020 phone survey. Following recent literature, we use a regularized linear model (Ridge regression) rather than a

simple linear regression to maximize out-of-sample accuracy^{30,33}. For the 2018–2019 field survey, PMT consumption estimates are produced out-of-sample over tenfold cross validation. For the 2020 phone survey, we train the Ridge regression on the entire 2018–2019 field survey sample and use the fitted model to produce PMT consumption estimates for each phone survey observation. Over tenfold cross validation, the PMT explains 48.35% of the variance in log-transformed consumption expenditure in the 2018–2019 field survey. This explanatory power is similar to that of other national-scale PMTs reported in Indonesia, Peru and Jamaica^{3,22,26} (41%–66%). The weights for the PMT are included in Supplementary Table 3. As they are trained to predict consumption, PMT consumption estimates can be interpreted as estimated US\$ per day.

Rural-specific PMT

We follow another stepwise forward selection process using the 2018–2019 field survey restricted to households in rural areas ($n = 3,895$) to create a PMT specific to rural areas with 12 components. The weights for the rural-specific PMT are shown in Supplementary Table 4. Over tenfold cross-validation the rural-specific PMT explains 17% of the variation in log-transformed consumption expenditure in the 2018–2019 field survey restricted to rural areas. We note that this explanatory power is substantially lower than that of other rural-specific PMTs evaluated in past work in Jamaica and Burkina Faso^{47,48} (36%–45%). We produce out-of-sample values for the rural-specific PMT over cross validation for the 2018–2019 field survey, and use the fitted model to produce values for the 2020 phone survey. We mean-impute the rural-specific PMT for observations that do not have all necessary components in the 2020 phone survey dataset ($n = 18$). The correlation between the rural-specific PMT and general PMT is 0.75 in the 2018–2019 survey dataset restricted to rural areas, and 0.76 in the 2020 phone survey dataset.

Construction of occupation categories

We use self-reported occupation (of the household head for the 2018–2019 field survey, and of the respondent for the 2020 phone survey) to categorize occupations and later simulate occupation-based targeting. We first classify each of the self-reported occupations according to the occupation categories in the Novissi registry. We identify which of these categories are informal (in the Novissi registry, more than 2,000 unique occupations are considered informal—some of the most common ones are vendors, hairdressers, taxi drivers, tailors, construction workers and the unemployed). We further classify occupations in 10 broad categories according to the Afrostat system (<https://www.afristat.org/nomenclatures/>). Supplementary Table 5 records these categories, along with the proportion in each category in each of the two surveys and associated average consumption.

Summary statistics

Supplementary Table 6 presents summary statistics on each of the two surveys; for the 2018–2019 household survey, results are presented separately for households who provide phone numbers (further broken down into those with phones numbers that match to the mobile phone metadata and those whose phone numbers do not match), and those without phone numbers. Note that since phone numbers for the 2018–2019 household survey were collected for a recontact protocol, a household without a phone number could represent a household without a phone or one that refused to be contacted for further surveys. We find that households providing phone numbers (average consumption = US\$2.56 per day) are less poor than households not providing them (average consumption = US\$1.75 per day); among those associated with a phone number, households that do not match to mobile phone metadata (average consumption = US\$2.21 per day) are poorer than those that do (average consumption = US\$2.59 per day). These patterns are consistent with related work in Afghanistan in which phone numbers were collected for the purpose of matching to mobile phone metadata. That study found that households with phones were wealthier than those without, and households associated with a matched phone number were wealthier than those that did not match¹⁹.

Comparing summary statistics from the 2020 phone survey and 2018–2019 household survey, respondents to the 2020 survey tend to be poorer (average PMT = 1.62 versus 2.10), younger (average age = 33 versus 44), and more predominantly male (23% women vs 28% women). These differences are not surprising given that the 2020 survey was conducted in rural areas whereas the 2018–2019 household survey was designed to be nationally representative.

Poverty maps

To simulate geographic targeting, we rely on poverty maps of Togo's prefectures (admin-2 level, 40 prefectures) and cantons (admin-3 level, 397 cantons). In the 2018–2019 field survey, the latitude and longitude of each household were recorded by enumerators as part of the interview, so we map each observation to a prefecture and canton using the geographic coordinates. For the 2020 phone survey, we ask each respondent to report their prefecture and canton of residence.

Prefecture poverty map

INSEED completed a survey-based poverty mapping exercise in 2017. Specifically, a PMT was calibrated on a small consumption sample survey conducted in 2015 ($N=2,335$). 26,902 households were then surveyed in the field over three weeks in 530 EAs, sampled to be representative at the prefecture level. The interview included

questions on demographics, education, asset ownership, and household characteristics that made up the PMT. The calibrated PMT was then used to infer the ‘consumption’ of each household, and observations were aggregated to estimate the percentage of the population living under the Togo-specific poverty line of US\$1.79 per day in each prefecture. Supplementary Fig. 5 shows the resulting poverty map. For validation, we evaluate the correlation between prefecture-level poverty rates from the poverty mapping exercise and average consumption in the 2018–2019 field survey. The Pearson correlation coefficient is -0.78 , and the Spearman correlation coefficient is -0.70 .

Canton poverty map

When COVID-19 first appeared in Togo in early 2020, it had been at least ten years since a household survey had been conducted in Togo that was representative at the canton level. Togo’s last census was conducted in 2011, but did not include information on income, consumption, or asset ownership. We therefore rely on recently-produced publicly available satellite-based estimates of poverty which use deep learning models trained on Demographic and Health Surveys (DHS) data from neighbouring countries to estimate the average relative wealth of each 2.4km tile in Togo¹⁶. We overlay the resulting tile-level wealth estimates with high-resolution estimates of population density inferred from satellite imagery⁴⁹ to obtain population-weighted average wealth estimates for each canton, shown in Supplementary Fig. 5. As noted in ref. 16, the relative wealth measures are estimated with uncertainty. Thus, for validation, we evaluate the canton-level correlation between average wealth from the satellite-based poverty map and average consumption in the 2018–2019 field survey (though note that the latter survey is not representative at the canton level). The Pearson correlation coefficient is 0.57, and the Spearman correlation coefficient is 0.52.

Mobile phone metadata

We obtain mobile phone metadata (call detail records (CDR)) from Togo’s two mobile network operators for certain time periods in 2018–2021. We focus on three slices of mobile network data: October–December 2018, April–June 2019 and March–September 2020. The three-month periods in 2018 and 2019 are matched to households interviewed in the first and second wave of the field survey, respectively. The seven-month period in 2020 is matched to outcomes for individuals interviewed in the phone survey in September 2020. Summary statistics on network activity in these periods are shown in Supplementary Fig. 6.

Our CDR data contain the following information. Calls: caller phone number, recipient phone number, date and time of call, duration of call, ID of the cell tower through

which the call is placed; SMS messages: sender phone number, recipient phone number, date and time of the message, ID of the antenna through which the message is sent; mobile data usage: phone number, date and time of transaction, amount of data consumed (upload and download combined); mobile money transactions: Sender phone number, recipient phone number (if peer-to-peer), date and time of the transaction, amount of transaction, and broad category of transaction type (cash in, cash out, peer-to-peer or bill pay).

October–December 2018 and April–June 2019 CDR

Between 1 October and 30 December 2018, there were a total of 4.84 million unique mobile network subscribers between the two mobile phone networks (where a subscriber is any phone number that places at least one call or SMS on a network). Between 1 April and 30 June 2019, there were a total of 4.89 million mobile network subscribers. We identify spammers on the network as any phone number that placed an average of over 100 calls or 100 SMS messages per day, and remove any transactions associated with these numbers from our dataset. We remove 232 spammers in the 2018 time period and 162 spammers in the 2019 time period. In the 2018–2019 CDR, we observe only calls, SMS messages, and mobile money transactions (we do not observe mobile data usage).

March–September 2020 CDR

For data between March 1 and September 30, 2020, we observe a total of 5.83 million mobile network subscribers (note that this subscriber population does not necessarily reflect a 19% increase in subscribers from 2018–2019, since the slice is seven months rather than three months and there is significant month-to-month churn in subscribers; during the 3-month period from July–September 2020 we observe 5.20 million unique subscribers, a 6% increase from the 2019 period). We identify spammers as described above, resulting in the removal of transactions associated with 107 spammers from the 2020 CDR dataset. In the 2020 CDR, we observe calls, SMS messages, mobile data usage, and mobile money transactions.

Featurization

For each subscriber observed on the network in each of the three time periods, we calculate a set of 857–1,042 ‘CDR features’ that describe aspects of the subscriber’s mobile phone behaviour. These include:

Call and SMS features. We use open-source library bandicoot⁵⁰ to produce around 700 features relating to the calls and SMS messages each subscriber places and receives. These range from general statistics (for example, number of calls or SMS messages, or

balance of incoming versus outgoing transactions), to social network characteristics (for example, number and diversity of contacts), to measures of mobility based on cell tower locations (for example, number of unique towers and radius of gyration).

Location features. Based on the locations of each of the cell towers in Togo, we calculate information about where each subscriber places their transactions. Specifically, we calculate the number and percentage of calls placed in each of Togo's 40 prefectures, and the number of unique antennas, cantons, prefectures, and regions that each subscriber visits.

International transaction features. Using country codes associated with phone numbers, we calculate the number of outgoing international transactions, separately for calls and SMS messages. We also calculate the total time spent on outgoing international calls.

Mobile money features. For each of four variables relating to transaction size—transaction amount, percent of balance, balance before transaction, and balance after transaction—we calculate the mean, median, minimum, and maximum, separately for incoming and outgoing mobile money transactions. We also calculate the total transaction count for each subscriber (separately for incoming and outgoing) and the total number of unique mobile money contacts (separately for incoming and outgoing). We perform these calculations for all transactions together, as well as separately by transaction type (cash in, cash out, peer-to-peer, bill payments and other transactions).

Mobile data features. We calculate the total, mean, median, minimum, and maximum mobile data transaction for each subscriber, as well as the standard deviation in transaction size. We also calculate the total number of mobile data transactions and the number of unique days on which data is consumed. Note that mobile data features are only calculated for the 2020 CDR period, as our 2018–2019 CDR does not include mobile data records.

Operator. In our feature dataset we include a dummy variable for which of the two mobile network operators each subscriber is associated with.

Matching survey and CDR datasets

Using phone numbers collected in surveys, we match survey observations to CDR features. As noted in ‘Survey data’, there are 4,618 households in the 2018–2019 field survey that provide a phone number, of which 4,171 match to CDR (90% of households with phone numbers, and 68% of households overall). We match households surveyed in the first survey wave to features generated in the October–December 2018 CDR period, and households surveyed in the second survey wave to features generated in the April–June 2019 CDR period. To build intuition on the

relationships between phone-related features and poverty, Supplementary Fig. 7 compares four CDR features for those above and below the poverty line in the 2018–2019 household survey. As the 2020 survey was sampled based on the CDR dataset, all 8,915 observations in the 2020 survey dataset are matched to CDR.

Data privacy concerns

The CDR data we obtained for each subscriber contain personally identifying information (PII) in the form of the subscriber’s phone number (it does not contain the individual’s name, address or other PII), as well as other potentially sensitive information such as data about the subscriber’s network and cell tower locations. To protect the confidentiality of these data, we pseudonymized the CDR prior to analysis by hash-encoding each phone number into a unique ID. The data are stored on secure university servers to which access is limited based on a data management plan approved by UC Berkeley’s Committee for the Protection of Human Subjects.

We obtained informed consent from all research subjects in the phone survey prior to matching CDR records to survey responses. However, there are still open concerns around the use of CDR by bad actors, particularly as even pseudonymized datasets can frequently be de-anonymized for a subset of observations^{37,51}. Active research on applying the guarantees of differential privacy to CDR datasets and associated machine-learning models holds promise for balancing the utility of CDR data with privacy concerns^{52,53}. For additional discussion of these considerations, see Supplementary Discussion, section 2.

Predicting poverty from phone data

Machine-learning methods

We follow the machine-learning methods described in prior work^{17,18,19} to train models that predict poverty from CDR features. Specifically, we train a gradient boosting regressor with Microsoft’s LightGBM for the two matched survey-CDR datasets separately. We tune hyperparameters for the model over threefold cross validation, with parameters chosen from the following grid:

Winsorization of features: { No winsorization, 1% limit}

Minimum data in leaf: { 10, 20, 50}

Number of leaves: { 5, 10, 20}

Number of estimators: { 20, 50, 100}

Learning rate: { 0.05, 0.075, 0.1}

We train and evaluate the model over fivefold cross validation, with hyperparameters tuned independently on each fold, to obtain out-of-sample estimates of accuracy and out-of-sample predictions of poverty for each observation in our matched survey datasets. We then re-train the model on all survey data (for each of the two datasets separately), record feature importances (the total number of times a feature is split on over the entire forest), and use the final model to generate wealth predictions for every subscriber on the mobile phone network during the relevant time period.

We experiment with training models in this way for each of the relevant poverty outcomes: consumption expenditure, PMT, and asset index for the 2018–2019 field survey dataset and PMT and asset index for the 2020 phone survey dataset.

Evaluations of model accuracy are found in Extended Data Table 6. The correlation between the phone-based poverty predictions and a traditional PMT is 0.41, as trained and evaluated on the 2020 phone survey dataset (Extended Data Table 6, panel c). When trained and evaluated using the national 2018–2019 household survey with consumption data, the correlation between the phone-based poverty predictions and consumption is 0.46 (Extended Data Table 6, panel a).

Feature importances

Feature importances for each model are presented in Extended Data Table 3. We note that in examining the feature importances, location-related features (number and percent of calls placed in each prefecture of the country) are very important. The correlation between phone-based poverty predictions using only these location features and a standard PMT is 0.35 when trained and evaluated with the 2020 phone survey (versus 0.41 using all features). When trained and evaluated with the 2018–2019 field survey, the correlation between location-only phone-based poverty predictions and consumption is 0.42 (versus 0.46 when using all features). Given the relative importance of location features, we provide more in-depth analysis of the role of geography in phone-based targeting approaches in ‘Location-based targeting’. Other important features in the full phone-based poverty scores relate to nighttime calling behaviour, mobile data usage and mobile money usage.

Aggregate validation of CDR-based poverty estimates

Our machine-learning models use cross-validation to help limit the potential that the predictions are overfit to the specific surveys on which they are trained (and on which they are later evaluated in the targeting simulations). To provide a more independent test of the validity of the CDR-based estimates, we compare regional aggregates of wealth based on the CDR model to regional estimates of wealth based on household

survey data. In this exercise, we predict the consumption of roughly 5 million subscribers in Togo using the machine-learning model trained to predict consumption using the 2018–2019 national household survey, then calculate the average consumption of each prefecture and canton (where each subscribers' home location is inferred from CDR using standard methods described in Supplementary Methods, section 4).

Results, shown in Supplementary Fig. 8, indicate that the CDR-based estimates of regional poverty correlate with survey-based estimates of regional poverty. At the prefecture level, the Pearson and Spearman correlations of CDR-based consumption with survey-based consumption are 0.92 and 0.83, respectively; the correlations with the proportion of each prefecture living in poverty are −0.76 and −0.74. At the canton level, comparing the CDR-based estimates to the satellite-inferred canton poverty map from Supplementary Fig. 5, we find Pearson correlation = 0.84 and Spearman correlation = 0.68; compared to the average canton consumption in the 2018–19 field survey, Pearson correlation = 0.57 and Spearman correlation = 0.59. These correlations are toward the lower end of the range of correlations observed in prior efforts to estimate regional poverty with CDR^{14,15,17}.

Parsimonious phone expenditure method

In addition to the machine-learning method for wealth prediction described above, we are interested in the performance of an intuitive, parsimonious method for approximating poverty with CDR. We focus on a measure of ‘phone expenditure’ on the basis of costs of all calls placed and SMS messages sent by each subscriber. We apply standard rates for calls and SMS messages in Togo: 30 CFA (US\$0.06) to send an SMS message and 50 CFA (US\$0.09) per minute of call time. (These prices represent a typical Togolese phone plan, though there is considerable diversity in special promotions and friends-and-family plans available from Togo’s two mobile phone operators, Moov and Togocom.) We use these prices to infer the (approximate) amount spent by each subscriber from their outgoing mobile phone transaction logs. We find that the phone expenditures method is substantially less accurate than the machine-learning-based method, with a correlation of 0.13 with both the 2020 phone survey PMT and the 2018–2019 household survey’s consumption measure (Extended Data Table 6a, c).

Targeting evaluations

Experimental design

We simulate phone-based and counterfactual targeting methods for reaching the poorest individuals in Togo, using the two survey datasets described in ‘Survey Data.’

Specifically, for each dataset, we simulate providing benefits to the poorest 29% of observations in the dataset based on a suite of counterfactual targeting options (with sample weights applied), and compare the population targeted to the population that is ‘truly poor’, where ground truth poverty is determined using two different measurements. With the 2018–2019 in-person survey dataset, our main ground-truth wealth measure is based on consumption expenditure: we evaluate how well proxy measures of poverty reach those with the lowest consumption. For the 2020 phone survey dataset, our main ground-truth wealth measure is based on the PMT described in the section ‘Survey data’ (this is necessary because consumption information was not collected in the phone survey).

Our main targeting evaluations simulate targeting 29% of individuals because the Novissi programme had sufficient funds to target 29% of registrants in eligible cantons. The 29th percentile corresponds to a consumption threshold of US\$1.17 per day in the 2018–2019 field survey dataset, and a PMT threshold of US\$1.18 per day in the 2020 phone survey dataset. Our analysis shows how accurately each targeting method reaches the 29% truly poorest (Table 1), those below the extreme poverty line, defined as three-quarters of the poverty line, or US\$1.43 per day (Extended Data Table 1), and those below the international poverty line of US\$1.90 per day (Extended Data Table 2).

Our evaluations are designed to measure how effectively several different targeting methods, described below, are at reaching the poorest individual mobile phone owners in each of the two survey populations. We focus on individuals rather than households because the Novissi programme was designed and paid as an individual benefit. While social assistance programmes in other countries typically consider the household to be the unit of analysis that determines programme eligibility, there is no notion of a household unit in the Novissi programme (in part because the government does not possess data that links individuals to households). See Supplementary Discussion section 2 for additional discussion of the implications of individual versus household-level analysis.

Likewise, our focus on mobile phone owners reflects the fact that the Novissi system in Togo distributed payments via mobile money; as such, anyone without access to a phone could not receive benefits irrespective of the targeting method—see ‘Programme exclusions’ for a discussion of exclusion errors resulting from this constraint. In practice, this constraint only affects the analysis using the 2018–2019 in-person survey, where 4,171 of 6,171 respondents provided an active phone number. For analysis using the 2020 phone survey, we include all respondents, as every respondent had access to a phone. Future work could compare phone-based targeting to counterfactual targeting methods that could be implemented in-person, and thus account for exclusion errors resulting from phone ownership.

Targeting methods and counterfactuals

Our evaluations use the two survey datasets to measure the performance of three targeting methods that were feasible when implementing the Novissi programme: geographic blanketing (targeting everyone in certain geographies), occupation-based targeting (targeting everyone in certain occupation categories), and phone-based targeting. The location of subscribers targeted by each of these methods, in both the rural Novissi programme and the hypothetical national programme, are shown in Supplementary Fig. 9. Note that in the 2020 phone survey the unit of observation is the individual, while in the 2018–2019 field survey the unit of observation is the household: in practice, this means that our simulations with the 2018–2019 field survey dataset reflect a programme that would provide benefits only to heads of household, and we do not account for household size in considering exclusion errors or social welfare. Future work could model phone-based targeting on a household basis by collecting phone numbers for all household members and calculating aggregate benefits assigned to each household; given survey data limitations we cannot perform this analysis.

With geographic targeting, the primary counterfactual approach considered by the government of Togo in implementing its rural assistance programme, we assume that the programme would target geographic units in order from poorest to wealthiest, and that all individuals in targeted units would be eligible for benefits. We report results from two different approaches to geographic targeting: (1) a programme that targets the poorest prefectures (admin-2 region), defined as those prefectures with the lowest average predicted consumption based on a 2017 INSEED survey PMT; and (2) a programme that targets the poorest cantons (admin-3 region), defined as those cantons with the lowest average wealth based on high-resolution micro-estimates of wealth inferred from satellite imagery. When targeting the n poorest geographic regions would result in more than 29% of individual receiving benefits, then $n - 1$ regions are targeted fully, and individuals from the n th poorest region are selected randomly until the 29% threshold is reached. See Supplementary Fig. 5 and ‘Poverty maps’ for the poverty maps used for geographic targeting. (While this purely geographic approach was considered carefully by the Government of Togo, it is less common in non-emergency settings, when other data can inform targeting decisions. For instance, it is common to combine some degree of geographic targeting with community-based targeting and/or proxy means tests.)

In occupation-based targeting, we first evaluate the effectiveness of targeting informal workers, which is the eligibility criteria used by Novissi when it was first launched in April 2020, and which served as the basis for paying roughly 500,000 urban residents. In practice, this process involves categorizing the occupation of every individual respondent in both surveys as either formal or informal (including unemployed),

applying the same definition of informality that was used by the Novissi programme. In the simulations, informal workers are targeted first (in random order if there are more informal workers than can receive benefits) and formal workers are targeted last (also in random order, if the available benefits exceed the number of informal workers).

We also develop and test a hypothetical occupation-based approach, which we refer to as ‘optimal occupation-based targeting’, which assumes that the policymaker had high-quality consumption data on the consumption of workers in each occupation and used that information to target the poorest occupations first. Although this approach was not considered in Togo’s pandemic response, it was feasible with the data sources available in Togo at the time, and represents an upper-bound on the performance of a hypothetical occupation-based targeting system. We simulate this optimal occupation-based approach by calculating the average consumption of each occupation in the 2018–2019 field survey; occupations are then targeted in order of increasing average consumption. The average consumption of each occupation category is shown in Supplementary Table 5. Note that because agricultural workers are the poorest category and make up 29% of the observations in the 2018–2019 field survey dataset and 41% of the observations in the 2020 phone survey dataset, in practice the precision and recall metrics reported in our targeting simulations reflect systems of occupation-based targeting that would prioritize agricultural workers only.

Of primary interest in the targeting evaluation is the performance of the targeting approaches based on mobile phone data. The phone-based (machine-learning) approach is the one described in the main text, which uses machine learning to construct a poverty score from rich data on mobile phone use and prioritizes the individuals with the lowest poverty scores (‘Machine-learning methods’). For reference, we also calculate the performance of a more parsimonious ‘phone (expenditures)’ model, which prioritizes the individuals with the smallest total phone expenditures (‘Parsimonious phone expenditure method’).

For completeness, our simulations also include results from targeting methods that were not feasible for the Novissi programme, as the data required to implement those methods were not available when Novissi was launched (though Togo plans to create a foundational unique ID system and comprehensive social registry in 2022)⁵⁴. In particular, we simulate targeting using an asset-based wealth index, constructed as described in ‘Survey data.’ For the hypothetical national simulations using the 2018–2019 field survey dataset, we also simulate targeting using a PPI and PMT. Finally, when simulating targeting the hypothetical national programme restricted to rural areas (Supplementary Table 1), we also simulate targeting on a rural-specific PMT (see Differences in rural and national evaluations’). We cannot simulate PPI or PMT-based targeting using the 2020 phone survey since the necessary data were not collected.

An important caveat is that the PMT that we use in the 2018–2019 survey is ‘perfectly calibrated’ in the sense that it is both trained and evaluated on the same sample. In real-world settings, the predictive accuracy of a PMT declines as the time increases between the time of calibration and the time of application^{27,29}. As such, the performance of the PMT we report is likely an upper bound of the performance of a real-world PMT.

For the PMT in the 2018–2019 field survey dataset, as well as for CDR-based wealth estimates in both datasets, predictions are produced out-of-sample over cross validation so that they can be fairly evaluated in targeting simulations. Specifically, in each case, the training dataset is divided into ten cross validation folds; the machine-learning model is trained on nine of the ten folds and used to produce predictions for the final fold. The training-and-prediction regime is repeated for all ten folds.

Measures of targeting quality

For each targeting method, we calculate two ‘threshold-agnostic’ metrics of targeting accuracy—metrics that capture relationships between continuous measures of poverty rather than focusing on accuracy for targeting a specific portion of the population. These are:

Spearman correlation coefficient

Spearman’s rank correlation coefficient is the Pearson correlation between the rank values of the true and proxy measures of poverty. We focus on the Spearman correlation rather than standard Pearson correlation as a measure of targeting quality because targeting concerns itself only with the ordering of observations according to poverty. Spearman’s correlation coefficient is calculated as follows:

$$\rho = 1 - \frac{6 \sum_{i=1}^N ((r_i - \hat{r}_i)^2)}{N(N-1)}$$

where N is the total number of observations, r_i is the rank of observation i according to the ground truth poverty measure, and \hat{r}_i is the rank of observation i according to the proxy poverty measure.

ROC curves and area under the curve

Following ref. 3, we trace receiver operator characteristic (ROC) curves that describe the quality of a targeting method at counterfactual targeting thresholds (Extended Data Fig. 4, left figures). At each counterfactual targeting threshold T we simulate targeting $T\%$ of observations according to the proxy poverty measure in question and calculate

the true positive rate (TPR) and false positive rate (FPR) of the classifier with respect to reaching the $T\%$ poorest according to the ground-truth poverty measure. By varying T from 0% to 100%, we construct the ROC curves shown in Extended Data Fig. 4. The area under the curve (AUC) is used to summarize the targeting quality, with a random targeting method achieving an AUC of 0.5 and perfect targeting an AUC of 1. For convenience, we also include ‘coverage vs recall’ figures (right figures of Extended Data Fig. 4) that show how programme recall varies as the eligible percentage of the population increases. Note that since recall is another name for the true positive rate, Extended Data Fig. 4b,d represent a rescaling of the ROC curves in Extended Data Fig. 4a,c.

Targeting accuracy

Our analysis focuses on analysing the performance of a quota-based approach that ranks individuals from predicted poorest to predicted wealthiest, then targets the poorest 29% of individuals. We use the quota of 29% since the rural Novissi programme had sufficient funding to provide benefits to the poorest 29% of registrants in eligible cantons. (This quota-based approach is not the only way that poverty scores could be used in targeting, though it is the only approach that we evaluate: for instance, a threshold-based approach might target everyone below a threshold poverty score; alternative approaches might provide cash transfers of different sizes depending on the poverty score of the beneficiary⁴.) The 29th percentile corresponds to a consumption threshold of US\$1.17 per day in the 2018–2019 field survey dataset, and a PMT threshold of US\$1.18 per day in the 2020 phone survey dataset. We calculate the following metrics to describe how accurately targeting the poorest 29% according to each targeting method reaches (1) the 29% truly poorest, (2) those below the international poverty line of US\$1.90 per day (57% of observations in the 2018–2019 field survey, and 76% of observations in the 2020 phone survey), and (3) those below the extreme poverty line, which was defined as three-quarters of the poverty line, or US\$1.43 per day (41% of observations in the 2018–2019 field survey, and 53% of observations in the 2020 phone survey):

- Accuracy: Classification accuracy measures the proportion of observations that are identified correctly (targeted observations that are poor according to the ground-truth poverty measure, and non-targeted observations that are not poor according to the ground-truth wealth measure).

$$\{\{\backslash rm\{ Accuracy\}\}=\backslash frac\{ \{\backslash rm\{ TP\}\}+\{\backslash rm\{ TN\}\} \}{\{\{\backslash rm\{ TP\}\}+\{\backslash rm\{ FP\}\} + \{\backslash rm\{ TN\}\}+\{\backslash rm\{ FN\}\}\}}\}.$$
- Recall: Recall measures the proportion of all poor observations that are reached by a given targeting method.

$$\{\{\backslash rm\{ Recall\}\}=\backslash frac\{ \{\backslash rm\{ TP\}\}\}{\{\{\backslash rm\{ TP\}\} + \{\backslash rm\{ FN\}\}\}}\}.$$
 Recall is closely related to the concept of exclusion errors (that is,

the fraction of true poor who do not receive benefits, $\frac{\text{FN}}{\text{TP} + \text{FN}}$, since $\text{Recall} = 1 - \text{Exclusion error}$.

- Precision: Precision measures the proportion of targeted observations that are poor according to the ground-truth poverty measure. $\frac{\text{Precision}}{\text{Precision}} = \frac{\text{TP}}{\text{TP} + \text{FP}}$. Precision is closely related to the concept of inclusion errors (that is, the fraction beneficiaries who are non-poor, $\frac{\text{FP}}{\text{TP} + \text{FP}}$), since $\text{Precision} = 1 - \text{Inclusion error}$.
- Exclusion error: The proportion of true poor excluded from benefits. Defined as $\frac{\text{FN}}{\text{TP} + \text{FN}}$.
- Inclusion error: The proportion of beneficiaries who are not poor, that is, $\frac{\text{FP}}{\text{TP} + \text{FP}}$.

Note that the poverty lines are applied to consumption expenditure in the 2018–2019 field survey dataset, and to the PMT estimates in the 2020 phone survey dataset.

Differences in rural and national evaluations

The results in Table 1 indicate that the phone-based targeting approach—as well as the counterfactual targeting approaches—was more effective in the actual rural Novissi programme (columns 3 to 6 of Table 1) than it would have been in a hypothetical nationwide programme (columns 7 to 10 of Table 1). There are several factors that may account for these differences. Some of these factors are difficult for us to test empirically, for instance the fact that the surveys were conducted at different points in time, used different teams of enumerators, and different data collection modalities (phone versus in person). We investigate two factors that we can explore empirically: the geographic concentration of each survey and the ground truth measure of poverty (consumption versus PMT). We additionally explore whether targeting results are sensitive to the use of a nationwide PMT versus a rural-specific PMT.

Geographic concentration

Whereas the rural Novissi evaluation focuses on Togo’s 100 poorest cantons, the hypothetical national programme is evaluated nationwide (397 cantons). We therefore present results in Supplementary Table 1 that restrict the simulation of the hypothetical national programme to the 2,306 households in rural areas (out of 4,171 total). Comparing the results in Supplementary Table 1 to the last four columns of Table 1, we find that the performance of all methods drops, as would be expected when the

beneficiary population is more homogeneous. The relative difficulty of estimating poverty among rural populations is also evident in Extended Data Table 6: the CDR-based method's performance at predicting both consumption and the PMT is lower when the analysis of the 2018–2019 survey is restricted to the rural population (panel A vs panel B). Importantly, we also observe that the relative performance of phone-based targeting increases: whereas the CDR-based method performed worse than the asset index and only slightly better than canton-based targeting in the full nationwide evaluation (last four columns of Table 1), the CDR-based method is on par with the asset index and substantially better than canton-based targeting when the nationwide survey is limited to rural areas (Supplementary Table 1).

Consumption versus PMT

Whereas the national evaluation uses a measure of consumption as ground truth, the rural Novissi evaluation uses a PMT as ground truth. Supplementary Table 7 therefore simulates the hypothetical national programme using a PMT as ground truth.

Comparing the results in Supplementary Table 7 to the last four columns in Table 1, we find that using a PMT rather than consumption as ground truth increases targeting accuracy across all of the targeting methods. However, switching from consumption to the PMT does not substantially improve the performance of the phone-based method relative to the counterfactual approaches. This latter finding suggests that the use of the PMT is likely not a major source of the difference between the relative performance of the CDR-based method in the rural Novissi programme (columns 3 to 6 of Table 1) and the hypothetical nationwide programme (columns 7 to 10 of Table 1).

National PMT versus rural PMT

As the best predictors of welfare differ for rural and urban populations, we explore whether targeting results change when the PMT is calibrated using a rural rather than national population. Specifically, we construct a rural-specific PMT using the same methodology described in ‘Survey data’, but restricting the training data to observations in the 2018–2019 field survey that are in rural areas. This rural PMT explains 17% of the variation in log-transformed consumption in rural areas, and is highly correlated (Pearson correlation = 0.75) with the general PMT. We then produce rural PMT estimates for respondents to the 2020 phone survey, and retrain the phone-based poverty prediction model to predict the rural-specific PMT in that population. Supplementary Table 8 then presents results from simulating with the rural PMT as ground truth. Comparing Supplementary Table 8 to columns 3 to 6 of Table 1, we observe a noticeable improvement in the performance of the asset index, but other results are largely unchanged.

Relatedly, Extended Data Table 3 shows the feature importances for different phone-based prediction models. Panels A and B show the top-10 features for the main models presented in Table 1, that is, for predicting a PMT in the 2020 rural phone survey, and predicting consumption in the 2018–19 nationwide household survey. Panels C and D show the top-10 features for predicting a PMT in the 2018–19 survey, and predicting a PMT in the 2018–2019 household survey, restricted to rural areas. The feature importances for the two national-scale models are similar, suggesting the role of the ground truth poverty measure may not be as important as the role of geography in creating the poverty prediction models. The feature importances for the two rural-focused models are less similar, which may be due to the fact that the 2020 phone survey is concentrated in the 100 poorest cantons, while in panel D we restrict to rural areas, but these rural areas still cover the entire country.

Taken together, the results in this subsection suggest that the benefits of phone-based targeting are likely to be greatest when the population under consideration is more homogeneous, and when there is less variation in other factors (such as place of residence) that are used in more traditional approaches to targeting.

Location-based targeting

Several results emphasize the importance of geographic information in effective targeting. In particular, we observe that basic geographic targeting performs nearly as well as phone-based targeting in specific simulations—in particular, in simulations of a nationwide programme that can afford to target a large proportion of the total population (for example, Extended Data Table 2). We also found that location-related features from the CDR are important in the phone-based prediction model ('Machine-learning methods').

For these reasons, Supplementary Table 9 explores the extent to which targeting could be based on a CDR–location model that only uses the CDR to infer an individual's home location (see Supplementary Methods section 4). As with the phone (expenditures) model, the CDR-location model may be attractive to implementers since the data and technical requirements are reduced⁵⁵. In Supplementary Table 9, we observe that geographic targeting using phone-inferred home location is of slightly lower quality than geographic targeting using survey-recorded home location, and substantially worse than targeting using the machine-learning approach.

We also investigate the correlation between different sources of information on an individual's location. Supplementary Table 10 compares three different methods for identifying an individual's location, using roughly 4,500 respondents to the 2020 phone survey. At the prefecture (admin-2) level, most people (90%) self-declare living in the same canton in which they are registered to vote; there is also strong overlap

between the individual's CDR-inferred location and self-declared location (70%). The accuracy is substantially lower at the canton level, which is likely due to error in the CDR-inference algorithm when spatial units are small, as well as to confusion among respondents as to which canton they live in (for example, most respondents were confident in naming their village, but did not always know their canton).

Supplementary Table 11 presents additional analysis to compare the mobile phone activity of each subscriber with their home location, as recorded in the survey and as inferred from their CDR. We find that 62–85% of the average subscriber's activity occurs in their home prefecture, and that all of the modal subscriber's activity occurs in their home prefecture. These results are consistent with the importance of location-related features in the prediction algorithm (and the relatively low mobility of the rural Togolese population).

This analysis may also provide some context for the difference in the accuracy of the geographic targeting methods between the rural evaluation and the national evaluation in Table 1. While canton-based targeting performs better in the national evaluation, which is consistent with past work showing that finer-resolution geographic targeting is preferred to lower-resolution geographic targeting^{21,56}, prefecture-based targeting counter-intuitively performs better in the rural evaluation. We suspect this discrepancy is caused by three main factors. First, we expect that the estimates of average canton wealth are likely to be noisier than the estimates of average prefecture wealth, because the prefecture estimates aggregate over a larger population and the canton estimates rely on satellite-based inferences. Second, in the rural evaluation the prefecture is an important component of the PMT that is used as the ground truth measure of poverty (see Supplementary Table 3), so prefecture targeting relies on information that is structurally incorporated into the ground truth outcome (unlike in the national evaluation, where the ground truth outcome is consumption). The results in Supplementary Table 7 are consistent with this second hypothesis: the gap between prefecture and canton targeting in the national evaluation in Table 1 is smaller when switching the ground-truth poverty outcome from consumption to the PMT. Third, locations in the rural phone survey were self-reported, whereas locations were recorded on GPS devices by enumerators in the national survey; as noted, many respondents expressed confusion about their home canton. (The results in Supplementary Table 9, however, are not consistent with this third hypothesis: they indicate that targeting on canton inferred from mobile phone data is weaker than targeting on prefecture inferred from mobile phone data, suggesting that a difference in response quality between prefecture and canton in the survey is not a major factor in the difference in outcomes in the targeting simulations.)

Temporal stability of results

When simulating the performance of phone-based targeting, our main analysis uses each survey dataset to both train the machine-learning model and, via cross-validation, to evaluate its performance. These measures of targeting performance thus indicate what should be expected when training data (that is, the ground truth measures of poverty and the matched CDR) are collected immediately prior to a programme's deployment. This best-case scenario is what occurred in Togo in 2020: the phone survey was completed in October 2020 and Novissi was expanded beginning in November 2020. In other settings, however, it may not be possible to conduct a survey before launching a new programme; it may likewise not be possible to access up-to-date mobile phone data.

To provide an indication of how long phone-based models and predictions remain accurate, Extended Data Table 4 compares (1) the best-case scenario to alternative regimes where (2) the training data are old but the CDR are current, and (3) the training data are old and the CDR are also old. In these simulations, the 'old' data are from the 2018–2019 national household survey and corresponding 2019 phone dataset; the 'current' data are the subset of 2020 phone survey respondents for whom CDR are available in 2019 and 2020 ($N = 7,064$). In all simulations, the 2020 PMT is used as the ground truth measure of poverty. Predictions for (1) are generated over tenfold cross validation; predictions for (2) and (3) are out-of-sample with respect to the training data, since the models are trained on the 2018–2019 field survey. (An additional issue with (3) is turnover on the mobile phone network: 1,851 (21%) of phone numbers collected in the 2020 survey were not on the mobile phone network in 2019, and therefore cannot be associated with a wealth prediction in (3). See also Supplementary Fig. 6 for detailed information on rates of turnover on the mobile phone network.)

The results in Extended Data Table 4 indicate that predictive performance decreases when the model is out of date, and decreases even further when the CDR are out of date. This is to be expected, since roughly two years elapsed between the old and current periods: in addition to changes in how people use their phones (which would disrupt the accuracy of the predictive model), the actual economic status of some individuals may have changed—for instance, owing to the COVID-19 pandemic. There are also other important differences between the 2018–19 national household survey and the 2020 phone survey that could affect the extent to which a model trained on the former could accurately predict outcomes in the latter (such as the mode of data collection, the geographic concentration of the sample, and so forth; see 'Differences in rural and national evaluations').

For the main simulations focused on reaching the poorest 29%, Extended Data Table 4 suggests that accuracy decreases by 3–4 percentage points (4–6%) and precision decreases by 5–7 percentage points (10–14%) when out of date models and CDR are used for targeting. These losses are nearly as large as the gains of phone-based

targeting over geographic targeting observed in Table 1, which emphasizes the importance of having current and representative training data for real-world deployment of phone-based targeting. However, in absolute levels, the phone-based predictions remain reasonably accurate despite the two-year gap between the training and test environments (that is, the Spearman correlation (ρ) with ground truth is 0.35–0.36.

Social welfare

Using the two matched survey-CDR datasets, we calculate aggregate utility under each of the targeting methods using a social welfare function. Following ref. 3 we rely on CRRA utility, which models individual utility as a function of pre-transfer consumption and transfer size:

$$\$U=\frac{1}{N} \sum_{i=0}^N ((y_i + b_i)^{1-\rho})^{1/\rho}$$

Where N is the population size, y_i is the consumption of individual i , and b_i are the benefits assigned to the individual. Following ref. 3, we use a coefficient of relative risk-aversion $(\rho = 3)$. To reflect the policy design of the Novissi programme, we assume that all beneficiaries who receive a benefit receive the same value $b_i = b$. (In principle, the benefit b_i paid to i could depend on characteristics of i , such as i 's level of poverty. Although such an approach would substantially increase total welfare, in practice it is much more difficult to implement). To construct the social welfare curves, we:

- Calculate a total budget available for each of the two datasets. We focus on programmes that have a budget size analogous to that of rural Novissi, which aimed to distributed approximately US\$4 million among the 154,238 programme registrants, or US\$25.93 per registrant. We therefore assign each dataset a total budget of US\$25.93 N , where N is the total size of the dataset.
- Simulate targeting $T\%$ of observations on the basis of each of our counterfactual targeting approaches.
- Assign equal benefits to each of the targeted observations, with the budget divided evenly among targeted observations (so lower targeting thresholds T correspond to more benefits for targeted individuals).
- Calculate aggregate utility by summing over benefits and consumption for each individual with the CRRA utility function. Note that non-targeted individuals are included in the welfare calculation; they are merely assigned 0 benefits. For the

2018–2019 field survey dataset we use consumption expenditure for y_i ; for the 2020 phone survey dataset we use the PMT estimates.

- By varying T between 0% and 100% of observations targeted, we trace out the social welfare curves shown in Fig. 2.

Fairness

We are interested in auditing our targeting methods for fairness across sensitive subgroups. Note that that notions of parity and fairness are debated in machine learning and policy communities: ref. 57 describes how the three most popular parity criteria—demographic parity (benefits assigned to subgroups proportionally to their size), threshold parity (use of the same classification threshold for all subgroups), and error rate parity (equal classification error across subgroups)—are in tension with one another. Moreover, ref. 33 describe how tensions over parity criteria, prioritized subgroups, and positive discrimination lead to complicated prioritization compromises in the administration of targeted social protection programmes.

Here we focus on two targeting-specific parity criteria:

Demographic parity. A targeting method satisfying demographic parity will assign benefits to a subgroup proportionally to the subgroup’s presence in the population of interest. We evaluate demographic parity among the poor: that is, we compare the proportion of each subgroup living in poverty (below the 29th percentile in terms of consumption) to the proportion of each subgroup that is targeted (below the 29th percentile in terms of the proxy poverty measure used for targeting).

$$\$ \$ \{ \text{\rm DP} \} = \frac{ \{ \text{\rm TruePositives} \} + \{ \text{\rm FalsePositives} \} }{ \{ \text{\rm N} \} } - \frac{ \{ \text{\rm TruePositives} \} + \{ \text{\rm FalseNegatives} \} }{ \{ \text{\rm N} \} } \$ \$$$

Normalized rank residual. We are interested in whether certain subgroups are consistently ranked higher or consistently ranked lower than they ‘should’ be by the counterfactual targeting approaches. We therefore compare the distributions of rank residuals across subgroups and targeting methods:

$$\$ \$ \{ \text{\rm RR} \} _i = \frac{ \{ \hat{r}_i \} - \{ r_i \} }{ \{ N \} } \$ \$$$

where $\{ \hat{r}_i \}$ is the poverty rank of individual i according to the proxy poverty measure and r_i is the poverty rank of individual i according to the ground-truth poverty measure.

We focus on seven dimensions for parity: gender, ethnicity, religion, age group, disability status, number of children, and marital status. We also evaluate parity across whether an individual is ‘vulnerable’, where vulnerability is defined as one of the following traits: { female, over age 60, has a disability, has more than five children, is single}. We conduct this analysis using demographic information about the head of the household in the 2018–2019 field survey dataset, as these demographic variables were not all collected in the 2020 phone survey.

Programme exclusions

In Table 2, we present information on sources of exclusion from the Novissi programme that are not inherently related to targeting. These estimates are drawn from diverse sources of administrative and survey data, specifically:

Voter ID penetration. According to government administrative datasets, 3,633,898 individuals were registered to vote in Togo by late 2019. The electoral commission of Togo reports that this corresponds to 86.6% of eligible adults. Although the total adult population in Togo is hard to pin down (the last census was in 2011), Togo’s national statistical agency (<https://inseed.tg/>) estimates that there are 3,715,318 adults in Togo, whereas the United Nations estimates 4.4 million adults in Togo⁴⁵, implying a voter ID penetration rates of 82.6% or 97.8%.

Phone penetration. In the 2018–2019 field survey, 65% of individuals reported owning a mobile phone (Supplementary Fig. 3a) and 85% of households included at least one individual who owns a phone (Supplementary Fig. 3b). In rural areas, these rates drop to 50% of individuals and 77% of households. Rates of phone ownership are substantially lower among women (53%) than among men (79%), especially in rural areas (33% for women and 71% for men). These household survey-based estimates likely represent a lower bound, given the steady increase in phone penetration between 2018 and 2020. The Togolese government estimates 82% SIM card penetration in the country (though some people may have multiple SIM cards)⁵⁸. On the basis of data from the mobile phone companies, we observe 5.83 million unique active SIMs in Togo between March and September 2020.

Past phone use. In order to construct a phone-based poverty estimate for a subscriber, they had to place at least one outgoing call or text on the mobile phone network in the period of mobile network observation prior to the programme’s launch (March – September 2020, with programme registrations in November–December 2020). In Togo, a lower bound on this source of exclusion is the typical monthly rate of mobile phone turnover, which we estimate to be roughly 2.5% (see Supplementary Fig. 6). An upper bound is closer to 27%, which is the number of SIM cards that registered for Novissi November–December 2020 who did not make an outgoing transaction in the

March-September. This discrepancy may be due to (1) individuals buying new SIM cards specifically to register for Novissi; or (2) individuals registering for Novissi using existing SIM cards that were not in active use, for instance the SIM cards in multi-SIM phones. Based on qualitative observation, multi-SIM phones are very common in Togo, and secondary or tertiary SIMs are infrequently used (or not used at all). It is possible that families registered one household member on a primary SIM and others on secondary or tertiary SIMs that may have had no previous network activity.

Programme awareness. Since individuals had to register for the Novissi programme to receive benefits, programme advertising and population awareness was a key goal. The programme was advertised via radio, SMS, field teams, and direct communication with community leaders at the prefecture and canton level. In total, 245,454 subscribers attempted to register for the programme. Although we do not observe the prefecture and canton of subscribers who attempt but do not succeed in registering in our administrative data, we know that 87% of successful registrants are in cantons eligible for benefits. Assuming the rate is approximately the same for attempters, we expect that around 213,545 of the attempters are in eligible cantons. The total voting population in eligible cantons is 528,562, for an estimated attempted registration rate of 40.40%.

Registration challenges. Registration for the Novissi programme required the completion of a short (5 question) USSD survey. Of the 245,454 subscribers that attempted to register for the programme, 176,517 succeed, for a 71.91% rate of registration success.

Overlaps among sources of exclusion

The above sources of exclusion are not independent and are therefore not cumulative. For instance, individuals who are not registered to vote may also be systematically less likely to have a mobile phone. For this reason, Extended Data Table 5 uses the 2020 phone survey dataset—restricted to respondents who report living in an eligible canton—to calculate overlaps in sources of exclusion to the poor, including voter ID possession, programme awareness, registration challenges, and targeting errors using the phone-based targeting method. We cannot account for mobile phone ownership in this analysis since the 2020 survey was conducted over the phone, and sampled based on past CDR (see Supplementary Methods, section 5).

The final three columns of Extended Data Table 5 show, based on the 2020 phone survey dataset, average characteristics of the population ‘succeeding’ at each step: average PMT, per cent women and average age. The first panel shows successive exclusions for the entire population; the second panel focuses on just the poorest 29%

(that is, those who ‘should’ be receiving aid, were everyone to register for the programme and were the targeting algorithm perfect). In panel A, we observe that to a certain extent the ‘right’ types of people are dropping out at each step, which would be consistent with self-targeting observed in other contexts²⁶: in particular, those who attempt to register are poorer than the overall population (average PMT = 1.45 vs 1.62). There are little differences in the share of the successful population who are women or average age, except in the targeting stage.

Comparing panels A and B of Extended Data Table 5, we observe that the recall of the targeting algorithm is substantially higher among the population that owns a voter ID and succeeds in registration for the programme (61%, as shown in Extended Data Table 5, last row) than the overall population surveyed in the 2020 phone survey (47%, as shown in Table 1, row 4). This may be due to self-selection (that is, the type of poor people who register for Novissi tend to also have low phone-based poverty scores). However, it could alternatively suggest that the phone-based targeting algorithm is best at identifying the poor among the types of subscribers who are aware of and register to the Novissi programme.

Reporting summary

Further information on research design is available in the Nature Research Reporting Summary linked to this paper.

Data availability

The data used in this analysis include data that are available from public online repositories, data that are available upon request of the data provider, and data that are not publicly available because of restrictions by the data provider. The micro-estimates of wealth and population density used to derive satellite-based poverty maps are available from the Humanitarian Data Exchange (<https://data.humdata.org/dataset/relative-wealth-index> and <https://data.humdata.org/dataset/highresolutionpopulationdensitymaps-tgo>). The survey datasets are available upon request from the Institut National de la Statistique et des Études Economiques et Démographiques (<https://inseed.tg/> and inseed@inseed.tg). The mobile phone data and administrative data from the Novissi programme contain proprietary and sensitive information, and cannot be publicly released. Upon reasonable request, we can provide information to academic researchers on how to contact mobile network operators and the Togolese government to request these datasets.

Code availability

The code used for these analyses is publicly available at the GitHub repository located at <https://github.com/emilylaiken/togo-targeting-replication/>.

References

1. Egger, D. et al. Falling living standards during the COVID-19 crisis: quantitative evidence from nine developing countries. *Sci. Adv.* **7**, eabe0997 (2021).
2. Gentilini, U., Almenfi, M., Orton, I. & Dale, P. *Social Protection and Jobs Responses to COVID-19: A Real-Time Review of Country Measures* World Bank Policy Brief (World Bank, 2020).
3. Hanna, R. & Olken, B. A. Universal basic incomes versus targeted transfers: anti-poverty programs in developing countries. *J. Econ. Perspect.* **32**, 201–226 (2018).
4. Lindert, K., Karippacheril, T. G., Caillava, I. R. & Chávez, K. N. *Sourcebook on the Foundations of Social Protection Delivery Systems* (World Bank, 2020).
5. Lakner, C., Yonzan, N., Mahler, D., Aguilar, R. A. & Wu, H. Updated estimates of the impact of COVID-19 on global poverty: looking back at 2020 and the outlook for 2021. *World Bank Blogs* <https://blogs.worldbank.org/opendata/updated-estimates-impact-covid-19-global-poverty-looking-back-2020-and-outlook-2021> (2021).
6. Mirrlees, J. A. An exploration in the theory of optimum income taxation. *Rev. Econ. Stud.* **38**, 175–208 (1971).
7. Jerven, M. *Poor Numbers: How we are Misled by African Development Statistics and What to Do About It* (Cornell Univ. Press, 2013).
8. Serajuddin, U., Wieser, C., Uematsu, H., Dabalen, A. L. & Yoshida, N. *Data Deprivation: Another Deprivation to End* (World Bank, 2015); <http://documents.worldbank.org/curated/en/700611468172787967/Data-deprivation-another-deprivation-to-end>
9. Yeh, C. et al. Using publicly available satellite imagery and deep learning to understand economic well-being in Africa. *Nat. Commun.* **11**, 2583 (2020).
10. Bank, W. *World Development Report 2021: Data for Better Lives* (World Bank, 2021).

11. Coady, D., Grosh, M. & Hoddinott, J. Targeting outcomes redux. *World Bank Res. Obs.* **19**, 61–85 (2004).
12. Jean, N. et al. Combining satellite imagery and machine learning to predict poverty. *Science* **353**, 790–794 (2016).
13. Engstrom, R., Hersh, J. S. & Newhouse, D. L. Poverty from space: using high-resolution satellite imagery for estimating economic well-being (World Bank, 2017); <http://documents.worldbank.org/curated/en/610771513691888412/Poverty-from-space- using-high-resolution-satellite-imagery-for- estimating-economic-well-being>
14. Steele, J. E. et al. Mapping poverty using mobile phone and satellite data. *J. R. Soc. Interface* **14**, 20160690 (2017).
15. Pokhriyal, N. & Jacques, D. C. Combining disparate data sources for improved poverty prediction and mapping. *Proc. Natl Acad. Sci. USA* **114**, E9783–E9792 (2017).
16. Chi, G., Fang, H., Chatterjee, S. & Blumenstock, J. E. Micro-estimates of wealth for all low- and middle-income countries. *Proc. Natl Acad. Sci. USA* **119**, e2113658119 (2022).
17. Blumenstock, J. E., Cadamuro, G. & On, R. Predicting poverty and wealth from mobile phone metadata. *Science* **350**, 1073–1076 (2015).
18. Blumenstock, J. E. Estimating economic characteristics with phone data. *Am. Econ. Rev.* **108**, 72–76 (2018).
19. Aiken, E., Bedoya, G., Coville, A. & Blumenstock, J. E. Targeting development aid with machine learning and mobile phone data: evidence from an anti-poverty intervention in Afghanistan. In *Proc. 3rd ACM SIGCAS Conf. Comput. Sustainable Soc.* 310–311 (2020).
20. Nichols, A. L. & Zeckhauser, R. J. Targeting transfers through restrictions on recipients. *Am. Econ. Rev.* **72**, 372–377 (1982).
21. Baker, J. L. & Grosh, M. E. Poverty reduction through geographic targeting: how well does it work? *World Development* **22**, 983–995 (1994).
22. Grosh, M. E. & Baker, J. L. *Proxy Means Tests for Targeting Social Programs* (World Bank, 1995).

23. Alderman, H. Do local officials know something we don't? Decentralization of targeted transfers in Albania. *J. Public Econ.* **83**, 375–404 (2002).
24. Galasso, E. & Umapathi, N. Improving nutritional status through behavioral change: lessons from Madagascar (World Bank, 2007);
<https://openknowledge.worldbank.org/handle/10986/7607>
25. Alatas, V., Banerjee, A., Hanna, R., Olken, B. A. & Tobias, J. Targeting the poor: evidence from a field experiment in Indonesia. *Am. Econ. Rev.* **102**, 1206–1240 (2012).
26. Alatas, V. et al. Self-targeting: evidence from a field experiment in Indonesia. *J. Political Econ.* **124**, 371–427 (2016).
27. Brown, C., Ravallion, M. & van de Walle, D. A poor means test? Econometric targeting in Africa. *J. Dev. Econ.* **134**, 109–124 (2018).
28. Blumenstock, J. Machine learning can help get COVID-19 aid to those who need it most. *Nature* <https://doi.org/10.1038/d41586-020-01393-7> (2020).
29. Skoufias, E., Diamond, A., Vinha, K., Gill, M. & Dellepiane, M. R. Estimating poverty rates in subnational populations of interest: an assessment of the Simple Poverty Scorecard. *World Dev.* **129**, 104887 (2020).
30. McBride, L. & Nichols, A. Retooling poverty targeting using out-of-sample validation and machine learning. *World Bank Econ. Rev.* **32**, 531–550 (2018).
31. Eubanks, V. *Automating Inequality: How High-Tech Tools Profile, Police, and Punish the Poor* (St Martin's Press, 2018).
32. Barocas, S., Hardt, M. & Narayanan, A. Fairness and Machine Learning (fairmlbook.org, 2018).
33. Noriega-Campero, A. et al. Algorithmic targeting of social policies: fairness, accuracy, and distributed governance. In *Proc. 2020 Conference on Fairness, Accountability, and Transparency* 241–251 (Association for Computing Machinery, 2020).
34. Kleinberg, J., Mullainathan, S. & Raghavan, M. Inherent trade-offs in the fair determination of risk scores. In *Proc. 8th Innov. Theor. Comp. Sci. Conf.* 43:1–43:23 (2017).
35. Dwork, C., Hardt, M., Pitassi, T., Reingold, O. & Zemel, R. Fairness through awareness. In *Proc. 3rd Innov. Theor. Comp. Sci. Conf.* 214–226 (2012).

36. Skoufias, E. Economic crises and natural disasters: coping strategies and policy implications. *World Dev.* **31**, 1087–1102 (2003).
37. de Montjoye, Y.-A., Hidalgo, C. A., Verleysen, M. & Blondel, V. D. Unique in the crowd: the privacy bounds of human mobility. *Sci. Rep.* **3**, 1376 (2013).
38. Mann, L. Left to other peoples' devices? A political economy perspective on the big data revolution in development. *Dev. Change* **49**, 3–36 (2018).
39. Kerry, C. F., Kendall, J. & de Montjoye, Y.-A. *Enabling Humanitarian Use of Mobile Phone Data* (Brookings Institute, 2014).
40. Abebe, R. et al. Narratives and counternarratives on data sharing in Africa. In *Proc. 2021 ACM Conf. Fairness, Accountability Transparency* 329–341 (Assoc. Comp. Machinery, 2021).
41. Taylor, L. No place to hide? The ethics and analytics of tracking mobility using mobile phone data. *Environ. Plan D* **34**, 319–336 (2016).
42. Oliver, N. et al. Mobile phone data for informing public health actions across the COVID-19 pandemic life cycle. *Sci. Adv.* **6**, eabc0764 (2020).
43. Blumenstock, J. E. Don't forget people in the use of big data for development. *Nature* **561**, 170–172 (2018).
44. République Togolaise. 86,6% des Togolais Ont une carte d'Électeur. RepublicOfTogo.com <https://www.republicoftogo.com/toutes-les-rubriques/politique/86-6-des-togolais-ont-une-carte-d-electeur> (2020).
45. United Nations Department of Economic and Social Affairs. *2019 Revision of World Population Prospects* (United Nations, 2019).
46. A COVID Cash Transfer Programme that Gives More Money to Women in Togo. *The Innovation Dividend Podcast Episode 9* (UNDP Regional Innovation Centre, 2020); <https://undp-ric.medium.com/cina-lawson-a-covid-cash-transfer-programme-that-gives-more-money-to-women-in-togo-2386c5dff49>
47. Gunnemann, J. *PMT Based Targeting in Burkina Faso* (World Bank, 2016).
48. Grosh, M. E. & Baker, J. L. *Proxy Means Tests for Targeting Social Programs* (World Bank, 1995).
49. Tiecke, T. G. et al. Mapping the world population one building at a time. Preprint at <https://arxiv.org/abs/1712.05839> (2017).

50. De Montjoye, Y.-A., Rocher, L. & Pentland, A. S. bandicoot: a Python toolbox for mobile phone metadata. *J. Mach. Learn. Res.* **17**, 6100–6104 (2016).
51. Cecaj, A., Mamei, M. & Bicocchi, N. Re-identification of anonymized CDR datasets using social network data. In *2014 IEEE Int. Conf. Pervasive Comp. Communication Workshops* 237–242 (2014).
52. Alaggan, M., Gambs, S., Matwin, S. & Tuhin, M. in *Data and Applications Security and Privacy XXIX* (ed. Samarati, P.) 223–230 (Springer, 2015).
53. Mir, D., Isaacman, S., Caceres, R., Martonosi, M. & Wright, R. DP-WHERE: differentially private modeling of human mobility. In *2013 IEEE Int. Conf. Big Data* 580–588 (2013).
54. Togolese deputies approve biometric ID project. *Togo First* <https://www.togofirst.com/en/public-management/0409-6177-togolese-deputies-approve-biometric-id-project> (2020).
55. Kabemba, P. B., Bermeo, L. and François. Cash and the city: digital COVID-19 social response in Kinshasa. *Brookings Institute: Future Development Series* <https://www.brookings.edu/blog/future-development/2021/09/08/cash-and-the-city-digital-covid-19-social-response-in-kinshasa/> (2021).
56. Smythe, I. & Blumenstock, J. E. Geographic micro-targeting of social assistance with high-resolution poverty maps. Preprint at <https://www.jblumenstock.com/files/papers/SmytheBlumenstockPreprint.pdf> (2020).
57. Barocas, S., Hardt, M. & Narayanan, A. *Fairness and Machine Learning Limitations and Opportunities*. <https://www.semanticscholar.org/paper/Fairness-and-Machine-Learning-Limitations-and-Barocas-Hardt/bae7f0b3448a3eac77886f2a683c0cf9256bb8bf> (2018).
58. République Togolaise. Programme Digital de Transferts Monétaires en Réponse à la COVID-19. <http://www.fondation-farm.org/zoe/doc/colocnovissi.pdf> (2020).
59. GIS Geography Togo map. *GIS Geography* <https://gisgeography.com/togo-map/> (accessed 5 January, 2022).

Acknowledgements

I. O. Falomir, S. Mehra, S. Nair, A. Dar Serapio, N. Ver Steeg and R. Warren provided invaluable research assistance on this project. This project would not have been

possible without the dedication of our project partners in Togo, especially C. Lawson, S. Bakari, L. Mills, K. Ekouhoho, M. Koudeka and A. Byll. The data collection for the 2020 phone survey was made possible by the hard work of a dedicated team of enumerators from Institut National de la Statistique et des Études Economiques et Démographiques (INSEED), led by S. Telou and R. Ogoumedi. The team at GiveDirectly was instrumental in implementing the Novissi expansion studied in this paper (especially H. S. Chia, M. Cooke, K. Lee, A. Nawar and D. Quinn). We thank E. Duflo, L. Encinas, T. George, R. Hanna, E. Ligon and B. Olken for helpful feedback. We are grateful for financial support from Google.org, data.org, the Center for Effective Global Action, the Jameel Poverty Action Lab, the Global Poverty Research Lab at Northwestern University, and the World Bank, which financed the phone surveys and data collection under the WURI programme. Blumenstock is supported by National Science Foundation award IIS—1942702 and Bellue is supported by the DAAD. Authors retained full intellectual freedom in conducting this research, and as such all opinions and errors are our own.

Author information

Author notes

1. These authors jointly supervised this work: Emily Aiken, Joshua Blumenstock

Affiliations

1. School of Information, University of California, Berkeley, CA, USA

Emily Aiken & Joshua E. Blumenstock

2. Department of Economics, University of Mannheim, Mannheim, Germany

Suzanne Bellue

3. Kellogg School of Management, Global Poverty Research Lab, Northwestern University, Evanston, IL, USA

Dean Karlan

4. Department of Economics, Global Poverty Research Lab, Northwestern University, Evanston, IL, USA

Chris Udry

Contributions

E.A. and J.B. jointly supervised this project. E.A., S.B. and J.B. analysed data and prepared figures. E.A. and J.B. wrote the paper. All authors conceived the project and edited and revised the manuscript.

Corresponding author

Correspondence to [Joshua E. Blumenstock](#).

Ethics declarations

Competing interests

The authors declare no competing interests.

Peer review

Peer review information

Nature thanks Matthew Wai-Poi and the other, anonymous reviewers for their contribution to the peer review of this work.

Additional information

Publisher's note Springer Nature remains neutral with regard to jurisdictional claims in published maps and institutional affiliations.

Extended data figures and tables

[Extended Data Fig. 1 Overview of targeting methodology.](#)

a) Regional targeting. Satellite imagery of Togo⁵⁹ is used to construct micro-estimates of poverty (middle)¹⁶, which are overlayed with population data to produce canton-level estimates of wealth. Individuals registered in the 100 poorest cantons (right) are eligible for benefits. Inset images © 2019 Google. **b)** Individual targeting. A machine-learning algorithm is trained using representative survey data to predict consumption from features of phone use (Methods, ‘Machine-learning methods’). The algorithm constructs poverty scores that are correlated with ground-truth measures of consumption (left). Subscribers who register for the program in targeted cantons with estimated consumption less than USD \$1.25/day are eligible for benefits (right). The red distribution shows the predicted wealth distribution of the entire population of

Togo; the blue distribution shows the predicted wealth distribution in the 100 poorest cantons; and the green section indicates the predicted wealth distribution of Novissi beneficiaries.

Extended Data Fig. 2 Fairness with normalized rank residuals.

Boxplots showing distributions of normalized rank residuals (see [Methods](#), ‘Fairness’) aggregated by subgroup, using the 2018–2019 field survey dataset ($N=4,171$). Boxes show the 25th and 75th percentiles, and the centre line shows the median of the distribution. Left-shifted boxes indicate groups that are consistently under-ranked by a given targeting mechanism, right-shifted boxes indicate groups that are consistently over-ranked by a given targeting mechanism.

Extended Data Fig. 3 Fairness with demographic parity.

We evaluate demographic parity across subgroups by comparing the proportion of a subgroup targeted under counterfactual approaches to the proportion of the subgroup that falls into the poorest 29% of the population (using data from the 2018–2019 field survey matched to CDR, $N=4,171$). Bubbles show the percentage point difference between the proportion of the subgroup that is targeted and the proportion that is poor according to ground-truth data. Large red bubbles indicate groups that are over-targeted; large blue bubbles indicate groups that are under-targeted.

Extended Data Fig. 4 Targeting performance at different levels of program coverage.

Top figures (**a** and **b**) show performance for the rural Novissi program, evaluated using 2020 phone survey. Bottom figures (**c** and **d**) correspond to the hypothetical national program, evaluated using the 2018–2019 field survey. ROC curves on left (**a** and **c**) indicate the true positive and false positive rates at different targeting thresholds. Coverage vs. Recall figures on right (**b** and **d**) show how precision and recall vary as the percentage of the population receiving benefits increases, i.e., they indicate the precision and recall for reaching the poorest $k\%$ of the population in programs that target the poorest $k\%$. (Precision and recall are thus the same for each value of k by construction; see [Methods](#), ‘Measures of targeting quality’).

Extended Data Table 1 Performance of targeting households below the extreme poverty line

Extended Data Table 2 Performance of targeting households below the poverty line

Extended Data Table 3 Feature importances

Extended Data Table 4 How quickly does the accuracy of a phone-based targeting model degrade?

Extended Data Table 5 Overlapping sources of exclusion from rural Novissi

Extended Data Table 6 Performance of phone-based approach to predicting wealth and consumption

Supplementary information

Supplementary Information

This file contains Supplementary Discussion, Methods, Supplementary Figs. 1–11, Tables 1–13 and references.

Supplementary Information

Reporting Summary.

Rights and permissions

Open Access This article is licensed under a Creative Commons Attribution 4.0 International License, which permits use, sharing, adaptation, distribution and reproduction in any medium or format, as long as you give appropriate credit to the original author(s) and the source, provide a link to the Creative Commons license, and indicate if changes were made. The images or other third party material in this article are included in the article's Creative Commons license, unless indicated otherwise in a credit line to the material. If material is not included in the article's Creative Commons license and your intended use is not permitted by statutory regulation or exceeds the permitted use, you will need to obtain permission directly from the copyright holder. To view a copy of this license, visit <http://creativecommons.org/licenses/by/4.0/>.

Reprints and Permissions

About this article

Cite this article

Aiken, E., Bellue, S., Karlan, D. *et al.* Machine learning and phone data can improve targeting of humanitarian aid. *Nature* **603**, 864–870 (2022).

<https://doi.org/10.1038/s41586-022-04484-9>

- Received: 15 July 2021

- Accepted: 25 January 2022
- Published: 16 March 2022
- Issue Date: 31 March 2022
- DOI: <https://doi.org/10.1038/s41586-022-04484-9>

Share this article

Anyone you share the following link with will be able to read this content:

[Get shareable link](#)

Sorry, a shareable link is not currently available for this article.

[Copy to clipboard](#)

Provided by the Springer Nature SharedIt content-sharing initiative

Machine learning can help get COVID-19 aid to those who need it most

- Joshua Blumenstock

World View 14 May 2020

The vest that can hear your heartbeat

- Benjamin Thompson
- Shamini Bundell

Nature Podcast 16 Mar 2022

This article was downloaded by **calibre** from <https://www.nature.com/articles/s41586-022-04484-9>

- Article
- Open Access
- [Published: 23 March 2022](#)

The development and evolution of inhibitory neurons in primate cerebrum

- [Matthew T. Schmitz](#)^{1,2},
- [Kadelyn Sandoval](#)^{2,3},
- [Christopher P. Chen](#) [ORCID: orcid.org/0000-0002-0800-444X](#)^{1,2},
- [Mohammed A. Mostajo-Radji](#) [ORCID: orcid.org/0000-0002-1634-7514](#)^{1,2},
- [William W. Seeley](#)²,
- [Tomasz J. Nowakowski](#) [ORCID: orcid.org/0000-0003-2345-4964](#)^{3,4,5,6,7},
- [Chun Jimmie Ye](#) [ORCID: orcid.org/0000-0001-6560-3783](#)^{7,8,9,10},
- [Mercedes F. Paredes](#)^{2,3} &
- [Alex A. Pollen](#) [ORCID: orcid.org/0000-0003-3263-8634](#)^{1,2,3,7}

Nature volume 603, pages 871–877 (2022)

- 13k Accesses
- 108 Altmetric
- [Metrics details](#)

Subjects

- [Cell type diversity](#)
- [Developmental neurogenesis](#)
- [Neuronal development](#)

Abstract

Neuroanatomists have long speculated that expanded primate brains contain an increased morphological diversity of inhibitory neurons (INs)¹, and recent studies have identified primate-specific neuronal populations at the molecular level². However, we know little about the developmental mechanisms that specify

evolutionarily novel cell types in the brain. Here, we reconstruct gene expression trajectories specifying INs generated throughout the neurogenic period in macaques and mice by analysing the transcriptomes of 250,181 cells. We find that the initial classes of INs generated prenatally are largely conserved among mammals. Nonetheless, we identify two contrasting developmental mechanisms for specifying evolutionarily novel cell types during prenatal development. First, we show that recently identified primate-specific *TAC3* striatal INs are specified by a unique transcriptional programme in progenitors followed by induction of a distinct suite of neuropeptides and neurotransmitter receptors in new-born neurons. Second, we find that multiple classes of transcriptionally conserved olfactory bulb (OB)-bound precursors are redirected to expanded primate white matter and striatum. These classes include a novel peristriatal class of striatum laureatum neurons that resemble dopaminergic periglomerular cells of the OB. We propose an evolutionary model in which conserved initial classes of neurons supplying the smaller primate OB are reused in the enlarged striatum and cortex. Together, our results provide a unified developmental taxonomy of initial classes of mammalian INs and reveal multiple developmental mechanisms for neural cell type evolution.

[Download PDF](#)

Main

To examine the diversity of primate inhibitory neurons (INs) during development, we dissected progenitor zones in the ventral telencephalon and migratory destinations in the cortex and basal nuclei of prenatal rhesus macaque brains. We focused on the lateral, medial and caudal ganglionic eminences (LGE, MGE and CGE, respectively) and ventromedial forebrain (VMF) regions including the septum, preoptic area and preoptic hypothalamus, where distinct configurations of transcription factors specify initial IN classes^{3,4,5,6}. We also sampled migratory destinations in the cortex and basal nuclei, where local signals further influence the maturation and postmitotic refinement of neuron classes⁷. In total, we collected 71 samples across 9 specimens, spanning the onset of cortical neurogenesis, postconception day 40 (PCD40), to the conclusion, PCD100 (ref. ⁸; Fig. [1a](#) and Extended Data Fig. [1](#)). We performed single-cell RNA sequencing using the 10x Chromium Controller, incorporating recent data from PCD110 (ref. ⁹) and mouse studies from PCD13 to PCD21 (refs [10,11](#)) as well as adult olfactory bulb (OB)¹² (Supplementary Table [1](#)). We applied stringent quality control, batch correction, dimensionality reduction, Leiden clustering and RNA velocity trajectory analysis to identify transcriptionally similar classes of progenitors and postmitotic INs among 109,112 macaque cells and 141,065 mouse cells, which were identified by expression of *DLX* and *GAD* genes ([Methods](#)).

Fig. 1: Transcriptional diversity of IN precursors in developing macaque and mouse telencephalon.

 figure 1

a, Regions dissected for single-cell RNA sequencing, labelled on PCD80 macaque lateral, medial and frontal coronal section traces. Columns of stacked boxes represent samples from each individual, with each box representing a region dissected and sampled. PCD110 samples from Zhu et al.⁹. PFC, prefrontal cortex; POH, preoptic hypothalamus; POA, preoptic area. **b**, Model of inhibitory neurogenesis. **c**, **d**, UMAP projections coloured by progenitor state and initial class for mice (**c**) and macaques (**d**). Insets in **c**, **d** show the dissection region from **a**, the scVelo dynamical RNA velocity shared latent time and age.

Macaque and mouse IN progenitors clustered mainly by cell cycle phase rather than spatial origin (Fig. [1b–d](#) and Extended Data Figs. [1–3](#)). Similarly, the most immature new-born neurons clustered by both class and differentiation stage, according to the RNA velocity latent time (Fig. [1b–d](#) and Extended Data Figs. [1–3](#)). From the Leiden clusters, we delineated 11 discrete initial classes of macaque postmitotic neurons, which resolved to 17 initial classes in mouse (Fig. [1c, d](#)). We found that canonical marker genes for established progenitor territories exhibited significant correlations among the progenitors, suggesting that core transcriptional regulatory programmes that are present at or before the last cell division predict the identity of postmitotic neurons in the initial classes. For example, signatures reflecting spatial origin and subtypes in the CGE (*NR2F1* and *NR2F2*), LGE (*MEIS2*, *EBF1* and *ISL1*), MGE (*MAF*, *LHX6* and *CRABPI*) and VMF (*ZIC1* and *ZIC2*) were visible in G1 progenitors, and signatures related to four distinct LGE initial classes further emerged

in dividing cells as correlations of the pan-LGE marker *MEIS2* to *PAX6*, *FOXP2*, *ISL1* or *PENK* (Extended Data Fig. 1d). These observations support a model in which we refer to differentiating postmitotic neuron clusters that are largely defined by germinal zone regional transcription factors as initial classes of new-born neurons. This terminology reflects the idea that a small number of discrete transcriptional classes are initially produced following a neuron's final cell division and that each of these immature transcriptional states is later partitioned into one or many different mature classes by nurture and circumstance as neurons migrate and integrate into the circuitry (Fig. 1b)⁷. Although many studies have demonstrated that these transcriptionally defined classes result from shared lineage relationships¹³, we refrain from referring to classes as lineages in the absence of direct lineage tracing data.

Conserved and divergent initial classes

To construct a taxonomy of IN development, we sought to identify evolutionarily conserved cell classes and to link them to candidate adult populations¹⁴. We found most well-known initial class markers to be conserved between species (Fig. 2a and Extended Data Fig. 4). Gene expression signatures for each progenitor and postmitotic initial class in macaques correlated strongly with at least one comparable class in mice (Extended Data Fig. 4). Most classes had one-to-one relationships, although subclasses such as LGE_FOXP1/ISL1/NPY1R and LGE_MEIS2/PAX6/SCGN as well as a number of VMF classes were apparent in the mouse data but were undersampled in macaques. Because cell type correlation methods depend on clustering resolution in each species, we further examined homology at the level of individual cells. Mutual nearest-neighbour analysis showed that all telencephalic initial classes present in mice were also present in macaques (Fig. 2b). To infer the putative fates of the initial classes in the absence of lineage tracing, we compiled the most complete available data of adult mouse brains (Extended Data Fig. 5). We then computed the terminal class absorption probabilities for prenatal neurons using nearest-neighbour relationships and RNA velocity with equal weight in CellRank's Markov chain model¹⁵. Our predicted mapping of postmitotic differentiation and partitioning of each initial class using transcriptional similarities recapitulated known lineage relationships and made a number of unexpected predictions that support unresolved linkages in the literature, as summarized in Fig. 2c, such as an *NKX2-1*⁺ MGE-derived *LAMP5*⁺ cortical chandelier population^{16,17,18} and a shared origin of amygdala intercalated cells (ITCs) and striatal eccentric spiny neurons^{19,20,21}. The widespread distribution and diversity of derivatives from some initial classes such as MGE_LHX6/NPY also highlights the shared genetic programmes underlying the initial specification of populations that later diversify according to regional destinations, where terminal classes are commonly subdivided into many transcription types and morphotypes. Although our results suggest that the initial classes are largely uniform, minor axes of variation may already

exist within classes, which could trigger downstream cascades that bias terminal fate partitioning. However, such variation cannot be identified here without knowing a cell's fate a priori.

Fig. 2: Unified taxonomy of Euarchontogliiran telencephalic IN specification.

 figure 2

a, Heatmap of macaque initial class marker expression, scaled by column. Stacked barplots correspond to region of origin for cells in each class. The dendrogram represents complete linkage of the Pearson correlation distance of mean expression values. Stacked bar plots show the regional distribution of each class. **b**, Sankey diagram in which the thickness of the lines between the left and middle columns represents the number of mutual nearest-neighbour (MNN) cells shared between each class and that between the middle and right columns reflects the initial class (IC) identity of the 100 cells with the highest (CellRank) probabilities of being absorbed in each terminal class (TC). **c**, Summarized taxonomy of initial and terminal classes observed in macaques and mice. Forked lines represent subclasses that become apparent postmitotically. Initial classes of INs are organized by the presumptive birthplace based on the expression of regional marker genes and putative birthdates, presented in the manner of Lim et al.⁵. Inferred terminal fates are based on our gene expression and histology analysis and the literature, as denoted and discussed in detail in Supplementary Table 4. S/DWMIN, superficial/deep white matter inhibitory neuron; BN, basal nuclei. RMTW_ZIC1/RELN and VMF_TMEM163/OTP were not included because they are excitatory cortical and hypothalamic classes, respectively.

Recent comparative studies of adult primate, rodent and ferret telencephalon showed a primate-specific population of striatal INs that express the neuropeptide TAC3 (ref. 2), although the developmental origin of this evolutionarily novel population remains

unclear. These striatal INs are important exceptions to the one-to-one conservation of initial classes between primates and rodents (Fig. 2b). Instead, mice have a single ancestral class of MGE_CRABP1/MAF neurons that shows strong homology to the MGE_CRABP1/MAF and MGE_CRABP1/TAC3 clusters in macaques (Extended Data Fig. 4c). We further examined the gene networks that define this primate-specific population (Fig. 3a,b and Extended Data Fig. 6). Using RNAscope, we quantified the co-expression of the dividing cell marker *MKI67* and the initial class markers *CRABP1*, *TAC3*, *MAF* and *LHX8* across the rostrocaudal expanse of the MGE and striatum at PCD65. Our results showed a bias of MGE_CRABP1/MAF neurons rostrally and MGE_CRABP1/TAC3 neurons caudally in the MGE progenitor zone (Fig. 3c,d). In addition, we detected a low fraction of cells co-expressing *CRABP1*, *TAC3* and *MKI67* that were displaced from the ventricle, suggesting that subventricular zone (SVZ) progenitors upregulate the programme for this novel initial class at or before their final cell division (Extended Data Fig. 7). In the striatum, both classes showed uniform distributions, which was also confirmed by RNAscope for *STXBP6*, *ANGPT2* and *RBP4* in two additional individuals (Extended Data Figs. 7 and 8). *LHX8* expression was restricted to a subset of *CRABP1*⁺*TAC3*⁺ cells outside the MGE (Fig. 3d), highlighting early postmitotic specification of a *TAC3/LHX8* subclass observed in adult marmosets². Interestingly, although they were clearly distinct from primate MGE_CRABP1/TAC3 neurons, mouse cholinergic and pallidal neurons (VMF_CRABP1/LHX8) also expressed *Zic1* and *Lhx8* (Fig. 3a), hinting that a combination of transcriptional programmes used by neighbouring initial classes may define the novel *TAC3* population. Differential expression and regulon analysis showed that the earliest molecular programmes that distinguish *TAC3* INs involve distinct neuropeptides, acetylcholine receptors and immediate early gene networks (Extended Data Fig. 6 and Supplementary Table 6), suggesting that *TAC3* neurons may receive signals from nearby cholinergic neurons. Notably, the primate-specific *TAC3* population emerged as a distinct class as cells became postmitotic by PCD65. This occurred far earlier in development than the conserved *PTHLH*⁺, *PVALB*⁺ and *TH*⁺ terminal fates that ultimately arise from the related MGE_CRABP1/MAF class^{2,22}. Lastly, we found that MGE_CRABP1 classes emerged in vitro as rare populations in human pluripotent stem cell-derived telencephalon organoids (Extended Data Fig. 6).

Fig. 3: Emergence of primate-specific MGE_CRABP1/TAC3 striatal INs.

 **figure 3**

a, Dot plot of expression of striatal IN marker genes. **b**, Schematic summarizing properties distinguishing new-born MGE $CRABP1^+TAC3^+$ and $CRABP1^+MAF^+$ neurons, from markers given in Supplementary Table 6. **c**, Line plots showing the Rostro–Caudal distribution of classes of $CRABP1^+$ cells. $TAC3^-$ (MAF) denotes that the MAF class is inferred by the lack of $TAC3$, as distinct positive markers for this class are not apparent until later in differentiation. Each point is the sum of all cells in at least five random fields of view in each section/region. Cells were counted from whole-section scans of RNAscope *in situ* hybridization on representative sections (full size shown in Extended Data Fig. 8). The solid (dotted) outlines of the GE region in the images represents MGE (LGE). One individual was used with four pairs of tandem sections interspersed with four single sections. **d**, Representative image of MGE_—CRABP1/MAF (blue arrows), MGE_—CRABP1/TAC3 (pink arrows), MGE_—CRABP1/TAC3/LHX8 (yellow arrows) and VMF_—CRABP1/LHX8 INs ($LHX8^+TAC3^-$ cells) in the putamen from section 66 (Extended Data Fig. 8c). Scale bar 50 μ m.

Reuse of OB neurons in primate cerebrum

We next analysed the initial classes of neurons detected within and probably derived from the LGE⁶. Two classes, LGE_FOXP2/TSHZ1 and LGE_MEIS2/PAX6, showed unexpected enrichment in the cortical frontal lobe in addition to the ventral telencephalon (Fig. 4a,b and Extended Data Fig. 9). LGE_MEIS2/PAX6 neurons express *ETV1*, *SP8*, *MEIS2*, *SALL3*, *TSHZ1* and *PAX6* during differentiation, all of which are markers of and are required for proper production of OB granule cells and dopaminergic TH^+ periglomerular cells (PGCs)^{23,24}. Indeed, the transcriptomes of cells in this class showed strong correlations to mouse adult-born granule cells (OB-GC_MEIS2/PAX6; Extended Data Fig. 4c). Similarly, trajectory analysis linked the mouse LGE_FOXP2/TSHZ1 class to OB-PGC_FOXP2/CALB1 PCGs of the OB, connecting each LGE class to distinct olfactory populations (Fig. 2b).

Fig. 4: Redistribution of LGE_MEIS2/PAX6 granule cells.

 figure 4

a, Approximate ganglionic eminence transcription factor territories in PCD80 macaque brain, showing estimated section planes. **b**, Dot plot of expression of markers of LGE- and CGE-derived classes showing overlap of transcription factor domains. The expression values are scaled from 0–1 for each gene. The dot size represents the percentage of cells that express each gene. Stacked bar plots show the regional distribution of each class. NAc, nucleus accumbens. **c–f**, Immunohistochemistry for LGE class markers in macaque and human. **c**, Coronal–axial section of the A-dLGE and PFC at PCD80 with the inset highlighting DLX2⁺SP8⁺FOXP2[−] parenchymal

chains. **d**, Arc–ACC SCGN⁺MEIS2⁺ cells (teal arrows) shown migrating within the boundary of dense TH⁺ axons at PCD120. **e**, Whole PCD120 coronal section from **d** showing the Arc–ACC and RMS wrapping around the striatum from the A-dLGE. Box marked ED13 corresponds to Extended Data Fig. 13f. **f**, Low-magnification sagittal image of a human postconception week 33 (PCW33) specimen showing large streams of MEIS2⁺SP8⁺ neurons originating from the A-dLGE; these neurons contribute to the RMS and the Arc. LV, left ventricle; Str, striatum. **g**, Schematic of a macaque brain. Multiple streams extend from the anterior pole of the dLGE, or the SVZ at later stages, to the RMS leading to the OB, the Arc extending dorsomedially and the Arc–ACC subsidiary stream extending to the ACC.

We performed immunofluorescence microscopy to visualize the spatial distribution of the LGE_FOXP2/TSHZ1 and LGE_MEIS2/PAX6 classes, using combinations of MEIS2 together with FOXP2/FOXP4 and SCGN/SP8/PAX6, respectively. Both populations appeared to emanate from the dorsal LGE (dLGE) but showed complementary distributions. LGE_FOXP2/TSHZ1 cells immunoreactive for FOXP2, FOXP4 and SCGN were found mainly in the dorsolateral dLGE (DL-dLGE; Extended Data Figs. 10 and 11) but were not detected in the anterior dLGE (A-dLGE) or rostral migratory stream (RMS). Instead, cells of this class migrated directly into the striatum, via the lateral migratory stream (LMS) to the outer OB and ventromedially to cortical superficial white matter (Extended Data Figs. 10–12). Consistent with trajectory analysis, markers of dLGE origin (*ETV1*, SCGN and SP8) were downregulated, whereas *FOXP2*, *CASZ1*, *OPRM1* and projection neuron markers were upregulated, as the cells differentiated and migrated into the striatum (Extended Data Figs. 9 and 10). The expression of *TSHZ1*, *LYPD1*, *PCDH8* and *CASZ1*, the absence of expression for the canonical medium spiny projection neuron markers *NPY* and *FOXP1*, and the results of RNA velocity analysis all imply that the LGE_FOXP2/TSHZ1 initial class also explains the previously unknown developmental origin of recently described striatal projection neurons in adult mice, eccentric spiny projection neurons (eSPNs)²¹ and amygdala ITCs (Fig. 2 and Extended Data Fig. 9). This linkage is consistent with reports that cells in mouse dLGE initially express SP8 and maintain TSHZ1 expression as they migrate via the LMS to become amygdala ITCs^{19,25}. This developmental perspective suggests that these cells are not eccentric deviations from canonical spiny projection neuron development; instead, the LGE_FOXP2/TSHZ1 class converges on a similar striatal and amygdaloid projection neuron transcription profile despite its distinct origin.

By contrast, we observed MEIS2⁺PAX6⁺SP8⁺SCGN⁺ cells representing the LGE_MEIS2/PAX6 class continuously from the anterior end of the dLGE along the RMS to the OB granule cell layer (Fig. 4c and Extended Data Figs. 11 and 12). Notably, we observed dense parenchymal chains²⁶ of these cells radiating from the dLGE at PCD80 ($n = 3$ hemispheres; Fig. 4c and Extended Data Fig. 12h,i). At

PCD120, we found large numbers of LGE_MEIS2/PAX6 precursors that express SCGN extending dorsomedially and caudally in the Arc migratory stream²⁷ in addition to the RMS (Extended Data Fig. 13). These cells were densest in chains running along the entire striatum in the primary tier of the Arc with fewer cells radially²⁷.

Unexpectedly, we also observed a robust stream diverted from the Arc that stretched from the A-dLGE into the anterior cingulate cortex (ACC; Fig. 4d,e). This stream, referred to as the Arc-ACC, appeared to be bounded by TH⁺ fibres in superficial white matter (Fig. 4d). Cells from the Arc and Arc-ACC were common in dorsomedial cortex deep white matter but were rarely found lateral or ventral to the striatum; however, many CGE-derived MEIS2⁻SP8⁺NR2F2⁺ neurons were observed throughout the white matter (Extended Data Fig. 13), highlighting regional heterogeneity in the composition of white matter INs.

We confirmed that LGE_MEIS2/PAX6 neurons from the A-dLGE also contribute to the RMS, Arc and Arc-ACC in perinatal humans (Fig. 4f) and postnatal macaques (Extended Data Fig. 13). We further found that these neurons persist postnatally in the deep white matter of the cingulate cortices and the superior corona radiata (Extended Data Fig. 13l,m). By contrast, in postnatal day 2 (P2) mice, we identified only rare instances of LGE_MEIS2/PAX6 cells in deep white matter (Extended Data Fig. 14a-c), consistent with recent reports that sparse MEIS2⁺HTR3A⁺ neurons in the white matter integrate into cortical circuitry perinatally²⁸. Instead, the vast majority of these cells appeared in the anterior SVZ and RMS in mice (Extended Data Fig. 14). Overall, we found that neurons derived from the dLGE are more widely distributed than previously recognized in primates, representing a major source of neurons in the primate Arc migratory streams and persisting in the deep white matter.

Our analysis identified a third presumed dLGE-derived class in and around the striatum, insula and claustrum, which we refer to as striatum laureatum neurons (SLNs or Str-SLN_TH/SCGN). Likely derived from the LGE_MEIS2/PAX6 initial class, SLNs are named for the wreath shape they form around the striatum. At both PCD120 and 7 months postnatally, SLNs were immunoreactive for PAX6, MEIS2, SP8, TH and SCGN but not for FOXP2, NKX2-1 or NR2F2, which is also characteristic of TH⁺ PCGs (OB-PGC_TH/SCGN) of the OB (Fig. 5a-d and Extended Data Figs. 13f and 15). This distribution matches observations of TH⁺ cells circumscribing the primate striatum and their reported absence in rodents and illuminates their molecular identity and origin²⁹. Indeed, we did not identify MEIS2⁺PAX6⁺SCGN⁺TH⁺ cells along the mouse striatum border or the claustrum (Extended Data Fig. 14e-g). Instead, these cells in mice were restricted to the OB, olfactory tract or olfactory tubercle, matching the macaque olfactory peduncle domain (Fig. 5e,f). We found that SLNs form a reticule at the white matter boundaries of the caudate and putamen of macaques, exist in humans and persist throughout life (Fig. 5a-h).

Fig. 5: Primate TH^+ SLNs and ancestral olfactory populations.

 figure 5

All immunofluorescence images in this figure are of MEIS2, SCGN and TH. **a**, Seven-month-postnatal macaque coronal section including the remnant RMS. **b**, TH^+ SLNs at the border of the striatum. MEIS2⁺SCGN⁺TH⁺ peristriatal SLNs are indicated by yellow arrows. **c**, SLNs in the claustrum with long, straight processes among dense TH⁺ midbrain–cortical fibre synapses including one TH⁺ process (orange arrowheads) and one TH⁻ process (white arrowheads). **d**, Anterior olfactory nucleus at the olfactory peduncle, with MEIS2⁺SCGN⁺TH⁻ cells (blue arrows) including SCGN⁺TH⁻ fibres entering the ventral cortex (inset) and triple-positive cells (yellow arrows). **e**, Coronal section of mouse P2 OB showing SLN-analogous TH⁺SCGN⁺ cells. **f**, Mouse P2 coronal section showing the olfactory tubercle (OT) and striatum (Str) outlined by dotted lines, with only MEIS2⁺TH⁺ or MEIS2⁺SCGN⁺ cells. **g**, Photograph of a brain coronal slab from an 88-year-old human. The box shows the approximate location of the inset section block. **h**, TH⁺SCGN⁺ human SLN, with double-positive processes highlighted with white arrowheads. Only two cells were observed across this section. **i**, Schematic summarizing the unequal scaling of cortical and olfactory structures. **j**, Schematic summarizing migration of dLGE neurons and unequal evolutionary scaling of their destinations. Relative values in the bar plots are arbitrary.

Discussion

By identifying transcriptional regulatory programmes distinguishing the earliest specification of initial classes, our study provides a resource for identifying conserved molecular mechanisms that specify cell type diversity. This resource can support rational in vitro derivation of these populations from pluripotent stem cells and

interpretation of the cellular substrates of genetic disorders of neural development. *TAC3*-expressing striatal INs represent an exceptional case in which an evolutionarily novel initial class of neurons emerges in differentiating progenitors. A limited number of gene networks distinguish the *TAC3* initial class from the related MGE_CRABP1/MAF class, consistent with a recent model of cell type evolution. Under this model, an ancestral cell type is partitioned into distinct subtypes by changes in transcription factor expression that enable genomic individuation of sister cell classes that still share many regulatory complexes and developmental trajectories³⁰. However, the conservation of nearly all other initial classes of INs between macaques and mice suggests that evolutionary diversification of primate INs arises mainly by radiation of conserved initial classes of new-born neurons and may be shaped by the expanded diversity of primate regional destinations⁷.

The neurons of the dLGE appeared to be particularly affected by primate brain reorganization. In both macaques and mice, the LGE_MEIS2/PAX6 class is among the latest-born INs and migrates to olfactory structures and deep white matter. However, the absolute migration distance of late-born A-dLGE neurons to the OB is more than two orders of magnitude longer in new-born macaques than in mice and increases further as the brain expands after birth^{27,31}. Similarly, the volume of white matter is more than three and five orders of magnitude larger in macaques and humans than in mice, respectively³², whereas the relative size of the primate OB is markedly smaller (Fig. 5*i, j*)³³. Thus, in mice, the birthplace is only several cell lengths from any point in the adjacent deep white matter. In macaques, however, these homologous cells traverse histologically distinct dorsal migratory streams and apparently reuse the chain migration strategy. OB granule cells derived from this class contribute to adult plasticity³⁴, and myelination is delayed for up to two decades in human frontal lobe white matter³⁵, potentially linking these cells to white matter plasticity. Notably, abnormal accumulations of frontal lobe white matter neurons have been reproducibly associated with schizophrenia and autism³⁶. With their prolonged migration to far-flung and ever-changing destinations, the A-dLGE neurons we identified here may be particularly vulnerable to environmental influences, and the markers we identified will be useful for assessing the molecular heterogeneity of disease-associated populations.

Finally, we identified SLNs, another likely OB sister type, which are redistributed to peristriatal regions and show a molecular resemblance to dopaminergic OB TH⁺ PGCs. Future studies can examine whether this primate striatal population partly explains the human-specific increase in TH-expressing striatal neurons^{37,38} and whether these neurons produce dopamine themselves or have an auxiliary role to compensate for increased demands on midbrain dopaminergic neurons^{39,40}. Crick and Koch⁴¹ speculated that, in the claustrum, hitherto undiscovered sparse INs resembling intraglomerular OB cells with dendrodendritic synapses could contribute to binding

information. Molecular access to SLNs will enable future circuit-level studies of this rare claustrum population. Together, our results highlight contrasting models for diversification of primate INs by specification of an entirely novel initial class and by redistribution of conserved initial classes that supply the OB into primate white matter migratory streams and peristriatal locations.

Methods

Samples

The Primate Center at the University of California, Davis, provided nine specimens of cortical tissue from PCD40, PCD50, PCD65 ($n = 3$), PCD80 ($n = 2$), PCD90 and PCD100 macaques. All animal procedures conformed to the requirements of the Animal Welfare Act, and protocols were approved before implementation by the Institutional Animal Care and Use Committee at the University of California, Davis. PCD40 represents embryonic Carnegie stage 20 and marks the approximate beginning of neurogenesis of both excitatory neurons and INs, whereas PCD100 is the approximate end of excitatory neurogenesis in the cortex⁴². Macaque data from PCD110 ($n = 2$) were taken from ref. ⁹. In addition, we used public mouse datasets, including for embryonic day 13.5 (E13.5) and E14.5 ganglionic eminences, which were enriched for DLX6⁺ cells¹⁰, and three samples from the 10x Genomics E18 mouse cortex example dataset with 1.3 million cells ([GSE93421](#); samples 1, 3 and 4). We also used mouse public datasets for E14, including neonatal cortex, subcortex¹¹ and whole-brain developmental structures as well as adult structures^{43,44}; P9 striatum⁴⁵, and adult OB¹². In total, we analysed single-cell transcriptomes from 109,112 cells from developing macaque, 76,828 cells from developing mouse and 141,065 total mouse cells. De-identified human tissue samples were collected with previous patient consent in strict observance of legal and institutional ethical regulations in accordance with the Declaration of Helsinki. Protocols were approved by the Human Gamete, Embryo, and Stem Cell Research Committee and the Committee on Human Research (institutional review board) at the University of California, San Francisco.

Single-cell RNA sequencing tissue processing

For the PCD40 to PCD100 macaques, dissections were performed in PBS under a stereo dissection microscope (Olympus SZ61). A number of regions were difficult to distinguish at earlier time points because key anatomical landmarks were still forming. Accordingly, presumptive regions were dissected such as motor versus somatosensory cortex before the appearance of the central sulcus or the anterior ends of the MGE and LGE. For single-cell dissociation, samples were cut into small pieces and incubated

with a prewarmed solution of papain (Worthington Biochemical Corporation) prepared according to the manufacturer's instructions for 10 min at 37 °C. After 30–60 min of incubation, samples were gently triturated with glass pipette tips, and the PCD100 macaque samples were further spun through an ovomucoid gradient to remove debris. Cells were then pelleted at 300g and resuspended in PBS supplemented with 0.1% BSA (Sigma). Samples for MULTIseq were prepared in strip tubes and were maintained at 4 °C for the labelling protocol, as described in McGinnis et al.⁴⁶. Single-cell RNA sequencing was completed using the 10x Genomics Chromium controller and version 2 or 3 3-prime RNA capture kits. Most samples were loaded at approximately 10,000 cells per well; up to 25,000 cells were loaded per lane for multiplexed samples. Transcriptome library preparation was completed using the associated 10x Genomics RNA library preparation kit. Multiseq barcode library preparation was completed as described in McGinnis et al.⁴⁶. Following library preparation, libraries were sequenced on Illumina HiSeq and NovaSeq platforms.

Alignments and gene models

Fastq files were generated from Illumina BCL files using bcl2fastq2. Genes were quantified using Kallisto release 0.46 (ref. ⁴⁷) and the RheMac10 genome assembly, newly annotated using the comparative annotation toolkit⁴⁸, as well as the transcript annotations of *Mus musculus* ENSEMBL release 100. A custom Kallisto reference for each species was created for the quantification of exons and introns together, in which introns were defined as the complement of exonic and intergenic space. The Kallisto index used *k*-mers of length 31. Public data were downloaded as raw fastq files or as BAM files that were converted back to fastq files. All data were processed from raw reads using the same Kallisto pipeline to minimize annotation and alignment artefacts.

Quality control

Kallisto–Bus output matrix files (including both introns and exons) were input to Cellbender (release 0.2.0; <https://github.com/broadinstitute/CellBender>), which was used to remove probable ambient RNA only. Only droplets with a greater than 0.99 probability of being cells (not ambient RNA), as calculated by the Cellbender model, were included in further analysis. Droplets with fewer than 800 genes detected, or greater than 40% ribosomal or 15% mitochondrial reads, were filtered from the dataset. Doublets were then detected and removed from the dataset using Scrublet (release 0.2.2; using threshold parameter 0.5).

Clustering and determination of homologous cell types

Much of the analysis pipeline was based on scanpy infrastructure and AnnData data structures⁴⁹. Counts in cells were normalized by read depth, log transformed and then scaled for each gene across all cells. Principal-component analysis was then performed using the top 12,000 most variable genes by applying the original Seurat variable gene selection method implemented in the scanpy package, with the 100 most variance-encompassing principal components used for the following steps. Batch correction was limited to the requirement that highly variable genes be variable in more than one sequencing sample and by application of batch-balanced k -nearest neighbours (BBKNN)⁵⁰ using the Euclidean distance of principal components to find 3 neighbours per batch in the developmental data and 12 neighbours per dataset in the developmental and adult merged mouse data. Leiden clustering using BBKNN-derived k -nearest-neighbour graphs was then applied according to the KNN graph with the scanpy resolution parameter set to 10 (or 7 in the developmental mouse dataset). Glia, along with excitatory progenitor and neuron clusters, were removed from the dataset in non-ganglionic eminence batches if their expression value was below the mean for two or more of the following genes: *GAD1*, *GAD2*, *DLX1*, *DLX2*, *DLX5* and *DLX6*. Cajal–Retzius cells (RMTW_ZIC1/RELN) met this threshold and served as a useful outgroup. These cells were considered to be derived from the rostromedial telencephalic wall (RMTW) on the basis of *ZIC1* and *RELN* expression even though they are known to have multiple origins⁵¹. After non-INs were removed, scaling, principal-component analysis and the following steps were repeated with this final IN dataset.

High-resolution Leiden clusters partitioned continuous differentiation trajectories of postmitotic initial classes into subclusters based on maturation stage. These high-resolution clusters were then manually merged to initial classes by using hierarchical clustering of cluster gene expression averages and distinctness of individual Leiden cluster markers as a guide. The nomenclature for merged clusters incorporates the presumptive spatial origin of the initial classes and specific marker genes. Spatial origin for each class was inferred according to the expression of canonical marker genes for the RMTW, MGE, LGE, CGE and VMF, such as *LHX5*, *NKX2.1*, *MEIS2*, *NR2F2* and *ZIC1* and was supported by immunostaining and the enrichment of these genes in cells from region-specific dissections. For merged species analysis, genes were normalized and scaled within species and were then merged for downstream analysis using BBKNN with 25 neighbours across and within species, the mutual nearest neighbours of which were used for Sankey plot comparison of developing macaques and mice. After clustering, the mean expression in each class was calculated for each gene that was among the original 12,000 most variable one-to-one orthologues from each dataset showing variability in both species (6,227 genes). These classes were then compared across species by Pearson correlation of their gene expression vectors.

Trajectory analysis of activating and inactivating macaque genes

We applied scVelo's dynamical model (release 0.2.3)⁵² to derive a shared latent time based on RNA velocity using spliced and unspliced counts from Kallisto. Next, we used the related CellRank (release 1.3.1) package¹⁵ to derive absorption probabilities for immature cells in the transition cluster to likely initial classes. This step was necessary because new-born neurons, like children, are more similar to each other than to their mature state. By using adjacency along the paths of differentiation, it is possible to infer which mature state is likely to absorb a given immature cell. We then classified the new-born neurons as cells below the 0.5 quantile of latent time for that class. Recent studies have indicated that these transcriptionally immature neurons correspond to new-born neurons as labelled by classical nucleoside-based methods⁵³. To identify genes that were activated or inactivated along trajectories, we used linear regression implemented in SciPy based on latent time values (x) versus gene expression values (y). This yielded linear regression coefficients and two-tailed P values for each gene, which were corrected for multiple-hypothesis testing using the Holm–Sidak method implemented in the statsmodels (release 0.12.2) package to derive q values. The gene sets were compared by calculating the Jaccard indices of set intersections, defined as the number of intersecting elements between two sets divided by the number of elements in the union of the two sets.

Linking developmental and adult data

Similarly to the reassignment of macaque transition cells, we also used CellRank-derived absorption probabilities, with equally weighted KNN and RNA velocity kernels, to estimate the precursor states of adult cells. Because absorption probabilities are biased by cell numbers in terminal states, and the goal this time was not to assign each developmental cell to a terminal state, we subsampled a maximum of 1,000 cells per class, with the rarest class having 707 cells from MGE_CRABP1/MAF, and we report the class identity of the 100 developing cells with the highest probability of being absorbed into each terminal class. This enabled us to provide an estimate of which developing class was the likely origin of the terminal classes, which is reflected in the weights of the edges in the Sankey diagram in Fig. 2. We also calculated the mean absorption probability for cells in each initial class to each terminal state to alleviate compositional effects, which we present as a heatmap. Notably, RMTW_ZIC1/RELN and VMF_TMEM163/OTP were not included because they are excitatory cortical and hypothalamic classes, respectively.

Immunohistochemistry tissue processing and imaging

Mouse, macaque and human tissues for histology were fixed in 4% paraformaldehyde in PBS overnight at 4 °C with constant agitation. The paraformaldehyde was then

replaced with fresh PBS (pH 7.4) and samples were cryopreserved by incubation for 24–48 h in 30% sucrose diluted in PBS (pH 7.4) before being embedded in a mixture of OCT (Tissue-Tek, VWR) and 30% sucrose. Tissue was then frozen at –80 °C and was cryosectioned at 16–20 µm. For RNAscope RNA in situ hybridization, fixed cryosections were stained according to the protocol for the Advanced Cell Diagnostics RNAscope Multiplex Fluorescent Reagent Kit V2 Assay (ACD, 323120). For immunostaining, antigen retrieval was performed by placing tissue slides in 95 °C citrate buffer and then allowing them to cool at room temperature. Antibodies were diluted in blocking buffer (0.1% Triton X-100, 5% donkey serum and 0.2% gelatine in PBS). Sections were incubated with primary antibodies overnight at room temperature under bright light to photobleach autofluorescence in a light box⁵⁴. The primary antibodies and dilutions used are recorded in Supplementary Table 7.

Alexa dye-conjugated donkey secondary antibodies were incubated in the dark at room temperature for 1 h. All tiled scans were acquired using an Evos M7000 microscope. All images were stitched using a custom Python script and ImageJ’s max correlation grid/collection stitching (release 1.2). They were then processed using ImageJ (release 1.53c) Rolling Ball background subtraction and manual brightness/contrast adjustment within an ImageJ macro. Image quantification of CRABP1⁺ cells was conducted using a custom ImageJ macro with the CRABP1⁺ area automatically thresholded using maximum entropy. Positivity for other gene products was classified manually for every cell in at least five random areas in the striatum or MGE and was defined as >1 puncta within CRABP1⁺ areas not clearly belonging to another cell.

Reporting summary

Further information on research design is available in the [Nature Research Reporting Summary](#) linked to this paper.

Data availability

The sequencing data have been deposited in the Gene Expression Omnibus under accession number [GSE169122](#); the data are browsable at <https://dev-inhibitory-neurons.cells.ucsc.edu/>. Scripts and annotation files for the study have been deposited on github at <https://github.com/mtvector/dev-and-evo-of-primate-inhibitory-neurons>.

References

1. DeFelipe, J. et al. New insights into the classification and nomenclature of cortical GABAergic interneurons. *Nat. Rev. Neurosci.* **14**, 202–216 (2013).

2. Krienen, F. M. et al. Innovations present in the primate interneuron repertoire. *Nature* **586**, 262–269 (2020).
3. Flames, N. et al. Delineation of multiple subpallial progenitor domains by the combinatorial expression of transcriptional codes. *J. Neurosci.* **27**, 9682–9695 (2007).
4. Hansen, D. V. et al. Non-epithelial stem cells and cortical interneuron production in the human ganglionic eminences. *Nat. Neurosci.* **16**, 1576–1587 (2013).
5. Lim, L., Mi, D., Llorca, A. & Marín, O. Development and functional diversification of cortical interneurons. *Neuron* **100**, 294–313 (2018).
6. Ma, T. et al. Subcortical origins of human and monkey neocortical interneurons. *Nat. Neurosci.* **16**, 1588–1597 (2013).
7. Fishell, G. & Kepecs, A. Interneuron types as attractors and controllers. *Annu. Rev. Neurosci.* **43**, 1–30 (2020).
8. Rakic, P. Neurons in rhesus monkey visual cortex: systematic relation between time of origin and eventual disposition. *Science* **183**, 425–427 (1974).
9. Zhu, Y. et al. Spatiotemporal transcriptomic divergence across human and macaque brain development. *Science* **362**, eaat8077 (2018).
10. Mayer, C. et al. Developmental diversification of cortical inhibitory interneurons. *Nature* **555**, 457–462 (2018).
11. Loo, L. et al. Single-cell transcriptomic analysis of mouse neocortical development. *Nat. Commun.* **10**, 134 (2019).
12. Tepe, B. et al. Single-cell RNA-seq of mouse olfactory bulb reveals cellular heterogeneity and activity-dependent molecular census of adult-born neurons. *Cell Rep.* **25**, 2689–2703 (2018).
13. Wagner, D. E. & Klein, A. M. Lineage tracing meets single-cell omics: opportunities and challenges. *Nat. Rev. Genet.* **21**, 410–427 (2020).
14. Miller, J. A. et al. Common cell type nomenclature for the mammalian brain. *eLife* **9**, e59928 (2020).
15. Lange, M. et al. CellRank for directed single-cell fate mapping. *Nat. Methods* **19**, 159–170 (2022).

16. Paul, A. et al. Transcriptional architecture of synaptic communication delineates GABAergic neuron identity. *Cell* **171**, 522–539 (2017).
17. Tasic, B. et al. Shared and distinct transcriptomic cell types across neocortical areas. *Nature* **563**, 72–78 (2018).
18. Valero, M. et al. Sleep down state-active ID2/Nkx2.1 interneurons in the neocortex. *Nat. Neurosci.* **24**, 401–411 (2021).
19. Kuerbitz, J. et al. Loss of intercalated cells (ITCs) in the mouse amygdala of *Tshz1* mutants correlates with fear, depression, and social interaction phenotypes. *J. Neurosci.* **38**, 1160–1177 (2018).
20. Märtin, A. et al. A spatiomolecular map of the striatum. *Cell Rep.* **29**, 4320–4333 (2019).
21. Saunders, A. et al. Molecular diversity and specializations among the cells of the adult mouse brain. *Cell* **174**, 1015–1030 (2018).
22. Muñoz-Manchado, A. B. et al. Diversity of interneurons in the dorsal striatum revealed by single-cell RNA sequencing and PatchSeq. *Cell Rep.* **24**, 2179–2190 (2018).
23. Agoston, Z. et al. Meis2 is a Pax6 co-factor in neurogenesis and dopaminergic periglomerular fate specification in the adult olfactory bulb. *Development* **141**, 28–38 (2014).
24. Cave, J. W. et al. Differential regulation of dopaminergic gene expression by Er81. *J. Neurosci.* **30**, 4717–4724 (2010).
25. Kuerbitz, J. et al. Temporally distinct roles for the zinc finger transcription factor Sp8 in the generation and migration of dorsal lateral ganglionic eminence (dLGE)-derived neuronal subtypes in the mouse. *Cereb. Cortex* **31**, 1744–1762 (2021).
26. Luzzati, F. et al. Glia-independent chains of neuroblasts through the subcortical parenchyma of the adult rabbit brain. *Proc. Natl Acad. Sci.* **100**, 13036–13041 (2003).
27. Paredes, M. F. et al. Extensive migration of young neurons into the infant human frontal lobe. *Science* **354**, aaf7073 (2016).
28. Frazer, S. et al. Transcriptomic and anatomic parcellation of 5-HT 3A R expressing cortical interneuron subtypes revealed by single-cell RNA sequencing.

Nat. Commun. **8**, 14219 (2017).

29. Dubach, M. et al. Primate neostriatal neurons containing tyrosine hydroxylase: immunohistochemical evidence. *Neurosci. Lett.* **75**, 205–210 (1987).
30. Arendt, D. et al. The origin and evolution of cell types. *Nat. Rev. Genet.* **17**, 744–757 (2016).
31. Paredes, M. F., Sorrells, S. F., Garcia-Verdugo, J. M. & Alvarez-Buylla, A. Brain size and limits to adult neurogenesis. *J. Comp. Neurol.* **524**, 646–664 (2016).
32. Zhang, K. & Sejnowski, T. J. A universal scaling law between gray matter and white matter of cerebral cortex. *Proc. Natl Acad. Sci. USA* **97**, 5621–5626 (2000).
33. Stephan, H. & Andy, O. J. Quantitative comparative neuroanatomy of primates: an attempt at a phylogenetic interpretation. *Ann. N.Y. Acad. Sci.* **167**, 370–387 (1969).
34. Lledo, P.-M., Alonso, M. & Grubb, M. S. Adult neurogenesis and functional plasticity in neuronal circuits. *Nat. Rev. Neurosci.* **7**, 179–193 (2006).
35. Miller, D. J. et al. Prolonged myelination in human neocortical evolution. *Proc. Natl Acad. Sci. USA* **109**, 16480–16485 (2012).
36. Duchatel, R. J., Shannon Weickert, C. & Tooney, P. A. White matter neuron biology and neuropathology in schizophrenia. *NPJ Schizophr.* **5**, 10 (2019).
37. Diederich, N. J., Surmeier, D. J., Uchihara, T., Grillner, S. & Goetz, C. G. Parkinson’s disease: is it a consequence of human brain evolution? *Movement Disord.* **34**, 453–459 (2019).
38. Sousa, A. M. M. et al. Molecular and cellular reorganization of neural circuits in the human lineage. *Science* **358**, 1027–1032 (2017).
39. Betarbet, R. et al. Dopaminergic neurons intrinsic to the primate striatum. *J. Neurosci.* **17**, 6761–6768 (1997).
40. Björklund, A. & Dunnett, S. B. Dopamine neuron systems in the brain: an update. *Trends Neurosci.* **30**, 194–202 (2007).
41. Crick, F. C. & Koch, C. What is the function of the claustrum? *Philos. Trans. R. Soc. B Biol. Sci.* **360**, 1271–1279 (2005).

42. Clancy, B., Darlington, R. B. & Finlay, B. L. Translating developmental time across mammalian species. *Neuroscience* **105**, 7–17 (2001).
43. La Manno, G. et al. Molecular architecture of the developing mouse brain. *Nature* **596**, 92–96 (2020).
44. Zeisel, A. et al. Molecular architecture of the mouse nervous system. *Cell* **174**, 999–1014 (2018).
45. Anderson, A. G., Kulkarni, A., Harper, M. & Konopka, G. Single-cell analysis of Foxp1-driven mechanisms essential for striatal development. *Cell Rep.* **30**, 3051–3066.e7 (2020).
46. McGinnis, C. S. et al. MULTI-seq: sample multiplexing for single-cell RNA sequencing using lipid-tagged indices. *Nat. Methods* **16**, 619–626 (2019).
47. Bray, N. L., Pimentel, H., Melsted, P. & Pachter, L. Near-optimal probabilistic RNA-seq quantification. *Nat. Biotechnol.* **34**, 525–527 (2016).
48. Fiddes, I. T. et al. Comparative Annotation Toolkit (CAT)—simultaneous clade and personal genome annotation. *Genome Res.* **28**, 1029–1038 (2018).
49. Wolf, F. A., Angerer, P. & Theis, F. J. SCANPY: large-scale single-cell gene expression data analysis. *Genome Biol.* **19**, 15 (2018).
50. Polański, K. et al. BBKNN: fast batch alignment of single cell transcriptomes. *Bioinformatics* **36**, 964–965 (2020).
51. Bielle, F. et al. Multiple origins of Cajal–Retzius cells at the borders of the developing pallium. *Nat. Neurosci.* **8**, 1002–1012 (2005).
52. Bergen, V., Lange, M., Peidli, S., Wolf, F. A. & Theis, F. J. Generalizing RNA velocity to transient cell states through dynamical modeling. *Nat. Biotechnol.* **38**, 1408–1414 (2020).
53. Habib, N. et al. Div-seq: single-nucleus RNA-seq reveals dynamics of rare adult newborn neurons. *Science* **353**, 925–928 (2016).
54. Sun, Y., Ip, P. & Chakrabartty, A. Simple elimination of background fluorescence in formalin-fixed human brain tissue for immunofluorescence microscopy. *J. Vis. Exp.* <https://doi.org/10.3791/56188>(2017).
55. Miyoshi, G. et al. Genetic fate mapping reveals that the caudal ganglionic eminence produces a large and diverse population of superficial cortical

- interneurons. *J. Neurosci.* **30**, 1582–1594 (2010).
56. Stenman, J., Toresson, H. & Campbell, K. Identification of two distinct progenitor populations in the lateral ganglionic eminence: implications for striatal and olfactory bulb neurogenesis. *J. Neurosci.* **23**, 167–174 (2003).
 57. Speir, M. L. et al. UCSC Cell Browser: visualize your single-cell data. *Bioinformatics* **37**, 4578–4580 (2021).
 58. Kanton, S. et al. Organoid single-cell genomic atlas uncovers human-specific features of brain development. *Nature* **574**, 418–422 (2019).
 59. Alzu’bi, A. & Clowry, G. J. Multiple origins of secretagogin expressing cortical GABAergic neuron precursors in the early human fetal telencephalon. *Front. Neuroanat.* **14**, 61 (2020).

Acknowledgements

We thank A. Bhaduri, A. Alvarez-Buylla, J. Rubenstein, C. Harwell, M. Turrero Garcia, M. Andrews, S. Nolbrant, J. Wallace, S. Salama, I. Fiddes and members of the Pollen and Ye laboratories for helpful discussion and A. Li, S. Gaus, S. Wang, B. Alvarado, A. Tarantal and A. Fox for providing samples for genomic and histological analyses, and K. Probst for drawing the artwork in Fig. 4g. This study was supported by NIH awards F31NS124333 (M.T.S.), DP2MH122400-01 (A.A.P.), U01MH114825 (A.A.P., T.J.N.), R01AI136972 (C.J.Y.) and DP2NS122550-01 (M.F.P.); the Roberta and Oscar Gregory Endowment (M.F.P.); the Schmidt Futures Foundation (A.A.P., T.J.N.); the Chan Zuckerberg Biohub (C.J.Y., A.A.P., T.J.N.); and a grant from the Shurl and Kay Curci Foundation to the Innovative Genomics Institute (A.A.P.). A.A.P is a New York Stem Cell Foundation Robertson Investigator and member of the UCSF Kavli Institute for Fundamental Neuroscience.

Author information

Affiliations

1. Eli and Edythe Broad Center for Regeneration Medicine and Stem Cell Research, University of California, San Francisco, San Francisco, CA, USA

Matthew T. Schmitz, Christopher P. Chen, Mohammed A. Mostajo-Radji & Alex A. Pollen

2. Department of Neurology, University of California, San Francisco, San Francisco, CA, USA

Matthew T. Schmitz, Kadelyn Sandoval, Christopher P. Chen, Mohammed A. Mostajo-Radji, William W. Seeley, Mercedes F. Paredes & Alex A. Pollen

3. Weill Institute for Neurosciences, University of California, San Francisco, San Francisco, CA, USA

Kadelyn Sandoval, Tomasz J. Nowakowski, Mercedes F. Paredes & Alex A. Pollen

4. Department of Anatomy, University of California, San Francisco, San Francisco, CA, USA

Tomasz J. Nowakowski

5. Department of Psychiatry and Behavioral Sciences, University of California, San Francisco, San Francisco, CA, USA

Tomasz J. Nowakowski

6. Department of Neurological Surgery, University of California, San Francisco, San Francisco, CA, USA

Tomasz J. Nowakowski

7. Chan Zuckerberg Biohub, San Francisco, CA, USA

Tomasz J. Nowakowski, Chun Jimmie Ye & Alex A. Pollen

8. Institute for Human Genetics, University of California, San Francisco, San Francisco, CA, USA

Chun Jimmie Ye

9. Department of Epidemiology and Biostatistics, University of California, San Francisco, San Francisco, CA, USA

Chun Jimmie Ye

10. Parker Institute for Cancer Immunotherapy, San Francisco, CA, USA

Chun Jimmie Ye

Contributions

M.T.S., T.J.N., M.F.P. and A.A.P. designed the methodology. M.T.S. K.S., C.P.C., M.A.M., T.J.N. and A.A.P. performed the experiments. W.W.S., M.F.P., T.J.N. and A.A.P. acquired the analysis resources. M.T.S., C.P.C. and K.S. conducted the microscopic analysis. M.T.S., M.A.M., T.J.N. and A.A.P. performed the single-cell RNA sequencing processing. M.T.S. implemented the software and analysed the study data. M.T.S. and A.A.P. wrote the manuscript with input from all authors. M.T.S., T.J.N., M.F.P., C.J.Y. and A.A.P. acquired the funding. M.T.S., M.F.P. and A.A.P. conceptualized the study. T.J.N., C.J.Y., M.F.P. and A.A.P. supervised the project.

Corresponding author

Correspondence to [Alex A. Pollen](#).

Ethics declarations

Competing interests

C.J.Y. is a scientific advisory board member for and holds equity in Related Sciences and ImmunAI, is a consultant for and holds equity in Maze Therapeutics, and is a consultant for TReX Bio. C.J.Y. has received research support from the Chan Zuckerberg Initiative, the Chan Zuckerberg Biohub and Genentech.

Peer review

Peer review information

Nature thanks Gord Fishell, Jhumku Kohtz and the other, anonymous, reviewer(s) for their contribution to the peer review of this work. Peer reviewer reports are available.

Additional information

Publisher's note Springer Nature remains neutral with regard to jurisdictional claims in published maps and institutional affiliations.

Extended data figures and tables

[Extended Data Fig. 1 Birthdates of initial classes of INs in macaque.](#)

a. Drawings of the lateral view of developing macaque brains across stages surveyed in this study and estimated comparable human and mouse stages based on the translating time model⁴² of cortical neurogenesis. **b.** Spatiotemporal distribution of new-born neurons, as determined by RNA velocity latent time, from each class as a proxy for birthdate. Bars represent the proportion of cells from each class in each region, at each timepoint (columns sum to 1). Cajal-Retzius neurons, MGE-derived cortical interneurons, and LGE-derived projection neurons first appeared early in development, starting at PCD40, followed by the later appearance of immature CGE-derived cortical interneurons and LGE_MEIS2/PAX6 neurons, consistent with broad patterns of temporal ordering in mouse^{51,55,56}. **c.** UMAP showing which cells are new-born in red (latent time < 0.5 quantile of latent time for each class) or maturing (>0.5 quantile) in blue. Clearly cycling progenitors are not included. **d.** Kamada-Kawai graph visualization of Pearson correlations between a gene pair's expression highlight the emergence of initial class gene co-expression patterns during macaque neuronal differentiation. Edges shown are Holm-Šídák corrected q value < 0.05 calculated by bootstrap, with thickness and color representing correlation. **e.** Stacked bar chart showing number of macaque cells collected at each timepoint, colored by region from which the cells are derived. Note undersampling of VMF structures between PCD50 and PCD100. **f.** Normalized stacked bar chart showing regions from which each macaque initial class is derived across the whole dataset. **g.** Violin plot showing the distribution of genes detected per cell for each macaque batch. **h.** Violin plot showing the distribution genes per cell detected for each mouse dataset.

[Extended Data Fig. 2 Macaque single cell RNAseq gene expression landscape.](#)

a. Macaque scRNAseq UMAP colored by post conception day from which cells are sampled. **b.** UMAP projection colored by cell-cycle phase as classified by scanpy score_genes_cell_cycle function. **c.** UMAP projection colored by Leiden clusters. Although cell intrinsic differences within initial classes may predict their further subclass partitioning, the fine-grained Leiden clusters did not yield groups appearing to match terminal classes and mainly varied by neuronal differentiation trajectories. **d–i.** Scaled and normalized expression of **d**, dividing and new-born neuron marker genes **e**, CGE-derived neuron markers **f**, dLGE-derived neuron markers **g**, LGE-derived projection neuron markers **h**, MGE-derived cortical neuron markers **i**, MGE-derived striatal interneuron markers. An interactive browser for exploring the transcriptional features of inhibitory neuron development is available (<https://dev-inhibitory-neurons.cells.ucsc.edu/>)⁵⁷.

[Extended Data Fig. 3 Mouse single cell RNAseq gene expression landscape.](#)

a. Mouse scRNAseq UMAP colored by public dataset from which the cells are derived. **b.** UMAP projection colored by cell-cycle phase as classified by scanpy score_genes_cell_cycle function. **c.** UMAP projection colored by Leiden clusters. **d–i** Scaled and normalized expression of **d**, dividing and new-born neuron marker genes **e**, CGE-derived neuron markers **f**, dLGE-derived neuron markers **g**, LGE-derived projection neuron markers **h**, MGE-derived cortical neuron markers **i**, MGE-derived striatal interneuron markers **j**, VMF-derived markers.

Extended Data Fig. 4 Markers of mouse and macaque initial classes.

a. Heatmap of mouse initial class marker genes selected from the top markers of each, scaled by column. **b.** Scatterplots of log 2 fold changes of each initial class vs the rest of the dataset for mouse vs macaque, with selected gene families of interest labeled. Conserved represents genes significantly upregulated in class vs rest in both species, Mouse-specific in mouse but not macaque, etc. N.S.= Not Significant in either species. Significance defined as $|\log_{2}fc| > 1.2$ and adjusted p value $< .01$, with significance marked "signif" in Supplementary Table 3. MGE_CRABP1/TAC3* is the comparison of macaque MGE_CRABP1/TAC3 vs mouse MGE_CRABP1/MAF, as this is the ancestral class comparison. Note that more genes show specific correlations to the macaque MGE_CRABP1/TAC3 class versus the macaque MGE_CRABP1/MAF class in the comparison to the single mouse MGE_CRABP1/MAF class. **c.** Pairwise Pearson correlations of mean gene expression in classes across species.

Extended Data Fig. 5 Inhibitory neurons of the developing and adult mouse forebrain.

a. UMAP projection of developing and adult mouse single cell RNAseq data, with initial and terminal classes labeled. **b.** UMAP of all mouse data, labeled by the post conception timepoint from which the cells are derived. **c.** UMAP of all mouse data, labeled by Leiden clusters used to determine terminal classes. **d.** UMAP of all mouse data, labeled by the scVelo dynamical shared latent time of each cell. **e.** Normalized stacked barplot, showing proportion of total cells of each class from each region. **f.** UMAP of all mouse data, labeled by the region from which the cells are derived. **g.** UMAP of all mouse data, labeled by the public dataset from which cells are derived. **h.** Heatmap representing the mean absorption probabilities of cells in each initial class to each terminal class. **i.** Selected genes differentially expressed in all terminal classes over all initial classes. **j.** Selected genes differentially expressed in initial classes over terminal classes.

Extended Data Fig. 6 Expression of CRABP1+/TAC3+ and MAF+ striatal interneuron markers in developing macaque.

a. UMAP projection of NKX2-1/CRABP1+/ETV1+ cells only colored by scaled and normalized expression of TAC3 or MAF class markers. **b.** Allen Institute E15.5 mouse brain in situ hybridization showing expression of CRABP1+ neuron-related regional transcription factors. Green circle denotes boundary between *Lhx8*+ MGE and rostroventral MGE/septum known to produce cholinergic neurons and the *Etv1*+ MGE thought to produce CRABP1+ striatal interneurons, indicating partitioning of *Etv1* and *Lhx8* domains in mouse MGE. **c.** SCENIC module scores (Y-axis) vs log2 fold change of hub transcription factor predicted to regulate the module (X-axis). Significance represents multiple testing corrected q-value < 0.1 for both diffxpy differential expression in macaque and also q-value < 0.1 SCENIC logistic regression coefficient q-value calculated by shuffling class labels. Size represents the proportion of all CRABP1+ cells which also express the gene. **d.** UMAP projection showing the region from which macaque cells are derived. **e.** UMAP projection showing classes in cells expressing 2 or more of (CRABP1, ETV1, ANGPT2). **f.** Subclustering of rare NKX2-1+ cells from organoid dataset⁵⁸, labeled by Leiden subclusters. **g.** NKX2-1+ cells from organoid dataset⁵⁸, labeled by the experimental conditions of the differentiation. **h.** Dotplot of expression of MGE_CRABP1 related markers in Leiden subclusters showing cluster 6 likely contains MGE_CRABP1/MAF and MGE_CRABP1/TAC3 cells.

Extended Data Fig. 7 Spatial distribution of CRABP1+/TAC3+ and MAF+ striatal interneuron marker expression.

a. PCD65 macaque brain section, from different individual than main text quantifications showing RNA expression of alternative markers of both CRABP1 classes (*ANGPT2*), the MGE_CRABP1/MAF class (*RBP4*) and the MGE_CRABP1/TAC3 class (*STXBP6*). Note that *RBP4* expression is rare at PCD65, but much more common at PCD80 (see **c, d**). **b.** Montage from **a** showing MGE_CRABP1/MAF (cyan arrows), MGE_CRABP1/TAC3 (magenta arrows) and STXBP6+/RBP4+ cells (green arrows). **c.** PCD80 macaque brain section showing RNA expression of alternative markers of both CRABP1 classes (*ANGPT2*), the MGE_CRABP1/MAF class (*RBP4*) and MGE_CRABP1/TAC3 (*STXBP6*). **d.** Montage from **c** showing MGE_CRABP1/MAF (cyan arrows), MGE_CRABP1/TAC3 (magenta arrows) and STXBP6+/RBP4+ cells (green arrows). **e.** PCD65 macaque brain section showing RNA expression of *CRABP1*, marking both CRABP1 classes, *ETV1*, marking both CRABP1 classes, the dLGE, and the GP, *TAC3* marking the MGE_CRABP1/TAC3 class and MKI67 marking dividing cells. Labeled regions are abbreviated LV: Lateral Ventricle, MGE: Medial Ganglionic Eminence, Str: Striatum, GP: Globus Pallidus, AC: Anterior Commissure **f.** Montage from **e** showing MGE_CRABP1/TAC3 (magenta arrows) and TAC3+/MKI67+ cells (red arrows).

Extended Data Fig. 8 CRABP1+/TAC3+ and MAF+ striatal interneuron marker expression.

Full size tile scanned representative images from Fig. 3c. **a-d**. Sections 0, 37, 66, and 101 four color in situ hybridization for CRABP1, LHX8, MAF, TAC3.

Extended Data Fig. 9 Spatial, temporal, and molecular distinctions among initial LGE-derived neurons.

a. Bar plot of the proportion of cells from each initial class across cortical regions for CGE-, LGE- and MGE-derived classes highlights frontal lobe enrichment of LGE classes during sampling. **b.** Schematic for c, showing cartoon scatter plots for the expression of two genes in individual cells regressed against latent time (left) to describe genes that activate or inactivate during neuronal differentiation, followed by Venn diagrams showing the overlap of dynamically regulated genes between pairs of initial classes used to calculate Jaccard indices. **c.** Heatmap of Jaccard indices of significantly overlapping lists of dynamic genes between cell classes of Holm-Šídák corrected linear regression q value < 0.05 on scaled and normalized gene expression to address the extent of shared versus cell type-specific trajectories during post-mitotic differentiation of initial classes. Bar graphs on axes represent the total number of significant genes activating/inactivating. Direct and indirect medium spiny neurons (LGE_FOXP1/ISL1 and LGE_FOXP1/PENK) show strong overlap of both activating and inactivating genes, despite early partitioning as distinct initial classes, while presumed eccentric spiny neurons from LGE_FOXP2/TSHZ1 show strong overlap of activating genes (see also g) but not inactivating genes. Conversely, MGE_CRABP1/MAF and MGE_CRABP1/TAC3 classes show strong overlap of inactivating genes among a smaller overall set of dynamically regulated genes, but little overlap in activating genes. **d.** Heatmap of selected marker expression of LGE-derived striatal initial and terminal classes, scaled by gene. **e.** Gene expression of dynamic dLGE marker genes in macaque LGE_FOXP2/TSHZ1 cells across shared latent time, ordered by latent time value and divided into 10 equally sized bins to provide stable mean expression values. **f.** Gene expression of dynamic marker genes in macaque cells across shared latent time, grouped by initial class, ordered by latent time value and divided into 30 equally sized bins to provide stable mean expression values. **g.** Venn diagram of intersections of significantly activating gene sets in LGE initial classes. In contrast to LGE_MEIS2/PAX6, the LGE_FOXP2/TSHZ1 class activates a large set of shared SPN genes during neuronal differentiation as inferred by latent time trajectories.

Extended Data Fig. 10 Emergence of Str-eSPN_FOXP2/TSHZ1 from LGE_FOXP2/TSHZ1 in the dLGE.

a. PCD80 macaque coronal section showing RNA expression of eSPN markers. The Lateral Migratory Stream (LMS) is noted as is shown in Kuerbitz et al¹⁹. **b.** Montage of magnified dLGE at the striatum-GE boundary. **c.** Montage from the box in **b** showing TSHZ1/CASZ1/OPRM1- (top arrow) and TSHZ1/CASZ1/OPRM1+ (bottom arrow) Str-eSPN_FOXP2/TSHZ1 cells (blue arrows) within the GE.

Extended Data Fig. 11 Distribution of dLGE-derived LGE FOXP2/TSHZ1 precursors in the superficial white matter.

a. Medial sagittal section of PCD80 macaque brain. The SCGN+ RMS originating at the anterior pole of the dLGE is seen extending from the olfactory ventricle to the OB. **b.** FOXP2+/PAX6+ cells from lateral migratory streams converge with RMS and enter periglomerular layers of OB (see also Extended Data Fig. 1). Note that FOXP2+ OB-PGC_FOXP2/CALB1 cells are largely absent from the RMS but are found ventral of the nucleus accumbens (NAc), anterior olfactory nucleus (AON) and in outer olfactory tract sheath. **c.** SCGN+/PAX6+ granule cells (OB-GC_MEIS2/PAX6) (cyan arrows), TH+ PGCs (OB-PGC_TH/SCGN) (yellow arrows) and FOXP2+ PGCs (OB-PGC_FOXP2/CALB1) (blue arrows) in OB. **d–f.** Human gestation week 20.5 sagittal cortex section shows new-born FOXP2+/SCGN+/PROX1- neurons (blue arrows) migrating into the ventral cortex superficial white matter. SCGN+ expression decreases as cells mature. **g.** Lateral sagittal section of PCD80 macaque brain. **h.** Immunofluorescence FOXP2+/FOXP4+/SCGN+ dLGE-derived projection class neurons (blue arrows) are seen in large numbers in the dLGE portion dorsal of the caudate, and in adjacent cortical white matter and striatum. **i.** 7 month old macaque coronal section. **j.** Montage from box in **i** with rare DLX2/FOXP2+ superficial white matter IN (SWMIN) marked with a blue arrow.

Extended Data Fig. 12 dLGE migration streams.

a–d. PCD 80 macaque brain sagittal section. Blue arrows represent SP8+/FOXP2+ cells in **(b)** septum and fornix (it is unclear whether these cells are born here, or arrive via an RMS dorsal extension or via a cortex-indusium griseum-fornix route, possibly seen in⁵⁹) **(c)** anterior olfactory nucleus (these cells appear to be near the point where the LMS is converging with the RMS, suggesting a lateral source of FOXP2+ PGCs) and **(d)** vmPFC. **e, f.** Coronal section of macaque PCD80 brain shows large numbers of SP8+/FOXP2+ cells and SP8+/MKI67+ cells in DL-dLGE. **g.** Sagittal section of anterior olfactory nucleus. New-born dLGE-derived PAX6+/SCGN+/FOXP2- labeled with yellow arrows. **h.** Oblique coronal-axial section of dLGE and PFC with insets highlighting DLX2+/SP8+/FOXP2- parenchymal chains. **i.** Oblique coronal-horizontal section of dLGE and PFC with insets highlighting MEIS2+/SCGN+/PROX1- parenchymal chains. **j.** Coronal section of PCD65 macaque brain with lateral ventricle (LV), striatum (Str), dLGE and approximate lateral migratory stream (LMS) labeled.

Extended Data Fig. 13 A-dLGE cells in the Arc.

a. Low magnification stitching of oblique horizontal section showing large stream of MEIS2+/SCGN+ chains in the Arc along the dorsomedial edge of the TH+ striatum. **b.** Further dorsal oblique horizontal section showing dorsal and lateral migratory streams. **c.** Enlargement of Arc-ACC. Cyan arrows denote MEIS2+/SCGN+ dLGE cells. Note that the stream is continually bounded by the increased density of TH+ fibers. **d.** Chains caudal of the striatum are of mixed classes. **e.** White matter neurons lateral of the striatum are nearly all MEIS2-negative (green arrows). Also note peristriatal SP8+/MEIS2+/TH+ *striatum laureatum* neurons (SLNs) at lateral border of striatum (yellow arrows). **f.** Coronal section of PCD120 macaque striatum showing an array of TH+ peristriatal SLNs(yellow arrows) at the edge of the caudate nucleus, from Fig. 3b, at the same location as 7 month postnatal, but not yet having developed SCGN+/TH+ processes tangential to the external capsule. **g, h.** Coronal section of PCD120. Sparse MKI67+ cells at ventricle, with SCGN+ cells away from the ventricle being MKI67-. **i, j.** Chains in Arc do not appear to be MKI67+. **k.** PCD120 SCGN/TH+ peristriatal SLNs (yellow arrows) are NR2F2 negative (NR2F2+ DWMINs labeled with green arrows). Note that the LGE_MEIS2/PAX6 and LGE_FOXP2/TSHZ1 classes very sparsely expressed the transcript encoding tyrosine hydroxylase (TH), a rate limiting enzyme in dopamine production, and were the only cortical IN classes to do so at developmental stages (see Fig. 4b). **l.** Coronal section of macaque cortex at 7 months. **m.** PAX6+/SCGN+/NR2F2- deep white matter neurons in postnatal macaque cingulate cortex (cyan arrows). These DWMINs were found in the cingulate white matter and corona radiata, though not in the corpus callosum itself and rarely near the deep layers of the cortical plate and external capsule white matter.

Extended Data Fig. 14 Distribution of LGE MEIS2/PAX6-derived cells in postnatal mouse.

a. Mouse sagittal section showing **b** and approximate **c** magnification locations. **b.** LGE_MEIS2/PAX6 cells in deep white matter (cyan arrows) **c.** Lateral sagittal section **d.** Panel showing SP8+/MEIS2+/PAX6+ cells in remainder of dLGE, likely homologous to dLGE chains in Arc. **e.** Lateral sagittal section of mouse postnatal day 2. **f.** MEIS2+/SCGN+/TH+ periglomerular cells in lateral OB. **g.** Striatum shown with dense TH+ projection fibers and synapses, but no MEIS2+/SCGN+/TH+ cell bodies.

Extended Data Fig. 15 Full montages of Fig. 5 peristriatal striatum laureatum neurons.

a. Remnant immature neurons of the RMS from 7m macaque (large white arrow) with migrating morphology MEIS2+/SCGN+ cells (teal arrows). **b.** Montage of edge of

striatum with arrows pointing to MEIS2+/SCGN+/TH+ SLNs. **c.** Montage of claustrum with yellow arrows pointing to MEIS2+/SCGN+/TH+ peristriatal SLNs. The TH+/SCGN+ process is labeled with orange arrowheads while TH-/SCGN+ process is labeled with white arrowheads. **d.** Photograph of 88 year old brain with approximate region of **e** in box. **e.** Montage of separate channels of the SLN shown in Fig. 5h.

Supplementary information

Reporting Summary

Peer Review File

Supplementary Table 1

Sample metadata. Region, stage, individual and sequencing quality-control metrics for each sample.

Supplementary Table 2

Cell metadata. Region, stage and individual for each cell in the macaque and mouse samples.

Supplementary Table 3

Class-specific marker genes. Table of logistic regression and diffxpy differential expression output values of each class versus all for determination of class markers. *q* values are the diffxpy multiple-hypothesis testing-corrected, two-sided *P* values.

Supplementary Table 4

Dictionary of initial and terminal classes. Qualitative definitions of classes explored in the atlas with extended explanations for inferences about initial–terminal class relationships.

Supplementary Table 5

Class-specific postmitotic trajectory genes. Linear regression coefficients, regression *P* values and Holm–Sidak *q* values of latent time regressed against normalized expression for each gene. Also includes logistic regression coefficients of class versus all markers.

Supplementary Table 6

MAF versus TAC3 differentially expressed genes. Table of diffxpy differential expression output values of MGE_CRABP1/TAC3 versus MGE_CRABP1/MAF. *q* values are the diffxpy multiple-hypothesis testing-corrected, two-sided *P* values.

Supplementary Table 7

Antibody information. Dilutions, manufacturers and lots of antibodies used in this study.

Rights and permissions

Open Access This article is licensed under a Creative Commons Attribution 4.0 International License, which permits use, sharing, adaptation, distribution and reproduction in any medium or format, as long as you give appropriate credit to the original author(s) and the source, provide a link to the Creative Commons license, and indicate if changes were made. The images or other third party material in this article are included in the article's Creative Commons license, unless indicated otherwise in a credit line to the material. If material is not included in the article's Creative Commons license and your intended use is not permitted by statutory regulation or exceeds the permitted use, you will need to obtain permission directly from the copyright holder. To view a copy of this license, visit <http://creativecommons.org/licenses/by/4.0/>.

Reprints and Permissions

About this article

Cite this article

Schmitz, M.T., Sandoval, K., Chen, C.P. *et al.* The development and evolution of inhibitory neurons in primate cerebrum. *Nature* **603**, 871–877 (2022).
<https://doi.org/10.1038/s41586-022-04510-w>

- Received: 19 March 2021
- Accepted: 01 February 2022
- Published: 23 March 2022
- Issue Date: 31 March 2022

- DOI: <https://doi.org/10.1038/s41586-022-04510-w>

Share this article

Anyone you share the following link with will be able to read this content:

[Get shareable link](#)

Sorry, a shareable link is not currently available for this article.

[Copy to clipboard](#)

Provided by the Springer Nature SharedIt content-sharing initiative

This article was downloaded by **calibre** from <https://www.nature.com/articles/s41586-022-04510-w>

| [Section menu](#) | [Main menu](#) |

- Article
- Open Access
- [Published: 16 March 2022](#)

A multidimensional coding architecture of the vagal interoceptive system

- [Qiancheng Zhao^{1,2},](#)
- [Chuyue D. Yu^{1,2,3},](#)
- [Rui Wang^{1,2},](#)
- [Qian J. Xu^{1,2,3},](#)
- [Rafael Dai Pra](#) [ORCID: orcid.org/0000-0001-5282-0682²](#),
- [Le Zhang⁴](#) &
- [Rui B. Chang](#) [ORCID: orcid.org/0000-0001-6953-2943^{1,2}](#)

Nature volume **603**, pages 878–884 (2022)

- 16k Accesses
- 125 Altmetric
- [Metrics details](#)

Subjects

- [Autonomic nervous system](#)
- [Neurophysiology](#)
- [Sensory processing](#)

Abstract

Interoception, the ability to timely and precisely sense changes inside the body, is critical for survival^{1,2,3,4}. Vagal sensory neurons (VSNs) form an important body-to-brain connection, navigating visceral organs along the rostral–caudal axis of the body and crossing the surface–lumen axis of organs into appropriate tissue layers^{5,6}. The brain can discriminate numerous body signals through VSNs, but the underlying coding strategy remains poorly understood. Here we show that VSNs code visceral

organ, tissue layer and stimulus modality—three key features of an interoceptive signal—in different dimensions. Large-scale single-cell profiling of VSNs from seven major organs in mice using multiplexed projection barcodes reveals a ‘visceral organ’ dimension composed of differentially expressed gene modules that code organs along the body’s rostral–caudal axis. We discover another ‘tissue layer’ dimension with gene modules that code the locations of VSN endings along the surface–lumen axis of organs. Using calcium-imaging-guided spatial transcriptomics, we show that VSNs are organized into functional units to sense similar stimuli across organs and tissue layers; this constitutes a third ‘stimulus modality’ dimension. The three independent feature-coding dimensions together specify many parallel VSN pathways in a combinatorial manner and facilitate the complex projection of VSNs in the brainstem. Our study highlights a multidimensional coding architecture of the mammalian vagal interoceptive system for effective signal communication.

[Download PDF](#)

Main

Sensing the body’s internal state is a critical life-ensuring process that maintains physiological homeostasis, provides motivational drivers and shapes our thoughts and emotions^{1,2,3,4}. As a key body–brain axis in interoception, VSNs in the nodose and jugular ganglia transmit numerous signals from visceral organs in the respiratory, cardiovascular, gastrointestinal, endocrine and immune systems into the brainstem^{5,6}. Signals communicated through VSNs are precisely discriminated in the brain for highly specific responses⁵, yet how this is achieved remains unclear. Extensive data show that VSNs are highly heterogeneous in multiple characteristics, including developmental origins, electrical properties, response patterns, molecular identities, terminal morphologies, sensory mechanisms, anatomical connections and physiological roles^{5,6,7,8,9,10,11,12,13,14,15,16,17,18,19}. However, despite the accumulation of a large amount of data over the past seven decades describing the complexity of VSN characteristics, little is known about how such heterogeneity and diversity facilitates interoceptive coding at a systems level.

The physiological role of an interoceptive signal can be specified by three important features: visceral organ; tissue layer; and stimulus modality. Stimuli that differ in these features represent different body changes. For example, stretching the arterial wall implicates an increase in blood pressure, whereas stretching the stomach wall signals food ingestion^{15,20}. Similarly, the same bioactive signal (such as serotonin) released from different tissue layers within the intestine communicates different organ information to the brain²¹. We reasoned that a faithful coding of these features in VSNs is necessary for accurate signal discrimination in the brain. Here we developed

several techniques to determine whether and how these essential features of interoceptive signals are coded in VSNs.

‘Visceral organ’ coding in VSNs

A gross topographic organization of visceral organs exists in paravertebral ganglia along the sympathetic chain and dorsal root ganglia (DRG) along the spinal cord^{22,23}. Whether a viscerotopic map exists in the nodose ganglion, where most visceral-organ-innervating VSNs are located⁶, is a subject of debate^{12,24,25,26,27}. Using retrograde adeno-associated virus (AAVrg), we show that VSNs labelled from various visceral organs are largely non-overlapping (Extended Data Fig. [1a–d](#)), which suggests that organ information is encoded within VSNs. However, their salt-and-pepper distribution patterns indicate that a viscerotopic map is missing in the nodose ganglion.

We therefore hypothesize that visceral organs are coded by specific genes in VSNs. We developed a single-cell sequencing approach named ‘Projection-seq’ for unbiased, high-throughput genetic and anatomical dissection of complex neural circuits (Fig. [1a](#)). Engineered from AAVrgs, Projection-seq AAVs encode a series of unique projection barcodes (UPBs) composed of exogenous nucleotide sequences, thus enabling large-scale multiplex sequencing with neuronal projection information. We injected Projection-seq AAVs with different UPBs into seven major visceral organs of the same mice, including the lung, heart, stomach, oesophagus, duodenum, pancreas and transverse colon (Fig. [1a](#)). AAVrgs cover most subregions in all examined organs and specificity is ensured by no labelling of vagal motor neurons (Extended Data Fig. [1e–w](#)). VSNs that project to adjoining regions between two organs, such as the oesophageal and pyloric sphincters, can be accurately identified with UPBs from both organs as AAVrg slightly diffuses to adjacent areas (Extended Data Fig. [1v,w](#)). The infection efficiencies of Projection-seq AAVs were comparable to regular AAVrgs, and UPBs were successfully detected from retrogradely infected VSNs (Extended Data Fig. [2a–c](#)).

Fig. 1: ‘Visceral organ’ coding in VSNs.

 **figure 1**

a, Schematic illustration of Projection-seq analysis of VSNs innervating the lung, heart, oesophagus, stomach, duodenum, transverse colon and pancreas. Organ illustrations were adapted from BioRender.com. **b**, UMAP plot from Projection-seq of 14,590 *Phox2b*⁺ VSNs (30 mice divided into 4 samples) showing 52 clusters (A1–L2)

in 12 VSN subpopulations (A–L) (top) or VSNs expressing UPBs representing 7 visceral organs (colour-coded) (bottom). **c**, Two-dimensional (2D) (top) and three-dimensional (3D) (bottom) UMAP plots of VSNs innervating different physiological systems. E-VSNs were excluded. The three heart VSN groups (red, arrowheads) are clustered together away from other gut VSNs (green) in the 3D UMAP plot. **d**, Dot plot showing transcription factors that are differentially expressed in lung, heart, gut and pancreas VSNs. **e**, UMAP plot of VSN clusters, coloured by target preference (weighted organ position score), showing a ‘visceral organ’ trajectory (arrow) coding visceral organs along the body’s rostral–caudal axis. **f**, Correlation between the normalized position of the indicated organs along the body’s rostral–caudal axis (mean; $n = 4$) and the position of VSNs expressing indicated organ UPBs along the ‘visceral organ’ trajectory (organ trajectory score; mean \pm s.e.m.; n as indicated). Linear regression $R^2 = 0.7547$. **g**, Histograms showing the distributions of UPB-labelled VSNs (colour-coded) along the identified ‘visceral organ’ trajectory. The bars underneath indicate normalized organ positions along the body’s rostral–caudal axis (beginning–end; mean \pm s.e.m.; $n = 4$).

Source Data

In total 14,590 *Phox2b*⁺ placode-derived nodose VSNs^{13,17,18} (of 25,393 cells after quality filtering) were grouped into 12 subpopulations (A–L) and 52 clusters (A1–L2) on the basis of differentially expressed genes (DEGs) using Seurat and visualized using uniform manifold approximation and projection (UMAP) (Fig. 1b, Extended Data Fig. 2d). VSNs labelled from each of the seven organs were identified using corresponding UPBs with extremely high detection efficiency (Fig. 1b, Extended Data Fig. 2c). The distribution of UPBs recapitulated AAVrg coverage in the organs (Extended Data Fig. 2e). VSN clusters and patterns of gene expression were similar among control label-free single-cell RNA sequencing (scRNA-seq), RNAscope HiPlex *in situ* hybridization and Projection-seq data (Extended Data Fig. 2f–n), showing that viral infection did not alter gene expression in VSNs. The genetic identities of organ-UPB-marked VSNs were further validated using RNAscope (Extended Data Fig. 2o–q). VSNs that are damaged by cell dissociation and viral infection can be easily identified (VSN subpopulation E, referred as E-VSNs; same for other subpopulations) and removed from analysis (Extended Data Fig. 3a–d). Together, Projection-seq results faithfully represent VSN clusters, gene expression and neuronal projections.

Projection-seq analysis reveals a genetic segregation of VSNs that innervate organs in the respiratory (lung), cardiovascular (heart), gastrointestinal (oesophagus, stomach, duodenum and transverse colon) and exocrine–endocrine (pancreas) systems (Fig. 1c, Extended Data Fig. 3e). Gut VSN clusters exhibit unique preferences for specific gastrointestinal regions (Extended Data Fig. 3f). DEG analysis identified a set of

transcription factors that may help define VSN identity for visceral organs (Fig. 1d, Extended Data Fig. 3g–h), many of which are critically involved in the development and differentiation of sensory neurons^{28,29,30,31,32}. Of note, it seems that VSNs are primed for the functions of their target organs. For example, the stomach contains several anatomically and functionally distinct subregions: the proximal region similar to the oesophagus and the distal region similar to the intestine³³. Accordingly, UPB-stomach⁺/UPB-oesophagus⁺ VSNs are genetically similar to oesophagus VSNs, whereas UPB-stomach⁺/UPB-duodenum⁺ VSNs are closer to duodenum VSNs (Extended Data Fig. 3f). Consistent with this notion, cell–cell interaction analyses suggest that VSNs use different ligand–receptor complexes to communicate with cells in different organ systems (Extended Data Fig. 3i). Together, our results reveal that VSNs use differential gene module expression to code visceral organs.

Notably, we further identified a genetic trajectory that represents visceral organs along the body’s rostral–caudal axis (Fig. 1e). The relative positions of VSNs along this trajectory (‘visceral organ’ trajectory score) on the UMAP plot had a strong linear relationship with the locations of their target organs along the body’s rostral–caudal axis (Fig. 1f,g). Anatomically, most vagal afferents travel together along a general path before branching off to their target organs, instead of making organ-specific projection pathways⁶. Our discovery of a genetic ‘visceral organ’ trajectory is in accordance with this long-standing observation, suggesting that VSNs might follow morphogen gradients to their target spots. Indeed, signalling gradients formed by secreted morphogens help to establish an anterior–posterior patterning³⁴ and specify peripheral targets for vagal motor neurons³⁵. Together, our data show that instead of a topographic organization, VSNs use a genetic trajectory to code visceral organs along the body’s rostral–caudal axis.

‘Tissue layer’ coding specifies VSN endings

We also discovered a second orthogonal trajectory and identified its associated DEGs, which include *Gpr65*, *Sst*, *Trpv1*, *Drd2* and *Agtr1a* (Fig. 2a, Extended Data Fig. 3j). To determine whether this second trajectory also encodes essential interoceptive information, we labelled DEG⁺ VSNs through nodose ganglion injection¹¹ of AAV-FLEX-tdTomato in corresponding Cre mouse lines (hereafter referred as DEG^{tdT} mice) and examined the innervation of tdTomato⁺ sensory fibres in whole-mount cleared organs. Notably, VSNs along this second trajectory project to different tissue layers (Extended Data Fig. 3k): *Gpr65*⁺ VSNs projected almost exclusively to the innermost mucosal layer in the oesophagus, stomach and duodenum but were largely absent from the heart and lung; *Sst*⁺ VSNs similarly innervated the mucosal layer mainly in the stomach around the pyloric sphincter; *Drd2*⁺ VSNs heavily terminated in the middle muscular layer across all gastrointestinal organs and the heart; and *Agtr1a*⁺

VSNs mostly terminated in the outer myenteric or epicardial layers composed of connective collagenous matrix. To better quantify the locations of VSN endings along the surface–lumen axis of organs, we gave each tissue layer an index (innermost mucosal or epithelial layer, 0; middle muscular layer, 1; outermost connective tissue layer, 2) (Fig. 2a) and calculated the average tissue layer index score for DEG⁺ VSNs in each examined organ ([Methods](#)). The tissue layer index scores of DEG⁺ VSNs correlated well with their relative positions along this trajectory ('tissue layer' trajectory score; Fig. 2a–c), demonstrating that the second trajectory we identified encodes the tissue layer information of VSN endings. Notably, within the same tissue layer, VSNs with lower trajectory scores—such as *Sst*⁺ and *Gpr65*⁺ VSNs—terminated significantly deeper than *Trpv1*⁺ VSNs with higher trajectory scores (Extended Data Fig. 3l, m), suggesting that this trajectory also encodes the relative position of VSN endings along the organ's surface–lumen axis; this implies that vagal afferents may follow morphogen gradients into deeper tissue layers.

Fig. 2: A 'tissue layer' dimension coding VSN ending locations and structures.

 **figure 2**

a, UMAP plots of identified DEGs (top) and their expression measures (middle) along a ‘tissue layer’ trajectory. Bottom, DEG^+ VSN ending locations, quantified as ‘tissue layer’ index score in corresponding DEG^{tdT} mice (mean; number of mice: *Gpr65*-oesophagus, 3; *Gpr65*-stomach, 7; *Gpr65*-duodenum, 4; *Sst*-stomach, 5; *Trpv1*-

oesophagus, 3; *Trpv1*-stomach, 7; *Trpv1*-duodenum, 4; *Trpv1*-colon, 4; *Trpv1*-heart, 10; *Drd2*-oesophagus, 3; *Drd2*-stomach, 6; *Drd2*-duodenum, 3; *Drd2*-colon, 2; *Drd2*-heart, 6; *Agtr1a*-oesophagus, 4; *Agtr1a*-stomach, 12; *Agtr1a*-duodenum, 4; *Agtr1a*-colon, 3; *Agtr1a*-heart, 6). **b**, UMAP plot of VSN clusters, coloured by average tissue index determined in *Gpr65*^{tdT} (F1–F4 clusters; golden), *Sst*^{tdT} (F5 cluster; yellow), *Drd2*^{tdT} (J2–J4, H2, H4 and I1 clusters; orange), and *Agtr1a*^{tdT} (I2 and I4–6 clusters; orange-red) mice, showing a continuous trajectory coding tissue layers along the organ’s surface–lumen axis. **c**, Correlation between mean ‘tissue layer’ trajectory score of DEG⁺ VSNs and their ‘tissue layer’ index score in corresponding *DEG*^{tdT} mice (mean ± s.e.m.; *n* as in **a**). Linear regression $R^2 = 0.6315$. **d**, VSN ending types characterized in *Vglut2*^{tdT} mice show stereotypical structures along various tissue layers across multiple visceral organs. Scale bars, 100 μm . **e**, Projection-seq-guided anterograde tracing (schematic illustration, left) reveals genetic identities of stereotypical VSN ending types illustrated on the UMAP plot (right). VSN clusters forming various VSN ending types followed the ‘tissue layer’ trajectory well (dashed arrow). **f**, Model for combinatorial coding of the body’s internal space in VSNs using a 2D genetic matrix.

Source Data

We then asked whether VSNs form organ-specific ending structures in various tissue layers. Although VSN endings have been extensively characterized in individual organs^{6,7,8,9,15,16,17}, it is unclear how they contribute to interoceptive coding. Systematic analyses of VSN terminals within the lung, heart, oesophagus, stomach, duodenum and colon in *Vglut2*^{tdT} mice revealed that there is a marked similarity between many stereotypical VSN ending types in the same tissue layer across visceral organs (Fig. 2d, Extended Data Fig. 4a,b), including (1) plates of terminal puncta lying in a collagenous and elastic environment; (2) varicose free endings in the fibrous adventitia; (3) parallel intramuscular arrays (pIMAs); (4) irregular muscular endings innervating muscle bundles facing different directions with circular parent neurites (cIMAs); (5) free endings beneath the luminal epithelial lining (absent in the heart and arteries, in which endoderm-derived epithelium is missing³⁶); and (6) bud endings wrapped around specialized sensory epithelial cell clusters. Our data thus suggest that VSN ending structures are predominantly organ-independent but tightly associated with tissue layers.

To further ask whether morphologically stereotypical VSN endings across organs have similar molecular identities, we performed Projection-seq-guided anterograde tracing to determine the genetic signatures of VSN ending structures. For each organ or anatomical region (oesophageal and pyloric sphincters), we (1) identified enriched VSN clusters and their DEGs on the basis of Projection-seq data; (2) labelled DEG⁺ VSNs by nodose infection of AAV-FLEX-tdTomato in corresponding Cre mice; and

(3) determined the sensory structures formed by DEG⁺ VSNs in the target organ or region using whole-organ clearing and volumetric imaging (Fig. 2e, Extended Data Fig. 4). With this approach, we determined the molecular identity of VSN endings in the heart, lung, stomach, oesophagus, duodenum and colon (Extended Data Figs. 5–8; see annotation details in Methods). VSN clusters forming various VSN ending types followed the tissue layer trajectory well (Fig. 2e), showing that from both an anatomical and a genetic perspective, VSN ending structures are specialized for their local tissue layer environments rather than for visceral organs.

The fact that ‘visceral organ’ and ‘tissue layer’ trajectories are orthogonal shows that they are coded in parallel rather than hierarchically. DEGs among VSNs that innervate different visceral organs and along the ‘tissue layer’ trajectory were both predominantly linked with Gene Ontology (GO) biological processes for neuron development, cell–cell signalling and synaptic signalling or ion transportation (Extended Data Fig. 8s), suggesting that VSN specifications for visceral organs and tissue layers are achieved using genes that have similar biological functions.

Compared to hierarchical coding, a parallel coding structure can effectively reduce the number of genes required, which aligns with the efficient coding hypothesis that sensory neurons use as few resources as possible to code the maximum information^{37,38}. Together, our results reveal a two-dimensional genetic representation of the body’s internal space in VSNs that codes the precise anatomical location of interoceptive signals (Fig. 2f).

A third ‘stimulus modality’ coding dimension

Next, we sought to understand how stimulus modality is coded in VSNs. VSNs might develop visceral-organ- or tissue-layer-specific sensory mechanisms or use more generalized mechanisms for similar stimulus modalities across the body. However, as VSN identity cannot be accurately determined using only one or two marker genes^{17,18}, it is challenging to uncover stimulus modality coding without more systems-based approaches.

We developed a technique named ‘vagal calcium imaging transformed fluorescence in situ hybridization’ (vCatFISH) (Fig. 3a). First, the neuronal activity in hundreds of VSNs was simultaneously imaged *in vivo* in response to various body stimuli including lung inflation, oesophagus and stomach stretch, intestine stretch and a series of chemical challenges delivered to the intestinal lumen (water, salt, nutrient and acid) using *Gpr65-ires-Cre; lox-tdTomato; Snap25-2a-GCaMP6s-D* (*Gpr65*^{tdT}-GCaMP6s) mice. VSN identity was then determined post hoc in cryo-sectioned nodose ganglia using RNAscope against 21 marker genes that together faithfully represent VSN subpopulations (Extended Data Fig. 9a–d). Finally, tdTomato⁺ cells were used as landmarks to register VSNs between calcium imaging and RNAscope assays

(Extended Data Figs. 9e, 10a). The proper density (13.8%) and scattered distribution of tdTomato⁺ VSNs in Gpr65^{tdT}-GCaMP6s mice ensure the successful registration of tdTomato⁻ VSNs. In total, 57.5% (349/607) responsive VSNs were unambiguously registered from six mice (Fig. 3b, Extended Data Fig. 10b, c). VSNs responding to stimuli applied to organs along the body's rostral–caudal axis closely followed the ‘visceral organ’ trajectory (Extended Data Fig. 10d). The vCatFISH results are consistent with previous reports regarding individual marker genes^{11,12,13,39,40}, and provide the precise identity of responsive VSNs.

Fig. 3: vCatFISH analysis reveals a third ‘stimulus modality’ coding dimension in VSNs.



a, Schematic illustration of vCatFISH analysis. Organ illustrations were adapted from BioRender.com. **b**, Time-resolved responses ($\Delta F/F$; colour-coded) of 311 single VSNs to the indicated stimuli (lung stretch: oxygen, 600 ml min^{-1} , 20 s; oesophagus and stomach stretch: saline, 100, 300, 600 μl , 30 s; duodenum stretch: saline, 600 μl) in Gpr65^{tdT}-GCaMP6s mice ($n = 6$) with RNAscope codes (Extended Data Fig. 9c) and annotated subpopulations (A–L). **c**, VSN subpopulations show stereotypical response patterns across organs ($\Delta F/F$; mean \pm s.e.m.; number of VSNs as indicated). Lung stretch responses were aligned at the activation frame (red arrowhead) to reveal response kinetics. Bars represent oesophagus and stomach stretch; black arrowheads

represent duodenal stretch (saline, 600 µl). **d**, VSN endings are uncoupled from response patterns. Left, F-VSNs ($\text{Gpr}65^{\text{tdT}}$) and G-VSNs (Vip^{tdT}) form indistinguishable mucosal villi endings (ME) in the intestine but respond to different sensory cues (bottom, 5 mice). Middle, pIMAs formed by H/J-VSNs ($\text{P2ry}1^{\text{tdT}}$) and C-VSNs ($\text{Piezo}2^{\text{tdT}}$) have distinct response kinetics to oesophagus and stomach stretch (bottom, $\Delta F/F$ at post-activation frame 15 (f15), mean ± s.e.m., 5 mice, *** $P < 0.001$, $P = 7.4 \times 10^{-7}$, two-tailed t -test). Right, IGLEs formed by C-VSNs ($\text{Piezo}2^{\text{tdT}}$) and I-VSNs ($\text{Agtr}1\alpha^{\text{tdT}}$) have different preferences between mechanical and chemical stimuli (bottom, 5 mice). **e**, Different ending types formed by C-VSNs in the lung, oesophagus and stomach ($\text{Piezo}2^{\text{tdT}}$). Scale bars, 100 µm (**d**, **e**). **f**, Correlation maps showing all mapped connections among various VSN characteristics. One-to-one connection pattern indicates perfect correlation; all-to-all connection pattern indicates no correlation. Magenta (top right) and gold (bottom right) connections indicate strong correlations between VSN subpopulation and response pattern and between tissue layer and ending type. **g**, Correlation index between pairs of VSN characteristics, calculated on the basis of the number and pattern of connections shown in **f**, showing three independent feature-coding dimensions in VSNs.

Source Data

Although VSNs in different subpopulations typically show distinct response patterns, all of the examined stimuli activated multiple subpopulations of VSNs (Fig. 3b, Extended Data Fig. 10b,e), indicating that VSN subpopulations are primed for an individual decomposed stimulus instead of coding complex physiological changes directly. Several lung-stretch-sensitive VSN types were identified. $\text{Piezo}2^+$ VSNs (55.1%) were activated significantly faster than $\text{Piezo}2^-$ K/L-VSNs (Extended Data Fig. 11a,b). $\text{Piezo}2^+P2ry1^-$ C-VSNs exhibited a rapid and sustained response, whereas $\text{Piezo}2^+P2ry1^+$ A-VSNs responded more transiently (Extended Data Fig. 11c, d), providing evidence that different $\text{Piezo}2^+$ subtypes have distinct response kinetics. For oesophagus- or stomach-stretch-sensitive VSNs, *Slit2* or *Grm5* and *Glp1r* differentially defined oesophagus and stomach C-VSNs (Extended Data Fig. 11e–g). C-VSNs (56.3%) and I-VSNs (9.0%) had sustained stretch responses, whereas H/J-VSNs (34.1%) responded only transiently (Extended Data Fig. 11f,g). Of note, VSNs sensitive to intestinal stretch were predominantly $\text{Piezo}2^-$ (94.1%). *Uts2b*⁺*Vip*⁺*Glp1r*⁺*Cckar*⁺ G-VSNs represented a large fraction (39.2%) of intestinal stretch responders (Extended Data Fig. 11h–j), with little response to various intestinal luminal stimuli (7.9%) or mechanical challenges in other organs (lung, 0%; intestine, 3.6%), whereas I-VSNs responded to both chemical challenges to intestinal lumen and mechanical stimuli in several organs. Our results thus show that—unlike what the multi-sensor theory proposes⁴¹, that fibres with distinct response patterns originate

from the same VSNs—response heterogeneity is generated by different subpopulations of VSNs.

VSNs in the same subpopulation often responded to a similar stimulus across multiple visceral organs (Fig. 3c). *Piezo2*⁺ C-VSNs responded to stretch in the lung, oesophagus, stomach and duodenum with similar sustained kinetics. By contrast, H-/J-VSNs showed transient response kinetics to stretch in organs along the gastrointestinal tract (Fig. 3c, Extended Data Fig. 11), suggesting that they are well suited to the detection of gastrointestinal dynamics. I-VSNs responded broadly to both stretch in many gastrointestinal organs and various intestinal luminal stimuli, indicating that they are polymodal sensors. Thus, our data show that instead of developing specialized sensory mechanisms for individual body–brain pathways, VSNs are organized into modular sensory units to code categorized stimulus modalities across visceral organs.

We then integrated vCatFISH results with Projection-seq-guided anterograde tracing data and generated a comprehensive road map (Extended Data Figs. 11k, 12). Unlike DRG neurons, which sense diverse somatosensory cues through highly specialized afferent terminals⁴², VSN response patterns are not well correlated with their ending structures. VSNs with the same ending structures often show multiple response patterns (Fig. 3d), suggesting that they could be primed for different stimulus modalities. For example, morphologically indistinguishable intestinal villi endings can sense luminal contents (F-VSNs) or mechanical changes (G-VSNs). Notably, mechanosensitive *Piezo2*⁺ enterochromaffin cells in the intestinal villi convert force into serotonin release⁴³, and the serotonin receptors *Htr3a* and *Htr3b* are highly expressed in G-VSNs^{16,18} (Extended Data Fig. 12), raising the question of whether G-VSNs are intrinsically mechanosensitive. Our data also provide functional evidence that IMAs are mechanosensitive. Genetically distinct IMAs have different response kinetics: transient (H/J-VSNs) or sustained (C-VSNs). Intraganglionic laminar endings (IGLEs) could be mechanosensitive (C-VSNs) or polymodal (I-VSNs); the latter would be ideal sensors for food ingestion, consistent with their roles in food intake¹⁶. Although IGLE mechanosensitivity is thought to be intrinsic⁴⁴, luminal sensation in IGLEs must be indirect, probably through communication with enteric neurons. It is also worth noting that many more VSN types could be polymodal as the appropriate stimulus may not have been examined. On the other hand, the same VSN sensory unit, such as *Piezo2*⁺ C-VSNs, could form different ending structures in different organs (oesophagus, stomach and lung) (Fig. 3e), suggesting that irrespective of ending structures, VSNs use the same sensory mechanism to monitor similar interoceptive signals from different locations. Thus, our data show that VSN endings are not specialized for coding stimulus modality. Notably, *Piezo2*⁺ C-VSNs that recapitulate the classical slowly adapting receptors terminate at bronchi bifurcations, where the highest shear stress occurs during inspiration⁴⁵. Together, our results identify a third ‘stimulus modality’ coding dimension in VSNs.

A multidimensional coding scheme in VSNs

To better quantify the relationship between VSN characteristics, we systematically mapped all characterized connections among the five VSN characteristics (Fig. 3f). In this model, a perfect correlation (index = 1) between two characteristics would have a ‘one-to-one’ pattern with the minimum number of possible connections, whereas a complete uncorrelation (index = 0) would have an ‘all-to-all’ pattern with the maximum number of possible connections. We thus calculated the correlation index between each pair on the basis of the number and pattern of connections (Fig. 3g). This quantitative analysis further demonstrates key organization principles of the vagal interoceptive system: (1) VSN endings are tightly linked with tissue layers but not specialized for visceral organs and not well correlated with response patterns, indicating that VSN ending structures are primarily developed for adaptation to local tissue layers across organs; (2) VSN subpopulations defined by unbiased single-cell clustering show much stronger correlation with response patterns than with visceral organs or tissue layers, suggesting that they are more primed to code stimulus modalities; and (3) visceral organ, tissue layer and sensory modality—the three most important features that together define the physiological role of an interoceptive signal—are coded in independent dimensions in VSNs. With this coding strategy, VSNs are specified into only a few groups for each dimension, but in the combination of three dimensions, a large number of parallel pathways are generated to ensure precise and effective body-to-brain signal communication. Together, our results reveal a fundamental multidimensional coding architecture of the vagal interoceptive system.

Complex VSN projections in the brainstem

Finally, we asked how this multidimensional coding architecture facilitates the organization of VSN afferents in the brain. Central projection specificity for both organ-labelled and genetically defined VSNs has been extensively described^{7,11,12,13,16,19,26,46,47}. Consistently, VSN central projections labelled using AAVrg-tdTomato from respiratory, cardiovascular and digestive systems were largely segregated, whereas vagal afferents from functionally related organs terminated in more overlapping areas (Extended Data Fig. 13), suggesting that parallel vagal pathways might innervate designated, non-overlapping brainstem regions (Fig. 4a).

Fig. 4: Complex organization of parallel VSN pathways in the brainstem.

 **figure 4**

a, Models for central projection patterns of parallel VSN pathways. **b**, Schematic illustration of Projection-seq-guided retrograde tracing of 11 VSN pathways (colour-coded), each with a unique combination of VSN characteristics, via injection of AAVrg-FLEX-tdTomato in the indicated organs and Cre mice. Fluorescence-labelled afferent terminals from different VSN pathways in the brainstem at bregma level -7.48 mm are illustrated. AP, area postrema; CC, central canal; DMV, dorsal motor nucleus of the vagus; Sol-C, commissural NTS; Sol-DL, dorsolateral NTS; Sol-G, gelatinosus NTS; Sol-IM, intermediate NTS; Sol-M, medial NTS Sol-V, ventral NTS; Sol-VL, ventrolateral NTS. Organ illustrations were adapted from BioRender.com. Mouse brain illustration adapted with permission from ref. [11](#). **c**, Innervation density of the 11 VSN pathways, expressed as fluorescence in indicated area/fluorescence in total area, along the rostral-caudal axis of the brainstem, from Bregma -7.2 mm to -8.0 mm (mean; colour-coded; $n = 3$ per pathway). Sol-IL, interlateral NTS. N/A, no signal. **d**, Model for a complex divergent-convergent organization of parallel VSN pathways in the brainstem.

[Source Data](#)

To test this idea, we performed Projection-seq-guided pathway-specific tracing using organ injection of AAVrg-FLEX-tdTomato in various Cre mouse lines for 11 individual vagal pathways, each representing a unique ‘visceral organ–tissue layer–stimulus modality’ combination (Fig. 4b). Notably, pathway-specific tracing did not result in a more distinguishable topographic map in the brainstem (Fig. 4b–d, Extended Data Fig. 14). All 11 of the examined vagal pathways projected to multiple brainstem regions, and vice versa, most brainstem regions received convergent inputs from many VSN pathways (Fig. 4c). The projection of VSNs to different brainstem regions depends on different features of interoceptive signals. Visceral organ is a main factor that determines the projection of VSNs to the lateral versus the medial nucleus of the solitary tract (NTS): all targeted VSN pathways from the lung and heart projected to the dorsolateral NTS, which integrates cardiopulmonary inputs⁴⁷, whereas the medial NTS received various interoceptive signals from all gastrointestinal organs with indistinguishable patterns, therefore functioning as a general gastrointestinal centre. Similarly, stimulus modality drives a marked segregation of gut VSNs in some brainstem regions: mechanosensitive C- and H-VSNs projected extensively to the DMV for real-time regulation of gastrointestinal motility, whereas F- and I-VSNs—both sensing intestinal luminal contents—heavily innervated the gelatinous and commissural NTS. Our results thus show that parallel VSN pathways are no longer processed in serial in the brainstem but in a more complex manner of divergence and convergence (Fig. 4d).

Discussion

A major challenge in interoception is to communicate an enormous and diverse set of body changes to the brain in an accurate and effective manner. The vagus nerve is a key interoceptive system that surveys various visceral organs. Our study, through a high-throughput large-scale integration of genetic signatures, response patterns and neuronal projections, uncovers a multidimensional coding architecture of the sensory vagus nerve that enables the massively parallel presentation of interoceptive signals in an efficient manner (Fig. 5).

Fig. 5: A multidimensional coding architecture of the vagal interoceptive system.

 figure 5

Model illustrating the three coding dimensions for three key features of interoceptive signals—visceral organ (red shades), tissue layer (blue shades) and sensory modality (green shades)—in VSNs. This multidimensional coding architecture together specifies many parallel VSN pathways in a combinatorial manner to precisely and effectively present body signals to the brain. Parallel VSN pathways are no longer organized in serial, but in a more complex divergent and convergent manner in the brainstem, based on multiple features of interoceptive signals. The multidimensional coding architecture further facilitates the extensive regrouping of parallel VSN pathways in the brain.

Special coding strategies develop to accommodate different sensory needs. The olfactory system uses combinatorial codes to discriminate numerous odours, and taste receptor cells are organized into labelled lines to distinguish five taste modalities^{48,49,50}. Like gustatory cells, VSNs are grouped into separate and parallel processing streams¹². However, it is unclear how such organization could satisfy the considerable processing needs. Our results demonstrate that each body region, composed of a unique combination of visceral organ and tissue layer, is surveyed by designated VSNs that are specialized by two independent sets of genes (Fig. 2f). Physically connected organs or tissue layers are generally coded through continuous changes of gene expression in VSNs, which further increases the coding efficiency. As a whole, this strategy ensures a precise coding of the body's internal space with minimal genes. Our vCatFISH study suggests that VSNs form broad functional units, each with a unique response pattern that recognizes a specific stimulus modality. Although future studies are required to reveal the exact sensory inputs for most VSN subpopulations, our work shows that through this mechanism, VSNs can sense categorized inputs with minimal specialized sensory mechanisms for visceral organs or tissue layers. Together, the vagal interoceptive system codes essential features of interoceptive signals in independent dimensions and uses a combinatorial strategy to effectively expand diversity. This multidimensional coding architecture not only enables the generation of many parallel VSN processing streams but also facilitates the complex projection of vagal afferents in the brain. Thus, the coding mechanism that

we have identified here is a good demonstration of the ‘efficient sensory coding theory’^{[37,38](#)} in the interoceptive system.

Abnormal presentation of interoceptive signals often leads to global dysfunction, which causes multiple psychological and physiological disorders⁴. Looking forward, the presented integrative approach will provide an effective blueprint for systematically unravelling the molecular and functional architecture of the interoceptive system, and will inspire innovative therapies for disease treatment.

Methods

Mice

All animal husbandry and procedures were performed in compliance with Yale University’s Institutional Animal Care and Use Committee and National Institute of Health (NIH) guidelines. All mice were age- and gender-matched adults (older than 8 weeks) and no differences between sexes were observed.

Mouse lines

Wild-type C57BL/6J (000664), *Glp1r-ires-Cre* (029283), *Gpr65-ires-Cre* (029282), *Npy2r-ires-Cre* (029285), *P2ry1-ires-Cre* (029284), *Agtr1a-Cre* (030553), *Calb2-ires-Cre* (010774), *Nts-Cre* (017525), *Vglut2-ires-Cre* (016963), *Sst-ires-Cre* (013044), *Twist2-Cre* (008712), *Vip-ires-Cre* (010908), *Piezo2-GFP-ires-Cre* (027719), *Trpv1-Cre* (017769), *Pvalb-Cre* (017320), *Vglut1-ires2-Cre* (023527), *Chat-ires-Cre* (031661), *lox-ChR2* (024109), *lox-tdTomato* (007914), and *Snap25-2A-GCaMP6s-D* (025111) were from the Jackson Laboratory. *Drd2-Cre* (032108-UCD) mice were from the Mutant Mouse Resource and Research Center (MMRRC). *lox-L10-GFP* mice were described before^{[11,12](#)}.

Generation of Projection-seq AAVs

UPB sequences were cloned from coding sequences of hChR2 (Addgene, plasmid 28017), hM3Dq (Addgene, plasmid 50474) and hM4Di (Addgene, plasmid 50475) and inserted right before the SV40 poly (A) of AAVrg-CAG-tdTomato-WPRE-SV40 (Addgene, plasmid 59462) using the In-Fusion HD Cloning Kit (Takara, 638909). Projection-seq AAVs (at titre > 10¹²–10¹³ viral genomes per ml) were generated at the UNC Vector Core. Plasmids have been deposited to Addgene.

UPB sequences (5'-3'):

UPB-oesophagus (UPB5, Addgene plasmid 180783):

```
ACAGCACCATCCTCAACTCCACCAAGTTACCCTCATCGGACAACCTGCAGG  
TGCCTGAGGAGGAGCTGGGATGGTGGACTTGGAGAGGAAAGCCGACAAG  
CTGCAGGCCAGAAGAGCGTGGACGATGGAGGCAGTTCCAAAAAGCTT  
CTCCAAGCTTCCATCCAGCTAGAGTCAGCCGTGGACACAGCTAACAGACTTC  
TGACGTCAACTCCTCAGTGGTAAGAGCACGGCCACTCTACCTCTGTCCTT  
CAAGGAAGCCACTCTGGCCAAGAGGTTGCTCTGAAGACCAGAAGTCAGA  
TCACTAAGCGGA.
```

UPB-stomach (UPB1, Addgene plasmid 180784):

```
ATGGACTATGGCGGCGTTGTCTGCCGTGGACCGAACCTTGTTCGTTA  
CTAACCTGTGGTGGTAACGGGTCCGTCTGGTCCCTGAGGATCAATGTTA  
CTGTGCCGGATGGATTGAATCTGCCGGCACGAACGGCGCTCAGACCGCGTC  
AAATGTCCTGCAGTGGCTTGCAGCAGGATTCAAGCATTGCTGCTGATGTT  
TATGCCTACCAAACCTGGAAATCTACATGCCGGCTGGAGGAGATCTATGTGT  
GCGCCATTGAAATGGTAAGGTGATTCTCGAGTTCTTGTGAGTTAAGAA  
TCCCTCTATGCTCTACCTT.
```

UPB-duodenum (UPB6, Addgene plasmid 180785):

```
AATGGCAGCTCGGGCAATCAGTCCGTGCGCCTGGTCACGTACATCCCAC  
AATCGCTATGAGACGGTGGAAATGGTCTTCATTGCCACAGTGACAGGCTCC  
CTGAGCCTGGTACTGTCGTGGCAACATCCTGGTATGCTGTCATCAAG  
GTCAACAGGCAGCTGCAGACAGTCAACAACACTTCCTCTCAGCCTGGCG  
TGTGCTGATCTCATCATAGGCGCCTCTCCATGAACCTCTACACCGTGTACAT  
CATCAAGGGCTACTGGCCCTGGCGCCGTGGTCTGCGACCTGTGGCTGGC  
CCTGGACTGCGTGGTGAGCAACGCCCTCGTCATGAACCTCTCATCATCAG  
CTTGACCGCTACTTCTGCGTCA.
```

UPB-colon (UPB4, Addgene plasmid 180786):

```
ATCGATGGGCCTTAGGAACTTGGCCTGTGACCTCTGGCTGCCATTGACTG  
CGTAGCCAGCAATGCCCTGTTATGAATCTCTGGTCATCAGCTTGACAGA  
TACTTTCCATCACGAGGCCGCTCACGTACCGAGCCAAACGAACAAACAAAG  
AGAGCCGGTGTGATGATCGGTCTGGCTGGGTATCTCCTTGTCCCTTGGG  
CTCCTGCCATCTGTTCTGGCAACTTGTGGAAAGAGAACTGTGCCTCC  
GGGAGAGTGCTTCATTCAAGTCCCTCAGTGAGGCCACCATTACTTTGGCACA  
GCCATCGCTGGTT.
```

UPB-pancreas (UPB7, Addgene plasmid 180787):

AAGATGGCAGGCCTCATGATTGCTGCTGCCTGGGTACTGTCCTCGTGCTCT
GGGCGCCTGCCATCTGTTCTGGCAGTTGTGGTGGTAAGCGGACGGTGC
CCGACAACCAGTGCTTCATCCAGTCAGTCCCTGTCCAACCCAGCAGTGACCTTG
GCACAGCCATTGCTGGCTTCTACCTGCCTGTGGTCATCATGACGGTGCTGTA
CATCCACATCTCCCTGGCCAGTCGAGCCACAAGCACCGGGCCGA
GGGCCCGAAGGAGAAGAAAGCCAAGACGCTGGCCTTCATAAGAGCCCAC
TAATGAAGCAGA.

UPB-lung (UPB2, Addgene plasmid 180788):

ACAGGACACCGGGTGCAGTGGCTGCGCTATGCAGAGTGGCTGCTCACTTGT
CCTGTCATCCTTATCCGCCTGAGCAACCTCACCGGCCTGAGCAACGACTAC
AGCAGGAGAACCATGGACTCCTGTCTCAGACATCGGGACTATCGTGTGG
GGGGCTACCAGCGCCATGGCAACCGGGCTATGTTAAAGTCATCTCTTTGTC
TTGGATTGTGCTATGGCGCGAACACATTTTCACGCCGCCAAAGCATATAT
CGAGGGTTATCATACTGTGCCA.

UPB-heart (UPB8, Addgene plasmid 180789):

AGGACACTTCAAATGAGTCCAGCTCAGGCAGTGCCACCCAGAACACCAAG
GAACGCCAGCCACAGAGCTGTCCACCACAGAGGCCACCACGCCGCAT
GCCCGCCCCCTCCCTGCAGCCGGGCCCTCAACCCAGCCTCCAGATGGTC
CAAGATCCAGATTGTGACGAAGCAGACAGGCAATGAGTGTGTGACAGCCAT
TGAGATTGTGCCCTGCCACGCCGGCTGGCATGCGCCCTGCCGGCAACGTGGC
CCGCAAGTTGCCAGCATCGCTCGCAACCAGGTGCGCAAGAACGGCAGA
TGGCGGCCGGAGCGCAAAGTGACACGAACGATCTTGCCTTGCTGG
CCTTCATCCT.

AAV infection of visceral organs

Retrograde adeno-associated virus (AAVrg)⁵¹ represents a powerful genetic tool in VSN studies^{52,53,54}. AAVrg-tdTomato and AAVrg-GFP were purchased from the UNC vector core. AAVrg-FLEX-tdTomato (28306-AAVrg), AAVrg-CAG-FLEX-rc [Jaws-KGC-GFP-ER2] (84445-AAVrg) and pAAVrg-hSyn-Con/Fon hChR2(H134R)-EYFP (55645-AAVrg) were purchased from Addgene. All viruses contained 10^{12} – 10^{13} viral genomes per ml, and 0.05% Fast Green FCF (Sigma-Aldrich, F7252-5G) was occasionally used to facilitate visualization.

In all surgeries, mice were anaesthetized with 1–2% isoflurane on a heating pad, followed by subcutaneous injections of meloxicam (5 mg kg⁻¹) and buprenorphine (1.5 mg kg⁻¹). Lung: virus (5 µl diluted with 75 µl of saline) was injected through a tracheal catheter into the lung using a Hamilton syringe. Heart: the mouse was

ventilated (tidal volume 0.21 ml, respiration rate 110 breaths per minute) using a mouse ventilator (SAR-1000, CWE) via an intubated angi catheter. The heart was gently exposed via thoracotomy. Virus (5 μ l) was injected intramurally (20 nl per second) using a Nanoject III injector at multiple sites covering most of the area of the heart. Stomach, duodenum, colon and pancreas: the target organ was gently exposed via an abdominal incision. Virus was injected intramurally at multiple sites covering most of the area (stomach: 5 μ l; all subregions in both dorsal and ventral sides; duodenum: 2.5 μ l, a length of 1.5 cm from the pyloric sphincter; transverse colon: 2.5 μ l, a length of 1.5 cm; pancreas: 5 μ l). Oesophagus: the cervical oesophagus underneath the trachea was surgically exposed via a neck incision. The abdominal oesophagus and the oesophageal sphincter were gently exposed via an abdominal incision. Virus was injected into oesophageal muscularis and serosa layers (cervical: 2.5 μ l; abdominal: 1 μ l, between the diaphragm and the oesophageal sphincter).

To visualize and quantify the anatomical location of VSNs innervating various visceral organs in the nodose ganglion (Extended Data Fig. 1a–c), the following AAVrgs were injected into visceral organs in wild-type mice for Extended Data Fig. 1a–c: heart (tdTomato)/lung (GFP), heart (tdTomato)/stomach (GFP), heart (tdTomato)/oesophagus (GFP), pancreas (tdTomato)/stomach (GFP), heart (tdTomato)/duodenum (GFP), and colon (tdTomato). To compare infection efficiencies of AAVrg and the conventional neural tracer cholera toxin B subunit (CTb), AAVrg-tdTomato (2.5 μ l) and Alexa Fluor 647-conjugated CTb (1.0 mg ml⁻¹, 2.5 μ l, Thermo Fisher Scientific, C34778) were mixed and co-injected into the stomach in wild-type mice (Extended Data Fig. 1d). AAVrg and CTb labelled partially overlapping VSNs with similar efficiencies, raising the possibility that AAVrg might have some preferential tropism for specific VSN populations over CTb. However, it is worth noting that co-infection of VSNs with two similar AAVs (AAV9-FLEX-tdTomato, AAV9-GFP) via nodose injection also resulted in similar partially overlapping labelling¹¹, suggesting that this likelihood is low. This possibility is further reduced by the extensive validation of Projection-seq results using anterograde tracing in 14 Cre mouse lines as described in Extended Data Figs. 4–8.

To verify the level of coverage of injected virus within the organ (Extended Data Fig. 1e–q, s–u), AAVrg-tdTomato or Fast Green FCF (5% w/v, same volume as AAVrg) were injected into wild-type mice as described above. Organs were processed as described in ‘Histology and immunohistochemistry’. Injected dye or virus were able to cover most subregions and virus-infected cells were observed in most tissue layers including the pulmonary alveoli, stomach and intestinal villi, and the entire myocardial layer of the heart ventricles. We also noticed that the atria and bronchial walls were not well covered. To examine whether AAVrgs could label vagal motor neurons in the DMV, AAVrg-FLEX-tdTomato (2.5 μ l) and AAVrg-GFP (2.5 μ l) were mixed and co-injected into the stomach of *Chat-ires-Cre* mice (Extended Data Fig. 1r). To examine

the degree of viral spread (Extended Data Fig. 1y, w), AAVrg-tdTomato and AAVrg-GFP were separately injected into indicated organs in the same mice. To determine the infection efficiency of Projection-seq AAVs (Extended Data Fig. 2a, b), Projection-seq AAVs and AAVrg-GFP were injected into the stomach. For Projection-seq analysis (Fig. 1), Projection-seq AAVs with UPB-lung, UPB-heart, UPB-oesophagus, UPB-stomach, UPB-duodenum, UPB-colon and UPB-pancreas were injected into corresponding organs. The heart, cervical oesophagus and lung were sequentially injected on the first day, and abdominal oesophagus, stomach, duodenum, pancreas and colon were sequentially injected into the same mice on the second day.

Approximately 30% of VSNs were labelled from the seven organs (Extended Data Fig. 2c). For RNAscope HiPlex assays of retrogradely labelled VSNs (Extended Data Fig. 2p, q), AAVrgs encoding reversed transcripts of fluorescent proteins, including AAVrg-FLEX-tdTomato (heart, stomach, duodenum), AAVrg-CAG-FLEX-rc [Jaws-KGC-GFP-ER2] (lung, oesophagus, pancreas) and AAVrg-hSyn Con/Fon hChR2(H134R)-EYFP (colon) were used to avoid potential contamination of RNAscope results from virus-introduced fluorescent signals.

For tracing the central targets of diverse vagal pathways, AAVrg-tdTomato was injected into visceral organs of wild-type mice (Extended Data Fig. 13), and AAVrg-FLEX-tdTomato was injected into visceral organs of indicated Cre lines (Fig. 4, Extended Data Fig. 14). Vagal ganglia were collected seven days after surgery and brains were collected two to three weeks after surgery.

PCR analysis of VSNs

Vagal ganglia were collected from control mice or mice with stomach injection of AAVrg-tdTomato-UPB2. RNA was extracted using the Monarch Total RNA Miniprep Kit (NEB, T2010S) and reverse-transcribed into cDNA using the SuperScript IV First-Strand Synthesis System (Thermo Fisher Scientific, 18091050). Primer sets used (Extended Data Fig. 2b):

UPB2 (5'-3'): CATCGATACCGTCGACACAGGACACCGGGTGCAGTG (forward);
CTGCTCGAAGCGGCCGCTGGCACAGTATGATAACCCTCG (reverse). UPB4
(5'-3'): CATCGATACCGTCGACATCGATGGCCTAGGGAAC (forward);
TGCTCGAAGCGGCCGCAACCAGCGATGGCTGTGCC (reverse).

scRNA-seq and Projection-seq of VSNs innervating various visceral organs

Neuron isolation and sequencing

For control scRNA-seq, vagal ganglia (left and right) were collected from 40 age- and gender-matched C57BL/6J wild-type mice (10 mice per sample) and VSNs were acutely isolated and enriched using previously described methods^{11,12,17}.

Approximately 5,000–10,000 VSNs were loaded in each channel of the 10X microfluidic device to target 3,000–6,000 cells as an output of one sample. Single-cell cDNA libraries were prepared at the Yale Center for Genomic Analysis (YCGA) and sequenced using an Illumina NovaSeq S4 sequencer at 150–300 million reads to achieve a fine sequencing depth of 30,000–50,000 reads per cell. For Projection-seq, 30 age- and gender-matched wild-type mice (divided into four samples) were first injected with different Projection-seq AAVs into thoracic and abdominal organs (details in ‘AAV infection of visceral organs’). Vagal ganglia were collected seven days later. Of the examined VSNs, 29.5% (102/346) were tdTomato⁺. VSNs were sequenced as mentioned above.

Bioinformatic processing

Transcriptomic data were aligned to the mm10 mouse genome reference (control scRNA-seq) or a custom mouse genome reference with additional sequence information of UPBs (Projection-seq) using the Cell Ranger software v.3.0.2 (10X Genomics). The following quality control metrics were applied to filter low-quality cells in scRNA-seq: number of genes per cell > 500; number of genes per cell < 8,000; percentage of mitochondria genes < 10%. A total of 56,575 cells were sequenced (31,182 control scRNA-seq samples: 7,842, 7,580, 7,939, 7,821; 25,393 Projection-seq samples: 6,403, 6,381, 5,803, 6,806). Control scRNA-seq and Projection-seq data were then integrated and processed using the R package Seurat v.3⁵⁵, and 42 cell clusters identified using the top 30 principal components (PCs) were visualized using UMAP⁵⁶ (Extended Data Fig. 2f). A total of 32,558 neurons selected from 25 *Slc17a6*⁺ clusters (16,267 control scRNA-seq samples: 4,961, 3,894, 4,288, 3,124; 16,291 Projection-seq samples: 3,863, 3,431, 4,449, 4,548) were re-clustered into 67 populations with the top 100 PCs (Extended Data Fig. 2g, top). A total of 27,800 placode-derived neurons selected from 52 *Phox2b*⁺ clusters (13,210 control scRNA-seq samples: 3,835, 3,091, 3,452, 2,832; 14,590 Projection-seq samples: 3,443, 2,973, 4,019, 4,155) were re-clustered into 52 clusters with the top 100 PCs and visualized with UMAP separately (Fig. 1b for Projection-seq; Extended Data Fig. 2g, bottom for control scRNA-seq) or together (Extended Data Fig. 2h). DEGs for the 52 clusters were identified using the Wilcoxon rank-sum test implemented in Seurat from the Projection-seq dataset (Extended Data Fig. 2d). VSN clusters were then manually grouped into 12 subpopulations on the basis of expression of DEGs and their locations on the UMAP plot. E-VSNs selectively express markers for damaged sensory neurons, such as *Sprrla* and *Ecell*^{16,57,58} (Extended Data Fig. 3a). The percentage of E-VSNs increased after the Projection-seq process (control: $n = 627$, 4.7%; Projection-seq: $n = 1,528$,

10.5%), and consistently more *Sprrla*⁺ VSNs were observed after AAVrg injection (Extended Data Fig. 3b–d), demonstrating that neurons damaged during both cell dissociation and Projection-seq procedures can be easily identified. Thus, E-VSNs were removed from further analysis.

Projection-seq analysis

Further analysis was performed for the Projection-seq dataset. A total of 42 out of 1,701 *Prdm12*⁺ (2.5%) neural-crest-derived jugular VSNs and 4,791 out of 14,590 (32.8%) *Phox2b*⁺ placode-derived nodose VSNs^{18,59} were recognized as UPB-positive (expression level > 0.8), suggesting that VSNs retrogradely labelled from the seven major visceral organs in our study mainly originate from the nodose but not the jugular ganglia. We therefore focused on nodose VSNs. After removing E-VSNs, 3,539 out of 4,609 UPB-marked nodose VSNs (76.8%) expressed a single barcode (lung-UPB, 855; oesophagus-UPB, 595; heart-UPB, 177; stomach-UPB, 1,166; duodenum-UPB, 110; pancreas-UPB, 356; colon-UPB, 280), and 740 out of 4,609 (16.1%) VSNs expressed were marked by two UPBs. A correlation matrix (Extended Data Fig. 2e) was calculated on the basis of the numbers of single-UPB and dual-UPB marked VSNs across the seven examined visceral organs and plotted using the R pheatmap package. Correlation analysis indicates that the two UPBs were predominantly from physically adjacent rather than random organs (Extended Data Fig. 2e). This observation was consistent with retrograde tracing results (Extended Data Fig. 1b, v, w), demonstrating that (1) UPB leakage was minimal during sample preparation; and (2) dual-labelled VSNs innervate regions close to both organs. Single UPB-labelled VSNs were designated as organ-specific VSNs, VSNs dual labelled with UPB-stomach and UPB-oesophagus were designated as oesophageal-sphincter projecting neurons and VSNs dual labelled with UPB-stomach and UPB-duodenum were designated as pyloric-sphincter projecting neurons. To examine VSNs that innervate different physiological systems, VSNs singly marked by oesophagus, stomach, duodenum and colon-UPBs were combined as gut VSNs (Fig. 1c, d). A 3D UMAP plot (Fig. 1c, bottom) was generated using a previously published method⁶⁰ (<https://github.com/Dragonmasterx87/Interactive-3D-Plotting-in-Seurat-3.0.0>). DEGs for organ-specific VSNs, or between thoracic (combination of oesophagus, heart and lung-UPB labelled) and abdominal (combination of stomach, duodenum, colon and pancreas-UPB labelled) VSNs were identified using the Wilcoxon rank-sum test (Extended Data Fig. 3e). Mouse transcription factors were identified (Fig. 1d, Extended Data Fig. 3g) by comparing DEGs with the AnimalTFDB 3.0 mouse database⁶¹ (<http://bioinfo.life.hust.edu.cn/AnimalTFDB/#/>). For example, *Pou4f1*, which is essential for DRG neuron specification³², is preferentially expressed in lung VSNs (Extended Data Fig. 3g). Regulatory networks in UPB-labelled VSNs (Extended Data Fig. 3h) showing the expression of *Pou4f1* downstream regulators

including *Runx1* and *Isl2* were predicted by IPA analysis (Qiagen) using the Upstream Analysis (Upstream Regulators) module. For cell–cell interaction analysis between organ-innervating VSNs and various organ cell types (Extended Data Fig. 3*i*), UPB⁺ VSNs labelled from the indicated organ were first extracted from the Projection-seq data and then integrated with a previously published scRNA-seq dataset containing various cell types from that corresponding organ using the R package Seurat v.3⁵⁵. The following datasets were used: heart⁶² (CM, cardiomyocyte; EDC, endothelial cell; EP, epicardial cell; FB, fibroblast), lung⁶³ (ATI, alveolar epithelial type I cell; ATII, alveolar epithelial type II cell; B, B cell; C&S, ciliated and secretory cell; DC, dendritic cell; EDC, endothelial cell; FB, fibroblast; MO, monocyte; Mac, macrophage; NK, natural killer cell; Neutro, neutrophil; Peri, pericyte; T, T cell), colon⁶⁴ (Endo, endothelial cell; Immu, immune cell; EN, enteric neuron; Glia, glial cell; Entero, enteroendocrine cell; Mus/Fb, muscle cell and fibroblast), duodenum⁶⁵ (duodenal enteric neuron subtypes: EXMN, excitatory motor neuron; INMN, inhibitory motor neuron; IN, inter neuron; IPAN, intrinsic primary afferent neuron) and pancreas⁶⁰ (ISL, islet cell; ACI, acinar cell; DUCT, duct cell; MES, mesenchymal cell; IMVS, immune and vascular cell). Cell–cell interactions between organ-innervating UPB⁺ VSNs and indicated organ cell types (or duodenal enteric neuron subtypes) were then analysed using the CellPhoneDB⁶⁶ (<https://github.com/Teichlab/cellphonedb>, v.2.0.0) Python package. GO pathway analyses of DEGs in heart, lung, gut and pancreas VSNs, and along the tissue trajectory (Extended Data Fig. 8*s*), were performed using the Gene Ontology Resource GO Enrichment Analysis tool^{67,68,69} (<http://geneontology.org>).

Calculation of trajectory score

Distances from the nodose ganglia to the beginning and the end of various organs were measured and normalized to the body length from the neck to the rectum (Fig. 1*e–g*). The mean distances were calculated as Position_{organ} (lung: 0.241 ± 0.005; heart: 0.280 ± 0.005; oesophagus: 0.228 ± 0.005; stomach: 0.469 ± 0.006; duodenum: 0.567 ± 0.006; transverse colon: 0.589 ± 0.005; pancreas: 0.545 ± 0.007; *n* = 4 mice). The organ position score for VSN clusters (Fig. 1*e*), indicating their target preference along the body’s rostral–caudal axis, was calculated as the weighted average of Position_{organ} using the percentage of organ-specific VSNs in the cluster ($P_{\text{organ-cluster}} = \text{Number of UPB}_{\text{organ}}^+ \text{ VSNs in the target cluster}/\text{Number of all UPB}_{\text{organ}}^+ \text{ VSNs}$) as the weight value for each organ, expressed as $\sum(P_{\text{organ-cluster}} \times \text{Position}_{\text{organ}})/\sum P_{\text{organ-cluster}}$. The organ trajectory score of an organ-specific VSN (Fig. 1*f,g*) was measured as its projection position along the organ trajectory on the UMAP plot (as shown in Fig. 1*e*). Tissue layer trajectory was identified using Slingshot⁷⁰, and DEGs along this trajectory were discovered using tradeSeq⁷¹. Tissue layer trajectory scores of DEG⁺

VSNs were measured as their relative positions along the tissue layer trajectory by Slingslot using the pseudotime function. On the basis of the inner–outer position, each tissue type was given an index score (mucosa or inner epithelium, 0; muscle, 1; connective tissue, 2), and the tissue layer index for DEG⁺ VSNs (Fig. [2a–c](#)) in each organ was calculated based on the percentage of DEG⁺ VSN endings in the target tissue layer and the tissue layer index across multiple tissue layers as $\Sigma((\text{Number of DEG}^+ \text{ VSN endings in the target tissue layer}) / (\text{Number of DEG}^+ \text{ VSN endings in all tissue layers})) \times \text{Index}_{\text{tissue}}$ (Fig. [2a–c](#)).

AAV infection of vagal ganglia

Vagal ganglia injection was performed as previously described^{[11,12](#)}. In brief, mice were anaesthetized with 1–2% isoflurane and maintained on a heating pad. Both left and right vagal ganglia were surgically exposed. A virus mix containing a 1:1 dilution of AAV9-FLEX-tdTomato and AAV5-CAG-GFP with 0.05% (w/v) Fast Green FCF was injected (160 nl for each side, 20 nl per second) using a Nanoject III injector (Drummond). Mice were euthanized four weeks after surgery for tissue collection (see ‘Histology and immunohistochemistry’).

RNAscope HiPlex assay

RNAscope HiPlex assays were performed following the manufacturer's protocol (Advanced Cell Diagnostics). Vagal ganglia were acutely dissected and freshly frozen in cryo-embedding medium (OCT). Cryosections (10 µm for vCatFISH; 14 µm for others) were cut using a cryostat (Thermo Fisher Scientific), mounted onto Superfrost Plus slides (Thermo Fisher Scientific), and stored at -80 °C until use. Slides were immediately immersed into fresh 4% paraformaldehyde (PFA) in RNase-free PBS for 60 min at room temperature, followed by dehydration with 50%, 70% and 100% ethanol. Samples were then digested with protease IV for 30 min at room temperature. After hybridization with designed probes (Supplementary Table 1) for 2 h at 40 °C, the sections were treated with HiPlex Amp 1–3, and then HiPlex Fluoro T1–T3, before counterstaining and mounting. The slides were imaged using a Leica SP8 confocal microscope equipped with a motorized stage, a PMT detector, a HyD SP detector, four laser lines (405 nm, 488 nm, 552 nm and 638 nm) and a 20× objective (HC PL APO 20×/0.75 CS2). Imaging loci were exactly recorded in the LAS X software in the first group for image registration, and then applied for imaging the same sections for the following groups. After each group, the fluorophores were cleaved by 10% cleaving solution (ACD, 324130). The sections were then hybridized with HiPlex Fluoro T4–T6 in group 2, HiPlex Fluoro T7–T9 in group 3 and HiPlex Fluoro T10–T12 in group 4. In total, 12 genes were detected on a single section. The following changes were made for vCatFISH: (1) slides were not mounted after HiPlex Fluoro and instead imaged in 4× SSC with a 16× immersion objective (HC FLUOTAR L 16×/0.8 IMM motCORR VISIR); (2) after the first-round imaging (4 groups, 12 probes), probes were removed using the HiPlexUp reagent, and sections were hybridized with another 12 probes (2 h, 40 °C) for the second-round analysis. In total, 22 genes were analysed (see 'vCatFISH analysis').

Histology and immunohistochemistry

Mice were anaesthetized with urethane (1.5 g per kg) and transcardially perfused with 15 ml cold PBS (pH 7.4) containing 10 U ml⁻¹ heparin (Sigma-Aldrich, H4784), followed by 25 ml cold 4% PFA. Fast Green FCF

injected organs (Extended Data Fig. 1e,g,j,s–u) were dissected and imaged under a Stereo Microscope with a digital camera (AmScope). For all others, visceral organs and/or vagal ganglia were dissected, post-fixed in 4% PFA at 4 °C (overnight for visceral organs, 30 min for ganglia), and then kept in cold PBS at 4 °C. Brains were post-fixed (4% PFA, overnight, 4 °C), cryoprotected in 30% sucrose PBS solution for two days at 4 °C, frozen in OCT and then stored at –80 °C until cryosection.

For brain samples, 40-μm cryosections were mounted onto Superfrost Plus slides. Cryosections were washed (3× PBS), permeabilized (0.1% Triton X-100, PBS), blocked (5% normal donkey serum, PBST (PBS, 0.05% Tween-20)) and incubated with primary antibodies (chicken anti-GFP, 1:1,000, Aves Labs; rabbit anti-RFP, 1:1,000, Rockland) diluted in blocking buffer for 2 h at room temperature. Then, the slides were washed (3× PBST), and incubated with fluorophore-conjugated secondary antibodies (Alexa Fluor 647-conjugated AffiniPure donkey anti-chicken IgY, 1:1,000; Alexa Fluor 594-conjugated AffiniPure donkey anti-rabbit IgG(H+L), 1:1,000, Jackson ImmunoResearch) diluted in blocking buffer for 2 h at room temperature. After incubation, the samples were washed (3× PBST), and mounted with Fluoromount-G with DAPI before imaging with the Leica SP8 confocal microscope.

Visceral organs were cleared with the CUBIC method⁷² and stained with the following protocol unless specifically mentioned. In brief, the dissected organ was immersed into 1/2-water-diluted reagent-1 (25 wt% urea, 25 wt% Quadrol, 15 wt% Triton X-100) with shaking at 37 °C for 3–6 h, followed by reagent-1 (R1) with shaking at 37 °C for 7 days. R1 was replaced fresh every two days. Next, the tissue was washed (3× PBS/0.01% NaN₃), blocked (2% normal donkey serum, 0.1% Triton X-100, PBS/0.01% NaN₃) and incubated with primary antibodies (chicken anti-GFP, 1:200; rabbit anti-RFP, 1:200) in blocking buffer with shaking for 7 days at room temperature. Samples were then washed (0.1% Triton X-100, PBS/0.01% NaN₃) and incubated with fluorophore-conjugated secondary antibodies diluted in blocking buffer with shaking for five days at room temperature. After antibody incubation, the samples were washed and immersed in 1/2-PBS-diluted reagent-2 (25 wt% urea, 50 wt% sucrose, 10 wt% triethanolamine) overnight at room temperature, and then reagent-2 (R2) at

37 °C for 2 days. The samples were finally immersed in oil for at least 1 h and flattened to approximately 500 µm in a custom-built imaging chamber and imaged using the Leica SP8 confocal microscope as described above, with a 10× objective (HC PL APO 10×/0.40 CS2, working distance: 2.1 mm) or a 40× objective (HC PL FLUOTAR L 40×/0.60 CORR, working distance: 3.3 mm). Some heart samples were similarly processed but not flattened and imaged with a LaVision Vltramicroscope II light-sheet microscope at the CNNR Imaging Core at Yale University (Extended Data Fig. 5a) or the Leica SP8 confocal microscope with a 16× immersion objective (HC FLUOTAR L 16×/0.8 IMM motCORR VISIR, working distance: 8 mm). Heart slices (1 mm thickness) and gastrointestinal organs to determine viral spread (Extended Data Fig. 1f, v, w) were imaged under a Leica M205FCA Fluorescent Stereo Microscope with a CoolLED pE300 white illumination, GFP and DSR Filter sets, 1× objective (Plan M-series) and a Leica DFC7000 T camera. The pancreas was excluded from anatomical analysis owing to multiple technical challenges (keeping its original structure and distinguishing various tissue layers after clearing, antibody penetration and imaging efficiency).

A modified CUBIC protocol was used for clearing vagal ganglia: samples were cleared in R1 for one day, incubated in primary and secondary antibodies (chicken anti-GFP, 1:1,000; rabbit anti-RFP, 1:1,000; Alexa Fluor 647-conjugated AffiniPure donkey anti-chicken IgY, 1:1,000; Alexa Fluor 594-conjugated AffiniPure donkey anti-rabbit IgG(H+L), 1:1,000) overnight, respectively, and treated with R2 for one day. Cleared ganglia were imaged with the Leica SP8 confocal microscope.

vCatFISH analysis

Surgery, stimulus delivery and imaging

Gpr65^{tdT}-GCaMP6s mice were continuously anaesthetized (1–2% isoflurane/oxygen) during the experiment. A tracheal tube was inserted for air injection. The upper oesophagus and pyloric sphincter were cannulated and flushed with saline multiple times to remove residual food particles. The duodenum (around 0.5 cm below the pyloric sphincter) was cannulated with a bundle of six PE-10 tubing for separate delivery of saline, water and

glucose (1 M), Ensure (Ensure Original Vanilla Nutrition Shake), 10× PBS and 150 mM HCl (pH = 0.84). Left vagal ganglia were exposed and immobilized on a stable platform¹². During calcium imaging, a series of stimuli were delivered to the same mice in the following sequence: (1) lung inflation for 20 s with 600 ml min⁻¹ flow (oxygen through the tracheal tube), twice with a 2-min interval; (2) small intestine stretch via fast injection of 600 µl saline through the duodenal cannula; stomach stretch with 100 µl, 300 µl and 600 µl saline through the oesophageal cannula for 30 s (duration precisely controlled by closing or opening of the pyloric cannula); (4) small intestine infusion with 100 µl saline, water, 1 M glucose, Ensure, 10× PBS and 150 mM HCl in sequence with a 3-min interval between infusions. GCamp6s fluorescence was measured from two focal planes 15 µm apart using a two-photon microscope (920 nm excitation, Leica TCS SP8, Mai Tai laser from Spectra-Physics, HyD SP detector). The imaging frequency for each plane was 1.72 s per frame. At the end, electrical stimulation was applied to the vagus nerve and a z-stack of the ganglia was taken for both GCaMP and tdTomato (552 nm, one photon excitation) signals for cell registration.

RNAscope and registration

After GCaMP imaging, vagal ganglia were immediately embedded in OCT, frozen in situ, and cut into 10 µm cryosections. RNAscope HiPlex assays for the following 22 genes were performed (Fig. 3b, Extended Data Fig. 9): *Trpa1* (R1T1), *Runx3* (R1T2), *Uts2b* (R1T3), *Gabra1* (R1T4), *Slit2* (R1T5), *Kcng1* (R1T6), *Piezo2* (R1T7), *Ddc* (R1T8), *Vip* (R1T9), *Trpv1* (R1T10), *tdTomato* (R1T11), *Gpr65* (R1T12), *Chodl* (R2T1), *Glp1r* (R2T2), *Grm5* (R2T3), *Slc17a7* (R2T4), *P2ry1* (R2T5), *Tmc3* (R2T6), *Car8* (R2T7), *Nts* (R2T8), *Cckar* (R2T9) and *Calca* (R2T11). The following criteria were used to categorize VSN subpopulations (Fig. 3b, Extended Data Fig. 9): A-VSNs: *Runx3*⁺ and/or *Piezo2*⁺/*P2ry1*⁺, *Tmc3*⁻; B-VSNs: *Gabra1*⁺; C-VSNs: multiple hits for *Slit2*⁺, *Piezo2*⁺, *Ddc*⁺, *Tmc3*⁺, *Trpv1*⁻, *P2ry1*⁻. D-VSNs: *Tmc3*⁺, *Trpv1*⁻; F-VSNs: *Gpr65*⁺; G-VSNs: *Trpv1*⁺, multiple hits for *Uts2b*⁺, *Vip*⁺, *Glp1r*⁺, *Cckar*⁺; H-VSNs: *Trpv1*⁺, *Tmc3*⁻, *Trpa1*⁺; I-VSNs: multiple hits for *Tmc3*⁺, *Car8*⁺, *Cckar*⁺, *Piezo2*⁻. J-VSNs: *Trpv1*⁺, *Calca*⁺ and some *P2ry1*⁺, *Piezo2*⁻; K-VSNs: *Trpa1*⁺, *Kcng1*⁺, *Trpv1*⁺,

Calca⁺; L-VSNs: *P2ry1*⁺, *Trpv1*⁻. tdTomato⁺ neurons that serve as geographic landmarks for cell registration were registered first between in vivo GCaMP images and RNAscope images (Extended Data Fig. 9e). Coordinates of registered tdTomato⁺ cells were then used to calculate the transformation matrix between in vivo 3D images and RNAscope sections. We reason that tdTomato⁺ cells from a given RNAscope section should also be located in the same plane in the transformed in vivo image stack, therefore we used a plane correction script simulating a virtual plane with minimum total projection distances for tdTomato⁺ cells from multiple RNAscope sections. The transformation matrix was then applied to the in vivo image stack (3D extension/plug-in in LASX software) to generate successive in vivo imaging planes that resemble RNAscope sections. tdTomato⁻ neurons were then registered on the basis of their relative distance and depth to their neighbouring tdTomato⁺ cells (Extended Data Fig. 9e–g). Registration for each sample was performed by at least two people independently. In total, 57.5% (349/607, 6 mice) of responsive VSNs were unambiguously registered, which is comparable to a similar approach developed in the trigeminal ganglion⁷³. Cells that were not successfully registered were removed from further analysis.

Analysis of neural activity

Regions of interest were manually extracted from GCaMP images. The stimulus induction frame was set as 0 unless specifically mentioned. Baseline signal (F) was defined as the average GCaMP6s fluorescence over a 10-frame period (17.2 s, frame -20 to frame -10) before stimulus induction and neuronal activity was calculated as $\Delta F/F$. Cells were coded as responsive to a given stimulus if the maximum GCaMP6s fluorescence was more than 100% above baseline during stimulus period (lung inflation and stomach stretch: between stretch on and off; intestine stretch: within 40 frames/68.8 s after injection; intestine infusion: within 90 frames/154.8 s after infusion). Peak response was identified as the maximum $\Delta F/F$ within the stimulus period. To compare adaptation rates in lung stretch-sensitive VSNs, GCaMP6s traces were aligned at activation frame (Extended Data Fig. 11c, arrow, set as 0), and the activation duration was calculated as the number of frames between the prior and post peak frames at which VSN

activity ($\Delta F/F$) reached 10% of the peak response (Extended Data Fig. [11d](#)). For intestine stretch, activation frame was defined as the prior peak frame at which VSN activity ($\Delta F/F$) reached 10% of peak response.

Projection-seq-guided anterograde tracing in visceral organs

The percentage of gene⁺ VSNs targeted in various Cre lines in individual clusters (Extended Data Fig. [4c](#)) was calculated as the number of gene⁺ VSNs normalized by the number of all VSNs in each cluster using the control scRNA-seq dataset. Fold enrichment of gene⁺ VSNs in each cluster (Extended Data Fig. [4d](#)) was calculated as the percentage of gene⁺ VSNs in the target cluster normalized by the overall percentage of gene⁺ VSNs in all clusters.

Identification of enriched clusters and DEGs

Primary oesophagus, stomach, duodenum, colon, heart and lung VSN clusters were identified as clusters containing more than 4% of corresponding UPB single-labelled VSNs (Extended Data Figs. [5c](#), [6b](#), [7c](#), [8a](#), [e](#), [k](#), [l](#)), with the following additions: G2, G5-duodenum VSNs (both 3.64%) and I4-heart VSNs (3.95%). VSN clusters enriched for stomach regions 4, 6–8 (Extended Data Fig. [7e](#), [h](#)) were defined using the following criteria: (1) the cluster contains more than 4% of dual-UPB (region 4: oesophagus/stomach; region 6: stomach/pancreas; region 7: stomach/colon; region 8: stomach/duodenum, respectively) labelled VSNs; and (2) in the cluster, the percentage of dual-UPB labelled VSNs is at least 5% higher than both the percentage of stomach-UPB labelled VSNs and the percentage of the other UPB (oesophagus, pancreas, colon, duodenum, respectively) labelled VSNs. VSN clusters enriched for stomach region 5 (fundus, S-only, Extended Data Fig. [7h](#)) were defined as: (1) the cluster contains more than 4% of stomach-UPB labelled VSNs; and (2) in the cluster, the percentage of stomach-UPB labelled VSNs is at least 5% higher than the percentages of stomach/oesophagus, stomach/pancreas, stomach/colon and stomach/duodenum dual-UPB labelled VSNs. Among the eight primary duodenum VSN clusters (F1, F4, G2, G5, H2, H3, I5 and J3), three (F1, H2, J3) were more enriched in stomach/duodenum dual-

labelled VSNs, suggesting that they preferentially project to the pyloric sphincter over the duodenum. Therefore, the other five duodenum VSN clusters were focused on for DEG analysis (Extended Data Fig. [8a](#)). Fractions of DEGs (Extended Data Figs. [5e](#), [6c](#), [7f](#), [8b,f,l](#)) were calculated as the number of DEG⁺ VSNs in the indicated cluster divided by the number of DEG⁺ VSNs in all enriched clusters indicated in the panel. Percentages of gene⁺ VSNs in identified enriched clusters (Extended Data Figs. [5d](#), [6d](#), [8h](#)) were calculated as the number of gene⁺ VSNs divided by the total number of VSNs in that cluster.

Histology analysis

Four types of gut VSN ending types, three types of heart VSN ending types and five types of lung VSN ending types were classified on the basis of their morphologies and locations using whole-mount preparations in Vglut2^{tdT} mice (Fig. [2d](#), Extended Data Figs. [4b](#), [5b](#), [6a](#); $n = 4–7$). For quantitative analyses of MEs and IMAs in the indicated gastrointestinal regions; alveoli, longitudinal and patch-terminals in the lung; and varicose endings and IMAs in the heart (Extended Data Figs. [5f](#), [6l](#), [7b](#), m, [8d,j,n](#)), the area covered by each sensory ending type was measured using the Leica Application Suite X software and divided by the total area of each sample to derive the innervation intensity. For IGLEs in the gastrointestinal tract, neuroepithelial body (NEB) endings in the lung and flower-spray endings in the heart, the number of terminal clusters was counted (Extended Data Figs. [5f](#), [6l](#)). The number of IGLEs was divided by the total area of each sample to derive the innervation intensity. Normalized innervation intensity for gastrointestinal endings (Extended Data Figs. [7b](#), m, [8d,j,n](#)) was calculated as the innervation intensity of the indicated sensory ending type formed in indicated Cre^{tdT} mice divided by the innervation intensity of the indicated sensory ending type formed in Vglut2^{tdT} mice. Fold changes for various sensory ending types in indicated stomach regions (Extended Data Fig. [7d](#), [j](#)) were calculated as the innervation intensity of the corresponding sensory ending type over the indicated stomach region divided by the innervation intensity of the corresponding sensory ending type over the entire stomach in Vglut2^{tdT} mice ($n = 4$).

Annotation of VSN clusters

Heart VSNs were predominantly distributed in four clusters (Extended Data Fig. 5), with the following DEGs: D1 (*Piezo2*), H4 (*Drd2*) and I3/I4 (*Agtr1a*). In *Piezo2*^{tdT} mice, most cardiac afferents were varicose surface endings. In *Drd2*^{tdT} mice, cardiac afferents densely innervated myocardium with both branched and parallel IMAs. *Agtr1a*⁺ VSNs predominantly formed flower-spray endings in the heart and the aortic arch. Our results thus reveal the identity of various VSN cardiac ending types (Extended Data Fig. 5h).

Although five types of lung VSN endings were characterized, only two large groups of primary lung VSN clusters were revealed (Extended Data Fig. 6). A3-VSN fibres labelled in *Agtr1a*^{tdT}, *Vglut1*^{tdT}, *Pvalb*^{tdT} and *P2ry1*^{tdT} mice travelled along segmental bronchi and terminated at airway bifurcations wrapping around NEBs. Of note, VSN fibres in *Agtr1a*^{tdT} and *P2ry1*^{tdT} mice also formed similar endings wrapping around taste buds in the larynx¹⁷ and the upper oesophagus (Extended Data Fig. 6h), suggesting that VSN bud endings in different organs are likely to have similar genetic signatures. K1–3/L2-VSNs labelled in *Twist2*^{tdT} and *P2ry1*^{tdT} mice formed alveoli endings. The other three VSN lung endings that were not effectively marked by Projection-seq were all on bronchial airways, consistent with our observation that lumen-delivered virus did not effectively cover bronchial walls (Extended Data Fig. 1i). *Npy2r*⁺ afferents formed dense longitudinal endings wrapping around the bronchioles; both *Npy2r*⁺ and *P2ry1*⁺ VSNs formed patchy endings on segmental bronchi or around bronchial bifurcations; *Piezo2*⁺ pulmonary afferents mainly formed two ending types: (1) bud ending wrapping around NEBs (Extended Data Fig. 6g) as *Piezo2* is partially in A3-VSNs; and (2) near the bronchial bifurcation with branch endings (Fig. 3e, left), largely from the C3 cluster (1.5% of lung-UPB-marked VSNs). Annotations for lung VSN types are summarized in Extended Data Fig. 6m).

Most stomach VSNs were distributed in nine clusters (Extended Data Fig. 7c). We divided the stomach into five regions based on their proximation to other UPB-targeted organs (Extended Data Fig. 7a,b) and took advantage

of dual-UPB labelled VSNs that innervate regions close to both organs to decode each region individually (region 4: stomach/oesophagus-UPB dual-labelled VSNs; region 6: stomach/pancreas-UPB dual-labelled VSNs; region 7: stomach/colon-UPB dual-labelled VSNs; region 8: stomach/duodenum-UPB dual-labelled VSNs). Compared to other stomach regions, pIMAs and cIMAs but no other endings were enriched around the oesophageal sphincter (Extended Data Fig. 7d, top). Accordingly, three clusters (J1, J3 and I1) were enriched in stomach/oesophagus-UPB dual-labelled VSNs (Extended Data Fig. 7e,f, top). We then identified DEGs (*P2ry1* for J1/J3 and *Calb2* for I1) and examined IMAs around pyloric sphincters in *P2ry1*^{tdT} and *Calb2*^{tdT} mice. Most (75.0%) of the *P2ry1*⁺ IMAs around the oesophageal sphincter were pIMAs and all *Calb2*⁺ IMAs were cIMAs (Extended Data Fig. 7g), suggesting that J1/J3-VSNs form pIMAs and I1-VSNs form cIMAs. In addition to J1- and I1-VSNs, three clusters were enriched in S/D-VSNs with the following DEGs: F1 (*Sst*, *Gpr65*), H2 (*Vip*) and C4 (*Glp1r*, *Piezo2*), whereas all afferent types in *Vglut2*^{tdT} mice were enriched in region 8 around the pyloric sphincter. Both *Sst*⁺ and *Gpr65*⁺ VSNs formed MEs on the stomach, as reported^{12,16}, with *Sst*⁺ endings mainly in the antrum and *Gpr65*⁺ endings more evenly distributed across the stomach, indicating that F1-VSNs form MEs. Both *Glp1r*⁺ and *Piezo2*⁺ VSNs predominantly formed IGLEs, suggesting that C4-VSNs form stomach IGLEs. *Vip*⁺ VSNs exhibited pIMA morphology in region 8, suggesting that H2-VSNs also form pIMAs (Extended Data Fig. 7d–g).

We also used anatomical tracing results to facilitate the annotation of other stomach VSN clusters. We first determined the relative innervation intensity (referred as anatomical fold change or AF_{afferent type-stomach region}) for each ending type (ME, pIMA, cIMA and IGLE) in each stomach region (4, 6, 7 and 8), calculated as the innervation intensity of corresponding ending types in various stomach regions normalized by the innervation intensity of the same ending type in the entire stomach in *Vglut2*^{tdT} mice (Extended Data Fig. 7j). According to anatomical results (Extended Data Figs. 7, 8), F- and G-VSNs formed mucosal endings (MEs); H2-, H4-, J1- and J3-VSNs formed pIMAs; I1-VSNs formed cIMAs; and C4-VSNs formed IGLEs. We then performed sensory ending type simulation for seven VSN clusters (I2,

I4, I5, I6, I7, J2 and J4) in the stomach (Extended Data Fig. 7*i*) using a MATLAB script, assuming that each could form one of the four ending types (ME, pIMA, cIMA and IGLE) independently. Therefore, in total $4^7 = 16,384$ possibilities were tested. For each possibility, the relative innervation intensity derived from Projection-seq data (referred as Projection-seq fold change or SF_{afferent type-stomach region}) of each ending type (ME, pIMA, cIMA and IGLE) in each stomach region (4, 6, 7 and 8) was calculated as the percentage of corresponding dual-labelled VSNs forming this ending type normalized to the percentage of stomach-UPB single-labelled VSNs forming this ending type, expressed as $\Sigma(\text{percentage of dual-labelled VSNs for this stomach region in all VSN clusters that form the corresponding ending type}) / \Sigma(\text{percentage of stomach-UPB single-labelled VSNs in all VSN clusters that form the corresponding ending type})$. We then calculated the total variance between anatomically and Projection-seq-derived innervation intensities in all stomach regions across all ending types, expressed as $\Sigma(n = \text{region } 4, 6, 7, 8) (\text{SF}_{\text{ME}-n} - \text{AF}_{\text{ME}-n})^2 + \Sigma(n = \text{region } 4, 6, 7, 8) (\text{SF}_{\text{pIMA}-n} - \text{AF}_{\text{pIMA}-n})^2 + \Sigma(n = \text{region } 4, 6, 7, 8) (\text{SF}_{\text{cIMA}-n} - \text{AF}_{\text{cIMA}-n})^2 + \Sigma(n = \text{region } 4, 6, 7, 8) (\text{SF}_{\text{IGLE}-n} - \text{AF}_{\text{IGLE}-n})^2$. The trial with the lowest variance was defined as the best fit. AF_{afferent type-stomach region} and SF_{afferent type-stomach region} for this condition were plotted together (Extended Data Fig. 7*j*). Simulation indicated that J2, J4 and I7 account for cIMAs, and I2 and I4–I6 for IGLEs. This prediction was further supported by our data and previous findings¹⁶ that both *Agtr1a*⁺ and *Oxtr*⁺ VSNs, mainly I-VSNs, formed IGLEs close to the stomach antrum (Extended Data Fig. 7*k,l*).

Five clusters enriched for duodenum VSNs over stomach/duodenum dual-labelled VSNs were characterized with the following DEGs: *Gpr65* (F4), *Vip* (H3/G2/G5), *Glp1r* (G2/G5), and *Agtr1a* (I5) (Extended Data Fig. 8*a*). *Gpr65*⁺ and *Vip*⁺ VSNs predominantly formed indistinguishable MEs arborizing intestinal villi in the duodenum (the density of *Vip*⁺ MEs was much lower), suggesting that both F- and G-VSN clusters form MEs. By contrast, *Agtr1a*⁺ neurons representing I5-VSNs primarily formed IGLEs in the duodenum (Extended Data Fig. 8*b–d*). Similarly, of the five primary colon VSN clusters, *Agtr1a* is a DEG for I-VSNs and *Agtr1a*⁺ VSNs mainly

formed IGLEs in the colon (Extended Data Fig. [8e–g](#)). *Trpv1* is highly expressed in both I- and H4- but only partially in F3-VSNs, and the percentage of IGLE, IMA and ME endings formed by *Trpv1*⁺ VSNs correlated well with the percentage of *Trpv1*⁺ VSNs in I, H4 and F3 clusters (Extended Data Fig. [8h–j](#)). Extensive *Trpv1*⁺ IMAs were observed in the oesophagus, and *Trpv1* is highly expressed in J3 among the five primary oesophagus VSN clusters, consistent with the notion that J3 VSNs form IMAs in the stomach. Piezo2⁺ vagal oesophageal afferents—predominantly from C5–8 clusters—formed dense IMAs, suggesting that unlike C4-VSNs (stomach IGLEs), C5–C8 VSNs also form oesophageal IMAs. Probably owing to low infection efficiency, no apparent oesophageal ME or IGLE clusters were revealed. Notably, among all Cre lines examined, afferents in NTS^{tdT} mice preferentially formed oesophageal IGLEs (Extended Data Fig. [8n](#)) and were later used to study the central projections of oesophageal IGLEs. Nevertheless, oesophageal MEs were predominantly formed by *Trpv1*⁺ and *Gpr65*⁺ VSNs, suggesting they might have similar genetic signatures to MEs in other gastrointestinal organs (Extended Data Fig. [8n, p](#)). Annotations for gut VSN types are summarized in Extended Data Fig. [8q](#).

Correlation analysis

Correlations among various VSN characteristics, including 7 visceral organs (lung, heart, oesophagus, stomach, pancreas, duodenum and colon), 4 tissue layer types (epithelium, specialized epithelial cells, muscle and elastic connective tissue), 6 VSN ending types (epithelial, budding, pIMA, cIMA, plate of puncta and varicose), 11 VSN subpopulations and 4 response patterns (mechanical sustained, mechanical transient, polymodal and chemical), were plotted in Fig. [3f](#). Correlation indexes between pairs of VSN characteristics (Fig. [3g](#)) were calculated on the basis of the number and pattern of connections between variables in the two characteristics, with two assumptions: (1) correlation is negatively related to the total number of connections: two characteristics are perfectly correlated (correlation index = 1) if every variable of one characteristic is only connected with one variable of the other characteristic (meaning a one-to-one correlation with the minimum number of possible connections), and two characteristics are

completely uncorrelated (correlation index = 0) if every variable of one characteristic is connected to every variable of the other characteristic (meaning the maximum number of possible connections); and (2) with the same number of connections, correlation is stronger if the connections are more evenly distributed, meaning a smaller statistical variance of the number of connections among all variables within both characteristics. We first counted the number of variables within each characteristic (variables with no connections were removed from the analysis) and the number of connections between each pair of characteristics. We then calculated the normalized number of connections (C), expressed as (number of connections – minimum number of possible connections)/(maximum number of possible connections – minimum number of possible connections), for each pair of characteristics. We next calculated the statistical variance of connections per variable for both characteristics ($v1$ and $v2$). As both variances contribute to the correlation equally, the correlation index was finally calculated as $(1 - C)/((v1 + 1) \times (v2 + 1))$.

Projection-seq-guided retrograde tracing in the brainstem

Mouse line and organ combinations were selected on the basis of Projection-seq anterograde tracing results: lung alveoli ending (Twist2-ires-Cre, lung), lung NEB ending (Agtr1a-Cre, lung), oesophageal IGLE (Nts-Cre, oesophagus), oesophageal IMA (Piezo2-GFP-ires-Cre, oesophagus), heart IMA (Drd2-Cre, heart), stomach IGLE (Glp1r-ires-Cre, stomach), stomach mucosal ending (Gpr65-ires-Cre, stomach), stomach IMA (Vip-ires-Cre, stomach), duodenal IGLE (Agtr1a-Cre, duodenum), duodenal mucosal ending (Gpr65-ires-Cre, duodenum) and colon IGLE (Agtr1a-Cre, colon). Organ injection of AAVrgs is described in ‘AAV infection of visceral organs’. Brain processing and imaging is described in ‘Histology and immunochemistry’.

Quantitative analyses of vagal central projections in the brainstem

Area innervated by vagal afferents retrogradely labelled from various visceral organs at different Bregma levels (-7.20 , -7.32 , -7.48 , -7.56 , -7.76 , -7.92 , -8.0 mm) were measured using Fiji (ImageJ) (Extended Data Fig. [13c](#)). The percentage innervation of indicated brainstem sub-nucleus at

certain Bregma level (Fig. 4c, Extended Data Fig. 13d, e) was calculated with the following steps: (1) the fluorescence intensity in each sub-nucleus ($FI_{Bregma-subnucleus}$) was calculated as average fluorescence in the sub-nucleus minus background fluorescence measured in a region in the sub-nucleus with no fluorescence-labelled vagal fibres; (2) the area of each sub-nucleus ($A_{Bregma-subnucleus}$) was measured; (3) the total fluorescence (TF_{Bregma}) was calculated as $\Sigma(Bregma, subnucleus) (FI_{Bregma-subnucleus} \times A_{Bregma-subnucleus})$; and (4) the percentage innervation (PI) of a sub-nucleus at a certain Bregma was calculated as $FI_{Bregma-subnucleus} \times A_{Bregma-subnucleus} / TF \times 100$. The correlation variance between VSNs labelled from various visceral organs (Extended Data Fig. 13f) was calculated as $\Sigma(all subnuclei, all Bregma level) (PI_{pathway 1} - PI_{pathway 2})^2$ and a phylogenetic tree was generated based on the correlation variance matrix using the seqlinkage function in MATLAB.

Statistics and reproducibility

All statistical analyses were performed using GraphPad Prism 8. All data are reported as mean \pm s.e.m. unless specifically mentioned. Significance for pair comparisons was determined and P values were reported using a two-tailed Student's t test. Significance for multiple comparisons was first determined using a one-way ANOVA and adjusted P value was then reported using Tukey's multiple comparisons test.

The sample sizes represent the number of mice used for experiments and data analysis, which is determined according to the consistency of the results. No significant inter-individual variability was observed in our results, suggesting that the sample sizes were sufficient to demonstrate the findings. The precise number of mice is reported in the figure legends and Methods. The study did not report contrasts between treatment and control groups, so randomization was not applicable. For sequencing and tracing experiments, there were no treatment and control groups, and no hypothesis was tested regarding molecular identities. Thus, blinding was not applicable.

Representative images and experiments were repeated independently in multiple mice with similar results: Fig. [2d](#), Plate of puncta: stomach ($n = 4$), heart ($n = 3$); varicose: heart ($n = 5$), aorta ($n = 6$); pIMA: colon ($n = 3$), heart ($n = 6$); cIMA: stomach ($n = 4$), oesophagus ($n = 3$); epithelial: stomach ($n = 4$), lung ($n = 5$); bud: lung ($n = 5$), oesophagus ($n = 3$); Extended Data Fig. [1a](#), $n = 3$; Extended Data Fig. [1f](#), $n = 2$; Extended Data Fig. [1h](#), [i](#), $n = 3$; Extended Data Fig. [1k](#)–[q](#), $n = 3$; Extended Data Fig. [1r](#), $n = 2$; Extended Data Fig. [1s](#), [t](#), $n = 3$; Extended Data Fig. [1v](#), $n = 2$; Extended Data Fig. [1w](#), $n = 4$; Extended Data Fig. [2a](#), $n = 5$; Extended Data Fig. [2b](#), $n = 2$; Extended Data Fig. [2k](#), [l](#), $n = 4$; Extended Data Fig. [2p](#), $n = 4$; Extended Data Fig. [3c](#), $n = 4$; Extended Data Fig. [4b](#), oesophagus ($n = 3$), stomach ($n = 4$), duodenum ($n = 3$), colon ($n = 3$), aorta ($n = 6$); Extended Data Fig. [4e](#), $n = 3$; Extended Data Fig. [5a](#), $n = 4$; Extended Data Fig. [5g](#), *Piezo2* ($n = 9$), *Drd2* ($n = 6$), *Agtr1a* ($n = 3$), *Npr2r* ($n = 2$); Extended Data Fig. [6e](#), $n = 4$; Extended Data Fig. [6g](#)–[k](#), *Npy2r* ($n = 3$), *Trpv1* ($n = 5$), *P2ry1* ($n = 6$), *Agtr1a* ($n = 4$), *Piezo2* ($n = 9$), *Vglut1* ($n = 4$), *Pvalb* ($n = 3$), *Twist2* ($n = 3$); Extended Data Fig. [7g](#), [l](#), *P2ry1* ($n = 4$), *Calb2* ($n = 3$), *Glp1r* ($n = 5$), *Vip* ($n = 5$), *Gpr65* ($n = 7$), *Sst* ($n = 5$), *Agtr1a* ($n = 12$); Extended Data Fig. [8c](#), *Glp1r* ($n = 3$), *Agtr1a* ($n = 4$); Extended Data Fig. [8g](#), *Trpv1* ($n = 4$), *Agtr1a* ($n = 3$); Extended Data Fig. [8o](#), [p](#), *Nts* ($n = 5$), *Trpv1* ($n = 3$), *Agtr1a* ($n = 4$), *Gpr65* ($n = 3$); Extended Data Fig. [9a](#), [e](#), [f](#), $n = 5$; Extended Data Fig. [10a](#), $n = 5$; Extended Data Fig. [13a](#), lung ($n = 3$), heart ($n = 3$), oesophagus ($n = 2$), stomach ($n = 3$), duodenum ($n = 3$), colon ($n = 3$), pancreas ($n = 3$); Extended Data Fig. [14](#), $n = 3$ for all groups.

Reporting summary

Further information on research design is available in the [Nature Research Reporting Summary](#) linked to this paper.

Data availability

The scRNA-seq and Projection-seq data that were produced for this study are available in the Gene Expression Omnibus (GEO) under the accession number [GSE192987](#). The publicly available genome reference mm10 (refdata-cellranger-mm10-3.0.0, ensemble 93) from 10X Genomics was

used for scRNA-seq analysis and the generation of Projection-seq genome reference. The AnimalTFDB 3.0 mouse database (<http://bioinfo.life.hust.edu.cn/AnimalTFDB/#/>) was used for transcription factor analysis. The Gene Ontology Resource database (<http://geneontology.org>, release date 1 July 2021) was used for GO pathway analysis. Additional data related to this paper may be requested from the authors. [Source data](#) are provided with this paper.

Code availability

Code for Seurat, Slingshot, tradeSeq and CellPhoneDB is available at <https://github.com>. Additional code is available upon request.

References

1. Chen, W. G. et al. The emerging science of interoception: sensing, integrating, interpreting, and regulating signals within the self. *Trends Neurosci.* **44**, 3–16 (2021).
2. Berntson, G. G. & Khalsa, S. S. Neural circuits of interoception. *Trends Neurosci.* **44**, 17–28 (2021).
3. Quigley, K. S., Kanoski, S., Grill, W. M., Barrett, L. F. & Tsakiris, M. Functions of interoception: from energy regulation to experience of the self. *Trends Neurosci.* **44**, 29–38 (2021).
4. Bonaz, B. et al. Diseases, disorders, and comorbidities of interoception. *Trends Neurosci.* **44**, 39–51 (2021).
5. Paintal, A. S. Vagal sensory receptors and their reflex effects. *Physiol. Rev.* **53**, 159–227 (1973).
6. Berthoud, H. R. & Neuhuber, W. L. Functional and chemical anatomy of the afferent vagal system. *Auton. Neurosci.* **85**, 1–17 (2000).
7. Mazzone, S. B. & Undem, B. J. Vagal afferent innervation of the airways in health and disease. *Physiol. Rev.* **96**, 975–1024 (2016).

8. Berthoud, H. R., Blackshaw, L. A., Brookes, S. J. & Grundy, D. Neuroanatomy of extrinsic afferents supplying the gastrointestinal tract. *Neurogastroenterol. Motil.* **16**, 28–33 (2004).
9. Powley, T. L. et al. Vagal innervation of the stomach reassessed: brain-gut connectome uses smart terminals. *Ann. N. Y. Acad. Sci.* **1454**, 14–30 (2019).
10. Coleridge, H. M. & Coleridge, J. C. Pulmonary reflexes: neural mechanisms of pulmonary defense. *Annu. Rev. Physiol.* **56**, 69–91 (1994).
11. Chang, R. B., Strochlic, D. E., Williams, E. K., Umans, B. D. & Liberles, S. D. Vagal sensory neuron subtypes that differentially control breathing. *Cell* **161**, 622–633 (2015).
12. Williams, E. K. et al. Sensory neurons that detect stretch and nutrients in the digestive system. *Cell* **166**, 209–221 (2016).
13. Nonomura, K. et al. Piezo2 senses airway stretch and mediates lung inflation-induced apnoea. *Nature* **541**, 176–181 (2017).
14. Zeng, W. Z. et al. PIEZOs mediate neuronal sensing of blood pressure and the baroreceptor reflex. *Science* **362**, 464–467 (2018).
15. Min, S. et al. Arterial baroreceptors sense blood pressure through decorated aortic claws. *Cell Rep.* **29**, 2192–2201 (2019).
16. Bai, L. et al. Genetic identification of vagal sensory neurons that control feeding. *Cell* **179**, 1129–1143 (2019).
17. Prescott, S. L., Umans, B. D., Williams, E. K., Brust, R. D. & Liberles, S. D. An airway protection program revealed by sweeping genetic control of vagal afferents. *Cell* **181**, 574–589 (2020).
18. Kupari, J., Haring, M., Agirre, E., Castelo-Branco, G. & Ernfors, P. An atlas of vagal sensory neurons and their molecular specialization. *Cell Rep.* **27**, 2508–2523 (2019).

19. Kim, S. H. et al. Mapping of sensory nerve subsets within the vagal ganglia and the brainstem using reporter mice for Pirt, TRPV1, 5-HT3, and Tac1 expression. *eNeuro* **7**, ENEURO.0494–19.2020 (2020).
20. Hajishafiee, M., Bitarafan, V. & Feinle-Bisset, C. Gastrointestinal sensing of meal-related signals in humans, and dysregulations in eating-related disorders. *Nutrients* **11**, 1298 (2019).
21. Terry, N. & Margolis, K. G. Serotonergic mechanisms regulating the GI tract: experimental evidence and therapeutic relevance. *Handb. Exp. Pharmacol.* **239**, 319–342 (2017).
22. Takahashi, Y., Chiba, T., Kurokawa, M. & Aoki, Y. Dermatomes and the central organization of dermatomes and body surface regions in the spinal cord dorsal horn in rats. *J. Comp. Neurol.* **462**, 29–41 (2003).
23. Karemaker, J. M. An introduction into autonomic nervous function. *Physiol. Meas.* **38**, R89–R118 (2017).
24. Hopkins, D. A. & Armour, J. A. Ganglionic distribution of afferent neurons innervating the canine heart and cardiopulmonary nerves. *J. Auton. Nerv. Syst.* **26**, 213–222 (1989).
25. Zhuo, H., Ichikawa, H. & Helke, C. J. Neurochemistry of the nodose ganglion. *Prog. Neurobiol.* **52**, 79–107 (1997).
26. Altschuler, S. M., Bao, X. M., Bieger, D., Hopkins, D. A. & Miselis, R. R. Viscerotopic representation of the upper alimentary tract in the rat: sensory ganglia and nuclei of the solitary and spinal trigeminal tracts. *J. Comp. Neurol.* **283**, 248–268 (1989).
27. Browning, K. N. & Mendelowitz, D. Musings on the wanderer: what's new in our understanding of vago-vagal reflexes?: II. Integration of afferent signaling from the viscera by the nodose ganglia. *Am. J. Physiol. Gastrointest. Liver Physiol.* **284**, G8–G14 (2003).
28. Dykes, I. M., Tempest, L., Lee, S. I. & Turner, E. E. Brn3a and Islet1 act epistatically to regulate the gene expression program of sensory

- differentiation. *J. Neurosci.* **31**, 9789–9799 (2011).
29. Chang, I. & Parrilla, M. Expression patterns of homeobox genes in the mouse vomeronasal organ at postnatal stages. *Gene Expr. Patterns* **21**, 69–80 (2016).
 30. Faure, L. et al. Single cell RNA sequencing identifies early diversity of sensory neurons forming via bi-potential intermediates. *Nat. Commun.* **11**, 4175 (2020).
 31. Huang, C., Lu, F., Li, P., Cao, C. & Liu, Z. Tlx3 Function in the dorsal root ganglion is pivotal to itch and pain sensations. *Front. Mol. Neurosci.* **10**, 205 (2017).
 32. Zou, M., Li, S., Klein, W. H. & Xiang, M. Brn3a/Pou4f1 regulates dorsal root ganglion sensory neuron specification and axonal projection into the spinal cord. *Dev. Biol.* **364**, 114–127 (2012).
 33. Navarro, M., Ruberte, J., Carretero, A., Nacher, V. & Dominguez, E. in *Morphological Mouse Phenotyping* (eds Ruberte, J., Carretero, A. & Navarro, M.) Ch. 5 (Elsevier, 2017).
 34. Gilmour, D., Rembold, M. & Leptin, M. From morphogen to morphogenesis and back. *Nature* **541**, 311–320 (2017).
 35. Isabella, A. J., Barsh, G. R., Stonick, J. A., Dubrulle, J. & Moens, C. B. Retinoic acid organizes the zebrafish vagus motor topographic map via spatiotemporal coordination of Hgf/Met signaling. *Dev. Cell* **53**, 344–357 (2020).
 36. Moorman, A., Webb, S., Brown, N. A., Lamers, W. & Anderson, R. H. Development of the heart: (1) formation of the cardiac chambers and arterial trunks. *Heart* **89**, 806–814 (2003).
 37. Yerxa, T. E., Kee, E., DeWeese, M. R. & Cooper, E. A. Efficient sensory coding of multidimensional stimuli. *PLoS Comput. Biol.* **16**, e1008146 (2020).

38. Barlow, H. B. in *Sensory Communication* (ed. Rosenblith, W. A.) 217–234 (MIT Press, 1961).
39. Frisby, C. L. et al. Inhibition of transient lower esophageal sphincter relaxation and gastroesophageal reflux by metabotropic glutamate receptor ligands. *Gastroenterology* **129**, 995–1004 (2005).
40. Jensen, J. et al. Transient lower esophageal sphincter relaxations in dogs are inhibited by a metabotropic glutamate receptor 5 antagonist. *Eur. J. Pharmacol.* **519**, 154–157 (2005).
41. Yu, J. Spectrum of myelinated pulmonary afferents (III) cracking intermediate adapting receptors. *Am J Physiol. Regul. Integr. Comp. Physiol.* **319**, R724–R732 (2020).
42. Li, L. et al. The functional organization of cutaneous low-threshold mechanosensory neurons. *Cell* **147**, 1615–1627 (2011).
43. Alcaino, C. et al. A population of gut epithelial enterochromaffin cells is mechanosensitive and requires Piezo2 to convert force into serotonin release. *Proc. Natl Acad. Sci. USA* **115**, E7632–E7641 (2018).
44. Zagorodnyuk, V. P., Chen, B. N., Costa, M. & Brookes, S. J. Mechanotransduction by intraganglionic laminar endings of vagal tension receptors in the guinea-pig oesophagus. *J. Physiol.* **553**, 575–587 (2003).
45. Xia, G., Tawhai, M. H., Hoffman, E. A. & Lin, C. L. Airway wall stiffening increases peak wall shear stress: a fluid-structure interaction study in rigid and compliant airways. *Ann. Biomed. Eng.* **38**, 1836–1853 (2010).
46. Andresen, M. C. & Paton, J. F. R. in *Central Regulation of Autonomic Functions* (eds Llewellyn-Smith, I. J. & Verberne, A. J. M.) Ch. 2 (Oxford Univ. Press, 2011).
47. Cutsforth-Gregory, J. K. & Benarroch, E. E. Nucleus of the solitary tract, medullary reflexes, and clinical implications. *Neurology* **88**,

1187–1196 (2017).

48. Liman, E. R., Zhang, Y. V. & Montell, C. Peripheral coding of taste. *Neuron* **81**, 984–1000 (2014).
49. Yarmolinsky, D. A., Zuker, C. S. & Ryba, N. J. Common sense about taste: from mammals to insects. *Cell* **139**, 234–244 (2009).
50. Grabe, V. & Sachse, S. Fundamental principles of the olfactory code. *Biosystems* **164**, 94–101 (2018).
51. Tervo, D. G. et al. A designer AAV variant permits efficient retrograde access to projection neurons. *Neuron* **92**, 372–382 (2016).
52. Han, W. et al. A neural circuit for gut-induced reward. *Cell* **175**, 887–888 (2018).
53. Fontaine, A. K. et al. Optical vagus nerve modulation of heart and respiration via heart-injected retrograde AAV. *Sci Rep.* **11**, 3664 (2021).
54. Kim, W. S. et al. Organ-specific, multimodal, wireless optoelectronics for high-throughput phenotyping of peripheral neural pathways. *Nat. Commun.* **12**, 157 (2021).
55. Stuart, T. et al. Comprehensive integration of single-cell data. *Cell* **177**, 1888–1902 (2019).
56. McInnes, L., Healy, J. & Melville, J. UMAP: uniform manifold approximation and projection for dimension reduction. Preprint at <https://arxiv.org/abs/1802.03426> (2018).
57. Bonilla, I. E., Tanabe, K. & Strittmatter, S. M. Small proline-rich repeat protein 1A is expressed by axotomized neurons and promotes axonal outgrowth. *J. Neurosci.* **22**, 1303–1315 (2002).
58. Kiryu-Seo, S. et al. Damage-induced neuronal endopeptidase (DINE) is a unique metallopeptidase expressed in response to neuronal damage

- and activates superoxide scavengers. *Proc. Natl Acad. Sci. USA* **97**, 4345–4350 (2000).
59. Baker, C. V. & Schlosser, G. The evolutionary origin of neural crest and placodes. *J Exp. Zool. B Mol. Dev. Evol.* **304**, 269–273 (2005).
 60. Qadir, M. M. F. et al. Single-cell resolution analysis of the human pancreatic ductal progenitor cell niche. *Proc. Natl Acad. Sci. USA* **117**, 10876–10887 (2020).
 61. Hu, H. et al. AnimalTFDB 3.0: a comprehensive resource for annotation and prediction of animal transcription factors. *Nucleic Acids Res.* **47**, D33–D38 (2019).
 62. Li, G. et al. Single cell expression analysis reveals anatomical and cell cycle-dependent transcriptional shifts during heart development. *Development* **146**, dev173476 (2019).
 63. Angelidis, I. et al. An atlas of the aging lung mapped by single cell transcriptomics and deep tissue proteomics. *Nat. Commun.* **10**, 963 (2019).
 64. Drokhlyansky, E. et al. The human and mouse enteric nervous system at single-cell resolution. *Cell* **182**, 1606–1622 (2020).
 65. Morarach, K. et al. Diversification of molecularly defined myenteric neuron classes revealed by single-cell RNA sequencing. *Nat. Neurosci.* **24**, 34–46 (2021).
 66. Efremova, M., Vento-Tormo, M., Teichmann, S. A. & Vento-Tormo, R. CellPhoneDB: inferring cell–cell communication from combined expression of multi-subunit ligand-receptor complexes. *Nat. Protoc.* **15**, 1484–1506 (2020).
 67. Ashburner, M. et al. Gene Ontology: tool for the unification of biology. *Nat. Genet.* **25**, 25–29 (2000).

68. Gene Ontology Consortium. The Gene Ontology resource: enriching a GOld mine. *Nucleic Acids Res.* **49**, D325–D334 (2021).
69. Mi, H., Muruganujan, A., Ebert, D., Huang, X. & Thomas, P. D. PANTHER version 14: more genomes, a new PANTHER GO-slim and improvements in enrichment analysis tools. *Nucleic Acids Res.* **47**, D419–D426 (2019).
70. Street, K. et al. Slingshot: cell lineage and pseudotime inference for single-cell transcriptomics. *BMC Genomics* **19**, 477 (2018).
71. Van den Berge, K. et al. Trajectory-based differential expression analysis for single-cell sequencing data. *Nat. Commun.* **11**, 1201 (2020).
72. Susaki, E. A. et al. Advanced CUBIC protocols for whole-brain and whole-body clearing and imaging. *Nat. Protoc.* **10**, 1709–1727 (2015).
73. von Buchholtz, L. J. et al. Decoding cellular mechanisms for mechanosensory discrimination. *Neuron* **109**, 285–298 (2021).

Acknowledgements

We thank L. Young, S. Tomita, I. Hsu, E. Gracheva, and P. De Camilli for comments on the manuscript; S. Tomita, S. Bagriantsev, J. Cardin, J. Demb, R. DiLeone, and J. Zhou for sharing mice; Y. Sun and J. Guo for testing Projection-seq AAV vectors; S. Wilson and the Yale CNNR Imaging Core for assistance with microscopy; G. Wang and the Yale Center for Genome Analysis (YCGA) for assistance with single-cell sequencing; J. Greenwood and the Yale Neuroscience Technology Core for making imaging apparatus and chambers; and X. Zhao for help drawing cartoon depictions.

BioRender.com was used in generating some of the illustrations. Funding was provided by the National Institutes of Health (NIH) (K01DK113047, R01HL150449 and DP2HL151354 to R.B.C); the Yale Spector Fund Award (R.B.C.); a YCGA pilot grant (R.B.C. and L.Z.); the Yale Kavli Innovative Research Award (R.B.C. and L.Z.); the CSC–Yale World Scholars Program in Biomedical Sciences (C.D.Y. and Q.J.X.); the Yale-CAPES Scholars

Program from Coordenação de Aperfeiçoamento de Pessoal de Nível Superior (CAPES - Brazil, Finance Code 001, R.D.P); and a Kavli Postdoctoral Fellowship (Q.Z.).

Author information

Affiliations

1. Department of Neuroscience, Yale University School of Medicine, New Haven, CT, USA

Qiancheng Zhao, Chuyue D. Yu, Rui Wang, Qian J. Xu & Rui B. Chang

2. Department of Cellular and Molecular Physiology, Yale University School of Medicine, New Haven, CT, USA

Qiancheng Zhao, Chuyue D. Yu, Rui Wang, Qian J. Xu, Rafael Dai Pra & Rui B. Chang

3. Interdepartmental Neuroscience Program, Yale University School of Medicine, New Haven, CT, USA

Chuyue D. Yu & Qian J. Xu

4. Department of Neurology, Yale University School of Medicine, New Haven, CT, USA

Le Zhang

Contributions

Q.Z., L.Z. and R.B.C. designed experiments, analysed data and wrote the manuscript. Q.Z. led and performed all experiments. C.D.Y and Q.Z. performed vCatFISH. R.W. and R.D.P. helped with anatomical tracing. Q.J.X. helped with statistics. L.Z. and R.B.C. analysed scRNA-seq data.

Corresponding authors

Correspondence to [Le Zhang](#) or [Rui B. Chang](#).

Ethics declarations

Competing interests

The authors declare no competing interests.

Peer review

Peer review information

Nature thanks Ulrika Marklund and the other, anonymous, reviewer(s) for their contribution to the peer review of this work.

Additional information

Publisher's note Springer Nature remains neutral with regard to jurisdictional claims in published maps and institutional affiliations.

Extended data figures and tables

[Extended Data Fig. 1 Developing and applying Projection-seq in VSNs.](#)

a, Retrograde labelling of VSNs in vagal ganglia from the heart (AAVrg-tdTomato, red) and the stomach (AAVrg-GFP, green). **b**, The numbers of VSNs singly (red or green) or dual (orange) labelled from indicated organs. n = 3-4 mice. **c**, Distance from a random neuron labelled from indicated organs to the centre of the ganglion (top) or between two neurons labelled from the same or two different organs (bottom). mean ± SEM, one-way

ANOVA. L- lung; H- heart; S- stomach; E- oesophagus; D- duodenum; C- colon; P- pancreas. **d**, A representative image (left) and quantification (right, mean \pm SEM, n = 6) of VSNs retrogradely labelled from the stomach using AAVrg-tdTomato (red) and Alexa FluorTM 647 conjugated CTb (green), showing that VSNs are labelled by AAVrgs and CTb with comparable efficiencies. **e**, Mouse hearts without (top) and with (bottom) Fast Green FCF injection. **f**, A series of transverse heart sections (1 mm thickness) with heart injection of AAVrg-tdTomato, showing that AAVrg can cover all tissue layers of most ventricles. **g**, Whole-mount view (left) and transverse-section view (right, as indicated by the parallelogram in the left) of mouse lung lobes without (top) and with (bottom) lung injection of Fast Green FCF through a tracheal cannula. **h, i**, Whole-mount (**h**) and zoom-in (**i**) view of a lung lobe with lung injection of AAVrg-tdTomato, showing that AAVrg can cover alveoli cells in most regions of the lung. Arrow, bronchi; arrowheads, infected alveoli cells. **j**, Mouse stomachs without (top) and with (surface view, left bottom; lumen view, right bottom) Fast Green FCF injection. Cartoon image (top right) shows injected stomach regions. **k**, Whole-mount view (max projection of stacked images) of a stomach with AAVrg-tdTomato injection, showing that AAVrg can cover most subregions of the stomach. **l, m**, transverse view around the pyloric region (**l**) and the pyloric sphincter (**m**) of a stomach with AAVrg-tdTomato injection, showing infection of the mucosal lining (arrowhead). **n–p**, lumen view of cardiac mucosa (**n**) and body mucosa (**o**, max projection (left) and at three different levels towards the lumen (right); **p**, 3D projection, colour-coded) of a stomach with AAVrg-tdTomato injection, showing infection of the mucosal lining. **q**, Infected enteric neurons in indicated subregions of a stomach with AAVrg-tdTomato injection. **r**, stomach injection with AAVrg-FLEX-tdTomato and AAVrg-GFP in Chatires-Cre mice (left) extensive labelled VSN central projections (green) but not DMV neurons (red). Organ illustration was adapted from BioRender.com. **s–u**, Mouse oesophagus (**s**), duodenum (**s**, cartoon image on the right showing injection areas), transverse colon (**t**) and pancreas (**u**) with corresponding organ injection of Fast Green FCF. **v**, Oesophagus (AAVrg-tdTomato) and stomach (AAVrg-GFP) co-injection, showing the distribution of infected tdTomato⁺ and GFP⁺ cells along subregions of the gastrointestinal tract. Oesophagus cells are heavily infected by tdTomato and stomach cells by GFP. Co-infection was only observed in region 3

around the oesophageal sphincter. UE, upper oesophagus; LE, lower oesophagus. **w**, Duodenum (AAVrg-tdTomato) and stomach (AAVrg-GFP) co-injection, showing the distribution of infected tdTomato⁺ and GFP⁺ cells along subregions of the gastrointestinal tract. Duodenum cells, including mucosal epithelial cells in the villi, are heavily infected by tdTomato and stomach cells by GFP. Co-infection was only observed in region 6 and 7 around the antrum and pyloric sphincter. Scale bars: 5 mm (**e, g, j, s, t, u**), 1 mm (**f, h, k, v, w**), 100 µm (others). Cartoon illustrations in **a, j, s-w** adapted with permission from ref. [11](#).

Source Data

Extended Data Fig. 2 Projection-seq analysis faithfully reveals the molecular architecture and organ projection of VSNs.

a, VSNs retrogradely labelled from the stomach using Projection-seq AAV (UPB-stomach, top) or AAVrg-GFP (bottom). **b**, RT-PCR analysis of vagal ganglia cDNA from mice with stomach injection of Projection-seq AAV-UPB2 (red) or control (grey) mice using primers that recognize UPB2 (dark colour) or UPB4 (light colour) sequences. For gel source data, see Supplementary Fig. [1](#). **c**, Percentage of tdTomato⁺ neurons after acute VSN dissociation (blue) and UPB marked neurons after Projection-seq analysis (red). **d**, Dot plot of expression of indicated marker genes in 12 VSN subpopulations (A-L)/52 VSN clusters (A1-L2). **e**, Correlation scores for VSNs labelled with UPBs from indicated visceral organs. **f**, UMAP plots of 31,182 cells from control scRNA-seq, coloured by expression of indicated genes. Dashed circle indicates *Syn1*⁺/*Slc17a6*⁺ neuronal clusters. **g**, (top) UMAP plot of 16,476 neurons from neuronal clusters indicated in (**f**), coloured by expression of indicated genes, showing the two developmental origins of VSNs. *Prdm12* (blue) labels neural crest derived VSNs in the jugular ganglia. *Phox2b*⁺ placode derived clusters (red, dashed circle) containing 13,210 VSNs in the nodose ganglia from control scRNA-seq data are re-clustered and plotted on the UMAP plot (bottom), coloured by VSN subpopulations. **h**, UMAP plot of 27,800 *Phox2b*⁺ placode-derived VSNs from integrated Projection-seq (cyan) and control scRNA-seq (red) data. **i**, Percentage of neurons in 49 VSN clusters from control scRNA-seq

(blue) and Projection-seq (red) datasets. E-VSNs were excluded. **j**, UMAP plots of VSNs colour by expression of indicated marker genes from control scRNA-seq (top) and Projection-seq (bottom) data. **k**, RNAscope HiPlex Assay in the nodose/jugular ganglia for indicated marker genes identified from Projection-seq. **l**, Zoom-in images from the dashed regions in (k). The numbers of VSNs expressing one gene (red or green) or both genes (yellow) were counted. Consistent with Projection-seq data as shown in (d), *Trpa1* and *Tmc3* were largely expressed in non-overlapping VSNs, whereas *Ut2sb*, *Runx3*, *Gabra1*, and *Gm765* each labelled a distinct VSN subset. **m**, VSN subpopulations determined from RNAscope HiPlex Assays using indicated genes identified by Projection-seq. One neuron per column as indicated in the bottom. X, unlabelled; Jg, jugular neurons. **n**, Cumulative percentage of neurons in 11 VSN subpopulations revealed by Projection-seq, control scRNA-seq, or RNAscope. X, unlabelled. **o**, Dot plot of expression of UPBs representing indicated organs in 12 VSN subpopulations (A-L)/52 clusters (A1-L2). **p**, RNAscope HiPlex Assays for indicated genes. VSNs were retrogradely labelled from indicated organs with AAVrgs and visualized using corresponding RNAscope probes. *, VSNs from oesophagus, lung, or colon. +, VSNs from stomach, heart, or duodenum. #, double-labelled VSNs. **q**, Cumulative percentage of neurons in 11 VSN subpopulations expressing organ UPBs from Projection-seq analysis (top) and retrogradely labelled from indicated organs from RNAscope analysis (bottom). X, unlabelled. Scale bars: 100 µm (a, k), 20 µm (l, p).

[Source Data](#)

[**Extended Data Fig. 3 ‘Visceral organ’ and ‘tissue layer’ coding in VSNs.**](#)

a, UMAP plots of VSNs showing that *Sprrl1a* (top) and *Ecell1* (bottom), genes upregulated in damaged sensory neurons, are selectively expressed in E-VSNs (dashed circles, control scRNA-seq data). **b**, Percentage of E-VSNs in label-free control scRNA-seq data (blue) and Projection-seq (red) data. **c**, Detection of *Sprrl1a* using RNAscope in vagal ganglia from control (top) and AAVrg stomach injected (bottom) mice. Dashed lines indicate the shape of vagal ganglia. *Sprrl1a*⁺ neurons are indicated in red dashed circle.

Scale bar: 100 μ m. **d**, Percentage of *Sprrla⁺* VSNs in control versus AAVrg stomach injected mice. mean \pm SEM, n = 4. *p < 0.05, p = 0.0204, two-tailed t-test. **e**, Heat map of genes differentially expressed in VSNs innervating indicated organs. **f**, Percentage of VSNs marked by UPBs from different gut regions in indicated clusters, coloured per cluster. **E** (oesophageal)-Sphincter VSNs express both UPB-oesophagus and UPB-stomach. **P** (pyloric)-Sphincter VSNs express both UPB-stomach and UPB-duodenum. **g**, Differential expression of transcription factors in UPB-marked VSNs innervating indicated organs. From left: *Atf3*, *Terf1*, *Runx1*, *Sox4*, *Tshz2*, *Pou4f1*, *Cebpb*, *Irf6*, *Esr1*, *Tbx3*, *Id3*, *Hoxb5*, *Carhsp1*, *Hoxb6*, *Mef2c*, *Zfhx3*, *Tcf4*, *Egr1*, *Klf2*, *Klf5*, *Casz1*, *Etv1*, *Epas1*, *Nfkbia*, *Scrt2*, *St18*, *Scx*, *Klf4*, and *Nhh2*. **h**, IPA predicted regulatory network of *Pou4f1* in lung VSNs. Orange arrows, predicted activation; grey arrow, unknown. **i**, Dot plots of cell-cell signalling between organ-UPB labelled VSNs and various cell types in corresponding organs, predicted by CellPhoneDB. (top left), HVSN, heart-VSN; CM, cardiomyocyte; EDC, endothelial cell; EP, epicardial cell; FB, fibroblast. (top right), LVSN, lung-VSN; ATI, alveolar epithelial type I cell; ATII, alveolar epithelial type II cell; B, B cell; C&S, ciliated and secretory cell; DC, dendritic cell; EDC, endothelial cell; FB, fibroblast; MO, monocyte; Mac, macrophage; NK, natural kill cell; Neutro, neutrophil; Peri, pericyte; T, T cell. (bottom left), CVSN, colon-VSN; Endo, endothelial cell; Immu, immune cell; EN, enteric neuron; Glia, glial cell; Entero, enteroendocrine cell; Mus/Fb, muscle cell and fibroblast. (bottom middle), DVSN, duodenum-VSN; EXMN, excitatory motor neuron; INMN, inhibitory motor neuron; IN, inter neuron; IPAN, intrinsic primary afferent neuron. (bottom right), PVSN, pancreas-VSN; ISL, islet cell; ACI, acinar cell; DUCT, duct cell; MES, mesenchymal cell; IMVS, immune and vascular cell. **j**, Scatterplots of expression measures vs tissue layer trajectory scores for indicated DEGs along the tissue layer trajectory. Bars: 0–3. **k**, Fraction of DEG⁺ VSN endings characterized in *Gpr65^{tdT}*, *Drd2^{tdT}*, and *Agtr1a^{tdT}* mice in indicated tissue layers of indicated organs. mean \pm SEM, number of mice: *Gpr65*-Oesophagus (3), *Gpr65*-Stomach (7), *Gpr65*-Duodenum (4), *Drd2*-Oesophagus (3), *Drd2*-Stomach (6), *Drd2*-Duodenum (3), *Drd2*-Colon (2), *Drd2*-Heart (6), *Agtr1a*-Oesophagus (4), *Agtr1a*-Stomach (12), *Agtr1a*-Duodenum (4), *Agtr1a*-Colon (3), *Agtr1a*-Heart (6). **l**, Expression of *Gpr65* and *Trpv1* in F-VSNs (left) and maximum depths of duodenal MEs, normalized to the thickness of the sample, in *Trpv1^{tdT}* and

$\text{Gpr65}^{\text{tdT}}$ mice (right). mean \pm SEM, 15 endings from 3 mice for Trpv1 , 26 endings from 4 mice for Gpr65 . *** $p < 0.001$, $p = 6.6 \times 10^{-6}$, two-tailed t -test. **m**, Expression of Sst and Trpv1 in F1-VSNs (left) and the number of stomach gland tips innervated in the antrum and corpus, normalized to the innervation area, in $\text{Trpv1}^{\text{tdT}}$ and Sst^{tdT} mice (right). mean \pm SEM, 11 endings from 5 mice for Trpv1 , 10 endings from 5 mice for Sst , ** $p < 0.01$, $p = 0.0031$, two-tailed t -test.

[Source Data](#)

[Extended Data Fig. 4 AAV-guided anatomical tracing using various Cre mouse lines.](#)

a, Schematic illustration of imaging DEG⁺ VSN endings in intact cleared visceral organs using nodose ganglia injection of AAV-FLEX-tdTomato in corresponding Cre mouse lines. A mouse heart before and after CUBIC clearing was shown. Leftmost panel adapted with permission from ref. ¹¹; remainder of the illustration was adapted from BioRender.com. **b**, Stereotypical VSN sensory endings characterized in various visceral organs in $\text{Vglut2}^{\text{tdT}}$ mice. **c**, UMAP plots of VSN clusters, coloured by the percentage of gene⁺ VSNs in each cluster. **d**, UMAP plots of VSN clusters, coloured by fold enrichment, calculated as the percentage of gene⁺ VSNs in the target cluster normalized by the overall percentage of gene⁺ VSNs in all clusters. **e**, Representative images of vagal ganglia from the following mice: $\text{Sst-Cre};\text{lox-L10-GFP}$, $\text{Gpr65}^{\text{tdT}}$, $\text{Glp1r}^{\text{tdT}}$, $\text{P2ry1}^{\text{tdT}}$, $\text{Trpv1}^{\text{tdT}}$, $\text{Piezo2}^{\text{tdT}}$, $\text{Vip-Cre};\text{lox-L10-GFP}$, $\text{Pvalb-Cre};\text{lox-tdT}$, $\text{Twist2}^{\text{tdT}}$, $\text{Agtr1a}^{\text{tdT}}$, Nts^{tdT} , $\text{Vglut1-Cre};\text{lox-ChR2-eYFP}$, $\text{Calb2}^{\text{tdT}}$ and Drd2^{tdT} . Scale bars: 0.5 cm (**a**), 100 μm (**b**, **e**).

[Extended Data Fig. 5 Projection-seq-guided mapping of heart VSNs.](#)

a, Light sheet image of a cleared heart from $\text{Vglut2}^{\text{tdT}}$ mice showing the projection of vagal cardiac afferents. **b**, Distribution of the three vagal afferent ending types in the heart. Purple circles, plate of puncta (flower

spray) endings; blue squares, parallel intramuscular arrays; orange circles, varicose surface endings. RA, right atrium. LA, left atrium. RCV, right cardiac vein. AO, aorta. PT, pulmonary trunk. **c**, 4 primary VSN clusters for heart UPB-labelled neurons, visualized on the UMAP plot (top) or column graph (bottom, red stars). **d**, Percentage of VSNs expressing indicated genes targeted in various Cre mouse lines in the 4 primary heart clusters. **e**, Fraction of DEG⁺ VSNs in indicated clusters, calculated as the number of DEG⁺ VSNs in the indicated cluster normalized by the total number of DEG⁺ VSNs in all the 4 primary heart clusters. **f**, Innervation density of heart ending types formed by indicated VSNs in corresponding Cre^{tdT} mice (mean ± SEM, n = 3–10 samples), indicating that the three VSN heart ending types are formed by different VSN subpopulations. **g**, Representative cardiac endings formed by indicated VSNs in corresponding Cre^{tdT} mice. Depth of IMAs labelled in Drd2^{tdT} mice are colour-coded. **h**, UMAP plot of VSN clusters indicating corresponding ending types in the heart. Scale bars: 1 mm (**a**), 100 µm (**g**).

[Source Data](#)

[Extended Data Fig. 6 Projection-seq-guided mapping of lung VSNs.](#)

a, Cartoon depiction of VSN ending types in the lung. **b**, 5 primary VSN clusters for lung UPB-labelled neurons, visualized on the UMAP plot (left) or column graph (right, red stars). **c**, Fraction of DEG⁺ VSNs across indicated primary clusters. **d**, Percentage of VSNs expressing indicated genes targeted in various Cre mouse lines in indicated clusters. **e**, RNAscope HiPlex Assay for various A3 cluster marker genes as shown in (**d**) in vagal ganglia. VSNs projecting to the lung were retrogradely labelled with AAVrg and visualized using an RNAscope probe. **f**, Expression of indicated genes in retrogradely labelled lung VSNs (one neuron per column). Note that A3 cluster markers including *P2ry1*, *Agtr1a*, *Pvalb*, and *Slc17a7* were largely co-expressed in the same subset of lung VSNs. **g**, Bud endings around pulmonary neuroepithelial bodies in P2ry1^{tdT}, Agtr1a^{tdT}, Vglut1^{tdT}, Piezo2^{tdT}, and Pvalb^{tdT} mice. **h**, Bud endings (arrow heads) wrapping around taste buds in the larynx and upper oesophagus in P2ry1^{tdT}

and Agtr1a^{tdT} mice (see [Methods](#)-Annotation of VSN clusters). **i**, Alveoli endings in Twist2^{tdT}, P2ry1^{tdT}, Trpv1^{tdT}, and Npy2r^{tdT} mice. **j, k**, 3D projection of stacked confocal images showing patchy endings along the bronchi (top) and around bronchi bifurcations (bottom) in P2ry1^{tdT} mice (**j**) and longitudinal endings wrapping around bronchioles in Npy2r^{tdT} mice (**k**). Fibre depths are colour-coded. **l**, Innervation density of lung VSN ending types formed by indicated VSNs in corresponding Cre^{tdT} mice (mean ± SEM, number of mice as indicated). **m**, UMAP plot of VSN clusters indicating corresponding ending types in the lung. Scale bars: 20 µm (**e, g**), 100 µm (**h–k**).

[Source Data](#)

[Extended Data Fig. 7 Projection-seq-guided mapping of stomach VSNs.](#)

a, Cartoon depiction of the 11 regions along the gastrointestinal tract with injection sites indicated. Cartoon illustration adapted with permission from ref. [11](#). **b**, Innervation intensity of various vagal afferent ending types (innervated area/total area for mucosal endings and IMAs, number of terminals/total area for IGLEs) along indicated regions on the gastrointestinal tract in Vglut2^{tdT} mice. (mean ± SEM, n = 3-4). E.S., oesophageal sphincter; P.S., pyloric sphincter; D, duodenum; C, transverse colon. Regions 1–3, upper, middle, and lower oesophagus. Regions 4–8 correlate with stomach regions as shown in **(a)**. **c**, 9 primary VSN clusters for stomach UPB-labelled neurons, visualized on the UMAP plot (top, red) or column graph (bottom, red stars). **d**, Innervation density of vagal ending types around the oesophageal (top) and pyloric (bottom) sphincters, normalized to the density across the entire stomach (mean ± SEM, n = 4). **e**, UMAP plots of VSN clusters enriched for the oesophageal (top, VSNs dual labelled with oesophagus and stomach UPBs) and pyloric (bottom, VSNs dual labelled with stomach and duodenum UPBs) sphincters over other stomach regions. Light red indicates clusters containing more than 4% of dual UPB labelled VSNs. Red indicates clusters enriched (>1.05 fold) in dual UPB labelled VSNs over stomach UPB labelled VSNs. **f**, Fraction of DEG⁺ VSNs among indicated clusters, calculated as the number of DEG⁺

VSNs in the indicated cluster normalized by the total number of DEG⁺ VSNs in all shown clusters. **g**, Representative stomach endings formed by DEG⁺ VSNs around the oesophageal or pyloric sphincter in corresponding Cre^{tdT} mice. **h**, UMAP plots of VSN clusters (red) enriched for the stomach regions 5, 6, and 7 as shown in **(a)**. Light red indicates clusters containing more than 4% of stomach/colon (region 7) or stomach/pancreas (region 6) dual UPB labelled, or stomach UPB single labelled (region 5) VSNs. Red indicates clusters enriched (>1.05 fold) in dual UPB labelled VSNs over stomach UPB labelled VSNs (for region 6 and 7), or in stomach UPB labelled VSNs over all other 4 groups of dual UPB labelled VSNs (for region 5). **i**, Simulation results for VSN clusters I2, I4–7, J2, and J4 (see [Methods](#)). Arrow indicates the trial with the lowest variation (red dots, ending types listed on the right). **j**, Innervation density of four VSN ending types in different stomach regions normalized to the intensity across the entire stomach. Quantified in Vglut2^{tdT} mice (blue, mean ± SEM, n = 4) or predicted by Projection-seq (red). **k**, UMAP plots of VSNs showing *Agtr1a* and *Oxtr* expression in I-VSNs. **l**, Representative stomach IGLE endings formed by I-VSNs in Agtr1a^{tdT} mice. **m**, Innervation intensity (innervated area/total area for ME, pIMA, and cIMA; number/total area for IGLE, normalized to Vglut2^{tdT}) of stomach afferent ending types formed by indicated VSNs in corresponding Cre^{tdT} mice (mean ± SEM, n = 3–12). Scale bars: 100 μm.

[Source Data](#)

[Extended Data Fig. 8 Projection-seq-guided mapping of oesophagus, duodenum and colon VSNs.](#)

a, 8 primary duodenum UPB-labelled VSN clusters (top) and 8 primary S/D (stomach/duodenum) dual UPB-labelled VSN clusters (bottom), visualized on the UMAP plot (left, light red indicates clusters containing more than 4% labelled VSNs; red indicates enriched clusters) or column graph (right, red stars). Five VSN clusters enriched in duodenum VSNs over S/D VSNs were labelled (top left, red) and marked with orange bars (top right). **b**, Fraction of DEG⁺ VSNs among the five clusters identified in **(a)**. **c**, Representative sensory endings formed by DEG⁺ VSNs in the duodenum in

corresponding Cre^{tdT} mice. **d**, Innervation intensity (innervated area/total area for ME; number/total area for IGLE, normalized to $\text{Vglut2}^{\text{tdT}}$, same for **j**, **m**, and **n**) of duodenal afferent ending types formed by indicated VSNs in corresponding Cre^{tdT} mice (mean \pm SEM, n = 3–5). **e**, 5 primary VSN clusters for colon UPB-labelled neurons, visualized on the UMAP plot (top, red) or column graph (bottom, red stars). **f**, Fraction of Agtr1a^+ VSNs among the five clusters identified in (e). **g**, Colon IGLE formed in $\text{Agtr1a}^{\text{tdT}}$ mice. **h**, Innervation density of Trpv1^+ VSN ending types in the colon, determined via anatomical tracing in $\text{Trpv1}^{\text{tdT}}$ mice (blue, innervated area/total area for ME and pIMA; number/total area for IGLE, normalized to $\text{Vglut2}^{\text{tdT}}$, mean \pm SEM, n = 4) or predicted by Projection-seq (red). **i**, Representative colon IMA and IGLE endings formed in $\text{Trpv1}^{\text{tdT}}$ mice. **j**, Innervation intensity of colon afferent ending types formed by indicated VSNs in corresponding Cre^{tdT} mice (mean \pm SEM, n = 3–4). **k**, 6 primary VSN clusters for oesophagus UPB-labelled neurons, visualized on the UMAP plot (top, red) or column graph (bottom, red stars). A4-VSNs (1.68%, blue star) was characterized to form rare bud endings wrapping around taste buds in the upper oesophagus (see Extended Data Fig. 6). **l**, Fraction of Piezo2^+ and Trpv1^+ VSNs among the five clusters identified in (k). **m**, Innervation intensity of oesophageal afferent ending types formed in $\text{Piezo2}^{\text{tdT}}$ and $\text{Trpv1}^{\text{tdT}}$ mice (mean \pm SEM, n = 3). **n**, Innervation intensity of oesophageal afferent ending types formed by indicated VSNs in corresponding Cre^{tdT} mice (mean \pm SEM, n = 3–5). **o**, Representative oesophageal IGLEs formed in Nts^{tdT} (top) and $\text{Agtr1a}^{\text{tdT}}$ (bottom) mice. **p**, Representative oesophageal mucosal endings formed in $\text{Trpv1}^{\text{tdT}}$ (top) and $\text{Gpr65}^{\text{tdT}}$ (bottom) mice. **q**, UMAP plots of VSN clusters indicating corresponding ending types in the oesophagus, stomach, duodenum, and colon, and all examined gastrointestinal organs. **r**, 6 primary pancreas UPB-labelled VSN clusters, visualized on the UMAP plot (left, red) or column graph (right, red stars). **s**, Top GO pathways of DEGs in heart, lung, gut, and pancreas VSNs, and along the tissue layer trajectory, coloured by physiological functions. Number of DEGs used are indicated. FDR, false discovery rate. Scale bars: 100 μm .

[Source Data](#)

Extended Data Fig. 9 Development of vCatFISH analysis.

a, RNAscope HiPlex Assay of VSNs for the indicated 22 genes in cryo-sectioned vagal ganglia after in vivo calcium imaging. Scale bar: 100 μm . **b**, Percentage of neurons expressing the indicated 22 genes in 11 VSN subpopulations (A-L, colour-coded, from bottom to top) in Projection-seq data ($n = 12,583$). **c**, VSN subpopulations (A-L, colour-coded, from bottom to top) determined using expression of indicated genes from RNAscope HiPlex Assays. One neuron per row as indicated on the right ($n = 982, 136$ (13.8%) of which were *tdTomato* $^+$). **d**, Cumulative percentage of neurons revealed by Projection-seq or RNAscope in 11 VSN subpopulations. **e**, GCaMP6s and *tdTomato* signals recorded from in vivo ganglion imaging (left) and RNAscope signal against *tdTomato* in a series of cryosections (depth colour-coded) of the same nodose ganglion (right), showing a perfect registration of *tdTomato* $^+$ VSNs between in vivo ganglion imaging and post-hoc RNAscope cryosections. Dashed lines indicate bright *tdTomato* $^+$ cells in the imaging plane. Arrows indicate weak *tdTomato* $^+$ cells off (below) the imaging plane. **f**, GCaMP6s signals ($\Delta F/F$, colour-coded) as in (e, left) showing VSNs from in vivo ganglion imaging (left) and increased background signal from RNAscope against *Grm5* showing all VSNs from post-hoc nodose ganglion cryosections (right). Dashed circles and arrows indicate bright and weak *tdTomato* $^+$ cells as shown in (e). **g**, Zoom-in images from the box in (f), with numbered VSNs showing registration between in vivo ganglion imaging and post-hoc RNAscope analysis. Scale bars: 100 μm (a), 20 μm (e, f).

Source Data

Extended Data Fig. 10 vCatFISH reveals genetic identity of VSNs responsive to various body stimuli.

a, Representative images showing VSN GCaMP responses and expression of marker genes. (top) A *Gpr65* $^+$ VSN (*tdTomato* labelled, magenta; background GCaMP6s signal in blue showing the shape of all VSNs) and GCaMP6s responses ($\Delta F/F$, colour-coded) to indicated stimuli in a representative vagal ganglion of *Gpr65* tdT -GCaMP6s mice. Responses

($\Delta F/F$) of indicated VSNs are shown on the right. (bottom) RNAscope analysis of the same VSNs for indicated genes in vagal ganglion cryosections. Scale bars: 20 μm . **b**, Time-resolved responses ($\Delta F/F$, colour-coded) of 38 single VSNs to indicated chemicals (saline, water, 1 M glucose, Ensure, 10 x Phosphate-Buffered Saline (PBS), 150 mM HCl, 100 μl) injected into duodenal lumen in Gpr65^{tdT}-GCaMP6s mice ($n = 5$). RNAscope codes are in the same sequence as shown in Fig. [3b](#) and Extended Data Fig. [9b,c](#). Annotated subpopulations (colour-coded) for responsive VSNs are indicated on the right. **c**, Genetic compositions of all VSNs (grey) or VSN cohorts activated by various indicated stimuli (colour-coded), showing by the percentage of neurons expressing indicated genes. **d**, Subpopulations of VSNs activated by indicated stimuli. (top), UMAP plots of VSN subpopulations (A-L), coloured by the percentage of neurons activated by the indicated stimulus in each subpopulation, showing that VSNs responsive to stimuli from thoracic and abdominal organs follow the ‘visceral organ’ trajectory (dashed arrow). (bottom), Pie chart indicating the percentage of VSN subpopulations in all VSNs or VSN cohorts responding to indicated stimuli. **e**, Summary of VSN groups responsive to diverse stimuli, with key marker genes, response patterns, and VSN subpopulations determined using RNAscope, showing modular VSN sensory units across multiple visceral organs.

Source Data

Extended Data Fig. 11 VSN subpopulations specify response patterns.

a, b, GCaMP responses to lung stretch (**a**) and quantification of activation kinetics (**b**) in A/C-VSNs ($n = 50$) and K/L-VSNs ($n = 39$) from 5 mice. **c**, GCaMP responses with activation frame (arrow) aligned showing C-VSNs ($n = 34$) and A-VSNs ($n = 16$) have different adaptation rates to lung stretch. **d**, Quantification of adaptation kinetics as shown in (**c**). **e**, Percentage of UPB-labelled VSNs from indicated gastrointestinal organs/regions expressing *Slit2* (left) and *Grm5* (right) in Projection-seq data. **f, g**, GCaMP responses to oesophagus/stomach stretch (600 μl) (**f**) and quantification (**g**) in *Slit2⁺* C- ($n = 41$), *Slit2⁻* C- ($n = 53$), H/J- ($n = 52$), and I- ($n = 15$) VSN subpopulations from 6 mice. *Slit2⁺* C-VSNs were activated significantly

faster with lower activation threshold, consistent with them being mechano-sensors in the oesophagus. **h–j**, GCaMP responses (**h**) to intestine stretch (saline, 600 µl, arrow) and quantification of response magnitudes (**i**) and activation kinetics (**j**) in H- (n = 14), G- (n = 20), and I- (n = 12) VSN subpopulations from 5 mice. **k**, Comprehensive UMAP plot of VSNs from integration of Projection-seq, vCatFISH, and Projection-seq-guided anterograde tracing analyses. VSN subpopulations (A-L) are colour-coded as in Fig. [1b](#). Organs are indicated by coloured lines. Ending structures are indicated using italic. Sensory properties are labelled in bold. Dashed arrow indicates a continuous representation of gut organs along the gastrointestinal tract. Arrow indicates a potential gradual shift of sensory inputs from chemical to mechanical sensation in the intestine. Some VSN clusters with similar characteristics are indicated by dashed lines. Imaging frequency: 1.72 second/frame. mean ± SEM. *p < 0.05, **p < 0.01, ***p < 0.001, two-tailed t-test for (**b**), one-way ANOVA and Tukey's multiple comparisons test for (**d, g, i, j**). P values for shown comparisons from left to right are as follows: **b**, 0.002, 0.3057, 0.0017, 0.0492, 0.2255; **d**, 0.043, 0.015, 0.021; **g**, 4.1×10^{-6} , 4.6×10^{-7} , 1.7×10^{-4} , 0.01084, 0.00570, 1.3×10^{-4} , 2.3×10^{-6} , 0.0004, 1.3×10^{-6} , 3.0×10^{-5} , 0.0363; **i**, 0.1623, 0.9692, 0.2918; **j**, 0.6378, 0.8140, 0.9766, 5.2×10^{-5} , 0.0159.

[Source Data](#)

[Extended Data Fig. 12 A comprehensive road map of genetically defined VSN subpopulations.](#)

a, A comprehensive comparison of various characteristics of VSN clusters revealed between our data and previously published results. DEGs for VSN subpopulations (left column) and clusters (second to left column) are listed. **b**, UMAP plot of VSNs, coloured by expression of *Htr3a* (left) and *Htr3b* (right) in VSNs.

[Extended Data Fig. 13 Central targets of VSNs innervating various visceral organs.](#)

a, Representative brainstem images at indicated Bregma levels containing central projections of VSNs retrogradely labelled from indicated visceral organs using *AAVrg-tdTomato*. Scale bar: 100 µm. **b**, Distribution of central VSNs terminals retrogradely labelled from indicated visceral organs (colour-coded) along the rostral-caudal axis. **c**, Brainstem area innervated by VSNs from indicated organs along the rostral-caudal axis (mean ± SEM, number of mice: 2 (oesophagus), 3 (others)). **d**, Percentage innervation, calculated as vagal afferent fluorescence in indicated subnuclei normalized to the fluorescence in all vagal afferent targets, for various brainstem subnuclei along the rostral-caudal axis (mean ± SEM, n as in c). **e**, Quantitative analysis of innervation density in indicated brainstem regions from Bregma -7.2 mm to -8.0 mm by VSNs from various visceral organs, expressed as fluorescence in indicated area/fluorescence in total area (mean, colour-coded, n as in c). **f**, Correlation variance matrix among organ pairs showing that VSNs from functionally related organs terminated in similar brainstem regions.

Source Data

Extended Data Fig. 14 Central projections of 11 individual VSN pathways.

Representative brainstem images at indicated Bregma levels along the rostral-caudal axis containing central projections of 11 VSN pathways shown in Fig. 4b. Visceral organ, ending type, and Cre lines used (red) are indicated. Scale bar: 100 µm.

Supplementary information

Supplementary Figure 1

Original source image for electrophoresis, related to Extended Data Fig. 2b. Red box indicates how the gel was cropped for the final figure.

Reporting Summary

Supplementary Table 1

Detailed information for RNAscope probes.

Source data

Source Data Fig. 1

Source Data Fig. 2

Source Data Fig. 3

Source Data Fig. 4

Source Data Extended Data Fig. 1

Source Data Extended Data Fig. 2

Source Data Extended Data Fig. 3

Source Data Extended Data Fig. 5

Source Data Extended Data Fig. 6

Source Data Extended Data Fig. 7

Source Data Extended Data Fig. 8

Source Data Extended Data Fig. 9

Source Data Extended Data Fig. 10

Source Data Extended Data Fig. 11

Source Data Extended Data Fig. 13

Rights and permissions

Open Access This article is licensed under a Creative Commons Attribution 4.0 International License, which permits use, sharing, adaptation, distribution and reproduction in any medium or format, as long as you give appropriate credit to the original author(s) and the source, provide a link to the Creative Commons license, and indicate if changes were made. The images or other third party material in this article are included in the article's Creative Commons license, unless indicated otherwise in a credit line to the material. If material is not included in the article's Creative Commons license and your intended use is not permitted by statutory regulation or exceeds the permitted use, you will need to obtain permission directly from the copyright holder. To view a copy of this license, visit <http://creativecommons.org/licenses/by/4.0/>.

Reprints and Permissions

About this article

Cite this article

Zhao, Q., Yu, C.D., Wang, R. *et al.* A multidimensional coding architecture of the vagal interoceptive system. *Nature* **603**, 878–884 (2022).
<https://doi.org/10.1038/s41586-022-04515-5>

- Received: 26 March 2021
- Accepted: 04 February 2022
- Published: 16 March 2022
- Issue Date: 31 March 2022
- DOI: <https://doi.org/10.1038/s41586-022-04515-5>

Share this article

Anyone you share the following link with will be able to read this content:

[Get shareable link](#)

Sorry, a shareable link is not currently available for this article.

[Copy to clipboard](#)

Provided by the Springer Nature SharedIt content-sharing initiative

This article was downloaded by **calibre** from <https://www.nature.com/articles/s41586-022-04515-5>

| [Section menu](#) | [Main menu](#) |

- Article
- [Published: 14 February 2022](#)

A human brain vascular atlas reveals diverse mediators of Alzheimer's risk

- [Andrew C. Yang](#) [ORCID: orcid.org/0000-0002-6756-4746](#)^{1,2,3},
- [Ryan T. Vest](#)^{3 na1},
- [Fabian Kern](#) [ORCID: orcid.org/0000-0002-8223-3750](#)^{3,4 na1},
- [Davis P. Lee](#)³,
- [Maayan Agam](#)³,
- [Christina A. Maat](#)³,
- [Patricia M. Losada](#)³,
- [Michelle B. Chen](#)¹,
- [Nicholas Schaum](#)³,
- [Nathalie Khoury](#)³,
- [Angus Toland](#)⁵,
- [Kruti Calcuttawala](#)³,
- [Heather Shin](#)³,
- [Róbert Pálovics](#)³,
- [Andrew Shin](#)³,
- [Elizabeth Y. Wang](#)⁶,
- [Jian Luo](#) [ORCID: orcid.org/0000-0002-2064-8467](#)⁷,
- [David Gate](#) [ORCID: orcid.org/0000-0003-0481-9657](#)³,
- [Walter J. Schulz-Schaeffer](#) [ORCID: orcid.org/0000-0001-5886-2322](#)⁸,
- [Pauline Chu](#)⁴,
- [Julie A. Siegenthaler](#)⁹,
- [M. Windy McNerney](#)¹⁰,
- [Andreas Keller](#) [ORCID: orcid.org/0000-0002-5361-0895](#)^{3,4} &
- [Tony Wyss-Coray](#) [ORCID: orcid.org/0000-0001-5893-0831](#)^{2,3,11,12}

[Nature](#) volume 603, pages 885–892 (2022)

- 37k Accesses
- 2 Citations

- 281 Altmetric
- [Metrics details](#)

Subjects

- [Blood–brain barrier](#)
- [Cellular neuroscience](#)
- [Neurodegeneration](#)
- [Transcriptomics](#)

Abstract

The human brain vasculature is of great medical importance: its dysfunction causes disability and death¹, and the specialized structure it forms—the blood–brain barrier—impedes the treatment of nearly all brain disorders^{2,3}. Yet so far, we have no molecular map of the human brain vasculature. Here we develop vessel isolation and nuclei extraction for sequencing (VINE-seq) to profile the major vascular and perivascular cell types of the human brain through 143,793 single-nucleus transcriptomes from 25 hippocampus and cortex samples of 9 individuals with Alzheimer’s disease and 8 individuals with no cognitive impairment. We identify brain-region- and species-enriched genes and pathways. We reveal molecular principles of human arteriovenous organization, recapitulating a gradual endothelial and punctuated mural cell continuum. We discover two subtypes of human pericytes, marked by solute transport and extracellular matrix (ECM) organization; and define perivascular versus meningeal fibroblast specialization. In Alzheimer’s disease, we observe selective vulnerability of ECM-maintaining pericytes and gene expression patterns that implicate dysregulated blood flow. With an expanded survey of brain cell types, we find that 30 of the top 45 genes that have been linked to Alzheimer’s disease risk by genome-wide association studies (GWASs) are expressed in the human brain vasculature, and we confirm this by immunostaining. Vascular GWAS genes map to endothelial protein transport, adaptive immune and ECM pathways. Many are microglia-specific in mice, suggesting a partial evolutionary transfer of Alzheimer’s disease risk. Our work uncovers the molecular basis of the human brain vasculature, which will inform our understanding of overall brain health, disease and therapy.

[Download PDF](#)

Main

Brain health depends on brain vascular health. The brain is one of the most highly perfused organs in the body, which is necessary to meet its unique metabolic needs⁴. Brain vascular dysfunction contributes to stroke¹, congenital neurological disorders⁵ and age-related neurodegenerative disease^{5,6}. The brain vasculature forms a special structure—the blood–brain barrier (BBB)—that mediates selective and haemodynamically responsive movement of molecules between the blood and the brain^{2,3}. Although necessary for optimal neuronal function⁴, the BBB frustrates the pharmacological treatment of nearly all brain disorders^{7,8}, and extensive efforts are underway to discover targets on the human BBB to enhance drug delivery.

Specialized brain vascular properties arise from a complex community of interacting cell types^{9,10,11}: endothelial cells, adjacent mural smooth muscle cells (SMCs) and pericytes, perivascular immune cells, and surrounding astrocytes that differ across brain regions and vary along an arteriovenous gradient¹². Heterogeneity along this gradient produces functionally segmented circulatory, metabolic and permeability properties that are necessary for brain health^{3,5}.

Previous work has profiled the mouse brain vasculature^{12,13,14,15}, but it remains unclear how conserved these findings are in humans. Single-nucleus studies have elucidated the cellular heterogeneity of the human brain in health and disease^{16,17,18,19}. However, although vascular cell density^{20,21} (70,000 cells per mm³) approaches total glia density²⁰, previous studies have depleted human brain vascular cells for unknown reasons. Although human brain microvessels can be isolated for bulk assays, at present no method exists—to our knowledge—to extract nuclei from microvessels for analysis at single-cell resolution.

Given the scientific, medical and pharmacological importance of the human brain vasculature, we set out to create a single-cell atlas of the human brain vasculature of the hippocampus and cortex on the basis of samples from individuals with no cognitive impairment (NCI) and from individuals with Alzheimer’s disease (AD).

Cells of the human brain vasculature

Extracting nuclei from brain microvessels is challenging because the method must dissociate the vessel basement membrane to release nuclei without damaging the nuclei themselves. We systematically explored enzymatic, chemical and physical approaches. Most resulted in damaged nuclei devoid of RNA reads. We found success in adapting a gentle protocol for splenocyte isolation (Methods), and combined it with extensive clean-up using sucrose and fluorescence-activated cell sorting (FACS) to ensure high-quality data (Fig. 1a, Extended Data Fig. 1). We used our method, VINE-seq (vessel isolation and nuclei extraction for sequencing), to process 25 samples: the

hippocampus of 9 individuals with AD and 8 age- and sex-matched individuals with NCI, as well as the superior frontal cortex from a subset of 8 individuals (4 per group) (Supplementary Table 1). Samples included a range of *APOE* genotypes, and NCI samples exhibited no significant vascular pathologies in the studied hippocampus and cortex tissue (Supplementary Table 1, Extended Data Fig. 2a). After quality control (Methods), we obtained 143,793 single-nucleus transcriptomes. Visualization in uniform manifold approximation and projection (UMAP) space separated nuclei into 15 major cell types (Fig. 1b), including all known vascular and perivascular cell types: endothelial cells (arterial, capillary and venous), SMCs, pericytes, astrocytes, macrophages, T cells, and both perivascular and meningeal fibroblasts. The number of cerebrovascular nuclei captured here exceeds those in the literature by several hundred-fold (Supplementary Table 2, Extended Data Fig. 2b,c). Vascular cell-type markers were validated in situ (Fig. 1c). Data can be browsed at https://tvc-stanford.shinyapps.io/human_bbb.

Fig. 1: Cells of the human brain vasculature.

 figure 1



a, VINE-seq method to enrich vascular nuclei from post-mortem human brain samples. **b**, Enrichment of vascular and perivascular cell types from the human cortex and hippocampus. UMAP of 143,793 nuclei from 25 human hippocampus and superior frontal cortex samples across 17 individuals, coloured by cell type and labelled with numbers of nuclei. M. fibro., meningeal fibroblast; oligo., oligodendrocyte; OPC, oligodendrocyte precursor cell; P. fibro., perivascular fibroblast; P. macrophage, perivascular macrophage. **c**, Immunohistochemical validation of cell-type-specific gene markers. Scale bars, 50 µm. Image credit: Human Protein Atlas²⁵ (<http://www.proteinatlas.org>). **d**, Enriched biological pathways in BECs from the hippocampus compared to the superior frontal cortex, in individuals with NCI ($P < 0.05$, cumulative hypergeometric test). **e**, Left, scatter plot depicting mRNA expression levels (logCPM) of mouse and human genes with one-to-one orthologues in BECs. Divergently expressed genes are coloured (>10 -fold difference,

minimum $0.5 \log_2 \text{CPM}$ expression). Right, proportion of the transcriptome of each brain cell type that is specific to human versus mouse (same thresholds). **f**, Immunohistochemical validation of A2M protein specifically in the human but not mouse vasculature. Scale bars, $50 \mu\text{m}$.

VINE-seq captured three types of immune cell in the human brain: microglia, macrophages and T cells. Over 300 genes differentiated brain border macrophages and microglia, yielding new markers for human studies (Extended Data Fig. 2d–f). Analysis of canonical markers indicated our capture of brain memory CD8 cytotoxic and CD4 T cells (Extended Data Fig. 2g). Brain regional transcriptome differences were evident (Supplementary Table 3). Astrocyte transcriptional identity was the most influenced by brain region (Extended Data Fig. 2h–k). Moreover, hippocampal endothelial cells showed greater baseline inflammation—indicated for example by higher levels of interferon- γ (IFN γ) signalling—than did those in the cortex (Fig. 1d). Such inflammatory signalling may inhibit hippocampal neurogenesis, and, together with accelerated hippocampal pericyte loss (Extended Data Fig. 1h), provides a molecular hypothesis for the vulnerability and dysfunction of the hippocampal vasculature²².

We next compared nuclei transcriptomes between human and mouse endothelial cells and pericytes. Using a strict cut-off ($>10\times$ difference, log-transformed counts per million (CPM) > 0.5) (Supplementary Table 4), we found hundreds of species-enriched genes in brain endothelial cells (BECs) and pericytes (Fig. 1e). Understanding species differences in neurons and glia has been a subject of intense study. Together with microglia²³, we find that BECs and pericytes exhibit the greatest transcriptional divergence (Fig. 1e, Extended Data Fig. 3). Several vascular solute transporters (for example, the γ -aminobutyric acid (GABA) transporter encoded by *SLC6A12*) vary by species, which suggests differences in brain metabolism (Extended Data Fig. 3g). Several genes of disease and pharmacological importance also vary (Extended Data Figs. 3, 4). Together, the VINE-seq method opens the human brain vasculature for molecular study and provides a data resource for investigating its diverse cell types.

Endothelial and mural cell organization

With our large-scale capture of vascular nuclei (more than 30 times the number previously reported in mice¹² and more than 200 times that previously reported in humans, to our knowledge^{16,17}), we sought to comprehensively characterize the molecular basis of endothelial and mural cell organization along the arteriovenous axis of the human brain vasculature. Changes along this axis are referred to as zonation^{12,15}. Beginning with BECs, we clustered 36,825 nuclei into known arterial, capillary and venous segments (Fig. 2a, Extended Data Fig. 5). Clusters were defined

by established zonation markers, such as arterial *VEGFC* and *ALPL*; capillary *MFS2A* and *SLC7A5*; and venous *ILIR1* and *NR2F2*^{12,15}. Although capillaries represent most (around 90%) of the endothelium, VINE-seq captured rarer arterial (at 19%) and venous (27%) BECs, because of better strainer retention or nuclei liberation. We noticed a small cluster (571 nuclei, around 0.1%) outside conventional zonation. This cluster expressed genes characteristic of ‘tip’ cells (for example, *PLAUR* and *LAMBI*) as well as ‘proteostatic’ heat shock proteins.

Fig. 2: Organizing principles of human BECs.

 figure 2

a, UMAP of 36,825 human BEC nuclei, coloured by zonation. **b**, Zonal expression of transcripts across human BECs ordered by Monocle pseudotime. LOWESS regression line (orange) and density of black lines (counts) correspond with expression levels. A, arterial; C, capillary; V, venous. **c**, Heat map of zonation-dependent gene expression in human BECs (36,825 nuclei). **d**, Scatter plot depicting the specificity of transcripts for venous BECs in mice¹² versus humans. Venous specificity score =average(logFC(vein/capillary), logFC(vein/artery)) (in which FC refers to fold change). For example, *VWF* is predicted to be more specific to venous BECs in mice than it is in humans. See Extended Data Fig. 9 for arterial and capillary specificity plots. **e**, Immunohistochemical validation of *VWF* specificity to venous BECs in mice but not in humans. Scale bars, 50 μm.

We next ordered endothelial nuclei along a one-dimensional pseudotime²⁴ axis to recapitulate the anatomical arteriovenous axis. Arterial and venous markers peaked at opposite ends, with capillary markers in between (Fig. 2b). We used the 665 most significantly variable cluster genes to unbiasedly order endothelial nuclei and observed 7 gradually changing patterns of gene expression, representing arterial, capillary or venous markers, and combinations thereof (Fig. 2c). We confirmed that the Monocle range represented a cell order matching anatomical arteriovenous zonation through immunostaining²⁵ (Extended Data Fig. 6a). Our patterns recapitulate the gradual zonation continuum described in mice—but, notably, this similar overall continuum arises from significantly different component zonation markers (Supplementary Tables 2, 5).

We thus wondered whether established zonation markers in mice would be conserved in humans. We calculated a score (Methods) measuring the specificity of each gene to a given zonation (for example, arterial, capillary or venous). Indeed, we observed in each vessel segment a significant number of markers that lost their zonation specificity between species (Fig. 2d, Extended Data Fig. 6). For example, the blood clotting gene von Willebrand factor (*VWF*) is largely expressed in mouse venous endothelial cells^{12,15}. However, *VWF* is expressed throughout the human cerebrovasculature, even in small-diameter capillaries (Fig. 2d,e). *VWF* abundance predisposes for ischaemic stroke²⁶, which raises implications for translational studies of stroke.

Next, with mural cells, we clustered 34,508 nuclei into arterial smooth muscle cells (aSMCs), arteriolar SMCs (aaSMCs), and notably, two subclusters of pericytes (Fig. 3a,b). One pericyte subcluster enriched for small-molecule transmembrane transport, which we call T-pericytes (for transport), whereas the other subcluster enriched for extracellular matrix (ECM) organization, (M-pericytes, for matrix). Thus, function rather than anatomical location may be the major driver of human pericyte transcriptional identity. M-pericytes may therefore contribute to small-vessel diseases such as CADASIL (cerebral autosomal dominant arteriopathy with subcortical infarcts and leukoencephalopathy), CARASIL (cerebral autosomal recessive arteriopathy with subcortical infarcts and leukoencephalopathy) and collagen IV deficiencies for which perturbations in the cerebrovascular ECM cause disease²⁷. Moreover, human T-pericytes—but not mouse pericytes—express transporters like the GABA transporter *SLC6A1* (involved in epilepsy) and the glutamate transporter *SLC1A3* (Extended Data Fig. 3g). Because recent mouse pericyte datasets¹² have cautioned against endothelial contamination, we assessed and found no such contamination in our human pericyte nuclei (Extended Data Fig. 2c).

Fig. 3: Organizing principles of human brain mural cells.

 **figure 3**

a, UMAP of 34,508 human pericyte and SMC nuclei, coloured by cell subtype. **b**, Enriched biological pathways in T- and M-pericytes compared to the remaining SMC and pericyte populations ($P < 0.05$, cumulative hypergeometric test). **c**, Heat map of gene expression in human SMCs and pericytes (34,508 human mural nuclei). Solid line delineating aaSMCs and aSMCs from pericytes reflects an abrupt transcriptomic transition. Unlike BECs, mural cell ordering does not reflect anatomical arteriovenous ordering. **d**, Mapping the expression of mouse mural cell markers onto human mural cell types. The top 500 mouse markers were aggregated into four distinct modules ('aSMCs', 'aaSMCs', capillary 'pericytes' and venous smooth muscle cells 'vSMCs')¹² and their expression was assessed in the four transcriptionally distinct human mural cell types. **e**, Overlap between the top 100 human endothelial and mural cell subtype markers and those identified in mice. A more lenient set of 500 mouse markers¹² was used for comparison for robust results. Species conservation of a cell-type marker depends both on species-specific changes in the given cell type and on changes among the remaining cell types.

To study mural cell zonation, we used the 670 most significantly variable and robustly expressed cluster genes to order all mural cell nuclei and observed the expected order of aSMC markers on one end (for example, *ACTA2* and *TAGLN*), followed by aaSMC (for example, *SLIT3* and *CTNNA3*); and pericyte markers on the other end (for example, *ABCC9* and *PTN*), confirmed *in situ* (Fig. 3c, Extended Data Fig. 6d). Recapitulating patterns described in mice¹²—and as opposed to the gradual zonation

pattern in BECs—, human mural cells exhibited an abrupt gene expression transition between SMCs and pericytes (Fig. 3c). To determine whether the ordering of T- and M-pericytes (Fig. 3c) reflects anatomical arteriovenous order, we mapped them to mouse mural cell markers¹² and found no differences in their expression of mouse capillary ‘pericyte’ versus venous mural cell ‘vSMC’ markers (Fig. 3d). This suggests that T- and M-pericytes do not segregate by arteriovenous segment. Immunostaining confirmed that T- and M-pericyte markers are each present across both small- and large-diameter brain vessels (Extended Data Fig. 6d).

Together, these data suggest that human pericytes transcriptionally identify more by functional specialization than by arteriovenous location; and that whereas aSMCs and aaSMCs reside on arterial and arteriolar vessels, respectively, T- and M-pericytes intermix along the capillary and venous vasculature. As with BECs, we find that only a minority of top mouse SMC and pericyte markers retain their predictive value in humans (Fig. 3e, Extended Data Figs. 3b, 6d). Because proteins encoded by zonation marker genes perform a variety of key functions at defined arteriovenous locations, species-specific endothelial and mural cell differences are likely to reflect fundamental differences in brain vascular properties that can now be studied.

Brain fibroblasts molecularly defined

Using annotations from previous mouse studies^{12,28}, we noticed fibroblasts from both the vascular and the meningeal barriers of the human brain (Fig. 4a). Cooperating with the vascular BBB, the recently (re)discovered meningeal lymphatics has important roles in waste clearance and neuroimmune surveillance^{29,30}. Fibroblasts transcriptionally segregated according to anatomical location: vascular versus meningeal (Fig. 4a, b); but they also separated according to meningeal layers (Extended Data Fig. 7a, b). Pathway enrichment analysis of marker genes revealed specialized fibroblast functions (Fig. 4b): perivascular fibroblasts showed enriched expression for ECM structural components or its modifiers or receptors (for example, ‘TGFβ regulation of ECM’), whereas meningeal fibroblasts enriched for solute transporters. Fibrotic scars arise from the pathological deposition of collagen I (COL1)-rich ECM. Consistent with mouse lineage-tracing studies³¹, our work indicates that human perivascular fibroblasts are the main producers of COL1 in the brain and thus are likely to form fibrotic scars after brain injury (Extended Data Fig. 7c).

Fig. 4: Molecular definitions for brain perivascular and meningeal fibroblasts.

 **figure 4**

a, Anatomical reference of the human meninges (dura and arachnoid) and perivascular space, each with a resident fibroblast population. **b**, Brain fibroblast heterogeneity. UMAP of 2,985 human perivascular fibroblast-like nuclei and 428 meningeal fibroblast nuclei. Enriched biological pathways derived from respective fibroblast cell-

type markers (Supplementary Table 2; $P < 0.05$, cumulative hypergeometric test). **c**, DEGs between perivascular (left, orange) and meningeal (right, brown) fibroblasts (MAST, Benjamini–Hochberg correction; false discovery rate (FDR) < 0.01 and $\log_2\text{FC} > 0.5$ ($\log_2\text{FC} > 0.72$) to be coloured significant). **d**, Expression of all differentially expressed (from **c**) SLC and ABC family members across perivascular (peri.) and meningeal (menin.) fibroblasts. **e**, Immunostaining validation of polarized meningeal and perivascular fibroblast transporter expression: the meningeal fibroblast-specific influx pump SLC4A4 (left, green) stains selectively in the meninges but not in the cortical vasculature (red); and vice versa for the perivascular-specific efflux pump ABCA8 (right, green). Scale bars, 50 μm .

Closer comparison of differentially expressed genes (DEGs) between fibroblast populations revealed a polarization of solute influx and efflux pumps: meningeal fibroblasts specifically expressed SLC influx solute transporters, whereas perivascular fibroblasts exclusively expressed ABC efflux pumps (Fig. 4d). We confirmed this polarized expression *in situ* (Fig. 4e, Extended Data Fig. 7d, e). Perivascular fibroblasts reside in the Virchow–Robin space, and thus like meningeal fibroblasts, bathe in the cerebrospinal fluid (CSF). This cooperative circuit of polarized transporters suggests fibroblast regulation of solute exchange between the brain and the CSF³². Finally, as in endothelial and mural cells, perivascular fibroblast-like cell markers varied by species (Extended Data Fig. 7f). Together, these data provide a characterization of human brain fibroblast diversity, revealing the molecular basis of their anatomical specialization and a cooperative circuit for CSF solute exchange.

Vascular cell-type perturbations in AD

AD is a neurodegenerative disorder with progressive impairment of cognitive function leading to dementia. Impairment arises from complex perturbations in cell composition and gene expression. We thus sought to profile changes in the AD human brain vasculature at single-cell resolution. We defined our patient groups by clinical diagnosis and confirmed the presence of β -amyloid plaques in the hippocampus and cortex (Extended Data Fig. 8a–c).

Previous studies have identified context-dependent, disease-associated glial subpopulations^{16,17,33}. We did not observe the emergence of new vascular cell subclusters in AD (Fig. 5a, Extended Data Fig. 8d). By contrast, we found a strong loss of brain vascular nuclei—across endothelial cells, SMCs, pericytes and fibroblast-like cells (Fig. 5a, b). Thus, beyond focal cerebrovascular damage, vascular loss may be widespread across the arteriovenous axis. Among pericytes, M-pericytes involved in ECM organization exhibited selective vulnerability (Fig. 5b), providing a molecular hypothesis for the structural breakdown of the BBB that is reported in AD²². However, FACS and single-nucleus RNA sequencing (snRNA-seq) approaches may not always

yield reliable cell quantifications. Thus, we stained hippocampal tissue to quantify the number of Hoechst⁺ vascular cells within collagen IV⁺ cerebrovasculature. Although we found no significant differences in the area of collagen IV⁺ vessels or in the total number of Hoechst⁺ nuclei, we found a significant decrease with AD in the number of Hoechst⁺ nuclei within collagen IV⁺ vessels, consistent with reports of ‘string vessels’ in disease³⁴ (Fig. 5b, Extended Data Fig. 8d, e). In short, we find selective vulnerability of specific vascular cell subpopulations in AD.

Fig. 5: Vascular cell-type-specific perturbations in Alzheimer’s disease.

 figure 5



a, Selective vascular cell vulnerability. Left, proportion of cell types captured in individuals with AD and individuals with NCI (left). Right, proportion of BEC and pericyte subpopulations in AD and NCI (right) ($n = 8$ NCI, $n = 9$ AD; two-sided t -test; mean \pm s.e.m.). ** $P = 0.002$ (BEC), ** $P = 0.003$ (pericyte), * $P = 0.0461$ (fibroblast) (left). * $P < 0.05$ (right). **b**, Immunohistochemical validation of a loss of vascular cell density in AD (number of Hoechst⁺ nuclei within collagen IV⁺ vasculature). Scale bars, 50 μm ($n = 5$ NCI and AD; nested two-sided t -test; mean \pm s.e.m.). Yellow arrows denote example vascular nuclei. **c**, DEG counts for each cell

type in AD. The intensity of the blue colour and the size of the squares are proportional to entry values. **d**, Enriched biological pathways from AD DEGs in pericytes, SMCs and perivascular fibroblast-like cells, plotted by pathway representation (in a given pathway, what proportion of all members are DEGs) and significance ($-\log_{10}P$) of pathway enrichment. ROS, reactive oxygen species. **e**, Enriched biological pathways from genes upregulated in individuals with AD who are carriers of *APOE4*, in capillary and venous endothelial cells ($P < 0.05$, cumulative hypergeometric test). **f**, Venn diagram comparing BEC DEGs in samples from individuals with AD compared to those from the Thy1-hAPP T41B^{Lon,Swe} amyloidosis mouse model³⁷. Only genes with human–mouse orthologues are shown, and the absolute logFC threshold for calling DEGs in mouse APP BECs was lowered to 0.15 (by half) to ensure that claims of limited overlap with human BECs were robust.

We next examined cell-type-specific changes in gene expression in AD (Methods). We identified 463 unique DEGs using more stringent thresholds (Methods, Fig. 5c, Supplementary Table 6). Overall, mural cells exhibited the strongest changes, and other cell types exhibited a signature of gene repression: 61–78% of DEGs were downregulated (Fig. 5c). DEGs were robustly detected across different levels of expression (Supplementary Table 6). Most DEGs were cell-type- and zonation-specific (Extended Data Fig. 8f), suggesting a heterogenous response to AD pathology across the vasculature. Notably, several DEGs are risk genes implicated in GWASs of AD and small-vessel disease (Extended Data Fig. 8g,h). At the pathway level, DEGs in mural cells and fibroblasts implicated dysregulated vasoconstriction and compromised blood flow (Fig. 5d). This provides a potential molecular mechanism for the cerebral hypoperfusion that is discernible in magnetic resonance imaging (MRI) scans of patients with AD³⁵.

Carriers of the *APOE4* allele may exhibit accelerated breakdown of the BBB before cognitive impairment³⁶. We found marked interferon inflammation in the endothelium of *APOE4* carriers (Fig. 5e, Extended Data Fig. 8i–k, Supplementary Table 7). Next, we compared AD DEGs in human BECs with those in mouse models of AD. Such models have facilitated mechanistic study of β-amyloid pathology, but recent reports describe significant species differences in various cell types, like microglia²³. We isolated BECs from 12–14-month-old Thy1-hAPP^{Lon,Swe} mice³⁷ (and littermate wild-type controls) and processed them for single-cell sequencing. Of note, we observed minimal overlap between human AD and mouse hAPP BEC DEGs (Fig. 5f). Finally, because AD pathology begins and spreads through a very consistent regional pattern, we assessed the effect of AD on brain regional vascular specialization. We found that regional differences in cell density and transcriptional profiles were largely erased in AD (Extended Data Fig. 8l,m)—suggesting impairments in brain-region-specific vascular functions.

Together, these findings show that patients with AD exhibit heterogeneous cell-type-, zonation-, region- and species-specific vulnerabilities and perturbations across the brain vasculature that require single-cell approaches to profile.

AD GWAS variants in human BBB cell types

A major goal of biomedical research is to understand how genetic variation contributes to disease. GWASs have nominated genes that contribute to AD risk (hereafter referred to as AD GWAS genes). Previous studies strongly implicate microglia as the major cell type that expresses AD GWAS genes^{23,38,39,40,41}. We wondered, however, whether the unintended depletion of brain vascular cells prematurely dismissed their potential contributions. We curated AD GWASs^{39,40,41} to order the top 45 risk genes. With our expanded survey of brain cell types, we calculated the cell-type proportional expression for each GWAS gene using expression weighted cell type enrichment (EWCE)⁴². We indeed observed among brain parenchymal cells a specific microglial signature for top AD GWAS genes such as *TREM2*, *MS4A6A*, *CRI* and *SPI1* that are now under intense mechanistic study (Fig. 6a, right).

Fig. 6: GWAS disease variants are enriched in the human brain vasculature.

 **figure 6**

a, Proportional expression of the top 45 AD GWAS genes across all major brain cell types. Expression values for a given gene sums to 1 across cell types using the EWCE method⁴². Genes ordered in approximate risk strength^{39,40,41,51}. Asterisks denote the strongest expressing cell types. Cells to the left of the dashed line are from the

vasculature, newly added here; to the right, parenchymal cells captured before. Numbers on the bottom summarize the number of GWAS genes enriched in a given cell type. *MS4A6A* represents the average expression of *MS4A6A*, *MS4A4A* and *MS4A4E*; likewise, *HLA-DRB1* averages *HLA-DRB1* and *HLA-DRB5*. *EPHA1* was not robustly detected. **b**, Immunohistochemical confirmation of the vascular localization of proteins encoded by top AD GWAS genes from **a**. Scale bars, 25 µm. Arrowheads in APOE point to signal around larger-diameter vessels, consistent with SMC expression. Image credit: Human Protein Atlas²⁵ (<http://www.proteinatlas.org>). **c**, Examples of genes expressed specifically in mouse microglia but then also expressed in human brain vascular cell types (*n* of around 3,500 whole-cell mouse transcriptomes¹², mean value ± s.e.m.). Asterisk denotes human cell types that express the AD risk gene. **d**, BEC heat map of top AD GWAS genes coloured by logFC(human/mouse) and labelled by the linear fold change (human/mouse) value. **e**, Quantification of the number of AD and AD-related trait GWAS genes¹⁷ most expressed in a given cell type. 383 of 650 genes (59%) mapped to vascular or perivascular cell types. Protein–protein interaction (PPI) network of gene ontology (GO) cellular components ($P < 0.05$, cumulative hypergeometric test). EC, endothelial cells (A, arterial; C, capillary; V, venous). In myeloid cells, Mg, microglia; Mφ, macrophage. In fibroblasts, M, meningeal; P, perivascular. In mural cells, S, SMC; P, pericyte. OPC, oligodendrocyte precursor cell. **f**, Human enrichment of the AD-related trait GWAS genes¹⁷ that are most highly expressed in BECs (left) and in mural cells (right). In contrast to GWAS genes, the ratio of human to mouse expression across the overall transcriptome (Tx) is less than or around 1 for both cell types (bottom, paired two-sided *t*-test, *** $P < 0.0001$ and *** $P = 0.0002$).

We noticed that several GWAS genes were strongly expressed in human brain vascular and perivascular cell types (Fig. 6a, left, Extended Data Fig. 9). These included two genes previously implicated in the mouse vasculature, *PICALM* and *CD2AP*^{43,44}. But they also included surprising genes, such as the immune-related *PLCG2* and *HLA-DRB1* or *HLA-DRB5* in arterial cells, endocytic *INPP5D* and *USP6NL* in capillaries, and ECM-related *ADAMTS1*, *ADAMTS4*, *FERMT2* and *AGRN* in SMCs and pericytes (Fig. 6a). Within pericytes, expression varied across M- and T-pericyte subtypes (Extended Data Fig. 9a). *APOE*, linked to myeloid cells and astrocytes, was robustly expressed in human SMCs and meningeal fibroblasts. Several GWAS genes such as *ABCA7* and *CLNK* enrich in T cells, and independent datasets show minimal expression in other brain cell types (Extended Data Fig. 9b). Several genes such as *ABCA1*, *FHL2*, *HESX1* and *IL34* enrich in fibroblasts. Notably, we confirmed our findings by immunostaining of proteins encoded by vascular GWAS genes, such as *CASS4*, *FERMT2*, *PLCG2* and *FHL2* (Fig. 6b, Extended Data Fig. 9c). Most GWAS genes were expressed similarly between the hippocampus and cortex (Extended Data Fig. 9d). In total, at least 30 of the top 45 AD GWAS genes are enriched in cells of the

human brain vasculature (not including those solely in perivascular macrophages), suggesting thorough vascular and perivascular involvement in AD.

We next wondered whether these genes are expressed in different cell types between mice and humans. Many genes, like *APOE*, *CASS4*, *INPP5D* and *HLA-DRB1*, were predominately microglial in mice¹² but then also exhibited vascular expression in humans (Fig. 6c, Extended Data Fig. 9e). Nearly every top AD GWAS gene expressed in BECs showed greater expression in humans (Fig. 6d). Together, these data suggest a partial evolutionary transfer of AD risk genes and pathways from microglia to the vasculature from mice to humans (Extended Data Fig. 9f).

We broadened our scope to hundreds of GWAS genes for AD and AD-related traits¹⁷. We observed robust, cell-type-specific vascular and perivascular expression (Extended Data Fig. 10). For each gene, we assigned the cell type with the strongest expression, and discovered that BECs contained the most AD-related GWAS genes, followed by microglia or macrophages (Fig. 6e, Supplementary Table 8). Within BECs, AD-related GWAS genes enriched in protein endo- and transcytosis components, such as receptor and clathrin vesicle components (Fig. 6d,e). A decline in BEC clathrin-mediated transcytosis with age has recently been demonstrated⁸ with age, suggesting one mechanism by which ageing and risk genes converge to increase AD risk. In total, over half of AD-related GWAS genes mapped to vascular or perivascular cell types (383 of 651). As with top GWAS genes, we observed enhanced human over mouse expression of AD-related genes in BECs and pericytes (Fig. 6f). Of note, this human-enhanced expression is not observed for the whole transcriptome.

Together, these data provide a more comprehensive understanding of the diverse cell types that contribute to AD risk. We suggest that an evolutionarily expanded vascular–microglia axis underlies the genetic risk for AD through shared protein clearance (BEC–microglia) and inflammatory pathways (BEC–T cell–microglia) (Fig. 6e, Extended Data Fig. 9f).

Discussion

We report here 143,793 single-cell, genome-wide quantitative transcriptomes from the human brain vasculature in health and AD. We molecularly define the principal vascular cell types; their differences by brain region and species; and the organizational principles of endothelial, mural and fibroblast-like cells. We reveal selective vulnerability of vascular subpopulations and transcriptomic perturbations associated with clinically diagnosed AD; and the expression of AD GWAS genes across human brain vascular cell types, confirmed *in situ*. Data are available to browse at https://twc-stanford.shinyapps.io/human_bbb.

AD has been linked to β -amyloid metabolism, cholesterol and lipid metabolism, innate immunity and endocytosis pathways operating in neurons and glia⁴³. We expand the cell types involved; for example, debris clearance through BEC clathrin-mediated endocytosis, and adaptive T cells in addition to innate immunity. We propose that the expansion of the human brain, brain activity and activity by-products (like β -amyloid⁴⁵) necessitate enhanced clearance mechanisms and neuroimmune surveillance. In this model, microglia are still frontline participants in AD pathogenesis. But more than in mice, human vascular and perivascular cells take part. For example, microglial clearance functions can become overwhelmed⁴⁶, diverting debris to BECs. Indeed, microglial depletion results in cerebral amyloid angiopathy⁴⁷. But unlike microglia, vascular cells do not proliferate efficiently. Thus, constant vascular exposure to debris like β -amyloid triggers cell death, dysfunction and impaired blood and CSF flow. Previous work identified a population of CD8 T_{EMRA} cells that is clonally expanded in AD CSF⁴⁸, potentially influenced by T cell GWAS genes. Together, we suggest an intertwined microglia–vascular axis expanded in humans, with vascular cells having an auxiliary role through shared endocytosis and inflammatory pathways. We note though the likelihood of additional human brain vascular contributions, as evidenced by SMC-, pericyte- and fibroblast-enriched GWAS genes of unclear function. In general, disease risk variants enrich in gene-expression-regulating enhancer regions⁴⁹ that undergo accelerated species divergence⁵⁰, providing one potential explanation for human-specific expression and dysregulation of AD risk genes in cerebrovascular cell types.

The field now has a near-complete census of human brain cell types. This atlas markedly expands the number of human brain vascular cell type and zonation markers to inform research, such as identifying vessels, validating organoid fidelity or deconvoluting bulk RNA-seq datasets. Our work also facilitates translational opportunities. This dataset provides targets for antibodies and other modalities to deliver therapeutic agents to the brain. VINE-seq enables the study of brain vascular contributions to various diseases, such as stroke, multiple sclerosis and COVID-19. But as with previous snRNA-seq studies^{16,17,18,19}, it will be important to distinguish which vascular transcriptional perturbations respond to versus drive disease, clarify their links to clinical and pathological traits, and investigate the mechanisms by which vascular-expressed AD variants confer disease risk. Overall, VINE-seq and the ensuing single-cell atlas provide a blueprint for studying the molecular basis of the human brain vasculature.

Methods

Isolation of vascular nuclei from frozen post-mortem brain tissue

Post-mortem fresh-frozen hippocampus and superior frontal cortex tissue were obtained from the Stanford/VA/NIA Aging Clinical Research Center (ACRC) with approval from local ethics committees and patient consent. Group characteristics are presented in Supplementary Table 1. Individuals were grouped by clinical diagnosis, with two of the individuals with NCI exhibiting β -amyloid plaque staining in the hippocampus, although not to a sufficient degree for an expert pathologist to diagnose AD by histopathological criteria. Clinical instead of pathological diagnosis was chosen because of potentially vascular contributions to AD independent of the well-known hallmarks of AD, β -amyloid and tau pathophysiology⁶. All procedures were carried out on ice in a 4 °C cold room as rapidly as possible. Brain tissue (0.3 grams or more) was thawed on ice for 5 min with 5 ml of nuclei buffer (NB): 1% BSA containing 0.2 U μl^{-1} RNase inhibitor (Takara, 2313A) and EDTA-free protease inhibitor cocktail (Roche, 11873580001). Tissue was quickly minced and homogenized with 7-ml glass douncers (357424, Wheaton) until no visible chunks of debris remained. Similar to before⁵², homogenates were transferred into 50-ml tubes containing 35 ml of chilled 32% dextran (D8821, Sigma) in HBSS. Samples were vigorously mixed before centrifugation at 4,400g for 20 min with no brake. After centrifugation, samples separate into a top myelin layer, middle parenchymal layer and vascular-enriched pellet. The myelin layer was aspirated, tips were changed and the parenchymal layer was carefully removed without disturbing the pellet. Pellets were resuspended in 8 ml of 32% dextran, transferred to 15-ml falcon tubes, and centrifuged again. Vascular-enriched pellets were gently resuspended in 1 ml of NB and added to pre-wetted 40- μm strainers sitting on top of 50-ml falcon tubes. From here diverging from prior protocol, strainers were washed with 10 ml of cold 0.32 M sucrose in PBS and 90 ml PBS until flow through the strainers was unimpeded to deplete contaminating parenchymal cells from trapped microvessels. At this step, retained microvessels turn white in colour, indicating the removal of circulating blood cells. Strainers were switched to new collection 50-ml falcon tubes. Various techniques were tested and optimized to extract vascular cells from the isolated microvessels (for example, enzymatic digestion, TissueRuptor, sonication and so on), but nearly all resulted in loss of nuclei integrity or low nuclei complexity (fewer than 50 median genes per nucleus). Eventually, adapting a method for the isolation of mouse splenocytes proved successful: vascular fragments were mashed four times through the cell strainer using the plunger end of a 3-ml syringe, with intermittent elution via 10 ml of 0.32 M sucrose and 40 ml of PBS. Liberated vascular cells were pelleted at 500g for 10 min and resuspended in 1.5 ml of EZ Prep Lysis Buffer (Sigma, NUC101) spiked with 0.2 U μl^{-1} RNase inhibitor (Takara, 2313A) and EDTA-free protease inhibitor cocktail (Roche, 11873580001). Nuclei were homogenized with 2-ml glass douncers (D8938, Sigma) 20 times with pestle B (pestle A optional). Spiked EZ lysis buffer was added to samples up to 4 ml and incubated on ice for 5 min before pelleting at 500g for 6 min. This incubation step was repeated. Debris was depleted via a sucrose gradient before flow cytometry isolation of nuclei. In brief, pelleted nuclei were resuspended in 0.5 ml

of NB before the addition of 0.9 ml of 2.2 M sucrose in PBS. This mixture was layered on top of 0.5 ml of 2.2 M sucrose and samples were centrifuged at 14,000g for 45 min at 4 °C, with no brake. Pellets were aspirated in 1 ml of NB, filtered through a 40-µm strainer (Flowmi), transferred to FACS tubes, stained with Hoechst 3342 (1:2,000, Thermo Fisher Scientific) and rabbit monoclonal anti-NeuN Alexa Fluor 647 (1:500, Abcam, ab190565), and nuclei collected on a SH800S Cell Sorter into chilled tubes containing 1 ml of NB without protease inhibitor. In pilot runs, we noticed that the cytometer overestimated nuclei counts by around 3.4 times, and thus we sorted around 34,000 nuclei to target around 10,000 nuclei per sample. Sorted samples were inspected for lack of debris on a bright-field microscope. We note that an iodixanol gradient⁵³ can substitute for the 2.2 M sucrose, but that unfortunately with either gradient, flow sorting is required—unlike parenchymal myelin debris, vascular debris is not sufficiently removed by gradient centrifugation alone. Vascular debris will confound downstream cDNA traces with higher background and low molecular weight peaks.

Droplet-based snRNA-seq

For droplet-based snRNA-seq, libraries were prepared using the Chromium Single Cell 3' v3 according to the manufacturer's protocol (10x Genomics), targeting 10,000 nuclei per sample after flow sorting (Sony SH800S Cell Sorter). Fifteen PCR cycles were applied to generate cDNA before 16 cycles for final library generation. Generated snRNA-seq libraries were sequenced on S4 lanes of a NovaSeq 6000 (150 cycles, Novogene).

snRNA-seq quality control

Gene counts were obtained by aligning reads to the hg38 genome (refdata-gex-GRCh38-2020-A) using CellRanger software (v.4.0.0) (10x Genomics). To account for unspliced nuclear transcripts, reads mapping to pre-mRNA were counted. As previously published, a cut-off value of 200 unique molecular identifiers (UMIs) was used to select single nuclei for further analysis^{16,54}. As initial reference, the entire dataset was projected onto two-dimensional space using UMAP on the top 30 principal components⁵⁵. Three approaches were combined for strict quality control: (1) outliers with a high ratio of mitochondrial (more than 5%, fewer than 200 features) relative to endogenous RNAs and homotypic doublets (more than 5,000 features) were removed in Seurat⁵⁶; (2) after scTransform normalization and integration, doublets and multiplets were filtered out using DoubletFinder⁵⁷; and (3) after DoubletFinder, nuclei were manually inspected using known cell-type-specific marker genes, with nuclei expressing more than one cell-type-specific marker further filtered^{16,18,57,58,59,60,61}. For example, BEC nuclei containing any reads for the following cell type markers

were subsequently filtered: *MOBP*, *MBP*, *MOG*, *SLC38A11*, *LAMA2*, *PDGFRB*, *GFAP*, *SLC1A2* and *AQP4*. We note that the vascular nuclei in previous human single-cell datasets exhibit contamination with other cell-type-specific gene markers, which potentially confounds downstream analysis. After applying these filtering steps, the dataset contained 143,793 high-quality, single nuclei.

Cell annotations and differential gene expression analysis

Seurat's integration function was used to align data with default settings. Genes were projected into principal component (PC) space using the principal component analysis (RunPCA). The first 30 dimensions were used as inputs into Seurat's FindNeighbors, FindClusters (at 0.2 resolution) and RunUMAP functions. In brief, a shared-nearest-neighbour graph was constructed based on the Euclidean distance metric in PC space, and cells were clustered using the Louvain method. RunUMAP functions with default settings were used to calculate two-dimensional UMAP coordinates and search for distinct cell populations. Positive differential expression of each cluster against all other clusters (model-based analysis of single-cell transcriptomics; MAST) was used to identify marker genes for each cluster⁶². We annotated cell-types using previously published marker genes^{16,19,61,63}. For BECs, zonation specificity scores for each gene were calculated separately for arterial, capillary, and venous segments as in the following example for a given gene in capillaries:

$$\$ \$ \{ \text{\rm Capillary} \} \backslash, \{ \text{\rm specificity} \} \backslash, \{ \text{\rm score} \} = \{ \text{\rm Average} \} \backslash \left[\log \left(\frac{ \{ \text{\rm Capillary} \} \backslash, \{ \text{\rm logCPM} \} }{ \{ \text{\rm Arterial} \} \backslash, \{ \text{\rm logCPM} \} } \right) \right] \backslash, \mathbf{log} \left(\frac{ \{ \text{\rm Capillary} \} \backslash, \{ \text{\rm logCPM} \} }{ \{ \text{\rm Veinous} \} \backslash, \{ \text{\rm logCPM} \} } \right) \backslash \right] \$ \$$$

Differential gene expression of genes comparing AD, ApoE4, and NCI samples—or comparing cell type subcluster markers—was done using the MAST⁶² algorithm, which implements a two-part hurdle model. Seurat natural log(fold change) > 0.5 (absolute value), adjusted *P* value (Bonferroni correction) < 0.01, and expression in greater than 10% of cells in both comparison groups were required to consider a gene differentially expressed for subcluster analysis and natural log(fold change) > 0.3 (absolute value), adjusted *P* value (Bonferroni correction) < 0.01, and expression in greater than 10% of cells in both comparison groups for AD and ApoE4 comparisons, both more stringent than the default Seurat settings. We incorporated age, gender and batch as covariates in our model. A more lenient threshold of the above but with natural log(fold change) > 0.2 (absolute value) was used for brain region (that is, hippocampus versus cortex). Biological pathway and gene ontology enrichment analyses were performed using Enrichr⁶⁴ or Metascape⁶⁵ with the input species set to *Homo sapiens*⁶⁵. UpSet plots were generated using identified DEGs as inputs using the R package UpSetR⁶⁶. Diagrams were created with BioRender.

Monocle trajectory analysis

Monocle was used to generate the pseudotime trajectory analysis in brain endothelial and mural cells²⁴. Cells were clustered in Seurat and cluster markers used as input into Monocle to infer arteriovenous relationships within endothelial cells and pericytes. Specifically, UMAP embeddings and cell subclusters generated from Seurat were converted to a cell_data_set object using SeuratWrappers (v.0.2.0) and then used as input to perform trajectory graph learning and pseudotime measurement through independent component analysis (ICA) with Monocle. Cluster marker genes identified in Seurat were used to generate a pseudotime route and plotted using the ‘plot_pseudotime_heatmap’ function. For mural cells, variable genes were limited to those with $\log[\text{average expression}] > 1$ (Seurat) for even more robust cell ordering.

Cell–cell communication

Cell–cell interactions based on the expression of known ligand–receptor pairs in different cell types were inferred using CellChatDB⁶⁷ (v.0.02). In brief, we followed the official workflow and loaded the normalized counts into CellChat and applied the preprocessing functions ‘identifyOverExpressedGenes’, ‘identifyOverExpressedInteractions’ and ‘projectData’ with standard parameters set. As database we selected the ‘Secreted Signaling’ pathways and used the pre-compiled human ‘Protein-Protein-Interactions’ as a priori network information. For the main analyses the core functions ‘computeCommunProb’, ‘computeCommunProbPathway’ and ‘aggregateNet’ were applied using standard parameters and fixed randomization seeds. Finally, to determine the senders and receivers in the network the function ‘netAnalysis_signalingRole’ was applied on the ‘netP’ data slot.

Mice

Aged C57BL/6 male mice (19 months old) were obtained from the National Institute on Aging rodent colony. Young male C57BL/6 mice (3 months old) were obtained from The Jackson Laboratory or Charles River Laboratories. Thy1-hAPP^{Lon,Swe} male mice and littermate wild-type control³⁷ mice were raised until 12–14 months of age. All mice were kept on a 12-h light–dark cycle and provided ad libitum access to food and water. All animal care and procedures complied with the Animal Welfare Act and were in accordance with institutional guidelines and approved by the V.A. Palo Alto Committee on Animal Research and the institutional administrative panel of laboratory animal care at Stanford University.

Mouse wild-type and APP T41B BEC single-cell and nuclei sequencing

Whole cell isolation from the central nervous system followed previously described methods^{68,69,70}. In brief, cortices and hippocampi were microdissected, minced and digested using the Neural Dissociation Kit (Miltenyi). Suspensions were filtered through a 100- μm strainer and myelin removed by centrifugation in 0.9 M sucrose. The remaining myelin-depleted cell suspension was blocked for 10 min with Fc preblock (CD16/CD32, BD 553141) on ice and stained for 20 min with antibodies to distinguish BECs (CD31 $^+$ /CD45 $^-$). BECs from 12–14-month-old Thy1-hAPP^{Lon,Swe} mice and littermate wild-type control³⁷ mice (pool of 4–6 mice per group) were sorted into PBS with 0.1% BSA. Nuclei isolation from 4–6 month-old mouse hippocampi followed protocols adapted from previous studies^{16,17,53,61,71}. In brief, tissue was homogenized using a glass douncer in 2 ml of ice-cold EZ PREP buffer (Sigma, N3408) and incubated on ice for 5 min. Centrifuged nuclei were resuspended in 1% BSA in PBS with 0.2 U μl^{-1} RNase inhibitor and filtered through a 40- μm cell strainer. Cells or nuclei were immediately counted using a Neubauer haemocytometer and loaded on a Chromium Single-Cell Instrument (10x Genomics) to generate single-cell gel-bead in emulsions (GEMs). The 10x Genomics v3 libraries were prepared as per the manufacturer’s instructions. Libraries were sequenced on an Illumina NextSeq 550 (paired-end; read 1: 28 cycles; i7 index: 8 cycles, i5 index: 0 cycles; read 2: 91 cycles). De-multiplexing was performed using the Cellranger toolkit (v.3.0.0) ‘cellranger mkfastq’ command and the ‘cellranger count’ command for alignment to the mouse transcriptome, cell barcode partitioning, collapsing UMIs to transcripts, and gene-level quantification. Around 70% sequencing saturation (more than 20,000 reads per cell) was achieved, for a median of around 2,000 genes detected per cell and around 16,500 genes detected in total. Downstream analysis using the Seurat package (v.3)⁷² was performed as previously described¹², applying standard algorithms for cell filtration, feature selection and dimensionality reduction. Samples with fewer than 1,000 and more than 4,000 unique feature counts, samples with more than 15% mitochondrial RNA, samples with more than 15% small subunit ribosomal genes (Rps), and counts of more than 10,000 were excluded from the analysis. Genes were projected into PC space using the principal component analysis (RunPCA). The first 30 dimensions were used as inputs into Seurat’s FindNeighbors and RunTsne functions. In brief, a shared-nearest-neighbour graph was constructed based on the Euclidean distance metric in PC space, and cells were clustered using the Louvain method. RunTsne functions with default settings was used to calculate two-dimensional t -distributed stochastic neighbour embedding (t -SNE) coordinates and search for distinct cell populations. Cells and clusters were then visualized using three-dimensional t -SNE embedding on the same distance metric. Differential gene expression analysis was done by applying MAST. Significant DEGs in Thy1-hAPP^{Lon,Swe} BECs were called by log(fold change) > 0.15 (absolute value), adjusted P value (Bonferroni correction) < 0.01 . This lowered log(fold change) was to ensure our claims of limited overlap with human AD BECs were robust.

GWAS analysis

For calculation of proportional cell-type-specific gene expression, we followed the EWCE method described in a previous study⁴², and used previously on human snRNA-seq data¹⁷. For AD analysis, we compiled a list of top GWAS risk genes from ref. ³⁹, ref. ⁴⁰ and ref. ⁴¹, sorted descending by approximate *P* value. The expression of each gene sums to 1 across the cell types, with each heat map cell showing the fraction of total gene expression as determined from EWCE analysis. The set of 720 AD and AD-related trait GWAS genes were obtained from ref. ¹⁷, and using EWCE analysis, the strongest expressing cell type was determined for each gene. The original list was slightly parsed to 720, as several genes were not detected as expressed in our dataset.

Immunohistochemistry

Fresh-frozen human brain tissue from individuals with NCI and from individuals with AD (hippocampus and superior frontal cortex adjacent to tissue processed for snRNA-seq as well as meninges) was subjected to immunohistochemistry (IHC). Ten-micrometre sections mounted on SuperFrost Plus glass slides were fixed with 4% paraformaldehyde (Electron Microscopy Services, 15714S) diluted in PBS at 4 °C for 15 min before dehydration via an ethanol series or air drying. Sections were blocked in TBS++ (TBS + 3% donkey serum (130787, Jackson ImmunoResearch) + 0.25% Triton X-100 (T8787, Sigma-Aldrich)) for 1.5 h at room temperature. Sections were incubated with primary antibodies at 4 °C overnight: goat polyclonal anti-collagen type IV (1:200, AB769, Sigma), rabbit polyclonal anti-CYP1B1 (1:100, HPA026863, Atlas Antibodies), rabbit polyclonal anti-SLC4A4 (1:100, HPA035628, Atlas Antibodies), rabbit polyclonal anti-SLC47A1 (1:100, HPA021987, Atlas Antibodies), rabbit polyclonal anti-ABCA8 (1:100, HPA044914, Atlas Antibodies), mouse monoclonal anti-CD31 (1:100, JC70A, Dako), rabbit polyclonal anti-VWF (1:100, GA527, Dako), rabbit polyclonal anti-SLC39A10 (1:100, HPA066087, Atlas Antibodies), rabbit polyclonal anti-ALPL (1:100, HPA007105, Atlas Antibodies), rabbit polyclonal anti-A2M (1:100, HPA002265, Atlas Antibodies), rabbit monoclonal anti-β-amyloid (1:500, clone D54D2 XP, CST) and mouse monoclonal anti-actin, α-smooth muscle–Cy3 (1:100, clone 1A4, Sigma). Sections were washed, stained with Alexa Fluor-conjugated secondary antibodies (1:250) and Hoechst 33342 (1:2,000, H3570, Thermo Fisher Scientific), mounted and coverslipped with ProLong Gold (Life Technologies) or VECTASHIELD (Vector Laboratories) before imaging on a confocal laser scanning microscope (Zeiss LSM880). Age-related autofluorescence was quenched before mounting with Sudan Black B, as before^{8,70}. National Institutes of Health ImageJ software was used to quantify the number of Hoechst⁺ nuclei per image, the percentage of vasculature (collagen IV), the number of Hoechst⁺ nuclei within collagen IV⁺ vasculature, or the predicted DEG SLC39A10 among CD31⁺

vasculature, following previously described protocols^{8,15,73}. In short, at least five images were stained per patient, and imaging and analyses were performed by a blinded observer.

Statistics and reproducibility

Immunostaining validation experiments were repeated independently at least twice with similar results. As indicated in the figure legends, some immunostaining images come from the Human Protein Atlas^{25,74} and are available at <https://www.proteinatlas.org/>.

Reporting summary

Further information on research design is available in the [Nature Research Reporting Summary](#) linked to this paper.

Data availability

Raw sequencing data have been deposited in the NCBI Gene Expression Omnibus (GEO) under accession code [GSE163577](#). Data are also available to explore via an interactive web browser: https://tvc-stanford.shinyapps.io/human_bbb.

References

1. Feigin, V. L. et al. Global and regional burden of stroke during 1990–2010: findings from the Global Burden of Disease Study 2010. *Lancet* **383**, 245–255 (2014).
2. Chow, B. W. & Gu, C. The molecular constituents of the blood–brain barrier. *Trends Neurosci.* **38**, 598–608 (2015).
3. Profaci, C. P., Munji, R. N., Pulido, R. S. & Daneman, R. The blood–brain barrier in health and disease: important unanswered questions. *J. Exp. Med.* **217**, e20190062 (2020).
4. Obermeier, B., Daneman, R. & Ransohoff, R. M. Development, maintenance and disruption of the blood–brain barrier. *Nat. Med.* **19**, 1584–1596 (2013).
5. Sweeney, M. D., Zhao, Z., Montagne, A., Nelson, A. R. & Zlokovic, B. V. Blood–brain barrier: from physiology to disease and back. *Physiol. Rev.* **99**, 21–78 (2019).

6. Iadecola, C. The pathobiology of vascular dementia. *Neuron* **80**, 844–866 (2013).
7. Pardridge, W. M. Drug transport across the blood–brain barrier. *J. Cereb. Blood Flow Metab.* **32**, 1959–1972 (2012).
8. Yang, A. C. et al. Physiological blood–brain transport is impaired with age by a shift in transcytosis. *Nature* **583**, 425–430 (2020).
9. Daneman, R., Zhou, L., Kebede, A. A. & Barres, B. A. Pericytes are required for blood–brain barrier integrity during embryogenesis. *Nature* **468**, 562–566 (2010).
10. Armulik, A. et al. Pericytes regulate the blood–brain barrier. *Nature* **468**, 557–561 (2010).
11. Janzer, R. C. & Raff, M. C. Astrocytes induce blood–brain barrier properties in endothelial cells. *Nature* **325**, 253–257 (1987).
12. Vanlandewijck, M. et al. A molecular atlas of cell types and zonation in the brain vasculature. *Nature* **554**, 475–480 (2018).
13. Sabbagh, M. F. et al. Transcriptional and epigenomic landscapes of CNS and non-CNS vascular endothelial cells. *Elife* **7**, e36187 (2018).
14. Kalucka, J. et al. Single-cell transcriptome atlas of murine endothelial cells. *Cell* **180**, 764–779 (2020).
15. Chen, M. B. et al. Brain endothelial cells are exquisite sensors of age-related circulatory cues. *Cell Rep.* **30**, 4418–4432 (2020).
16. Mathys, H. et al. Single-cell transcriptomic analysis of Alzheimer’s disease. *Nature* **570**, 332–337 (2019).
17. Grubman, A. et al. A single-cell atlas of entorhinal cortex from individuals with Alzheimer’s disease reveals cell-type-specific gene expression regulation. *Nat. Neurosci.* **22**, 2087–2097 (2019).
18. Jäkel, S. et al. Altered human oligodendrocyte heterogeneity in multiple sclerosis. *Nature* **566**, 543–547 (2019).
19. Veltmeshev, D. et al. Single-cell genomics identifies cell type–specific molecular changes in autism. *Science* **364**, 685–689 (2019).
20. Keller, D., Erö, C. & Markram, H. Cell densities in the mouse brain: a systematic review. *Front. Neuroanat.* **12**, 83 (2018).

21. Niedowicz, D. M. et al. Obesity and diabetes cause cognitive dysfunction in the absence of accelerated β -amyloid deposition in a novel murine model of mixed or vascular dementia. *Acta Neuropathol. Commun.* **2**, 64 (2014).
22. Montagne, A. et al. Blood–brain barrier breakdown in the aging human hippocampus. *Neuron* **85**, 296–302 (2015).
23. Geirsdottir, L. et al. Cross-species single-cell analysis reveals divergence of the primate microglia program. *Cell* **179**, 1609–1622 (2019).
24. Trapnell, C. et al. The dynamics and regulators of cell fate decisions are revealed by pseudotemporal ordering of single cells. *Nat. Biotechnol.* **32**, 381–386 (2014).
25. Uhlén, M. et al. Tissue-based map of the human proteome. *Science* **347**, 1260419 (2015).
26. De Meyer, S. F., Stoll, G., Wagner, D. D. & Kleinschmitz, C. Von Willebrand factor: an emerging target in stroke therapy. *Stroke* **43**, 599–606 (2012).
27. Mao, M., Alavi, M. V., Labelle-Dumais, C. & Gould, D. B. Type IV collagens and basement membrane diseases: cell biology and pathogenic mechanisms. *Curr. Top. Membr.* **76**, 61–116 (2015).
28. DeSisto, J. et al. Single-cell transcriptomic analyses of the developing meninges reveal meningeal fibroblast diversity and function. *Dev. Cell* **54**, 43–59 (2020).
29. Louveau, A. et al. Structural and functional features of central nervous system lymphatic vessels. *Nature* **523**, 337–341 (2015).
30. Aspelund, A. et al. A dural lymphatic vascular system that drains brain interstitial fluid and macromolecules. *J. Exp. Med.* **212**, 991–999. (2015).
31. Dorrier, C. E. et al. CNS fibroblasts form a fibrotic scar in response to immune cell infiltration. *Nat. Neurosci.* **24**, 234–244 (2021).
32. Iliff, J. J. et al. A paravascular pathway facilitates CSF flow through the brain parenchyma and the clearance of interstitial solutes, including amyloid β . *Sci. Transl. Med.* **4**, 147ra111 (2012).
33. Keren-Shaul, H. et al. A unique microglia type associated with restricting development of Alzheimer’s disease. *Cell* **169**, 1276–1290 (2017).
34. Brown, W. R. A review of string vessels or collapsed, empty basement membrane tubes. *J. Alzheimer’s Dis.* **21**, 725–739 (2010).

35. Roher, A. E. et al. Cerebral blood flow in Alzheimer's disease. *Vasc. Health Risk Manag.* **8**, 599 (2012).
36. Montagne, A. et al. *APOE4* leads to blood–brain barrier dysfunction predicting cognitive decline. *Nature* **581**, 71–76 (2020).
37. Rockenstein, E., Mallory, M., Mante, M., Sisk, A. & Masliah, E. Early formation of mature amyloid- β protein deposits in a mutant APP transgenic model depends on levels of A β _{1–42}. *J. Neurosci. Res.* **66**, 573–582 (2001).
38. Nott, A. et al. Brain cell type-specific enhancer–promoter interactome maps and disease-risk association. *Science* **366**, 1134–1139 (2019).
39. Lambert, J. C. et al. Meta-analysis of 74,046 individuals identifies 11 new susceptibility loci for Alzheimer's disease. *Nat. Genet.* **45**, 1452–1458 (2013).
40. Kunkle, B. W. et al. Genetic meta-analysis of diagnosed Alzheimer's disease identifies new risk loci and implicates A β , tau, immunity and lipid processing. *Nat. Genet.* **51**, 414–430 (2019).
41. Jansen, I. E. et al. Genome-wide meta-analysis identifies new loci and functional pathways influencing Alzheimer's disease risk. *Nat. Genet.* **51**, 404–413 (2019).
42. Skene, N. G. & Grant, S. G. N. Identification of vulnerable cell types in major brain disorders using single cell transcriptomes and expression weighted cell type enrichment. *Front. Neurosci.* **10**, 16 (2016).
43. Karch, C. M. & Goate, A. M. Alzheimer's disease risk genes and mechanisms of disease pathogenesis. *Biol. Psychiatry* **77**, 43–51 (2015).
44. Zhao, Z. et al. Central role for PICALM in amyloid- β blood–brain barrier transcytosis and clearance. *Nat. Neurosci.* **18**, 978–987 (2015).
45. Cirrito, J. R. et al. Synaptic activity regulates interstitial fluid amyloid- β levels in vivo. *Neuron* **48**, 913–922 (2005).
46. Safaiyan, S. et al. Age-related myelin degradation burdens the clearance function of microglia during aging. *Nat. Neurosci.* **19**, 995–998 (2016).
47. Spangenberg, E. et al. Sustained microglial depletion with CSF1R inhibitor impairs parenchymal plaque development in an Alzheimer's disease model. *Nat. Commun.* **10**, 3758 (2019).

48. Gate, D. et al. Clonally expanded CD8 T cells patrol the cerebrospinal fluid in Alzheimer's disease. *Nature* **577**, 399–404 (2020).
49. Farh, K. K. H. et al. Genetic and epigenetic fine mapping of causal autoimmune disease variants. *Nature* **518**, 337–343 (2015).
50. Villar, D. et al. Enhancer evolution across 20 mammalian species. *Cell* **160**, 554–566 (2015).
51. Wightman, D. P. et al. Largest GWAS ($N = 1,126,563$) of Alzheimer's disease implicates microglia and immune cells. Preprint at <https://doi.org/10.1101/2020.11.20.20235275> (2020).
52. Lee, Y. K., Uchida, H., Smith, H., Ito, A., & Sanchez, T. The isolation and molecular characterization of cerebral microvessels. *Nat. Protoc.* **14**, 3059–3081 (2019).
53. Corces, M. R. et al. An improved ATAC-seq protocol reduces background and enables interrogation of frozen tissues. *Nat. Methods* **14**, 959–962 (2017).
54. Yang, A. C. et al. Dysregulation of brain and choroid plexus cell types in severe COVID-19. *Nature* **595**, 565–571 (2021).
55. McInnes, L., Healy, J. & Melville, J. UMAP: uniform manifold approximation and projection for dimension reduction. Preprint at <https://arxiv.org/abs/1802.03426> (2018).
56. Satija, R., Farrell, J. A., Gennert, D., Schier, A. F., & Regev, A. Spatial reconstruction of single-cell gene expression data. *Nat. Biotechnol.* **33**, 495–502 (2015).
57. McGinnis, C. S., Murrow, L. M., & Gartner, Z. J. DoubletFinder: doublet detection in single-cell RNA sequencing data using artificial nearest neighbors. *Cell Syst.* **8**, 329–337 (2019).
58. Zeisel, A. et al. Molecular architecture of the mouse nervous system. *Cell* **174**, 999–1014 (2018).
59. Zeisel, A. et al. Cell types in the mouse cortex and hippocampus revealed by single-cell RNA-seq. *Science* **347**, 1138–1142 (2015).
60. Yang, A. C. et al. Dysregulation of brain and choroid plexus cell types in severe COVID-19. *Nature* **595**, 565–571 (2021).

61. Zhou, Y. et al. Human and mouse single-nucleus transcriptomics reveal TREM2-dependent and TREM2-independent cellular responses in Alzheimer's disease. *Nat. Med.* **26**, 131–142 (2020).
62. Finak, G. et al. MAST: a flexible statistical framework for assessing transcriptional changes and characterizing heterogeneity in single-cell RNA sequencing data. *Genome Biol.* **16**, 278 (2015).
63. Lake, B. B. et al. Integrative single-cell analysis of transcriptional and epigenetic states in the human adult brain. *Nat. Biotechnol.* **36**, 70–80 (2018).
64. Chen, E. Y. et al. Enrichr: interactive and collaborative HTML5 gene list enrichment analysis tool. *BMC Bioinformatics* **14**, 128 (2013).
65. Zhou, Y. et al. Metascape provides a biologist-oriented resource for the analysis of systems-level datasets. *Nat. Commun.* **10**, 1523 (2019).
66. Conway, J. R., Lex, A. & Gehlenborg, N. UpSetR: an R package for the visualization of intersecting sets and their properties. *Bioinformatics* **33**, 2938–2940 (2017).
67. Jin, S. et al. Inference and analysis of cell–cell communication using CellChat. *Nat. Commun.* **12**, 1088 (2021).
68. The Tabula Muris Consortium. Single-cell transcriptomics of 20 mouse organs creates a *Tabula Muris*. *Nature* **562**, 367–372 (2018).
69. Zuchero, Y. J. Y. et al. Discovery of novel blood–brain barrier targets to enhance brain uptake of therapeutic antibodies. *Neuron* **89**, 70–82 (2016).
70. Yousef, H., et al. Aged blood impairs hippocampal neural precursor activity and activates microglia via brain endothelial cell VCAM1. *Nat. Med.* **25**, 988–1000 (2019).
71. Swiech, L. et al. In vivo interrogation of gene function in the mammalian brain using CRISPR–Cas9. *Nat. Biotechnol.* **33**, 102–106 (2015).
72. Butler, A., Hoffman, P., Smibert, P., Papalexi, E. & Satija, R. Integrating single-cell transcriptomic data across different conditions, technologies, and species. *Nat. Biotechnol.* **36**, 411–420 (2018).
73. Yang, A. C. et al. Multiple click-selective tRNA Synthetases expand mammalian cell-specific proteomics. *J. Am. Chem. Soc.* **140**, 7046–7051 (2018).

74. Thul, P. J. et al. A subcellular map of the human proteome. *Science* **356**, eaal3321 (2017).
75. Butovsky, O. et al. Identification of a unique TGF- β -dependent molecular and functional signature in microglia. *Nat. Neurosci.* **17**, 131–143 (2014).
76. Szabo, P. A. et al. Single-cell transcriptomics of human T cells reveals tissue and activation signatures in health and disease. *Nat. Commun.* **10**, 4706 (2019).
77. Iadecola, C., Anrather, J. & Kamel, H. Effects of COVID-19 on the nervous system. *Cell* **183**, 16–27 (2020).
78. Månberg, A. et al. Altered perivascular fibroblast activity precedes ALS disease onset. *Nat. Med.* **27**, 640–646 (2021).
79. Parker, K. R. et al. Single-cell analyses identify brain mural cells expressing CD19 as potential off-tumor targets for CAR-T immunotherapies. *Cell* **183**, 126–142 (2020).
80. Vanlandewijck, M. et al. A molecular atlas of cell types and zonation in the brain vasculature. *Nature* **554**, 475–480 (2018).
81. Zhang, Y. et al. Purification and characterization of progenitor and mature human astrocytes reveals transcriptional and functional differences with mouse. *Neuron* **89**, 37–53 (2016).

Acknowledgements

We thank T. Iram, E. Tapp, N. Lu, M. Haney, O. Hahn, M. J. Estrada, S. M. Shi and other members of the Wyss-Coray laboratory for feedback and support; H. Mathys, D. A. Bennett and participants in the CSHL BBB 2021 meeting for advice; and H. Zhang and K. Dickey for laboratory management. This work was funded by the NOMIS Foundation (T.W.-C.), the National Institute on Aging (T32-AG0047126 to A.C.Y. and 1RF1AG059694 to T.W.-C), Nan Fung Life Sciences (T.W.-C.), the Bertarelli Brain Rejuvenation Sequencing Cluster (an initiative of the Stanford Wu Tsai Neurosciences Institute) and the Stanford Alzheimer’s Disease Research Center (P30 AG066515). This work was supported by a grant from the Simons Foundation Award (811253TWC). A.C.Y. was supported by a Siebel Scholarship. F.K. and A.K. are part of the CORSAAR study supported by the State of Saarland, the Saarland University and the Rolf M. Schwiete Stiftung. This study was supported by the AHA–Allen Initiative in Brain Health and Cognitive Impairment (19PABHI34580007). The statements in this work are solely the responsibility of the authors and do not

necessarily represent the views of the American Heart Association (AHA) or the Paul G. Allen Frontiers Group. Graphics were created with BioRender.com.

Author information

Author notes

1. These authors contributed equally: Ryan T. Vest, Fabian Kern

Affiliations

1. Department of Anatomy, University of California San Francisco, San Francisco, CA, USA

Andrew C. Yang & Michelle B. Chen

2. Bakar Aging Research Institute, University of California San Francisco, San Francisco, CA, USA

Andrew C. Yang & Tony Wyss-Coray

3. Department of Neurology and Neurological Sciences, Stanford University School of Medicine, Stanford, CA, USA

Andrew C. Yang, Ryan T. Vest, Fabian Kern, Davis P. Lee, Maayan Agam, Christina A. Maat, Patricia M. Losada, Nicholas Schaum, Nathalie Khouri, Kruti Calcuttawala, Heather Shin, Róbert Pálovics, Andrew Shin, David Gate, Andreas Keller & Tony Wyss-Coray

4. Chair for Clinical Bioinformatics, Saarland University, Saarbrücken, Germany

Fabian Kern, Pauline Chu & Andreas Keller

5. Department of Pathology, Stanford University School of Medicine, Stanford, CA, USA

Angus Toland

6. Department of Surgery, Icahn School of Medicine at Mount Sinai, New York, NY, USA

Elizabeth Y. Wang

7. Veterans Administration Palo Alto Healthcare System, Palo Alto, CA, USA

Jian Luo

8. Institute for Neuropathology, Saarland University Hospital and Medical Faculty of Saarland University, Homburg, Germany

Walter J. Schulz-Schaeffer

9. Department of Pediatrics, University of Colorado Anschutz Medical Campus, Aurora, CO, USA

Julie A. Siegenthaler

10. Department of Psychiatry, Stanford University School of Medicine, Stanford, CA, USA

M. Windy McNerney

11. Wu Tsai Neurosciences Institute, Stanford University, Stanford, CA, USA

Tony Wyss-Coray

12. Paul F. Glenn Center for the Biology of Aging, Stanford University School of Medicine, Stanford, CA, USA

Tony Wyss-Coray

Contributions

A.C.Y. and T.W.-C. conceptualized the study. A.C.Y. devised the isolation method. M.W.M. and W.J.S.-S. provided and A.C.Y. organized tissue samples. D.P.L. and A.C.Y. performed tissue dissociations. N.S., R.T.V., D.G., K.C., H.S. and A.C.Y. prepared libraries for sequencing. R.T.V., F.K., A.K., C.A.M., M.B.C., R.P., A.S., N.K., J.A.S. and A.C.Y. performed computational analysis. D.P.L., C.A.M., M.A., D.G., E.Y.W., J.L. A.T., P.C. and A.C.Y. performed immunohistochemical stains. P.M.L. developed the searchable web interface (Shiny app). C.A.M. and A.C.Y. drew diagrams. A.C.Y. wrote the manuscript with input from all authors. A.C.Y. and T.W.-C. supervised the study.

Corresponding authors

Correspondence to [Andrew C. Yang](#) or [Tony Wyss-Coray](#).

Ethics declarations

Competing interests

T.W.-C. is a co-founder and scientific advisor of Alkahest. A.C.Y., R.T.V. and T.W.-C. are co-founders and scientific advisors of Qinotto.

Peer review

Peer review information

Nature thanks Trygve Bakken, Neelroop Parikshak and the other, anonymous, reviewer(s) for their contribution to the peer review of this work.

Additional information

Publisher's note Springer Nature remains neutral with regard to jurisdictional claims in published maps and institutional affiliations.

Extended data figures and tables

[Extended Data Fig. 1 Enhanced capture and characterization of human brain vascular nuclei.](#)

a, Detailed schematic of the VINE-seq method to capture human brain vascular and immune cell types for single-nucleus sequencing. **b**, Total number of nuclei, median number of unique molecular identifiers (UMI), and median number of genes for each human sample sequenced from hippocampus and superior frontal cortex. **c**, Quantification of the median number of genes detected per nuclei across groups ($n = 17$ hippocampus and $n = 8$ cortex; $n = 8$ NCI and $n = 9$ AD, two-sided t -test; mean \pm s.e.m.). **d**, **e**, Quantification of the number (**d**) and proportion (**e**) of cerebrovascular cell types captured via the VINE-seq method introduced here compared to recent snRNA-seq studies^{16,17}. **f**, Summary quantification of the proportion of captured cell types, by individuals with NCI and individuals with AD. **g**, Quantification of the proportion of captured cell types across individuals. **h**, Summary (left) and quantification (right) of the proportion of captured cell types by brain region ($n = 17$ hippocampus and $n = 8$ cortex; $n = 8$ NCI and $n = 9$ AD, two-sided t -test; mean \pm s.e.m.).

Extended Data Fig. 2 Diversity and heterogeneity of human brain vascular cell types.

a, Representative H&E images used by two neuropathologists to evaluate NCI cortical and hippocampal tissue for vascular pathology. No significant vascular pathology was observed. Scale bars, 200 µm. **b**, Discovery of the top cell-type-specific marker genes across the major classes of cells captured. The colour bar indicates gene expression from low (blue) to high (yellow). **c**, Validation of cell-type annotations and confirmation of minimal doublet contamination using established cell-type markers. **d**, UMAP projection of captured myeloid cells, forming two distinct clusters corresponding to parenchymal microglia and brain barrier macrophages. Example marker genes listed. **e**, Immunohistochemical validation of microglial and perivascular macrophage markers. Scale bars, 50 µm. Image credit: Human Protein Atlas^{25,74} (<http://www.proteinatlas.org>). **f**, Global view of DEGs comparing human brain macrophages and microglia (left, MAST, Benjamini–Hochberg correction; FDR < 0.01 and logFC>0.5 [log₂FC>0.72] to be coloured significant). Pathways enriched in microglia versus macrophages (right), recapitulating interesting biology such as the unique TGF-β molecular signature in microglia⁷⁵. **g**, Expression of top gene markers for various T cell subtypes (top), and quantification of their expression as a module (bottom)⁷⁶. Brain T cells exhibit highest expression of markers corresponding to CD8 cytotoxic and CD4 Naive/Central memory (NV/CM) T cells. **h**, UMAP projection of captured astrocytes, forming two distinct clusters, and split by brain region. Example marker genes listed. **i–j**, Quantification of astrocyte cluster 0 (**b**) and 1 (**c**) frequency in the cortex and hippocampus ($n = 8$ cortex and $n = 17$ hippocampus, Mann-Whitney *t*-test; mean +/- s.e.m.). **k**, Immunohistochemical validation of the brain region-specific astrocyte marker *TENM4*. Scale bars, 50 µm.

Extended Data Fig. 3 Species-specific gene expression across brain cell types and their pharmacological relevance.

a–f, Identification of species-specific genes. Both mouse and human transcriptomes were generated and analysed similarly via single-nucleus

RNA-sequencing. Mice were 19 months of age to match the average age of our human cohort. Species-specific/enriched are coloured. **g**, Immunohistochemical confirmation of genes predicted to be enriched or specific to human cerebrovascular cells compared to mouse (isolated mouse nuclei and per Vanlandewijck, et al., 2018)¹², in terms of overall expression or zonation. In parenthesis is the cell type predicted to be uniquely or exhibiting enriched expressed in human over mouse. Scale bars, 50 µm. Image credit: Human Protein Atlas^{25,74} (<http://www.proteinatlas.org>). **h–i**, Mouse and human BEC expression of genes mediating protein transcytosis (**h**) and small molecule influx and efflux (**i**).

Extended Data Fig. 4 Human brain vascular expression of genes relevant to disease.

a, Brain vascular expression of genes relevant to SARS-CoV-2 brain entry, as summarized in Iadecola, et al. 2020⁷⁷. **b**, Expression of the mouse perivascular fibroblast-like gene *Spp1* is instead specifically expressed in human myeloid cells and oligodendrocytes (*SPP1*, top)⁷⁸. **c**, No expression of the immuno-oncology target *CD19* and its chaperone *CD81* across human adult brain pericytes and SMCs⁷⁹. Note: cells with any finite expression are ordered to the front to ensure all expression is visible, but this carries the potential to visually overestimate average expression.

Extended Data Fig. 5 Brain endothelial and mural cell zonation and subpopulations.

a, UMAP projection of captured BECs, organizing by arteriovenous zonation. Bottom, tip cell markers expressed in the tip-like/ proteostatic EC cluster. **b**, Validation of BEC zonation clusters using established zonation markers¹². Violin plots are centred around the median, with their shape representing cell distribution. **c**, **d**, As in **a**, **b** but for pericytes and SMCs. Note that the anatomical locations of pericyte 0 and 1 have not yet been determined. **e**, Immunohistochemical validation of *ACTA2* (α-SMA) expression in human SMCs and less so in capillary pericytes. A denotes arterial and C denotes capillary. Arrowheads specify capillary pericytes

expressing *ACTA2*. Scale bars, 50 µm. **f, g**, As in **a, b** but for perivascular fibroblast-like cells, as recently discovered in mice¹².

Extended Data Fig. 6 Brain endothelial zonation and mural cell subtype markers.

a, Immunohistochemical validation of zonation and cell subtype markers in BECs. Scale bars, 50 µm. Image credit: Human Protein Atlas^{25,74} (<http://www.proteinatlas.org>). **b**, Comparison of the zonal specificity of genes in arterial, capillary, and venous cells. Axis plot a specificity score, as defined in the Methods. For example, specificity score for capillaries = avg(logFC(cap/ven), logFC(cap/art)). **c**, Immunohistochemical validation of capillary expression in human brains of the mouse venous-specific marker VWF and CA4, with similar patterns observed across multiple primary antibody clones. Scale bars, 100 µm. Image credit: Human Protein Atlas^{25,74} (<http://www.proteinatlas.org>). **d**, Immunohistochemical validation of zonation and cell subtype markers in brain SMCs and pericytes. Scale bars, 50 µm. Image credit: Human Protein Atlas^{25,74} (<http://www.proteinatlas.org>).

Extended Data Fig. 7 Specialization and functions of human brain fibroblasts.

a, Expression of example markers demarcating perivascular from meningeal fibroblasts. **b**, UMAP of 428 meningeal fibroblast nuclei, subclustering into anatomically segregated dural and arachnoid space fibroblasts. **c**, Expression of the genes constituting the major fibrotic scar component collagen I in pericytes and fibroblasts. Collagen I is composed of two components, COL1A1 and COL1A2. Column annotations: T-PC = solute transport pericyte and M-PC = Extracellular matrix regulating pericyte, P. FB = Perivascular fibroblast, and M. FB = Meningeal fibroblast. **d, e**, Protein immunostaining validation of polarized expression of human brain meningeal and perivascular fibroblast pumps: the common marker CYP1B1 (**d**, serves as a control) and the meningeal fibroblast-specific influx pump SLC47A1 (**e**). Scale bars, 50 µm. **f**, Overlap between the top 100 perivascular fibroblast-like cell markers and those identified in mice. A

more lenient set of 500 (instead of 100) mouse markers⁸⁰ were used for comparison to ensure claims of species-specificity were robust. Note: the species-conservation of a cell-type marker depends on species-specific changes in the given cell type and changes amongst the remaining background cell types.

Extended Data Fig. 8 Vascular cell-type-specific perturbations in patients with AD and ApoE4 carriers.

a, Immunohistochemistry with anti- β -amyloid antibody (D54D2, white), Thioflavin S (green), and Hoechst (blue) in the hippocampus of individuals with NCI and individuals with AD. Scale bars, 40 μm . **b**, Quantification of β -amyloid immunostaining in **a** for overall β -amyloid ($n = 4$ NCI and AD, two-sided *t*-test; mean \pm s.e.m.). **c**, As in **b** but for cored and neuritic β -amyloid plaques ($n = 3$ NCI and AD, two-sided *t*-test; mean \pm s.e.m.). **d**, UMAP of 143,793 nuclei captured from 17 human hippocampus and superior frontal cortex samples, coloured by AD diagnosis. **e**, Quantification controls for Fig. 5b. Quantification of Collagen IV⁺ vasculature (left) and number of total (regardless of Collagen IV⁺ overlap) Hoechst⁺ nuclei ($n = 5$ NCI and AD, nested two-sided *t*-test; mean \pm s.e.m.). **f**, Matrix layout for intersections of AD DEGs shared across and specific to each cell type. Circles in the matrix indicate sets that are part of the intersection, showing that most DEGs are cell-type-specific. **g**, Example DEGs in AD: arterial (Art), capillary (Cap), venous (Vein), pericyte (Peri), perivascular fibroblast-like cell (P. fibro), and SMC. Blue arrow indicates upregulated and grey arrow downregulated genes. **h**, Summary of the number of AD DEGs by pericyte class: T-, M-, and all pericytes combined to evaluate DEGs that could arise due to a disproportionate loss of M-pericytes in AD. **i**, DEG counts for each cell type in ApoE4 carriers ($n = 5$ ApoE3/3, $n = 11$ ApoE3/4 or ApoE4/4): arterial (Art), capillary (Cap), venous (Vein), pericyte (Peri), perivascular fibroblast-like cell (P. fibro), and SMC. The intensity of the blue colour and the size of the squares are proportional to entry values. **j**, Matrix layout for intersections of ApoE4 DEGs shared across and specific to each cell type. Circles in the matrix indicate sets that are part of the intersection, showing that most DEGs are cell-type-specific. **k**, Immunohistochemical validation of the predicted

upregulated anti-inflammatory DEG *SLC39A10* in venous BECs of ApoE4 carriers. Scale bars, 50 µm ($n = 4$ ApoE3/3 and ApoE4 carriers, nested two-sided *t*-test; mean \pm s.e.m.). **I**, Among patients with both hippocampus and superior frontal cortex profiled ($n = 4$ NCI and $n = 4$ AD), quantification of the relative abundance of major vascular cell types (NCI hippocampus set as reference, unpaired two-sided *t*-test; mean \pm s.e.m.). *BEC $P = 0.0260$, **BEC $P = 0.0023$, *Pericyte P (left) = 0.0357, *Pericyte P (mid) = 0.0237, **Pericyte $P = 0.0077$, **SMC $P = 0.0075$, *Fibroblast $P = 0.0109$, *Astrocyte $P = 0.0357$. **m**, As in **(I)**, but comparison of the number of DEGs between brain regions for each cerebrovascular cell type. Analysis done separately for NCI and AD samples ($n = 7$ cell types, unpaired two-sided *t*-test; mean \pm s.e.m.).

Extended Data Fig. 9 Re-evaluation and characterization of top AD GWAS genes expressed in the human brain vasculature.

a, Heterogeneous expression of AD GWAS genes across T- and M-pericyte subtypes. **b**, RNA-seq data of the predicted T cell-specific AD GWAS genes *EPHA1* and *ABCA7* in an independent dataset⁸¹, corroborating minimal expression across resident/ parenchymal brain cells. **c**, Immunohistochemical confirmation of vascular localization of proteins encoded by 12 top AD GWAS genes from **a**. Scale bars, 25 µm. Arrowheads in APOE point to signal around larger-diameter vessels, consistent with predicted SMC expression. Image credit: Human Protein Atlas^{25,74} (<http://www.proteinatlas.org>). **d**, Heat map comparing expression patterns of top AD GWAS genes in the hippocampus and superior frontal cortex: e.g., several microglia-expressed GWAS genes like *APOE*, *MS4A4A*, and *TREM2* are more highly expressed in hippocampal compared to cortical microglia/ macrophages. **e**, GWAS genes found to be expressed specifically in microglia among cells captured using the conventional nuclei isolation process (from Grubman et al. 2019)¹⁷ are also expressed in vascular cells (asterisks). **f**, Summary of AD GWAS genes enriched in microglia and vascular cells mediating common pathways in protein clearance and inflammation. Mouse and human superscripts denote whether expression has been confirmed in that species for a given gene. Proposed model is described in Discussion.

Extended Data Fig. 10 Brain vascular and perivascular expression of AD and AD-related GWAS genes.

a, Expression of AD and AD-related GWAS risk genes (from Grubman et al. 2019)¹⁷ across human vascular cells. **b**, Enriched biological pathways amongst AD and AD-related trait GWAS genes expressed in each cell type. **c**, For each cell type, the top 10 most specifically expressed AD and AD-related trait GWAS genes.

Supplementary information

Reporting Summary

Supplementary Table 1

Patient samples.

Supplementary Table 2

Cell type markers.

Supplementary Table 3

Brain region enriched genes.

Supplementary Table 4

Mouse versus human gene expression.

Supplementary Table 5

Vascular cell subtype markers.

Supplementary Table 6

Vascular Alzheimer's disease differentially expressed genes.

Supplementary Table 7

Vascular ApoE4 carrier disease differentially expressed genes.

Supplementary Table 8

Expression of top Alzheimer's disease and related GWAS genes.

Rights and permissions

Reprints and Permissions

About this article

Cite this article

Yang, A.C., Vest, R.T., Kern, F. *et al.* A human brain vascular atlas reveals diverse mediators of Alzheimer's risk. *Nature* **603**, 885–892 (2022).
<https://doi.org/10.1038/s41586-021-04369-3>

- Received: 23 April 2021
- Accepted: 17 December 2021
- Published: 14 February 2022
- Issue Date: 31 March 2022
- DOI: <https://doi.org/10.1038/s41586-021-04369-3>

Share this article

Anyone you share the following link with will be able to read this content:

[Get shareable link](#)

Sorry, a shareable link is not currently available for this article.

[Copy to clipboard](#)

Provided by the Springer Nature SharedIt content-sharing initiative

Further reading

- [**Neutrophil-vascular interactions drive myeloperoxidase accumulation in the brain in Alzheimer's disease**](#)

- Leon C. D. Smyth
- Helen C. Murray
- Mark B. Hampton

Acta Neuropathologica Communications (2022)

- [**Transcriptomic mapping of the human cerebrovasculature**](#)

- Masafumi Ihara
- Yumi Yamamoto

Nature Reviews Neurology (2022)

[**Molecular map of the human blood–brain barrier reveals links to Alzheimer's disease**](#)

Research Briefing 14 Feb 2022

[**Transcriptomic mapping of the human cerebrovasculature**](#)

- Masafumi Ihara
- Yumi Yamamoto

News & Views 23 Mar 2022

This article was downloaded by **calibre** from <https://www.nature.com/articles/s41586-021-04369-3>

| [Section menu](#) | [Main menu](#) |

- Article
- [Published: 14 February 2022](#)

Single-cell dissection of the human brain vasculature

- [Francisco J. Garcia](#)^{1,2,3} na1,
- [Na Sun](#)^{3,4,5} na1,
- [Hyeseung Lee](#)^{2,3},
- [Brianna Godlewski](#)^{6,7},
- [Hansruedi Mathys](#)^{2,3,8},
- [Kyriaki Galani](#)^{3,4,5},
- [Blake Zhou](#)^{2,3},
- [Xueqiao Jiang](#)^{2,3},
- [Ayesha P. Ng](#)^{2,3},
- [Julio Mantero](#)^{3,4,5},
- [Li-Huei Tsai](#)^{1,2,3},
- [David A. Bennett](#)⁹,
- [Mustafa Sahin](#) ORCID: orcid.org/0000-0001-7044-2953^{6,7},
- [Manolis Kellis](#) ORCID: orcid.org/0000-0001-7113-9630^{3,4,5} &
- [Myriam Heiman](#) ORCID: orcid.org/0000-0002-6365-8673^{1,2,3}

Nature volume **603**, pages 893–899 (2022)

- 12k Accesses
- 1 Citations
- 131 Altmetric
- [Metrics details](#)

Subjects

- [Blood-brain barrier](#)
- [Transcriptomics](#)

Abstract

Despite the importance of the cerebrovasculature in maintaining normal brain physiology and in understanding neurodegeneration and drug delivery to the central nervous system¹, human cerebrovascular cells remain poorly characterized owing to their sparsity and dispersion. Here we perform single-cell characterization of the human cerebrovasculature using both ex vivo fresh tissue experimental enrichment and post mortem *in silico* sorting of human cortical tissue samples. We capture 16,681 cerebrovascular nuclei across 11 subtypes, including endothelial cells, mural cells and three distinct subtypes of perivascular fibroblast along the vasculature. We uncover human-specific expression patterns along the arteriovenous axis and determine previously uncharacterized cell-type-specific markers. We use these human-specific signatures to study changes in 3,945 cerebrovascular cells from patients with Huntington's disease, which reveal activation of innate immune signalling in vascular and glial cell types and a concomitant reduction in the levels of proteins critical for maintenance of blood–brain barrier integrity. Finally, our study provides a comprehensive molecular atlas of the human cerebrovasculature to guide future biological and therapeutic studies.

This is a preview of subscription content

Access options

Subscribe to Nature+

Get immediate online access to the entire Nature family of 50+ journals

\$29.99

monthly

[Subscribe](#)

Subscribe to Journal

Get full journal access for 1 year

\$199.00

only \$3.90 per issue

[Subscribe](#)

All prices are NET prices.

VAT will be added later in the checkout.

Tax calculation will be finalised during checkout.

Buy article

Get time limited or full article access on ReadCube.

\$32.00

[Buy](#)

All prices are NET prices.

Additional access options:

- [Log in](#)
- [Learn about institutional subscriptions](#)

Fig. 1: snRNA-seq profiling of the human cerebrovasculature.

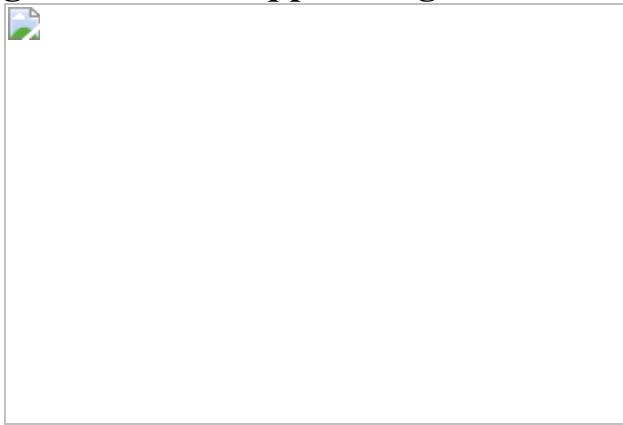


Fig. 2: Integrative analysis of human ex vivo, post mortem and mouse cerebrovascular cell types.



Fig. 3: Molecular zonation of human brain endothelial and mural cells.

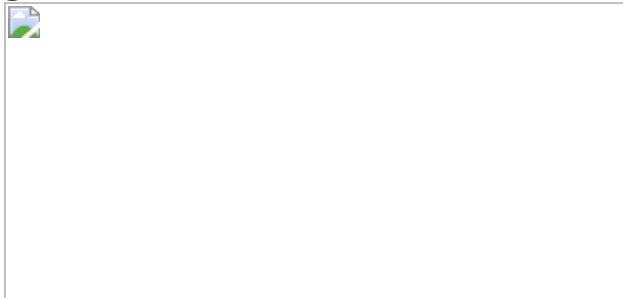


Fig. 4: Perivascular fibroblasts in the human cerebrovasculature.

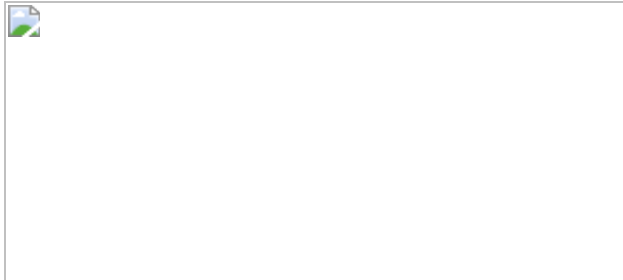
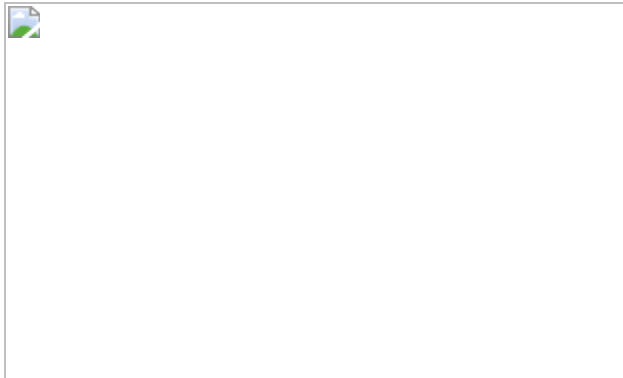


Fig. 5: Innate immune activation related to cerebrovascular dysfunction in HD.



Data availability

Count matrices for all cells analysed in this study have been uploaded with this submission at <http://compbio.mit.edu/scBBB/>. An interactive website is available at <https://nsun.shinyapps.io/scbbb/>. Raw sequencing data associated with Figs. 1–5 are available in the National Center for Biotechnology Information Gene Expression Omnibus under accession number [GSE173731](#). Sample identifiers for ROSMAP and HD human tissue samples are listed in Supplementary Table 1. With these identifiers, data/sample acquisition for the HD samples can be accessed at <https://neurobiobank.nih.gov/>. ROSMAP samples and data can be accessed at <https://www.radc.rush.edu>. This website includes detailed documentation on variables and cross-calculations of selected variables, and the relevant Data Use Agreement and Material Transfer Agreement can also be downloaded from this site. Samples (and data regarding them) from the Boston Children’s Hospital were collected for the use of Boston Children’s Hospital investigators and their collaborators, and are not freely available. Further enquiries regarding these samples can be directed to the corresponding authors.

Code availability

The code used in this study is available at <http://compbio.mit.edu/scBBB/>. Code used in this study is also available upon reasonable request from the corresponding authors.

References

1. Sweeney, M. D., Zhao, Z., Montagne, A., Nelson, A. R. & Zlokovic, B. V. Blood-brain barrier: from physiology to disease and back. *Physiol. Rev.* **99**, 21–78 (2019).
2. Saunders, A. et al. Molecular diversity and specializations among the cells of the adult mouse brain. *Cell* **174**, 1015–1030 (2018).

3. Sabbagh, M. F. et al. Transcriptional and epigenomic landscapes of CNS and non-CNS vascular endothelial cells. *eLife* **7**, e36187 (2018).
4. Vanlandewijck, M. et al. A molecular atlas of cell types and zonation in the brain vasculature. *Nature* **554**, 475–480 (2018).
5. Montagne, A. et al. Blood-brain barrier breakdown in the aging human hippocampus. *Neuron* **85**, 296–302 (2015).
6. Sweeney, M. D., Kisler, K., Montagne, A., Toga, A. W. & Zlokovic, B. V. The role of brain vasculature in neurodegenerative disorders. *Nat. Neurosci.* **21**, 1318–1331 (2018).
7. Lee, Y.-K., Uchida, H., Smith, H., Ito, A. & Sanchez, T. The isolation and molecular characterization of cerebral microvessels. *Nat. Protoc.* **14**, 3059–3081 (2019).
8. Mathys, H. et al. Single-cell transcriptomic analysis of Alzheimer’s disease. *Nature* **570**, 332–337 (2019).
9. Lee, H. et al. Cell type-specific transcriptomics reveals that mutant Huntingtin leads to mitochondrial RNA release and neuronal innate immune activation. *Neuron* **107**, 891–908 (2020).
10. Bennett, D. A. et al. Religious Orders Study and Rush Memory and Aging Project. *J. Alzheimer’s Dis.* **64**, S161–S189 (2018).
11. Zhao, Z. et al. Central role for PICALM in amyloid- β blood-brain barrier transcytosis and clearance. *Nat. Neurosci.* **18**, 978–987 (2015).
12. Lim, Y.-H. et al. Identification of long noncoding RNAs involved in muscle differentiation. *PLoS ONE* **13**, e0193898 (2018).
13. Joutel, A. et al. *Notch3* mutations in CADASIL, a hereditary adult-onset condition causing stroke and dementia. *Nature* **383**, 707–710 (1996).
14. Park, C., Kim, T. M. & Malik, A. B. Transcriptional regulation of endothelial cell and vascular development. *Circ. Res.* **112**, 1380–1400

(2013).

15. Ley, K., Laudanna, C., Cybulsky, M. I. & Nourshargh, S. Getting to the site of inflammation: the leukocyte adhesion cascade updated. *Nat. Rev. Immunol.* **7**, 678–689 (2007).
16. Attwell, D., Mishra, A., Hall, C. N., O’Farrell, F. M. & Dalkara, T. What is a pericyte? *J. Cereb. Blood Flow Metab.* **36**, 451–455 (2016).
17. Morrone, C. D., Bishay, J. & McLaurin, J. Potential role of venular amyloid in Alzheimer’s disease pathogenesis. *Int. J. Mol. Sci.* **21**, 1985 (2020).
18. Rajan, A. M., Ma, R. C., Kocha, K. M., Zhang, D. J. & Huang, P. Dual function of perivascular fibroblasts in vascular stabilization in zebrafish. *PLoS Genet.* **16**, e1008800 (2020).
19. Muhl, L. et al. Single-cell analysis uncovers fibroblast heterogeneity and criteria for fibroblast and mural cell identification and discrimination. *Nat. Commun.* **11**, 3953 (2020).
20. Fernández-Klett, F. et al. Early loss of pericytes and perivascular stromal cell-induced scar formation after stroke. *J. Cereb. Blood Flow Metab.* **33**, 428–439 (2013).
21. Zeisel, A. et al. Molecular architecture of the mouse nervous system. *Cell* **174**, 999–1014 (2018).
22. Dorrier, C. E. et al. CNS fibroblasts form a fibrotic scar in response to immune cell infiltration. *Nat. Neurosci.* **24**, 234–244 (2021).
23. Bonney, S. K., Sullivan, L. T., Cherry, T. J., Daneman, R. & Shih, A. Y. Distinct features of brain perivascular fibroblasts and mural cells revealed by in vivo two-photon imaging. *J. Cereb. Blood Flow Metab.*, <https://doi.org/10.1177/0271678X211068528> (2021).
24. Chinnery, P. F. et al. Clinical features and natural history of neuroferritinopathy caused by the *FTL1* 460InsA mutation. *Brain* **130**,

110–119 (2007).

25. Tadic, V. et al. Primary familial brain calcification with known gene mutations. *JAMA Neurol.* **72**, 460–467 (2015).
26. MacDonald, M. E. et al. A novel gene containing a trinucleotide repeat that is expanded and unstable on Huntington’s disease chromosomes. *Cell* **72**, 971–983 (1993).
27. Drouin-Ouellet, J. et al. Cerebrovascular and blood–brain barrier impairments in Huntington’s disease: potential implications for its pathophysiology. *Ann. Neurol.* **78**, 160–177 (2015).
28. Chen, J. J., Salat, D. H. & Rosas, H. D. Complex relationships between cerebral blood flow and brain atrophy in early Huntington’s disease. *Neuroimage* **59**, 1043–1051 (2012).
29. Harris, G. J. et al. Reduced basal ganglia blood flow and volume in pre-symptomatic, gene-tested persons at-risk for Huntington’s disease. *Brain* **122**, 1667–1678 (1999).
30. Hua, J., Unschuld, P. G., Margolis, R. L., van Zijl, P. C. M. & Ross, C. A. Elevated arteriolar cerebral blood volume in prodromal Huntington’s disease. *Mov. Disord.* **29**, 396–401 (2014).
31. Di Pardo, A. et al. Impairment of blood–brain barrier is an early event in R6/2 mouse model of Huntington disease. *Sci Rep.* **7**, 41316 (2017).
32. Padel, T. et al. Brain pericyte activation occurs early in Huntington’s disease. *Exp. Neurol.* **305**, 139–150 (2018).
33. Liu, H. et al. Huntingtin silencing delays onset and slows progression of Huntington’s disease: a biomarker study. *Brain* **144**, 3101–3113 (2021).
34. Ben-Zvi, A. et al. Mfsd2a is critical for the formation and function of the blood–brain barrier. *Nature* **509**, 507–511 (2014).

35. Lim, R. G. et al. Huntington's disease iPSC-derived brain microvascular endothelial cells reveal WNT-mediated angiogenic and blood-brain barrier deficits. *Cell Rep.* **19**, 1365–1377 (2017).
36. Daniels, B. P. & Klein, R. S. Viral sensing at the blood–brain barrier: new roles for innate immunity at the CNS vasculature. *Clin. Pharmacol. Ther.* **97**, 372–379 (2015).
37. Song, H. W. et al. Transcriptomic comparison of human and mouse brain microvessels. *Sci Rep.* **10**, 12358 (2020).
38. Mondo, E. et al. A developmental analysis of juxtavascular microglia dynamics and interactions with the vasculature. *J. Neurosci.* **40**, 6503–6521 (2020).
39. Fujioka, T., Kaneko, N. & Sawamoto, K. Blood vessels as a scaffold for neuronal migration. *Neurochem. Int.* **126**, 69–73 (2019).
40. Wingo, A. P. et al. Shared proteomic effects of cerebral atherosclerosis and Alzheimer's disease on the human brain. *Nat. Neurosci.* **23**, 696–700 (2020).
41. Butler, A., Hoffman, P., Smibert, P., Papalexi, E. & Satija, R. Integrating single-cell transcriptomic data across different conditions, technologies, and species. *Nat. Biotechnol.* **36**, 411–420 (2018).
42. McGinnis, C. S., Murrow, L. M. & Gartner, Z. J. DoubletFinder: doublet detection in single-cell RNA sequencing data using artificial nearest neighbors. *Cell Syst.* **8**, 329–337 (2019).
43. Wang, D. et al. Comprehensive functional genomic resource and integrative model for the human brain. *Science* **362**, eaat8464 (2018).
44. Finak, G. et al. MAST: a flexible statistical framework for assessing transcriptional changes and characterizing heterogeneity in single-cell RNA sequencing data. *Genome Biol.* **16**, 278 (2015).

45. Chen, E. Y. et al. Enrichr: interactive and collaborative HTML5 gene list enrichment analysis tool. *BMC Bioinform.* **14**, 128 (2013).
46. Xie, Z. et al. Gene set knowledge discovery with Enrichr. *Curr. Protoc.* **1**, e90 (2021).
47. Kuleshov, M. V. et al. Enrichr: a comprehensive gene set enrichment analysis web server 2016 update. *Nucleic Acids Res.* **44**, W90–W97 (2016).
48. Ashburner, M. et al. Gene Ontology: tool for the unification of biology. *Nat. Genet.* **25**, 25–29 (2000).
49. The Gene Ontology Consortium. The Gene Ontology resource: 20 years and still GOing strong. *Nucleic Acids Res.* **47**, D330–D338 (2019).
50. Cao, J. et al. The single-cell transcriptional landscape of mammalian organogenesis. *Nature* **566**, 496–502 (2019).
51. Mohammadi, S., Davila-Velderrain, J. & Kellis, M. A multiresolution framework to characterize single-cell state landscapes. *Nat. Commun.* **11**, 5399 (2020).
52. Ritchie, M. E. et al. limma powers differential expression analyses for RNA-sequencing and microarray studies. *Nucleic Acids Res.* **43**, e47 (2015).

Acknowledgements

This research was supported in part by the Intellectual and Developmental Disability Research Center (financed by NIH U54 HD090255 and P50 HD105351) and the Rosamund Stone Zander Translational Neuroscience Center at the Boston Children’s Hospital (to M.S.), a Picower Institute Innovation Fund Award and a Walter B. Brewer (1940) MIT Fund Award (to M.H.), and NIH AG054012, AG058002, AG062377, NS110453, NS115064, AG067151, AG062335, MH109978, MH119509 and

HG008155 and Cure Alzheimer's Fund CureAlz-CIRCUITS (to M.K.). ROSMAP was supported by National Institute on Aging grants P30AG10161, R01AG15819, R01AG17917 and U01AG61356. We thank A. H. Effenberger for assistance in graphics design; S. S. Pineda for assistance with differential gene expression analysis; P. Ge for assistance with the western blot experiments; and L.-L. Ho and Z. Peng, for collaborative and scientific input on experimental profiling. We also thank the NIH NeuroBioBank and the University of Alabama at Birmingham for providing the human HD and control samples used in this study.

Author information

Author notes

1. These authors contributed equally: Francisco J. Garcia, Na Sun

Affiliations

1. Department of Brain and Cognitive Sciences, MIT, Cambridge, MA, USA

Francisco J. Garcia, Li-Huei Tsai & Myriam Heiman

2. Picower Institute for Learning and Memory, Cambridge, MA, USA

Francisco J. Garcia, Hyeseung Lee, Hansruedi Mathys, Blake Zhou, Xueqiao Jiang, Ayesha P. Ng, Li-Huei Tsai & Myriam Heiman

3. Broad Institute of MIT and Harvard, Cambridge, MA, USA

Francisco J. Garcia, Na Sun, Hyeseung Lee, Hansruedi Mathys, Kyriaki Galani, Blake Zhou, Xueqiao Jiang, Ayesha P. Ng, Julio Mantero, Li-Huei Tsai, Manolis Kellis & Myriam Heiman

4. Department of Electrical Engineering and Computer Science, MIT, Cambridge, MA, USA

Na Sun, Kyriaki Galani, Julio Mantero & Manolis Kellis

5. MIT Computer Science and Artificial Intelligence Laboratory,
Cambridge, MA, USA

Na Sun, Kyriaki Galani, Julio Mantero & Manolis Kellis

6. Rosamund Stone Zander Translational Neuroscience Center, F.M.
Kirby Neurobiology Center, Department of Neurology, Boston
Children's Hospital, Boston, MA, USA

Brianna Godlewski & Mustafa Sahin

7. Department of Neurology, Harvard Medical School, Boston, MA,
USA

Brianna Godlewski & Mustafa Sahin

8. Department of Neurobiology, University of Pittsburgh School of
Medicine, Pittsburgh, PA, USA

Hansruedi Mathys

9. Rush Alzheimer's Disease Center, Rush University Medical Center,
Chicago, IL, USA

David A. Bennett

Contributions

F.J.G. designed the human and mouse studies and developed the BVE protocol; N.S. conducted data analysis with assistance from F.J.G. and H.L.; B.G. and M.S. assisted in ex vivo human tissue sample acquisition; H.L. assisted with BVE snRNA-seq sample preparation; B.Z. performed vascular-related experiments and quantification; K.G. and J.M. conducted snRNA-seq post mortem sample profiling; H.M., X.J., A.P.N. and L.-H.T. provided pre-publication ROSMAP data; D.A.B. provided post mortem

samples; F.J.G., N.S., M.K. and M.H. wrote the paper with comments from all authors; and M.K. and M.H. supervised the project.

Corresponding authors

Correspondence to [Manolis Kellis](#) or [Myriam Heiman](#).

Ethics declarations

Competing interests

The authors declare no competing interests.

Peer review

Peer review information

Nature thanks the anonymous reviewers for their contribution to the peer review of this work.

Additional information

Publisher's note Springer Nature remains neutral with regard to jurisdictional claims in published maps and institutional affiliations.

Extended data figures and tables

[Extended Data Fig. 1 Validation of Blood Vessel Enrichment \(BVE\) protocol.](#)

a. qPCR of canonical cell type markers for endothelial *Cldn5* ($p < 0.0001$), *Abcb1a* ($p = 0.0002$), *Mfsd2a* ($p = 0.9556$), mural *Pdgfrb* ($p = 0.0388$), *Acta2* ($p < 0.0001$), *Myh11* ($p < 0.0001$), astrocytes *Aqp4* ($p > 0.9999$), *Aldh1l1* ($p > 0.9999$), oligodendrocytes *Mog* ($p > 0.9999$), neurons *Rbfox3*

($p > 0.9999$), and microglia *Aif1* ($p > 0.9999$) from mouse cortex, ordinary one-way ANOVA, * $p < 0.05$, ** $p < 0.01$, *** $p < 0.001$, **** $p < 0.0001$, n.s. = not significant. Error bars denote standard deviation of the mean from $n = 3$ independent biological replicates. **b.** Representative immunofluorescence of blood vessels enriched from mouse cortex using the BVE protocol. $n = 3$ independent biological replicates for immunostaining. Brightness and contrast enhanced for visualization. Scale bar, 20 μm .

Extended Data Fig. 2 Characterization of human snRNA-seq data from human temporal cortex.

a. UMAP of *ex vivo* dataset by patient ID. **b.** UMAP of *ex vivo* dataset by experimental protocol. **c.** Heatmap of top cell-type differentially-expressed genes (ctDEGs) in major cell types from *ex vivo* human tissue. **d.** UMAP sub-clustering of excitatory neurons. **e.** UMAP sub-clustering of inhibitory neurons. **f.** Correlation heatmap between *ex vivo* and *post mortem* vascular cell types.

Extended Data Fig. 3 Integrative analysis of *ex vivo*, *post mortem*, and mouse datasets.

a. UMAP plot of integrated human snRNA-seq datasets without covariate correction shown by platform and cell type and **b.** with covariate correction by platform and cell type **c.** Cell fraction distribution of single nuclei across all datasets by cerebrovasculature cell type. **d.** Cell number distribution of single nuclei across all datasets by cerebrovasculature cell type. **e.** Venn diagram overlap of genes between human *post mortem* vs. mouse and human *ex vivo* vs. mouse. **f.** Cell fraction and **g.** gene comparison of vascular cell types between mouse and human datasets. **h–i.** Representative functional enriched terms of human- and mouse-specific/highly expressed genes in endothelial (**h**) and pericytes (**i**). Human-mouse differentially expressed genes (hmDEGs) smooth muscle cells (**j, left**), and fibroblast (**k, left**). X-axis represents the log-transformed fold change and y-axis represents the maximal expression level. The top genes are highlighted in blue for mouse and red for human. Genes that were also cell type markers

are bolded. **j–k.** (right panels), the representative functional enriched terms of human- and mouse-specific/highly expressed genes.

Extended Data Fig. 4 Zonation gene expression analysis of human endothelial cells.

- a.** Heatmap of 147 zonated transcription factors along the endothelial gradient. **b.** Heatmap of 76 zonated transporters along the endothelial gradient.

Extended Data Fig. 5 Zonation in human brain endothelial cells.

- a.** Gene zonation analysis of mouse brain endothelial cells from Vanlandewick et al. **b.** Integrated zonation analysis of human and mouse brain endothelial cell profiles. Pearson correlation coefficient of shared genes shown on right. **c.** Indirect immunofluorescence of TSHZ2 expression in human and mouse brain cortex. **d.** Indirect immunofluorescence of MT1E/MT1 expression in human and mouse brain cortex. **e.** Indirect immunofluorescence of MT2A/MT2 expression in human and mouse brain cortex. **f.** Enriched Gene Ontology terms in endothelial zones. Representative images in **c., d.,** and **e.** from $n = 3$ independent biological replicates for each marker. Brightness and contrast enhanced for visualization. Scale bar, 20 μm .

Extended Data Fig. 6 Zonation gene expression analysis of human pericytes.

- a.** Heatmap of zonated transcription factors along the pericyte gradient. **b.** Heatmap of zonated transporters along the pericyte gradient.

Extended Data Fig. 7 Zonation gene expression analysis of human SMCs.

- a.** Heatmap of zonated transcription factors along the SMC gradient. **b.** Heatmap of zonated transporters along the SMC gradient. **c.** Overlap matrix

across the zonated pericyte and SMC clusters.

Extended Data Fig. 8 Zonation in human brain mural cells.

a. Indirect immunofluorescence of SLC30A10 expression in human and mouse brain cortex. **b.** Indirect immunofluorescence of GRM8 expression in human and mouse brain cortex. **c.** Indirect immunofluorescence of FRMD3 expression in human and mouse brain cortex. **d.** Indirect immunofluorescence localization of FRMD3 on ACTA2+ (known SMC marker) vessels. **e.** Enriched Gene Ontology terms in mural zones. Representative images in **a–d** from $n = 3$ independent biological replicates for each marker. Brightness and contrast enhanced for visualization. Scale bar, 20 μm .

Extended Data Fig. 9 Validation and pathway analyses of perivascular fibroblast subtypes.

a. Immunofluorescence staining of Type III fibroblast marker KCNMA1 on ACTA2+ vessels in human. **b.** Enriched Gene Ontology analysis in perivascular fibroblast subtypes. **c.** Pseudotime analysis of *ex vivo* fibroblast subtypes. **d.** Pseudotime analysis of *ex vivo* fibroblast subtypes and Pericyte 2 (note: Pericyte 1 not shown as it did not fall within any pseudotime trajectory). Representative image in **a.** from $n = 3$ independent biological replicates for each marker. Brightness and contrast enhanced for visualization. Scale bar, 20 μm .

Extended Data Fig. 10 Cerebrovascular profiling in Huntington's disease.

a. UMAP of integrated single nuclei from *post mortem* control and HD human patient samples. **b.** UMAP of integrated cerebrovasculature cells in *post mortem* control and HD human patients. **c.** Comparison of cerebrovasculature cell annotations (in cell numbers) in this study vs. Lee et al. **d.** UMAP analysis of astrocyte subclusters in HD. Vascular-related astrocytes outlined in blue. **e.** UMAP analysis of microglia subclusters in HD. Vascular-related microglia outlined in blue. **f.** ChEA prediction of top

10 regulators of upregulated genes in HD endothelial, mural, and fibroblasts cells. **g.** Pathway analysis of the top 10 enriched upregulated pathways in HD endothelial, mural, and fibroblasts cells. **h.** PKR immunoreactivity in the R6/2 HD mouse model engulfs blood vessels with low CLDN5 expression. **i.** Western blots for tight junction proteins CLDN5 and TJP1 from human HD and control samples. Representative images in **h.** from $n = 3$ independent biological replicates for each immunostaining. Brightness and contrast in immunofluorescence enhanced for visualization. Scale bar, 20 μm .

Supplementary information

Reporting Summary

Supplementary Table 1

Patient and sample information for ex vivo, post mortem ROSMAP, and post mortem HD and controls.

Supplementary Table 2

DEGs in cerebrovasculature cell types, as reported by snRNA-seq from ex vivo and post mortem samples. Differential expression analysis is based on the non-parametric Wilcoxon rank sum test.

Supplementary Table 3

DEGs from comparisons between cross-modal ex vivo versus post mortem and cross-species human versus mouse, as reported by snRNA-seq. Differential expression analysis is based on the non-parametric Wilcoxon rank sum test.

Supplementary Table 4

DEGs in endothelial, mural and fibroblasts, as reported by snRNA-seq from the caudate nucleus and putamen of patients with HD (compared to

controls), as well as WikiPathways, KEGG and GOBP analysis. The differential gene expression analysis was performed at cell-type-specific pseudo-bulk level using ACTIONNet and limma with age, sex, PMI and disease group as design covariates and gene-wise single-cell-level variances as weights for the linear model.

Supplementary Table 5

DEGs in vascular-related astrocyte and microglia subclusters, as reported by snRNA-seq from the caudate nucleus and putamen of patients with HD (compared to controls). Differential expression analysis is based on the non-parametric Wilcoxon rank sum test.

Supplementary Table 6

List of antibody information.

Rights and permissions

Reprints and Permissions

About this article

Cite this article

Garcia, F.J., Sun, N., Lee, H. *et al.* Single-cell dissection of the human brain vasculature. *Nature* **603**, 893–899 (2022). <https://doi.org/10.1038/s41586-022-04521-7>

- Received: 06 April 2021
- Accepted: 04 February 2022
- Published: 14 February 2022
- Issue Date: 31 March 2022

- DOI: <https://doi.org/10.1038/s41586-022-04521-7>

Share this article

Anyone you share the following link with will be able to read this content:

[Get shareable link](#)

Sorry, a shareable link is not currently available for this article.

[Copy to clipboard](#)

Provided by the Springer Nature SharedIt content-sharing initiative

Further reading

- [**Transcriptomic mapping of the human cerebrovasculature**](#)
 - Masafumi Ihara
 - Yumi Yamamoto

Nature Reviews Neurology (2022)

[**Transcriptomic mapping of the human cerebrovasculature**](#)

- Masafumi Ihara
- Yumi Yamamoto

News & Views 23 Mar 2022

This article was downloaded by **calibre** from <https://www.nature.com/articles/s41586-022-04521-7>

- Article
- [Published: 16 March 2022](#)

Bacterial inhibition of Fas-mediated killing promotes neuroinvasion and persistence

- [Claire Maudet](#) [ORCID: orcid.org/0000-0001-8856-0819](#)^{1, na1},
- [Marouane Kheloufi](#)^{1, na1},
- [Sylvain Levallois](#) [ORCID: orcid.org/0000-0002-5805-1092](#)¹,
- [Julien Gaillard](#)¹,
- [Lei Huang](#)¹,
- [Charlotte Gaultier](#)¹,
- [Yu-Huan Tsai](#)^{1, nAff4},
- [Olivier Disson](#)¹ &
- [Marc Lecuit](#) [ORCID: orcid.org/0000-0002-4491-1063](#)^{1,2,3}

[Nature](#) volume **603**, pages 900–906 (2022)

- 4094 Accesses
- 1 Citations
- 182 Altmetric
- [Metrics details](#)

Subjects

- [Blood-brain barrier](#)
- [Immune evasion](#)

- [Infection](#)
- [Listeria](#)
- [Pathogens](#)

Abstract

Infections of the central nervous system are among the most serious infections^{1,2}, but the mechanisms by which pathogens access the brain remain poorly understood. The model microorganism *Listeria monocytogenes* (*Lm*) is a major foodborne pathogen that causes neurolisteriosis, one of the deadliest infections of the central nervous system^{3,4}. Although immunosuppression is a well-established host risk factor for neurolisteriosis^{3,5}, little is known about the bacterial factors that underlie the neuroinvasion of *Lm*. Here we develop a clinically relevant experimental model of neurolisteriosis, using hypervirulent neuroinvasive strains⁶ inoculated in a humanized mouse model of infection⁷, and we show that the bacterial surface protein InlB protects infected monocytes from Fas-mediated cell death by CD8⁺ T cells in a manner that depends on c-Met, PI3 kinase and FLIP. This blockade of specific anti-*Lm* cellular immune killing lengthens the lifespan of infected monocytes, and thereby favours the transfer of *Lm* from infected monocytes to the brain. The intracellular niche that is created by InlB-mediated cell-autonomous immune resistance also promotes *Lm* faecal shedding, which accounts for the selection of InlB as a core virulence gene of *Lm*. We have uncovered a specific mechanism by which a bacterial pathogen confers an increased lifespan to the cells it infects by rendering them resistant to cell-mediated immunity. This promotes the persistence of *Lm* within the host, its dissemination to the central nervous system and its transmission.

This is a preview of subscription content

Access options

Subscribe to Nature+

Get immediate online access to the entire Nature family of 50+ journals

\$29.99

monthly

[Subscribe](#)

Subscribe to Journal

Get full journal access for 1 year

\$199.00

only \$3.90 per issue

[Subscribe](#)

All prices are NET prices.

VAT will be added later in the checkout.

Tax calculation will be finalised during checkout.

Buy article

Get time limited or full article access on ReadCube.

\$32.00

[Buy](#)

All prices are NET prices.

Additional access options:

- [Log in](#)
- [Learn about institutional subscriptions](#)

Fig. 1: Infected inflammatory monocytes transfer *Lm* to the CNS by cell-to-cell spread.

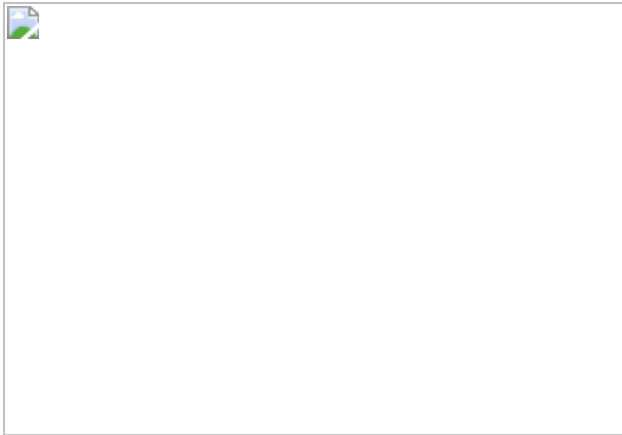


Fig. 2: InlB is involved in *Lm* neuroinvasion and increases the infection of inflammatory monocytes.



Fig. 3: InlB blocks the CD8⁺ T cell-mediated cell death of monocytes.

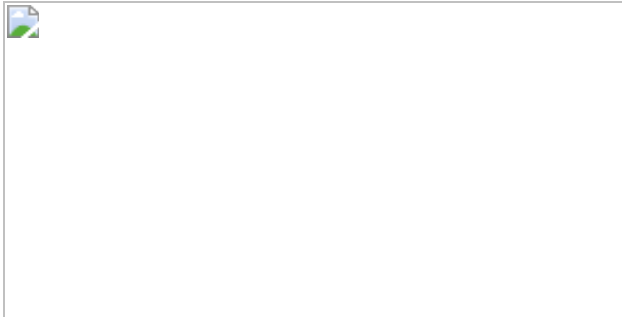
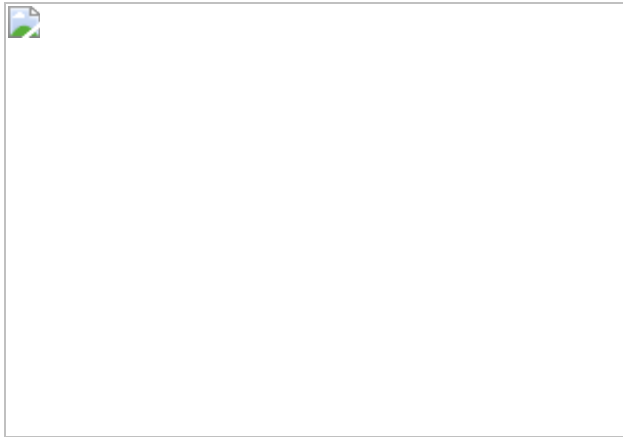


Fig. 4: InlB blocks CD8⁺ T cell-mediated killing through c-Met–PI3K–FLIP, and favours the persistence of *Lm* in the gut.



Data availability

The datasets generated and/or analysed during this study are available as Source Data. [Source data](#) are provided with this paper.

References

1. Schuchat, A. et al. Bacterial meningitis in the United States in 1995. *N. Engl. J. Med.* **337**, 970–976 (1997).
2. van de Beek, D. et al. Clinical features and prognostic factors in adults with bacterial meningitis. *N. Engl. J. Med.* **351**, 1849–1859 (2004).
3. Charlier, C. et al. Clinical features and prognostic factors of listeriosis: the MONALISA national prospective cohort study. *Lancet Infect. Dis.* **17**, 510–519 (2017).
4. Mailles, A. & Stahl, J. Infectious encephalitis in France in 2007: a national prospective study. *Clin. Infect. Dis.* **49**, 1838–1847 (2009).
5. Skogberg, K. et al. Clinical presentation and outcome of listeriosis in patients with and without immunosuppressive therapy. *Clin. Infect. Dis.* **14**, 815–821 (1992).
6. Maury, M. M. et al. Uncovering *Listeria monocytogenes* hypervirulence by harnessing its biodiversity. *Nat. Genet.* **48**, 308–313

(2016).

7. Disson, O. et al. Conjugated action of two species-specific invasion proteins for fetoplacental listeriosis. *Nature* **455**, 1114–1118 (2008).
8. Drevets, D. A., Jelinek, T. A. & Freitag, N. E. *Listeria monocytogenes*-infected phagocytes can initiate central nervous system infection in mice. *Infect. Immun.* **69**, 1344–1350 (2001).
9. Join-Lambert, O. F. et al. *Listeria monocytogenes*-infected bone marrow myeloid cells promote bacterial invasion of the central nervous system. *Cell. Microbiol.* **7**, 167–180 (2005).
10. Cantinelli, T. et al. “Epidemic clones” of *Listeria monocytogenes* are widespread and ancient clonal groups. *J. Clin. Microbiol.* **51**, 3770–3779 (2013).
11. Bécavin, C. et al. Comparison of widely used *Listeria monocytogenes* strains EGD, 10403S, and EGD-e highlights genomic variations underlying differences in pathogenicity. *mBio* **5**, e00969-14 (2014).
12. Pizarro-Cerdá, J., Lecuit, M. & Cossart, P. in *Molecular Cellular Microbiology* Vol. 31 (eds Sansonetti, P. & Zychlinsky, A.) 161–177 (Academic Press, 2002).
13. Boring, L. et al. Impaired monocyte migration and reduced type 1 (Th1) cytokine responses in C-C chemokine receptor 2 knockout mice. *J. Clin. Invest.* **100**, 2552–2561 (1997).
14. Kocks, C. et al. *L. monocytogenes*-induced actin assembly requires the *actA* gene product, a surface protein. *Cell* **68**, 521–531 (1992).
15. Tilney, L. G. & Portnoy, D. A. Actin filaments and the growth, movement, and spread of the intracellular bacterial parasite, *Listeria monocytogenes*. *J. Cell Biol.* **109**, 1597–1608 (1989).
16. Lecuit, M. et al. A transgenic model for listeriosis: role of internalin in crossing the intestinal barrier. *Science* **292**, 1722–1725 (2001).

17. Moura, A. et al. Whole genome-based population biology and epidemiological surveillance of *Listeria monocytogenes*. *Nat. Microbiol.* **2**, 16185 (2016).
18. Gaillard, J. L., Jaubert, F. & Berche, P. The *inlAB* locus mediates the entry of *Listeria monocytogenes* into hepatocytes in vivo. *J. Exp. Med.* **183**, 359–369 (1996).
19. Braun, L. et al. InlB: an invasion protein of *Listeria monocytogenes* with a novel type of surface association. *Mol. Microbiol.* **25**, 285–294 (1997).
20. Dramsi, S. et al. Entry of *Listeria monocytogenes* into hepatocytes requires expression of InlB, a surface protein of the internalin multigene family. *Mol. Microbiol.* **16**, 251–261 (1995).
21. Lane, F. C. & Unanue, E. R. Requirement of thymus (T) lymphocytes for resistance to listeriosis. *J. Exp. Med.* **135**, 1104–1112 (1972).
22. Schlüter, D. et al. Systemic immunization induces protective CD4⁺ and CD8⁺ T cell-mediated immune responses in murine *Listeria monocytogenes* meningoencephalitis. *Eur. J. Immunol.* **25**, 2384–2391 (1995).
23. Khanna, K. M., McNamara, J. T. & Lefrançois, L. In situ imaging of the endogenous CD8 T cell response to infection. *Science* **318**, 116–120 (2007).
24. Doherty, P. Cell-mediated cytotoxicity. *Cell* **75**, 607–612 (1993).
25. Muzio, M. et al. FLICE, a novel FADD-homologous ICE/CED-3-like protease, is recruited to the CD95 (Fas/APO-1) death-inducing signaling complex. *Cell* **85**, 817–827 (1996).
26. Shen, Y., Naujokas, M., Park, M. & Ireton, K. InlB-dependent internalization of *Listeria* is mediated by the Met receptor tyrosine kinase. *Cell* **103**, 501–510 (2000).

27. Bierne, H. et al. A role for cofilin and LIM kinase in *Listeria*-induced phagocytosis. *J. Cell Biol.* **155**, 101 (2001).
28. Weidner, K. M. et al. Interaction between Gab1 and the c-Met receptor tyrosine kinase is responsible for epithelial morphogenesis. *Nature* **384**, 173–176 (1996).
29. Bowers, D. C. et al. Scatter factor/hepatocyte growth factor protects against cytotoxic death in human glioblastoma via phosphatidylinositol 3-kinase- and AKT-dependent pathways. *Cancer Res.* **60**, 4277–4283 (2000).
30. Xiao, G.-H. et al. Anti-apoptotic signaling by hepatocyte growth factor/Met via the phosphatidylinositol 3-kinase/Akt and mitogen-activated protein kinase pathways. *Proc. Natl Acad. Sci. USA* **98**, 247–252 (2001).
31. Tsai, Y. H. L., Orsi, R. H., Nightingale, K. K. & Wiedmann, M. *Listeria monocytogenes* internalins are highly diverse and evolved by recombination and positive selection. *Infect. Genet. Evol.* **6**, 378–389 (2006).
32. Louie, A., Zhang, T., Becattini, S., Waldor, M. K. & Portnoy, D. A. A multiorgan trafficking circuit provides purifying selection of *Listeria monocytogenes* virulence genes. *mBio* **10**, e02948-19 (2019).
33. Coureuil, M., Lécuyer, H., Bourdoulous, S. & Nassif, X. A journey into the brain: insight into how bacterial pathogens cross blood–brain barriers. *Nat. Rev. Microbiol.* **15**, 149–159 (2017).
34. Devraj, G. et al. HIF-1 α is involved in blood–brain barrier dysfunction and paracellular migration of bacteria in pneumococcal meningitis. *Acta Neuropathol.* **140**, 183–208 (2020).
35. Liu, Y., Li, J. Y., Chen, S. T., Huang, H. R. & Cai, H. The rLrp of *Mycobacterium tuberculosis* inhibits proinflammatory cytokine production and downregulates APC function in mouse macrophages

- via a TLR2-mediated PI3K/Akt pathway activation-dependent mechanism. *Cell. Mol. Immunol.* **13**, 729–746 (2016).
36. Quan, J. H. et al. Intracellular networks of the PI3K/AKT and MAPK pathways for regulating *Toxoplasma gondii*-induced IL-23 and IL-12 production in human THP-1 cells. *PLoS One* **10**, e0141550 (2015).
 37. Klenerman, P. & Hill, A. T cells and viral persistence: lessons from diverse infections. *Nat. Immunol.* **6**, 873–879 (2005).
 38. Protzer, U., Maini, M. K. & Knolle, P. A. Living in the liver: hepatic infections. *Nat. Rev. Immunol.* **12**, 201–213 (2012).
 39. Mackaness, G. B. Cellular resistance to infection. *J. Exp. Med.* **116**, 381–406 (1962).
 40. Pamer, E. G. Immune responses to *Listeria monocytogenes*. *Nat. Rev. Immunol.* **4**, 812–823 (2004).
 41. Shen, H. et al. Recombinant *Listeria monocytogenes* as a live vaccine vehicle for the induction of protective anti-viral cell-mediated immunity. *Proc. Natl Acad. Sci. USA* **92**, 3987–3991 (2006).
 42. Spranger, S., Bao, R. & Gajewski, T. F. Melanoma-intrinsic β -catenin signalling prevents anti-tumour immunity. *Nature* **523**, 231–235 (2015).
 43. Tauriello, D. V. F. et al. TGF β drives immune evasion in genetically reconstituted colon cancer metastasis. *Nature* **554**, 538–543 (2018).
 44. Ricci, A. et al. *Listeria monocytogenes* contamination of ready-to-eat foods and the risk for human health in the EU. *EFSA J.* **16**, 5134 (2018).
 45. Maury, M. M. et al. Spontaneous loss of virulence in natural populations of *Listeria monocytogenes*. *Infect. Immun.* **85**, e00541-17 (2017).

46. Shinkai, Y. et al. RAG-2-deficient mice lack mature lymphocytes owing to inability to initiate V(D)J rearrangement. *Cell* **68**, 855–867 (1992).
47. Malissen, M. et al. Altered T cell development in mice with a targeted mutation of the CD3-epsilon gene. *EMBO J.* **14**, 4641–4653 (1995).
48. Kitamura, D., Roes, J., Kühn, R. & Rajewsky, K. A B cell-deficient mouse by targeted disruption of the membrane exon of the immunoglobulin μ chain gene. *Nature* **350**, 423–426 (1991).
49. Jung, S. et al. Analysis of fractalkine receptor CX₃CR1 function by targeted deletion and green fluorescent protein reporter gene insertion. *Mol. Cell. Biol.* **20**, 4106–4114 (2000).
50. Hameyer, D. et al. Toxicity of ligand-dependent Cre recombinases and generation of a conditional Cre deleter mouse allowing mosaic recombination in peripheral tissues. *Physiol. Genomics* **31**, 32–41 (2007).
51. Buch, T. et al. A Cre-inducible diphtheria toxin receptor mediates cell lineage ablation after toxin administration. *Nat. Methods* **2**, 419–426 (2005).
52. Matsuzawa, A. et al. A new allele of the lpr locus, lprcg, that complements the gld gene in induction of lymphadenopathy in the mouse. *J. Exp. Med.* **171**, 519–531 (1990).
53. Kägi, D. et al. Cytotoxicity mediated by T cells and natural killer cells is greatly impaired in perforin-deficient mice. *Nature* **369**, 31–37 (1994).
54. Huang, Q. Q. et al. FLIP: a novel regulator of macrophage differentiation and granulocyte homeostasis. *Blood* **116**, 4968–4977 (2010).
55. Huh, C.-G. et al. Hepatocyte growth factor/c-met signaling pathway is required for efficient liver regeneration and repair. *Proc. Natl Acad.*

Sci. USA **101**, 4477–4482 (2004).

56. Canli, Ö. et al. Myeloid cell-derived reactive oxygen species induce epithelial mutagenesis. *Cancer Cell* **32**, 869–883 (2017).
57. Monk, I. R., Gahan, C. G. M. & Hill, C. Tools for functional postgenomic analysis of *listeria monocytogenes*. *Appl. Environ. Microbiol.* **74**, 3921–3934 (2008).
58. Arnaud, M., Chastanet, A. & Débarbouillé, M. New vector for efficient allelic replacement in naturally nontransformable, low-GC-content, Gram-positive bacteria. *Appl. Environ. Microbiol.* **70**, 6887–6891 (2004).
59. Argov, T., Rabinovich, L., Sigal, N. & Herskovits, A. A. An effective counterselection system for *Listeria monocytogenes* and its use to characterize the monocin genomic region of strain 10403S. *Appl. Environ. Microbiol.* **83**, e02927-16 (2017).
60. Balestrino, D. et al. Single-cell techniques using chromosomally tagged fluorescent bacteria to study *Listeria monocytogenes* infection processes. *Appl. Environ. Microbiol.* **76**, 3625–3636 (2010).
61. Quereda, J. J. et al. A dual microscopy-based assay to assess *Listeria monocytogenes* cellular entry and vacuolar escape. *Appl. Environ. Microbiol.* **82**, 211–217 (2016).
62. Disson, O. et al. Modeling human listeriosis in natural and genetically engineered animals. *Nat. Protoc.* **4**, 799–810 (2009).
63. Lu, H. et al. Subcutaneous angiotensin II infusion using osmotic pumps induces aortic aneurysms in mice. *J. Vis. Exp.* **103**, e53191 (2015).

Acknowledgements

We thank P. Bousso and A. Fischer for discussions and the members of the Biology of Infection Unit for their support, in particular L. Travier for

technical help on brain microscopy and L. Hafner for contributing to data analysis, and the National Reference Center *Listeria*. We thank the Cytometry and Biomarkers Unit of Technology and Service (CB UTechS), the Center for Animal Resources and Research (C2RA) and D. Ershov and J.-Y. Tinevez from the Image Analysis Hub at Institut Pasteur. We are grateful to G. de Saint Basile and F. Sepuvelda for the *Prf1* KO mice, F. Rieux-Laucat for the *Fas^{lpr-cg}* mice, R. Pope for the *Flip^{flox/flox}* mice, F. Greten for the *LysM-CreER^{T2}* mice, A. Eychene for the *Met^{flox/flox}* mice and J. Pizarro-Cerda and P. Cossart for the pAD β-lactamase plasmid. Figures 1j, 4l and Extended Data Figs. 5l, 9a were created with BioRender. Work in the M.L. laboratory is funded by the Institut Pasteur, Inserm, ERC, ANR, DIM1HEALTH, Labex IBEID (ANR-10-LABX-62-IBEID) and the Fondation Le Roch-Les Mousquetaires. C.M. and M.K. were recipients of the Roux-Cantarini fellowship of the Institut Pasteur. L.H., C.G. and J.G. were supported by the Université de Paris; Y.-H.T. by the Pasteur–Paris University (PPU) International PhD Program under the European Union’s Horizon 2020 research and innovation program, Marie Skłodowska-Curie grant agreement no 665807; and S.L. by FRM (ECO201906009119) and ‘Ecole Doctorale FIRE-Programme Bettencourt’. M.L. is a member of the Institut Universitaire de France.

Author information

Author notes

1. Yu-Huan Tsai

Present address: Institute of Microbiology and Immunology, National Yang-Ming University, Taipei, Taiwan

2. These authors contributed equally: Claire Maudet, Marouane Kheloufi

Affiliations

1. Institut Pasteur, Université de Paris, Inserm U1117, Biology of Infection Unit, Paris, France

Claire Maudet, Marouane Kheloufi, Sylvain Levallois, Julien Gaillard, Lei Huang, Charlotte Gaultier, Yu-Huan Tsai, Olivier Disson & Marc Lecuit

2. Institut Pasteur, National Reference Center and WHO Collaborating Center Listeria, Paris, France

Marc Lecuit

3. Necker-Enfants Malades University Hospital, Division of Infectious Diseases and Tropical Medicine, APHP, Institut Imagine, Paris, France

Marc Lecuit

Contributions

M.L. initiated and coordinated the study. C.M., M.K., S.L. and M.L. conceived and designed the experimental strategy. C.M. and M.K. performed in vivo and cell sorting for ex vivo experiments. C.M. performed flow cytometry experiments. S.L. and Y.-H.T. performed in vivo experiments and imaging of CNS tissue samples. J.G. performed in vivo experiments and imaging of infected intestinal tissue. O.D. and M.K. did ex vivo monocyte imaging. C.M., L.H. and C.G. designed and performed qPCR with reverse transcription experiments. C.M. and L.H. performed cloning and mutagenesis. M.K. performed western blotting experiments. C.M., M.K., S.L., J.G., O.D., Y.-H.T. and M.L. analysed the data. C.M., S.L. and M.L. wrote the manuscript, M.K. and O.D. edited it and all authors agreed on its final version.

Corresponding author

Correspondence to [Marc Lecuit](#).

Ethics declarations

Competing interests

The authors declare no competing interests.

Peer review

Peer review information

Nature thanks Keith Ireton, Junying Yuan and the other, anonymous, reviewer(s) for their contribution to the peer review of this work. Peer reviewer reports are available.

Additional information

Publisher's note Springer Nature remains neutral with regard to jurisdictional claims in published maps and institutional affiliations.

Extended data figures and tables

[Extended Data Fig. 1 Infected inflammatory monocytes transfer *Lm* to the brain.](#)

(a) Bacterial load in the spleen and liver 5 days after oral inoculation with CC4-*Lm*, in mice treated with gentamicin intraperitoneally every day from day 1 post-inoculation, related to Fig. [1b](#). **(b)** Bacterial load in organs after iv inoculation with CC4-*Lm*, immediately followed by intravenous injection of gentamicin, assessing the bactericidal effect of gentamicin on extracellular circulating *Lm*. **(c)** Bacterial load in the blood after oral inoculation with CC1/CC4/CC6-*Lm*, related to Fig. [1a](#). **(d)** Repartition of the 3 main infected cell subsets in the blood and spleen after iv inoculation with CC4-*Lm*. **(e)** Number of infected inflammatory monocytes in the spleen and liver of B6-WT mice 3 days after iv inoculation with CC4-*Lm*, showing that monocytes are infected in the spleen by an order of magnitude more than in the liver. **(f)** Number of inflammatory monocytes in the blood and spleen of B6-WT or *Ccr2*^{-/-} mice. **(g)** Number of bacteria in transferred infected monocytes, collected from spleen of mice 3 days after inoculation with CC4, related to Fig. [1f](#). **(h)** Schematic pipeline of the transfer

experiment in *LysM*-CreER^{T2} × iDTR mice. (i) Bacterial load in the spleen, liver and brain of gentamicin- and diphtheria toxin-treated recipient *LysM*-CreER^{T2+/-} × *Rosa26*-iDTR^{+/-} and littermate mice, 4 days after injection of infected monocytes collected from infected donor tamoxifen-treated *LysM*-CreER^{T2+/-} × *Rosa26*-iDTR^{+/-} or littermate mice. (j, k) Representative fluorescence microscopy images of brain sections with infected inflammatory monocytes adhering to endothelial cells after iv inoculation with 5×10^5 CFU CC1-*Lm*. Adhering infected cells are Ly6C⁺ (j) and Ly6G⁻ (k). (l) Number of infected monocytes adhering to brain blood vessels of mice inoculated with WT-CC4 or CC4Δ*inlB* with or without perfusion of vasculature. (m) Representative fluorescence microscopy image of a brain section with infected inflammatory monocytes adhering to endothelial cells after iv inoculation with 5×10^5 CFU CC1-*Lm*. Arrow: *Lm* polymerizing actin in a monocyte; arrowheads: infected monocytes. (n) Representative fluorescence microscopy image of splenocytes 5 days after iv inoculation with 10^4 CFU CC4-*Lm*, in which intracellular *Lm* are found polymerizing actin (top insets) or in LAMP-1 positive vacuole (right insets). (o, p) Proportion of *Lm* detected polymerizing actin in each infected monocyte (o), or overall fraction of *Lm* associated with actin or LAMP-1 vacuoles (p) in monocytes from the spleen or from the blood vasculature of mice after inoculation with CC4-*Lm*. Values in (o) are compared with a *t*-test and proportions in (p) compared with a χ^2 test. Data were obtained from two (a, l) or three (b–h, j–k, m–p) and four (i) independent experiments.

[Source data](#)

[Extended Data Fig. 2 The expression level of InlB is a major determinant of *Lm* neuroinvasiveness, whereas InlA is not involved.](#)

(a) Optical density at 600 nm of indicated bacterial strains measured over time after 1:100 dilution in BHI of an overnight culture. (b, c) Bacterial load after oral inoculation (b) or after iv inoculation (c) with a 1:1 mix of CC4-WT expressing tdTomato or GFP. (d) Bacterial load in brain after iv inoculation with a 1:1 mix of WT and Δ*inlA* isogenic strains, related to Fig. 2a. (e) Bacterial load in brain after iv inoculation with a 1:1 mix of WT and

$\Delta inlB$ isogenic strains, related to Fig. 2b. (f, g) Competition indexes (f) and bacterial load (g) in brain after iv inoculation with a 1:1 mix of CC4-WT and either CC4 $\Delta inlA$, CC4 $\Delta inlB$, CC4 $\Delta inlAB$ or CC4 $\Delta inlB$ complemented with *inlB* ($\Delta inlB + inlB$), related to Fig. 2a, b and panels d, e. (h) Bacterial load in brain after oral inoculation with a 1:1 mix of WT strain and $\Delta inlB$ isogenic strains, related to Fig. 2c. (i, j) Bacterial load in brain after iv inoculation with 5×10^3 CFU (i) or oral inoculation with 10^9 CFU (j) of either CC4-WT or CC4 $\Delta inlB$. (k, l) Bacterial load in brain across time after iv inoculation (k) and after oral inoculation (l) with a 1:1 mix of CC4-WT and CC4 $\Delta inlB$, related to Fig. 2f, g. (m) Transcription levels of *inlA* relative to EGDe in mid-log phase in BHI. For CC1/4/6, each dot corresponds to a different clinical isolate and triangles represent the strains used throughout the rest of the study and referred to as CC1, CC4 and CC6, related to panel (o). (n) Transcription levels of *inlA* relative to EGDe in infected splenocytes 2 days after iv inoculation with 2×10^5 CFU in mice, related to Fig. 2h. (o) Transcription levels of *inlB* relative to EGDe in mid-log phase in BHI. Each dot for CC1/4/6 corresponds to a different clinical isolate and triangles point out the strains used throughout the rest of the study and referred to as CC1, CC4 and CC6. (p) Representative Western blot (left) and quantification (right) of InlB expression, normalized to that of EF-Tu, relative to EGDe in mid-log phase in BHI. (q) Bacterial load in brain after inoculation with either WT-EGDe, EGDe $\Delta inlB$ and WT-CC4. (r) Transcription levels of *inlB*, relative to EGDe, in infected splenocytes 2 days after iv inoculation with 2×10^5 CFU of EGDe-WT, CC4-WT and strains complemented with either *inlB* from EGDe or from CC4. (s) Bacterial load in brain after inoculation with a 1:1 mix of the indicated bacterial strains, related to Fig. 2i. (t) Bacterial load in brain after inoculation with a 1:1 mix of EGDe $\Delta inlB$ and CC4 $\Delta inlB$, related to Fig. 2i. Data were obtained from three independent experiments.

[Source data](#)

[**Extended Data Fig. 3 InlB is not involved in *Lm* invasion of monocytes.**](#)

(a, b) Competition indexes (a) and bacterial load (b) in blood after iv inoculation with a 1:1 mix of CC4-WT and CC4 $\Delta inlB$. (c) Number of

infected monocytes in the spleen after inoculation with CC4-WT or CC4 Δ *inlB*. (d) Bacterial load from 10⁵ sorted monocytes (infected or not) retrieved from mice after inoculation with CC4-WT or CC4 Δ *inlB*. (e) Number of infected monocytes across time in the spleen after inoculation with either CC4-WT or CC4 Δ *inlB*. (f) Number of bacteria per infected monocyte collected from mice after inoculation with either CC4-WT or CC4 Δ *inlB*. (g) Number of infected monocytes in the spleen after inoculation with CC4-WT, CC4 Δ *inlB* or EGDe-WT. (h) Bacterial load in brain of B6-WT or *Ccr2*^{-/-} mice after inoculation with a 1:1 mix of CC4-WT and CC4 Δ *inlB*, related to Fig. 2i. (i, j) Bacterial load in blood (i) and brain (j) after iv inoculation with 5 \times 10⁵ CFU of either CC4-WT or CC4 Δ *inlB*. (k, l) Competition index (k) and bacterial load (l) in brain 1 day after intracranial inoculation with a 1:1 mix of CC4-WT and CC4 Δ *inlB*. (m-o) Number of infected monocytes (m), percentage of infected monocytes (n) and bacterial load (o) in monocytes 1 h after *in vitro* infection of primary bone marrow mouse monocytes with WT-Lm or Δ *inlB* isogenic mutants, at a MOI of 5. Data were obtained from two (k-l), three (a-j) and four (m-o) independent experiments.

Source data

Extended Data Fig. 4 Lm neuroinvasion depends on InlB only in the presence of functional CD8⁺ T cells.

(a) Number of infected monocytes in the blood and spleen of cyclosporin and gentamicin-treated mice after oral inoculation with EGDe. (b, c) Bacterial load in brain (b) and ratio of brain/blood bacterial load (c) in cyclosporin \pm gentamicin-treated mice after oral inoculation with EGDe. (d, e) Bacterial load in brain of cyclosporin-treated mice after oral (d) and iv (e) inoculation with a 1:1 mix of EGDe-WT and EGDe Δ *inlB*. (f, g) Bacterial load in brain (f) and in blood (g) of *Rag2*^{-/-} mice after inoculation with a 1:1 mix of CC4-WT and CC4 Δ *inlB*, related to Fig. 3f. (h) Competition indexes in brain of *Rag2*^{-/-} mice after inoculation with a 1:1 mix of WT strain and Δ *inlB* isogenic strains. (i, j) Bacterial load in brain (f) and in blood (g) after inoculation with a 1:1 mix of CC4-WT and CC4 Δ *inlB* in control B6 WT mice and in mice lacking functional T (CD3 ϵ ^{-/-}), B

lymphocytes ($\text{muMt}^{-/-}$) or both ($Rag2^{-/-}$), related to Fig. 3d. (k) Ratio of brain/blood bacterial loads in B6 WT, $Rag2^{-/-}$, $\text{CD3}\varepsilon^{-/-}$ and $\text{muMt}^{-/-}$ mice, related to Fig. 3d. (l) Bacterial load in brain of mice after inoculation with a 1:1 mix of CC4-WT and CC4 $\Delta inlB$ after CD8 $^{+}$ T cells depletion, related to Fig. 3e. (m) Representative dot plots (left) and proportion of CD8 $^{+}$ T cells (right) among CD45 $^{+}$ CD3 $^{+}$ cells in the spleen, after CD8 $^{+}$ T cells depletion, related to Fig. 3e. Data were obtained from two (m) or three independent experiments.

[Source data](#)

Extended Data Fig. 5 InlB does not alter the induction and differentiation of specific anti-Lm CD8 $^{+}$ T cells.

(a, b) Percentage (left) and number (right) of LLO-specific CD8 $^{+}$ T cells in mesenteric lymph nodes (MLN) (a) and spleen (b) of BALB/c mice after iv inoculation with CC4-WT strain or CC4 $\Delta inlB$. (c, d) Percentage (left) and number (right) of LLO-specific CD8 $^{+}$ T cells in MLN (c) and spleen (d) of iFABP-hEcad mice after oral inoculation with CC4-WT strain or CC4 $\Delta inlB$. (e–j) Percentage (left) and number (right) of Perforin $^{+}$ (e), CD69 $^{+}$ (f), Granzyme-B $^{+}$ (g), CD127 $^{+}$ (h), IFN γ $^{+}$ (i) and KLRG1 $^{+}$ (j) CD8 $^{+}$ T cells after iv inoculation with CC4-WT or CC4 $\Delta inlB$. (k) Bacterial load in spleen and liver after oral inoculation with CC4-WT in mice challenged 30 days before with 5×10^7 CFU of CC4-WT or CC4 $\Delta inlB$. (l) Schematic pipeline of the cytotoxic lymphocyte (CTL) assay. (m) Level of caspase-3 cleavage of infected spleen monocytes, collected after iv inoculation with CC4-WT or CC4 $\Delta inlB$, and incubated with CD8 $^{+}$ T cells from similarly infected (WT and $\Delta inlB$) or control (PBS) mice at the indicated effector to target ratio, related to Fig. 3i. Results are normalized to the level of caspase-3 cleavage in absence of CD8 $^{+}$ T cells. (n) Level of caspase-3 cleavage of uninfected spleen monocytes, collected after iv inoculation with CC4-WT or CC4 $\Delta inlB$, and incubated with CD8 $^{+}$ T cells from similarly infected (WT and $\Delta inlB$) or control (PBS) mice at an effector to target ratio of 5, related to Fig. 3i. Results are normalized to the level of caspase-3 cleavage in

absence of CD8⁺ T cells. Data were obtained from three independent experiments.

[Source data](#)

Extended Data Fig. 6 Membrane-associated InlB protects infected monocytes from CD8[±] T cell-mediated cell death and increases their lifespan, favouring their adhesion to blood brain vessels.

(a) Schematic representation of WT (full length) InlB and its anchored and released variants. **(b)** Competition indexes in the brain of mice after inoculation with a 1:1 mix of CC4-WT and CC4Δ*inlB* transformed with a plasmid expressing either full-length WT InlB, cell wall-anchored InlB or released InlB. **(c)** Representative fluorescence microscopy images of centrifugated CC4Δ*inlB* transformed with a plasmid expressing either full length InlB (left panel), anchored InlB (central panel) or released InlB (right panel). Scale bars: 5 μm. **(d)** Transcription level of *inlB* in CC4Δ*inlB* transformed with a plasmid expressing InlB variants in mid-log phase in BHI, relative to CC4Δ*inlB* expressing full length InlB. **(e)** Proportion of infected monocytes containing 1 to 7 bacteria. For monocytes containing more than 1 bacteria, number of GFP- or tdTomato-expressing bacteria in each monocyte is shown. Monocytes were collected 3 days after inoculation with a 1:1 mix of CC4-WT expressing GFP or tdTomato. **(f)** Level of caspase-3 cleavage of non-infected spleen monocytes, collected from mice infected for 3 days with CC4-WT or CC4Δ*inlB*, incubated *ex vivo* with FasL, related to Fig. 3m. **(g)** Percentage of infected spleen monocytes expressing Fas at their surface (left), and the mean fluorescence intensity (MFI) of Fas signal (right), after inoculation with CC4-WT or CC4Δ*inlB*. **(h, i)** Competition indexes (h) and bacterial load (i) in brain after inoculation with a 1:1 mix of CC4-WT and CC4Δ*inlB* and treatment with caspase-8 inhibitor. **(j)** Proportion of dye-positive transferred monocytes among infected monocytes in the blood and the spleen after inoculation of B6 WT mice (plain lines) or *Rag2*^{-/-} (dotted lines) with CC4-WT or CC4Δ*inlB*. Calculated half-lives of infected monocytes are shown in the table. **(k)** Number of infected monocytes adhering to brain vessels 2 days

after inoculation with 5×10^6 CFU of CC4-WT or CC4 Δ *inlB*, expressing tdTomato, of B6 WT mice immunized 2 days before with 10^3 CFU of CC4-WT expressing GFP. Each dot corresponds to the average number of monocytes counted on two slides (representative median sagittal sections, 40 μ m thickness) for one mouse. (I) Number of infected monocytes adhering to brain vessels 2 days after inoculation with 10^6 CFU of CC4-WT and CC4 Δ *inlB*, expressing tdTomato, of *Rag2*^{-/-} mice immunized 2 days before with 10^3 CFU of CC4-WT expressing GFP. Each dot corresponds to the average number of monocytes counted on two slides (representative median sagittal sections, 40 μ m thickness) for one mouse. Data were obtained from two (k, l) or three independent experiments.

Source data

Extended Data Fig. 7 InlB recruits c-Met in LAMP-1⁺ vacuoles in infected monocytes.

(a) Representative fluorescence microscopy images of spleen monocytes (not permeabilized) collected from tamoxifen-treated *LysM-CreER*^{T2} \times *Met*^{fl/fl} (*Met*^{LysMΔ/Δ}) and their littermates, showing specific surface expression of c-Met. (b) Percentage of *Lm* co-localizing with c-Met *in vitro* in Vero cells 15 min (left), 30 min (middle) and 45 min (right) after infection at MOI 50 with CC4 Δ *inlB* expressing either WT InlB, released InlB or cell wall-anchored InlB. (c, d) Representative fluorescence microscopy images of spleen monocytes collected after inoculation with CC4-WT, showing intra-vacuolar *Lm* surrounded with LAMP-1 (c) and co-localizing with both c-Met and LAMP-1 (d) related to Supplementary Video 4. (e) Representative fluorescence microscopy images of spleen monocytes collected after inoculation with CC4 Δ *inlB*, showing no colocalization with c-Met. (c–e) Maximum intensity projection over a z-stack. (f) Quantification of intracellular *Lm* co-localizing or not with c-Met and LAMP-1 in infected spleen monocytes collected after inoculation with CC4-WT or CC4 Δ *inlB*. Individual cells are plotted in top panel and samples are compared in bottom panel. (g) Representative fluorescence microscopy images of spleen monocytes collected after inoculation with CC4-WT, co-localizing with both c-Met and GAB1 related to Supplementary Video 5.

Maximum intensity projection over a *z*-stack. (h) Bacterial load in brain after inoculation with a 1:1 mix of CC4-WT and CC4 Δ *inlB* in mice treated with capmatinib, related to Fig. 4a. (i) Proportion of infected spleen monocytes positive for c-Met signal in flow cytometry after inoculation of *Met*^{LysM Δ/Δ} mice and their littermates with CC4-WT. Data were obtained from three independent experiments (a, h and i) or from three microscopic field of views (f).

[Source data](#)

Extended Data Fig. 8 InlB-mediated neuroinvasion involves the c-Met–PI3K α –FLIP pathway in infected monocytes.

(a) Representative fluorescence microscopy images of spleen monocytes collected after inoculation with CC4-WT or CC4 Δ *inlB*, showing cytosolic and nuclear phosphorylation of AKT, related to Supplementary Video 6. Images are maximum intensity projection over a *z*-stack. (b) Proportion of infected spleen monocytes positive for phospho-AKT signal in flow cytometry after inoculation with CC4-WT or CC4 Δ *inlB*. (c, d) Competition indexes (c) and bacterial load (d) in brain after inoculation with a 1:1 mix of CC4-WT and CC4 Δ *inlB* in mice treated with wortmannin. (e) Competition indexes in brain after inoculation with a 1:1 mix of CC4-WT and CC4 Δ *inlB* in mice treated with PI3K δ inhibitor (IC87114). (f) Bacterial load in the brain after inoculation with a 1:1 mix of CC4-WT and CC4 Δ *inlB* in mice treated with BYL-719 or IC87114, related to Fig. 4d and to panel e. (g) Proportion of infected spleen monocytes positive for FLIP signal in flow cytometry after inoculation with CC4-WT, CC4 Δ *inlB* or EGDe-WT. (h) Representative dot plot of FLIP expression in infected inflammatory spleen monocytes, after inoculation with CC4-WT or CC4 Δ *inlB*, related to Fig. 4e. (i) Proportion of infected spleen monocytes positive for FLIP signal in flow cytometry after inoculation with CC4-WT of *Met*^{LysM Δ/Δ} mice and their littermates after tamoxifen treatment. (j) Level of caspase-3 cleavage of infected spleen monocytes, collected 3 days after inoculation with CC4-WT or CC4 Δ *inlB* of tamoxifen-treated *Rosa26*-CreER^{T2} × *Cflar*^{+/+} (*Flip*^{Rosa^{+/+}}) littermate mice and incubated with CD8 $^+$ T cells from similarly infected mice at an effector to target ratio of 5, related to Fig. 4g. (k) Proportion of infected spleen monocytes positive for FLIP signal in flow cytometry, after

inoculation with CC4-WT of tamoxifen-treated *LysM*-CreER^{T2} × *Cflar*^{fl/fl} (*Flip*^{LysMΔ/Δ}) mice and their littermates (*Flip*^{LysM+/+}), and after tamoxifen treatment. (l) Bacterial load in tamoxifen-treated (*Flip*^{LysMΔ/Δ}), *LysM*-CreER^{T2} × *Cflar*^{fl/+} (*Flip*^{LysMΔ/+}) and their littermates, after inoculation with a 1:1 mix of CC4-WT and CC4Δ*inlB* and tamoxifen treatment, related to Fig. 4h. Of note, only female mice were used for *Flip*^{LysMΔ/+}, whereas both male and female mice were included for *Flip*^{LysMΔ/Δ} and their littermates. (m–o) Proportion of infected spleen monocytes positive for phospho-AKT signal (m), FLIP signal (n) and Zombie signal (o) in flow cytometry, after inoculation with CC4-WT or CC4Δ*inlB* and treatment with HGF. Data were obtained from two (m–o) or three independent experiments.

[Source data](#)

Extended Data Fig. 9 In the intestinal tract, *Lm* infects CX3CR1[±] macrophages of the lamina propria, in an InlB-dependent manner.

(a) Representation of InlB-activated pathway of infected monocytes survival to Fas-mediated cell death. (b–d) Bacterial load in luminal content of KIE16P (b) and B6 WT (d) or intestinal tissue of B6 WT (c) mice after oral (b) and iv (c, d) inoculation with a 1:1 mix of CC4-WT and CC4Δ*inlB*, related to Fig. 4j, k, Extended Data Fig. 10a, c, e, g. (e) Number of infected CD11b⁺ CX3CR1⁺ macrophages of the lamina propria of the small intestine of B6 WT mice in flow cytometry after inoculation with CC4-WT or CC4Δ*inlB*. (f, g) Representative fluorescence microscopy images of infected CX3CR1⁺ infected macrophages in the colon lamina propria of mice after inoculation with CC4-WT, related to Supplementary Videos 7, 8. Data were obtained from three independent experiments. SI = small intestine.

[Source data](#)

Extended Data Fig. 10 InlB-mediated *Lm* gut persistence involves resistance to CD8⁺ T cells and FLIP expression in myeloid cells.

(a) Competition indexes in intestinal tissue of B6 WT and *Rag2*^{-/-} mice after inoculation with a 1:1 mix of CC4-WT and CC4Δ*inlB*, related to Extended Data Figs. 9c, d and to panels b–d. **(b)** Bacterial load in intestinal tissue of *Rag2*^{-/-} mice after inoculation with a 1:1 mix of CC4-WT and CC4Δ*inlB*, related to a, c, d. **(c)** Competition indexes in luminal content of B6 WT and *Rag2*^{-/-} mice after inoculation with a 1:1 mix of CC4-WT and CC4Δ*inlB*, related to Extended Data Fig. 9c, d and to panels a, b, d. **(d)** Bacterial load in luminal content of *Rag2*^{-/-} mice after inoculation with a 1:1 mix of CC4-WT and CC4Δ*inlB*, related to panels a–c. **(e)** Competition indexes in intestinal tissue of mice after inoculation with a 1:1 mix of CC4-WT and CC4Δ*inlB* and treated with an anti-CD8⁺ T cells antibody, related to Extended Data Fig. 9d and to panels f–h. **(f)** Bacterial load in intestinal tissue of mice after inoculation with a 1:1 mix of CC4-WT and CC4Δ*inlB* and treated with an anti-CD8⁺ T cells antibody, related to e–h. **(g)** Competition indexes in luminal content of mice after inoculation with a 1:1 mix of CC4-WT and CC4Δ*inlB* and treated with an anti-CD8⁺ T cells antibody, related to Fig. 4j, Extended Data Fig. 9b and to panels e–h. **(h)** Bacterial load in luminal content of mice after inoculation with a 1:1 mix of CC4-WT and CC4Δ*inlB* and treated with an anti-CD8⁺ T cells antibody, related to e–g. **(i)** Competition indexes in intestinal tissue of *Flip*^{LysMΔ/Δ} mice and their littermates after inoculation with a 1:1 mix of CC4-WT and CC4Δ*inlB*, related to Fig. 4k and to panels j–m. **(j)** Bacterial load in intestinal tissue of littermates of *Flip*^{LysMΔ/Δ} mice after inoculation with a 1:1 mix of CC4-WT and CC4Δ*inlB*, related to Fig. 4k and to panels i, k–m. **(k)** Competition indexes in luminal content of *Flip*^{LysMΔ/Δ} mice and their littermates after inoculation with a 1:1 mix of CC4-WT and CC4Δ*inlB*, related to Fig. 4k and to panels i, j, l, m. **(l)** Bacterial load in luminal content of littermates of *Flip*^{LysMΔ/Δ} mice after inoculation with a 1:1 mix of CC4-WT and CC4Δ*inlB*, related to Fig. 4k and to panels i–k, m. **(m)** Bacterial load in luminal content of *Flip*^{LysMΔ/Δ} mice after inoculation with a 1:1 mix of CC4-WT and CC4Δ*inlB*, related to Fig. 4k and to panels i–l.

(n, o) Bacterial load in intestinal tissue (n) and luminal content (o) of mice after inoculation with either CC4-WT or CC4 Δ inlB and treated with caspase-8 inhibitor, related to Fig. 3k. Data were obtained from three independent experiments. SI = small intestine.

[Source data](#)

Supplementary information

[Supplementary Information](#)

This file contains Supplementary Figs 1–2 and Supplementary Tables 1-7.

[Reporting Summary](#)

[Peer Review File](#)

[41586_2022_4505_MOESM4_ESM.mp4](#)

Supplementary Video 1 Polymerization of actin comet tails by *Lm* within a monocyte adhering to the blood–brain barrier. CX3CR1^{GFP/+} KIE16P mice were infected iv with 5x10⁵ CFUs of CC6 for 48 hours. Labels: DNA in blue, CX3CR1 in green, *Lm* in red, actin in white. 46 optical sections of a 20 μ m thick brain sample were imaged with a Zeiss LSM700 confocal microscope. 3D reconstruction was performed using the Arivis Vison 4D software.

[41586_2022_4505_MOESM5_ESM.mp4](#)

Supplementary Video 2 Polymerization of actin comet tails by *Lm* within a monocyte adhering to the blood–brain barrier. KIE16P mice were infected iv 5x10⁵ CFUs of CC4 for 48 hours. Labels: DNA in blue, Ly6C in green, *Lm* in red, actin in white. Ly6C stains both endothelial cells and monocytes. 100 optical sections of a 20 μ m thick brain sample were imaged with a Zeiss LSM900 confocal microscope. 3D reconstruction was performed using the Arivis Vison 4D software.

41586 2022 4505 MOESM6 ESM.mp4

Supplementary Video 3 ***Lm* associated with LAMP-1 and *Lm* actin comet tails in infected spleen.** KIE16P mice were infected iv with 5×10^3 CFUs of CC4 for 5 days. Labels: DNA in blue, LAMP-1 in red, *Lm* in green, actin in white. 126 optical sections of a 22.5 μm thick spleen sample were imaged with a Zeiss LSM900 confocal microscope. 3D reconstruction was performed using the Arivis Vison 4D software.

41586 2022 4505 MOESM7 ESM.mp4

Supplementary Video 4 ***Lm* co-localization with c-Met and LAMP-1 in sorted spleen monocytes.** KIE16P mice were infected iv with 10^4 CFUs of CC4 for 4 days. CD45 $^+$ CD3 $^-$ CD19 $^-$ Ly6G $^-$ CD11C $^-$ Ly6C $^\text{hi}$ spleen monocytes were sorted. Labels: *Lm* in blue, LAMP-1 in green, c-Met in red and DNA in white. 25 optical sections of a 3.8 μm thick spleen sample were imaged with a Zeiss LSM900 confocal microscope. 3D reconstruction was performed using the Arivis Vison 4D software.

41586 2022 4505 MOESM8 ESM.mp4

Supplementary Video 5 ***Lm* co-localization with c-Met and GAB1 in sorted spleen monocytes.** KIE16P mice were infected iv with 10^4 CFUs of CC4 for 4 days. CD45 $^+$ CD3 $^-$ CD19 $^-$ Ly6G $^-$ CD11C $^-$ Ly6C $^\text{hi}$ spleen monocytes were sorted. Labels: *Lm* in blue, GAB1 in green, c-Met in red and DNA in white. 20 optical sections of a 3.6 μm thick spleen sample were imaged with a Zeiss LSM900 confocal microscope. 3D reconstruction was performed using the Arivis Vison 4D software.

41586 2022 4505 MOESM9 ESM.mp4

Supplementary Video 6 ***Lm* co-localization with c-Met and p-AKT in sorted spleen monocytes.** KIE16P mice were infected iv with 10^4 CFUs of CC4 for 4 days. CD45 $^+$ CD3 $^-$ CD19 $^-$ Ly6G $^-$ CD11C $^-$ Ly6C $^\text{hi}$ spleen monocytes were sorted. Labels: *Lm* in blue, p-AKT in green, c-Met in red and DNA in white. 37 optical sections of a 6.5 μm thick spleen sample were

imaged with a Zeiss LSM900 confocal microscope. 3D reconstruction was performed using the Arivis Vison 4D software.

41586_2022_4505_MOESM10_ESM.mp4

Supplementary Video 7 **Infection focus of *Lm* in the colon.** CX3CR1^{GFP/+} KIE16P mice were infected iv with 5×10^3 CFUs of CC4 for 5 days. Labels : DNA in blue, CX3CR1 in green, *Lm* in red, CD11b in white. 16 optical sections of a 5,43 μm thick colon sample were imaged with a Zeiss LSM710 confocal microscope. 3D reconstruction was performed using the Arivis Vison 4D software.

41586_2022_4505_MOESM11_ESM.mp4

Supplementary Video 8 ***Lm*- infected CX3CR1⁺ cells in the colon.** CX3CR1^{GFP/+} KIE16P mice were infected iv with 5×10^3 CFUs of CC4 for 5 days. Labels : DNA in blue, CX3CR1 in green, *Lm* in red, CD8 in white. 33 optical sections of a 11,10 μm thick colon sample were imaged with a Zeiss LSM900 confocal microscope. 3D reconstruction was performed using the Arivis Vison 4D software.

Source data

Source Data Fig. 1

Source Data Fig. 2

Source Data Fig. 3

Source Data Fig. 4

Source Data Extended Data Fig. 1

Source Data Extended Data Fig. 2

[**Source Data Extended Data Fig. 3**](#)

[**Source Data Extended Data Fig. 4**](#)

[**Source Data Extended Data Fig. 5**](#)

[**Source Data Extended Data Fig. 6**](#)

[**Source Data Extended Data Fig. 7**](#)

[**Source Data Extended Data Fig. 8**](#)

[**Source Data Extended Data Fig. 9**](#)

[**Source Data Extended Data Fig. 10**](#)

Rights and permissions

[Reprints and Permissions](#)

About this article

Cite this article

Maudet, C., Kheloufi, M., Levallois, S. *et al.* Bacterial inhibition of Fas-mediated killing promotes neuroinvasion and persistence. *Nature* **603**, 900–906 (2022). <https://doi.org/10.1038/s41586-022-04505-7>

- Received: 20 November 2020
- Accepted: 03 February 2022
- Published: 16 March 2022
- Issue Date: 31 March 2022

- DOI: <https://doi.org/10.1038/s41586-022-04505-7>

Share this article

Anyone you share the following link with will be able to read this content:

[Get shareable link](#)

Sorry, a shareable link is not currently available for this article.

[Copy to clipboard](#)

Provided by the Springer Nature SharedIt content-sharing initiative

Further reading

- [**Listeria hitches a ride**](#)

- Andrea Du Toit

Nature Reviews Microbiology (2022)

This article was downloaded by **calibre** from <https://www.nature.com/articles/s41586-022-04505-7>

| [Section menu](#) | [Main menu](#) |

- Article
- [Published: 16 March 2022](#)

Human gut bacteria produce T_H17-modulating bile acid metabolites

- [Donggi Paik](#) ORCID: orcid.org/0000-0003-1031-0371¹ nal,
- [Lina Yao](#) ORCID: orcid.org/0000-0003-1018-5646² nal,
- [Yancong Zhang](#) ORCID: orcid.org/0000-0002-2768-2975^{3,4},
- [Sena Bae](#)^{4,5},
- [Gabriel D. D'Agostino](#)²,
- [Minghao Zhang](#)⁶,
- [Eunha Kim](#) ORCID: orcid.org/0000-0001-7041-1727¹,
- [Eric A. Franzosa](#) ORCID: orcid.org/0000-0002-8798-7068^{4,5},
- [Julian Avila-Pacheco](#) ORCID: orcid.org/0000-0001-9388-3946³,
- [Jordan E. Bisanz](#) ORCID: orcid.org/0000-0002-8649-1706⁷,
- [Christopher K. Rakowski](#)⁸,
- [Hera Vlamakis](#) ORCID: orcid.org/0000-0003-1086-9191^{3,9},
- [Ramnik J. Xavier](#) ORCID: orcid.org/0000-0002-5630-5167^{3,9,10,11},
- [Peter J. Turnbaugh](#) ORCID: orcid.org/0000-0002-0888-2875^{7,12},
- [Randy S. Longman](#)¹³,
- [Michael R. Krout](#)⁸,
- [Clary B. Clish](#) ORCID: orcid.org/0000-0001-8259-9245³,
- [Fraydoon Rastinejad](#)⁶,
- [Curtis Huttenhower](#) ORCID: orcid.org/0000-0002-1110-0096^{3,4,5},
- [Jun R. Huh](#) ORCID: orcid.org/0000-0002-1540-6244^{1,14} &
- [A. Sloan Devlin](#) ORCID: orcid.org/0000-0001-5598-3751²

- 10k Accesses
- 192 Altmetric
- [Metrics details](#)

Subjects

- [Chemical biology](#)
- [Immunology](#)
- [Microbiology](#)

Abstract

The microbiota modulates gut immune homeostasis. Bacteria influence the development and function of host immune cells, including T helper cells expressing interleukin-17A (T_H17 cells). We previously reported that the bile acid metabolite 3-oxolithocholic acid (3-oxoLCA) inhibits T_H17 cell differentiation¹. Although it was suggested that gut-residing bacteria produce 3-oxoLCA, the identity of such bacteria was unknown, and it was unclear whether 3-oxoLCA and other immunomodulatory bile acids are associated with inflammatory pathologies in humans. Here we identify human gut bacteria and corresponding enzymes that convert the secondary bile acid lithocholic acid into 3-oxoLCA as well as the abundant gut metabolite isolithocholic acid (isoLCA). Similar to 3-oxoLCA, isoLCA suppressed T_H17 cell differentiation by inhibiting retinoic acid receptor-related orphan nuclear receptor- γ t, a key T_H17 -cell-promoting transcription factor. The levels of both 3-oxoLCA and isoLCA and the 3α -hydroxysteroid dehydrogenase genes that are required for their biosynthesis were significantly reduced in patients with inflammatory bowel disease. Moreover, the levels of these bile acids were inversely correlated with the expression of T_H17 -cell-associated genes. Overall, our data suggest that bacterially produced bile acids inhibit T_H17 cell function, an activity that may be relevant to the pathophysiology of inflammatory disorders such as inflammatory bowel disease.

This is a preview of subscription content

Access options

Subscribe to Nature+

Get immediate online access to the entire Nature family of 50+ journals

\$29.99

monthly

[Subscribe](#)

Subscribe to Journal

Get full journal access for 1 year

\$199.00

only \$3.90 per issue

[Subscribe](#)

All prices are NET prices.

VAT will be added later in the checkout.

Tax calculation will be finalised during checkout.

Buy article

Get time limited or full article access on ReadCube.

\$32.00

[Buy](#)

All prices are NET prices.

Additional access options:

- [Log in](#)
- [Learn about institutional subscriptions](#)

Fig. 1: Human gut bacteria produce 3-oxoLCA, a T_H17-cell-modulating BA metabolite.

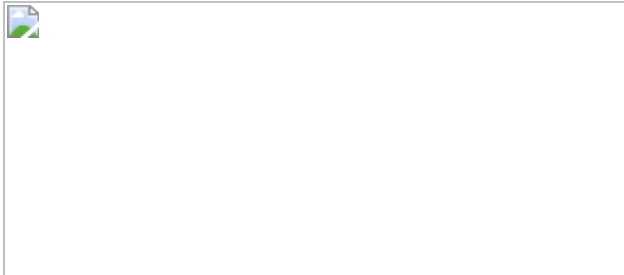


Fig. 2: The abundant gut bacterial metabolite isoLCA inhibits T_H17 cell differentiation.

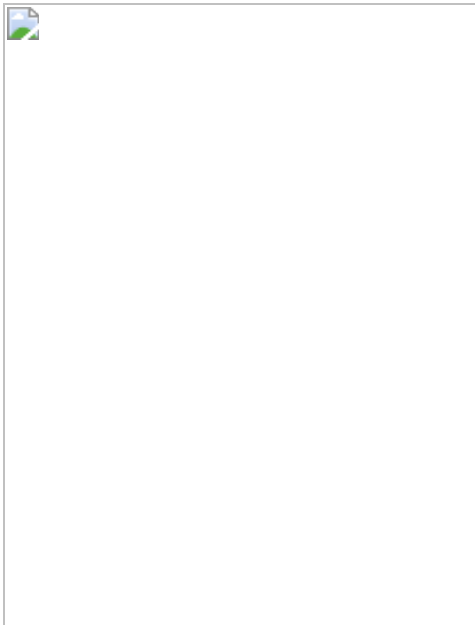


Fig. 3: Bacterial HSDHs convert LCA to 3-oxoLCA and isoLCA.

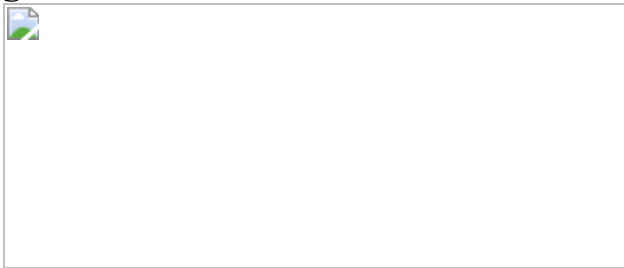
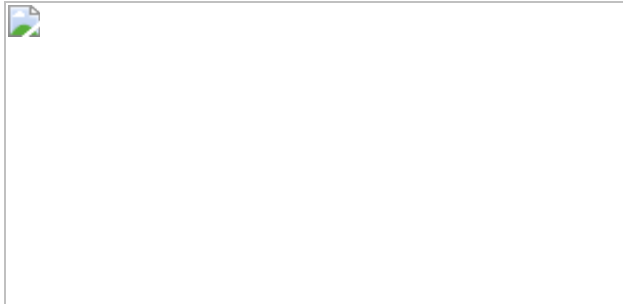


Fig. 4: 3-OxoLCA and isoLCA modulate the T_H17 cell response in vivo and are negatively correlated with CD in humans.



Data availability

The 16S amplicon and RNA-seq datasets are available through NCBI under BioProject ID [PRJNA675599](#) and GEO accession number [GSE179740](#), respectively. All mass spectra acquired for standards in this study were deposited at MoNA (<https://mona.fiehnlab.ucdavis.edu/>) under IDs MoNA031840 to MoNA031854 (Supplementary Table 12) and the <https://ibdmdb.org/> dataset and the metabolomics workbench study ST000923. [Source data](#) are provided with this paper.

Code availability

The software packages used in this study are free and open source. Source code for ElenMatchR is available at GitHub (<https://github.com/turnbaughlab/ElenMatchR>). MaAsLin2 is available online (<http://huttenhower.sph.harvard.edu/maaslin>) as source code and installable packages. The R package limma is available online (<https://www.bioconductor.org/packages/release/bioc/html/limma.html>). Analysis scripts using these packages are available from the authors on request.

References

1. Hang, S. et al. Bile acid metabolites control T_H17 and T_{reg} cell differentiation. *Nature* **576**, 143–148 (2019).

2. Fiorucci, S. & Distrutti, E. Bile acid-activated receptors, intestinal microbiota, and the treatment of metabolic disorders. *Trends Mol. Med.* **21**, 702–714 (2015).
3. Ridlon, J. M., Kang, D.-J. & Hylemon, P. B. Bile salt biotransformations by human intestinal bacteria. *J. Lipid Res.* **47**, 241–259 (2005).
4. Modica, S., Gadaleta, R. M. & Moschetta, A. Deciphering the nuclear bile acid receptor FXR paradigm. *Nucl. Recept. Signal.* **8**, e005 (2010).
5. Schaap, F. G., Trauner, M. & Jansen, P. L. M. Bile acid receptors as targets for drug development. *Nat. Rev. Gastroenterol.* **11**, 55–67 (2014).
6. Guo, C. et al. Bile acids control inflammation and metabolic disorder through inhibition of NLRP3 inflammasome. *Immunity* **45**, 944 (2016).
7. Ma, C. et al. Gut microbiome-mediated bile acid metabolism regulates liver cancer via NKT cells. *Science* **360**, eaan5931 (2018).
8. Cao, W. et al. The xenobiotic transporter Mdr1 enforces T cell homeostasis in the presence of intestinal bile acids. *Immunity* **47**, 1182–1196 (2017).
9. Duerr, R. H. et al. A genome-wide association study identifies *IL23R* as an inflammatory bowel disease gene. *Science* **314**, 1461–1463 (2006).
10. Nair, R. P. et al. Genome-wide scan reveals association of psoriasis with IL-23 and NF-κB pathways. *Nat. Genet.* **41**, 199–204 (2009).
11. Stahl, E. A. et al. Genome-wide association study meta-analysis identifies seven new rheumatoid arthritis risk loci. *Nat. Genet.* **42**, 508–514 (2010).
12. Sakaguchi, S. Naturally arising CD4⁺ regulatory T cells for immunologic self-tolerance and negative control of immune responses.

Annu. Rev. Immunol. **22**, 531–562 (2004).

13. Josefowicz, S. Z., Lu, L.-F. & Rudensky, A. Y. Regulatory T cells: mechanisms of differentiation and function. *Immunology* **30**, 531–564 (2012).
14. Campbell, C. et al. Bacterial metabolism of bile acids promotes generation of peripheral regulatory T cells. *Nature* **581**, 475–479 (2020).
15. Song, X. et al. Microbial bile acid metabolites modulate gut ROR γ^+ regulatory T cell homeostasis. *Nature* **577**, 410–415 (2020).
16. Ivanov, I. I. et al. The orphan nuclear receptor ROR γ t directs the differentiation program of proinflammatory IL-17 $^+$ T helper cells. *Cell* **126**, 1121–1133 (2006).
17. Yang, X. O. et al. T helper 17 lineage differentiation is programmed by orphan nuclear receptors ROR α and ROR γ . *Immunity* **28**, 29–39 (2008).
18. Hamilton, J. P. et al. Human cecal bile acids: concentration and spectrum. *Am. J. Physiol. Gastrointest. Liver Physiol.* **293**, G256–G263 (2007).
19. Hirano, S. & Masuda, N. Transformation of bile acids by *Eubacterium lentum*. *Appl. Environ. Microbiol.* **42**, 912–915 (1981).
20. Devlin, A. S. & Fischbach, M. A. A biosynthetic pathway for a prominent class of microbiota-derived bile acids. *Nat. Chem. Biol.* **11**, 685–690 (2015).
21. Ivanov, I. I. et al. Induction of intestinal T $_H$ 17 Cells by segmented filamentous bacteria. *Cell* **139**, 485–498 (2009).
22. Esplugues, E. et al. Control of T $_H$ 17 cells occurs in the small intestine. *Nature* **475**, 514–518 (2011).

23. Hong, P.-Y., Wu, J.-H. & Liu, W.-T. Relative abundance of *Bacteroides* spp. in stools and wastewaters as determined by hierarchical oligonucleotide primer extension. *Appl. Environ. Microbiol.* **74**, 2882–2893 (2008).
24. García-Bayona, L. & Comstock, L. E. Streamlined genetic manipulation of diverse *Bacteroides* and *Parabacteroides* isolates from the human gut microbiota. *mBio* **10**, e01762-19 (2019).
25. Sayin, S. I. et al. Gut microbiota regulates bile acid metabolism by reducing the levels of tauro-beta-muricholic acid, a naturally occurring FXR antagonist. *Cell Metab.* **17**, 225–235 (2013).
26. Franzosa, E. A. et al. Gut microbiome structure and metabolic activity in inflammatory bowel disease. *Nat. Microbiol.* **4**, 293–305 (2019).
27. Lloyd-Price, J. et al. Multi-omics of the gut microbial ecosystem in inflammatory bowel diseases. *Nature* **569**, 655–662 (2019).
28. Revu, S. et al. IL-23 and IL-1 β drive human T_H17 cell differentiation and metabolic reprogramming in absence of CD28 costimulation. *Cell Rep.* **22**, 2642–2653 (2018).
29. Lee, W. et al. Multi-omics reveal microbial determinants impacting responses to biologic therapies in inflammatory bowel disease. *Cell Host Microbe* **29**, 1294–1304 (2021).
30. Sato, Y. et al. Novel bile acid biosynthetic pathways are enriched in the microbiome of centenarians. *Nature* **599**, 458–464 (2021).
31. Bouladoux, N., Harrison, O. J. & Belkaid, Y. The mouse model of infection with *Citrobacter rodentium*. *Curr. Protoc. Immunol.* **119**, 19.15.1–19.15.25 (2017).
32. Huh, J. R. & Littman, D. R. Small molecule inhibitors of ROR γ t: targeting T_H17 cells and other applications. *Eur. J. Immunol.* **42**, 2232–2237 (2012).

33. Patro, R., Duggal, G., Love, M. I., Irizarry, R. A. & Kingsford, C. Salmon provides fast and bias-aware quantification of transcript expression. *Nat. Methods* **14**, 417–419 (2017).
34. Love, M. I., Huber, W. & Anders, S. Moderated estimation of fold change and dispersion for RNA-seq data with DESeq2. *Genome Biol.* **15**, 550 (2014).
35. Mi, H., Muruganujan, A. & Thomas, P. PANTHER in 2013: modeling the evolution of gene function, and other gene attributes, in the context of phylogenetic trees. *Nucleic Acids Res.* **41**, D377–D386 (2013).
36. Browne, H. P. et al. Culturing of “unculturable” human microbiota reveals novel taxa and extensive sporulation. *Nature* **533**, 543–546 (2016).
37. Hall, A. B. et al. A novel *Ruminococcus gnavus* clade enriched in inflammatory bowel disease patients. *Genome Med.* **9**, 103 (2017).
38. Yao, L. et al. A selective gut bacterial bile salt hydrolase alters host metabolism. *eLife* **7**, e37182 (2018).
39. Swann, J. R. et al. Systemic gut microbial modulation of bile acid metabolism in host tissue compartments. *Proc. Natl Acad. Sci. USA* **108**, 4523–4530 (2011).
40. Chen, I.-M. A. et al. IMG/M v.5.0: an integrated data management and comparative analysis system for microbial genomes and microbiomes. *Nucleic Acids Res.* **47**, D666–D677 (2019).
41. Mukherjee, S. et al. Genomes OnLine database (GOLD) v.7: updates and new features. *Nucleic Acids Res.* **47**, D649–D659 (2019).
42. Drozdetskiy, A., Cole, C., Procter, J. & Barton, G. J. JPred4: a protein secondary structure prediction server. *Nucleic Acids Res.* **43**, W389–W394 (2015).

43. Bisanz, J. E. et al. A genomic toolkit for the mechanistic dissection of intractable human gut bacteria. *Cell Host Microbe* **27**, 1001–1013 (2020).
44. Segata, N., Börnigen, D., Morgan, X. C. & Huttenhower, C. PhyloPhlAn is a new method for improved phylogenetic and taxonomic placement of microbes. *Nat. Commun.* **4**, 2304 (2013).
45. Yu, G., Lam, T. T.-Y., Zhu, H. & Guan, Y. Two methods for mapping and visualizing associated data on phylogeny using Ggtree. *Mol. Biol. Evol.* **35**, 3041–3043 (2018).
46. Truong, D. T. et al. MetaPhlAn2 for enhanced metagenomic taxonomic profiling. *Nat. Methods* **12**, 902–903 (2015).
47. Suzek, B. E., Huang, H., McGarvey, P., Mazumder, R. & Wu, C. H. UniRef: comprehensive and non-redundant UniProt reference clusters. *Bioinformatics* **23**, 1282–1288 (2007).
48. Franzosa, E. A. et al. Species-level functional profiling of metagenomes and metatranscriptomes. *Nat. Methods* **15**, 962–968 (2018).
49. Suzek, B. E. et al. UniRef clusters: a comprehensive and scalable alternative for improving sequence similarity searches. *Bioinformatics* **31**, 926–932 (2015).
50. Mallick, H. et al. Multivariable association discovery in population-scale meta-omics studies. *PLoS Comput. Biol.* **17**, e1009442 (2021).
51. Law, C. W., Chen, Y., Shi, W. & Smyth, G. K. voom: precision weights unlock linear model analysis tools for RNA-seq read counts. *Genome Biol.* **15**, R29 (2014).
52. Smyth, G. K. in *Bioinformatics and Computational Biology Solutions using R and Bioconductor* (eds Gentleman, R. et al.) 397–420 (Springer, 2015).

53. Barman, M. et al. Enteric salmonellosis disrupts the microbial ecology of the murine gastrointestinal tract. *Infect. Immun.* **76**, 907–915 (2008).
54. Sagaidak, S., Taibi, A., Wen, B. & Comelli, E. M. Development of a real-time PCR assay for quantification of *Citrobacter rodentium*. *J. Microbiol. Methods* **126**, 76–77 (2016).

Acknowledgements

We thank the members of the Devlin, Huh and Clardy laboratories (Harvard Medical School (HMS)) for discussions; the staff at the HMS ICCB-Longwood Screening Facility, BPF Genomics Core Facility at Harvard Medical School for their expertise and instrument support; N. Lee, J. Vasquez, C. Powell, B. Russell and M. Henke for technical support and advice; M. Trombly and S. Blacklow for reading the manuscript; L. E. Comstock for the pLGB30 plasmid (Addgene plasmid 126620); and L. García-Bayona for her technical support. We are grateful to the human patients who participated in the human stool screen, PRISM and HMP2 studies. We acknowledge NIH grant P30DK034854 and the use of the Harvard Digestive Disease Center's core services, resources, technology and expertise. This work was supported by National Institutes of Health grants R01 DK110559 (to J.R.H. and A.S.D.), R01AR074500 (P.J.T.), U54DE023798 (C.H.), R24DK110499 (C.H.), T32GM095450 and MIRA R35 GM128618 (A.S.D.), a Harvard Medical School Dean's Innovation Grant in the Basic and Social Sciences (A.S.D. and J.R.H.), a John and Virginia Kaneb Fellowship (A.S.D.), a Harvard Medical School Christopher Walsh Fellowship (L.Y.) and a Wellington Postdoctoral Fellowship (L.Y.). J.E.B. was the recipient of a Natural Sciences and Engineering Research Council of Canada Postdoctoral Fellowship and is supported by the National Institute of Allergy and Infectious Diseases (K99AI147165). P.J.T. is a Chan Zuckerberg Biohub investigator. The computations in this paper were run in part on the FASRC Cannon cluster supported by the FAS Division of Science Research Computing Group at Harvard University. The images in Figs. [2c](#), [4a](#), [d](#), Extended Data Figs. [1b](#), [c](#), [3i](#), [1](#) were created using BioRender.

Author information

Author notes

1. These authors contributed equally: Donggi Paik, Lina Yao

Affiliations

1. Department of Immunology, Blavatnik Institute, Harvard Medical School, Boston, MA, USA

Donggi Paik, Eunha Kim & Jun R. Huh

2. Department of Biological Chemistry and Molecular Pharmacology, Blavatnik Institute, Harvard Medical School, Boston, MA, USA

Lina Yao, Gabriel D. D'Agostino & A. Sloan Devlin

3. Broad Institute of MIT and Harvard, Cambridge, MA, USA

Yancong Zhang, Julian Avila-Pacheco, Hera Vlamakis, Ramnik J. Xavier, Clary B. Clish & Curtis Huttenhower

4. Department of Biostatistics, Harvard T. H. Chan School of Public Health, Boston, MA, USA

Yancong Zhang, Sena Bae, Eric A. Franzosa & Curtis Huttenhower

5. Department of Immunology and Infectious Diseases, Harvard T. H. Chan School of Public Health, Boston, MA, USA

Sena Bae, Eric A. Franzosa & Curtis Huttenhower

6. Target Discovery Institute, Nuffield Department of Medicine, University of Oxford, Oxford, UK

Minghao Zhang & Fraydoon Rastinejad

7. Department of Microbiology and Immunology, University of California San Francisco, San Francisco, CA, USA

Jordan E. Bisanz & Peter J. Turnbaugh

8. Department of Chemistry, Bucknell University, Lewisburg, PA, USA

Christopher K. Rakowski & Michael R. Krout

9. Center for Microbiome Informatics and Therapeutics, MIT, Cambridge, MA, USA

Hera Vlamakis & Ramnik J. Xavier

10. Center for Computational and Integrative Biology, Massachusetts General Hospital and Harvard Medical School, Boston, MA, USA

Ramnik J. Xavier

11. Department of Molecular Biology, Massachusetts General Hospital and Harvard Medical School, Boston, MA, USA

Ramnik J. Xavier

12. Chan Zuckerberg Biohub, San Francisco, CA, USA

Peter J. Turnbaugh

13. Jill Roberts Center for IBD, Weill Cornell Medicine, New York, NY, USA

Randy S. Longman

14. Evergrande Center for Immunologic Diseases, Harvard Medical School and Brigham and Women's Hospital, Boston, MA, USA

Jun R. Huh

Contributions

J.R.H. and A.S.D. conceptualized the study. D.P., L.Y., J.R.H. and A.S.D. conceived the project and designed the experiments. D.P. performed mouse experiments, in vitro T cell and reporter assays. L.Y. performed human isolate screening, bacterial in vitro culture experiments and BA profiling. G.D.D. performed HSDH enzyme characterization. Y.Z. and S.B. performed the bioinformatics analyses. E.A.F. and C.H. supervised the computational analyses. J.A.-P. and C.B.C.. performed LCA derivative identification in PRISM and HMP2 metabolomics. E.K. performed T cell RNA-seq analysis. M.Z. and F.R. performed in vitro protein-binding assays. J.E.B. performed comparative genomics on *E. lenta*. C.K.R. and M.R.K. synthesized some of the BA derivatives. J.E.B. and P.J.T. supervised the *E. lenta* human isolate studies. H.V. and R.J.X. provided bacterial strains and technical support. R.L. provided the patient stool samples. D.P., L.Y., Y.Z., S.B., G.D.D., E.A.F., J.R.H. and A.S.D. wrote the manuscript, with contributions from all of the authors.

Corresponding authors

Correspondence to [Jun R. Huh](#) or [A. Sloan Devlin](#).

Ethics declarations

Competing interests

A.S.D. is a consultant for Takeda Pharmaceuticals and Axial Therapeutics. J.R.H. is a consultant for CJ Research Center and Interon Laboratories and on the scientific advisory board for ChunLab. P.J.T. is on the scientific advisory board for Kaleido, Pendulum, Seres and SNIPRbiome. C.H. is on the scientific advisory boards of Seres Therapeutics, Empress Therapeutics, and ZOE Nutrition.

Peer review

Peer review information

Nature thanks Pieter Dorrestein and the other, anonymous, reviewer(s) for their contribution to the peer review of this work.

Additional information

Publisher's note Springer Nature remains neutral with regard to jurisdictional claims in published maps and institutional affiliations.

Extended data figures and tables

[Extended Data Fig. 1 3-oxoLCA biosynthetic pathway and microbial diversity from the human screen.](#)

a, Quantification of 3-oxoLCA and isoLCA in stool samples from patients after faecal microbiota transplant (FMT) ($n = 15$). Stool samples from patient p#3 (3-oxoLCA: 44 picomol/mg, isoLCA: 136 picomol/mg) and patient p#27 (3-oxoLCA: 83 picomol/mg, isoLCA: 213 picomol/mg) were used to screen for 3-oxoLCA producers. **b**, Schematic of the screen for bacterial producers of the LCA metabolite 3-oxoLCA from human stool samples. In total, 990 bacterial colonies were isolated, restreaked, and archived from two human stool samples. ① Replicate plates (assay plates) were then used for the screen. ② Individual isolates were incubated anaerobically with LCA (100 μ M) (see Fig. 1b) or 3-oxoLCA (100 μ M) (see Fig. 2b) for 48 h. Cultures were harvested, acidified, extracted, and BA metabolites were quantified by UPLC-MS. ③ Positive hits containing 3-oxoLCA were re-selected from the archived stock plates, and recovered on new plates. ④ Activity was verified and each producer species was identified by full-length 16S rRNA sequencing. Finally, bacterial enzymes responsible for the LCA metabolite production were identified (see Fig. 3), and ⑤ corresponding genes were utilized as query sequences in BLASTP searches for novel putative bacterial producers and enzymes. **c**, Sample preparation workflow for the determination of cultured bacteria from the human stool sample screen. For each patient, individual isolates were recovered and cultured for 48 h. These isolates were then pooled together, and genomic DNA was extracted from the pooled pellet. Illumina® MiSeq sequencing on the V3 and V4 hypervariable regions of 16S rRNA was then

performed. **d**, Genus and phylum-level microbial community composition for each human stool sample. **e**, 3-oxoLCA and/or isoLCA production was verified in the type strains of a subset of 3-oxoLCA-producing human isolates ($n = 3$ biological replicates per group, data are mean \pm SEM).

[Source data](#)

Extended Data Fig. 2 Supernatants from LCA metabolite-producing bacteria do not affect T_{reg} cell differentiation in vitro.

a, b, Representative FACS plots (**a**) and population frequencies (**b**) of CD4+ T cells, cultured under T_{reg} polarization conditions in vitro are presented. Bacterial culture supernatants were added 18 h after TCR activation ($n = 3$ biologically independent samples per group. Data are mean \pm SEM, one-way ANOVA followed by Tukey's multiple comparison test). **c**, A pure standard of isoLCA was spiked into a subset of bacterial culture extracts containing the new peak (#). Co-elution and an identical m/z match confirmed that the new compound (#) in Fig. **1b** was isoLCA. Total ion chromatograms are shown. **d**, isoLCA production from 3-oxoLCA (100 μ M) was verified in the type strains of a subset of isoLCA-producing human isolates ($n = 3$ biological replicates per group, data are mean \pm SEM).

[Source data](#)

Extended Data Fig. 3 IsoLCA neither affects T cell viability nor inhibits T_{reg} and T_{H1} cell differentiation in vitro.

a-c, IsoLCA does not reduce T cell viability or proliferation. Percentages of T_{H17} cells (**a**), viable cells (**b**) and total cell numbers (**c**) at the end of T cell culture under T_{H17} polarization conditions in the presence of LCA, 3-oxoLCA, or isoLCA at 40, 20, 10, 5, 2.5, 1.25 and 0.625 μ M ($n = 3$ biologically independent samples, data are mean \pm SEM, one-way ANOVA with Dunnett's multiple comparisons). **d-g**, IsoLCA does not affect T_{reg} or

T_{H1} cell differentiation in vitro. Flow cytometry and quantification of intracellular staining for FoxP3 (**d**, **e**) or IFN- γ (**f**, **g**). Mouse naive CD4 T cells from wild-type C57BL/6J mice were cultured under T_{H1} - or T_{reg} - polarizing conditions and DMSO or isoLCA was added 18 h after TCR activation ($n = 3$ biologically independent samples per condition, data are mean \pm SEM, two-tailed unpaired t-test). **h**, SFB colonization measured by qPCR analysis in Fig. 2c–f, calculated as SFB 16s rRNA copy number ($n = 8$ mice per group, pooled from two experiments, data are mean \pm SEM, two-tailed unpaired t-test). **i–k**, Experimental scheme of Th17 induction by SFB (**i**), representative FACS plots (**j**) and population frequencies of T_{H17} cells (**k**), isolated from the ileal lamina propria of control or isoLCA-treated mice ($n = 8$ mice for control, $n = 6$ mice for isoLCA-treated groups, pooled from two experiments). B6 Tac mice were fed a control or an isoLCA (0.3% w/w)-containing diet for 7 days (data are mean \pm SEM, two-tailed unpaired t-test). **l–o**, Experimental scheme of anti-CD3 experiment (**l**), representative FACS plots (**m**) and population frequencies of T_{H17} (**n**) and T_{reg} cells (**o**) of the ileal lamina propria of control or isoLCA-treated mice ($n = 15$ mice for control, 13 mice for isoLCA-treated groups, pooled from three experiments). B6 Tac mice were intraperitoneally injected with anti-CD3 and fed a control diet or an isoLCA-containing (0.3% w/w) diet during the experiments (data are mean \pm SEM, two-tailed unpaired t-test). **p**, ROR γ t luciferase reporter assay in HEK293 cells, treated with a synthetic ROR γ inhibitor ML209 (1 μ M), isoLCA (20 μ M, 10 μ M, 5 μ M), isoDCA (20 μ M, 10 μ M, 5 μ M) or DMSO. The fold ratio of firefly luciferase (FLuc) to Renilla luciferase (RLuc) activity is presented on the y-axis. DMSO-treated group set to 1 ($n = 7$ independent transfections per group, pooled from two experiments. Data are mean \pm SEM, one-way ANOVA with Dunnett's multiple comparison test, vehicle set as control). **q, r**, Differential scanning fluorimetry (DSF) analyses indicated robust binding of isoLCA (**q**), but not of isoDCA (**r**) to the ROR γ t ligand-binding domain (LBD). **s–v**, Surface plasmon resonance (SPR) indicated robust binding of isoLCA to the ROR γ t LBD. Sensorgrams for affinity (**s**) and kinetics (**t**) of isoLCA and affinity (**u**) and kinetics (**v**) of isoDCA with the ROR γ t LBD. **w**, Transcriptional profiling of wild-type (WT) T cells and ROR γ deficient (KO) T cells, cultured under T_{H17} cell polarization conditions. DMSO or BAs were added to cells 18 h after TCR activation. Cells were then

harvested, and RNA-sequencing was performed. Heat map represents 46 genes that are regulated by either 3-oxoLCA or isoLCA as well as ROR γ (n = 3 mice per condition, the Wald test with Benjamini-Hochberg correction was used to determine FDR-adjusted p value < 0.05, genes that were differentially expressed by both isoLCA and 3-oxoLCA are shown in magenta). **x**, Gene ontology enrichment analysis was performed on the 46 genes that were differentially regulated by either 3-oxoLCA or isoLCA and ROR γ t revealed that these BA treatments resulted in changes in the expression of genes involved in several biological processes, including IL-17-mediated signalling and cytokine production pathways.

Source data

Extended Data Fig. 4 Screen of the candidate HSDH enzymes from gut bacteria.

a–c, Results of lysis assay in which the *E. lenta* DSM2243 (Elen), *R. gnavus* ATCC29149 (Rumgna), and *B. fragilis* NCTC9343 (BF) candidate HSDH enzymes were expressed in *E. coli* BL21 pLysS and their ability to convert LCA to 3-oxoLCA (**a**, 3 α -HSDH activity), 3-oxoLCA to isoLCA (**b**, and **c**, left, 3 β -HSDH activity), and 3-oxoLCA back to LCA (**d**, right, reverse 3 α -HSDH activity) was analyzed by UPLC-MS. Data are reported as percent conversion to product (n = 3 biological replicates per group, data are mean \pm SEM). **d–g**, SDS-PAGE analysis of candidate gene expression from *E. lenta* DSM 2243 and *R. gnavus* ATCC 29149 (Elen_0358, Elen_690, Elen_1325, Elen_2515, Rumgna_00694, and Rumgna_02133) (n = 3 replicates) (**d**). Western blot of the expression of Elen_0198, Elen_0359, Elen_0360, and Rumgna_02133. Anti-His tag labeling (left). Amido black total protein stain of membrane (right) (n = 2 replicates) (**e**). Western blot of the expression of BF0083, BF0143, BF1060, BF1669, BF2144, and BF3320. Anti-His tag labeling (left). Amido black total protein stain of membrane (right) (n = 2 replicates) (**f**). Western blot of the expression of Bf3538 and Bf3932. Anti-His tag labeling (left). Amido black total protein stain of membrane (right) (n = 2 replicates) (**g**). For source gel data for **d–g**, see Fig. S1. **h**, DNA gel for the *B. fragilis* genetic knockout mutants' diagnostic PCR. IntF-UHF-BF3538/ Int-R-DHF-BF3538 PCR primers: lane 1–3 are *B. fragilis* Δ 3538 mutant colonies #1–#3; lane 4, 5, 7

are *B. fragilis* Δ3932 mutant colonies #1-#3; lanes 6 and 8 are *B. fragilis* WT; lane 9 is a non-template control. IntF-UHF-BF3932/ Int-R-DHF-BF3932 PCR primers: lane 11-13 are *B. fragilis* Δ3538 mutant colonies #1-#3; lane 14, 15, 17 are *B. fragilis* Δ3932 mutant colonies #1-#3; lanes 16 and 18 are *B. fragilis* WT; lane 19 is a non-template control. UNIV-16s-F/UNIV-16s-R PCR primers: lane 21-23 are *B. fragilis* Δ3538 mutant colonies #1-#3; lane 24, 25, 27 are *B. fragilis* Δ3932 mutant colonies #1-#3; lanes 26 and 28 are *B. fragilis* WT; lane 29 is a non-template control. Lane 10, 20, 30 are the 1kb DNA ladder ($n = 2$ replicates). For source gel data, see Fig. S1. **i, j**, *R. gnavus* isolates in red (*R. gnavus* RDX1118, *R. gnavus* RDX1119, *R. gnavus* RDX1124, *R. gnavus* RDX1125, *R. gnavus* RDX1126, *R. gnavus* RDX1128) that lack a homologue of Rumgna_02133 (Table S5) did not synthesize 3-oxoLCA or isoLCA from LCA (**i**). *R. gnavus* isolates in red that lack a homologue of Rumgna_02133 (Table S5) only produced isoLCA from 3-oxoLCA (**j**). All strains were incubated with 100 μM LCA as a substrate for 48 h ($n = 3$ biological replicates per group). **k, l**, The 3α-HSDH gene of *E. lenta* is required to suppress T_H17 cell differentiation in vitro. Representative FACS plots (**l**) and population frequencies of T_H17 cells (**k**) are presented. Naive CD4+ T cells from wild-type C57BL/6J mice were cultured under T_H17 cell polarizing conditions for 3 days. Culture supernatants of *E. lenta* DSM2243 or *E. lenta* DSM15644, an isolate lacking a 3α-HSDH, were added 18 h after TCR activation ($n = 3$ biologically independent samples per group, data are mean ± SEM, one-way ANOVA followed by Tukey's multiple comparison test. $p = 0.000081$ between column 4 and 6(**l**)). **m**, Production of 3-oxoLCA and isoLCA by “high” and “low” producer co-cultures. Production of 3-oxoLCA and isoLCA from LCA (100 μM) by co-cultures of human gut bacteria type strains in vitro are shown (high producer group: *E. lenta* DSM2243 + *B. fragilis* NCTC9343; low producer group: *E. lenta* DSM15644 + *B. fragilis* NCTC9343 ΔBF3538 and *C. citroniae* human isolate P2-B6 + *B. fragilis* NCTC9343 ΔBF3538; $n = 3$ biological replicates per co-culture, data are mean ± SEM).

[Source data](#)

Extended Data Fig. 5 Human gut bacteria affect T cell levels in gnotobiotic mice.

a, Representative FACS plots for IL-17A or IFN γ - producing CD4 T cells in the colonic lamina propria of GF mice (left) or in *C. rodentium* infected mice 5 days after infection (right). **b**, IsoLCA reduced IFN γ + T_H17 cell level but did not affect T_H1 and T_{reg} cell levels in GF mice following *C. rodentium* infection (n = 8 for control and isoLCA groups, data are mean ± SEM pooled from two experiments followed by two-tailed unpaired t test). **c**, IsoLCA inhibited T_H17 and IFN γ + T_H17 cell levels in a dose-dependent manner but not T_H1 and T_{reg} cell levels in GF mice treated with 0.08% or 0.4% (w/w) isoLCA-containing diet (linear regression, n = 12 mice pooled from two experiments; T_H17, R-squared = 0.4877, p = 0.0115; IFN γ + T_H17, R-squared = 0.5083, p = 0.0093; T_H1, R-squared = 0.0848, p = 0.3715; T_{reg}, R-squared = 0.006924, p = 0.7971). **d**, LCA did not affect IFN γ + T_H17 level while T_H1 and T_{reg} cell levels were negatively impacted in GF mice following *C. rodentium* infection. Mice were sorted into quartile groups based on LCA levels in caecal contents (see [Methods](#) for details, n = 5 mice for Q1, n = 6 for Q2, n = 6 for Q3 and n = 5 for Q4, data are mean ± SEM pooled from three experiments, one-way ANOVA followed by Tukey's multiple comparison test). **e**, LCA treatment did not affect T_H17 and IFN γ + T_H17 cell levels but negatively impacted T_H1 and T_{reg} cell levels in GF mice treated with 0.012%, 0.06%, 0.25% or 0.3% (w/w) LCA-containing diets (linear regression, n = 22 mice; T_H17, R-squared = 0.01291, p = 0.6141; IFN γ + T_H17, R-squared = 0.1783, p = 0.0503; T_H1, R-squared = 0.3818, p = 0.0022; T_{reg}, R-squared = 0.3989, p = 0.0016). **f**, 3-oxoLCA and isoLCA levels in mice colonized with the high producer bacterial group were significantly higher than those colonized with the low producer groups (linear regression, R-squared = 0.1434, p = 0.0564, n = 26 mice for low producers; R-squared = 0.4727, p = 0.0011, n = 19 for high producers; p = 0.0033 for the difference between two lines). **g**, GF mice colonized with bacterial producers of 3-oxoLCA and isoLCA affected IFN γ + T_H17 but not T_H1 or T_{reg} cell levels. Mice were sorted into quartile groups based on 3-oxoLCA+isoLCA levels in caecal contents (see [Methods](#) for details, n = 11

mice for Q1, n = 12 for Q2, n = 11 for Q3 and n = 11 for Q4, data are mean \pm SEM pooled from six experiments, one-way ANOVA followed by Tukey's multiple comparison test). **h**, GF mice colonized with low and high bacterial producers of 3-oxoLCA and isoLCA affected T_{H17} and $IFN\gamma^+$ T_{H17} but not T_{H1} or T_{reg} cell levels (linear regression, n = 26 for low producers, n = 19 mice for high producers; T_{H17} , R-squared = 0.02255, p = 0.4640 for low producers, R-squared = 0.3699, p = 0.0057 for high producers, p = 0.3007 for the interaction term (slope*bacterial groups); $IFN\gamma^+ T_{H17}$, R-squared = 0.03817, p = 0.3389 for low producers, R-squared = 0.3079, p = 0.0137 for high producers, p = 0.7402 for the interaction term (slope*bacterial groups); T_{H1} , R-squared = 0.1533, p = 0.0647 for low producers, R-squared = 0.006748, p = 0.2430 for high producers, p = 0.3013 for the interaction term (slope*bacterial groups); T_{reg} , R-squared = 0.0539, p = 0.2538 for low producers; R-squared = 0.1575, p = 0.0925 for high producers, p = 0.9930 for the interaction term (slope*bacterial groups)). **i**, T_{H17} cell percentages do not affect C. *rodentium*-encoded *espB* levels. *Citrobacter* colonization was measured by qPCR analyses detecting *espB* and plotted against T_{H17} cell percentages in mice used for bacterial colonization experiments shown in Fig. 4g, Extended Data Fig. 5g, h were determined by qPCR and plotted against percentage of Th17 cells in individual mice. n = 31, R squared = 0.02928 for goodness of fit, F = 0.9352, p = 0.3414 for slope by simple linear regression. Dotted lines are 95% confidence bands of the best fit line.

[Source data](#)

[Extended Data Fig. 6 Levels of BA metabolites detected in the PRISM cohort.](#)

Abundances of identifiable BAs in PRISM cohort. BA levels were not universally decreased in CD patients, indicating that decreased levels of LCA, 3-oxoLCA, and isoLCA were not due to lower levels of all BAs in these cohorts. Boxplots show median and lower/upper quartiles with outliers outside of boxplot 'whiskers' (indicating the inner fences of the data). n = 34 for CD, n = 52 for UC and n = 34 for non-IBD. The percentage

of zeros in each condition are added as x-axis tick labels. See Table S6 for full results.

[Source data](#)

Extended Data Fig. 7 Levels of BA metabolites detected in the HMP2 cohort.

Abundances of identifiable BAs in HMP2 cohort. BA levels were not universally decreased in dysbiotic CD patients, indicating that decreased levels of LCA, 3-oxoLCA, and isoLCA were not due to lower levels of all BAs in these cohorts. Boxplots show median and lower/upper quartiles with outliers outside of boxplot ‘whiskers’ (indicating the inner fences of the data). n = 47 for dysbiotic CD, n = 169 for non-dysbiotic CD, n = 12 for dysbiotic UC, n = 110 for non-dysbiotic UC and n = 122 for non-IBD. The percentage of zeros in each condition are added as x-axis tick labels. See Table S6 for full results.

[Source data](#)

Extended Data Fig. 8 Correlation between $T_{H17}/IL-17$ -related features and LCA metabolite abundance in HMP2.

$T_{H17}/IL-17$ -related genes upregulated in IBD were significantly negatively correlated with 3-oxoLCA and isoLCA (FDR-adjusted *p*-value < 0.25) but not the other 3 control BAs (LCA, DCA, and CDCA). Differentially expressed $T_{H17}/IL-17$ -related genes with at least one significant association are shown. This analysis was based on a subset of n = 71 participant-unique samples with matched metagenomic, metabolomic, and host transcriptomic profiling in the HMP2 cohort (33 CD, 21 UC, and 17 non-IBD controls, Spearman correlation with FDR adjusted *p*-value < 0.25). Correlations were based on residual transcript and metabolite abundance after correcting for diagnosis, consent age, and antibiotic use. See Table S8 for full results.

[Source data](#)

Extended Data Fig. 9 Correlation between 3 α , β -HSDH-related microbial features and LCA metabolite abundance in HMP2.

a–b, Relative abundance distributions of differentially abundant 3 α -HSDH (**a**) and 3 α -HSDH (**b**) homologues profiled from HMP2 metagenomes ($n = 1,595$ samples from 130 subjects; linear mixed-effects model coefficient for dysbiosis within diagnosis, FDR-adjusted p -values < 0.05). Boxplots show median and lower/upper quartiles with outliers outside of boxplot ‘whiskers’ (indicating the inner fences of the data). The percentage of zeros in each condition are added as x-axis tick labels. See Table S9 for full results. **c–f**, LCA metabolites show significant differential abundance after adjusting for variation in underlying taxonomic abundance. Accounting for underlying variation in the taxonomic abundance of the major producers of isoLCA (Actinobacteria and Firmicutes), we used the phyla abundances as additional covariates to normalize the abundance of LCA metabolites and enzymes. 3-OxoLCA (**c**) and isoLCA (**d**) as derived from metabolomic profiles of HMP2 cohorts are significantly depleted in HMP2 dysbiotic CD samples ($n = 48$) relative to non-dysbiotic controls ($n = 169$). Meanwhile, 3 α -HSDH (**e**) and 3 β -HSDH (**f**) homologues were also profiled from HMP2 metagenomes ($n = 1,595$ samples from 130 participants; linear mixed-effects model coefficient for dysbiosis within diagnosis, FDR-adjusted p -values < 0.05). The percentage of zeros in each condition are added as x-axis tick labels. Boxplot ‘boxes’ indicate the first, second (median), and third quartiles of the data. The points outside of boxplot whiskers are outliers. Statistical analysis was performed using a linear mixed-effect model and its coefficient and significance, FDR-adjusted p -values, are shown.

[Source data](#)

Extended Data Fig. 10 3 α - and 3 β -HSDH homologues and species with 3 α -/ 3 β -HSDH activity are likely to be positively correlated with 3-oxoLCA/ isoLCA in HMP2.

a, Differentially abundant 3 α -/ 3 β -HSDH homologues (FDR adjusted p -value < 0.05) with at least one significant metabolite association (Spearman

correlation with FDR adjusted p-value < 0.25). Correlations were computed over a subset of paired metabolomes and metagenomes from the HMP2 cohort derived from 106 participants (CD, n = 50; UC, n = 30; Non-IBD, n = 26). **b**, Differentially abundant species with validated 3 α -/ 3 β -HSDH activity (FDR adjusted p-value < 0.05) with at least one significant metabolite association (Spearman correlation with FDR adjusted p-value < 0.25) with five metabolites are shown for the paired metabolome and metagenome samples from 106 participants (CD, n = 50; UC, n = 30; Non-IBD, n = 26) in HMP2.

[Source data](#)

Supplementary information

[Supplementary Information](#)

Supplementary Notes, Supplementary Figs. 1–8, Supplementary Tables 1–12; a sequence summary report and Supplementary References

[Reporting Summary](#)

Source data

[Source Data Fig. 1](#)

[Source Data Fig. 2](#)

[Source Data Fig. 3](#)

[Source Data Fig. 4](#)

[Source Data Extended Data Fig. 1](#)

[Source Data Extended Data Fig. 2](#)

[**Source Data Extended Data Fig. 3**](#)

[**Source Data Extended Data Fig. 4**](#)

[**Source Data Extended Data Fig. 5**](#)

[**Source Data Extended Data Fig. 6**](#)

[**Source Data Extended Data Fig. 7**](#)

[**Source Data Extended Data Fig. 8**](#)

[**Source Data Extended Data Fig. 9**](#)

[**Source Data Extended Data Fig. 10**](#)

Rights and permissions

[Reprints and Permissions](#)

About this article

Cite this article

Paik, D., Yao, L., Zhang, Y. *et al.* Human gut bacteria produce T_H17-modulating bile acid metabolites. *Nature* **603**, 907–912 (2022). <https://doi.org/10.1038/s41586-022-04480-z>

- Received: 04 December 2020
- Accepted: 27 January 2022
- Published: 16 March 2022
- Issue Date: 31 March 2022

- DOI: <https://doi.org/10.1038/s41586-022-04480-z>

Share this article

Anyone you share the following link with will be able to read this content:

[Get shareable link](#)

Sorry, a shareable link is not currently available for this article.

[Copy to clipboard](#)

Provided by the Springer Nature SharedIt content-sharing initiative

This article was downloaded by **calibre** from <https://www.nature.com/articles/s41586-022-04480-z>

| [Section menu](#) | [Main menu](#) |

- Article
- Open Access
- [Published: 03 February 2022](#)

ACE2 binding is an ancestral and evolvable trait of sarbecoviruses

- [Tyler N. Starr](#) [ORCID: orcid.org/0000-0001-6713-6904^{1,2}](#) [na1](#),
- [Samantha K. Zepeda](#) [ORCID: orcid.org/0000-0003-0005-9793³](#) [na1](#),
- [Alexandra C. Walls](#) [ORCID: orcid.org/0000-0002-9636-8330³](#),
- [Allison J. Greaney^{1,4}](#),
- [Sergey Alkhovsky](#) [ORCID: orcid.org/0000-0001-6913-5841⁵](#),
- [David Veesler](#) [ORCID: orcid.org/0000-0002-6019-8675^{2,3}](#) &
- [Jesse D. Bloom](#) [ORCID: orcid.org/0000-0003-1267-3408^{1,2,4}](#)

Nature volume 603, pages 913–918 (2022)

- 14k Accesses
- 2 Citations
- 177 Altmetric
- [Metrics details](#)

Subjects

- [Molecular evolution](#)
- [SARS-CoV-2](#)
- [Viral evolution](#)
- [Viral proteins](#)
- [Virus–host interactions](#)

Abstract

Two different sarbecoviruses have caused major human outbreaks in the past two decades^{1,2}. Both of these sarbecoviruses, SARS-CoV-1 and SARS-CoV-2, engage

ACE2 through the spike receptor-binding domain^{2,3,4,5,6}. However, binding to ACE2 orthologues of humans, bats and other species has been observed only sporadically among the broader diversity of bat sarbecoviruses^{7,8,9,10,11}. Here we use high-throughput assays¹² to trace the evolutionary history of ACE2 binding across a diverse range of sarbecoviruses and ACE2 orthologues. We find that ACE2 binding is an ancestral trait of sarbecovirus receptor-binding domains that has subsequently been lost in some clades. Furthermore, we reveal that bat sarbecoviruses from outside Asia can bind to ACE2. Moreover, ACE2 binding is highly evolvable—for many sarbecovirus receptor-binding domains, there are single amino-acid mutations that enable binding to new ACE2 orthologues. However, the effects of individual mutations can differ considerably between viruses, as shown by the N501Y mutation, which enhances the human ACE2-binding affinity of several SARS-CoV-2 variants of concern¹² but substantially decreases it for SARS-CoV-1. Our results point to the deep ancestral origin and evolutionary plasticity of ACE2 binding, broadening the range of sarbecoviruses that should be considered to have spillover potential.

[Download PDF](#)

Main

Both SARS-CoV-2 and SARS-CoV-1 use human ACE2 as their receptor^{2,3,4,5,6}. Sampling of bats has identified multiple lineages of sarbecoviruses with receptor-binding domains (RBDs) exhibiting different ACE2-binding properties^{7,8,9,10,11,13,14,15,16,17,18,19} that are exchanged through recombination^{8,19,20}. Before the emergence of SARS-CoV-2, all bat sarbecoviruses with a demonstrated ability to bind to any ACE2 orthologue contained RBDs related to SARS-CoV-1 and were sampled from *Rhinolophus sinicus* and *Rhinolophus affinis* bats in Yunnan province in southwest China^{7,8,11,21,22}. More recently, sarbecoviruses related to SARS-CoV-2 that bind to ACE2 have been found more widely across Asia and from a broader diversity of *Rhinolophus* species^{2,16,23,24,25}. However, ACE2 binding has not been observed within a prevalent group of sarbecovirus RBDs sampled in southeast Asia (RBD clade 2)^{7,8,17}, nor has it been observed in distantly related sarbecoviruses from Africa and Europe (RBD clade 3)^{7,19} (Fig. 1a). It is therefore unclear whether ACE2 binding is an ancestral trait of sarbecovirus RBDs that has been lost in some RBD lineages, or a trait that was acquired more recently in a subset of Asian sarbecovirus RBDs^{19,20}. As ACE2 is also variable among *Rhinolophus* bats, particularly in the surface recognized by sarbecoviruses^{26,27,28}, it is important to understand how sarbecoviruses acquire the ability to bind to new ACE2 orthologues, including that of humans, through amino acid mutations.

Fig. 1: High-throughput survey of sarbecovirus ACE2 binding.

 **figure 1**

a, Maximum likelihood phylogeny of sarbecovirus RBDs constructed from RBD nucleotide sequences. The node labels indicate bootstrap support values. Details on rooting are shown in Extended Data Fig. 1. Scale bar, 0.5 nucleotide substitutions per site. **b**, Binding avidities of sarbecovirus RBDs for eight ACE2 orthologues determined using high-throughput yeast-displayed RBD titration assays (Extended Data Fig. 2). **c**, Alignment of tested ACE2 orthologues within RBD-contact positions (4 Å cut-off in Protein Data Bank (PDB) [6M0J](#) or [2AJF](#)). **d**, Representative ACE2-binding curves from high-throughput titrations. Underlying titration curves for individual replicate-barcoded representatives of a genotype are shown in light grey, and the average binding across all barcodes is indicated in black. **e**, BLI binding analysis of 1 μM *R. affinis* ACE2–Fc binding to biotinylated BtKY72 RBD immobilized at the surface of streptavidin biosensors (see Extended Data Fig. 3a for analysis of the robustness of the result to ACE2–Fc concentration). Data are representative of three assays using independent preparations of RBD (biological triplicate). **f**, Entry of VSV particles pseudotyped with the BtKY72 spike into HEK293T cells transiently expressing *R. affinis* ACE2 alleles 9479 or 787. Each point represents the mean of technical triplicates for assays performed with independent preparation of pseudoviral particles (biological duplicate). The geometric mean is

shown by the horizontal line. The normalized pseudovirus western blot, and mock (VSV prepared without spike plasmid) pseudovirus entry in *R. affinis* ACE2 HEK293T cells are shown in Extended Data Fig. 3c,d.

Survey of sarbecovirus ACE2 binding

To trace the evolutionary history of sarbecovirus binding to ACE2, we assembled a gene library encoding 45 sarbecovirus RBDs spanning all four known RBD phylogenetic clades (Fig. 1a,b and Extended Data Fig. 1). We cloned the RBD library into a yeast-surface display platform that enables high-throughput measurement of ACE2-binding avidities using titration assays combining fluorescence-activated cell sorting (FACS) and deep sequencing¹² (Extended Data Fig. 2a-d). We also assembled a panel of recombinant, dimeric ACE2 proteins from human, civet, pangolin and mouse, as well as two alleles each from *R. affinis* and *R. sinicus* bats²⁶ (Fig. 1c). The *R. affinis* alleles encode the two distinct RBD-interface sequences found among 23 *R. affinis* bats from Yunnan and Hubei, China. The *R. sinicus* alleles encode two out of the eight distinct RBD-interface sequences found among 25 *R. sinicus* bats from Yunnan, Hubei, Guangdong and Guangxi provinces, and Hong Kong²⁶, including one allele (3364) that is closest to consensus among the 8 RBD-interface sequences, and another (1434) that does not support entry by some clade 1a sarbecoviruses²⁶. We measured the apparent dissociation constant ($K_{D,\text{app}}$) of each RBD for each of the eight ACE2 orthologues (Fig. 1b,d and Extended Data Fig. 2). We performed all of the experiments in duplicate using independently constructed libraries, and the measurements were highly correlated between replicates ($R^2 > 0.99$; Extended Data Fig. 2g).

Consistent with a previous survey of human ACE2-mediated cellular infectivity⁷, human ACE2 binding is restricted to RBDs within the SARS-CoV-1 and SARS-CoV-2 clades (Fig. 1b), although binding affinities vary among RBDs within these clades. Specifically, the RBDs from SARS-CoV-2 and related viruses from pangolins bind to human ACE2 with high affinity, whereas the RBD from the bat virus RaTG13 exhibits much lower affinity¹⁶. The RBDs of SARS-CoV-1 isolates from the 2002–2003 epidemic bind to human ACE2 strongly, whereas RBDs from civet and sporadic 2004 human isolates (GD03T0013, GZ0402) show weaker binding, consistent with their civet origin and limited transmission^{29,30}. SARS-CoV-1-related bat virus RBDs bind to human ACE2, in some cases with higher affinity than SARS-CoV-1 itself.

Binding to civet ACE2 was detected only within the SARS-CoV-1 clade, whereas pangolin ACE2 binding is more widespread within the SARS-CoV-2 clade, consistent with viruses isolated from civet or pangolin partitioning specifically within each of these clades. Mice are not a natural host of sarbecoviruses, and RBDs from the SARS-

CoV-1 and SARS-CoV-2 clades bind to mouse ACE2 only sporadically, typically with modest to weak affinity relative to other ACE2 orthologues. The highest binding affinity for mouse ACE2 is found in the cluster of RBDs related to RsSHC014, which can mediate infection and pathogenesis in mice³¹.

Binding to ACE2 of *R. affinis* and particularly *R. sinicus* bats varies considerably among strains in the SARS-CoV-1 and SARS-CoV-2 clades, consistent with an evolutionary arms race driving ACE2 variation in *Rhinolophus* bats^{26,27}. The two *R. sinicus* bat ACE2 proteins tested interacted only with SARS-CoV-1 isolates and the bat RsSHC014-cluster RBDs, which are notable for their broad ACE2-binding specificity in our assay. By contrast, we detected strong binding to both *R. affinis* ACE2 proteins among many RBDs in the SARS-CoV-1 and SARS-CoV-2 clades. However, the RBDs of the two viruses sampled from *R. affinis* in our panel bound only modestly (LYRa11) or very weakly (RaTG13) to the *R. affinis* ACE2s that we tested.

Strikingly, we detected binding to *R. affinis* ACE2 proteins by the RBD of the BtKY72 virus from Kenya¹³ (Fig. 1b,d), the first described binding to any ACE2 orthologue for a sarbecovirus outside of Asia^{7,19}. To validate this finding, we purified the BtKY72 RBD and *R. affinis* ACE2–Fc fusion proteins recombinantly expressed in human cells and characterized their interaction using biolayer interferometry (BLI). In agreement with the yeast-display results, the BtKY72 RBD bound to the *R. affinis* 9479 ACE2 and more weakly to the *R. affinis* 787 allele (Fig. 1e and Extended Data Fig. 3a). Furthermore, HEK293T cells transfected with the *R. affinis* 9479 or 787 ACE2 alleles supported the entry of vesicular stomatitis virus (VSV) particles pseudotyped with the BtKY72 spike, thereby demonstrating that ACE2 is a bona fide entry receptor for this virus (Fig. 1f and Extended Data Fig. 3c,d). The geographical range of *R. affinis* does not extend outside of Asia¹⁵, but this result indicates that BtKY72 may bind to ACE2 orthologues of bats found in Africa, although the full range of non-Asian bat species that harbour sarbecoviruses and their ACE2 sequences are underexplored^{13,14,19,32}.

We did not detect ACE2 binding by any of the clade 2 RBDs. In our panel, 9 out of the 23 clade 2 RBDs were sampled from *R. sinicus*, in some cases from the same caves—and even found co-infecting the same *R. sinicus* bats⁸—as ACE2-utilizing SARS-CoV-1-related RBDs. We tested binding by two clade 2 RBDs isolated from *R. sinicus* (YN2013 from Yunnan and HKU3-1 from Hong Kong Special Administrative Region) to an expanded ACE2 panel comprising all RBD-interface sequences observed in *R. sinicus* bats²⁶, including those sampled in Yunnan and Hong Kong Special Administrative Region. In contrast to SARS-CoV-1 Urbani and RsSHC014 (a clade 1a RBD isolated from *R. sinicus* in Yunnan¹¹), YN2013 and HKU3-1 RBDs did not bind to any of the eight *R. sinicus* ACE2 proteins (Extended Data Fig. 4). Previous experiments with clade 2 RBDs have also demonstrated a lack of binding to *R.*

*pearsonii*¹⁷ and human^{7,8,12,17} ACE2. Clade 2 RBDs have two large deletions within the receptor-binding motif^{7,8,19}, which has led to the hypothesis that this clade uses an unidentified alternative receptor, which could be bound by either the RBD or the spike N-terminal domain^{33,34,35,36}. Our results are consistent with this hypothesis, although we cannot rule out that clade 2 RBDs bind to other ACE2 orthologues that have not yet been tested.

Ancestral origins of ACE2 binding

Our finding that the BtKY72 RBD binds to ACE2 suggests that ACE2 binding was present in the ancestor of all sarbecoviruses before the split of Asian and non-Asian RBD clades (Fig. 2a). To test this hypothesis, we used ancestral sequence reconstruction³⁷ to infer plausible sequences representing ancestral nodes on the sarbecovirus RBD phylogeny (Fig. 2a and Extended Data Fig. 5a). We evaluated ACE2 binding for the most probable reconstructed ancestral sequences (Fig. 2b and Extended Data Fig. 5b) and in alternative reconstructions that incorporate statistical or phylogenetic ambiguities inherent to ancestral reconstruction (Extended Data Fig. 6). Consistent with the distribution of ACE2 binding among extant sarbecoviruses, the reconstructed ancestor of all sarbecovirus RBDs (AncSarbecovirus) bound to the *R. affinis* 9479 ACE2 (Fig. 2b). Broader ACE2 binding (including to human ACE2) was acquired on the branch connecting AncSarbecovirus to the ancestor of the three Asian sarbecoviruses RBD clades (AncAsia). ACE2 binding was then lost along the branch to the clade 2 ancestor (AncClade2), due to the combination of 48 amino-acid substitutions and 2 deletions within the ACE2-binding region that occurred along this branch (Fig. 2c).

Fig. 2: Ancestral origins of sarbecovirus ACE2 binding.



a, Clade-collapsed RBD phylogeny. The circles represent nodes at which ancestral sequences were inferred. The bars indicate putative gains and losses in ACE2 binding. **b**, ACE2 binding of ancestrally reconstructed, yeast-displayed RBDs (Extended Data Figs. 5 and 6). **c**, ACE2 binding of AncAsia RBD plus introduction of the 48 substitutions or 2 sequence deletions that occurred on the phylogenetic branch leading to AncClade2 RBD.

This evolutionary history of ACE2 binding is robust to some but not all analyses of uncertainty in our phylogenetic reconstructions^{38,39}. The key phenotypes represented in Fig. 2b are robust to uncertainties in the topology of the RBD phylogeny (Extended Data Fig. 6a, b) or possible recombination within the RBD impacting the cluster of RBDs related to RsSHC014 (Extended Data Fig. 6c–f). However, statistical uncertainty in the identity of some ACE2-contact positions affects our inferences, with some reasonably plausible ‘second-best’ reconstructed states altering ancestral phenotypes (Extended Data Fig. 6b). Nonetheless, our hypothesis of an ancestral origin of sarbecovirus ACE2 binding is supported by the most plausible ancestral reconstructions as well as the distribution of ACE2 binding among the directly sampled sarbecovirus RBDs in Fig. 1a, b.

Evolvability of ACE2 binding

To examine how easily RBDs can acquire ACE2 binding through single amino-acid mutations, we constructed mutant libraries in 14 RBD backgrounds spanning the RBD phylogeny. In each background, we introduced all single amino acid mutations at six RBD positions previously implicated in the evolution of receptor binding in SARS-CoV-2 and SARS-CoV-1 (refs. 12,40) (SARS-CoV-2 residues Leu455, Phe486, Gln493, Ser494, Gln498 and Asn501; Fig. 3a; we use SARS-CoV-2 numbering for mutations in all of the homologues below). We recovered nearly all 1,596 of the intended mutations, and measured the binding of each mutant RBD to each ACE2 orthologue using high-throughput titrations as described above.

Fig. 3: Evolutionary plasticity of ACE2 binding.

 **figure 3**

a, The structural context of positions targeted for mutagenesis. Green cartoon, RBD; grey cartoon, ACE2 interaction motifs; blue spheres, residues targeted through mutagenesis (SARS-CoV-2 identities). **b**, Mutational scanning measurements. The red bars mark the binding avidity of the parental RBD, and the points mark mutant avidities (see Extended Data Fig. 7 for mutation-level measurements). **c**, The fraction of the 14 RBD backgrounds for which the parental RBD binds to the indicated ACE2 orthologue ($-\log_{10}(K_{D,app}) > 7$), a single mutant binds but the parental RBD does not, or no tested mutants bind. **d**, Binding of 1 μM human ACE2–Fc to biotinylated RBDs immobilized at the surface of streptavidin biosensors (see Extended Data Fig. 3b for an analysis of the robustness of the result to ACE2–Fc concentration). Data are representative of three assays using independent preparations of RBD (biological triplicate). **e**, Entry of BtKY72 spike-pseudotyped VSV in HEK293T cells stably expressing human ACE2. Each point represents the mean of technical triplicates in assays performed with independent preparation of pseudoviral particles (biological triplicate). The horizontal line shows the geometric mean. Mock, VSV particles produced in cells in which no spike gene was transfected. A western blot of pseudotyped particles is shown in Extended Data Fig. 3c, and entry into HEK293T cells lacking ACE2 is shown in Extended Data Fig. 3e. **f**, Titration curves illustrating

the effect of mutation to tyrosine 501 (SARS-CoV-2 numbering) in the SARS-CoV-2 and SARS-CoV-1 Urbani RBD backgrounds. **g**, Epistatic turnover in mutation effects. Each point represents, for a pair of RBDs, the mean absolute error (residual) in their correlated mutant avidities for human ACE2 (Extended Data Fig. 9a) versus their pairwise amino acid sequence identity. Correlations were computed only for pairs in which the parental RBDs bind with $-\log_{10}(K_{D,app}) > 7$. Data are LOESS mean (blue line) $\pm 95\%$ confidence intervals trendline (grey shading) (see Extended Data Fig. 9b for an analysis across all ACE2 orthologues).

The results show that ACE2 binding is a remarkably evolvable trait (Fig. 3b,c and Extended Data Fig. 7). In almost all cases in which a parental RBD binds to a particular ACE2, there are single amino acid mutations that improve binding by greater than fivefold. Thus, ACE2 binding can easily be enhanced by mutation, which may facilitate the frequent host jumps seen among sarbecoviruses⁴¹. Notably, our data on mouse ACE2 binding could inform the development of mouse-adapted sarbecovirus strains for in vivo studies^{31,42,43,44}, including potentially safer strains that bind to mouse but not human ACE2 (Extended Data Fig. 8).

In the majority of cases in which an RBD does not bind to a particular ACE2 orthologue, single mutations can confer low to moderate binding affinity (Fig. 3b,c). The only exceptions are BM48-31 and AncClade2, for which none of the tested mutations enabled binding to any of the ACE2 variants. We found that the mutation K493Y in AncSarbecovirus enables binding to human ACE2 (Fig. 3b and Extended Data Fig. 7), although this particular mutation did not occur on the branch to AncAsia where we inferred that human ACE2 binding was historically acquired, illustrating the existence of multiple evolutionary paths to acquiring human ACE2 binding. We identified single mutations at positions 493, 498 and 501 that enable the BtKY72 RBD to bind to human ACE2 (Fig. 3b and Extended Data Fig. 7), suggesting that human ACE2 binding is evolutionarily accessible in this lineage.

We validated that the mutations K493Y and T498W enable the RBD of the African sarbecovirus BtKY72 to interact with human ACE2 using purified recombinant proteins. Binding to human ACE2–Fc is not detectable with the parental BtKY72 RBD using BLI but is conferred by T498W and enhanced for the K493Y/T498W double mutant (Fig. 3d and Extended Data Fig. 3b). To evaluate whether the observed binding translated into cell entry, we generated VSV particles pseudotyped with the wild-type or mutant BtKY72 spikes and tested entry in HEK293T cells expressing human ACE2. We detected robust spike-mediated entry for the K493Y/T498W double mutant but not the T498W single mutant (Fig. 3e and Extended Data Fig. 3c,e), reflecting their apparent avidities (Fig. 3d) and confirming the evolvability of human ACE2 binding in this African sarbecovirus lineage.

Finally, we examined how the mutations that enhance ACE2 binding differ among sarbecovirus backgrounds, reflecting epistatic turnover in mutation effects^{12,45}. For example, the N501Y mutation increases human ACE2-binding affinity for SARS-CoV-2 where it has arisen in variants of concern⁴⁶, but the homologous mutation in the SARS-CoV-1 RBD (position 487) is highly deleterious for human ACE2 binding (Fig. 3f). More broadly, variation in mutant effects increases as RBD sequences diverge (Fig. 3g and Extended Data Fig. 9). However, the rate of this epistatic turnover varies across positions—for example, the effects on human ACE2 binding for mutations at positions 486 and 494 remain relatively constant across sequence backgrounds, whereas variability in the effects of mutations at positions 498 and 501 increases substantially as RBDs diverge.

New sarbecovirus lineages bind to ACE2

Given that ACE2 binding is an ancestral sarbecovirus trait with plastic evolutionary potential, unsampled sarbecoviruses lineages probably have the ability to bind to ACE2 and evolve to bind to human ACE2 unless these traits have been specifically lost as occurred in clade 2. To test this idea, we investigated sarbecoviruses reported after the initiation of our study, including viruses from Africa¹⁹ and Europe^{32,47} and a new RBD lineage represented by RsYN04 from a *Rhinolophus stheno* bat in Yunnan, China¹⁵, which branches separately from the four RBD clades previously described (Fig. 4a).

Fig. 4: Newly sampled sarbecovirus lineages bind to ACE2.

 **figure 4**

a, Phylogenetic placement of the newly described sarbecovirus RBDs. The new sequences are shown in bold font. RBDs are coloured according to the key in Fig. 1a (Extended Data Fig. 10). Scale bar, expected nucleotide substitutions per site. **b–d**, Binding curves for newly described sarbecovirus RBDs from Europe (**b**), Africa (**c**) and Asia (**d**), and candidate mutations that confer human ACE2 binding. Measurements were performed with yeast-displayed RBDs and purified dimeric ACE2 proteins, measured using flow cytometry. Data are from a single experimental replicate.

We determined the ACE2-binding abilities of these RBDs using our yeast-display platform. We found that two newly described sarbeco-viruses from the Caucasus region of Russia³² bind to ACE2 (Fig. 4b): the Khosta-1 RBD binds to *R. affinis* ACE2s with avidity that is improved by the T498W mutation and, strikingly, the Khosta-2 RBD binds to human ACE2 even in the absence of mutations. The Khosta-2 RBD was also recently shown to enable cell entry through human ACE2 (refs. 48,49). This finding indicates that the evolvability of human ACE2 binding that we describe

for other African and European sarbecoviruses has been realized in naturally circulating viruses that are geographically and phylogenetically separated from the southeast Asian clades from which spillover has been described to date. Our results also reinforce our observation of ACE2 binding in African sarbecoviruses (Fig. 4c)—similar to BtKY72, RBDs of the newly described African sarbecoviruses PDF-2380 and PRD-0038 (ref. 19) bind to *R. affinis* ACE2s, and the K493Y/T498W double mutant confers human ACE2 binding to the PRD-0038 RBD as it does for BtKY72. Finally, the uniquely branching RsYN04 RBD binds to *R. affinis* 787 ACE2 (Fig. 4d), as was recently shown for the closely related RaTG15 spike⁵⁰. The RsYN04 RBD can also acquire binding to human ACE2 through the single T498W mutation. Incorporation of newly described sarbecovirus sequences into an updated phylogenetic reconstruction of the AncSarbecovirus RBD sequence reaffirms the conclusion that the ancestral sarbecovirus binds to bat ACE2 and can evolve human ACE2 binding through single amino-acid mutation (Extended Data Fig. 10). These results illustrate that the ancestral traits of ACE2 binding and ability to evolve human ACE2 binding are maintained in geographically and phylogenetically diverse sarbecoviruses, including lineages that are just beginning to be described^{13,15,19,32,50}.

Discussion

Our experiments reveal that binding to bat ACE2 is an ancestral trait of sarbecoviruses that is also present in viruses from outside of Asia^{13,19,32}. Binding to human ACE2 arose in the common ancestor of SARS-CoV-1- and SARS-CoV-2-related RBDs before their divergence, and human ACE2 binding is evolvable in other phylogenetic clades. Binding to the ACE2 orthologues that we tested was then lost on the branch leading to the clade 2 RBDs, which either bind to an alternative receptor or ACE2 orthologues that were not evaluated here. These results imply that unsampled RBD lineages in the phylogenetic interval between BtKY72 and SARS-CoV-1/SARS-CoV-2 probably use ACE2 as an entry receptor and have the ability to evolve affinity for human ACE2. Indeed, the Khosta-2 virus from Russia provides an example of a RBD for which this evolutionary potential for human ACE2 binding has been realized.

Our research also shows that ACE2 binding is a highly evolvable trait of sarbecovirus RBDs. For every ACE2-binding RBD that we studied, there were single amino acid mutations that enhanced affinity for ACE2 orthologues that a RBD could already bind to or that conferred binding to new ACE2 orthologues from different species. Host jumps are common among the wide diversity of bats that are naturally infected with these viruses^{8,15,41}. In addition to frequent exchange of RBDs among viral backbones through recombination^{8,19,20}, the evolutionary plasticity of RBD binding to ACE2 is probably a key contributor to the ecological dynamics of sarbecoviruses, and perhaps other coronaviruses that frequently transmit across species⁵¹. As the effects of RBD

mutations on ACE2 binding can differ across sarbecovirus backgrounds, it is not trivial to predict the ACE2-binding properties of a given RBD solely from its sequence. Thus, high-throughput approaches such as the one we have used here, which enables rapid and comprehensive measurement of ACE2-binding affinities of RBD variants in a non-viral context, can aid efforts to understand the evolutionary diversity and dynamics of sarbecoviruses and develop broadly protective therapeutics.

Sarbecoviruses are of particular concern, as two different strains have caused human outbreaks. Although human infectivity depends on many factors, the ability to bind to human receptors is certainly a key factor. Our results show that the ability of sarbecoviruses to bind to human ACE2 is evolvable and has arisen independently in regions outside of southeast Asia. Our high-throughput yeast-display platform enables the study of possible host tropism of sarbecoviruses without requiring work with replication-competent viruses that can pose biosafety concerns. The geographical breadth of ACE2 binding that we describe suggests that care should be taken in the sampling and study of replication-competent sarbecoviruses even outside regions such as southeast Asia in which spillover potential is considered greatest, and that efforts to develop vaccines and antibody therapeutics for pandemic preparedness should consider sarbecoviruses circulating worldwide.

Methods

Phylogenetics and ancestral sequence reconstruction

All steps of the bioinformatic analysis, including specific programmatic commands, alignments, raw data and output files are provided at GitHub (https://github.com/jbloomlab/SARSr-CoV_homolog_survey/tree/master/RBD_ASR).

A panel of unique sarbecovirus RBD sequences was assembled incorporating the RBD sequences curated in ref. 7, all unique RBD sequences among SARS-CoV-1 human and civet strains reported in ref. 30, and recently reported sarbecoviruses BtKY72 (ref. 13), RaTG13 (ref. 2) GD-Pangolin-CoV (consensus RBD sequence reported in figure 3a of ref. 23) and GX-Pangolin-CoV²³ (P2V, ambiguous nucleotide in codon 515 (SARS-CoV-2 numbering) was resolved to retain amino acid Phe515, which is conserved across all other sarbecoviruses). We also incorporated newly described sarbecovirus sequences RsYN04 (ref. 15), PDF-2370 and PRD-0038 (ref. 19), Khosta-1 and Khosta-2 (ref. 32), RhGB01 (ref. 47), RshSTT182 (ref. 25) and Rc-o319 (ref. 24) into updated phylogenies and functional work after the initiation of our study (Fig. 4 and Extended Data Fig. 10). The Hibecovirus sequence Hp-BetaCoV/Zhejiang2013 (GenBank: [KF636752](#)) was used to root the sarbecovirus phylogeny. For Extended Data Figs. 1 and 10a–d, additional betacoronavirus outgroups were included in

rooting. All virus names, species and location of sampling, and sequence accessions or citations are provided at GitHub (https://github.com/jbloomlab/SARSr-CoV_homolog_survey/blob/master/RBD_ASR/RBD_accessions.csv).

Amino acid sequences were aligned by mafft (v.7.471)⁵² with a gap opening penalty of 4.5. RBD sequences were subsetted from spike alignments according to our domain boundary defined for SARS-CoV-2 (Wuhan-Hu-1 GenBank: [MN908947](#), residues Asn331–Thr531). Nucleotide alignments were constructed from amino acid alignments using PAL2NAL (v.14)⁵³. Phylogenies were inferred with RAxML (v.8.2.12)⁵⁴ using the LG+Γ substitution model for amino acid sequence alignments or GTR+Γ with separate data partitions applied to the first, second and third codon positions for nucleotide sequence alignments. Constraint files specifying specific clade relationships (but free topologies within clades) were used to fix particular topologies in Extended Data Fig. 6a (alternative relationships between RBD clades 1a, 1b and 2) and Fig. 4a (monophyletic Europe and Africa RBD clade; Extended Data Fig. 10a–d). RBD gene segments were used as our primary boundary for phylogenetic inference and ancestral sequence reconstruction due to the presence of frequent recombination within broader spike alignments^{19,20}.

Marginal likelihood ancestral sequence reconstruction was performed with FastML (v.3.11)⁵⁵ using the amino acid sequence alignment, the maximum likelihood nucleotide tree topology from RAxML, the LG+Γ substitution matrix, re-optimization of branch lengths and FastML’s likelihood-based indel reconstruction model. The maximum a posteriori ancestral sequences at nodes of interest were determined from the marginal reconstructions as the string of amino acids at each alignment site with the highest posterior probability, censored by deletions as inferred from the indel reconstruction. To test the robustness of ancestral phenotypes to statistical uncertainty in reconstructed ancestral states, we also constructed ‘alt’ ancestors in which all second-most-probable states with posterior probability > 0.2 were introduced simultaneously³⁸.

To identify potential recombination breakpoints within the RBD alignment, we used GARD (v.0.2)⁵⁶, which identified a possible recombination breakpoint (Extended Data Fig. 6c) that produces two alignment segments exhibiting phylogenetic incongruence with a gain in overall likelihood sufficient to justify the duplication of phylogenetic parameters ($\Delta\text{AIC} = -85$). To determine the impact of this possible recombination on ancestral sequence reconstructions, the alignment was split into separate segments at the proposed breakpoint. Phylogenies were inferred and ancestral sequences reconstructed on separate segments as described above, and reconstructed ancestral sequences at matched nodes for each segment were concatenated, as shown in Extended Data Fig. 6e.

RBD library construction

Genes encoding all 73 unique extant and ancestral RBD amino acid sequences were ordered from Twist Bioscience, Genscript, and IDT. Gene sequences are provided at GitHub (https://github.com/jbloomlab/SARSr-CoV_homolog_survey/blob/master/RBD_ASR/parsed_sequences/RBD_sequence_set_annotated.csv). Genes were cloned in bulk into the pETcon yeast surface-display vector (plasmid 2649) as described previously¹². As described in this previous publication, randomized N16 barcodes were appended by PCR downstream from RBD coding sequences. RBD sequences were pooled and barcoded in two independently processed replicates. The pooled, barcoded parental RBD libraries were electroporated into *Escherichia coli* and plated at an estimated bottleneck of ~22,000 colony-forming units, yielding an estimated ~300 barcodes per parental RBD within each library replicate.

In parallel, we cloned site saturation mutagenesis libraries of six positions in select RBD backgrounds. The positions targeted correspond to SARS-CoV-2 positions 455, 486, 493, 494, 498 and 501. The RBD-indexed position targeted in each background is provided at GitHub (https://github.com/jbloomlab/SARSr-CoV_homolog_survey/blob/master/RBD_ASR/parsed_sequences/RBD_sequence_set_annotated.csv). Precise site saturation mutagenesis pools were produced by Genscript, provided as plasmid libraries. Failed positions in the Genscript mutagenesis libraries (all six positions in SARS-CoV-1 Urbani, position 494 in SARS-CoV-2, and position 455 in RaTG13 and GD-Pangolin) or backgrounds chosen for mutagenesis subsequent to initial library design (BtKY72) were produced in-house by PCR-based mutagenesis using NNS degenerate mutagenic primers followed by Gibson Assembly of the mutagenized fragments. In duplicate, mutant libraries were pooled and N16 barcodes were appended downstream from the RBD coding sequence. The pooled, barcoded mutant libraries were electroporated into *E. coli* and plated at a target bottleneck corresponding to an average of 20 barcodes per mutant within each library replicate.

Colonies from bottlenecked transformation plates were scraped and plasmids were purified. Parental RBD and mutant pools were combined at ratios corresponding to expected barcode diversity, yielding the two separately barcoded library replicates used in high-throughput experiments. Plasmid libraries were transformed into yeast (AWY101 strain⁵⁷) according to a previously described protocol⁵⁸, transforming 10 µg of plasmid at 10× scale.

PacBio sequencing and analysis

As described previously¹², PacBio sequencing was used to acquire long sequence reads spanning the N16 barcode and RBD coding sequence. PacBio sequencing constructs were prepared from library plasmid pools by NotI digestion and gel purification, followed by SMRTbell ligation. Each library was sequenced across three SMRT Cells on a PacBio Sequel using 20 h video collection times. PacBio circular consensus sequences (CCSs) were generated from subreads using the ccs program (v.5.0.0), requiring 99.9% accuracy and a minimum of 3 passes. The resulting CCSs are available on the NCBI Sequence Read Archive (SRA), BioSample [SAMN18316101](#).

CCSs were processed using alignparse (v.0.1.6)⁵⁹ to identify the RBD target sequence, call any mutations and determine the associated N16 barcode sequence, requiring no more than 18 nucleotide mutations from the intended target sequence, an expected 16-nucleotide-length barcode sequence and no more than 3 mismatches across the sequenced portions of the vector backbone.

We next used processed CCSs to link each barcode to the associated RBD sequence. We first filtered sequences with ccs-determined accuracies of <99.99% or indels. The empirical sequencing accuracy estimated by comparing RBD variants associated with barcode sequences sampled across multiple CCSs

(https://jbloomlab.github.io/alignparse/alignparse_consensus.html#alignparse_consensus.empirical_accuracy) was 99.0% and 98.4% in libraries 1 and 2, respectively. For barcodes sampled across multiple CCSs, we derived consensus RBD variant sequences, discarding barcodes of which CCSs with identical barcodes exhibited >1 point mutation or >2 indels, or of which >10% or >25% of CCSs with an identical barcode contained a secondary non-consensus mutation or indel, respectively. The CCS processing pipeline is available at GitHub (https://github.com/jbloomlab/SARS-CoV_homolog_survey/blob/master/results/summary/process_ccs.md). The final barcode-variant lookup table, which links each N16 barcode with its associated RBD sequence, is available at GitHub (https://github.com/jbloomlab/SARS-CoV_homolog_survey/blob/master/results/variants/nucleotide_variant_table.csv).

ACE2 proteins for yeast-display assays

Recombinant dimeric ACE2 proteins for yeast-display binding assays were purchased or produced from commercial sources. Recombinant human ACE2 (UniProt: [Q9BYF1-1](#)) was purchased from ACROBiosystems (AC2-H82E6), consisting of residues 18–740 spanning an intrinsic dimerization domain, followed by a His tag and biotinylated Avitag used for downstream detection. Civet (*Paguma larvata*) ACE2 (UniProt: [Q56NL1-1](#)) was purchased from ACROBiosystems (AC2-P5248), consisting of residues 18–740 spanning an intrinsic dimerization domain, with an N-terminal His tag used for downstream detection. Mouse (*Mus musculus*) ACE2

(UniProt: [Q8R0I0-1](#)) was purchased from Sino Biological (50249-M03H), consisting of residues 18–740 spanning an intrinsic dimerization domain, followed by a His tag and human IgG1 Fc domain used for downstream detection.

The remaining ACE2s for yeast-display binding assays (with the exception of Extended Data Fig. 4) were produced by Genscript. Specifically, pangolin (*Manis javanica*, GenBank: [XP_017505746.1](#)), *R. affinis* 787 (GenBank: [QMQ39222](#)), *R. affinis* 9479 (GenBank: [QMQ39227](#)), *R. sinicus* 3364 (GenBank: [QMQ39219](#)) and *R. sinicus* 1434 (GenBank: [QMQ39216](#)) ACE2 residues 19–615 were cloned with a C-terminal human IgG1 Fc domain for dimerization and downstream detection. pcDNA3.4 expression plasmids were transfected into HD 293F cells for protein expression. ACE2–Fc fusion proteins were purified from day six culture supernatants by Fc-tag affinity purification.

Library measurements of RBD expression and RBD⁺ enrichment

Transformed yeast library aliquots were grown overnight in a shaker at 30 °C in SD-CAA medium (6.7 g l⁻¹ yeast nitrogen base, 5.0 g l⁻¹ casamino acids, 2.13 g l⁻¹ MES and 2% (w/v) dextrose, pH 5.3). To induce RBD expression, yeast was washed and resuspended in SG-CAA + 0.1% D medium (6.7 g l⁻¹ yeast nitrogen base, 5.0 g l⁻¹ casamino acids, 2.13 g l⁻¹ MES, 2% (w/v) galactose and 0.1% (w/v) dextrose, pH 5.3) at an initial optical density at 600 nm (OD₆₀₀) of 0.67, and incubated at room temperature for 16–18 h with mild agitation.

For each library, 45 OD₆₀₀ of induced culture was washed twice with PBS-BSA (0.2 mg ml⁻¹), and RBD surface expression was labelled by a C-terminal c-Myc tag with 1:100 diluted FITC-conjugated chicken anti-c-Myc antibodies (Immunology Consultants Lab, CMYC-45F) in 3 ml PBS-BSA. Labelled cells were washed twice in PBS-BSA, and resuspended in PBS for FACS analysis.

Yeast library sorting experiments were conducted on the BD FACSAria II system with FACSDiva software (v.8.0.2). For high-throughput measurements of RBD expression levels, cells were gated for single cells (Extended Data Fig. 2b) and partitioned into 4 bins of FITC fluorescence (Extended Data Fig. 2c), where bin 1 captures 99% of unstained cells, and bins 2–4 split the remaining library population into tertiles. Cells were sorted into 5 ml tubes pre-wet with 1 ml of SD-CAA with 1% BSA. We recovered ~8 million cells per library across the 4 bins. Sorted cells were resuspended to 2 × 10⁶ cells per ml in fresh SD-CAA with 1:100 penicillin–streptomycin, and grown overnight at 30 °C. Plasmids were purified from post-sort yeast samples of <4 × 10⁷ cells per miniprep column using the Zymo Yeast Miniprep II kit (D2004) according to the manufacturer's instructions, with the addition of an extended (>2 h)

Zymolyase treatment and a -80°C freeze–thaw cycle before cell lysis. N16 barcodes were PCR amplified from each plasmid aliquot as described previously¹² and submitted for Illumina HiSeq 50 bp single-end sequencing.

To enrich properly expressing RBD variants for downstream titration experiments, we also sorted around 2×10^7 cells per library using the RBD⁺ (FITC⁺) bin (Extended Data Fig. 2b). RBD⁺-enriched populations were resuspended to 1×10^6 cells per ml for overnight outgrowth, and frozen at -80°C in 9 OD₆₀₀ aliquots for subsequent titration experiments.

A pool of mutants that were added after the first set of experiments (mutations at position 455 in RaTG13 and GD-Pangolin, and mutations at all six positions in BtKY72) were not RBD⁺ enriched and were not part of the bulk expression Sort-seq measurement, but were pooled with the RBD⁺-enriched population of the primary libraries for subsequent titration assays.

Library measurements of ACE2-binding affinities

For high-throughput measurements of ACE2-binding affinities, yeast libraries were induced for RBD expression as described above. Induced cultures were aliquoted at 8 OD₆₀₀ per titration sample and washed twice with PBS-BSA. Cells were resuspended across a range of ACE2 concentrations from 1×10^{-6} M to 1×10^{-13} M in 1 M intervals, plus a 0 M ACE2 concentration. The samples were incubated overnight at room temperature with mild agitation. The samples were washed twice in ice-cold PBS-BSA, and resuspended in 1 ml secondary label (1:100 Myc-FITC and 1:200 PE-conjugated streptavidin (Thermo Fisher Scientific, S866) for human ACE2, 1:200 iFluor647-conjugated mouse anti-His (Genscript, A01802) for civet ACE2 and 1:200 PE-conjugated goat anti-human IgG (Jackson ImmunoResearch Labs 109-115-098) for all other Fc-tagged ACE2 ligands), and incubated for 1 h on ice. Cells were washed twice with PBS-BSA and resuspended in PBS for FACS analysis.

Titration samples were binned for single RBD-expressing cells (Extended Data Fig. 2b), which were then partitioned into four bins on the basis of ACE2 binding (Extended Data Fig. 2d). At each concentration, a minimum of 5×10^6 cells were collected across the 4 bins. Sorted cells were resuspended in 1 ml SD-CAA with 1:100 penicillin–streptomycin, and grown overnight at 30°C in deep-well plates. Plasmid aliquots from each population were purified using the Zymo Yeast 96-Well Miniprep kit (D2005) according to the manufacturer’s instructions, with the addition of an extended (>2 h) Zymolyase treatment and a -80°C freeze–thaw cycle before cell lysis. N16 barcodes were PCR amplified from each plasmid aliquot as described previously¹² and submitted for Illumina HiSeq 50 bp single-end sequencing.

For the pool of mutants that were added after the first set of experiments (mutations at position 455 in RaTG13 and GD-Pangolin, and mutations at all six positions in BtKY72), duplicate titrations were already conducted with the primary pool for human ACE2 and *R. affinis* 787 ACE2. Titrations with this smaller library sub-pool with these ACE2 ligands were conducted as described above, but scaled to 1.6 OD₆₀₀ per sample, collecting >1 million cells per concentration.

Illumina barcode sequencing analysis

Demultiplexed sequence reads (available on the NCBI SRA, BioSample [SAMN20174027](#)) were aligned to library barcodes as determined from PacBio sequencing using dms_variants (v.0.8.5), yielding a count of the number of times each barcode was sequenced within each FACS bin. Read counts within each FACS bin were downweighted by the ratio of total reads from a bin compared to the number of cells that were actually sorted into that bin. The table giving downweighted counts of each barcode in each FACS bin is available at GitHub (https://github.com/jbloomlab/SARSr-CoV_homolog_survey/blob/master/results/counts/variant_counts.csv).

We estimated the RBD expression level of each barcoded variant on the basis of its distribution of counts across FACS bins and the known log-transformed fluorescence boundaries of each sort bin using a maximum likelihood approach^{12,60}, implemented with the fitdistrplus package (v.1.0.14)⁶¹ in R. Expression measurements were retained for barcodes for which greater than 20 counts were observed across the four FACS bins. The full pipeline for computing per-barcode expression values is described at GitHub (https://github.com/jbloomlab/SARSr-CoV_homolog_survey/blob/master/results/summary/compute_expression_meanF.md).

We estimated the level of ACE2 binding of each barcoded variant at each titration concentration on the basis of its distribution of counts across FACS bins calculated as a simple mean⁶⁰, as described previously¹². We determined the apparent binding constant $K_{D,app}$ describing the affinity of each barcoded variant for each ACE2 along with free parameters a (titration response range) and b (titration curve baseline) with nonlinear least-squares regression using the standard non-cooperative Hill equation relating the mean bin response variable to the ACE2 labelling concentration:

$$\text{\$}\$\{\text{\rm{bin}}\} = a \times [\text{\rm{ACE}}]_2 / ([\text{\rm{ACE}}]_2 + \{K\}_{\{\text{\rm{D}}\}}, \{\text{\rm{app}}\}) + b\$$$

The measured mean bin value at a given ACE2 concentration was excluded from a variant's curve fit if fewer than 10 counts were observed across the four FACS bins at that concentration. Individual concentration points were also excluded from the curve

fit if they demonstrated evidence of bimodality ($>40\%$ of counts of a barcode were found in each of two non-consecutive bins $1 + 3$ or $2 + 4$, or $>20\%$ of counts of a barcode were found in each of the boundary bins $1 + 4$). To avoid errant fits, we constrained the fit baseline parameter b to be between 1 and 1.5, the response parameter a to be between 2 and 3, and the $K_{D,\text{app}}$ parameter to be between 1×10^{-15} and 1×10^{-5} . The fit for a barcoded variant was discarded if the average count across all sample concentrations was below 10, or if $>20\%$ of sample concentrations were missing due to counts below 10. We also discarded curve fits in cases in which the normalized mean square residual (residuals normalized from 0 to 1 relative to the fit response parameter a) is $>10\times$ the median normalized mean square residual across all titrations with all ACE2s. $K_{D,\text{app}}$ binding constants were expressed as $-\log_{10}(K_{D,\text{app}})$, where higher values indicate higher-affinity binding. The full pipeline for computing per-barcode binding affinities is described at GitHub (https://github.com/jbloomlab/SARSr-CoV_homolog_survey/blob/master/results/summary/compute_binding_Kd.md).

To derive our final measurements we collapsed measurements across internally replicated barcodes representing each RBD genotype. For each RBD genotype, we discarded the top and bottom 5% (expression measurements) or 2.5% (titration affinities) of per-barcode measurements, and computed the mean value across the remaining barcodes within each library. The correlations in these barcode-averaged measurements between independently barcoded and assayed library replicates are shown in Extended Data Fig. 2g. Final measurements were determined as the mean of the barcode-collapsed mean measurements from each replicate. The total number of barcodes collapsed into these final measurements from both replicates is shown in the histograms in Extended Data Fig. 2f. Final measurements for an RBD genotype were discarded if the RBD genotype was not sampled with at least one non-filtered barcode in each replicate, or sampled with at least five non-filtered barcodes in a single replicate. The full pipeline for barcode collapsing is described at GitHub (https://github.com/jbloomlab/SARSr-CoV_homolog_survey/blob/master/results/summary/barcode_to_genotype_phenotype_s.md). The final processed measurements of expression and ACE2 binding for parental and mutant RBDs can be found at GitHub (https://github.com/jbloomlab/SARSr-CoV_homolog_survey/blob/master/results/final_variant_scores/wt_variant_scores.csv and https://github.com/jbloomlab/SARSr-CoV_homolog_survey/blob/master/results/final_variant_scores/mut_variant_scores.csv).

Isogenic ACE2-binding assays

For RBDs assayed subsequent to library experiments (Fig. 4 and Extended Data Figs. 4, 6f and 10e), RBDs were cloned as isogenic stocks into the 2649 plasmid, sequence

verified and transformed individually into yeast using the LiAc/ssDNA transformation method⁶². Cultures were induced for RBD expression and labelled across ACE2 concentration series as described above in V-bottom 96-well plates with 0.067 OD₆₀₀ yeast per well. ACE2 labelling of RBD⁺ cells was measured using the BD LSRFortessa X50 flow cytometer and data were processed using FlowJo (v.10). Binding curves of PE (ACE2) mean fluorescence intensity versus ACE2 labelling concentration were fit as above, with the inclusion of a Hill coefficient slope parameter *n*.

Transient expression of *R. affinis* and *R. sinicus* ACE2–Fc

The *R. affinis* 787 (GenBank: [QMQ39222.1](#)), *R. affinis* 9479 (GenBank: [QMQ39227.1](#)), *R. sinicus* 1446 (GenBank: [QMQ39213.1](#)), *R. sinicus* WJ1 (GenBank: [QMQ39206.1](#)), *R. sinicus* GQ262791 (GenBank: [ACT66275.1](#)), *R. sinicus* 3364 (GenBank: [QMQ39219.1](#)), *R. sinicus* WJ4 (GenBank: [QMQ39200.1](#)), *R. sinicus* 1438 (GenBank: [QMQ39203.1](#)), *R. sinicus* 1434 (GenBank: [QMQ39216.1](#)) and *R. sinicus* 3358 (GenBank: [QMQ39212.1](#)) ACE2 ectodomains constructs were synthesized by GenScript and placed into a pCMV plasmid. The domain boundaries for the ectodomain are residues 19–615. The native signal tag was identified using SignalP-5.0 (residues 1–18) and replaced with an N-terminal mu-phosphatase signal peptide. These constructs were then fused to a sequence encoding a thrombin cleavage site and a human Fc fragment at the C-terminus. All ACE2–Fc constructs were produced in Expi293F cells (Thermo Fisher Scientific, A14527) in Gibco Expi293 Expression Medium at 37 °C in a humidified 8% CO₂ incubator rotating at 130 rpm. The cultures were transfected using PEI-25K (Polyscience) with cells grown to a density of 3 million cells per ml and cultivated for 4–5 days. Proteins were purified from clarified supernatants using a 1 ml HiTrap Protein A HP affinity column (Cytiva), concentrated and flash-frozen in 1× PBS, pH 7.4 (10 mM Na₂HPO₄, 1.8 mM KH₂PO₄, 2.7 mM KCl, 137 mM NaCl). Cell lines were not authenticated or tested for mycoplasma contamination.

Transient expression of BtKY72 parental and mutant RBDs

BtKY72 RBD construct (BtKY72 S residues 318–520) was synthesized by GenScript into a CMVR plasmid with an N-terminal mu-phosphatase signal peptide and a C-terminal hexa-histidine tag (-HHHHHH) joined by a short linker (-GGSS) to an Avi tag (-GLNDIFEAQKIEWHE). BtKY72 mutant constructs T498W (BtKY72 S residue 487) and K493Y/T498W (BtKY72 S residue 482/487) were subcloned by GenScript from the BtKY72 RBD construct. BtKY72 and BtKY72 mutant RBD constructs were produced in Expi293F cells in Gibco Expi293 Expression Medium at 37 °C in a humidified 8% CO₂ incubator rotating at 130 rpm. The cultures were

transfected using PEI-25K with cells grown to a density of 3 million cells per ml and cultivated for 3–5 days. Proteins were purified from clarified supernatants using a 1 ml HisTrap HP affinity column (Cytiva), concentrated and then biotinylated using a commercial BirA kit (Avidity). Proteins were then purified from the BirA enzyme by affinity purification using a 1 ml HisTrap HP affinity column (Cytiva), concentrated and flash-frozen in 1× PBS, pH 7.4. Cell lines were not authenticated or tested for mycoplasma contamination.

BLI analysis

Assays were performed on an Octet Red (Forte Bio) instrument at 30 °C with shaking at 1,000 rpm. Streptavidin biosensors were hydrated in water for 10 min before incubation for 60 s in 10× kinetics buffer (undiluted). Biotinylated RBDs were loaded at 5–10 µg ml⁻¹ in 10× kinetics buffer for 100–600 s before baseline equilibration for 120 s in 10× kinetics buffer. Association of ACE2–Fc (dimeric) was performed at 1 µM in 10× kinetics buffer. These data were baseline-subtracted. The experiments were performed with three separate purification batches of BtKY72 RBDs. All RBDs were immobilized to identical levels, that is, 1 nm shift. The data were plotted in GraphPad Prism and a representative plot is shown.

Generation of VSV pseudovirus

The BtKY72 S construct was synthesized by GenScript and cloned into an HDM plasmid with a C-terminal 3× Flag tag. The BtKY72 mutant S constructs T498W (BtKY72 S residue 487) and K493Y/T498W (BtKY72 S residue 482/487) were subcloned by GenScript from the BtKY72 S construct. Pseudotyped VSV particles were prepared using HEK293T (ATCC CRL-11268) cells seeded into 10 cm dishes. HEK293T cells were transfected using Lipofectamine 2000 (Life Technologies) with a S-encoding plasmid in Opti-MEM transfection medium and incubated for 5 h at 37 °C with 8% CO₂ supplemented with DMEM containing 10% FBS. One day after transfection, cells were infected with VSV (G*ΔG-luciferase) and, after 2 h, infected cells were washed five times with DMEM before adding medium supplemented with anti-VSV G antibodies (I1-mouse hybridoma supernatant diluted 1:40, ATCC CRL-2700). Pseudotyped particles were collected 18–24 h after inoculation, clarified from cellular debris by centrifugation at 3,000g for 10 min, concentrated 100× using a 100 MWCO membrane for 10 min at 3,000 rpm and frozen at –80 °C. Mock pseudotyped VSV pseudovirus was generated as above but in the absence of S. Cell lines were not authenticated or tested for mycoplasma contamination.

VSV pseudovirus entry assays

HEK293T cells (ATCC CRL-11268) and HEK293T cells with stable transfection of human ACE2 (ref. [63](#)) were cultured in 10% FBS, 1% penicillin–streptomycin DMEM at 37 °C in a humidified 8% CO₂ incubator. Cells were plated into poly-lysine-coated 96-well plates. For *R. affinis* ACE2 entry, transient transfection of *R. affinis* ACE2 in HEK293T cells was performed 36–48 h before infection using Lipofectamine 2000 (Life Technologies) and an HDM plasmid containing full length *R. affinis* ACE2 (synthesized by GenScript) in Opti-MEM. After 5 h incubation at 37 °C in a humidified 8% CO₂ incubator, DMEM with 10% FBS was added and cells were incubated at 37 °C in a humidified 8% CO₂ incubator for 36–48 h. Cell lines were not authenticated or tested for mycoplasma contamination.

Immediately before infection, HEK293T cells with stable expression of human ACE2, transient expression of *R. affinis* ACE2 or not transduced to express ACE2 were washed once with DMEM, then plated with normalized pseudovirus in DMEM. Infection in DMEM was performed with cells between 60–80% confluence (human ACE2-293T) or between 80–90% confluence (*R. affinis* ACE2-293T) for 2.5 h before adding FBS and penicillin–streptomycin to final concentrations of 10% and 1%, respectively. After 24 h of infection, One-Glo-EX (Promega) was added to the cells and incubated in the dark for 5 min before reading on a Synergy H1 Hybrid Multi-Mode plate reader (Biotek). Normalized cell entry levels of pseudovirus generated on different days (biological replicates) were plotted in GraphPad Prism as individual points, and average cell entry across biological replicates was calculated as the geometric mean.

BtKY72 S parental and mutant pseudoviral particle inputs for the above cell entry assays were normalized to spike incorporation quantified using western blotting. Detection of S was performed using mouse monoclonal anti-Flag M2 antibodies (Sigma-Aldrich, F3165) and Alexa Fluor 680 AffiniPure Goat Anti-Mouse IgG, light chain specific (Jackson ImmunoResearch Labs, 115-625-174). Detection of the VSV backbone was performed using anti-VSV-M [23H12] antibodies (Kerafast, EB0011) and Alexa Fluor 680 AffiniPure Goat Anti-Mouse IgG, light chain specific (Jackson ImmunoResearch Labs 115-625-174). A representative blot is shown in Extended Data Fig. [3c](#). Expression of the *R. affinis* ACE2 alleles was not quantified or normalized.

Biosafety considerations

We characterized the human ACE2 binding of sarbecovirus RBDs and identified point mutants that increase the affinity of some RBDs. This work includes identifying sarbecovirus RBDs from outside southeast Asia that can naturally bind to human ACE2 (Khosta-2 RBD from Russia) or adapt to bind to human ACE2 with just a few mutations (BtKY72 RBD from Kenya). We verified this latter finding using non-replicative spike-pseudotyped VSV particles. None of our experiments pose a

biosafety risk, as they involve only RBD protein (purified or expressed in yeast) or non-replicative pseudotyped VSV viral particles, and not live virus. However, it is possible that another researcher could perform experiments on actual sarbecoviruses with RBDs such as the ones we described, and such experiments could pose a risk. Against that possible information misuse, we weigh the following benefits of the information conveyed by our study: (1) as stated in the concluding paragraph of the Discussion, we used safe methods to highlight the need for care when sampling sarbecoviruses including those from outside southeast Asia; (2) we identified a broader swath of spike proteins that should be included in biochemical studies to engineer countermeasures (such as broad antibodies^{64,65} or stabilized spike immunogens); (3) we characterized mutations that could enable safer mouse-adapted laboratory strains with reduced human ACE2 affinity (Extended Data Fig. 8c); (4) we provide data that can improve sequence-based phenotypic predictions. We emphasize that our research indicates that live-virus experiments with any new sarbecovirus should involve careful consideration of risks, as human ACE2 binding may be widespread. The actual ability of a sarbecovirus to infect humans will depend not only on its ACE2 affinity, but also other properties including proteolytic activation of the spike protein⁶⁶, innate immunity and other poorly understood factors.

Reporting summary

Further information on research design is available in the [Nature Research Reporting Summary](#) linked to this paper.

Data availability

PacBio CCSs are available from the NCBI SRA, BioSample [SAMN18316101](#). Illumina sequences for barcode counting are available from the NCBI SRA, BioSample [SAMN20174027](#). A table of measurements of ACE2 binding and expression for all parental RBDs is available at GitHub (https://github.com/jbloomlab/SARSr-CoV_homolog_survey/blob/master/results/final_variant_scores/wt_variant_scores.csv). A table of measurements of ACE2 binding and expression for all single mutant RBDs is available at GitHub (https://github.com/jbloomlab/SARSr-CoV_homolog_survey/blob/master/results/final_variant_scores/mut_variant_scores.csv). For bioinformatics analyses, tables of all virus names, species and location of sampling, and sequence accessions (NCBI GenBank or GISAID) or citations are provided at GitHub (https://github.com/jbloomlab/SARSr-CoV_homolog_survey/blob/master/RBD_ASR/RBD_acccessions.csv).

Code availability

All code for data analysis is available at GitHub (https://github.com/jbloomlab/SARSr-CoV_homolog_survey). A summary of the computational pipeline and links to individual notebooks detailing steps of analysis is available at GitHub (https://github.com/jbloomlab/SARSr-CoV_homolog_survey/blob/master/results/summary/summary.md).

References

1. Cui, J., Li, F. & Shi, Z.-L. Origin and evolution of pathogenic coronaviruses. *Nat. Rev. Microbiol.* **17**, 181–192 (2019).
2. Zhou, P. et al. A pneumonia outbreak associated with a new coronavirus of probable bat origin. *Nature* **579**, 270–273 (2020).
3. Li, W. et al. Angiotensin-converting enzyme 2 is a functional receptor for the SARS coronavirus. *Nature* **426**, 450–454 (2003).
4. Walls, A. C. et al. Structure, function, and antigenicity of the SARS-CoV-2 spike glycoprotein. *Cell* **181**, 281–292 (2020).
5. Wrapp, D. et al. Cryo-EM structure of the 2019-nCoV spike in the prefusion conformation. *Science* **367**, 1260–1263 (2020).
6. Hoffmann, M. et al. SARS-CoV-2 cell entry depends on ACE2 and TMPRSS2 and is blocked by a clinically proven protease inhibitor. *Cell* **181**, 271–280 (2020).
7. Letko, M., Marzi, A. & Munster, V. Functional assessment of cell entry and receptor usage for SARS-CoV-2 and other lineage B betacoronaviruses. *Nat. Microbiol.* **5**, 562–569 (2020).
8. Hu, B. et al. Discovery of a rich gene pool of bat SARS-related coronaviruses provides new insights into the origin of SARS coronavirus. *PLoS Pathog.* **13**, e1006698 (2017).
9. Li, W. et al. Bats are natural reservoirs of SARS-like coronaviruses. *Science* **310**, 676–679 (2005).
10. Lau, S. K. P. et al. Severe acute respiratory syndrome coronavirus-like virus in Chinese horseshoe bats. *Proc. Natl Acad. Sci. USA* **102**, 14040–14045 (2005).
11. Ge, X.-Y. et al. Isolation and characterization of a bat SARS-like coronavirus that uses the ACE2 receptor. *Nature* **503**, 535–538 (2013).

12. Starr, T. N. et al. Deep mutational scanning of SARS-CoV-2 receptor binding domain reveals constraints on folding and ACE2 binding. *Cell* **182**, 1295–1310 (2020).
13. Tao, Y. & Tong, S. Complete genome sequence of a severe acute respiratory syndrome-related coronavirus from Kenyan bats. *Microbiol. Resour. Announc.* **8**, e00548–19 (2019).
14. Drexler, J. F. et al. Genomic characterization of severe acute respiratory syndrome-related coronavirus in European bats and classification of coronaviruses based on partial RNA-dependent RNA polymerase gene sequences. *J. Virol.* **84**, 11336–11349 (2010).
15. Zhou, H. et al. Identification of novel bat coronaviruses sheds light on the evolutionary origins of SARS-CoV-2 and related viruses. *Cell* **184**, 4380–4391 (2021).
16. Liu, K. et al. Binding and molecular basis of the bat coronavirus RaTG13 virus to ACE2 in humans and other species. *Cell* **184**, 3438–3451 (2021).
17. Ren, W. et al. Difference in receptor usage between severe acute respiratory syndrome (SARS) coronavirus and SARS-like coronavirus of bat origin. *J. Virol.* **82**, 1899–1907 (2008).
18. Becker, M. M. et al. Synthetic recombinant bat SARS-like coronavirus is infectious in cultured cells and in mice. *Proc. Natl Acad. Sci. USA* **105**, 19944–19949 (2008).
19. Wells, H. L. et al. The evolutionary history of ACE2 usage within the coronavirus subgenus Sarbecovirus. *Virus Evol.* **7**, veab007 (2021).
20. Boni, M. F. et al. Evolutionary origins of the SARS-CoV-2 Sarbecovirus lineage responsible for the COVID-19 pandemic. *Nat. Microbiol.* **5**, 1408–1417 (2020).
21. He, B. et al. Identification of diverse alphacoronaviruses and genomic characterization of a novel severe acute respiratory syndrome-like coronavirus from bats in China. *J. Virol.* **88**, 7070–7082 (2014).
22. Yang, X.-L. et al. Isolation and characterization of a novel bat coronavirus closely related to the direct progenitor of severe acute respiratory syndrome coronavirus. *J. Virol.* **90**, 3253–3256 (2015).
23. Lam, T. T.-Y. et al. Identifying SARS-CoV-2-related coronaviruses in Malayan pangolins. *Nature* **583**, 282–285 (2020).

24. Murakami, S. et al. Detection and characterization of bat Sarbecovirus phylogenetically related to SARS-CoV-2, Japan. *Emerg. Infect. Dis.* **26**, 3025–3029 (2020).
25. Delaune, D. et al. A novel SARS-CoV-2 related coronavirus in bats from Cambodia. *Nat. Commun.* **12**, 6563 (2021).
26. Guo, H. et al. Evolutionary arms race between virus and host drives genetic diversity in bat severe acute respiratory syndrome-related coronavirus spike genes. *J. Virol.* **94**, e00902–20 (2020).
27. Demogines, A., Farzan, M. & Sawyer, S. L. Evidence for ACE2-utilizing coronaviruses (CoVs) related to severe acute respiratory syndrome CoV in bats. *J. Virol.* **86**, 6350–6353 (2012).
28. Mou, H. et al. Mutations derived from horseshoe bat ACE2 orthologs enhance ACE2-Fc neutralization of SARS-CoV-2. *PLoS Pathog.* **17**, e1009501 (2021).
29. Li, W. et al. Receptor and viral determinants of SARS-coronavirus adaptation to human ACE2. *EMBO J.* **24**, 1634–1643 (2005).
30. Song, H.-D. et al. Cross-host evolution of severe acute respiratory syndrome coronavirus in palm civet and human. *Proc. Natl Acad. Sci. USA* **102**, 2430–2435 (2005).
31. Menachery, V. D. et al. A SARS-like cluster of circulating bat coronaviruses shows potential for human emergence. *Nat. Med.* **21**, 1508–1513 (2015).
32. Alkhovsky, S. et al. SARS-like coronaviruses in horseshoe bats (*Rhinolophus* spp.) in Russia, 2020. *Viruses* **14**, 113 (2022).
33. Reguera, J., Mudgal, G., Santiago, C. & Casasnovas, J. M. A structural view of coronavirus-receptor interactions. *Virus Res.* **194**, 3–15 (2014).
34. Tortorici, M. A. & Veesler, D. Structural insights into coronavirus entry. *Adv. Virus Res.* **105**, 93–116 (2019).
35. Tortorici, M. A. et al. Structural basis for human coronavirus attachment to sialic acid receptors. *Nat. Struct. Mol. Biol.* **26**, 481–489 (2019).
36. Bosch, B. J., Huizinga, E. G. & De Groot, R. J. Human coronaviruses OC43 and HKU1 bind to 9-O-acetylated sialic acids via a conserved receptor-binding site in spike protein domain A. *Proc. Natl Acad. Sci. USA* **116**, 2681–2690 (2019).

37. Thornton, J. W. Resurrecting ancient genes: experimental analysis of extinct molecules. *Nat. Rev. Genet.* **5**, 366–375 (2004).
38. Eick, G. N., Bridgham, J. T., Anderson, D. P., Harms, M. J. & Thornton, J. W. Robustness of reconstructed ancestral protein functions to statistical uncertainty. *Mol. Biol. Evol.* **34**, 247–261 (2017).
39. Hanson-Smith, V., Kolaczkowski, B. & Thornton, J. W. Robustness of ancestral sequence reconstruction to phylogenetic uncertainty. *Mol. Biol. Evol.* **27**, 1988–1999 (2010).
40. Wan, Y., Shang, J., Graham, R., Baric, R. S. & Li, F. Receptor recognition by the novel coronavirus from Wuhan: an analysis based on decade-long structural studies of SARS coronavirus. *J. Virol.* **94**, e00127–20 (2020).
41. Latinne, A. et al. Origin and cross-species transmission of bat coronaviruses in China. *Nat. Commun.* **11**, 4235 (2020).
42. Dinnon, K. H. III et al. A mouse-adapted model of SARS-CoV-2 to test COVID-19 countermeasures. *Nature* **586**, 560–566 (2020).
43. Roberts, A. et al. A mouse-adapted SARS-coronavirus causes disease and mortality in BALB/c mice. *PLoS Pathog.* **3**, e5 (2007).
44. Menachery, V. D. et al. SARS-like WIV1-CoV poised for human emergence. *Proc. Natl Acad. Sci. USA* **113**, 3048–3053 (2016).
45. Starr, T. N. & Thornton, J. W. Epistasis in protein evolution. *Protein Sci.* **25**, 1204–1218 (2016).
46. Tao, K. et al. The biological and clinical significance of emerging SARS-CoV-2 variants. *Nat. Rev. Genet.* **22**, 757–773 (2021).
47. Crook, J. M. et al. Metagenomic identification of a new sarbecovirus from horseshoe bats in Europe. *Sci. Rep.* **11**, 14723 (2021).
48. Seifert, S. N. & Letko, M. C. A Sarbecovirus found in Russian bats uses human ACE2. Preprint at <https://doi.org/10.1101/2021.12.05.471310> (2021).
49. Roelle, S. M., Shukla, N., Pham, A. T., Bruchez, A. M. & Matreyek, K. A. Expanded ACE2 dependencies of diverse SARS-like coronavirus receptor binding domains. Preprint at <https://doi.org/10.1101/2021.12.25.474149> (2021).

50. Guo, H. et al. Identification of a novel lineage bat SARS-related coronaviruses that use bat ACE2 receptor. *Emerg. Microbes Infect.* **10**, 1507–1514 (2021).
51. Menachery, V. D., Graham, R. L. & Baric, R. S. Jumping species-a mechanism for coronavirus persistence and survival. *Curr. Opin. Virol.* **23**, 1–7 (2017).
52. Katoh, K. & Standley, D. M. MAFFT multiple sequence alignment software version 7: improvements in performance and usability. *Mol. Biol. Evol.* **30**, 772–780 (2013).
53. Suyama, M., Torrents, D. & Bork, P. PAL2NAL: robust conversion of protein sequence alignments into the corresponding codon alignments. *Nucleic Acids Res.* **34**, W609–W612 (2006).
54. Stamatakis, A. RAxML version 8: a tool for phylogenetic analysis and post-analysis of large phylogenies. *Bioinformatics* **30**, 1312–1313 (2014).
55. Ashkenazy, H. et al. FastML: a web server for probabilistic reconstruction of ancestral sequences. *Nucleic Acids Res.* **40**, W580–W584 (2012).
56. Kosakovsky Pond, S. L., Posada, D., Gravenor, M. B., Woelk, C. H. & Frost, S. D. W. Automated phylogenetic detection of recombination using a genetic algorithm. *Mol. Biol. Evol.* **23**, 1891–1901 (2006).
57. Wentz, A. E. & Shusta, E. V. A novel high-throughput screen reveals yeast genes that increase secretion of heterologous proteins. *Appl. Environ. Microbiol.* **73**, 1189–1198 (2007).
58. Gietz, R. D. & Schiestl, R. H. Large-scale high-efficiency yeast transformation using the LiAc/SS carrier DNA/PEG method. *Nat. Protoc.* **2**, 38–41 (2007).
59. Crawford, K. H. D. & Bloom, J. D. alignparse: a Python package for parsing complex features from high-throughput long-read sequencing. *J. Open Source Softw.* **4**, 1915 (2019).
60. Peterman, N. & Levine, E. Sort-seq under the hood: implications of design choices on large-scale characterization of sequence-function relations. *BMC Genomics* **17**, 206 (2016).
61. Delignette-Muller, M. & Dutang, C. fitdistrplus: An R Package for fitting distributions. *J. Stat. Softw.* **64**, 1–34 (2015).
62. Gietz, R. D. & Schiestl, R. H. High-efficiency yeast transformation using the LiAc/SS carrier DNA/PEG method. *Nat. Protoc.* **2**, 31–34 (2007).

63. Crawford, K. H. D. et al. Protocol and reagents for pseudotyping lentiviral particles with SARS-CoV-2 spike protein for neutralization assays. *Viruses* **12**, 513 (2020).
64. Starr, T. N. et al. SARS-CoV-2 RBD antibodies that maximize breadth and resistance to escape. *Nature* **597**, 97–102 (2021).
65. Tortorici, M. A. et al. Broad sarbecovirus neutralization by a human monoclonal antibody. *Nature* **597**, 103–108 (2021).
66. Johnson, B. A. et al. Loss of furin cleavage site attenuates SARS-CoV-2 pathogenesis. *Nature* **591**, 293–299 (2021).
67. Adams, R. M., Mora, T., Walczak, A. M. & Kinney, J. B. Measuring the sequence-affinity landscape of antibodies with massively parallel titration curves. *eLife* **5**, e23156 (2016).
68. Frieman, M. et al. Molecular determinants of severe acute respiratory syndrome coronavirus pathogenesis and virulence in young and aged mouse models of human disease. *J. Virol.* **86**, 884–897 (2012).
69. Gu, H. et al. Adaptation of SARS-CoV-2 in BALB/c mice for testing vaccine efficacy. *Science* **369**, 1603–1607 (2020).
70. Huang, K. et al. Q493K and Q498H substitutions in spike promote adaptation of SARS-CoV-2 in mice. *EBioMedicine* **67**, 103381 (2021).
71. Montagutelli, X. et al. The B1.351 and P.1 variants extend SARS-CoV-2 host range to mice. Preprint at <https://doi.org/10.1101/2021.03.18.436013> (2021).

Acknowledgements

We thank the staff at the Fred Hutch Flow Cytometry and Genomics facilities and the Scientific Computing group supported by ORIP grant S10OD028685; Z. Shi for sharing *R. sinicus* and *R. affinis* ACE2 sequences from a preprint before formal publication; H. Tani for providing the reagents necessary for preparing VSV pseudotyped viruses; S. Goldstein and A. Chan for discussions; and all sequence contributors, including contributors to GISAID (https://github.com/jbloomlab/SARS-CoV_homolog_survey/tree/master/RBD_ASR/gisaid). This study was supported by the National Institute of Allergy and Infectious Diseases (DP1AI158186 and HHSN272201700059C to D.V., and R01AI141707 to J.D.B.), the National Institute of General Medical Sciences (R01GM120553 to D.V., and 5T32GM008268-32 to S.K.Z.), a Pew Biomedical Scholars Award (to D.V.), Investigators in the Pathogenesis

of Infectious Disease Awards from the Burroughs Wellcome Fund (to D.V. and J.D.B.), Fast Grants (to D.V.), the Bill & Melinda Gates Foundation (OPP1156262 to D.V., and INV-004949 to J.D.B.) and the Russian Foundation for Basic Research (20-04-60154 ‘An analysis of genetic diversity of zoonotic viruses in Russian populations of bats and rodents’ to S.A.). T.N.S. is an HHMI Fellow of the Damon Runyon Cancer Research Foundation. D.V. and J.D.B. are investigators of the Howard Hughes Medical Institute.

Author information

Author notes

1. These authors contributed equally: Tyler N. Starr, Samantha K. Zepeda

Affiliations

1. Basic Sciences Division, Fred Hutchinson Cancer Research Center, Seattle, WA, USA

Tyler N. Starr, Allison J. Greaney & Jesse D. Bloom

2. Howard Hughes Medical Institute, Seattle, WA, USA

Tyler N. Starr, David Veesler & Jesse D. Bloom

3. Department of Biochemistry, University of Washington, Seattle, WA, USA

Samantha K. Zepeda, Alexandra C. Walls & David Veesler

4. Department of Genome Sciences, University of Washington, Seattle, WA, USA

Allison J. Greaney & Jesse D. Bloom

5. N.F. Gamleya National Center of Epidemiology and Microbiology, Ministry of Health of the Russian Federation, Moscow, Russia

Sergey Alkhovsky

Contributions

Conceptualization: T.N.S., S.K.Z., D.V. and J.D.B. Phylogenetics: T.N.S. Yeast-display methodology: T.N.S. and A.J.G. Yeast-display experiments: T.N.S. BLI measurements: S.K.Z. Pseudovirus entry assays: S.K.Z. and

A.C.W. Data analysis: T.N.S. Khosta-1 and Khosta-2 sampling and sequencing: S.A. Supervision: D.V. and J.D.B. Writing—original draft: T.N.S., S.K.Z., D.V. and J.D.B. All of the authors read and edited the manuscript.

Corresponding authors

Correspondence to [Tyler N. Starr](#), [David Veesler](#) or [Jesse D. Bloom](#).

Ethics declarations

Competing interests

J.D.B. consults for Moderna on viral evolution and epidemiology and Flagship Labs 77 on deep mutational scanning. J.D.B. may receive a share of IP revenue as an inventor on a Fred Hutchinson Cancer Research Center-optioned technology/patent (US Patent and Trademark Office application WO2020006494) related to deep mutational scanning of viral proteins. The Veesler laboratory (S.K.Z., A.C.W. and D.V.) has received an unrelated sponsored research agreement from Vir Biotechnology.

Peer review

Peer review information

Nature thanks Zheng-Li Shi and the other, anonymous, reviewer(s) for their contribution to the peer review of this work. Peer review reports are available.

Additional information

Publisher's note Springer Nature remains neutral with regard to jurisdictional claims in published maps and institutional affiliations.

Extended data figures and tables

Extended Data Fig. 1 Robustness of the root of the sarbecovirus ingroup.

To establish robustness of our conclusion that the first sarbecovirus divergence is between sarbecoviruses from Africa and Europe and those from Asia, we inferred phylogenies based on alignments of RBD (SARS-CoV-2 spike residues N331-T531) (**a,b**) or the full spike gene (**c,d**) and nucleotide (**a, c**) or amino-acid (**b, d**) alignments and substitution models. In all four cases, the first sarbecovirus bipartition is placed between sarbecoviruses in Africa/Europe and those in Asia. The placement of the overall tree root is arbitrary with respect to the relationship among non-sarbecovirus outgroups, but this arbitrary placement does not impact the sarbecovirus ingroup rooting. The primary variations among trees includes a potential paraphyletic separation of BtKY72 and BM48–31 from Europe and Africa such that they do not form a monophyletic clade (**b**; also seen in Extended Data Fig. [10a-c](#)), and variation in the relationships among the three Asia sarbecovirus clades (whose relationship is also inferred with a very low bootstrap support value in our primary phylogeny in Fig. [1a](#)). Known recombination of RBDs with respect to other spike segments among viruses creates incongruencies between spike and RBD trees among Asian sarbecovirus lineages (e.g. ZC45 and ZXC21), though recombination has not been reported among the Africa and Europe spikes and those in Asia. Scale bar, expected number nucleotide or amino-acid substitutions per site. Node labels illustrate bootstrap support values for sarbecovirus and Asia sarbecovirus monophyly. Sequences colored by their RBD clade as in Fig. [1a](#).

Extended Data Fig. 2 Experimental details of Sort-seq assays.

a, RBD yeast-surface display enables detection of folded RBD expression and ACE2 binding. **b**, Representative gating for single (SSC-A versus FSC-A, SSC-W versus SSC-H, and FSC-W versus FSC-W), RBD+ (FITC versus FSC-A) cells. **c**, Representative bins drawn on single cells for expression Sort-seq measurements. **d**, Representative bins drawn on single, RBD+ cells for ACE2 Tite-seq^{[12,67](#)} measurements. **e**, Per-variant expression, shown as violin plots across replicate barcodes representing each variant within the gene libraries. **f**, Number of distinct barcodes for

each parental (top) or mutant (bottom) RBD genotype used in the determination of final pooled measurements across libraries. **g**, Correlation in measured phenotypes between independently assembled and barcoded gene library duplicates for parental (top) or mutant (bottom) RBD genotypes.

Extended Data Fig. 3 Normalization and controls for biolayer interferometry binding and pseudovirus entry assays.

a,b Biolayer interferometry binding analysis of a range of *R. affinis* ACE2-Fc (**a**) or human ACE2-Fc (**b**) concentrations to biotinylated BtKY72 RBD (parental or mutant) immobilized at the surface of streptavidin biosensors. **c**, Representative Western blots for quantification of spike incorporation into pseudoviral particles. Anti-FLAG (Sigma F3165) identifies incorporation of 3xFLAG-tagged spike, and anti-VSV-M (Kerafast EB0011) identifies level of VSV backbone. Viral inputs into cell entry assays were normalized across pseudoviral particles by S incorporation as determined in the anti-FLAG Western blot. Blot representative of biological duplicate generations of each pseudovirus. For gel source data, see Supplementary Fig. 1. **d**, Entry into *R. affinis* ACE2-expressing HEK293T cells by mock VSV particles produced in cells in which no spike gene was transfected. Each point represents the mean of technical triplicates for assays performed with independent preparation of pseudoviral particles (biological replicates). **e**, Entry of pseudoviral particles into HEK293T cells not transfected with any ACE2. Each point represents the mean of technical triplicates for assays performed with independent preparation of pseudoviral particles (biological replicates).

Extended Data Fig. 4 Clade 2 RBD binding to an expanded panel of *R. sinicus* ACE2 alleles.

Binding curves for Clade 1a (SARS-CoV-1 Urbani and RsSHC014) and Clade 2 (YN2013 and HKU3-1) sarbecovirus RBDs for 8 *R. sinicus* ACE2 alleles. Measurements performed with yeast-displayed RBDs and purified dimeric ACE2 proteins, measured by flow cytometry. Data from a single experimental replicate. Region of sampling for bat sarbecoviruses and *R.*

sinicus ACE2 alleles are provided. RsSHC014, YN2013, and HKU3-1 were all sampled from *R. sinicus* bats.

Extended Data Fig. 5 Full set of RBD ancestral sequence reconstructions.

a, Phylogeny with labelled nodes representing all ancestors tested, including nodes within the SARS-CoV-1 and SARS-CoV-2 clades leading to the human viruses. Branches are annotated with the number of amino-acid substitutions and indels that are inferred to have occurred along each branch. **b**, Phenotypes of all most plausible ancestral sequences (including repetition of the data represented in Fig. 2b).

Extended Data Fig. 6 Robustness to uncertainties in ancestral reconstructions.

a, We performed ancestral sequence reconstructions on phylogenies constraining sister relationships between SARS-CoV-2 clade and clade 2 (tree1) or SARS-CoV-1 and SARS-CoV-2 clades (tree2) due to ambiguity in these relationships (Fig. 1a and Extended Data Fig. 1). **b**, ACE2 binding of alternative reconstructions. “Alt” ancestors incorporate all secondary reconstructed states with posterior probability > 0.2;³⁸ “tree1” and “tree2” ancestors are inferred on the constrained trees in (a); and “ins117-118” tests the ambiguity of an indel separate from the remaining substitutions in AncSarbecovirus_alt. Sequence differences are listed at right relative to the maximum a posteriori (MAP) ancestors from Fig. 2b and Extended Data Fig. 5b. Mutations are colored red if they were sufficient to abolish the ancestral phenotype and blue if they reinforced it (Extended Data Fig. 7). Dramatic changes to inferred ancestral phenotypes are mostly observed in the alt ancestors which are the most probabilistically distant, while the tree1 and tree2 alternatives generally recapitulate the MAP phenotypes. The exception is AncSARS1a, where the tree1 and tree2 alternatives better match what would be expected based on the descendent RBD phenotypes (Fig. 1b). **c**, RBD amino acid alignment, indicating a potential recombination breakpoint identified by GARD⁵⁶ (from underlying nucleotide sequence). **d**, Relative support values for possible recombination

breakpoints. **e**, Phylogenies inferred for the putative non-recombinant RBD segments. Arrows point to key changes in the segment 2 sub-tree. Each change is supported by weak bootstrap support values, and this hypothesis introduces a non-parsimonious history with respect to an indel at position 482. We reconstructed AncSarbecovirus_GARD and AncAsia_GARD as concatenated segment 1 and 2 reconstructions. Mutations that distinguish the GARD and MAP ancestor are listed at bottom. **f**, Binding of GARD ancestors to human and *R. affinis* 9479 ACE2 was determined in isogenic yeast-display titrations.

Extended Data Fig. 7 Binding of RBD single mutants to each ACE2.

Each heatmap square illustrates the change in binding caused by the indicated mutation at the indicated position (SARS-CoV-2 numbering), according to the color key shown on the upper-right. Yellow, mutations that were absent from the library or not sampled with sufficient depth in a particular experiment. x markers indicate the wildtype state at each position in each RBD background.

Extended Data Fig. 8 Existing data on sarbecoviruses in mice, and affinities of RBDs and key mutants for mouse versus human ACE2.

a, Summary of infectivity and pathogenesis of natural sarbecovirus and mouse-adapted strains from prior studies^{31,42,43,44,68,69,70,71}. **b**, High-throughput titration curves for relevant genotypes from (a). Details as in Fig. 1d. Strength of binding to mouse ACE2 explains the infectivity and pathogenesis of SARS-CoV-1 Urbani and RsSHC014^{31,43}, relative to the weak or absent replication of WIV1⁴⁴ and SARS-CoV-2⁴² in mice. Mutagenesis data explain the inefficient mouse infectivity of the SARS-CoV-2 B.1.1.7 isolate⁷¹ which incorporates the N501Y RBD mutation, relative to the efficient replication of the mouse-adapted SARS-CoV-2 isolate containing Q498Y⁴² or the pathogenic WBP-1 strain containing Q493K and Q498H⁷⁰. **c**, An ideal mouse-adapted laboratory sarbecovirus strain would bind mouse ACE2 but not human ACE2 due to biosafety

considerations. The large red points indicate the affinity of the parental RBD for human and mouse ACE2. The smaller black points indicate mutations, and key mutations that enhance binding to mouse versus human ACE2 are labelled (using SARS-CoV-2 numbering). Further mouse ACE2 specificity may be enabled via mutations at other positions not surveyed in our set of six positions.

[Extended Data Fig. 9 Epistasis and turnover in mutational effects.](#)

a, Example correlations in binding affinities for mutants in distinct RBD backgrounds at each site for human ACE2. Plots illustrate mutant avidities for human ACE2 and mean absolute error (residual) in the correlation for mutation measurements in GD-Pangolin (top) and SARS-CoV-1 Urbani (bottom) versus SARS-CoV-2. Plotting symbols indicate amino acid for each measurement. **b**, Epistatic turnover in mutational effects across RBD backgrounds. Details as in Fig. 3g, but incorporating mutation effects among RBD pairs across all tested ACE2s. Blue line and shaded grey, LOESS mean and 95% CI trendline. See Extended Data Fig. 9b for analysis across all ACE2 orthologues.

[Extended Data Fig. 10 Robustness of rooting and AncSarbecovirus phenotype in a phylogeny incorporating newly reported sequences.](#)

a-d, Phylogenetic inference with inclusion of newly reported sarbecovirus sequences (Fig. 4a). As in Extended Data Fig. 1, we infer phylogenies with RBD (**a,b**) and full spike alignments (**c,d**), both on nucleotide sequences (**a,c**) and translated amino acid (**b,d**) sequence alignments. The full set of outgroup betacoronavirus sequences shown in Extended Data Fig. 1 were also included in this tree inference but truncated from the display for visual clarity. The phylogeny in Fig. 4a is a constrained version of the RBD nucleotide tree from (**a**) where we constrained a monophyletic relationship among Africa/Europe sarbecoviruses due to uncertainty in the exact placement of the root within or relative of the Africa/Europe sarbecovirus clade. **e**, ACE2 binding by parental RBD and candidate mutants in an

updated AncSarbecovirus sequence (“v2”) inferred from the phylogeny in Fig. 4a that incorporates many newly described sarbecovirus RBDs, including some in important new phylogenetic locations. The unconstrained tree in (a) leads to inference of an AncSarbecovirus sequence that is identical to Khosta-2 (which also binds ACE2). Sequence differences between the original MAP AncSarbecovirus and the “v2” reconstruction are listed at top. Measurements performed with yeast-displayed RBDs and purified dimeric ACE2 proteins, measured by flow cytometry. Data from a single experimental replicate.

Supplementary information

Supplementary Fig. 1

Uncropped images of the western blots in Extended Data Fig. 3c.

Reporting Summary

Peer Review File

Rights and permissions

Open Access This article is licensed under a Creative Commons Attribution 4.0 International License, which permits use, sharing, adaptation, distribution and reproduction in any medium or format, as long as you give appropriate credit to the original author(s) and the source, provide a link to the Creative Commons license, and indicate if changes were made. The images or other third party material in this article are included in the article’s Creative Commons license, unless indicated otherwise in a credit line to the material. If material is not included in the article’s Creative Commons license and your intended use is not permitted by statutory regulation or exceeds the permitted use, you will need to obtain permission directly from the copyright holder. To view a copy of this license, visit <http://creativecommons.org/licenses/by/4.0/>.

Reprints and Permissions

About this article

Cite this article

Starr, T.N., Zepeda, S.K., Walls, A.C. *et al.* ACE2 binding is an ancestral and evolvable trait of sarbecoviruses. *Nature* **603**, 913–918 (2022).
<https://doi.org/10.1038/s41586-022-04464-z>

- Received: 18 July 2021
- Accepted: 25 January 2022
- Published: 03 February 2022
- Issue Date: 31 March 2022
- DOI: <https://doi.org/10.1038/s41586-022-04464-z>

Share this article

Anyone you share the following link with will be able to read this content:

[Get shareable link](#)

Sorry, a shareable link is not currently available for this article.

[Copy to clipboard](#)

Provided by the Springer Nature SharedIt content-sharing initiative

Further reading

- [**SARS-CoV-2: tracing the origin, tracking the evolution**](#)
 - Konstantinos Voskarides

BMC Medical Genomics (2022)

This article was downloaded by **calibre** from <https://www.nature.com/articles/s41586-022-04464-z>

| [Section menu](#) | [Main menu](#) |

- Article
- Open Access
- [Published: 28 January 2022](#)

Memory B cell repertoire from triple vaccinees against diverse SARS-CoV-2 variants

- [Kang Wang^{1,na1}](#),
- [Zijing Jia^{1,2,na1}](#),
- [Linilin Bao^{3,na1}](#),
- [Lei Wang^{1,2,na1}](#),
- [Lei Cao^{1,na1}](#),
- [Hang Chi^{4,na1}](#),
- [Yaling Hu^{5,na1}](#),
- [Qianqian Li^{6,na1}](#),
- [Yunjiao Zhou^{7,na1}](#),
- [Yinan Jiang⁸](#),
- [Qianhui Zhu^{1,2}](#),
- [Yongqiang Deng](#) ORCID: [orcid.org/0000-0002-2306-1039⁴](https://orcid.org/0000-0002-2306-1039),
- [Pan Liu^{1,2}](#),
- [Nan Wang¹](#),
- [Lin Wang](#) ORCID: [orcid.org/0000-0002-2571-4320⁵](https://orcid.org/0000-0002-2571-4320),
- [Min Liu⁵](#),
- [Yurong Li⁵](#),
- [Boling Zhu¹](#),
- [Kaiyue Fan^{1,2}](#),
- [Wangjun Fu^{1,2}](#),
- [Peng Yang^{1,2}](#),
- [Xinran Pei¹](#),
- [Zhen Cui^{1,2}](#),
- [Lili Qin](#) ORCID: [orcid.org/0000-0002-0700-0180⁸](https://orcid.org/0000-0002-0700-0180),
- [Pingju Ge⁸](#),
- [Jiajing Wu⁶](#),

- [Shuo Liu⁶](#),
- [Yiding Chen⁸](#),
- [Weijin Huang](#) [ORCID: orcid.org/0000-0002-4246-8889⁶](#),
- [Qiao Wang⁷](#),
- [Cheng-Feng Qin](#) [ORCID: orcid.org/0000-0002-0632-2807⁴](#),
- [Youchun Wang](#) [ORCID: orcid.org/0000-0001-9769-5141⁶](#),
- [Chuan Qin](#) [ORCID: orcid.org/0000-0002-6261-1232³](#) &
- [Xiangxi Wang](#) [ORCID: orcid.org/0000-0003-0635-278X^{1,2}](#)

[Nature](#) volume 603, pages 919–925 (2022)

- 66k Accesses
- 174 Altmetric
- [Metrics details](#)

Subjects

- [Microbiology](#)
- [SARS-CoV-2](#)

Abstract

Omicron (B.1.1.529), the most heavily mutated SARS-CoV-2 variant so far, is highly resistant to neutralizing antibodies, raising concerns about the effectiveness of antibody therapies and vaccines^{1,2}. Here we examined whether sera from individuals who received two or three doses of inactivated SARS-CoV-2 vaccine could neutralize authentic Omicron. The seroconversion rates of neutralizing antibodies were 3.3% (2 out of 60) and 95% (57 out of 60) for individuals who had received 2 and 3 doses of vaccine, respectively. For recipients of three vaccine doses, the geometric mean neutralization antibody titre for Omicron was 16.5-fold lower than for the ancestral virus (254). We isolated 323 human monoclonal antibodies derived from memory B cells in triple vaccinees, half of which recognized the receptor-binding domain, and showed that a subset (24 out of 163) potently neutralized all SARS-CoV-2 variants of concern, including Omicron. Therapeutic treatments with representative broadly neutralizing monoclonal antibodies were highly protective against infection of mice with SARS-CoV-2 Beta (B.1.351) and Omicron. Atomic structures of the Omicron spike protein in complex with three classes of antibodies that were active against all five variants of concern defined the binding and neutralizing determinants and revealed a key antibody escape site, G446S, that confers greater resistance to a class of

antibodies that bind on the right shoulder of the receptor-binding domain by altering local conformation at the binding interface. Our results rationalize the use of three-dose immunization regimens and suggest that the fundamental epitopes revealed by these broadly ultrapotent antibodies are rational targets for a universal sarbecovirus vaccine.

[Download PDF](#)

Main

The ongoing evolution and emergence of SARS-CoV-2 variants has increased concerns about the effectiveness of monoclonal antibody therapies and vaccines^{3,4,5}, posing challenges for global pandemic control. These variants have been classed as variants of interest (VOI) or variants of concern (VOC) by the World Health Organization (WHO). The more recently identified Omicron variant, designated as a new VOC, has led to a surge in COVID-19 cases in South Africa and is now spreading across the world⁶. Omicron is the most heavily mutated variant to emerge so far, with more than 30 mutations in its spike (S) protein, 15 of which occur in the receptor binding domain (RBD). In addition, there are three small deletions and one three-residue insertion in the N-terminal domain (NTD) of the S1 subunit (Fig. 1a). The pattern of some of these alterations, similar to those noted in previous VOCs, such as Δ69–70 in Alpha (B.1.1.7), N501Y in Alpha, Beta and Gamma (P.1), and P681H in Alpha and Delta (B.1.617.2), are associated with enhanced transmissibility, whereas many substitutions, including G142D/Δ143–145, ins214EPE, K417N, T478K, E484A, Q493R and N501Y, are closely linked with resistance to neutralizing antibodies and vaccine induced humoral immunity^{3,5,7,8,9,10,11} (Fig. 1a, b).

Fig. 1: Evolution and neutralization characteristics of Omicron variant.

 **figure 1**

a, A linear representation of Omicron S with mutations indicated. The replacements are in red, deletions are in grey and insertions are in purple. **b**, Distribution of Omicron S mutations on the cryo-EM structure³⁴ of pre-fusion S trimer determined at pH 7.5 (Protein Data Bank (PDB) ID 7WG6). The mutations listed in **a** are indicated in the ‘up’ protomer shown in cartoon, with mutated residues highlighted as spheres and coloured as in **a**. The RBD, NTD, SD1 and S2 domains of this subunit are marked with arrows and coloured green, blue, magenta and yellow, respectively; the other two protomers are in the ‘down’ state and shown in surface representation in pale cyan and pale yellow. Alpha, B.1.1.7; Gamma, P.1; Lambda, C.37. **c**, The neutralizing antibody response against WT and Omicron SARS-CoV-2 authentic virus for sera from healthy vaccinees who received two ($n = 60$ volunteers) or three ($n = 60$ volunteers) doses of Coronavac. Data are geometric mean \pm s.d. of technical triplicates. The dotted line represents the detection limit. NT₅₀ values of less than 4 were plotted as 2. Fold difference in neutralizing antibody titre Delta or Omicron over WT for each group of sera is shown above each set of points.

Although COVID-19 vaccines have continued to be effective against severe diseases and deaths, including those caused by the circulating Delta variant, waning immunity and massive breakthrough infections caused by viral diversification warrant a third vaccine dose or new vaccines. To combat the current resurgence of the epidemic, the US Food and Drug Administration has authorized use of a third booster dose for all

adults after completion of primary vaccination with approved COVID-19 vaccine¹². This step seems essential, because preliminary studies have indicated that three doses of Pfizer-BioNTech mRNA vaccine neutralize the Omicron variant with an approximately 40-fold decline in viral titre, whereas two doses are less effective^{1,13}. However, these preliminary data on the sensitivity of Omicron to neutralization require further independent confirmation. The clinical effects of natural and vaccine-induced immunity in relation to protection from infection and severe disease require urgent investigation.

Authentic Omicron neutralization

CoronaVac, a β-propiolactone-inactivated SARS-CoV-2 vaccine against COVID-19, has been approved for emergency use and recommended for a booster (third) vaccination dose in older people by the WHO^{14,15}. We collected serum specimens from two groups of individuals who had received two doses ($n = 60$, at $t = 0$ and 1 month) or three doses ($n = 60$, at $t = 0, 1$ and 7 months) of CoronaVac to evaluate neutralization titres against the Omicron and Delta variants using live SARS-CoV-2. None of the volunteers recruited for vaccination were infected with SARS-CoV-2 before the study. Blood samples were collected from vaccinees four weeks after their last vaccination to compare neutralizing antibody titres against circulating SARS-CoV-2 variants. We used an early passage of isolated (CHK06 strain) and sequence-confirmed live Omicron virus for neutralization assays in this study. Among recipients of three doses of CoronaVac, the geometric mean half-maximal neutralizing titres (GMT NT₅₀) against live wild-type (WT) virus, Delta and Omicron variants were 253.9, 77.8 and 15.4, respectively. Compared with WT virus, neutralizing titres against Delta and Omicron were, on average, 3.3-fold and 16.5-fold lower, respectively (Fig. 1c). Only 3 out of 60 samples had a NT₅₀ titre of less than 8 against Omicron, with a seroconversion rate of 95% for neutralizing antibodies (Fig. 1c). However, the effectiveness of a two-dose vaccine regime against Omicron infection is relatively low. Among recipients of two doses of CoronaVac, the mean NT₅₀ titre against Delta was 6.6, 5.1-fold lower compared with WT virus, but none of the serum specimens had an NT₅₀ titre higher than 8 against Omicron (Fig. 1c). Compared with vaccinees who had received two doses, sera from vaccinees who had received three doses exhibited smaller reductions in neutralization titres against Delta, consistent with previous observations that three-dose administration of inactivated virus vaccine leads to enhanced neutralizing breadth against SARS-CoV-2 variants⁷.

Antibodies elicited by three-dose vaccination

We previously sorted immunoglobulin-expressing (IgG+) memory B cells from peripheral blood mononuclear cells (PBMCs) of four individuals who had received three doses of CoronaVac using prefusion SARS-CoV-2 S as a bait^{7,16}. In total, we sorted 1,800 SARS-CoV-2 S-specific memory B cells, obtained 422 paired heavy chain and light chain antibody sequences, and selected 323 antibodies for expression (Supplementary Table 1). Characterization by enzyme-linked immunosorbent assay (ELISA) showed that 163, 100 and 51 antibodies recognized the RBD, NTD and S2 domain, respectively and 9 antibodies did not bind S (Fig. 2a). Affinity measurements using biolayer interferometry (BLI) showed that nearly all RBD-directed antibodies bound to WT SARS-CoV-2 S at sub-nanomolar levels (Supplementary Table 1), and we selected 127 of these antibodies showing neutralization activities against both authentic and pseudotyped WT SARS-CoV-2 for further investigation. More than 93% of these antibodies exhibited broad binding activities to most VOCs and VOIs (Supplementary Table 1). Notably, 85% of these antibodies cross-reacted with the Omicron S RBD (Supplementary Table 1). Around 80% of the antibodies that bound the NTD did not bind Omicron S. Additionally, NTD antibodies also showed relatively poor cross-reactivity to S from the other four VOCs, owing to the increased diversity of the NTD compared with other regions of S (Fig. 1a, b, Supplementary Table 1).

Fig. 2: Characteristics of a subset of broadly neutralizing antibodies from recipients of a booster immunization.

 figure 2

a, Vertical slice chart shows the gross distribution of binding epitopes of monoclonal antibodies isolated from individuals who received three doses of inactivated SARS-CoV-2 vaccine. The total number of antibodies and the percentage of antibodies that recognize the RBD, NTD and S2 domain are indicated. **b**, Heat map representation of 41 selected representative monoclonal antibodies against pseudotyped viruses expressing WT or variant SARS-CoV-2 S. The colour bar on the right shows IC₅₀ values for the indicated monoclonal antibodies against pseudotyped viruses in **c**. Antibodies marked with star were selected for structural analysis. **c**, Heat map showing the competition ability of selected monoclonal antibodies with human ACE2. Competition ability is represented by the AUC, ranging from 1 (weakest) to 24 (strongest). **d**, Neutralization curves for the selected antibodies towards pseudotyped viruses expressing Omicron S. Data represent three groups of antibodies shown in **b**. Yellow indicates antibodies with high neutralizing activity against all five VOCs; green indicates antibodies with high neutralizing activity against four VOCs and intermediate neutralizing activity against Omicron; red indicates antibodies with high neutralizing activity against four VOCs and weak neutralizing activity against Omicron. XGv347, XGv282 and XGv265 were selected as representatives of each group. All experiments were performed in duplicate.

Monoclonal antibodies with broad neutralization

Results of pseudovirus neutralization assays performed using virus expressing the S of WT virus or VOCs^{17,18} identified 31 RBD-targeting antibodies that were particularly potent, with half-maximal inhibitory concentration (IC₅₀) values ranging from 0.002 to 0.800 µg ml⁻¹ against WT virus and the VOCs (Fig. 2b). Among these, 30 antibodies neutralized the virus by directly blocking the interactions between the RBD and its receptor, human angiotensin-converting enzyme 2 (ACE2), and 1 antibody used other mechanisms to neutralize viral infection (Fig. 2c, Extended Data Fig. 1). A subset of RBD antibodies (13 and 24) neutralized virus expressing Omicron S, with IC₅₀ values below 0.02 µg ml⁻¹ and 0.1 µg ml⁻¹, respectively. This neutralization is as potent as neutralization by best-in-class antibodies against virus expressing WT S (Fig. 2b,d, Supplementary Table 1, 2)—we obtained IC₅₀ values of 0.27 and 0.16 µg ml⁻¹ for the well-studied therapeutic antibodies VIR-7831 and DXP-604, respectively. These values are 10- to 40-fold higher than those of the subset antibodies (Extended Data Fig. 2, Supplementary Table 1). Neutralization activity of some antibody drugs, such as REGN10933, REGN10987, LY-CoV555, LY-CoV016, AZD1061 and AZD8895, was almost completely lost with virus expressing Omicron S² (Extended Data Fig. 2, Supplementary Table 1). Meanwhile, specific antibodies with high neutralizing potency against WT and some VOCs (IC₅₀ < 0.2 µg ml⁻¹) were identified and these comprised approximately 30% of the antibody repertoire (Supplementary Data Table

[1](#)). A previous study revealed that the numbers of nucleotide mutations in the V gene for RBD-specific antibodies in individuals who had received three doses of SARS-CoV-2 vaccine were substantially higher than in individuals who had received two doses, and antibodies from individuals who had received three doses exhibited higher binding activities than those from individuals who had received two doses^{[5](#)}—these results indicated the evolution of a wide range of antibodies over time. Experiments repeated using authentic virus, including WT virus and five circulating VOCs, showed similar neutralization patterns by all these antibodies (Extended Data Fig. [3](#)), further verifying the neutralizing potency and breadth for this subset of antibody repertoire elicited by three doses of vaccine.

Structures of Omicron S trimer and antibodies

Antibodies targeting the RBD can be categorized into six general classes (I–VI) on the basis of cluster analysis of epitopes of 265 available RBD–neutralizing antibody complex structures^{[7](#)}—these classes are related to the previously reported four classes on the basis of competition with the ACE2 for binding to S and recognition of the ‘up’ or ‘down’ states of the three RBDs in S^{[19,20,21](#)}. ELISA-based square competition-matrix analysis with the aid of existing structural data revealed the presence of three major groups in this subset of antibody repertoire (Extended Data Fig. [4](#)). To delineate the structural basis for antibody-mediated neutralization, we determined the cryo-electron microscopy (cryo-EM) structure of a prefusion-stabilized Omicron S trimer in complex with representative Fab fragments. The two highly potent antibodies against Omicron (XGv347 and XGv289, with IC₅₀ values of 0.006 and 0.016 µg ml⁻¹, respectively), one monoclonal antibody (XGv282 with IC₅₀ of 0.268 µg ml⁻¹) with intermediate neutralizing activities against Omicron, but high neutralizing activities against the other four VOCs, and a monoclonal antibody (XGv265 with IC₅₀ of 7.479 µg ml⁻¹) with more than 500-fold decreased neutralization against Omicron, but potent neutralization against four other VOCs were selected for structural investigations (Fig. [2b](#)). We obtained cryo-EM reconstructions of these complexes at 3.3–3.8 Å, and performed local refinement to further improve the densities around the binding interface between RBD and antibodies, enabling reliable analysis of the details of the interaction (Fig. [3](#), Extended Data Figs. [5](#)–[7](#), Extended Data Table [1](#)).

Fig. 3: Structural basis of the broad and potent neutralization of representative antibodies.

 **figure 3**

a, Side and top views of Cryo-EM maps of Omicron S trimer in complex with XGv347 (S states 1–3), XGv289, XGv282 and XGv265. State 1, one up RBD and one down RBD; state 2, three down RBDs; state 3, two up RBDs. **b**, Cartoon representations of the structures of Omicron S RBD in complex with XGv347 (top left), XGv289 (top right), XGv282 (bottom left) and XGv265 (bottom right). Two views are shown to illustrate the binding modes of the four antibodies. RBD is shown

in cyan. **c**, Interactions between the four antibodies and Omicron S RBD. The CDRs of the four antibodies that interact with the RBD are shown as cartoon over the light green surface of RBD. The mutation sites on Omicron S RBD are in red; the epitopes of antibodies are in deep green and the overlap of mutation sites and epitopes are in blue. Residues of each epitope are indicated in the corresponding regions. **d**, Superposition of Omicron and WT S trimers. Omicron S trimer is in cyan and WT S trimer is in yellow.

The strauctures of XGv347–Omicron S structures revealed three distinct conformational states: three XGv347 Fabs bound to a completely closed S with three RBDs in the down state; two XGv347 Fabs bound to RBD in either two up or one up and one down configuration (Fig. 3a). By contrast, each of the complex structures for XGv289, XGv282 and XGv265 showed only one configuration, in which three XGv289 Fabs bound to two up and one down RBDs; three XGv282 Fabs bound to one up and two down RBDs; two XGv265 Fabs bound to an S trimer with one down and one up RBD, although the XGv265-bound up RBD conformation was weakly resolved and therefore not modelled (Fig. 3a). XGv347 bound to an epitope at the tip of the RBD, largely overlapping with the patch targeted by ACE2 (Figs. 2c, 3b,c, Extended Data Fig. 1). Structural comparisons revealed that XGv347 is very similar to A23-58.1, an ultrapotent and broadly reactive neutralizing antibody effective against 23 SARS-CoV-2 variants²², but marked differences could be observed in the complementarity-determining region (CDR) domains (Extended Data Fig. 8). Furthermore, the residues of the epitope of XGv347 match with a major subset of those targeted by S2K146, another broadly cross-reactive sarbecovirus neutralizing antibody^{23,24}, highlighting a plausible capability of these neutralizing antibodies to cross-neutralize Omicron and circulating SARS-CoV-2 variants. Unexpectedly, the epitopes of XGv347, A23-58.1 as well as their sister neutralizing antibodies would be normally inaccessible for the RBD-down conformation in the WT S, but become accessible for either up or down RBDs in the Omicron S owing to a markedly outward expansion and clockwise rotation of approximately 10° of three RBDs, leading to an approximately 9 Å conformational movement of the receptor-binding motif (RBM) (Fig. 3d, Extended Data Fig. 9). The XGv347 paratope comprised 5 CDRs with heavy chain and light chain contributing 70% and 30% of the binding surface area, respectively (Fig. 3b,c, Extended Data Table 2). Overall XGv289, XGv282 and XGv265 bind patches surrounding the right shoulder of RBD with various orientations²⁰, but in a manner similar to those observed for LY-CoV1404, BD-812 and REGN10987—antibodies that are known to generally neutralize most VOCs with high potency^{25,26,27}—but showing decreased, to varying degrees, binding and neutralizing activities against Omicron owing to the presence of new N440K and G446S mutations (Fig. 2b, Extended Data Fig. 10, Extended Data Table 2). Notably, XGv265 and REGN10987 recognize almost the same epitopes, and both have almost no neutralizing activity against Omicron, despite retaining weak binding (Extended

Data Fig. 10). Structural superimpositions and competitive BLI assays reveal that XGv347 and either XGv289 or XGv265 can simultaneously bind to S, informing strategies to rationally design two-antibody combinations for potential therapeutics (Extended Data Figs. 11, 12).

Structural basis for immune escape

XGv347, XGv289, XGv282 and XGv265 bound Omicron S with 5- to 40-fold lower affinity compared with their binding to WT S, although the same binding modes were observed for the two orthologues (Fig. 3, Supplementary Table 1). XGv347 exhibited tight binding to WT S primarily owing to extensive hydrophobic interactions contributed by F456, Y473, F486 and Y489 from WT RBD, V32, V53, W51, P100 and F111 from the heavy chain, Y33 from the light chain, and nine hydrogen bonds (Extended Data Fig. 13, Table 3). Hydrophobic interactions between the Omicron RBD and XGv347 were largely maintained. However, substitutions of Y505H and K417N abolished three hydrogen bonds formed with K75, D31 and E104 from the heavy chain complementarity-determining regions (HCDRs), leading to conformational shifts in HCDR3 and the RBM tip (residues 470–490), which further perturbed six hydrogen bonds built by Y473, A475, S477, T478 and Q493 from WT RBD with T105, C107, A56, G55 and D109 from the HCDRs, albeit with an extra hydrogen bond established by the mutation Q493R and G55 from HCDR2 for Omicron (Extended Data Fig. 13). Similarly, a large patch of hydrophobic interactions constructed by V445, G446, Y449 and P499 from the WT RBD and F33, L50, I51, Y59 and W103 from the HCDRs as well as extensive hydrophilic interactions facilitate tight binding between XGv289 and WT S (Fig. 3, Extended Data Fig. 13). Substitution of G446S disrupts the hydrophobic microenvironment, substantially decreasing hydrophobic interactions between Omicron S and XGv289. Furthermore, mutations of N440K and Q498R, together with altered local conformation, also decrease hydrogen bonding formed by N439, K440, Y449, R498, T500 and Q506 from the Omicron RBD and D95, L98 from the light chain complementarity-determining regions (LCDRs) as well as Y59 and N62 from the HCDRs that would exist in the XGv289–WT S complex (Extended Data Fig. 13). Among these four representative antibodies, XGv282 showed a minimal reduction in binding affinity (fivefold), but a more substantial reduction in neutralization (approximately 40-fold), whereas XGv347 showed a 40-fold decrease in binding, but unchanged neutralization against Omicron when compared to WT S (Extended Data Table 3), suggesting that the epitopes, rather than binding affinity, might have more crucial roles in the neutralizing potency and breadth of an antibody. Consistent with XGv289, the substitution of G446S alters the hydrophobic microenvironment generally established by RBD and a group of antibodies bound at the right shoulder, including XGv289 and XGv282, triggering a conformational shift on CDRs and disrupting antibody recognition (Extended Data Fig. 13). In addition, the mutation E484A breaks the

hydrogen bond with R74 from XGv282 HCDR2 and losses of charge interactions between R346 and K444 on WT RBD, and D56 and D58 on XGv265 LCDR2 owing to conformational alterations, further decreasing the binding of XGv282 and XGv265 to the Omicron S, respectively (Extended Data Fig. 13). Together, G446S, acting as a critical mutation site, can alter the local conformation at the binding interface, conferring greater resistance to a class of antibodies bound at the right shoulder of the RBD.

Therapeutic activities of antibodies

Given the excellent neutralizing breadth and potency of these antibodies at the cellular level, we next sought to assess the correlation between in vitro neutralization and in vivo protection. A number of representative monoclonal antibodies with high neutralizing potency and breadth, belonging to different classes, such as XGv347, XGv289, XGv282, XGv265 and XGv052, produced in the HEK 293F cell line were selected for therapeutic evaluation in an established mouse model challenged with Beta virus²⁸. Upon intranasal challenge with Beta, adult BALB/c mice showed robust viral replication in the lungs at 3–5 days post inoculation (dpi). To evaluate the protection efficacy of these monoclonal antibodies, BALB/c mice challenged with the Beta variant were administered a single dose of 5 mg kg⁻¹ XGv347, XGv289, XGv282, XGv265 and XGv052 individually, or combinations of XGv282 and XGv347 (2.5 mg kg⁻¹ of each), and XGv052 and XGv289 (2.5 mg kg⁻¹ of each) in therapeutic settings (Fig. 4a). Heavy viral loads with high levels of viral RNA (more than 10⁹ copies per g) were detected in the lungs at day 5 after infection in the control group of mice treated with PBS. However, a single dose of XGv282 reduced the viral RNA loads by about 10,000-fold in the lungs compared with the control group (Fig. 4b). A single dose of XGv289, XGv265, XGv347, XGv052 or antibody cocktails of XGv282 and XGv347 or XGv052 and XGv289 resulted in a complete clearance of viral particles in the lungs (Fig. 4b,c). A potential synergistic effect was observed for combined XGv282 and XGv347 (Fig. 4b,c). In addition, histopathological examination revealed severe interstitial pneumonia, characterized by alveolar septal thickening, inflammatory cell infiltration and distinctive vascular system injury in mice belonging to the control group at day 5 (Fig. 4d). By contrast, no obvious lesions of alveolar epithelial cells or focal haemorrhage were observed in lung sections from mice that received the indicated antibody treatments (Fig. 4d, Extended Data Fig. 14). To further evaluate whether XGv347 could serve as a therapeutic intervention against Omicron in vivo, we tested the protective efficacy of XGv347 on transgenic mice expressing human ACE2²⁹ (K18-hACE2) and challenged with Omicron. We recorded the body weight of each mouse daily after infection for 5 days and found that mice in the treatment group maintained their body weight, whereas those in the control group lost weight (Fig. 4e), indicating that XGv347 applied after infection could greatly

improve the physiological condition of the Omicron-infected mice. Similar to the studies in mice using Beta, therapeutic administration of XGv347 provided a clear benefit in the K18-hACE2 mice infected with Omicron, as indicated by a complete clearance of viral RNA in the lungs and trachea at day 5 after challenge (Fig. 4f). Of note, K18-hACE2 mice infected with Omicron developed moderate interstitial pneumonia characterized by focal to multifocal widened alveolar interstitium accompanied by infiltration of inflammatory cells (Fig. 4g). No obvious pathological injury was observed in the lung from infected mice treated with XGv347 (Fig. 4g). Collectively, these results suggest that some antibodies—at least best-in-class antibodies such as XGv347—from the repertoire elicited by a three-dose vaccination regimen retain therapeutic potential against currently circulating VOCs.

Fig. 4: Protection against challenge by SARS-CoV-2 Beta and Omicron variants in mice.



a, Experimental design for protection assay against Beta variant challenge. $n=4$ mice in XGv347, XGv052 and XGv052 + XGv289 groups; $n=5$ mice in other groups. **b–d**, Lung tissues of mice challenged with Beta variant, collected at 5 dpi: virus titre (**b**), immunostaining (**c**) and haematoxylin and eosin staining (**d**). **b**, Viral subgenomic (sg) RNA loads in the lungs at 5 dpi were measured by quantitative PCR with reverse transcription. Data are mean \pm s.d. Dashed line represents the limit of detection. **c**, In situ hybridization with a SARS-CoV-2 specific probe. Brown staining indicates the presence of SARS-CoV-2 genomic RNA. **d**, Histopathological analysis of lung samples at 5 dpi. **e**, **f**, Weight change (**e**) and viral RNA in lung tissues (**f**) of K18-hACE2 mice challenged with Omicron variant of concern. $n=5$ mice in each group. **e**, The weight of each mouse in both groups was monitored and recorded daily following infection. Data are mean \pm s.d. **f**, Viral RNA loads in the lungs at 5 dpi were measured as in **b**. Data are mean \pm s.d. Dashed line represents the limit of detection. **g**, Histopathological analysis of lung tissues from infected mice treated with XGv347 or PBS. Micrographs in **c**, **d**, **g** are representative of two experiments.

Discussion

The ongoing COVID-19 pandemic has resulted in frequent occurrences of SARS-CoV-2 variants that increase transmissibility and reduce potency of vaccine-induced and therapeutic antibodies^{4,30}. More recently, there has been concern that the Omicron variant has increased antibody escape breadth owing to newly occurring and accumulated mutations in key epitopes of most neutralizing antibodies. Omicron nearly ablates the neutralization activity of most FDA-approved antibody drugs, including LY-CoV555, LY-CoV016, REGN10933, REGN10987, AZD8895 and AZD1061². These issues mean there is an urgent need to develop new antibody-based therapies that can neutralize these variants as well as future variants of concern. Previous studies revealed that a three-dose vaccination regimen (0, 1 and 7 months) with inactivated SARS-CoV-2 vaccine leads to an improved immune response with significantly enhanced neutralizing breadth via ongoing antibody somatic mutation and memory B cell clonal turnover^{7,31}. A subset of highly potent neutralizing antibodies with broad activities ($IC_{50} < 0.2 \mu\text{g ml}^{-1}$) against all circulating VOCs, including Omicron, was present in at least four individuals who had received three doses of inactivated ancestral SARS-CoV-2 vaccine. Some of these antibodies protected against Beta and Omicron infections in mice. Furthermore, our structural and functional analyses revealed that the G446S mutation might act as a critical antibody escape site, conferring greater resistance to one major class of antibodies bound at the right shoulder of RBD by altering microenvironments at the S-neutralizing antibody-binding interface.

In addition to evading currently available antibody therapies, Omicron can diminish the efficacy of clinically approved vaccines, including mRNA and inactivated virus vaccines^{[30,32](#)}. There is an ongoing debate about whether immune responses can be fine-turned to the Omicron variant by boosting with a tweaked (Omicron-based) vaccine. A major hurdle for this approach is the ‘original antigenic sin’, a phenomenon documented in some other infectious diseases, including flu^{[33](#)}. The presence of a subset of antibodies with broad neutralizing activities against all circulating VOCs in the memory B-derived antibody repertoire from the three-dose vaccinees suggests a possibility that selective and expeditious recall of humoral responses might be elicited by infection with Omicron or other variants, conferring a secondary protection directed by memory etched in the immune system. Further studies are warranted to examine the advantages and disadvantages of booster shots of an Omicron-specific vaccine or simply administration of a booster with the original vaccines. Last, the identification and characterization of broadly protective antibodies against all circulating VOCs will help in the development of universal vaccination strategies against sarbecoviruses.

Methods

Facility and ethics statements

All procedures associated with SARS-CoV-2 live virus were approved by the Animal experiment Committee Laboratory Animal Center, Beijing Institute of Microbiology and Epidemiology with an approval number of IACUC-IME-2021-022 and performed in Biosafety Level 3 (BSL-3) laboratories in strict accordance with the recommendations in the Guide for Care and Use of Laboratory Animals. The procedures about human participants were approved by the Ethics Committee (seal) of Beijing Youan Hospital, Capital Medical University with an approval number of LL-2021-042-K. All participants were provided written informed consent.

Viral stock and cell lines

SARS-CoV-2 WT strain CN01 was originally isolated from a patient during the early phase of COVID-19 endemic in China. SARS-CoV-2 variant of concern Beta strain GDPCC was isolated in a patient from South Africa and an Omicron strain was isolated from a patient in Hong Kong and now preserved in SinoVac Biotech Ltd. All virus strains were first purified by standard plaque assay as previously described^{[14](#)} and then inoculated into Vero cells (ATCC CCL-81) grown to 95% in 10% fetal bovine serum (FBS) supplemented Dulbecco’s minimal essential medium (DMEM) for amplification. Besides, 293T cells (ATCC CRL-3216) and Huh-7 cells (JCRB 0403) were used for pseudovirus neutralization assays; HEK293F cells (Thermo Fisher

Scientific 11625019) were used for protein expression; and HEK293 cells (ECACC 85120602) were used for antibody expression. All cells were confirmed to be negative for mycoplasma contamination.

Human sera samples

The serum samples were obtained from healthy volunteers who had no history of COVID-19 and were verified by PCR and serological assay and received two doses or three doses of CoronaVac (Sinovac) inactivated virus vaccine specific against SARS-CoV-2. The whole study was conducted in accordance with the requirements of Good Clinical Practice of China.

Authentic virus neutralization assay

The serum samples were first incubated at 56 °C for 30 min for inactivation. The heat-treated samples or monoclonal antibodies were subject to serial dilution from 1: 4 or 50 µg ml⁻¹ with DMEM in two-fold steps and mixed with a virus suspension containing 100 TCID₅₀ at 36. °C for 2 h, after which, the mixtures were added to wells seeded with confluence Vero cells and incubated at 36.5 °C for another 5 days in a humidified 5% CO₂ cell incubator. After that, the cytopathic effect of each well was observed under microscopes by three different individuals and the related dilutions and concentrations were recorded and used for the titration of samples tested by the method of Reed-Muench¹⁴.

Pseudovirus neutralization assay

The pseudotyped viruses bearing the S protein were generated, aliquoted and restored as previously described¹⁸. In brief, 293T cells were first transfected with the plasmid embedded with the S gene of WT or variant (Alpha, Beta, Gamma, Delta, Lambda and Omicron) SARS-CoV-2. The transfected 293T cells were infected with VSV G pseudotyped virus (G*ΔG-VSV) at a multiplicity of infection (MOI) of 4. After incubation for 5 h, cells were washed with PBS, and then complete culture medium was added. After another 24 h, the SARS-CoV-2 pseudoviruses were produced and collected. For the in vitro pseudotyped virus neutralization assay, the plasma samples or antibodies were diluted in DMEM starting from 1:10 or 10 µg ml⁻¹ with 6 additional threefold serial dilutions, each of which were mixed with the collected pseudovirus and incubated at 37 °C for 1 h. After that, the mixtures were added to Huh-7 cells and placed back for incubation for another 24 h. Then, the luciferase luminescence (RLU) of each well was measured with a luminescence microplate reader. The neutralization percentage was calculated as following: Inhibition (%) =

$(1 - (\text{sample RLU} - \text{blank RLU}) / (\text{positive control RLU} - \text{blank RLU}))$. Antibody neutralization titres were presented as 50% maximal inhibitory concentration (IC_{50}).

Protein expression and purification

The sequences of VOC Omicron full-length S protein (residues 1–1208), RBD (residues 319–541) and NTD (residues 1–304) were modified from the plasmids encoding the S, RBD and NTD of WT SARS-CoV-2 (GenBank: MN908947) in our lab by overlapping PCR. In addition to the reported mutations (A67V, Δ69–70, T95I, G142D, Δ143–145, Δ211, L212I, ins214EPE, G339D, S371L, S373P, S375F, K417N, N440K, G446S, S477N, T478K, E484A, Q493R, G496S, Q498R, N501Y, Y505H, T547K, D614G, H655Y, N679K, P681H, N764K, D796Y, N856K, Q954H, N969K and L981F) on Omicron, the proline substitutions at 817, 892, 899, 942, 986 and 987, ‘GSAS’ substitutions at the S1/S2 furin cleavage site (residues 682–685) and a C-terminal T4 foldon trimerization domain were also introduced in the Omicron S construct to stabilize the trimeric conformation of S protein. For protein expression, the plasmids of these proteins were transiently transfected into HEK 293F cells grown in suspension at 37 °C in an incubator supplied with 8% CO₂, rotating at 130 rpm. The cell supernatants were collected and concentrated three days post-transfection, and further purified by affinity chromatography using resin attached with streptavidin and size-exclusion chromatography (SEC) using a Superose 6 10/300 column (GE Healthcare Life Sciences) equilibrated with the buffer containing 20 mM Tris-HCl, pH 8.0, and 200 mM NaCl.

Single memory B cell isolation and sequencing

PBMCs were separated from the whole-blood samples obtained from four volunteers using Histopaque (Sigma) gradient centrifugation. After washing with Hank’s balanced salt solution (HBSS) (Solarbio) for three times, the cells were aliquoted and stored in liquid nitrogen in the presence of FBS and DMSO. For single memory B cell sorting, stored PBMCs were thawed and incubated with CD19 MicroBeads (Miltenyi Biotec) to screen out CD19+ B lymphocytes, which were then incubated with human Fc block (BD Biosciences), anti-CD20-PECy7 (BD1113 Biosciences), S-ECD-PE, and S-ECD-APC. The single memory B cells (CD20-1114 PECy7+ S-ECD-PE+ S-ECD-APC+) were further sorted into 96-well plates using a FACSAria II (BD Biosciences), and followed by sequencing and cloning as previously described³⁵.

Antibody expression and Fab generation

The selected 323 antibodies were subjected to gene codon optimization and construction with a plasmid encoding human IgG1 Fc as described previously⁷. Then

the clones were transiently transfected into mammalian HEK 293F cells and incubated for 5 days in a 5% CO₂ rotating incubator at 37 °C for antibody expression, which were further purified using protein A and dialyzed into phosphate buffered saline (PBS). The purified monoclonal antibodies XGv265, XGv282, XGv289 and XGv347 were then processed to obtain their Fab fragments using the Pierce FAB preparation kit (Thermo Scientific) as described previously³⁶. In brief, the samples were first applied to desalination columns to remove the salt and the flow-throughs were collected and incubated with papain that was attached with beads to cleave Fab fragments from the whole antibodies for 5 h at 37 °C. After that, the mixtures were transferred into protein A columns and the flow-throughs, that is, the Fab fragments were collected and dialyzed into PBS (ThermoFisher, catalogue (cat.) no. 10010023).

Bio-layer interferometry

BLI experiments were run on an Octet Red 384 instrument (ForteBio). To measure the binding affinities of monoclonal antibodies, monoclonal antibodies were immobilized onto Protein A biosensors (ForteBio) and threefold serial dilutions of WT RBD, Alpha RBD (ACROBiosystems, cat. no. SPD-C52Hn), Beta RBD (ACROBiosystems, cat. no. SPD-C52Hp), Gamma RBD (ACROBiosystems, cat. no. SPD-C52Hr), Delta RBD (ACROBiosystems, cat. no. SPD-C52Hh) and Omicron RBD (ACROBiosystems, cat. no. SPD-C522e) in PBS were used as analytes. Data were then analysed using software Octet BLI Analysis 12.2 (ForteBio) with a 1:1 fitting model. For the competitive assay by BLI, SARS-CoV-2 WT RBD tagged with His (ACROBiosystems, cat. no. SPD-C52H3) was loaded on NTA biosensors, which were pre-equilibrated in the buffer for at least 1 min. The loaded biosensors were immersed with the first monoclonal antibody for 300 s, followed by addition of the second monoclonal antibody for another 300 s. Data obtained were also analysed by Octet BLI Analysis 12.2.

ELISA

To evaluate whether the given monoclonal antibodies could block the interaction between human ACE2 (hACE2) and RBD, ACE2 competition ELISA was performed by using the SARS-CoV-2 (B.1.1.529) Inhibitor Screening Kit (ACROBiosystems, cat. no. EP-115) according to the recommended protocol. In brief, each of the 10 twofold dilution series of monoclonal antibodies (starting dilution of 25 µg ml⁻¹) and 0.8 µg ml⁻¹ of HRP-conjugated SARS-CoV-2 RBD were added into the ELISA plate wells which are pre-coated with hACE2 protein. After incubation at 37 °C for 1 h, the plates were washed three times with PBST (0.1% Tween) and the colorimetric signals were developed by addition of 3,3',5,5'-tetramethylbenzidine TMB (Thermo Fisher) for 10 min. The reaction was stopped by addition of 50 µl 1 M H₂SO₄. The absorbance

was measured at 450 nm with an ELISA microplate reader. For each monoclonal antibody, a blank control with no monoclonal antibody was added for inhibition calculation. The area under the curve (AUC) of each monoclonal antibody were determined using Prism V8.0 (GraphPad). For competitive ELISAs to identify the domain of a given monoclonal antibody, 96-well plates were first coated with RBD ($2 \mu\text{g ml}^{-1}$) and then blocked with 2% BSA in PBS. After incubation with the reference monoclonal antibodies, the blocking antibody ($15 \mu\text{g ml}^{-1}$), the wells were followed by directly adding the second biotinylated antibodies ($0.25 \mu\text{g ml}^{-1}$). Streptavidin-HRP (BD Biosciences) was then added for detection. Samples with no first antibody were used as a negative control for normalization.

Cryo-EM sample preparation, data collection

The purified S protein was mixed with each of the Fab fragments of XGv265, XGv282, XGv289 or XGv347 with a molar ratio of 1: 1.2 for 10 s ice incubation, and then dropped onto the pre-glow-discharged holey carbon-coated gold grid (C-flat, 300-mesh, 1.2/1.3, Protochips In.), blotted for 7 s with no force in 100% relative humidity and immediately plunged into the liquid ethane using Vitrobot (FEI). Cryo-EM data sets of these complexes were collected at 300 kV with an FEI Titan Krios microscope (FEI). Movies (32 frames, each 0.2 s, total dose of $60 \text{ e}^- \text{ \AA}^{-2}$) were recorded using a K3 Summit direct detector with a defocus range between 1.5–2.7 μm . Automated single particle data acquisition was carried out by SerialEM, with a calibrated magnification of 22,500 yielding a final pixel size of 1.07 \AA .

Cryo-EM data processing

A total of 3,752, 2,631, 3,955 and 5,014 micrographs of S–XGv265 complex, S–XGv282 complex, S–XGv289 complex and S–XGv347 complex, respectively were recorded and subjected to beam-induced motion correction using motionCorr in Relion 3.0 package³⁷. The defocus value of each image was calculated by Gctf. Then, 1,302,103, 756,508, 2,332,045 and 2,320,416 particles of the S–XGv265 complex, S–XGv282 complex, S–XGv289 complex and S–XGv347 complex, respectively, were picked and extracted for reference-free 2D alignment by cryoSPARC³⁸, based of which, 422,083, 190,154, 837,832 and 614,852 particles were selected and applied for 3D classification by Relion3.0 for S–XGv265 complex, S–XGv282 complex, S–XGv289 complex and S–XGv347 complex, respectively with no symmetry imposed to produce the potential conformations for the complexes. Afterwards, the candidate model for each complex was selected and processed by non-uniform auto-refinement and postprocessing in cryoSPARC to generate the final cryo-EM density for S–XGv265 complex, S–XGv282 complex, S–XGv289 complex and S–XGv347 complex. To improve the resolution of the interface between RBD and monoclonal

antibodies, the block-based reconstruction was performed to obtain the final resolution of the focused interfaces which contained the interfaces of RBD and monoclonal antibodies investigated here as described previously³⁹. The resolution of each structure was determined on the basis of the gold-standard Fourier shell correlation (threshold = 0.143) and evaluated by ResMap. All dataset processing is shown in Extended Data Fig. 3 and summarized in Extended Data Table 2.

Model fitting and refinement

The atomic models of the complexes were generated by first fitting the chains of the native apo SARS-CoV-2 S trimer (PDB number of 6VYB) and Fabs (PDB number of 7LSS and 7CZW for XGv265, 5MES and 5VAG for XGv282, 6UDA and 7MEG for XGv289 as well as 7E3K for XGv347) into the cryo-EM densities of the final S-Fab-complexes described above by Chimera, followed by manually adjustment and correction according to the protein sequences and densities in Coot, as well as real space refinement using Phenix. Details of the refinement statistics of the complexes are summarized in Extended Data Table 2.

Molecular dynamics simulation and ΔG estimation

Model of SARS-CoV-2 WT RBD in complex with XGv265, XGv282, XGv289 and XGv347 were generated in Chimera by superimposition of WT RBD and cryo-EM structure of Omicron RBD in complex with the four antibodies. Before molecular dynamics, all models were checked by WHAT IF Web Interface (<https://swift.cmbi.umcn.nl/servers/html/index.html>) to model missing sidechains and remove atomic clashes. After that, the structure was simulated by GROMACS-2021. In brief, we used OPLS force field with TIP3P water model to prepare the dynamic system and add Na⁺ and Cl⁻ ions to make the system electrically neutralized. Then, the system was subjected to energy minimization using the steepest descent algorithm until the maximum force of 1,000 kJ mol⁻¹ has been achieved. NVT ensemble via the Nose-Hoover method at 300 K and NPT ensemble at 1 bar with the Parrinello-Rahman algorithm were employed successively to make the temperature and the pressure equilibrated, respectively. Finally, molecular dynamics production runs of 100 ns were performed starting from random initial velocities and applying periodic boundary conditions. The non-bonded interactions were treated using Verlet cut-off scheme, while the long-range electrostatic interactions were treated using particle mesh Ewald method. The short-range electrostatic and van der Waals interactions were calculated with a cut-off of 12 Å. Average structure of the four complexes were generated using the last 10 ns frames and ΔG between the antibodies and RBD was estimated in ROSETTA by InterfaceAnalyzer. Atomic_burial_cutoff, sasa_calculator_probe_radius and interfaces_cutoff values were set to 0.01, 1.4 and 8.0 respectively.

In vivo protection against SARS-CoV-2 Beta and Omicron variants challenge in mice

The in vivo protection efficacies of single antibody or antibody cocktails were assessed by using a newly established mouse model based on a SARS-CoV-2 Beta variant strain²⁸. In brief, groups of 8-month-old female BALB/c mice were infected with 1×10^4 PFU of SARS-CoV-2 Beta variant strain, then infected mice were treated intraperitoneally with a single dose of different antibodies or antibody cocktails (5 mg kg^{-1}) at 1 h after infection. The protection efficacy of XGv347 was also assessed by using 10-week-old female K18-hACE2 mice, each challenged with $1 \times 10^2 \text{ TCID}_{50}$ of Omicron strain. And two 2 h post infection, mice were intraperitoneally treated with a single dose of XGv347 at 30 mg kg^{-1} or the same volume of PBS as control. The lung tissues of mice from both two groups were collected at 5 dpi for viral RNA loads assay and pathological examination. All mice were randomly allocated in each group; investigators were not blinded to allocation during the experiment and outcome assessment.

Viral burden determination

Viral burden in lung from mice were measured as described previously¹⁷. In brief, lung tissue homogenates were clarified by centrifugation and viral RNA was extracted using the QIAamp Viral RNA Mini Kit (Qiagen). Viral sgRNA quantification in each tissue sample was performed by quantitative reverse transcription PCR (RT-qPCR) targeting the S gene of SARS-CoV-2. RT-qPCR was performed using One-Step PrimeScript RT-PCR Kit (Takara).

Histology and RNA in situ hybridization

Lung tissues from mice were fixed with perfusion fixative (formaldehyde) for 48 h, and embedded in paraffin according to standard histological assays. For histopathology, lung tissues were stained with haematoxylin and eosin. Images were captured using Olympus BX51 microscope equipped with a DP72 camera. For RNA ISH assays were performed with an RNAscope 2.5 (Advanced Cell Diagnostics) according to the manufacturer's instruction. In brief, formalin-fixed paraffin-embedded tissue sections of $5 \mu\text{m}$ were deparaffinized by incubation for 60 min at 60 °C. Endogenous peroxidases were quenched with hydrogen peroxide for 10 min at room temperature. Slides were then boiled for 15 min in RNAscope Target Retrieval Reagents and incubated for 30 min in RNAscope Protease Plus before probe hybridization. The probe targeting 2019-nCoV RNA was designed and synthesized by Advanced Cell Diagnostics (cat. no. 848561). Tissues were counterstained with Gill's

haematoxylin and visualized with standard bright-field microscopy. Original magnification was 10 \times .

Reporting summary

Further information on research design is available in the [Nature Research Reporting Summary](#) linked to this paper.

Data availability

The atomic coordinates of XGv347 in complex with S trimer (state 1), XGv347 in complex with S trimer (state 2) and XGv347 in complex with S trimer (state 3) have been submitted to the Protein Data Bank with accession codes [7WEA](#), [7WEC](#) and [7WEB](#), respectively. The atomic coordinates of XGv265, XGv282 and XGv289 have been deposited in the Protein Data Bank under accession codes [7WE8](#), [7WE7](#) and [7WE9](#), respectively. Cryo-EM density maps in this study have been deposited at the Electron Microscopy Data Bank with accession codes [EMD-32444](#) (state 1), [EMD-32446](#) (state 2) and [EMD-32445](#) (state 3), [EMD-32441](#) (XGv282), [EMD-32442](#) (XGv265) and [EMD-32443](#) (XGv289). To reveal structural details of Fab binding mechanism, the local optimized method was used to optimized data progress and the related atomic models and EM density maps of optimized reconstructions of Fab interaction interfaces have been deposited under accession codes [7WEE](#) (XGv265), [7WED](#) (XGv347), [7WLC](#) (XGv282), [7WEF](#) (XGv289), [EMD-32447](#) (XGv347), [EMD-32448](#) (XGv265), [EMD-32581](#) (XGv282) and [EMD-32449](#) (XGv289).

References

1. Carreno, J. M. et al. Activity of convalescent and vaccine serum against a B. 1.1. 529 variant SARS-CoV-2 isolate. *Nature* <https://doi.org/10.1038/s41586-022-04399-5> (2021).
2. Cao, Y. R. et al. B. 1.1. 529 escapes the majority of SARS-CoV-2 neutralizing antibodies of diverse epitopes. *Nature* <https://doi.org/10.1038/s41586-021-04385-3> (2021).
3. Mlcochova, P. et al. SARS-CoV-2 B. 1.617. 2 Delta variant replication and immune evasion. *Nature* **599**, 114–119 (2021).
4. Wang, G.-L. et al. Susceptibility of circulating SARS-CoV-2 variants to neutralization. *N. Engl. J. Med.* **384**, 2354–2356 (2021).

5. Altmann, D. M., Boyton, R. J. & Beale, R. Immunity to SARS-CoV-2 variants of concern. *Science* **371**, 1103–1104 (2021).
6. Karim, S. S. A. & Karim, Q. A. Omicron SARS-CoV-2 variant: a new chapter in the COVID-19 pandemic. *Lancet* **398**, 2126–2128 (2021).
7. Wang, K. et al. A third dose of inactivated vaccine augments the potency, breadth, and duration of anamnestic responses against SARS-CoV-2. Preprint at <https://doi.org/10.1101/2021.09.02.21261735> (2021).
8. Hastie, K. M. et al. Defining variant-resistant epitopes targeted by SARS-CoV-2 antibodies: a global consortium study. *Science* **374**, 472–478 (2021).
9. Yuan, M. et al. Structural and functional ramifications of antigenic drift in recent SARS-CoV-2 variants. *Science* **373**, 818–823 (2021).
10. Zhang, J. et al. Membrane fusion and immune evasion by the spike protein of SARS-CoV-2 Delta variant. *Science* **374**, 1353–1360 (2021).
11. Saito, A. et al. Enhanced fusogenicity and pathogenicity of SARS-CoV-2 Delta P681R mutation. *Nature* **602**, 300–306 (2021).
12. Mbaeyi, S. et al. The Advisory Committee on Immunization Practices' interim recommendations for additional primary and booster doses of COVID-19 vaccines—United States, 2021. *Morb. Mortal. Wkly Rep.* **70**, 1545 (2021).
13. Garcia-Beltran, W. F. et al. mRNA-based COVID-19 vaccine boosters induce neutralizing immunity against SARS-CoV-2 Omicron variant. *Cell* **185**, 457–466.e4 (2022).
14. Gao, Q. et al. Development of an inactivated vaccine candidate for SARS-CoV-2. *Science* **369**, 77–81 (2020).
15. SAGE. Interim statement on booster doses for COVID-19 vaccination. *WHO* <https://www.who.int/news-room/detail/04-10-2021-interim-statement-on-booster-doses-for-covid-19-vaccination> (2021).
16. Wang, Z. et al. mRNA vaccine-elicited antibodies to SARS-CoV-2 and circulating variants. *Nature* **592**, 616–622 (2021).
17. Lv, Z. et al. Structural basis for neutralization of SARS-CoV-2 and SARS-CoV by a potent therapeutic antibody. *Science* **369**, 1505–1509 (2020).

18. Yao, H. et al. Rational development of a human antibody cocktail that deploys multiple functions to confer Pan-SARS-CoVs protection. *Cell Res.* **31**, 25–36 (2021).
19. Barnes, C. O. et al. SARS-CoV-2 neutralizing antibody structures inform therapeutic strategies. *Nature* **588**, 682–687 (2020).
20. Dejnirattisai, W. et al. The antigenic anatomy of SARS-CoV-2 receptor binding domain. *Cell* **184**, 2183–2200.e2122 (2021).
21. Tong, P. et al. Memory B cell repertoire for recognition of evolving SARS-CoV-2 spike. *Cell* **184**, 4969–4980.e4915 (2021).
22. Wang, L. et al. Ultrapotent antibodies against diverse and highly transmissible SARS-CoV-2 variants. *Science* **373**, eabh1766 (2021).
23. Park, Y.-J. et al. Antibody-mediated broad sarbecovirus neutralization through ACE2 molecular mimicry. *Science* **375**, 449–454 (2022).
24. Camerini, E. et al. Broadly neutralizing antibodies overcome SARS-CoV-2 Omicron antigenic shift. *Nature* <https://doi.org/10.1038/s41586-021-04386-2> (2021).
25. Kathryn, W. et al. LY-CoV1404 (bebtelovimab) potently neutralizes SARS-CoV-2 variants. Preprint at <https://doi.org/10.1101/2021.04.30.442182> (2022).
26. Zhu, L. et al. Double lock of a potent human therapeutic monoclonal antibody against SARS-CoV-2. *Natl Sci. Rev.* **8**, nwaa297 (2021).
27. Hansen, J. et al. Studies in humanized mice and convalescent humans yield a SARS-CoV-2 antibody cocktail. *Science* **369**, 1010–1014 (2020).
28. Chen, Q. et al. Transient acquisition of cross-species infectivity during the evolution of SARS-CoV-2. *Natl Sci. Rev.* **8**, nwab167 (2021).
29. Bao, L. et al. The pathogenicity of SARS-CoV-2 in hACE2 transgenic mice. *Nature* **583**, 830–833 (2020).
30. Wilhelm, A. et al. Reduced neutralization of SARS-CoV-2 Omicron variant by vaccine sera and monoclonal antibodies. Preprint at <https://doi.org/10.1101/2021.12.07.21267432> (2021).
31. Wang, Z. et al. Naturally enhanced neutralizing breadth against SARS-CoV-2 one year after infection. *Nature* **595**, 426–431 (2021).

32. Gardner, B. J. & Kilpatrick, A. M. Estimates of reduced vaccine effectiveness against hospitalization, infection, transmission and symptomatic disease of a new SARS-CoV-2 variant, Omicron (B. 1.1. 529), using neutralizing antibody titers. Preprint at <https://doi.org/10.1101/2021.12.10.21267594> (2021).
33. Biswas, A., Chakrabarti, A. K. & Dutta, S. Current challenges: from the path of “original antigenic sin” towards the development of universal flu vaccines: Flu vaccine efficacy encounters significant hurdles from pre-existing immunity of the host suggesting assessment of host immunity before vaccination. *Int. Rev. Immunol.* **39**, 21–36 (2020).
34. Cui, Z. et al. Structural and functional characterizations of altered infectivity and immune evasion of SARS-CoV-2 Omicron variant. Preprint at <https://doi.org/10.1101/2021.12.29.474402> (2021).
35. Zhou, Y. et al. Enhancement versus neutralization by SARS-CoV-2 antibodies from a convalescent donor associates with distinct epitopes on the RBD. *Cell Rep.* **34**, 108699 (2021).
36. Wang, N. et al. Structure-based development of human antibody cocktails against SARS-CoV-2. *Cell Res.* **31**, 101–103 (2021).
37. Zivanov, J. et al. New tools for automated high-resolution cryo-EM structure determination in RELION-3. *eLife* **7**, e42166 (2018).
38. Punjani, A., Rubinstein, J. L., Fleet, D. J. & Brubaker, M. cryoSPARC: algorithms for rapid unsupervised cryo-EM structure determination. *Nat. Methods* **14**, 290–296 (2017).
39. Sun, Y. et al. Structure-based development of three-and four-antibody cocktails against SARS-CoV-2 via multiple mechanisms. *Cell Res.* **31**, 597–600 (2021).

Acknowledgements

We thank X. Li, X. Huang and L. Chen for cryo-EM data collection at the Center for Biological imaging (CBI) at the Institute of Biophysics for EM work; Y. Chen, Z. Yang and B. Zhou for technical support on surface plasmon resonance. This work was supported by the Strategic Priority Research Program (XDB29010000, XDB37030000), CAS (YSBR-010), National Key Research and Development Program (2020YFA0707500, 2018YFA0900801, 2021YFA1301400), Beijing Municipal Science and Technology Project (Z201100005420017), National Natural Science Foundation of China (31872730 and 32070947) and Ministry of Science and Technology of China (EKGPG21-09 and CPL-1233). X.W. was supported by Ten

Thousand Talent Program and the NSFS Innovative Research Group (no. 81921005). K.W. was supported by the Special Research Assistant Project of the Chinese Academy of Sciences.

Author information

Author notes

1. These authors contributed equally: Kang Wang, Zijing Jia, Linlin Bao, Lei Wang, Lei Cao, Hang Chi, Yaling Hu, Qianqian Li, Yunjiao Zhou

Affiliations

1. CAS Key Laboratory of Infection and Immunity, National Laboratory of Macromolecules, Institute of Biophysics, Chinese Academy of Sciences, Beijing, China

Kang Wang, Zijing Jia, Lei Wang, Lei Cao, Qianhui Zhu, Pan Liu, Nan Wang, Boling Zhu, Kaiyue Fan, Wangjun Fu, Peng Yang, Xinran Pei, Zhen Cui & Xiangxi Wang

2. University of Chinese Academy of Sciences, Beijing, China

Zijing Jia, Lei Wang, Qianhui Zhu, Pan Liu, Kaiyue Fan, Wangjun Fu, Peng Yang, Zhen Cui & Xiangxi Wang

3. Key Laboratory of Human Disease Comparative Medicine, Chinese Ministry of Health, Beijing Key Laboratory for Animal Models of Emerging and Reemerging Infectious Diseases, Institute of Laboratory Animal Science, Chinese Academy of Medical Sciences and Comparative Medicine Center, Peking Union Medical College, Beijing, China

Linilin Bao & Chuan Qin

4. State Key Laboratory of Pathogen and Biosecurity, Beijing Institute of Microbiology and Epidemiology AMMS, Beijing, China

Hang Chi, Yongqiang Deng & Cheng-Feng Qin

5. Sinovac Biotech, Beijing, China

Yaling Hu, Lin Wang, Min Liu & Yurong Li

6. Division of HIV/AIDS and Sex-Transmitted Virus Vaccines, Institute for Biological Product Control, National Institutes for Food and Drug Control (NIFDC), Beijing, China

Qianqian Li, Jiajing Wu, Shuo Liu, Weijin Huang & Youchun Wang

7. Key Laboratory of Medical Molecular Virology (MOE/NHC/CAMS), Shanghai Institute of Infectious Disease and Biosecurity, Shanghai Frontiers Science Center of Pathogenic Microbes and Infection, School of Basic Medical Sciences, Shanghai Medical College, Fudan University, Shanghai, China

Yunjiao Zhou & Qiao Wang

8. Acrobiosystems, Beijing, China

Yinan Jiang, Lili Qin, Pingju Ge & Yiding Chen

Contributions

X.W., K.W., C.-F.Q., C.Q. Q.W. and Y.W. conceived, designed and analysed the whole experiment. Y.Z. performed B cell sorting and antibody cloning. Y.H., M.L., Y.L. and Lin Wang. performed authentic virus neutralization assays. Z.J., Q.L., X.P., J.W., S.L. and W.H. performed the pseudovirus neutralization assays. K.W., Y.J., L.Q., P.G., Z.C., Y.C. and K.F. performed plasmid construction, and protein and antibody expression. Q.Z. and P.Y. performed the BLI assay. L.B., H.C. and Y.D. performed animal experiments and analysed the results. K.W., Lei Wang, B.Z., L.C., P.L., W.F. and N.W. performed cryo-EM sample preparation, data collection, and processing. All authors analysed data. X.W., K.W., C.-F.Q., C.Q. and Y.W. wrote the manuscript with input from all co-authors.

Corresponding authors

Correspondence to [Qiao Wang](#), [Cheng-Feng Qin](#), [Youchun Wang](#), [Chuan Qin](#) or [Xiangxi Wang](#).

Ethics declarations

Competing interests

Y.H., Lin Wang and M.L. are employees of Sinovac Biotech Ltd. Y.J., P.G. and Y.C. are employees of Acrobiosystems Inc. The other authors declare no competing interests.

Peer review

Peer review information

Nature thanks the anonymous reviewers for their contribution to the peer review of this work.

Additional information

Publisher's note Springer Nature remains neutral with regard to jurisdictional claims in published maps and institutional affiliations.

Extended data figures and tables

[Extended Data Fig. 1 Antibody-hACE2 competition ELISA assay.](#)

Data shown are the curves of 31 antibodies used to compete with ACE2. All experiments were performed in duplicate.

[Extended Data Fig. 2 Characteristics of representative antibodies against pseudotyped viruses.](#)

a, Heatmap representation of five therapeutic mAbs approved or in clinical trials against pseudotyped viruses with the S proteins of wild-type or variants of concern or interest (Alpha, Beta, Gamma, Delta, Lambda and Omicron). **b**, Neutralization curves for these mAbs in correspondence with **a**. Mean of two experiments is shown.

[Extended Data Fig. 3 Heatmap representation of representative mAbs against WT and variants of concern.](#)

Color bar on the right showed the gradient of IC₅₀ of different antibodies against the authentic WT and variants of concern. All experiments were performed in duplicate.

[Extended Data Fig. 4 Data sheets of ELISA assay of representative mAbs against Omicron RBD.](#)

Different Classes of mAbs (Class I-VI) are colored by yellow, green, red, blue, brown and magenta, respectively. Values are filled with black (>75), grey (50–75), silver (25–50) and white (<25). Each data is the mean of three values from three independent experiments.

Extended Data Fig. 5 Flowcharts for cryo-EM data processing.

Flowcharts for Omicron S protein in complex with **a**, XGv347, **b**, XGv289, **c**, XGv282 and **d**, XGv265 are shown. Scala bar in micrographs, 100 nm.

Extended Data Fig. 6 Resolution estimation of the EM maps.

a, The gold-standard FSC curves of overall maps of Omicron S trimer in complex with Fab XGv347, XGv289, XGv282 and XGv265 and local maps of interfaces. **b**, Local resolution assessments of cryo-EM maps using ResMap are shown.

Extended Data Fig. 7 Density maps and atomic models.

Cryo-EM density maps of Omicron S trimer in complex with XGv347, XGv289, XGv282 and XGv265 and their interfaces are shown. Color scheme is the same as in Fig. 3a. Residues are shown as sticks with oxygen colored in red, nitrogen colored in blue and sulfurs colored in yellow.

Extended Data Fig. 8 Multiple sequence alignment of XGv347, CoV2-2196 and A23-58.1.

Multiple sequence alignments of heavy chains and light chains of XGv347, CoV2-2196 and A23-58.1 were performed, respectively. Paratopes of XGv347 binding to Omicron variant RBD are highlighted by green boxes.

Extended Data Fig. 9 Mechanism of XGv347 binding to 3 closed RBD.

a, Superimposition of A23-58.1 onto WT S trimer. **b**, Superimposition of XGv347 onto WT S trimer. **c**, complex of XGv347 and Omicron S trimer. All complexes are in the same orientation with close-ups of Fab-RBD binding modes showing potential clashes.

Extended Data Fig. 10 Binding modes of XGv289, 282 and 265.

Binding modes of XGv289, XGv282 and XGv265. RBD is colored in light cyan and color scheme of XGv289, XGv282 and XGv265 is the same as in Fig. 3a. LY-CoV1404, BD-812 and REGN10987 are colored in purple, deep pink and blue, respectively.

Extended Data Fig. 11 Structural fitting.

XGv265, XGv282 and XGv289 are superimposed onto XGv347 and all structure are shown as surface.

Extended Data Fig. 12 BLI assay for XGv347 competing with XGv289, XGv282 and XGv265.

Affinity curves of XGv347 to Omicron S protein competing with **a**, XGv265, **b**, XGv282 and **c**, XGv289. In each panel, (left) XGv347 was first injected, followed by the XGv265, XGv282 and XGv289 in **a–c**, respectively. (right) Also, XGv265 in **a**, XGv282 in **b** and XGv289 in **c**, was injected first and competed with the second injection of XGv347. Each curve is a representative of three independent experiments.

Extended Data Fig. 13 Interactions details between antibodies (XGv347, XGv289, XGv282 and XGv265) and SARS-CoV-2 WT (left) and Omicron RBD (right).

All the WT structures are predicted with GROMACS. Hydrophobic patches and hydrogen bonds are denoted by surface and dash lines. Color scheme is the same as in Fig. 3a. For hydrophobic patches of XGv289, XGv282 and XGv265, G446 and S446 are colored in magenta. The dash lines marked out the hydrophobic patches only found in WT RBD.

Extended Data Fig. 14 Histopathological analysis of lung samples from XGv282 treatment group at 5 dpi.

Shown here are the H&E staining of lung samples from each of the remaining four mice in XGv282 group. Each micrograph is representative of two separate experiments.

Extended Data Table 1 Statistics for cryo-EM data collection, refinement, and validation

Extended Data Table 2 List of interacting residues between Fabs and Omicron SARS-CoV-2 S trimer ($d < 4 \text{ \AA}$)

Extended Data Table 3 Statistics for molecular dynamics

Supplementary information

Reporting Summary

Supplementary Table 1

Information for the antibodies isolated individuals who received 3 doses of Coronavac vaccine.

Supplementary Table 2

Sequences of the 41 representative recombinant antibodies.

Rights and permissions

Open Access This article is licensed under a Creative Commons Attribution 4.0 International License, which permits use, sharing, adaptation, distribution and reproduction in any medium or format, as long as you give appropriate credit to the original author(s) and the source, provide a link to the Creative Commons license, and indicate if changes were made. The images or other third party material in this article are included in the article's Creative Commons license, unless indicated otherwise in a credit line to the material. If material is not included in the article's Creative Commons license and your intended use is not permitted by statutory regulation or exceeds the permitted use, you will need to obtain permission directly from the copyright holder. To view a copy of this license, visit <http://creativecommons.org/licenses/by/4.0/>.

Reprints and Permissions

About this article

Cite this article

Wang, K., Jia, Z., Bao, L. *et al.* Memory B cell repertoire from triple vaccinees against diverse SARS-CoV-2 variants. *Nature* **603**, 919–925 (2022).
<https://doi.org/10.1038/s41586-022-04466-x>

- Received: 22 December 2021
- Accepted: 20 January 2022
- Published: 28 January 2022
- Issue Date: 31 March 2022
- DOI: <https://doi.org/10.1038/s41586-022-04466-x>

Share this article

Anyone you share the following link with will be able to read this content:

[Get shareable link](#)

Sorry, a shareable link is not currently available for this article.

[Copy to clipboard](#)

Provided by the Springer Nature SharedIt content-sharing initiative

This article was downloaded by **calibre** from <https://www.nature.com/articles/s41586-022-04466-x>

| [Section menu](#) | [Main menu](#) |

- Article
- [Published: 16 March 2022](#)

A single-cell atlas of human and mouse white adipose tissue

- [Margo P. Emont](#) ORCID: orcid.org/0000-0001-9873-2784^{1,2},
- [Christopher Jacobs](#) ORCID: orcid.org/0000-0002-6034-1873^{1,2},
- [Adam L. Essene](#)¹,
- [Deepti Pant](#)¹,
- [Danielle Tenen](#)^{1,2},
- [Georgia Colleluori](#) ORCID: orcid.org/0000-0002-4908-9873³,
- [Angelica Di Vincenzo](#)³,
- [Anja M. Jørgensen](#)⁴,
- [Hesam Dashti](#)²,
- [Adam Stefek](#)²,
- [Elizabeth McGonagle](#) ORCID: orcid.org/0000-0001-9708-9272²,
- [Sophie Strobel](#)²,
- [Samantha Laber](#)²,
- [Saaket Agrawal](#)^{2,5},
- [Gregory P. Westcott](#) ORCID: orcid.org/0000-0002-4321-3992¹,
- [Amrita Kar](#)^{1,2},
- [Molly L. Veregge](#)¹,
- [Anton Gulko](#)¹,
- [Harini Srinivasan](#)^{1,2},
- [Zachary Kramer](#)¹,
- [Eleanna De Filippis](#) ORCID: orcid.org/0000-0002-5622-6709⁶,
- [Erin Merkel](#)¹,
- [Jennifer Ducie](#)⁷,
- [Christopher G. Boyd](#)⁸,

- [William Gourash⁹](#),
- [Anita Courcoulas⁹](#),
- [Samuel J. Lin¹⁰](#),
- [Bernard T. Lee¹⁰](#),
- [Donald Morris¹⁰](#),
- [Adam Tobias¹⁰](#),
- [Amit V. Khera^{2,5,10}](#),
- [Melina Claussnitzer^{2,12}](#),
- [Tune H. Pers](#) [ORCID: orcid.org/0000-0003-0207-4831⁴](#),
- [Antonio Giordano³](#),
- [Orr Ashenberg¹³](#),
- [Aviv Regev^{13,14,15}](#),
- [Linus T. Tsai](#) [ORCID: orcid.org/0000-0002-0134-6949^{1,2,11}](#) &
- [Evan D. Rosen](#) [ORCID: orcid.org/0000-0003-4603-708X^{1,2,11}](#)

[**Nature**](#) **volume 603**, pages 926–933 (2022)

- 12k Accesses
- 155 Altmetric
- [Metrics details](#)

Subjects

- [Fat metabolism](#)
- [Obesity](#)

Abstract

White adipose tissue, once regarded as morphologically and functionally bland, is now recognized to be dynamic, plastic and heterogenous, and is involved in a wide array of biological processes including energy homeostasis, glucose and lipid handling, blood pressure control and host defence¹. High-fat feeding and other metabolic stressors cause marked changes in adipose morphology, physiology and cellular composition¹, and

alterations in adiposity are associated with insulin resistance, dyslipidemia and type 2 diabetes². Here we provide detailed cellular atlases of human and mouse subcutaneous and visceral white fat at single-cell resolution across a range of body weight. We identify subpopulations of adipocytes, adipose stem and progenitor cells, vascular and immune cells and demonstrate commonalities and differences across species and dietary conditions. We link specific cell types to increased risk of metabolic disease and provide an initial blueprint for a comprehensive set of interactions between individual cell types in the adipose niche in leanness and obesity. These data comprise an extensive resource for the exploration of genes, traits and cell types in the function of white adipose tissue across species, depots and nutritional conditions.

This is a preview of subscription content

Access options

Subscribe to Nature+

Get immediate online access to the entire Nature family of 50+ journals

\$29.99

monthly

[Subscribe](#)

Subscribe to Journal

Get full journal access for 1 year

\$199.00

only \$3.90 per issue

[Subscribe](#)

All prices are NET prices.
VAT will be added later in the checkout.
Tax calculation will be finalised during checkout.

Buy article

Get time limited or full article access on ReadCube.

\$32.00

[Buy](#)

All prices are NET prices.

Additional access options:

- [Log in](#)
- [Learn about institutional subscriptions](#)

Fig. 1: A single-cell atlas of human white adipose tissue.

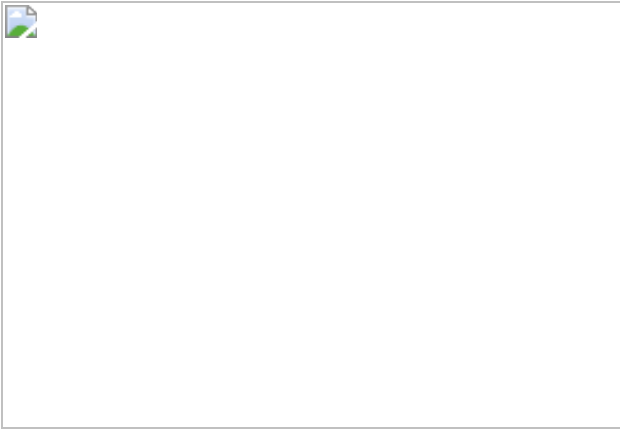


Fig. 2: A single cell atlas of mouse white adipose tissue.

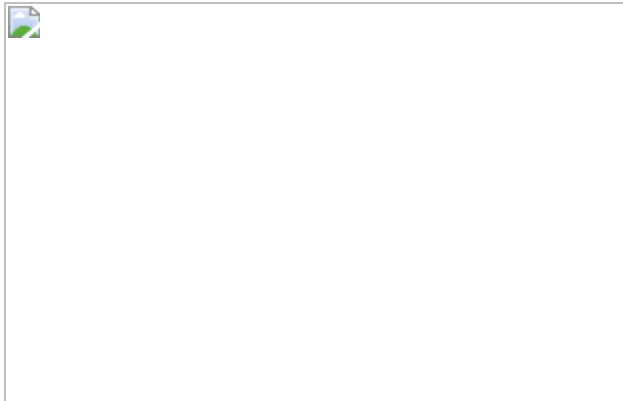


Fig. 3: Subclustering of human and mouse adipocytes reveals multiple distinct populations that vary across depot and diet.

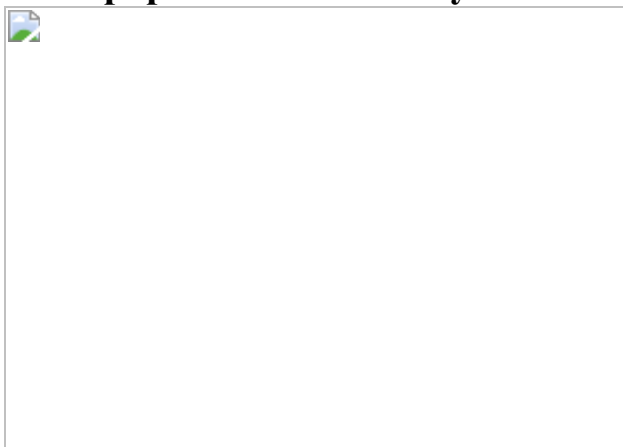
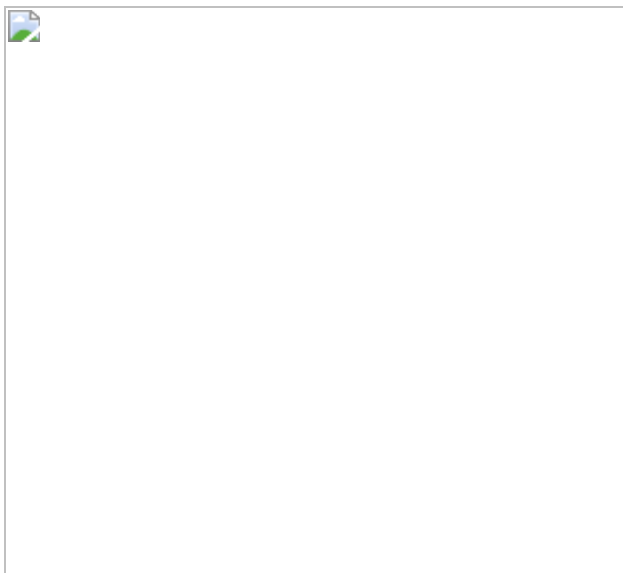


Fig. 4: Extensive cell–cell interactions in WAT and associations with human disease traits.



Data availability

Single-cell RNA expression and count data are deposited in the Single Cell Portal (study no. [SCP1376](#)). Processed count data for bulk RNA-seq and differential gene expression matrices for single-cell and single-nucleus RNA-seq have been deposited in the Gene Expression Omnibus (bulk-sequencing accession [GSE174475](#), scRNA-seq accession [GSE176067](#), sNuc-seq accession [GSE176171](#)); raw sequencing reads for mouse data are available in the Sequence Read Archive under study no. [SRP322736](#). FASTQ and SNP array files for human samples are deposited in dbGaP under accession [phs002766.v1.p1](#). [Source data](#) are provided with this paper.

Code availability

Data analysis pipelines used in this study for processing of raw sequencing data, integration and clustering can be obtained from
<https://gitlab.com/rosen-lab/white-adipose-atlas>.

References

1. Rosen, E. D. & Spiegelman, B. M. What we talk about when we talk about fat. *Cell* **156**, 20–44 (2014).
2. Kahn, S. E., Hull, R. L. & Utzschneider, K. M. Mechanisms linking obesity to insulin resistance and type 2 diabetes. *Nature* **444**, 840–846 (2006).
3. Schwalie, P. C. et al. A stromal cell population that inhibits adipogenesis in mammalian fat depots. *Nature* **559**, 103–108 (2018).
4. Burl, R. B. et al. Deconstructing adipogenesis induced by β 3-adrenergic receptor activation with single-cell expression profiling. *Cell Metab.* **28**, 300–309.e4 (2018).
5. Merrick, D. et al. Identification of a mesenchymal progenitor cell hierarchy in adipose tissue. *Science* **364**, eaav2501 (2019).
6. Hepler, C. et al. Identification of functionally distinct fibro-inflammatory and adipogenic stromal subpopulations in visceral

adipose tissue of adult mice. *eLife* **7**, e39636 (2018).

7. Vijay, J. et al. Single-cell analysis of human adipose tissue identifies depot- and disease-specific cell types. *Nat. Metab.* **2**, 97–109 (2020).
8. Rajbhandari, P. et al. Single cell analysis reveals immune cell–adipocyte crosstalk regulating the transcription of thermogenic adipocytes. *eLife* **8**, e49501 (2019).
9. Sárvári, A. K. et al. Plasticity of epididymal adipose tissue in response to diet-induced obesity at single-nucleus resolution. *Cell Metab.* **33**, 437–453.e5 (2021).
10. Sun, W. et al. snRNA-seq reveals a subpopulation of adipocytes that regulates thermogenesis. *Nature* **587**, 98–102 (2020).
11. Benites-Zapata, V. A. et al. High waist-to-hip ratio levels are associated with insulin resistance markers in normal-weight women. *Diabetes Metab. Syndr. Clin. Res. Rev.* **13**, 636–642 (2019).
12. Wang, X., Park, J., Susztak, K., Zhang, N. R. & Li, M. Bulk tissue cell type deconvolution with multi-subject single-cell expression reference. *Nat. Commun.* **10**, 380 (2019).
13. Raulerson, C. K. et al. Adipose tissue gene expression associations reveal hundreds of candidate genes for cardiometabolic traits. *Am. J. Hum. Genet.* **105**, 773–787 (2019).
14. Blüher, M. Transgenic animal models for the study of adipose tissue biology. *Best Pract. Res. Clin. Endocrinol. Metab.* **19**, 605–623 (2005).
15. Rinaldi, V. D. et al. An atlas of cell types in the mouse epididymis and vas deferens. *eLife* **9**, e55474 (2020).
16. Villani, A.-C. et al. Single-cell RNA-seq reveals new types of human blood dendritic cells, monocytes, and progenitors. *Science* **356**, eaah4573 (2017).

17. Hildreth, A. D. et al. Single-cell sequencing of human white adipose tissue identifies new cell states in health and obesity. *Nat. Immunol.* **22**, 639–653 (2021).
18. Suganami, T. & Ogawa, Y. Adipose tissue macrophages: their role in adipose tissue remodeling. *J. Leukoc. Biol.* **88**, 33–39 (2010).
19. Weisberg, S. P. et al. Obesity is associated with macrophage accumulation in adipose tissue. *J. Clin. Invest.* **112**, 1796–1808 (2003).
20. Reilly, S. M. & Saltiel, A. R. Adapting to obesity with adipose tissue inflammation. *Nat. Rev. Endocrinol.* **13**, 633–643 (2017).
21. Shi, M. & Shi, G.-P. Different roles of mast cells in obesity and diabetes: lessons from experimental animals and humans. *Front. Immunol.* **3**, 7 (2012).
22. Xu, H. et al. Chronic inflammation in fat plays a crucial role in the development of obesity-related insulin resistance. *J. Clin. Invest.* **112**, 1821–1830 (2003).
23. Ferrero, R., Rainer, P. & Deplancke, B. Toward a consensus view of mammalian adipocyte stem and progenitor cell heterogeneity. *Trends Cell Biol.* **30**, 937 (2020).
24. Wang, Q. A., Tao, C., Gupta, R. K. & Scherer, P. E. Tracking adipogenesis during white adipose tissue development, expansion and regeneration. *Nat. Med.* **19**, 1338–1344 (2013).
25. Jeffery, E., Church, C. D., Holtrup, B., Colman, L. & Rodeheffer, M. S. Rapid depot-specific activation of adipocyte precursor cells at the onset of obesity. *Nat. Cell Biol.* **17**, 376–385 (2015).
26. Bäckdahl, J. et al. Spatial mapping reveals human adipocyte subpopulations with distinct sensitivities to insulin. *Cell Metab.* **33**, 1869–1882.e6 (2021).

27. Stefan, N. et al. Circulating palmitoleate strongly and independently predicts insulin sensitivity in humans. *Diabetes Care* **33**, 405–407 (2010).
28. Laber, S. et al. Discovering cellular programs of intrinsic and extrinsic drivers of metabolic traits using LipocyteProfiler. Preprint at <https://doi.org/10.1101/2021.07.17.452050> (2021).
29. Rajakumari, S. et al. EBF2 determines and maintains brown adipocyte identity. *Cell Metab.* **17**, 562–574 (2013).
30. Pilit, S. L. et al. Meta-analysis of genome-wide association studies for body fat distribution in 694 649 individuals of European ancestry. *Hum. Mol. Genet.* **28**, 166–174 (2019).
31. Agrawal, S. et al. Inherited basis of visceral, abdominal subcutaneous and gluteofemoral fat depots. Preprint at <https://doi.org/10.1101/2021.08.24.21262564> (2021).
32. Willows, J. W. et al. Visualization and analysis of whole depot adipose tissue neural innervation. *iScience* **24**, 103127 (2021).
33. Roh, H. C. et al. Adipocytes fail to maintain cellular identity during obesity due to reduced PPAR γ activity and elevated TGF β –SMAD signaling. *Mol. Metab.* **42**, 101086 (2020).
34. Park, J. et al. Progenitor-like characteristics in a subgroup of UCP1 $^{+}$ cells within white adipose tissue. *Dev. Cell* **56**, 985–999.e4 (2021).
35. Priest, C. & Tontonoz, P. Inter-organ cross-talk in metabolic syndrome. *Nat. Metab.* **1**, 1177–1188 (2019).
36. Schling, P. & Löffler, G. Cross talk between adipose tissue cells: impact on pathophysiology. *News Physiol. Sci.* **17**, 99–104 (2002).
37. Kane, H. & Lynch, L. Innate immune control of adipose tissue homeostasis. *Trends Immunol.* **40**, 857–872 (2019).

38. Efremova, M., Vento-Tormo, M., Teichmann, S. A. & Vento-Tormo, R. CellPhoneDB: inferring cell–cell communication from combined expression of multi-subunit ligand–receptor complexes. *Nat. Protoc.* **15**, 1484–1506 (2020).
39. Cao, Y. Angiogenesis and vascular functions in modulation of obesity, adipose metabolism, and insulin sensitivity. *Cell Metab.* **18**, 478–489 (2013).
40. Hubert, A. et al. Selective deletion of leptin signaling in endothelial cells enhances neointima formation and phenocopies the vascular effects of diet-induced obesity in mice. *Arterioscler. Thromb. Vasc. Biol.* **37**, 1683–1697 (2017).
41. Scott, R. A. et al. An expanded genome-wide association study of type 2 diabetes in Europeans. *Diabetes* **66**, 2888–2902 (2017).
42. Shungin, D. et al. New genetic loci link adipose and insulin biology to body fat distribution. *Nature* **518**, 187–196 (2015).
43. Huang, L. O. et al. Genome-wide discovery of genetic loci that uncouple excess adiposity from its comorbidities. *Nat. Metab.* **3**, 228–243 (2021).
44. Timshel, P. N., Thompson, J. J. & Pers, T. H. Genetic mapping of etiologic brain cell types for obesity. *eLife* **9**, e55851 (2020).
45. O’Rahilly, S. & Farooqi, I. S. Human obesity as a heritable disorder of the central control of energy balance. *Int. J. Obes.* **32** (Suppl. 7), S55–S61 (2008).
46. Sailer, S., Keller, M. A., Werner, E. R. & Watschinger, K. The emerging physiological role of AGMO 10 years after its gene identification. *Life* **11**, 88 (2021).
47. Dupuis, J. et al. New genetic loci implicated in fasting glucose homeostasis and their impact on type 2 diabetes risk. *Nat. Genet.* **42**, 105–116 (2010).

48. Loh, N. Y. et al. RSPO3 impacts body fat distribution and regulates adipose cell biology in vitro. *Nat. Commun.* **11**, 2797 (2020).
49. Chi, J. et al. Three-dimensional adipose tissue imaging reveals regional variation in beige fat biogenesis and PRDM16-dependent sympathetic neurite density. *Cell Metab.* **27**, 226–236.e3 (2018).
50. Katz, A. et al. Quantitative insulin sensitivity check index: a simple, accurate method for assessing insulin sensitivity in humans. *J. Clin. Endocrinol. Metab.* **85**, 2402–2410 (2000).
51. Matthews, D. R. et al. Homeostasis model assessment: insulin resistance and β-cell function from fasting plasma glucose and insulin concentrations in man. *Diabetologia* **28**, 412–419 (1985).
52. Macosko, E. Z. et al. Highly parallel genome-wide expression profiling of individual cells using nanoliter droplets. *Cell* **161**, 1202–1214 (2015).
53. Drokhlyansky, E. et al. The human and mouse enteric nervous system at single-cell resolution. *Cell* **182**, 1606–1622.e23 (2020).
54. Slyper, M. et al. A single-cell and single-nucleus RNA-seq toolbox for fresh and frozen human tumors. *Nat. Med.* **26**, 792–802 (2020).
55. Delorey, T. M. et al. A single-cell and spatial atlas of autopsy tissues reveals pathology and cellular targets of SARS-CoV-2. Preprint at <https://doi.org/10.1101/2021.02.25.430130> (2021).
56. Dobin, A. et al. STAR: ultrafast universal RNA-seq aligner. *Bioinformatics* **29**, 15–21 (2013).
57. CellBender remove-background: a deep generative model for unsupervised removal of background noise from scRNA-seq datasets. Preprint at <https://doi.org/10.1101/791699> (2019).
58. Lun, A. T. L. et al. EmptyDrops: distinguishing cells from empty droplets in droplet-based single-cell RNA sequencing data. *Genome*

Biol. **20**, 63 (2019).

59. Wolock, S. L., Lopez, R. & Klein, A. M. Scrublet: computational identification of cell doublets in single-cell transcriptomic data. *Cell Syst.* **8**, 281–291.e9 (2019).
60. Patro, R., Duggal, G., Love, M. I., Irizarry, R. A. & Kingsford, C. Salmon provides fast and bias-aware quantification of transcript expression. *Nat. Methods* **14**, 417–419 (2017).
61. Srivastava, A. et al. Alignment and mapping methodology influence transcript abundance estimation. *Genome Biol.* **21**, 239 (2020).
62. Soneson, C., Love, M. I. & Robinson, M. D. Differential analyses for RNA-seq: transcript-level estimates improve gene-level inferences. *F1000Research* **4**, 1521 (2015).
63. Stuart, T. et al. Comprehensive integration of single-cell data. *Cell* **177**, 1888–1902.e21 (2019).
64. Hafemeister, C. & Satija, R. Normalization and variance stabilization of single-cell RNA-seq data using regularized negative binomial regression. *Genome Biol.* **20**, 296 (2019).
65. Hao, Y. et al. Integrated analysis of multimodal single-cell data. *Cell* **184**, 3573–3587.e29 (2021).
66. Yu, G., Wang, L.-G., Han, Y. & He, Q.-Y. clusterProfiler: an R package for comparing biological themes among gene clusters. *OMICS J. Integr. Biol.* **16**, 284–287 (2012).
67. Littlejohns, T. J. et al. The UK Biobank imaging enhancement of 100,000 participants: rationale, data collection, management and future directions. *Nat. Commun.* **11**, 2624 (2020).
68. Sudlow, C. et al. UK Biobank: an open access resource for identifying the causes of a wide range of complex diseases of middle and old age. *PLoS Med.* **12**, e1001779 (2015).

69. Agrawal, S. et al. Association of machine learning-derived measures of body fat distribution in >40,000 individuals with cardiometabolic diseases. Preprint at <https://doi.org/10.1101/2021.05.07.21256854> (2021).
70. Kichaev, G. et al. Leveraging polygenic functional enrichment to improve GWAS power. *Am. J. Hum. Genet.* **104**, 65–75 (2019).
71. Pruim, R. J. et al. LocusZoom: regional visualization of genome-wide association scan results. *Bioinformatics* **26**, 2336–2337 (2010).
72. Mahajan, A. et al. Fine-mapping type 2 diabetes loci to single-variant resolution using high-density imputation and islet-specific epigenome maps. *Nat. Genet.* **50**, 1505–1513 (2018).
73. Loh, P.-R., Kichaev, G., Gazal, S., Schoech, A. P. & Price, A. L. Mixed-model association for biobank-scale datasets. *Nat. Genet.* **50**, 906–908 (2018).
74. Finucane, H. K. et al. Partitioning heritability by functional annotation using genome-wide association summary statistics. *Nat. Genet.* **47**, 1228–1235 (2015).
75. Teslovich, T. M. et al. Biological, clinical and population relevance of 95 loci for blood lipids. *Nature* **466**, 707–713 (2010).
76. Bradfield, J. P. et al. A genome-wide meta-analysis of six type 1 diabetes cohorts identifies multiple associated loci. *PLoS Genet.* **7**, e1002293 (2011).
77. Loh, P.-R. et al. Reference-based phasing using the Haplotype Reference Consortium panel. *Nat. Genet.* **48**, 1443–1448 (2016).
78. Das, S. et al. Next-generation genotype imputation service and methods. *Nat. Genet.* **48**, 1284–1287 (2016).
79. Robinson, M. D., McCarthy, D. J. & Smyth, G. K. edgeR: a Bioconductor package for differential expression analysis of digital

gene expression data. *Bioinformatics* **26**, 139–140 (2010).

80. Büttner, M., Ostner, J., Müller, C., Theis, F. & Schubert, B. scCODA: a Bayesian model for compositional single-cell data analysis. *Nat. Commun.* **12**, 6876 (2021).

Acknowledgements

This work was supported by NIH grants RC2 DK116691 to E.D.R., L.T.T., A.C., O.A. and A.R., AHA POST14540015 and DoD PRMRP-DAW81XWH to L.T.T., Broad-BADERC Collaboration Initiative Award (NIH 5P30DK057521) to L.T.T. and E.D.R., and R01 DK102173 to E.D.R. M.P.E. is supported by NIH grant F32DK124914. Additional support includes PRIN 2017 (Italian Ministry of University, no. 2017L8Z2EM) to A. Giordano, T.H.P. acknowledges the Novo Nordisk Foundation (unconditional donation to the Novo Nordisk Foundation Center for Basic Metabolic Research; grant number NNF18CC0034900) and the Lundbeck Foundation (grant number R190-2014-3904), grants AMP-T2D RFB8b (FNIH) and UM1DK126185 (NIDDK) to M.C., Sarnoff Cardiovascular Research Foundation Fellowship to S.A., grants 1K08HG010155 and 1U01HG011719 to A.V.K. from the National Human Genome Research Institute, and a sponsored research agreement from IBM Research to the Broad Institute of MIT and Harvard to A.V.K. All single cell library construction and sequencing was performed through the Boston Nutrition Obesity Research Center Functional Genomics and Bioinformatics Core (NIH P30DK046200). We thank C. Usher for artistic support and M. Udler for helpful discussions.

Author information

Affiliations

1. Division of Endocrinology, Diabetes and Metabolism, Beth Israel Deaconess Medical Center, Boston, MA, USA

Margo P. Emont, Christopher Jacobs, Adam L. Essene, Deepti Pant, Danielle Tenen, Gregory P. Westcott, Amrita Kar, Molly L. Veregge, Anton Gulko, Harini Srinivasan, Zachary Kramer, Erin Merkel, Linus T. Tsai & Evan D. Rosen

2. Broad Institute of MIT and Harvard, Cambridge, MA, USA

Margo P. Emont, Christopher Jacobs, Danielle Tenen, Hesam Dashti, Adam Stefek, Elizabeth McGonagle, Sophie Strobel, Samantha Laber, Saaket Agrawal, Amrita Kar, Harini Srinivasan, Amit V. Khera, Melina Claussnitzer, Linus T. Tsai & Evan D. Rosen

3. Department of Experimental and Clinical Medicine, Center of Obesity, Marche Polytechnic University, Ancona, Italy

Georgia Colleluori, Angelica Di Vincenzo & Antonio Giordano

4. Novo Nordisk Foundation Center for Basic Metabolic Research, University of Copenhagen, Copenhagen, Denmark

Anja M. Jørgensen & Tune H. Pers

5. Center for Genomic Medicine, Department of Medicine, Massachusetts General Hospital, Boston, MA, USA

Saaket Agrawal & Amit V. Khera

6. Division of Endocrinology, Diabetes and Metabolism, Mayo Clinic Scottsdale, AZ, USA

Eleanna De Filippis

7. Division of Gynecologic Oncology, Department of Obstetrics and Gynecology, Beth Israel Deaconess Medical Center, Boston, MA, USA

Jennifer Ducie

8. Department of Surgery, Beth Israel Deaconess Medical Center, Boston, MA, USA

Christopher G. Boyd

9. Department of Surgery, University of Pittsburgh Medical Center, Pittsburgh, PA, USA

William Gourash & Anita Courcoulas

10. Division of Plastic Surgery, Department of Surgery, Beth Israel Deaconess Medical Center, Boston, MA, USA

Samuel J. Lin, Bernard T. Lee, Donald Morris, Adam Tobias & Amit V. Khera

11. Harvard Medical School, Boston, MA, USA

Linus T. Tsai & Evan D. Rosen

12. Diabetes Unit and Center for Genomic Medicine, Massachusetts General Hospital, Boston, Massachusetts, USA

Melina Claussnitzer

13. Klarman Cell Observatory, Broad Institute of MIT and Harvard, Cambridge, MA, USA

Orr Ashenberger & Aviv Regev

14. Howard Hughes Medical Institute, Koch Institute of Integrative Cancer Research, Department of Biology, Massachusetts Institute of Technology, Cambridge, MA, USA

Aviv Regev

15. Genentech, South San Francisco, CA, USA

Aviv Regev

Contributions

M.P.E., L.T.T. and E.D.R. conceived of the project. M.P.E. and E.D.R. wrote the manuscript with assistance from L.T.T., C.J., O.A. and A.R. M.P.E., A.L.E., D.P., D.T., G.C., A.D.V., A.S., E. McGonagle, S.S., S.L., G.P.W., M.L.V., A. Gulko and E. Merkel performed experiments. G.P.W., A. Gulko, Z.K., E.D.F., J.D., C.G.B., W.G., A.C., S.J.L., B.T.L., D.M. and A.T. collected samples. M.P.E., C.J., A.M.J., H.D., S.A., A.K. and H.S. performed computational analysis. A.V.K., M.C., T.H.P., A. Giordano, O.A. and A.R. provided additional intellectual input.

Corresponding author

Correspondence to [Evan D. Rosen](#).

Ethics declarations

Competing interests

S.A. has served as a scientific consultant to Third Rock Ventures. A.V.K. has served as a scientific advisor to Sanofi, Amgen, Maze Therapeutics, Navitor Pharmaceuticals, Sarepta Therapeutics, Novartis, Verve Therapeutics, Silence Therapeutics, Veritas International, Color Health, Third Rock Ventures and Columbia University (NIH); received speaking fees from Illumina, MedGenome, Amgen, and the Novartis Institute for Biomedical Research; and received a sponsored research agreement from the Novartis Institute for Biomedical Research. M.C. holds equity in Waypoint Bio and is a member of the Nestle Scientific Advisory Board. A.R. is a co-founder and equity holder of Celsius Therapeutics, an equity holder in Immunitas Therapeutics and a scientific advisory board member of Thermo Fisher Scientific, Syros Pharmaceuticals, Asimov and Neogene Therapeutics. A.R. is also an employee of Genentech. All other authors declare no competing interests.

Peer review

Peer review information

Nature thanks Bart Deplancke and the other, anonymous, reviewers for their contribution to the peer review of this work. Peer review reports are available.

Additional information

Publisher's note Springer Nature remains neutral with regard to jurisdictional claims in published maps and institutional affiliations.

Extended data figures and tables

[Extended Data Fig. 1 Additional analysis of the effects of depot and BMI on human WAT populations.](#)

a, UMAP projections of cells from the lowest and highest BMI ranges in the dataset, split by depot. To facilitate comparison, samples were randomly subset to contain the same number of cells in each plot ($n = 20,339$). **b**, Graph showing the proportion of sNuc-seq cells in each cluster per sample, split by depot and BMI, $n = 4$ SAT < 30 , 6 SAT > 40 , 3 VAT < 30 , 5 VAT > 40 . **C**, Estimated cell type proportions in bulk RNA sequencing data of subcutaneous adipose tissue from 331 individuals from the METSIM cohort calculated using sNuc-seq data as reference. Vascular cells include endothelial, lymphatic endothelial, pericytes, and smooth muscle cells. Myeloid immune includes macrophages, monocytes, dendritic cells, mast cells and neutrophils, and lymphoid immune includes B cells, NK cells, and T cells. For lines of best fit: Adipocytes $R^2 = 0.031$, ASCPs $R^2 = 0.034$, Vascular $R^2 = 0.076$, Myeloid Immune $R^2 = 0.13$, Lymphoid Immune $R^2 = 0.0049$. For scatterplots, error bands represent a confidence level of 0.95 and P values were calculated using an F -test with the null hypothesis that the slope = 0. For bar graphs, error bars represent SEM, * indicates credible depot effect and # indicates credible BMI effect, calculated using dendritic cells as reference.

[Source data](#)

Extended Data Fig. 2 Additional analysis of the effects of depot and diet on mouse WAT populations and association with human WAT populations.

a, UMAP projection of all mouse WAT cells split by depot. **b**, Proportion of cells in each cluster per sample, split by sex as well as by depot and diet, for male mice n = 4 ING Chow, 4 ING HFD, 3 EPI Chow, and 5 EPI HFD. For female mice, n = 2 per condition. **c**, Riverplot showing the relationship between mouse and human clusters. Mouse cells were mapped onto human sNuc-seq cells using multimodal reference mapping. The riverplot represents the relationship between manually assigned mouse cluster and mapped human cluster for every mouse cell. For bar graphs, error bars represent SEM, * indicates credible depot effect and # indicates credible diet effect, calculated using dendritic cells as reference.

[Source data](#)

Extended Data Fig. 3 Highly similar vascular cells in human and mouse WAT.

a, UMAP projection of 22,734 human vascular cells. **b**, Marker genes for 11 distinct clusters of human WAT vascular cells. **c**, UMAP projection of 7,632 mouse vascular cells. **d**, Marker genes for 9 distinct clusters of mouse WAT vascular cells. **e**, Riverplot showing the correlation between annotated mouse and human vascular clusters based on multimodal reference mapping for each mouse cell. **f**, **g**, Bar graphs showing the proportion of cells in each cluster per sample split by depot and BMI for human (**f**) and depot, diet, and sex for mouse (**g**). For humans, n = 9 SAT < 30, 6 SAT > 40, 3 VAT < 30, and 5 VAT > 40. For male mice n = 4 ING Chow, 4 ING HFD, 3 EPI Chow, and 5 EPI HFD. For female mice, n = 2 per condition. For bar graphs, error bars represent SEM, * indicates credible depot effect and # indicates credible BMI/diet effect, calculated using hEndoA2 (human) and mEndoA2 (mouse) as reference.

[Source data](#)

Extended Data Fig. 4 Comparison of immune cells in human and mouse WAT.

a, UMAP projection of 34,268 immune cells from human WAT. **b**, Marker genes for human immune cell clusters. **c**, UMAP projection of 70,547 immune cells from mouse WAT. **d**, Marker genes for mouse immune cell clusters. **e-f**, Riverplots showing the correlation between annotated mouse cluster and mapped human cluster for mouse (**e**) dendritic cells, mast cells, neutrophils, B cells, NK cells, and T cells and (**f**) monocytes and macrophages.

Extended Data Fig. 5 Human and mouse immune cells are differentially regulated by depot and BMI/diet.

a, b, UMAP projections of human (**a**) and mouse (**b**) WAT immune cells split by depot. **c, d**, UMAP projections of human (**c**) and mouse (**d**) WAT immune cells split by BMI (**c**) and diet (**d**). **e-f**, Bar graphs showing the proportion of cells in each cluster per sample split by depot and BMI for human (**e**) and depot, diet, and sex for mouse (**f**). For humans, n = 10 SAT < 30, 6 SAT > 40, 3 VAT < 30, and 5 VAT > 40. For male mice n = 4 ING Chow, 4 ING HFD, 3 EPI Chow, and 5 EPI HFD. For female mice, n = 2 per condition. For bar graphs, error bars represent SEM, * indicates credible depot effect and # indicates credible BMI/diet effect, calculated using hMono2 (human) and mcDC1 (mouse) as reference.

[Source data](#)

Extended Data Fig. 6 Subpopulations of human and mouse mesothelial cells.

a, UMAP projection of 30,482 human mesothelial cells. **b**, Marker genes for distinct human mesothelial populations. **c**, UMAP projection of 14,947 mouse mesothelial cells. **d** Marker genes for distinct mouse mesothelial populations. **e**, Riverplots showing relationship of mouse and human mesothelial clusters. **f, g**, Proportion of cells in each cluster per sample, split by BMI for human (**f**) and diet and sex for mouse (**g**). For humans, n =

3 VAT < 30, and 5 VAT > 40. For male mice n = 3 EPI Chow, and 5 EPI HFD. For female mice, n = 2 per condition. Error bars represent SEM, # indicates credible BMI/diet effect, calculated using hMes3 (human) and mMes1 (mouse) as reference.

[Source data](#)

Extended Data Fig. 7 Human and mouse ASPCs share commonalities with previously reported subtypes.

a, UMAP projection of 52,482 human ASPCs. **b**, Marker genes for distinct ASPC subpopulations. **c**, UMAP projection of 51,227 mouse ASPCs. **d**, Marker genes for distinct ASPC subpopulations. **e**, Riverplot depicting the relationship between mouse and human ASPC clusters. **f**, Integration of ASPCs from this paper with ASPCs from other groups.

Extended Data Fig. 8 Human ASPCs exhibit strong depot dependency while mouse ASPCs are dependent on both depot and diet.

a, b, UMAP projections of human (**a**) and mouse (**b**) ASPCs split by depot. **c-d**, UMAP projections of human (**c**) and mouse (**d**) ASPCs split by BMI/diet. **e, f**, Proportion of ASPC cells in each cluster per sample split by depot and BMI for human (**e**) and depot, diet, and sex for mouse (**f**). For humans, n = 11 SAT < 30, 6 SAT > 40, 3 VAT < 30, and 5 VAT > 40. For male mice n = 4 ING Chow, 4 ING HFD, 3 EPI Chow, and 5 EPI HFD. For female mice, n = 2 per condition. For bar graphs, error bars represent SEM, * indicates credible depot effect and # indicates credible BMI/diet effect, calculated using hASPC2 (human) and mASPC4 (mouse) as reference.

[Source data](#)

Extended Data Fig. 9 Human adipocyte subtypes are highly dependent on depot and may be responsible for distinct functions.

a, b, UMAP projections of human white adipocytes split by depot (**a**) and BMI (**b**). **c**, Proportion of cells in each human cluster by sample split by depot and BMI, n = 4 SAT < 30, 6 SAT > 40, 3 VAT < 30, and 5 VAT > 40. **D**, Quantification of immunofluorescence analysis of GRIA4+ cells in mature human adipocytes from two individuals. Each dot represents an image, n = 12 images from individual 1 and 9 images from individual 2 with a total of 704 counted cells. Only cells with visible nuclei were included in the quantification. **e**, Representative image of GRIA4+ cells, white arrows represent positive cells, grey represent negative, scale bar = 100 μ m. In total, there were 21 images from samples taken from two individuals. **f**, Expression of genes associated with adipokine secretion, insulin signaling, lipid handling, and thermogenesis across human adipocyte subclusters. **g–m**, Expression of genes associated with GO or KEGG pathways indicative of individual human adipocyte subclusters. For bar graph, error bars represent SEM, * indicates credible depot effect and # indicates credible BMI effect, calculated using hAd5 as reference.

[Source data](#)

[Extended Data Fig. 10 Human adipocytes differentiated *ex vivo* recapitulate many of the adipocyte subclusters found *in vivo*.](#)

a, Plot of estimated cell type proportion in *ex vivo* adipocyte cultures differentiated from subcutaneous or visceral preadipocytes for 14 days, ordered by estimated proportion. **b, c**, Scatterplots showing the relationship between estimated cell type proportion and the LipocyteProfiler-calculated features Large BODIPY objects (**b**) and Median BODIPY Intensity (**c**). *p* values were calculated using an *F*-test with the null hypothesis that the slope = 0. **d**, Representative images of hAd3 low/hAd5 or hAd3 high hAd5 low *ex vivo* differentiated cultures. Green represents BODIPY staining, blue represents Hoechst staining. Scale bars are 100 μ m, in total, 3 randomly selected images/sample were analyzed from 3 SAT samples and 3 VAT samples with the lowest and highest predicted proportions of hAd3 and hAd5.

[Source data](#)

Extended Data Fig. 11 Visceral-specific adipocyte subpopulation hAd6 is associated with thermogenic traits.

a, Regional visualization of associations of common genetic variants near EBF2 with VATadj. **b**, Effect size of association of rs4872393 with VATadj, ASATadj, GFATadj, and BMI per minor allele A; n = 37,641. Error bars reflect a 95% confidence interval around the effect size estimate from regression. **c**, VATadj raw data plotted according to rs4872393 carrier status; n = 36,185. For box plots, horizontal line = median, lower and upper bounds of the box = 1st and 3rd quartile respectively, lower and upper whisker = 1st quartile – 1.5 x interquartile range (IQR) and 3rd quartile + 1.5 x IQR respectively, outliers are plotted as points. **d**, Scatterplot showing the relationship between estimated cell type proportion and the LipocyteProfiler calculated feature Mitochondrial Intensity in visceral samples. **e**, Expression of mitochondrial and thermogenic genes in visceral *ex vivo* differentiated adipocytes stratified by estimated hAd6 proportion and matched for amount of differentiation using *PPARG* expression, n = 7 mAd6 low and 5 mAd6 high. Error bars represent SEM, P values were calculated using two tailed t-tests with no adjustments for multiple comparison, *, P < .05, **, P < .01. Exact P values: *EBF2* = 0.027, *TFAM* = 0.019, *CKMT1A* = 0.049, *CKMT1B* = 0.005. **f**, Representative images of hAd6 low and high visceral in vitro differentiated cultures. Green represents BODIPY staining, red represents MitoTracker staining, and blue represents Hoechst staining. Scale bars are 100 µm, in total 3 random images/sample were analyzed from 5 hAd6 low and 5 hAd6 high samples. **g**, Violin plot of sNuc-seq data showing axon guidance genes in adipocyte subclusters. **h**, Scatterplots showing the relationship between calculated proportion of visceral subpopulations hAd2 and hAd6 and expression of pan-neuronal markers on the ambient RNA of individual visceral sNuc-seq samples. For scatterplots, P values were calculated using an F-test with the null hypothesis that the slope = 0.

[Source data](#)

Extended Data Fig. 12 Mouse adipocytes appear to have distinct functionality but are not analogous to human adipocyte

subpopulations.

a, b, UMAP projections of mouse adipocytes split by depot (**a**) and diet (**b**). **c**, Proportion of cells in each mouse cluster per sample split by depot, diet, and sex. For male mice n = 4 ING Chow, 4 ING HFD, 3 EPI Chow, and 5 EPI HFD. For female mice, n = 2 per condition. **d**, Expression of genes associated with known adipocyte functions in mouse adipocyte subclusters. **e–k**, Expression of genes associated with GO or KEGG pathways indicative of individual mouse adipocyte subclusters. **l–n**, Riverplots of mouse cells showing the association between mouse and human adipocyte clusters from both subcutaneous and visceral depots (**l**), subcutaneous (ING and SAT) adipocytes only (**m**) or visceral (PG and VAT) adipocytes only (**n**). For depot comparisons, both mouse query objects and human reference objects were subset to the respective depot before mapping. For bar graph, error bars represent SEM, * indicates credible depot effect and # indicates credible diet effect, calculated using mAd6 as reference.

Source data

Extended Data Fig. 13 CellphoneDB identifies increasing numbers of cell-cell interactions within WAT during obesity.

a, Heatmap showing number of significant interactions identified between cell types in SAT of low (<30) and high (>40) BMI individuals as determined by CellphoneDB. **b**, Expression of ligand and receptor genes from Fig. [4b](#) in human adipocyte subclusters. **c**, Heatmaps showing number of significant interactions identified between cell types in ING and PG WAT of chow and HFD fed mice. **d**, Venn diagrams showing the overlap of significant interactions between adipocytes and endothelial cells, ASCPs, and macrophages between depot, BMI/diet, and species. **e**, Jitter plots of the relationship between number of WAT cell types expressing a ligand (y axis) vs. the number of cell types expressing the receptor (x axis) for all significant interactions in high BMI human VAT (left) and mouse HFD PG (right).

Extended Data Fig. 14 Association with GWAS data provides further insight into the contribution of white adipocytes to human traits.

a-c, Expression of *PPARG* in human adipocyte subclusters (**a**), and in METSIM SAT bulk RNA-seq plotted against WHR (**b**) or HOMA-IR (**c**). **d**, Expression of *PPARG* in isolated subcutaneous adipocyte bulk RNA-seq plotted against HOMA-IR. **e-h**, SNPs in the *PPARG* gene identified by DEPICT as associated with BMI-adjusted WHR plotted against *PPARG* gene expression (**e, g**) and HOMA-IR (**f, h**) in isolated subcutaneous adipocyte bulk RNA-seq data and cohort. For rs17819328 n = 7 for T/T, 30 for T/G, and 6 for G/G. For rs1797912 n = 7 for A/A, 31 for A/C, and 5 for C/C. For box plots, horizontal line = median, lower and upper bounds of the box = 1st and 3rd quartile respectively, lower and upper whisker = 1st quartile – 1.5 x interquartile range (IQR) and 3rd quartile + 1.5 x IQR respectively. *P* values were calculated using a Wilcoxon test. **i-j**, Expression of genes in human adipocyte subtypes from sNuc-seq data (**i**) and from isolated subcutaneous adipocyte bulk RNA-seq plotted against LDL (**j**). **k**, *p* values of the association between mouse cell types and GWAS studies. **l-m**, *p* values of the association between mouse adipocyte (**l**) or ASPC (**m**) subclusters with GWAS studies. For all graphs, the grey line represents *P* = 0.05 and the orange line represents significant *P* value after Bonferroni adjustment (*P* = 0.003 for all cell, *P* = 0.001 for subclusters), calculated based on number of cell types queried. For scatterplots, *P* values were calculated using an *F*-test with the null hypothesis that the slope = 0.

Extended Data Table 1 Subject information for Drop-Seq, sNuc-seq, and bulk RNA-seq of isolated subcutaneous human adipocytes
Extended Data Table 2 Numbers of cells in human and mouse single cell experiments broken down by cluster, depot, BMI/diet, and technology
Extended Data Table 3 GWAS studies used for CELLECT analysis

Supplementary information

Supplementary Information This file contains Supplementary Figs. 1–3 and Supplementary Note 1.

Reporting Summary

Peer Review File

Supplementary Table 1

Markers for human clusters and subclusters

Supplementary Table 2

Markers for mouse clusters and subclusters

Supplementary Table 3

GO and KEGG analysis of markers of human and mouse adipocyte subtypes

Supplementary Table 4

Significant interactions identified by CellphoneDB in human and mouse adipose tissue

Supplementary Table 5

Average expression of genes in clusters split by high or low BMI (human) or diet (mouse) for genes in interactions identified by CellphoneDB

Supplementary Table 6

Interactions between adipocytes and endothelial cells, ASCPs, and macrophages in human and mouse adipose tissue. TRUE refers to an interaction that is statistically significant under the given condition

Supplementary Table 7

CELLECT output for human and mouse clusters and subclusters

Source data

Source Data Fig. 2

Source Data Fig. 3

Source Data Extended Data Fig. 1

Source Data Extended Data Fig. 2

Source Data Extended Data Fig. 3

Source Data Extended Data Fig. 5

Source Data Extended Data Fig. 6

Source Data Extended Data Fig. 8

Source Data Extended Data Fig. 9

Source Data Extended Data Fig. 10

Source Data Extended Data Fig. 11

Source Data Extended Data Fig. 12

Rights and permissions

Reprints and Permissions

About this article

Cite this article

Emont, M.P., Jacobs, C., Essene, A.L. *et al.* A single-cell atlas of human and mouse white adipose tissue. *Nature* **603**, 926–933 (2022).
<https://doi.org/10.1038/s41586-022-04518-2>

- Received: 15 May 2021
- Accepted: 04 February 2022
- Published: 16 March 2022
- Issue Date: 31 March 2022
- DOI: <https://doi.org/10.1038/s41586-022-04518-2>

Share this article

Anyone you share the following link with will be able to read this content:

[Get shareable link](#)

Sorry, a shareable link is not currently available for this article.

[Copy to clipboard](#)

Provided by the Springer Nature SharedIt content-sharing initiative

This article was downloaded by **calibre** from <https://www.nature.com/articles/s41586-022-04518-2>

- Article
- Open Access
- [Published: 07 February 2022](#)

GD2-CAR T cell therapy for H3K27M-mutated diffuse midline gliomas

- [Robbie G. Majzner](#) ORCID: [orcid.org/0000-0001-6969-8011^{1,2,3}](https://orcid.org/0000-0001-6969-8011),
[Sneha Ramakrishna^{1,2}](#),
- [Kristen W. Yeom](#) ORCID: [orcid.org/0000-0001-9860-3368⁴](https://orcid.org/0000-0001-9860-3368),
- [Shabnum Patel¹](#),
- [Harshini Chinnasamy¹](#),
- [Liora M. Schultz^{1,2}](#),
- [Rebecca M. Richards^{1,2}](#),
- [Li Jiang⁵](#),
- [Valentin Barsan^{1,2}](#),
- [Rebecca Mancusi](#) ORCID: [orcid.org/0000-0002-4809-5569⁶](https://orcid.org/0000-0002-4809-5569),
- [Anna C. Geraghty⁶](#),
- [Zinaida Good](#) ORCID: [orcid.org/0000-0003-2343-5771^{1,3,7}](https://orcid.org/0000-0003-2343-5771),
- [Aaron Y. Mochizuki](#) ORCID: [orcid.org/0000-0003-1073-916X⁶](https://orcid.org/0000-0003-1073-916X),
- [Shawn M. Gillespie⁶](#),
- [Angus Martin Shaw Toland⁸](#),
- [Jasia Mahdi⁶](#),
- [Agnes Reschke^{1,2}](#),
- [Esther H. Nie⁶](#),
- [Isabelle J. Chau⁶](#),
- [Maria Caterina Rotiroti²](#),
- [Christopher W. Mount⁶](#),
- [Christina Baggott¹](#),
- [Sharon Mavroukakis¹](#),
- [Emily Egeler¹](#),
- [Jennifer Moon¹](#),
- [Courtney Erickson¹](#),
- [Sean Green²](#),
- [Michael Kunicki](#) ORCID: [orcid.org/0000-0001-6630-6289^{1,2}](https://orcid.org/0000-0001-6630-6289),

- [Michelle Fujimoto](#)^{1,2},
- [Zach Ehlinger](#)²,
- [Warren Reynolds](#)²,
- [Sreevidya Kurra](#)²,
- [Katherine E. Warren](#)⁵,
- [Snehit Prabhu](#)¹,
- [Hannes Vogel](#)⁸,
- [Lindsey Rasmussen](#)⁹,
- [Timothy T. Cornell](#)⁹,
- [Sonia Partap](#)⁶,
- [Paul G. Fisher](#) [ORCID: orcid.org/0000-0002-1196-1590](#)⁶,
- [Cynthia J. Campen](#) [ORCID: orcid.org/0000-0002-3519-1375](#)⁶,
- [Mariella G. Filbin](#)⁵,
- [Gerald Grant](#)¹⁰,
- [Bita Sahaf](#)^{1,2},
- [Kara L. Davis](#) [ORCID: orcid.org/0000-0002-7182-2592](#)^{1,2},
- [Steven A. Feldman](#)¹,
- [Crystal L. Mackall](#) [ORCID: orcid.org/0000-0001-6323-4304](#)^{1,2,3,11 na2} &
- [Michelle Monje](#) [ORCID: orcid.org/0000-0002-3547-237X](#)^{1,2,6,8,10,12 na2}

Nature volume **603**, pages 934–941 (2022)

- 14k Accesses
- 2 Citations
- 283 Altmetric
- [Metrics details](#)

Subjects

- [CNS cancer](#)
- [Paediatric research](#)

Abstract

Diffuse intrinsic pontine glioma (DIPG) and other H3K27M-mutated diffuse midline gliomas (DMGs) are universally lethal paediatric tumours of the central nervous system¹. We have previously shown that the disialoganglioside GD2 is highly expressed on H3K27M-mutated glioma cells and have demonstrated promising

preclinical efficacy of GD2-directed chimeric antigen receptor (CAR) T cells², providing the rationale for a first-in-human phase I clinical trial (NCT04196413). Because CAR T cell-induced brainstem inflammation can result in obstructive hydrocephalus, increased intracranial pressure and dangerous tissue shifts, neurocritical care precautions were incorporated. Here we present the clinical experience from the first four patients with H3K27M-mutated DIPG or spinal cord DMG treated with GD2-CAR T cells at dose level 1 (1×10^6 GD2-CAR T cells per kg administered intravenously). Patients who exhibited clinical benefit were eligible for subsequent GD2-CAR T cell infusions administered intracerebroventricularly³. Toxicity was largely related to the location of the tumour and was reversible with intensive supportive care. On-target, off-tumour toxicity was not observed. Three of four patients exhibited clinical and radiographic improvement. Pro-inflammatory cytokine levels were increased in the plasma and cerebrospinal fluid. Transcriptomic analyses of 65,598 single cells from CAR T cell products and cerebrospinal fluid elucidate heterogeneity in response between participants and administration routes. These early results underscore the promise of this therapeutic approach for patients with H3K27M-mutated DIPG or spinal cord DMG.

[Download PDF](#)

Main

This phase I dose-escalation trial of autologous GD2-CAR T cells (containing a GD2 binding domain, a 4-1BB co-stimulatory domain and a CD3Z signalling domain) in children and young adults with pontine and spinal cord DMG characterized by a K27M mutation in genes encoding histone H3 (H3K27M) was designed with the primary objectives of assessing feasibility of manufacturing, safety and tolerability, and identifying the maximally tolerated dose or recommended phase II dose (Fig. 1a, b). Assessment of clinical activity was a secondary objective and identifying biomarkers of response was an exploratory objective. We anticipated the development of neurological symptoms related to CAR T cell-mediated inflammation in sites of central nervous system (CNS) disease², which we have termed tumour inflammation-associated neurotoxicity (TIAN). To mitigate risks associated with TIAN, we excluded patients with bulky thalamic or cerebellar tumours, required placement of an Ommaya reservoir in patients with DIPG to monitor intracranial pressure (ICP), and instituted a TIAN toxicity management algorithm incorporating the removal of cerebrospinal fluid (CSF) via Ommaya, hypertonic saline, anti-cytokine agents and corticosteroids.

Fig. 1: Trial design and patients 1 and 2 with DIPG.

 **figure 1**

a, GD2–4-1BB–CD3Z CAR schematic. TM, transmembrane domain. **b**, Outline of clinical trial design. D0, day 0; LD, lymphodepleting chemotherapy. **c**, Post-mortem examination of participant 1 with DIPG (DIPG-1). From left to right: haematoxylin and eosin staining; CD3 immunohistochemistry (brown); *GD2-CAR* mRNA puncta (pink; haematoxylin counterstain for all cells in blue); and GD2 antigen (blue) immunohistochemistry (H3K27M⁺ nuclei in brown). **d**, qPCR for *GD2-CAR* DNA from autopsy samples from DIPG-1 exhibit the presence of GD2-CAR in tumour-involved midbrain and pons, but not her uninvolved cortex or brain tissue from an untreated individual (control). Resected temporal lobe tumour from patient 1 with spinal DMG (spinal DMG-1) following i.v. infusion reveals the presence of *GD2-CAR* DNA. Data represent mean \pm s.e.m., $n = 3$ technical replicates for each sample. **e**, MRI scan (axial T2, shown at the level of the lower pons) of participant 2 with DIPG (DIPG-2) before and 4 weeks after i.v. infusion (top row). An MRI scan before and 2 weeks following i.c.v. infusion is also shown (bottom row). A reduction in the tumour size is observed after each infusion (red arrows). **f**, Photographs of DIPG-2 demonstrate significant improvement in left facial strength 2 weeks after i.c.v. infusion. Photographs were obtained and published with informed consent. Schematics were created with BioRender.com.

[Source data](#)

Dose level 1

Beginning June 2020, four participants were enrolled on dose level 1 (DL1; 1×10^6 GD2-CAR T cells per kg administered intravenously; three participants with DIPG and one participant with spinal cord DMG; 5–25 years of age; one male and three female; Supplementary Table 1); all participants were more than 6 months from completion of standard radiotherapy. GD2-CAR T cells were successfully manufactured and met release criteria for all four patients (Supplementary Table 2). During cell manufacturing, patient 1 with spinal DMG experienced rapid tumour progression and was removed from the study but was treated at DL1 on a single-patient compassionate emergency investigational new drug application (eIND). Results are reported here with a data cut-off of March 2021.

Patient 1 with DIPG was a 14-year-old girl with H3K27M⁺ DIPG, with early radiographic signs of tumour progression, right sixth nerve palsy, left facial weakness, dysarthria, bilateral dysmetria and wide-based gait at the time of treatment. On day +6 following treatment with GD2-CAR T cells intravenously (i.v.), she experienced grade 1 cytokine release syndrome (CRS; 40.1 °C fever) together with worsening cranial nerve symptoms consistent with TIAN and was treated with tocilizumab (an IL-6 antagonist) and corticosteroids (Supplementary Table 3). On day +9, she experienced an acute episode of fever, hypertension, decreased responsiveness, hemiplegia and extensor posturing. Her Ommaya was immediately accessed; her ICP was elevated at 22 mmHg, 10 ml CSF was drained, and she returned to her neurological baseline within minutes. Anakinra (an IL-1R antagonist) was started. MRI demonstrated increased pontine oedema. She remained on corticosteroids, with transient improvement in her baseline dysarthria and dysmetria. One month post-infusion, increased disease (approximately 20% enlargement) was evident on MRI, followed by tumour progression resulting in death 3 months after infusion of GD2-CAR T cells, 3 months after radiographic progression was first noted and 13 months after diagnosis (Extended Data Fig. 1a,b). Post-mortem brain examination demonstrated substantial infiltration of lymphocytes in the tumour that is uncharacteristic for DIPG⁴; lymphocytic infiltration was not observed in areas of the normal brain (Fig 1c, Extended Data Fig. 1c). RNAscope identified cells expressing *GD2-CAR* mRNA transcript in the tumour, but not the unaffected cortex (Fig. 1c, Extended Data Fig. 1d). Similarly, the *GD2-CAR* transgene was detected by quantitative PCR (qPCR) of DNA from tumour tissue (Fig. 1d). GD2-antigen expression was substantially higher in the tumour than in the normal brain tissue (Fig. 1c, Extended Data Fig. 1e). Tumour microglial and other myeloid cell infiltration was prominent (Extended Data Fig. 1f, g).

Patient 2 with DIPG was a 21-year-old man with H3K27M⁺ DIPG exhibiting early signs of clinical and radiographic progression at the time of enrolment, with left sixth

nerve palsy, left facial weakness, decreased left facial sensation, trismus with difficulty opening his mouth that limited large bites of food, right lower extremity sensory loss and wide-based gait with inability to tandem walk. On day +7 following i.v. GD2-CAR T cell administration, he developed grade 2 CRS (fever to 39.4 °C and hypotension responsive to fluids) and transient worsening of baseline deficits consistent with TIAN affecting pontine function, including transiently worsened trismus limiting oral intake to eating through a straw, transient right upper extremity sensory loss and mild left hearing loss lasting 2 days. MRI demonstrated increased T2/FLAIR signal in the left trigeminal nucleus (Extended Data Fig. 2a), which controls the muscles of mastication, correlating with the symptom of trismus. He was treated with tocilizumab and anakinra, but no corticosteroids (Supplementary Table 3). By the second week, he experienced marked improvement in trismus (near-normal mouth opening and no limitations to eating), improvement in facial symmetry, resolution of baseline sensory loss and improvement in gait with the ability to tandem walk (Supplementary Table 4). By 1 month following treatment with GD2-CAR T cells, he exhibited a near-normal neurological examination, with only a residual sixth nerve palsy. MRI demonstrated areas of improved T2/FLAIR signal and mildly decreased (approximately 17% smaller) tumour volume (Fig. 1e, Extended Data Fig. 2b).

Clinical and radiographic improvement persisted until 2–3 months, when he experienced recrudescence of previous symptoms, including return of trismus, facial weakness and sensory loss, left hearing loss, increased weakness and sensory loss affecting the right side of his body, and gait instability that required wheelchair use for any distance beyond a few steps. He received a second dose of 30×10^6 GD2-CAR T cells administered intracerebroventricularly (i.c.v.) via Ommaya reservoir without lymphodepletion. He developed a fever (40 °C) within 24 h and approximately 48 h post-infusion developed acutely increased somnolence and new right third nerve palsy. His Ommaya reservoir was accessed, demonstrating elevated ICP of 34 mmHg; CSF was removed with immediate clinical improvement. Neuroimaging demonstrated obstructive hydrocephalus due to compression of the fourth ventricle by the expanded pons. The Ommaya was left accessed for continuous CSF drainage. Hypertonic saline, anakinra and systemic corticosteroids were administered (Supplementary Table 3). Hydrocephalus resolved without need for continued drainage of CSF after 2 days. Corticosteroids were discontinued after 4 days (on day +6). Two weeks post-i.c.v. infusion, his neurological examination had markedly improved, with near-normalization of facial strength (Fig. 1f) and sensation, improved trismus, hearing, right-sided weakness and dramatic improvement in gait that enabled independent walking for long distances (Supplementary Videos 1, 2, Supplementary Table 4). An MRI scan 2 weeks post-i.c.v. GD2-CAR T cell infusion demonstrated 27% reduction in tumour volume compared to his pre-i.c.v. infusion MRI (Fig. 1e, Extended Data Fig. 2b).

After the data cut-off of March 2021, he went on to receive three more i.c.v. infusions (five infusions total). Before the planned sixth infusion, he died due to an intratumoural haemorrhage in a known area of intratumoural vascular anomaly. Such intratumoural haemorrhages are relatively common in DIPG and risk increases with time from diagnosis⁵. He survived 26 months from diagnosis, 12 months after he began to exhibit radiographic and clinical progression, and 10 months after his first GD2-CAR T cell infusion.

Patient 3 with DIPG was a 5-year-old girl with H3K27M⁺ DIPG who enrolled before progression. She did not exhibit brainstem enlargement, only areas of infiltrative tumour evident as patchy abnormal T2/FLAIR signal in the left cerebral peduncle (corticospinal tract motor fibres) of the midbrain (Fig. 2a), anterior pons, medulla and left cerebellar peduncle. At baseline, she exhibited bilateral facial weakness, hypophonic voice, rightward tongue deviation, difficulty controlling oral secretions (drooling), chronic nausea, hypertonic right hemiparesis that limited use of the right arm and hand (her right hand was held in a flexed position; Fig. 2b), dysmetria and a hemiparetic, wide-based gait. On day 7 after i.v. administration of GD2-CAR T cells, she developed grade 1 CRS (fever of 40.4 °C) and transiently increased ataxia, consistent with TIAN. She was treated with tocilizumab and anakinra, but no corticosteroids (Supplementary Table 3). By 2 weeks post-infusion, her chronic nausea (present since diagnosis) had resolved, her right-sided motor function improved and she was using her right hand spontaneously in play, with improved ability to extend her fingers (Fig. 2b). By 1 month post-infusion, she was controlling oral secretions without drooling, taking bigger and stronger bites of food, speaking with a louder voice and showing improved facial strength that enabled a wide smile. These clinical improvements were accompanied by decreased T2/FLAIR MRI signal abnormality in the midbrain (Fig. 2a,c). By 6 weeks after i.v. GD2-CAR T cells, her balance, coordination and use of her right leg had improved, enabling her to ride a scooter using her right leg (Supplementary Table 4). With resolution of chronic nausea, her food intake improved; she increased from the sixth percentile to the thirtieth percentile for weight and grew 2 inches in height in the 2 months following i.v. GD2-CAR T cells.

Fig. 2: Patient 3 with DIPG and patient 1 with spinal DMG.

 **figure 2**

a, MRI images (axial T2) of participant 3 with DIPG (DIPG-3) showed a decrease in abnormal T2 signal (tumour) in the left cerebral peduncle corticospinal tract motor fibres (red arrows) 4 weeks following i.v. infusion that remained stably improved (MRI 2 weeks following i.c.v. infusion is also shown). **b**, The right hand of DIPG-3 at baseline, which exhibited poor strength, increased tone and was held in chronic flexion. Recovery of right-hand motor function was observed by 2 weeks after i.v. treatment, with increased movement and improved tone. **c**, Midbrain (left cerebral peduncle) tumour volume change over time in DIPG-3. **d**, Tumour volume change in the pons and medulla, and the middle cerebellar peduncles (MCP) and cerebellum over time in DIPG-3. **e**, Sagittal MRI images of patient 1 with spinal cord DMG (spinal DMG-1) show a decrease in the tumour (outlined in red) following i.v. treatment (blue arrow) and i.c.v. re-treatment (yellow arrow). **f**, Change over time in spinal cord tumour volume in spinal DMG-1. Grey shading indicates time period following i.c.v. infusion (**c,d,f**). **g**, Despite significant tumour reduction in **f**, a temporal lobe tumour (red arrow) in spinal DMG-1 did not respond (axial T2 MRI images). **h**, GD2 expression in the resected temporal lobe tumour from spinal DMG-1 was high and uniform by flow cytometry as compared to a fluorescence-minus-one control.

Source data

She was re-treated with 12.9×10^6 GD2-CAR T cells i.c.v. (equivalent to 1×10^6 per kg) without lymphodepletion 3 months after her i.v. infusion, when improvement in her clinical examination had plateaued and increased cerebellar peduncle disease was evident (Fig. 2d, Extended Data Fig. 2c). She experienced only mild headache. No anti-cytokine agents or steroids were used. Her clinical response was mixed. She demonstrated additional improvement in right-sided motor function (improved right ankle dorsiflexion and wrist extension, and further increased use of right hand) within 1 week of her second GD2-CAR T cell infusion (Supplementary Table 4). By contrast, her left-sided ataxia progressively worsened consistent with increased left cerebellar peduncle disease (Fig. 2d, Extended Data Fig. 2c).

After the data cut-off of March 2021, this participant received one more i.c.v. infusion but her tumour continued to progress. She died from tumour progression 20 months after diagnosis, 4 months after she had begun to exhibit tumour progression, and 7 months after her first GD2-CAR T cell infusion.

Patient 1 with spinal DMG was a 25-year-old woman with an H3K27M⁺ spinal cord DMG centred at thoracic levels T10–T12 who exhibited early signs of clinical and radiographic progression at the time of enrolment. After trial enrolment and during cell manufacturing, she experienced rapid tumour progression resulting in near-complete paraparesis, severe neuropathic pain, sensory loss below the T10 level, bladder dysfunction requiring urinary catheterization, and tumour spread to her temporal lobe. An urgent duraplasty was performed to relieve pressure in the spinal canal due to the rapidly expanding, tumour-infiltrated cord and to mitigate her severe neuropathic pain. Pain was moderately improved after duraplasty, but she still required a lidocaine drip and opiates for pain management. She no longer met criteria for GD2-CAR T cell infusion on-study due to rapid tumour progression with neurological deterioration and corticosteroid use before GD2-CAR T cell infusion and was removed from the protocol. She received GD2-CAR T cells (1×10^6 per kg) administered i.v. on an eIND. Beginning day +6, she exhibited grade 3 CRS (fever to 39.6 °C and hypotension requiring vasopressor support), which was treated with tocilizumab and corticosteroids for 3 days (days +8–11; Supplementary Table 3). Despite the trajectory of her rapid tumour progression before GD2-CAR T cell treatment, imaging demonstrated more than 90% reduction in volume of the spinal cord tumour by day +32 (Fig. 2e,f) accompanied by improved lower extremity motor and urinary function, resolution of neuropathic pain and discontinuation of all pain medications by 2 months post-infusion (Supplementary Table 4). By contrast, her brain metastasis did not exhibit improvement (Fig. 2g).

Both brain and spinal cord disease progressed by day +75 (Fig. 2e,f). The tumour had spread extensively throughout her brain (Extended Data Fig. 2d), and the bulkiest

component in the medial temporal lobe was resected. Flow cytometry of the resected tissue demonstrated robust tumour cell GD2 expression (Fig. 2h) but few infiltrating T cells. Low levels of the *GD2-CAR* transgene were detected by qPCR in the resected tumour of the temporal lobe (Fig. 1d). With limited therapeutic options, she was retreated with 50×10^6 GD2-CAR T cells administered i.c.v. following increased lymphodepletion, given the concern for immune rejection of the CAR T cells. The chosen dose for CAR T cells was within the range of cell doses administered i.c.v. on other brain tumour trials^{6,7}. She was the first patient chronologically to receive GD2-CAR T cells i.c.v., and her course informed the i.c.v. strategy described above. Within 48 h, she developed persistent fevers (up to 39.9 °C) and grade 3 encephalopathy (grade 4 immune effector cell-associated neurotoxicity (ICANS)), associated with no MRI changes in the normal brain and diffuse slowing with triphasic waves on continuous EEG monitoring, consistent with a reversible toxic/metabolic/inflammatory encephalopathy (Extended Data Fig. 3). Given the extensive tumour invasion of brain structures including the thalamus, hypothalamus, mammillary bodies, bilateral insula and bilateral frontal lobes, we were unable to distinguish between ICANS and TIAN as the primary cause for her encephalopathy. She was treated with anti-inflammatory therapy (anakinra, siltuximab (an IL-6 antagonist) and corticosteroids (i.v. and i.c.v.)) and oral dasatinib to dampen the activity of CAR T cells⁸ (Supplementary Table 3). Within 4 days, the encephalopathy resolved. Steroids were weaned and discontinued by day +24. Regression was again observed in her spinal tumour (more than 80% reduction over 3 weeks; Fig. 2e,f) as well as select areas of her brain disease (Extended Data Fig. 2d). Clinical improvement in spinal cord function was not observed after the second infusion as it was after the first (Supplementary Table 4). Both spinal and brain disease progressed further by 2 months following i.c.v. infusion and she received no further GD2-CAR T cell infusions. After the data cut-off of March 2021, she survived 20 months from diagnosis, 14 months from the beginning of tumour progression and 11 months after her first GD2-CAR T cell infusion.

Correlative findings

Serum and CSF samples were obtained routinely and at times of clinical intervention to assess markers of inflammation and correlates of response. Patient 1 with spinal DMG had CSF samples collected following only i.c.v. administration but not following i.v. administration, and limited CSF samples were obtained from patient 3 with DIPG due to her young age.

Correlating with tumour response, serum levels of lactate dehydrogenase increased in all patients after GD2-CAR T cell treatment and tracked with evidence of inflammation (Extended Data Fig. 4a). Using digital droplet PCR for the tumour-specific H3K27M mutation, cell-free tumour DNA was detected in CSF in two of four

patients (Extended Data Fig. 4b–f). CSF cell-free tumour DNA was elevated during peak inflammation post-i.c.v. treatment, a pattern expected with tumour cell killing⁹. Additional sampling may further elucidate the kinetics of tumour cell killing in future studies.

GD2-CAR T cell expansion and persistence was monitored using *GD2-CAR* transgene qPCR and flow cytometry of cell-surface CAR expression. GD2-CAR T cell expansion in blood assessed by qPCR was similar in magnitude to expansion of highly active CAR T cells for haematological malignancies^{10,11,12} (Fig. 3a). Flow cytometry-based GD2-CAR T cell detection in blood was limited, potentially due to decreased surface expression of GD2-CAR after activation¹³. GD2-CAR T cells were detected in CSF by flow cytometry, particularly following i.c.v. administration (Fig. 3b, Extended Data Fig. 6b).

Fig. 3: CAR T cell kinetics and cytokine production.

 figure 3



a, qPCR for *GD2-CARDNA* illustrates kinetics of CAR T cell expansion and persistence in the peripheral blood following i.v. (top) and i.c.v. (bottom) administration. Each point represents one technical replicate; $n = 3$ technical replicates per timepoint per patient, 4 patients (i.v.), 3 patients (i.c.v.). **b**, Flow cytometry of GD2-CAR demonstrated significantly higher proportion of CAR T cells in the CSF

following i.c.v. GD2-CAR T cell infusion than following i.v. infusion at peak inflammation timepoints. Each dot represents one patient. $n = 4$ patients (i.v.), 3 patients (i.c.v.). **c, d**, Pro-inflammatory cytokines in the blood and CSF after i.v. infusion (**c**), $n = 4$ patients, and after i.c.v. infusion (**d**), $n = 3$ patients. Note that the expression of IFN γ in the CSF of spinal DMG-1 on D1–3 after i.c.v. infusion was above the upper limit of detection of the assay. **e**, Levels of the immunosuppressive cytokines TGF β 1, TGF β 2 and TGF β 3 in the CSF after i.v. infusion. $n = 3$ patients. Heatmaps in **c–e** were generated from Luminex multiplex cytokine analysis of patient blood plasma and CSF in technical duplicates. Average pg ml $^{-1}$ results are represented by log₂ fold change from D0 timepoint.

[Source data](#)

In blood, cytokines implicated in CRS, including IL-6, were higher following i.v. than i.c.v. administration, consistent with the higher grade CRS observed after i.v. administration. In CSF, the levels of pro-inflammatory cytokines, including IFN γ , TNF, IL-2 and IL-6, were higher following i.c.v. administration than following i.v. administration (Fig. [3c, d](#), Extended Data Fig. [5a–c](#)). Patient 1 with DIPG exhibited increased levels of immunosuppressive cytokines, including TGF β , in the CSF (Fig. [4e](#), Extended Data Fig. [5d](#)) and prominent myeloid populations in tumour tissue (Extended Data Fig. [1f, g](#)), which may correlate with her lack of response. Cytokine analyses confirmed that anakinra (modified recombinant IL-1RA) crossed the blood-brain barrier, with detectable levels of IL-1RA found in both the blood and the CSF following i.v. administration of anakinra (Extended Data Fig. [5e](#)).

Fig. 4: Single-cell transcriptomic analyses identifies distinct myeloid subpopulations.

 **figure 4**

a, UMAP representation identifies cellular populations within GD2-CAR⁺ flow-sorted T cell products. $n = 20,000$ single cells (5,000 GD2-CAR⁺ cells from each of the 4 patient products). **b**, UMAP representation identifies cellular populations within CSF samples from patients. CSF cells by patient (left) and CSF cells by cell type (right) are shown. $n = 25,598$ single cells. **c**, UMAP highlighting FOXP3⁺ regulatory T (T_{reg}) cells (left). T_{reg} cell population (defined by CD4, FOXP3 and CD25 expression) identified in CSF samples at peak inflammation timepoints following i.v. or i.c.v. administration (right). $n = 523$ T_{reg} cells were analysed from a total of 17,699 CSF T cells from 3 participants after i.v. and 2 participants after i.c.v. administration. With a Bayesian model-based single-cell compositional data analysis (scCODA) framework, the log fold change was 0.6, the inclusion probability was 0.75 and the false discovery rate was less than 0.05. **d**, CSF sample single-cell RNA sequencing was filtered to isolate myeloid cells. Clustering was conducted after data integration by Harmony. $n = 6,497$ myeloid cells. **e**, Pie charts represent myeloid cluster proportions at different timepoints. A single UMAP was generated with myeloid cells from the CSF, and then individually visually represented based on timepoint of the sample, coloured by

patient. Note the alterations in the presence of myeloid clusters over time. **f**, Expression signature of ‘immune activating’, ‘immune suppressive’, ‘disease-associated myeloid (DAM) stage 1’, ‘DAM stage 2’, ‘myeloid-derived suppressor cell (MDSC)’ and ‘axon tract-associated microglial (ATM)’ cell states and associated representation within clusters based on single-cell expression scores (Z score).

Source data

Single-cell RNA sequencing was performed on cells isolated from CSF (Extended Data Fig. [6a](#)) as well as flow-sorted GD2-CAR-positive and GD2-CAR-negative T cells from the manufactured products (Fig. [4a, b](#)). We analysed 65,598 single cells: 25,598 cells from CSF and 40,000 cells from manufactured products. The cellular composition of CSF included lymphocytes, myeloid cells, rare astrocytes and B cells (Fig. [4b](#)). We observed a population of lineage doublets, raising the possibility of phagocytosis of T cells by myeloid cells (Fig. [4b](#)). We observed more GD2-CAR T cells in CSF at times of peak inflammation, and more CSF GD2-CAR T cells after i.c.v. versus i.v. administration for patient 2 with DIPG, the only patient in whom this comparison was possible (Extended Data Fig. [6b](#)). By single-cell RNA sequencing, we did not identify GD2-CAR T cells in the CSF of patients 1 and 3 with DIPG.

Comparing manufactured cell products for patient 1 with DIPG, who did not have a response, to patient 2 with DIPG, who exhibited radiographic and clinical benefit, revealed numerous transcriptional differences. These included baseline interferon and PD1 signalling activation pathways in patient 1 with DIPG, potentially indicating increased tonic signalling associated with reduced GD2-CAR T cell activity^{[14](#)} (Extended Data Fig. [6c, d](#)). Comparisons of other products are shown in Extended Data Fig. [6e, f](#). Assessing all lymphocytes from the CSF of all participants revealed that the T cell CD4:CD8 ratios in CSF differed over time between patients (Extended Data Fig. [7a](#)). Increased numbers of regulatory T (T_{reg}) cells were found in patient CSF after i.v. GD2-CAR T cell administration compared to i.c.v. administration (Fig. [4c](#), Extended Data Fig. [7b](#)).

Examination of all CSF myeloid cells from all patients after each administration route revealed seven distinct clusters of cells, including monocytes, microglia and macrophages expressing various functional signatures, and proliferating myeloid cells (Fig. [4d](#), Extended Data Fig. [8a](#), Supplementary Table [5](#)). We identified a myeloid population characterized by interferon response, present primarily at peak inflammation timepoints after i.c.v. administration (Fig. [4d, e](#)). This cluster exhibited a distinctly immune-activating signature (Fig. [4f](#), Extended Data Fig. [8b](#)), concordant with the pro-inflammatory CSF cytokine profile observed after i.c.v. administration (Fig. [3c, d](#)). By contrast, i.v. administration and late timepoints had CSF myeloid cell subpopulations that expressed prominent phagocytosis and lipid metabolism gene programmes. These cells also exhibited a strong immune-suppressive profile, which

aligned with transcriptional signatures of disease-associated microglia¹⁵, myeloid-derived suppressor cell and axon tract-associated microglia¹⁶ cell states (Fig. 4e,f, Extended Data Fig. 8). Comparison of the CSF myeloid cell fraction in patient 1 with DIPG to other patients at the time of peak inflammation highlighted differentially increased interleukin, chemokine and neutrophil degranulation processes (Extended Data Fig. 9a–c). Similarly, comparison of the CSF myeloid cell fraction in patient 2 with DIPG at peak inflammation following i.v. versus i.c.v. administration revealed increased myeloid activation processes following i.v. administration (Extended Data Fig. 9d).

Together, these correlative studies provide further evidence of GD2-CAR T cell activity against H3K27M⁺ DIPG and spinal cord DMG and begin to elucidate the heterogeneity observed in antitumour responses.

Discussion

H3K27M⁺ DIPG and spinal cord DMGs are extremely aggressive, universally fatal tumours with few therapeutic options. The average life expectancy is 10 months from diagnosis, and the 5-year survival is less than 1%¹⁷. Palliative radiotherapy is the only established treatment, and neither cytotoxic nor targeted pharmacological approaches have demonstrated improved prognosis to date¹⁸. Implementation of immunotherapy as treatment for tumours in these precarious neuroanatomical locations is both promising and dangerous. This phase I study was carefully designed to manage potential consequences of inflammation-induced swelling of an already expanded brainstem. The toxicities associated with GD2-CAR T cell infusions were manageable and reversible with intensive supportive care in the inpatient setting. CRS and ICANS were similar to that described with other CAR T cell therapies^{19,20}, but patients also developed signs and symptoms consistent with CAR T cell-mediated inflammation in sites of CNS disease, which we have termed TIAN. TIAN most often manifested as transient worsening of existing deficits but also resulted in episodes of increased ICP secondary to brainstem oedema and consequent obstructive hydrocephalus, which would have been life-threatening unless immediately and appropriately managed. Our toxicity management algorithm incorporated several pre-emptive measures that enabled safe delivery of this potent therapy. As increasingly efficacious CAR T cell and other immunotherapies are deployed for CNS tumours, TIAN is likely to emerge as an important axis of toxicity in neuro-immuno-oncology.

Two categories of TIAN were evident in these patients: the first category of TIAN relates to ICP and intracranial space constraints secondary to inflammation-induced tissue oedema and/or obstruction of CSF flow. This can require urgent and/or emergent management utilizing principles of neurocritical care. The second category

of TIAN relates to primary dysfunction of brain or spinal cord structures affected by inflammation, is typically transient, frequently manifests as worsening of pre-existing symptoms and can often be managed conservatively unless the neurological dysfunction involves critical functions such as respiratory drive.

Although patients developed symptoms of on-tumour neurotoxicity, they did not manifest any signs or symptoms of on-target, off-tumour toxicity. GD2 is expressed on normal neural tissues, including the brain and peripheral nerves, and treatment with the US Food and Drug Administration-approved anti-GD2 antibody dinutuximab for neuroblastoma is associated with transient painful neuropathy in most children^{21,22}. None of these four patients developed painful neuropathies or any other clinical or radiographic indication of on-target, off-tumour toxicity. This study adds to the growing evidence that GD2 can be safely targeted with CAR T cells^{23,24,25,26}, and is consistent with evidence that CAR T cells require high antigen density for full effector function^{10,13,27,28}. Indeed, autopsy tissue from patient 1 with DIPG confirmed robustly differential GD2 expression levels and T cell infiltration between the tumour and the uninvolved brain.

Although the clinical experience reported here is early and the number of participants treated to date is small, three of four patients derived radiographic and clinical benefit after i.v. administration of GD2-CAR T cells. The improvement observed in neurological function highlights the extent to which this diffusely infiltrating tumour chiefly integrates with and disrupts—rather than destroys—neural circuits²⁹, underscoring the potential that a tumour cell-specific therapy offers for functional recovery. i.c.v. administration of a second dose of GD2-CAR T cells provided additional radiographic and/or clinical benefit in three of three patients treated. In comparison to i.v. infusions, i.c.v. administrations were associated with less systemic toxicity such as CRS, and correlated with enhanced levels of pro-inflammatory cytokines and reduced immunosuppressive cell populations in CSF. The promising early experience with GD2-CAR T cells for DIPG and spinal cord DMG described here sets the stage for further optimization of this approach for this historically lethal CNS cancer. This clinical trial will continue to treat patients with H3K27M⁺ DIPG and spinal DMG using GD2-CAR T cell therapy to determine optimal dose, route and schedule, and to determine efficacy.

Methods

Clinical trial design

This phase I dose-escalation trial of GD2-CAR T cells in children and young adults with pontine and spinal H3K27M⁺ DMG uses a 3 + 3 design with the primary

objectives of assessing feasibility of manufacturing, safety and tolerability, and identifying the maximally tolerated dose or recommended phase II dose. Assessment of clinical activity is the secondary objective and identifying correlative biomarkers of response is an exploratory objective. Patients were eligible for enrolment if they had a pathologically confirmed diagnosis of H3K27M-mutated DIPG or spinal cord DMG, had completed standard radiotherapy and were not receiving corticosteroid therapy (additional eligibility and exclusion criteria below).

Toxicity management

In preclinical studies, a fraction of the mice exhibited brainstem oedema as a result of on-tumour inflammation that led to obstructive hydrocephalus due to the neuroanatomical location of these tumours². We anticipated the development of neurological symptoms related to CAR T cell-mediated inflammation in sites of CNS disease, which we have termed TIAN. To mitigate the risks associated with TIAN, we excluded patients with bulky thalamic or cerebellar tumours, required placement of an Ommaya reservoir in patients with DIPG, conducted both routine and symptom-prompted ICP measurements and instituted a toxicity management plan that included TIAN management (CSF removal via Ommaya, hypertonic saline and/or corticosteroids) and CRS management using anti-cytokine agents (tocilizumab, an IL-6R antagonist, and anakinra, an IL-1R antagonist) and corticosteroids. In addition, the CAR construct incorporated an iCasp9-inducible suicide switch, which could be activated with rimiducid in the event of life-threatening toxicity that is not manageable with the approaches and agents discussed above³⁰.

Oversight and informed consent

The clinical study and all amendments were approved by the Stanford University Institutional Review Board. An external data and safety monitoring board (DSMB) reviewed the protocol, amendments and all important patient events and outcomes. Before enrolment in the clinical trial, patients and/or their parents provided written, informed consent, and minor assent was obtained when appropriate. In addition, patients and/or their parents provided written, informed consent for use of photographs and videos that may be used in scientific presentations and publications in print and electronic formats.

CAR T cell manufacturing

Autologous peripheral blood mononuclear cells (PBMCs) were collected via apheresis and GD2-CAR T cells were manufactured using the closed-system CliniMACS Prodigy (Miltenyi). In brief, CD4 and CD8 T cells were selected and transduced with one bicistronic retroviral vector encoding an iCasp9 domain (Bellicum

Pharmaceuticals, Inc.), and a GD2–4-1BB–CD3Z CAR (Fig. 1a) containing the 14g2a scFv under control of an MSCV promoter. GD2-CAR T cells were expanded for 7 days in the presence of recombinant human IL-7 and IL-15, plus the addition of the tyrosine kinase inhibitor dasatinib on days 3 and 5 to improve T cell fitness³¹.

CAR T cell administration

Lymphodepleting chemotherapy (cyclophosphamide 500 mg m² daily and fludarabine 25 mg m² daily on days −4, −3 and −2) was administered followed by i.v. CAR T cell infusion on day 0 (Fig. 1b). Patients were monitored closely, including routine ICP measurements, in the inpatient setting through toxicity resolution. For patients receiving second infusions, CAR T cells were infused i.c.v. via the Ommaya. The first patient to be treated with i.c.v. administered CAR T cells (patient 1 with spinal DMG) received a flat dose of 50 million CAR T cells after increased lymphodepleting chemotherapy (cyclophosphamide 600 mg m² daily and fludarabine 30 mg m² daily on days −5, −4, −3 and −2) under a single-patient eIND (see below); subsequent patients received 30 million CAR T cells or the equivalent of their weight-based dose at DL1, whichever was lower, i.c.v. without lymphodepletion.

Clinical trial eligibility and exclusion criteria

Inclusion criteria

1. (1)

Disease status

1. (i)

Dose-escalation phase and DIPG expansion cohort: tissue diagnosis of H3K27M-mutated DIPG with radiographically evident tumour restricted to the brainstem, or

2. (ii)

Dose-escalation phase and spinal DMG expansion cohort: tissue diagnosis of H3K27M-mutated DMG of the spinal cord.

2. (2)

Age: greater than or equal to 2 years of age and less than or equal to 30 years of age.

3. (3)

Previous therapy:

1. (i)

At least 4 weeks following completion of front-line radiation therapy.

2. (ii)

At least 3 weeks post-chemotherapy or five half-lives, whichever is shorter, must have elapsed since any previous systemic therapy, except for systemic inhibitory/stimulatory immune checkpoint therapy, which requires 3 months.

4. (4)

Performance status: participants over 16 years of age, Karnofsky $\geq 60\%$ or Eastern Cooperative Oncology Group (ECOG) performance status of 0 or 1; participants 16 years of age or younger, Lansky scale $\geq 60\%$. Participants who are unable to walk because of paralysis, but who are up in a wheelchair, will be considered ambulatory for the purpose of assessing the performance score.

5. (5)

Normal organ and marrow function (supportive care is allowed per institutional standards, that is, filgrastim, transfusion):

1. (i)

Absolute neutrophil count (ANC) $\geq 1,000$ per μl

2. (ii)

Platelet count $\geq 100,000$ per μl

3. (iii)

Absolute lymphocyte count ≥ 150 per μl

4. (iv)

Haemoglobin $\geq 8 \text{ g dl}^{-1}$

5. (v)

Adequate renal, hepatic, pulmonary and cardiac function defined as:

6. (vi)

Creatinine within institutional norms for age that is, ≤ 2 mg dl $^{-1}$ in adults or according to the table below in children younger than 18 years of age) or creatinine clearance (as estimated by Cockcroft Gault equation) ≥ 60 ml min $^{-1}$

7. (vii)

Serum alanine transaminase/aspartate transaminase (ALT/AST) ≤ 3.0 upper limit of normal (ULN;grade 1)

8. (viii)

Total bilirubin ≤ 1.5 mg dl $^{-1}$, except in participants with Gilbert's syndrome

9. (ix)

Cardiac ejection fraction $\geq 45\%$, no evidence of physiologically significant pericardial effusion as determined by an echocardiogram, and no clinically significant electrocardiogram findings

10. (x)

Baseline oxygen saturation $> 92\%$ on room air

6. (6)

Female individuals of childbearing potential must have a negative serum or urine pregnancy test (female individuals who have undergone surgical sterilization are not considered to be of childbearing potential).

7. (7)

Contraception: participants of childbearing or child-fathering potential must be willing to practice birth control from the time of enrolment on this study and for 4 months after receiving the preparative lymphodepletion regimen or for as long as GD2-CAR T cells are detectable in peripheral blood or CSF.

8. (8)

Ability to give informed consent. Paediatric participants will be included in age appropriate discussion and written assent will be obtained for those 7 years of age or older, when appropriate.

Exclusion criteria

1. (1)

Bulky tumour involvement of the cerebellar vermis or hemispheres (pontocerebellar peduncle involvement is allowed), thalamic lesions that in the investigator's assessment place the participant at unacceptable risk for herniation.

2. (2)

Clinically significant swallowing dysfunction as judged by clinical assessment.

3. (3)

Current systemic corticosteroid therapy.

4. (4)

Previous CAR therapy.

5. (5)

Uncontrolled fungal, bacterial, viral or other infection. Previously diagnosed infection for which the patient continues to receive antimicrobial therapy is permitted if responding to treatment and clinically stable.

6. (6)

Ongoing infection with HIV or hepatitis B virus (HBsAg positive) or hepatitis C virus (anti-HCV positive). A history of hepatitis B or hepatitis C is permitted if the viral load is undetectable per qPCR and/or nucleic acid testing.

7. (7)

Clinically significant systemic illness or medical condition (for example, significant cardiac, pulmonary, hepatic or other organ dysfunction), that in the judgement of the principal investigator is likely to interfere with assessment of safety or efficacy of the investigational regimen and its requirements.

8. (8)

In the investigator's judgement, the participant is unlikely to complete all protocol-required study visits or procedures, including follow-up visits, or comply with the study requirements for participation.

9. (9)

Known sensitivity or allergy to any agents and/or reagents used in this study.

10. (10)

Primary immunodeficiency or history of autoimmune disease (for example, Crohns, rheumatoid arthritis and systemic lupus) requiring systemic immunosuppression and/or systemic disease-modifying agents within the past 2 years.

Response assessment

Radiographic responses were evaluated by gadolinium-enhanced MRI scans of the brain and/or spinal cord. Because DMGs are diffusely infiltrative of CNS structures and therefore are difficult to measure, volumetric tumour segmentation of T2/FLAIR signal abnormality was performed by a neuroradiologist (K.W.Y.) to measure radiographic change.

Clinical response was assessed by neurological examination. To quantify clinical change, a clinical improvement score (CIS) was calculated. The CIS represents an unweighted quantification of the neurological examination and is conducted by a neurologist who examines the participant before infusion and then at designated timepoints after therapy. For each neurological symptom or sign, one point is assigned. Improvement in a given symptom or sign from pre-infusion baseline add one point to the score, no change adds zero and one point is subtracted for symptom or sign worsening. The reported score is a sum of the positive and negative points. For example, a participant with improved right upper extremity strength and improved left sixth nerve palsy would receive a score of +2. A participant with improved right upper and lower extremity strength, improved left sixth nerve palsy but worsened left facial sensation would also receive a score of +2 (+3 – 1 = +2). The assessment cannot be conducted within 7 days of corticosteroid administration. Sample forms are available in Supplementary Tables [6](#), [7](#).

Cell-free DNA rare mutation detection

Patient CSF samples were collected at pre-determined and trigger timepoints throughout the treatment course. To gently separate the cellular compartment, samples were spun within 1 h of collection at 1,800g for 10 min at 4 °C followed by 20,000g

for 10 min. Supernatant was frozen at -80°C . DNA extraction was performed on 0.5–3 ml CSF supernatant aliquots using the QIAamp Circulating Nucleic Acids Kit (Qiagen) into 25 μl extraction buffer. All samples were assessed for cell-free DNA concentration by nanodrop and fragment size distribution with the BioAnalyzer (Agilent).

Forward and reverse primers and wild-type or mutant probes were designed to optimally detect the H3F3A K27M mutation through digital droplet polymerase chain reaction (ddPCR), and a dilution series of mutant H3K27M g-block against a wild-type H3 background was performed to validate linearity and confirm limit of detection. Seven PCR cycles for pre-amplification were performed on 10 μl of extracted cell-free DNA with Q5 Hot Start High-Fidelity Master Mix (New England Biolabs) for each timepoint. Preamplified reactions were immediately placed on ice after the final extension and diluted with 100 μl TE buffer, pH 8.0, to inactivate the Q5 polymerase. Samples were used immediately for ddPCR (40 cycles; Bio-Rad) and run as 4–6 technical replicates. The raw spectral data were analysed using the Bio-Rad software to plot the signal for mutant and wild-type alleles. All runs contained positive and negative controls. Results were analysed in R to plot variant allele frequency (VAF) as well as mutation count per volume over time.

qPCR measurement of *in vivo* GD2-CAR expansion

Patient blood and tumour tissue samples were processed and mononuclear cells were viably cryopreserved. DNA was extracted from whole blood (2×10^6 – 5×10^6 PBMCs) using QIAamp DNA Blood Mini Kit (51306, Qiagen) at baseline and multiple timepoints following CAR administration and from tumour tissue samples using DNeasy 96 Blood & Tissue Kit (69582, Qiagen). CAR presence was measured by qPCR using the primer and probe sequences provided as below and in Supplementary Table 8. For the standard curve, a custom Minigene plasmid (IDT) was designed containing a partial GD2–4-1BB–CD3Z sequence and a partial albumin sequence, which served as a control for normalization (Supplementary Table 8). The standard curve contained a tenfold serial dilution of plasmid between 5×10^8 and 5×10^0 copies. Both plasmid and patient DNA from each timepoint were run in triplicate, with each reaction containing 5 μl of DNA (50 ng total), 200 nM forward and reverse albumin primers (or 300 nM forward and reverse GD2–4-1BB–CD3Z primers), 150 nM probe suspended in 10 μl of TaqMan Fast Universal PCR Master Mix (2X), no AmpErase UNG (Thermo Fisher Scientific) and 24.5 μl (albumin) or 22.5 μl (GD2–4-1BB–CD3Z) of TE buffer (AM9935, Invitrogen). The Thermo Fisher Scientific QuantStudio 6 Pro Real-time qPCR Instrument was used for qPCR with 20 μl per reaction. The quality metrics for all qPCR standard curve results were $R^2 > 0.95$ and efficiency was 70–110%.

Albumin results from plate normalized to average albumin, then *GD2-CAR* copy number (copies per 50 ng DNA) adjusted to albumin and modified to copies per 100 ng DNA by the following equation: copy number (copies per 100 ng DNA) = $2 \times (\text{GD2-CAR copy number} \times (\text{albumin copy number/average albumin}))$. qPCR reagents included albumin probe (5'-/56'-FAM/CCTGTCATG/ZEN/CCCACACAAATCTCTCC/3IABkFQ/-3'), albumin forward primer (5'-GCTGTCATCTCTGTGGGCTGT-3'), albumin reverse primer (5'-ACTCATGGGAGCTGCTGGTTC-3'), GD2-CAR FAM probe (5'-/56'-FAM/TCATGTTGT/ZEN/AGCCGGTGA AGGAGC/3IABkFQ/-3'), GD2-CAR forward primer (5'-CTCTGTGATGATCTCCTGCAA-3'), GD2-CAR reverse primer (5'-CGATCCATTCCAGGCTCTT-3'), and GD2 Albumin Minigene Plasmid (does not include proprietary backbone sequence; 5'-GCTGGCCTTTGCTCACAGCTGGGTTGCTGTCATCTCTGTGGGCTGTA ATC ATCGTCTAGGCTTAAGAGTAATATTGCAAAACCTGTCATGCCACACAAATC TCT CCCTGGCATTGTTGTCTTGCAAGATGTCAGTGAAAGAGAACCGAGCAGCTCC CATG AGTCCCAAGCTATGTTCTTCCTGCGTTCTGGTGGAACCTGGCGCCTCT GTG ATGATCTCCTGCAAGGCCAGCGGCA GCTCCTTCACCGGCTACAACATGAACTGGG TGCGCCAGAACATCGGCAAGAGGCCTGGAATGGATCGGCGCCATCGACCCCT ACTACGGCGGCACCAGCT).

Real-time flow cytometry assay

A high-dimensional (Hi-D) immuno-phenotyping flow cytometry panel was designed for immune profiling of CAR T cells in real time. PBMCs were isolated from fresh whole blood by gradient centrifugation on ficoll (Ficoll-Paque Plus, GE Healthcare, Sigma-Aldrich). Two to five million PBMCs were stained with fixable live/dead aqua (Invitrogen) amine-reactive viability stain. Cells were then preincubated with Fc block (trustain, BioLegend) for 5 min, then stained at room temperature with the following fluorochrome-conjugated mAb in a 15-colour, 17-parameter staining combination (Supplementary Table 9).

CAR-tranduced T cells were used as positive control included in daily staining experiments. Stained and fixed cells were acquired on a LSR (BD BioSciences) five-laser (blue 488 nm, violet 405 nm, UV laser 355 nm, red 640 nm and green 532 nm lasers) analyser. At least 10^6 cells were acquired unless restricted by the number of cells isolated from 8 ml of whole blood or when acquiring isolated cells from CSF. The assay limit of detection for cells calculated as 1 in 10^4 of total acquired PBMCs. Representative gating is shown in Extended Data Fig. 10a.

Luminex cytokines

Patient blood and CSF samples were collected at pre-determined and trigger timepoints throughout treatment. Samples were spun at 250g for 6 min. Supernatant was frozen at -80°C until batched for assessment. Cytokine assessment was performed by the Immunoassay Team-Human Immune Monitoring Center at Stanford University. Panels include Luminex-EMD Millipore HIMC H80 (panel 1 is Milliplex HCYTA-60K-PX48; panel 2 is Milliplex HCP2MAG-62K-PX23; panel 3 includes the Milliplex HSP1MAG-63K-06 and HADCYMAG-61K-03 (resistin, leptin and HGF) to generate a 9 plex) and TGF β (TGFBMAG-64K-03). Kits were purchased from EMD Millipore Corporation and used according to the manufacturer's recommendations with modifications described. The assay setup followed recommended protocol. In brief, samples were diluted threefold (panels 1 and 2) or tenfold (panel 3). Of the diluted sample, 25 μl was mixed with antibody-linked magnetic beads in a 96-well plate and incubated overnight at 4°C with shaking. Cold and room temperature incubation steps were performed on an orbital shaker at 500–600 rpm. Plates were washed twice with wash buffer in a Biotek ELx405 washer (BioTek Instruments). Following 1-h incubation at room temperature with biotinylated detection antibody, streptavidin–phycoerythrin (PE) was added for 30 min with shaking. Plates were washed as described above and PBS was added to wells for reading in the Luminex FlexMap3D Instrument with a lower bound of 50 beads per sample per cytokine. Custom Assay Chex control beads were purchased and added to all wells (Radix Biosolutions). All wells collected met quality control metrics with a bead count >50 . Data are represented in pg ml^{-1} based on standard curves or heat maps of fold change from baseline timepoint. All samples were run in technical duplicate.

Single-cell RNA sequencing

Single-cell RNA sequencing (scRNA-seq) was performed using 5' v2 Single Cell Immune Profiling technology (10X Genomics) according to the manufacturer's protocol. In brief, cells from CSF samples collected at indicated timepoints before and after CAR T cell administration, as well as sorted CAR $^{+}$ and CAR $^{-}$ cells from the CAR T cell infusion products, were counted, resuspended to 700–1,200 cells per μl , and captured using Single Cell Chip A on the 10x Chromium Controller (10X Genomics) to generate gel bead-in emulsions (GEMs). Reverse transcription inside GEMs was performed using a C1000 Touch Thermal Cycler (Bio-Rad). Barcoded complementary DNA (cDNA) was recovered through post-GEM-RT cleanup and PCR amplification. Recovered cDNA was amplified and used to construct 5' whole-transcriptome libraries. Quality of cDNA and each library was assessed using Agilent 2100 Bioanalyzer. The libraries were indexed using a Chromium i7 Sample Index Kit, pooled and sequenced on NovaSeq 6000 System (Illumina) by Novogene.

Raw sequencing data were processed using the Cell Ranger software version 6.0.0 or higher (10X Genomics). Sequencer's base call files (BCLs) were demultiplexed into FASTQ files using the cellranger mkfastq pipeline. To optimize CAR sequence detection in the scRNA-seq data, we probed the FASTQ files using SeqKit³² in 50-base-pair segments from the *GD2-CAR* plasmid sequence. Once we identified the segments with the most hits, we created a custom reference by appending these segments to the GRCh38 5.0.0 human genome reference with the cellranger mkref pipeline. FASTQ files were aligned to this custom reference using the cellranger count pipeline.

Unique molecular identifier (UMI) count matrices from Cell Ranger were analysed using Seurat³³. Dead cells and cell debris with more than 15% of UMI counts mapping to mitochondrial genes or less than 300 genes detected were excluded from the analysis. Cell doublets containing more than 10,000 genes or more than 50,000 UMI counts were also excluded. Next, scRNA-seq data were subsampled to 5,000 cells per sample, and all data were normalized together to the sequencing depth using the SCTtransform pipeline³⁴. Data between patients were integrated using reciprocal principal component analysis (RPCA). PCA was performed using all variable genes with the exception of *TCR* and *BCR* genes to prevent clonotypes from driving the final layout. In addition, a set of curated genes relevant to T cell function or cell-type identification were included into the list of variable genes. UMAP embedding was performed using the first 50 principal components. Cell types were assigned to all cells based on canonical lineage marker expression. Cell-type doublets ('lineage doublets') were identified as cells expressing markers of more than one lineage: T cells (*CD2*, *CD3E*, *CD3D*, *CD3G*, *CD247*, *CD7* and *GD2-CAR*), B cells (*CD19*, *CD22* and *PAX5*), microglia/myeloid cells (*CD14*, *CD68*, *CD163*, *CSF1R* and *AIF1*) or astrocytes (*GFAP*). Differential expression analysis was performed on SCT counts modelled as a negative binomial distribution using the FindMarkers pipeline.

Further analysis of patient 1 with DIPG and other participant CSF samples was performed using the R-based 'Seurat' package³⁵ to assess transcriptional differences preceding and during CAR T cell administration. First, the large Seurat object was subset into various smaller objects to enable multiple comparisons across different DIPG CSF samples (see Fig. 4). Seurat objects subsequently underwent scaling and dimensionality reduction based on the UMAP algorithm³⁶. Myeloid fractions of the dataset were identified using the 'AddModuleScore' function in Seurat to isolate cells with relatively high expression of myeloid genes (*AIF1*, *CSF1R*, *CX3CR1*, *CD14*, *CD68* and *CD163*), compared to their expression of B cell-related (*CD19*, *CD22* and *PAX5*) and T cell-related (*CD2*, *CD3E*, *CD3D*, *CD3G*, *CD247* and *CD7*) genes. Scoring of cells based on disease-associated myeloid (DAM) or myeloid-derived suppressor cell (MDSC) gene expression was implemented using the 'AddModuleScore' and 'FeaturePlot' functions in Seurat. DAM genes included *SPP1*,

GPNMB, IGF1, CLEC7A, LPL, CD9, CD63, LGALS3, FABP5, ITGAX, APOE and *TYROBP*, based on previous noteworthy characterizations of myeloid cells in disease^{15,16,37,38}. MDSC genes included *CD33*, *CD14*, *CD15* and *IL4RA*³⁹. Volcano plot analysis was conducted using the R-based ‘EnhancedVolcano’ package⁴⁰. Gene ontology (GO) analysis was performed using the R-based ‘ReactomePA’ package⁴¹.

Single-cell expression scores were computed in a similar way as previously described⁴². Given a set of genes (G_j) for a gene set (for example, a DAM signature), a score, $SC_j(i)$, which quantifies the scaled expression (Z-score) of G_j for each cell i , was computed as the average scaled expression (Er) of the genes in G_j compared to the average scaled expression of a control gene set Gcont: $SC_j(i) = \text{average}[Er(G_j, i)] - \text{average}[Er(G_{\text{cont}}, i)]$. For each gene of the gene set, its control gene set contains 100 genes with the most similar aggregated expression level to that gene. Therefore, the control gene set represents a 100-fold larger but comparable distribution of expression levels to that of the considered gene set.

Graph-based clustering with data integration was adapted to identify cellular clusters. We selected highly variable genes (HVGs) using the FindVariableFeatures function in Seurat and used the scaled expression values of these HVGs for PCA. To disentangle sample-specific biological variations from cell subpopulation-specific variations and integrate multiple samples, we applied a linear adjustment method called Harmony to the first 30 principle components with default parameters to generate a corrected embedding⁴³. We chose the first 20 Harmony corrected dimensions for constructing UMAP embeddings by RunUMAP in Seurat and clustered cells by the Louvain algorithm based FindClusters in Seurat. Cells that were from different samples, but expressed similar gene programmes, were well mixed. We next identified differentially expressed genes (DEGs) by FindAllMarkers in Seurat and tested genes that were detected in a minimum of 30% of the cells within each cluster and that showed at least a 0.5-fold mean log difference. We utilized Wilcoxon rank-sum test with Bonferroni correction for multiple testing and only kept genes with adjusted $P < 0.05$. Cell clusters were annotated with manual inspection of their top DEGs. In addition, we tested for enrichment of described gene sets (GO biological processes) and compared expression programmes of each cell cluster with those of a published glioblastoma-associated myeloid cell dataset⁴⁴.

Histology, immunohistochemistry, immunofluorescence and RNAscope

Immunohistochemistry (other than for GD2 and H3K27M) was performed on formalin-fixed paraffin-embedded tissue sections per standard protocols including deparaffinization, antigen retrieval, incubation with primary antibody, and detection per the manufacturers’ instructions. The following antibodies were used: CD3 (790–4341, Ventana; rabbit polyclonal, prediluted), CD4 (NCL-CD4-368, Leica

(Novocastra); mouse monoclonal, 1:40 dilution), CD8 (M7103, Dako; monoclonal mouse, 1:400 dilution) and CD163 (760–4437, Ventana; monoclonal mouse, prediluted). Stains for CD3 and CD163 were performed on a Ventana BenchMark Ultra automated stainer using CC1 antigen retrieval. Stains for CD4 and CD8 were performed on a Leica Bond automated stainer using ER2 antigen retrieval.

For H3K27M and GD2 immunohistochemistry, primary tumour samples from patients were transferred to cryomolds and embedded in optimal-cutting temperature (OCT) compound (TissueTek). Cryosections (10 µm) were generated on a cryostat (Leica). Tissue was fixed with 4% PFA at 4 °C for 20 min then washed and endogenous peroxidase activity was neutralized (Bloxall, Vector Laboratories; 10 min at room temperature) before permeabilization (0.3% Triton X-100, TBS, 15 min at room temperature) and blocking (5% horse serum, Vector Laboratories; 20 min at room temperature). Sequential double-staining immunohistochemistry was conducted for H3K27M (ab190631, Abcam; 1:1,000, 1 h at room temperature) and GD2 (14g2a, BD; 1:500, 1 h at room temperature). H3K27M was developed with a peroxidase secondary (ImmPRESS VR anti-rabbit IgG, Vector Laboratories; 30 min at room temperature) and DAB substrate (BD). After quenching the DAB substrate development in TBS and staining with the 14g2a primary antibody, the GD2 signal was developed using a polymer-based alkaline phosphatase secondary antibody (ImmPRESS AP anti-mouse IgG, Vector Laboratories; 30 min at room temperature) and blue alkaline phosphatase substrate (Vector Blue AP substrate kit, Vector Laboratories; 5 min at room temperature). Alkaline phosphatase development was quenched in TBS, and samples were mounted and imaged by light microscopy (Zeiss Axio Imager M2).

For immunofluorescence, primary tumour samples from patients were fixed in 4% PFA overnight and then transferred to 30% sucrose until samples sunk (3–4 days). Serial 40-µm cryosections were generated on an automatic freezing microtome (HM450, Thermo Fisher) then incubated with 3% normal donkey serum in 0.3% Triton X-100 in TBS blocking solution at 1 h at room temperature. Sections were stained overnight at 4 °C in primary antibody. Antibodies used were mouse anti-H3K27M (ab190631, Abcam; 1:1000) and rabbit anti-IBA1 (019–19741, Wako; 1:500) diluted in 1% normal donkey serum in 0.3% Triton X-100 in TBS blocking solution. Sections were incubated in secondary antibody conjugated with either 594 or 488 for 2 h at room temperature (715-585-150 and 711-545-152, Jackson Immunoresearch; 1:500). Samples were mounted with ProLong Gold mounting medium (P36930, Life Technologies) and were imaged using confocal microscopy (LSM710, Zeiss). For RNAscope *in situ* hybridization to visualize the *GD2-CAR* construct, primary tumor samples from patients were transferred to cryomolds and embedded in optimal-cutting temperature (OCT) compound (TissueTek). 10-µm cryosections were generated on a cryostat (Leica). Slides were fixed with cold 4% PFA for 15 minutes at 4 °C and then dehydrated in increasing ethanol rinses. To

prepare for staining, tissue was pretreated with RNAscope hydrogen peroxide for 10 min at room temperature, then treated with RNAscope protease IV and incubated for 30 min at room temperature (ACD 322381). Tissue was then stained following the kit protocol for RNAscope 2.5 HD Duplex Assay (ACD, 322500). To stain control cells for *GD2-CAR* RNAscope, *GD2-CAR* T cells were thawed from frozen and prepared for staining according to the RNAscope Multiplex v2 Assay (ACD document MK-50 010). In short, cells were seeded in growth medium on chamber slides for 24 h and then fixed with 4% PFA for 30 min at room temperature. Cells were then dehydrated with ethanal and stored in 100% ethanol at -20 °C until staining. On the day of staining, cells were rehydrated with ethanol rinses and then pretreated with RNAscope hydrogen peroxide for 10 min at room temperature followed by RNAscope protease III diluted 1:15 with PBS for 10 min at room temperature (ACD 322381) and then stained alongside the tissue samples. A custom probe was designed to target the *GD2-CAR* construct using the following sequence:

AUGCUGCUGCUCGUGACAUUCUUCUGCUGAUCAGCCAGACCCUCU
ACCCCGCCUUUCUGCUGAUCCCCGAUAUCCUGCUGACCCAGACCCUCU
GAGCCUGCCUGUGUCUCUGGGCGAUCAGGCCAGCAUCAGCUGCAGAUCC
AGCCAGAGCCUGGUGCACCGAACGGAAACACCUACCUGCACUGGUUAUC
UGCAGAAAGCCGGCCAGAGCCCCAAGCUGCUGAUUCACAAGGUGUCCAA
CCGGUUCAGCGGCUGGCCAGAGAUUUUCUGGCAGCGGCUCCGGCACC
GACUUCACCCUGAAGAACUGAGCCGGGUGGAAGCCGAGGACCUGGGCGUGU
ACUUCUGCAGCCAGUCCACCCACGUGCCCCCCCUGACAUUUGGCGCCGG
AACAAAGCUGGAACUGAAGGGCAGCACAGCGGAGCGGCAAGCCUGGA
UCUGGCAGGGAAAGCACCAAGGGCGAAGUGAAGCUGCAGCAGAGCGGCC
CCUCUCUGGUGGAACCUGGCCUCUGUGAUGAUCUCCUGCAAGGCCAG
CGGCAGCUCCUUCACCGCUACAACAUGAACUGGGUGCGCCAGAACAU
GGCAAGAGCCUGGAUGGAUCGGCGCAUCGACCCUACUACGGCGCA
CCAGCUACAACCAGAACGUUCAAGGGCAGAGCCACCCUGACCGUGGACAA
GAGCAGCUCCACCGCCUACAUGCACCUGAACGUCCUGACCAGCGAGGAC
AGCGCCGUGUACUACUGCGUGUCCGGCAUGGAAUACUGGGGCCAGGGCA
CAAGCGUGACCGUGGUCCUCUGCGGCCGCAACCACGACGCCAGCGCCGCG
ACCACCAACACCGCGCCCACCAUCGCGUCGCAGCCCCUGUCCCUGCGCC
CAGAGGCUGGCCGGCCAGCGCGGGGGCGCAGUGCACACGAGGGGGCU
GGACUUCGCCUGUGAUACUACAUUCUGGGGCCUUGGCCGGACUUGU
GGGUCCUUCUCCUGUCACUGGUUAUCACCCUUUACUGCAAACGGGGCA
GAAAGAAACUCCUGUAUAUAUCAAACAAACCAUUUAUGAGACCAGUACAA
ACUACUCAAGAGGAAAUGGCUGUAGCUGCCGAUUUCCAGAAGAAGAAG
AAGGAGGAUGUAACUGAGAGUGAAGUUCAGCAGGAGCGCAGACGCC
GCGUACCAGCAGGGCCAGAACCAACGUCUAAACGAGCUAAUCUAGGAC
GAAGAGAGGAGUACGAUGUUUUGGACAAGAGAGACGUGGCCGGACCUA
GAUGGGGGAAAGCCGAGAAGGAAGAACCCUCAGAAGGCCUGUACAAU
GAACUGCAGAAAGAUAGAUGGCGGAGGCCUACAGUGAGAUUGGGAUG

AAAGGCGAGCGCCGGAGGGCAAGGGCACGAUGGCCUUUACCAGGGUC UCAGUACAGCCACCAAGGACACCUACGACGCCUUCACAUGCAGGCCU GCCCCCUCGC. After probe hybridization, amplification and detection according to the kit manual, slides were counterstained with 50% hematoxylin for 30 sec, followed by 0.02% ammonia water for blueing. Slides were dried at 60 °C for 15 min, then mounted and imaged by light microscopy (Zeiss Axio Imager M2).

Flow cytometry of resected tumour tissue

Tumour resection material was digested into single-cell suspensions as previously described⁴⁵. Single-cell suspensions were stained with the following antibodies (Supplementary Table 10) and gating was performed using fluorescence minus one controls (FMO) on a BD LSRII Fortessa. DIPG cells were gated to evaluate GD2 expression in the CD45⁻, B7-H3⁺ population. The gating strategy is depicted in Extended Data Fig. 10b.

Reporting summary

Further information on research design is available in the [Nature Research Reporting Summary](#) linked to this paper.

Data availability

All raw data are provided in the source data files. The single-cell RNA sequencing data have been uploaded to the Gene Expression Omnibus ([GSE186802](#)). [Source data](#) are provided with this paper.

References

1. Louis, D. N. et al. The 2016 World Health Organization Classification of Tumors of the Central Nervous System: a summary. *Acta Neuropathol.* **131**, 803–820 (2016).
2. Mount, C. W. et al. Potent antitumor efficacy of anti-GD2 CAR T cells in H3-K27M⁺ diffuse midline gliomas. *Nat. Med.* **24**, 572–579 (2018).
3. Theruvath, J. et al. Locoregionally administered B7-H3-targeted CAR T cells for treatment of atypical teratoid/rhabdoid tumors. *Nat. Med.* **26**, 712–719 (2020).
4. Lin, G. L. et al. Non-inflammatory tumor microenvironment of diffuse intrinsic pontine glioma. *Acta Neuropathol. Commun.* **6**, 51 (2018).

5. Broniscer, A. et al. Intratumoral hemorrhage among children with newly diagnosed, diffuse brainstem glioma. *Cancer* **106**, 1364–1371 (2006).
6. Brown, C. E. et al. Regression of glioblastoma after chimeric antigen receptor T-cell therapy. *N. Engl. J. Med.* **375**, 2561–2569 (2016).
7. Ahmed, N. et al. HER2-specific chimeric antigen receptor-modified virus-specific T cells for progressive glioblastoma: a phase 1 dose-escalation trial. *JAMA Oncol.* **3**, 1094–1101 (2017).
8. Weber, E. W. et al. Pharmacologic control of CAR-T cell function using dasatinib. *Blood Adv.* **3**, 711–717 (2019).
9. Stallard, S. et al. CSF H3F3A K27M circulating tumor DNA copy number quantifies tumor growth and in vitro treatment response. *Acta Neuropathol. Commun.* **6**, 80 (2018).
10. Fry, T. J. et al. CD22-targeted CAR T cells induce remission in B-ALL that is naive or resistant to CD19-targeted CAR immunotherapy. *Nat. Med.* **24**, 20–28 (2018).
11. Lee, D. W. et al. T cells expressing CD19 chimeric antigen receptors for acute lymphoblastic leukaemia in children and young adults: a phase 1 dose-escalation trial. *Lancet* **385**, 517–528 (2015).
12. Maude, S. L. et al. Chimeric antigen receptor T cells for sustained remissions in leukemia. *N. Engl. J. Med.* **371**, 1507–1517 (2014).
13. Walker, A. J. et al. Tumor antigen and receptor densities regulate efficacy of a chimeric antigen receptor targeting anaplastic lymphoma kinase. *Mol. Ther.* **25**, 2189–2201 (2017).
14. Long, A. H. et al. 4-1BB costimulation ameliorates T cell exhaustion induced by tonic signaling of chimeric antigen receptors. *Nat. Med.* **21**, 581–590 (2015).
15. Keren-Shaul, H. et al. A unique microglia type associated with restricting development of Alzheimer’s disease. *Cell* **169**, 1276–1290.e17 (2017).
16. Hammond, T. R. et al. Single-cell RNA sequencing of microglia throughout the mouse lifespan and in the injured brain reveals complex cell-state changes. *Immunity* **50**, 253–271.e6 (2019).
17. Cooney, T. et al. Contemporary survival endpoints: an International Diffuse Intrinsic Pontine Glioma Registry study. *Neuro-Oncol.* **19**, 1279–1280 (2017).

18. Robison, N. J. & Kieran, M. W. Diffuse intrinsic pontine glioma: a reassessment. *J. Neurooncol.* **119**, 7–15 (2014).
19. Lee, D. W. et al. ASTCT consensus grading for cytokine release syndrome and neurologic toxicity associated with immune effector cells. *Biol. Blood Marrow Transplant.* **25**, 625–638 (2019).
20. Brudno, J. N. & Kochenderfer, J. N. Toxicities of chimeric antigen receptor T cells: recognition and management. *Blood* **127**, 3321–3330 (2016).
21. Marconi, S. et al. Expression of gangliosides on glial and neuronal cells in normal and pathological adult human brain. *J. Neuroimmunol.* **170**, 115–121 (2005).
22. Yu, A. L. et al. Anti-GD2 antibody with GM-CSF, interleukin-2, and isotretinoin for neuroblastoma. *N. Engl. J. Med.* **363**, 1324–1334 (2010).
23. Louis, C. U. et al. Antitumor activity and long-term fate of chimeric antigen receptor-positive T cells in patients with neuroblastoma. *Blood* **118**, 6050–6056 (2011).
24. Pule, M. A. et al. Virus-specific T cells engineered to coexpress tumor-specific receptors: persistence and antitumor activity in individuals with neuroblastoma. *Nat. Med.* **14**, 1264–1270 (2008).
25. Straathof, K. et al. Antitumor activity without on-target off-tumor toxicity of GD2-chimeric antigen receptor T cells in patients with neuroblastoma. *Sci. Transl. Med.* **12**, eabd6169 (2020).
26. Heczey, A. et al. Anti-GD2 CAR-NKT cells in patients with relapsed or refractory neuroblastoma: an interim analysis. *Nat. Med.* **26**, 1686–1690 (2020).
27. Majzner, R. G. et al. Tuning the antigen density requirement for CAR T-cell activity. *Cancer Discov.* **10**, 702–723 (2020).
28. Majzner, R. G. et al. CAR T cells targeting B7-H3, a pan-cancer antigen, demonstrate potent preclinical activity against pediatric solid tumors and brain tumors. *Clin. Cancer Res.* **25**, 2560–2574 (2019).
29. Venkatesh, H. S. et al. Electrical and synaptic integration of glioma into neural circuits. *Nature* **573**, 539–545 (2019).
30. Di Stasi, A. et al. Inducible apoptosis as a safety switch for adoptive cell therapy. *N. Engl. J. Med.* **365**, 1673–1683 (2011).

31. Weber, E. W. et al. Transient rest restores functionality in exhausted CAR-T cells through epigenetic remodeling. *Science* **372**, eaba1786 (2021).
32. Shen, W., Le, S., Li, Y. & Hu, F. SeqKit: a cross-platform and ultrafast toolkit for FASTA/Q file manipulation. *PLoS ONE* **11**, e0163962 (2016).
33. Stuart, T. et al. Comprehensive integration of single-cell data. *Cell* **177**, 1888–1902.e21 (2019).
34. Hafemeister, C. & Satija, R. Normalization and variance stabilization of single-cell RNA-seq data using regularized negative binomial regression. *Genome Biol.* **20**, 296 (2019).
35. Hao, Y. et al. Integrated analysis of multimodal single-cell data. *Cell* **184**, 3573–3587.e29 (2021).
36. Becht, E. et al. Dimensionality reduction for visualizing single-cell data using UMAP. *Nat. Biotechnol.* **37**, 38–44 (2019).
37. Krasemann, S. et al. The TREM2-APOE pathway drives the transcriptional phenotype of dysfunctional microglia in neurodegenerative diseases. *Immunity* **47**, 566–581.e9 (2017).
38. Li, Q. et al. Developmental heterogeneity of microglia and brain myeloid cells revealed by deep single-cell RNA sequencing. *Neuron* **101**, 207–223.e10 (2019).
39. Gabrusiewicz, K., Colwell, N. A. & Heimberger, A. B. in *Translational Immunotherapy of Brain Tumors* (ed. Sampson, J. H.) 63–82 (2017).
40. Blighe, K., Rana, S. & Lewis, M. EnhancedVolcano: Publication-ready volcano plots with enhanced colouring and labeling. R package version 1.12.0. *GitHub* <https://github.com/kevinblighe/EnhancedVolcano> (2021).
41. Yu, G. & He, Q. Y. ReactomePA: an R/Bioconductor package for reactome pathway analysis and visualization. *Mol. Biosyst.* **12**, 477–479 (2016).
42. Gojo, J. et al. Single-cell RNA-seq reveals cellular hierarchies and impaired developmental trajectories in pediatric ependymoma. *Cancer Cell* **38**, 44–59.e9 (2020).
43. Korsunsky, I. et al. Fast, sensitive and accurate integration of single-cell data with Harmony. *Nat. Methods* **16**, 1289–1296 (2019).

44. Pombo Antunes, A. R. et al. Single-cell profiling of myeloid cells in glioblastoma across species and disease stage reveals macrophage competition and specialization. *Nat. Neurosci.* **24**, 595–610 (2021).
45. Lin, G. L. & Monje, M. A protocol for rapid post-mortem cell culture of diffuse intrinsic pontine glioma (DIPG). *J. Vis. Exp.* **121**, 55360 (2017).

Acknowledgements

We are grateful to our courageous patients and their families; A. Quinones-Hinojosa, K. Jaeckle, H. Tran, D. Poon, M. Casazza, D. Brown, S. Herrera, R. Taiwo, R. Jamiolkowski, A. Wu, S. Vaca, D. Herrick, D. Purger, D. Hong, A. Cluster, D. Limbrick, E. Mayne, C. Tesi-Rocha, C. Wusthoff, S. Lee, F. Baumer, J. Klotz, T. Nguyen and many others on the clinical teams for collaboration in the care of these patients; J. Senesac and Bellicum for providing study-enabling materials in the form of the viral vector and the AP1903 supply; J. S. Tamaresis for statistical support in the trial design; Y. Pan for help with figure formatting; S. Marsh and B. Stevens for input on myeloid cell transcriptional signatures; N. Lepori-Bui, T. Tutt and A.-L. Gramstrup Petersen for their expertise in cell formulation; and the Stanford Human Immune Monitoring Core (HIMC) for performing cytokine assays. This work was supported by the National Institutes of Health R01 CA263500-01 (C.L.M. and M.M.), the Parker Institute for Cancer Immunotherapy (C.L.M. and R.G.M.), CureSearch (C.L.M., M.M. and R.G.M.), a St. Baldrick's Foundation - Stand Up 2 Cancer Pediatric Cancer Dream Team translational research grant (SU2CAACR-DT1113; C.L.M., R.G.M., S.R. and M.M.), the Stella S. Jones Foundation (M.M.), The V Foundation (R.G.M.), NIH Director's Pioneer Award (DP1NS111132; M.M.), NIH Director's New Innovator Award (DP2-CA272092; R.G.M.), ChadTough Defeat DIPG (J. Mahdi), Waxman Family Research Fund (A.C.G.) and the Virginia and D.K. Ludwig Fund for Cancer Research (C.L.M. and M.M.). The St. Baldrick's Foundation partners with Stand Up 2 Cancer, a programme of the Entertainment Industry Foundation administered by the American Association for Cancer Research.

Author information

Author notes

1. These authors contributed equally: Robbie G. Majzner, Sneha Ramakrishna
2. These authors jointly supervised this work: Crystal L. Mackall, Michelle Monje

Affiliations

1. Stanford Center for Cancer Cell Therapy, Stanford Cancer Institute, Stanford University, Stanford, CA, USA

Robbie G. Majzner, Sneha Ramakrishna, Shabnum Patel, Harshini Chinnasamy, Liora M. Schultz, Rebecca M. Richards, Valentin Barsan, Zinaida Good, Agnes Reschke, Christina Baggott, Sharon Mavroukakis, Emily Egeler, Jennifer Moon, Courtney Erickson, Michael Kunicki, Michelle Fujimoto, Snehit Prabhu, Bita Sahaf, Kara L. Davis, Steven A. Feldman, Crystal L. Mackall & Michelle Monje

2. Division of Pediatric Hematology, Oncology, Stem Cell Transplantation & Regenerative Medicine, Department of Pediatrics, Stanford University, Stanford, CA, USA

Robbie G. Majzner, Sneha Ramakrishna, Liora M. Schultz, Rebecca M. Richards, Valentin Barsan, Agnes Reschke, Maria Caterina Rotiroti, Sean Green, Michael Kunicki, Michelle Fujimoto, Zach Ehlinger, Warren Reynolds, Sreevidya Kurra, Bita Sahaf, Kara L. Davis, Crystal L. Mackall & Michelle Monje

3. Parker Institute for Cancer Immunotherapy, San Francisco, CA, USA

Robbie G. Majzner, Zinaida Good & Crystal L. Mackall

4. Division of Neuroradiology, Department of Radiology, Stanford University, Stanford, CA, USA

Kristen W. Yeom

5. Division of Pediatric Neuro-Oncology, Dana Farber Cancer Institute, Boston, MA, USA

Li Jiang, Katherine E. Warren & Mariella G. Filbin

6. Department of Neurology and Neurological Sciences, Stanford University, Stanford, CA, USA

Rebecca Mancusi, Anna C. Geraghty, Aaron Y. Mochizuki, Shawn M. Gillespie, Jasia Mahdi, Esther H. Nie, Isabelle J. Chau, Christopher W. Mount, Sonia Partap, Paul G. Fisher, Cynthia J. Campen & Michelle Monje

7. Department of Biomedical Data Science, Stanford University, Stanford, CA, USA

Zinaida Good

8. Department of Pathology, Stanford University, Stanford, CA, USA

Angus Martin Shaw Toland, Hannes Vogel & Michelle Monje

9. Division of Critical Care Medicine, Department of Pediatrics, Stanford University, Stanford, CA, USA

Lindsey Rasmussen & Timothy T. Cornell

10. Department of Neurosurgery, Stanford University, Stanford, CA, USA

Gerald Grant & Michelle Monje

11. Division of Stem Cell Transplantation and Cell Therapy, Department of Medicine, Stanford University, Stanford, CA, USA

Crystal L. Mackall

12. Howard Hughes Medical Institute, Stanford University, Stanford, CA, USA

Michelle Monje

Contributions

M.M. is the principal investigator of the trial. C.L.M. is the Investigational New Drug (IND) holder. C.W.M., R.G.M., C.L.M. and M.M. conceived the project. S.M., E.E. and C.B. oversaw regulatory affairs. S.M., E.E., M.M., C.L.M., C.W.M., R.G.M., S. Partap, C.J.C., L.R., T.T.C., K.E.W. and G.G. planned, designed and/or wrote the clinical trial, amendments and treatment protocols. K.E.W. and M.M. designed the clinical improvement scale. S. Patel, H.C. and S.A.F. performed process development for cellular manufacturing and supervised cellular manufacturing. R.G.M., S.R., L.M.S., R.M.R., V.B., J. Moon, A.R., E.H.N., C.B., J. Mahdi, C.E., S.G., L.R., T.T.C., S. Partap, P.G.F., C.J.C., G.G., K.L.D., C.L.M. and M.M. participated in patient care. K.W.Y. read radiographs and performed volumetric analysis of MRI scans. I.J.C., M.C.R., C.B., J. Moon., M.K. and M.F. participated in the collection and/or processing of patient samples. A.C.G., V.B., R.G.M., Z.E., W.R., S.K. and B.S. performed correlative studies. A.C.G. performed GD2 tissue staining and designed and carried out RNAscope *in situ* hybridization. V.B. designed and carried out the ctDNA assay. S.R., L.J., R.M., Z.G., A.Y.M., S.M.G. and M.G.F. analysed scRNA-seq data. S. Prabhu., S.R., V.B., A.C.G., R.G.M., M.M. and C.L.M. analysed other correlative studies. A.M.S.T. and H.V. performed the brain autopsy for patient 1 with DIPG and

performed neuropathological examination and immunohistochemical analyses on the autopsy tissue. R.G.M., S.R., M.M. and C.L.M. prepared figures and wrote the manuscript. All authors reviewed and edited the manuscript. M.M. and C.L.M. supervised all aspects of the work.

Corresponding authors

Correspondence to [Crystal L. Mackall](#) or [Michelle Monje](#).

Ethics declarations

Competing interests

Stanford University is in the process of applying for a patent application covering treatment of H3K27M-mutated gliomas with GD2-CAR T cells that lists M.M., C.L.M., R.G.M and C.W.M. as inventors. C.L.M. is a cofounder and holds equity in Lyell Immunopharma and Syncopation Life Sciences, which are developing CAR-based therapies, Red Tree Venture Capital, Ensme and Mammoth and consults for Lyell, Syncopation, Red Tree, NeoImmune Tech, Apricity, Nektar, Immatics, Ensoma and Mammoth. R.G.M. is a cofounder of and holds equity in Syncopation Life Sciences; he is also a consultant for Lyell Immunopharma, Syncopation Life Sciences, NKarta, Gamma Delta Therapeutics, Aptorum Group, Illumina Radiopharmaceuticals, ImmunAI, Arovella Therapeutics and Zai Lab. M.M. is on the scientific advisory board for Cygnal Therapeutics.

Peer review

Peer review information

Nature thanks the anonymous reviewers for their contribution to the peer review of this work. Peer reviewer reports are available.

Additional information

Publisher's note Springer Nature remains neutral with regard to jurisdictional claims in published maps and institutional affiliations.

Extended data figures and tables

Extended Data Fig. 1 Additional correlative findings and imaging for DIPG-1.

a, MRI images (axial T2) of participant 1 with DIPG (DIPG-1) prior to and Day+28 following GD2-CART infusion showed no improvement. **b**, Tumour volume change over time in DIPG-1. **c**, Post-mortem pons tumour tissue of DIPG-1 shows evidence of CD4+ and CD8+ T-cells by immunohistochemistry (brown). Unaffected cortex CD4+ staining depicts rare leptomeningeal vascular CD4+ cells and serves as an internal positive control. **d**, RNAscope probe against the *GD2-CAR* construct mRNA identifies GD2-CAR T cells (*GD2-CAR* mRNA puncta, pink). Positive control GD2-CAR T cells in tissue culture and negative control cortex from a DIPG patient not treated with CAR T cells were used to validate the RNAscope probe. *GD2-CAR* mRNA expression detected by RNAscope identified GD2-CAR T cells in tumour tissue from DIPG-1. *GD2-CAR* mRNA puncta = pink, hematoxylin counterstain for all cells = blue. **e**, Normal human muscle tissue immunostained for GD2 as negative control for GD2 antigen immunohistochemistry. **f**, CD163+ myeloid cells (brown) in tumor tissue of DIPG-1 by immunohistochemistry. Unaffected cortex CD163 immunostaining demonstrates microglial cells in their "resting" perivascular location. CD163+ reactive microglia/macrophages were not evident in the normal cortex of DIPG-1. **g**, Confocal microscopy of DIPG-1 tumour tissue obtained at autopsy demonstrates significant myeloid cells (Iba1+ cells, green) infiltrating the tumor (H3K27M+ cells, red). Scale bars = 100 micrometers.

[Source data](#)

Extended Data Fig. 2 Additional MRI findings.

a, Participant 2 with DIPG (DIPG-2) MRI images (axial T2) at the level of the mid-pons demonstrate T2 signal abnormality in the trigeminal nucleus (red arrow) that worsened (increased T2 signal, consistent with pseudoprogression) at Day+7 and progressively decreased on the Day+14 and Day+21 scans. Together with this T2 signal change, trigeminal function (muscles of mastication and left facial sensation) worsened around Day+7 and then progressively improved clinically. The size of the intra-tumoral cyst near the trigeminal nucleus decreased in size after treatment (red arrowhead) and the size and shape of the fourth ventricle normalized. **b**, Tumor volume change over time in DIPG-2. **c**, MRIs (axial T2) of cerebellum from participant 3 with DIPG (DIPG-3) shows increased disease in cerebellum over time, despite GD2-CAR T cell treatments. Disease in the cerebellar peduncle was relatively stable at 1 month post-IV infusion, but by the time of ICV infusion (new ICV baseline, bottom row) the cerebellar peduncle and cerebellar disease had increased, consistent with tumour progression at this site. **d**, Patient 1 with spinal cord DMG (Spinal DMG-1) MRI brain (axial T2) prior to and 21 days after ICV GD2-CAR T cell

administration. Note the extensive spread of tumour throughout brain, which reduced following ICV treatment (for example, see arrows at the left inferior frontal lobe highlighting decreased infiltrative disease at Day 21).

[Source data](#)

[**Extended Data Fig. 3 Spinal DMG-1 EEG during episode of encephalopathy.**](#)

Electroencephalogram (EEG) demonstrates diffuse slowing with triphasic waves on Day 2-3 following ICV GD2-CAR T cell administration in Spinal DMG-1. Consistent with this EEG pattern that is often observed with reversible toxic/metabolic/inflammatory encephalopathy, mental status returned to baseline over the course of days.

[**Extended Data Fig. 4 Peripheral blood LDH kinetics, CSF cell-free tumor DNA \(ctDNA\) findings, and ctDNA validation.**](#)

a, Elevated Lactate Dehydrogenase (LDH) levels approximately 7–14 days following GD2-CAR T cell infusions (either IV or ICV) in N = 4 patients. Filled dot=IV, open dot=ICV. **b**, Cell-free tumor DNA (ctDNA) from patient CSF was evaluated using digital droplet PCR for the H3K27M mutation in the *H3F3A* gene. N=at least 4 technical replicates represented as Log₂ of mutations per mL CSF ± SEM. Each point equals one technical replicate at the indicated timepoint; Filled dot=IV, open dot=ICV. DIPG-2 and Spinal DMG-1 demonstrated increasing cfDNA levels directly following GD2-CAR T cell ICV infusion ($p < 0.0001$ calculated by t-test). All available CSF samples from patients with adequate DNA extraction are represented here. DIPG-1 and DIPG-3 exhibited below the limit of detection levels and are not shown (limit of detection = 1 mutation per mL). **c**, Workflow for cell-free tumor DNA (ctDNA) assay. Cell-free DNA (cfDNA) was extracted from 1–4ml of CSF and subjected to 7 cycles pre-amplification followed by 40 cycles of digital droplet PCR (ddPCR). Schematic created with BioRender.com. **d**, Representative bioanalyzer traces of patients demonstrate adequate cfDNA quantities in Spinal DMG-1 and DIPG-2 without detectable cfDNA in DIPG-1 and DIPG-3 (i.e. there was not enough total cell-free DNA to run the assay). **e**, Validation of ddPCR assay through serial dilution of mutant H3K27M gBlock (IDT) against a fixed background of wild type H3K27M gBlock demonstrates linear mutant H3K27M detection. Sample concentrations (copies/ul) and dilution factors are plotted at Log₁₀ scale. The QuantaSoft Pro Software calculates the starting concentration of each target DNA molecule by modeling as a Poisson distribution; the formula used for Poisson modeling is: Copies per droplet = $-\ln(1-p)$ where p = fraction of positive droplets. **f**, Inclusion of negative and positive controls for each ddPCR assay was performed alongside patient samples. Pre-amplified water

served as a negative control for every run. Conditioned medium from H3K27M-mutated DIPG cell cultures was used as a positive control. Serial dilutions of H3K27M-mutated DIPG cell culture medium demonstrate a reproducible variant allele frequency (VAF) of the positive control.

[Source data](#)

Extended Data Fig. 5 Absolute values of pro-inflammatory and suppressive cytokines in pg/mL and anakinra levels measured by IL1-Ra in CSF and serum.

a, Time-course of anti-inflammatory agents (tocilizumab, anakinra and corticosteroids) administered to patients following CAR T cell infusions represented graphically to provide context for interpreting cytokine levels at various timepoints. **b–d**, The same data in absolute values that is represented in heatmap form in Fig. 4. Each data point represents the pg/ml value of the indicated cytokine at the timepoint following GD2-CAR T cell infusion. **b**, Pro-inflammatory cytokine levels in blood and cerebrospinal fluid (CSF) following intravenous (IV) administration. N = 4 patients (blood) and 3 patients (CSF). **c**, Pro-inflammatory cytokine levels in blood and cerebrospinal fluid (CSF) following intra-cerebroventricular (ICV) administration. N = 3 patients. **d**, Immune-suppressive TGF β cytokine levels in the CSF following IV CAR T cell administration. N = 3 patients. **e**, Peak serum and CSF IL1-Ra levels during anakinra treatment. Anakinra is recombinant IL1-Ra. CSF levels of anakinra, which can cross the blood-brain barrier, were approximately one tenth those of serum levels. Data generated by Luminex multi-plex cytokine analysis of patient blood plasma and CSF samples. N = 3 patients. **b–e**, Each data point represents the mean of two technical replicates. Red=DIPG-1, Blue=DIPG-2, Purple= DIPG-3, Green=Spinal DMG-1. Filled dot=IV, open dot=ICV.

[Source data](#)

Extended Data Fig. 6 Single cell RNA-sequencing of GD2-CAR T cells in CSF and from manufactured product.

a, Schematic of single cell RNA sequencing (scRNA-seq) via 10X Genomics platform, conducted on sorted GD2-CAR+ and CAR- infusion products, as well as CSF samples at indicated timepoints throughout treatment. 65,598 single cells were sequenced, including 20,000 single cells from the CAR+ fraction of patient products and 25,598 cells obtained from patient CSF (shown in Fig. 4). Schematic created with BioRender.com. **b**, GD2-CAR+ T cells were identified in post-treatment CSF samples of DIPG-2 and Spinal DMG-1 following GD2-CAR T cell administration. T cells with detected GD2-CAR expression are represented as red dots. A single UMAP was

generated with flow-sorted GD2-CAR T cell product and cells from the CSF then individually visually represented based on day of the sample. Note alterations in GD2-CAR T cell profile over time. CSF studies were not obtained for Spinal DMG-1 following IV infusion. CSF studies were also limited in DIPG-3: Following ICV GD2-CAR T cell administration, DIPG-3 did not require CSF drainage during the period of peak inflammation and given her young age, elective CSF collection was more limited. Therefore, the only post-ICV timepoint for CSF collection from DIPG-3 was Day 14, at which point there were not enough cells in CSF to conduct scRNAseq. Blue arrow=IV infusion, Yellow arrow=ICV infusion. **c**, Volcano plot representing CAR T cell product of DIPG-1 compared to DIPG-2. **d–f**, Gene ontology term analysis of the most significantly enriched pathways in DIPG-1CAR+ product relative to DIPG-2 (**d**), Spinal DMG-1 (**e**), and DIPG-3 (**f**) CAR+ product prior to CAR T cell administration. The y-axis shows the enhanced gene ontology terms, while the x-axis (“GeneRatio”) corresponds to the overlap between the up-regulated genes and genes associated with the given gene ontology terms in the dataset. Color of the circle corresponds to the p-value significance of the pathway enrichment, relative to all other genes in the dataset. Size of the circle corresponds to the relative number of matching up-regulated genes in the given gene ontology term.

Extended Data Fig. 7 CD4:CD8 Ratios of T cells throughout treatment and gene ontology term analysis of CAR T cell products prior to CAR T cell treatment.

a, Pie charts represent CSF T cell CD4:CD8 ratios from patients at different timepoints following CAR T cell administration. **b**, Top panel: CSF T cell UMAP projections highlighting Tregs in scRNA-seq data. The Treg cell cluster is highlighted in purple, while all other T cells are colored grey. Bottom panel: UMAP projections highlighting Tregs in scRNA-seq data by expressions of canonical marker genes of Tregs (CD4, FOXP3, CD25, and IKZF2).

Source data

Extended Data Fig. 8 Expression of cell cluster-specific marker genes and myeloid signature genes.

a, CSF myeloid cell UMAP projections highlighting myeloid cell clusters in scRNA-seq data by top differentially expressed genes of each cell cluster. **b, c**, Expression of myeloid transcriptional signature genes (y-axis) of identified myeloid cell clusters (x-axis). Dot sizes represent the percentage of cells expressing the gene in the given cluster. Color scale shows scaled average expression. Genes of immune activating and suppressive (**b**), homeostatic, and DAM stage 1 and 2 signatures (**c**) are plotted.

Extended Data Fig. 9 Gene ontology term analysis of myeloid cells from CSF following GD2-CAR T cell treatment.

a–c, Gene ontology term analysis demonstrates the most significantly activated pathways in the myeloid fraction of DIPG-1 compared to DIPG-2 (**a**), DIPG-3 (**b**), and Spinal DMG-1 (**c**). **d**, Gene ontology term analysis demonstrates the most significantly enriched pathways in the myeloid fraction of DIPG-2 CSF sample on Day 8 of IV CAR T administration relative to the myeloid fraction of DIPG-2 CSF sample on Day 2 of ICV CAR T cell administration (time points of peak inflammation following IV or ICV administration for this patient). The y-axis shows the enhanced gene ontology terms, while the x-axis (“GeneRatio”) corresponds to the overlap between the up-regulated genes and genes associated with the given gene ontology term in the dataset. Color of the circle corresponds to the p-value significance of the pathway enrichment, relative to all other genes in the dataset. Size of the circle corresponds to the relative number of matching up-regulated genes in the given gene ontology term. Only myeloid cells in CSF are included in this analysis.

Extended Data Fig. 10 Representative gating for flow cytometry of patient samples.

a, Representative gating of a patient CSF sample by flow cytometry (identical gating was used for PBMC obtained from blood). **b**, Gating of tumour cells by flow cytometry from temporal lobe resection tissue from Spinal DMG-1.

Supplementary information

Supplementary Information

This file contains the Clinical Trial Protocol.

Reporting Summary

Peer Review File

Supplementary Tables

This file contains Supplementary Tables 1-10.

Supplementary Video 1

Baseline Gait in participant with DIPG 2 (DIPG-2) prior to intracerebroventricular GD2-CAR T cell infusion. Gait exam on the day of admission, prior to CAR T cell infusion (D0). Gait is wide-based and mildly unstable, with decreased right arm swing and right lower extremity circumduction. He takes several (6) steps to turn. He walks back across the room on toes, then turns again with multiple steps and attempts to perform tandem walking but is unable. Videos obtained and published with informed consent.

Supplementary Video 2

Gait in participant with DIPG 2 (DIPG-2) at two weeks following intracerebroventricular GD2-CAR T cell infusion. On Day +14 after ICV GD2-CAR T cell infusion, gait is markedly improved, with a narrow base, increased speed, improved right circumduction and improved arm swing. Note improved (two steps) turning. Videos obtained and published with informed consent.

Source data

[**Source Data Fig. 1**](#)

[**Source Data Fig. 2**](#)

[**Source Data Fig. 3**](#)

[**Source Data Fig. 4**](#)

[**Source Data Extended Data Fig. 1**](#)

[**Source Data Extended Data Fig. 2**](#)

[**Source Data Extended Data Fig. 4**](#)

[**Source Data Extended Data Fig. 5**](#)

[**Source Data Extended Data Fig. 7**](#)

Rights and permissions

Open Access This article is licensed under a Creative Commons Attribution 4.0 International License, which permits use, sharing, adaptation, distribution and

reproduction in any medium or format, as long as you give appropriate credit to the original author(s) and the source, provide a link to the Creative Commons license, and indicate if changes were made. The images or other third party material in this article are included in the article's Creative Commons license, unless indicated otherwise in a credit line to the material. If material is not included in the article's Creative Commons license and your intended use is not permitted by statutory regulation or exceeds the permitted use, you will need to obtain permission directly from the copyright holder. To view a copy of this license, visit <http://creativecommons.org/licenses/by/4.0/>.

Reprints and Permissions

About this article

Cite this article

Majzner, R.G., Ramakrishna, S., Yeom, K.W. *et al.* GD2-CAR T cell therapy for H3K27M-mutated diffuse midline gliomas. *Nature* **603**, 934–941 (2022).
<https://doi.org/10.1038/s41586-022-04489-4>

- Received: 02 August 2021
- Accepted: 28 January 2022
- Published: 07 February 2022
- Issue Date: 31 March 2022
- DOI: <https://doi.org/10.1038/s41586-022-04489-4>

Share this article

Anyone you share the following link with will be able to read this content:

[Get shareable link](#)

Sorry, a shareable link is not currently available for this article.

[Copy to clipboard](#)

Provided by the Springer Nature SharedIt content-sharing initiative

Further reading

- **The roles of thermal and mechanical stress in focused ultrasound-mediated immunomodulation and immunotherapy for central nervous system tumors**

- Chulyong Kim
- Michael Lim
- Costas D. Arvanitis

Journal of Neuro-Oncology (2022)

This article was downloaded by **calibre** from <https://www.nature.com/articles/s41586-022-04489-4>

| [Section menu](#) | [Main menu](#) |

- Article
- Open Access
- [Published: 23 March 2022](#)

Nivolumab plus chemotherapy or ipilimumab in gastro-oesophageal cancer

- [Kohei Shitara](#) ORCID: [orcid.org/0000-0001-5196-3630¹](https://orcid.org/0000-0001-5196-3630),
- [Jaffer A. Ajani](#) ORCID: [orcid.org/0000-0001-9946-0629²](https://orcid.org/0000-0001-9946-0629),
- [Markus Moehler](#)³,
- [Marcelo Garrido](#)⁴,
- [Carlos Gallardo](#)⁵,
- [Lin Shen](#)⁶,
- [Kensei Yamaguchi](#)⁷,
- [Lucjan Wyrwicz](#)⁸,
- [Tomasz Skoczyłas](#) ORCID: [orcid.org/0000-0002-1276-3828⁹](https://orcid.org/0000-0002-1276-3828),
- [Arinilda Campos Bragagnoli](#) ORCID: [orcid.org/0000-0002-5165-0797¹⁰](https://orcid.org/0000-0002-5165-0797),
- [Tianshu Liu](#)¹¹,
- [Mustapha Tehfe](#)¹²,
- [Elena Elimova](#)¹³,
- [Ricardo Bruges](#)¹⁴,
- [Thomas Zander](#)¹⁵,
- [Sergio de Azevedo](#)¹⁶,
- [Ruben Kowalszyn](#)¹⁷,
- [Roberto Pazo-Cid](#) ORCID: [orcid.org/0000-0002-8026-7391¹⁸](https://orcid.org/0000-0002-8026-7391),
- [Michael Schenker](#)¹⁹,
- [James M. Cleary](#)²⁰,
- [Patricio Yanez](#)²¹,
- [Kynan Feeney](#)²²,
- [Michalis V. Karamouzis](#) ORCID: [orcid.org/0000-0003-1369-8201²³](https://orcid.org/0000-0003-1369-8201),
- [Valerie Poulart](#)²⁴,
- [Ming Lei](#)²⁴,
- [Hong Xiao](#) ORCID: [orcid.org/0000-0003-3406-0186²⁴](https://orcid.org/0000-0003-3406-0186),

- [Kaoru Kondo²⁴](#),
- [Mingshun Li²⁴](#) &
- [Yelena Y. Janjigian](#) [ORCID: orcid.org/0000-0002-5357-5858²⁵](#)

[Nature](#) volume 603, pages 942–948 (2022)

- 12k Accesses
- 128 Altmetric
- [Metrics details](#)

Subjects

- [Gastric cancer](#)
- [Immunotherapy](#)

Abstract

Standard first-line chemotherapy results in disease progression and death within one year in most patients with human epidermal growth factor receptor 2 (HER2)-negative gastro-oesophageal adenocarcinoma^{1,2,3,4}. Nivolumab plus chemotherapy demonstrated superior overall survival versus chemotherapy at 12-month follow-up in gastric, gastro-oesophageal junction or oesophageal adenocarcinoma in the randomized, global CheckMate 649 phase 3 trial⁵ (programmed death ligand-1 (PD-L1) combined positive score ≥ 5 and all randomized patients). On the basis of these results, nivolumab plus chemotherapy is now approved as a first-line treatment for these patients in many countries⁶. Nivolumab and the cytotoxic T-lymphocyte antigen-4 (CTLA-4) inhibitor ipilimumab have distinct but complementary mechanisms of action that contribute to the restoration of anti-tumour T-cell function and induction of de novo anti-tumour T-cell responses, respectively^{7,8,9,10,11}. Treatment combining 1 mg kg⁻¹ nivolumab with 3 mg kg⁻¹ ipilimumab demonstrated clinically meaningful anti-tumour activity with a manageable safety profile in heavily pre-treated patients with advanced gastro-oesophageal cancer¹². Here we report both long-term follow-up results comparing nivolumab plus chemotherapy versus chemotherapy alone and the first results comparing nivolumab plus ipilimumab versus chemotherapy alone from CheckMate 649. After the 24.0-month minimum follow-up, nivolumab plus chemotherapy continued to demonstrate improvement in overall survival versus chemotherapy alone in patients with PD-L1 combined positive score ≥ 5 (hazard ratio 0.70; 95% confidence interval 0.61, 0.81) and all randomized patients (hazard ratio 0.79; 95% confidence interval 0.71, 0.88). Overall survival in patients with PD-L1

combined positive score ≥ 5 for nivolumab plus ipilimumab versus chemotherapy alone did not meet the prespecified boundary for significance. No new safety signals were identified. Our results support the continued use of nivolumab plus chemotherapy as standard first-line treatment for advanced gastro-oesophageal adenocarcinoma.

[Download PDF](#)

Main

We enrolled 3,185 patients, 2,031 of whom were randomized across the 3 treatment groups; of these, 1,581 patients were concurrently randomized to nivolumab plus chemotherapy or chemotherapy (April 2017 to May 2019) and 813 to nivolumab plus ipilimumab or chemotherapy (October 2016 to June 2018). Enrolment to the nivolumab-plus-ipilimumab group was closed early owing to increased rate of adverse events and early deaths relative to the other two study groups, per recommendation from the data monitoring committee. Among randomized patients, the number of patients who received one or more dose of study treatment and those that were discontinued at the data cut-off date for the current analysis (27 May 2021) are shown in Extended Data Fig. 1. The primary reason for treatment discontinuation was disease progression (Extended Data Fig. 1).

Baseline characteristics were balanced across the treatment groups ([Supplementary Information](#)). Most patients were of non-Asian race ($\geq 70\%$) and had gastric cancer ($\geq 69\%$), whereas approximately 18% and 12% had gastro-oesophageal junction (GEJ) cancer and oesophageal adenocarcinoma, respectively. Approximately 60% of patients across groups had tumours expressing PD-L1 combined positive score (CPS) ≥ 5 and 3% had microsatellite instability-high (MSI-H) tumours.

Efficacy of nivolumab plus chemotherapy

With a 24.0-month minimum follow-up (time from concurrent randomization of the last patient to clinical data cut-off), nivolumab plus chemotherapy continued to demonstrate improved overall survival versus chemotherapy in patients with PD-L1 CPS ≥ 5 ; median overall survival was 14.4 months (95% confidence interval 13.1, 16.2) versus 11.1 months (10.0, 12.1), respectively (Fig. 1a). There was a 30% reduction in the risk of death (hazard ratio 0.70 (95% confidence interval 0.61, 0.81)) and sustained separation of Kaplan–Meier curves; the proportion of patients alive at 24 months was 31% versus 19%, respectively. Similarly, improved overall survival with nivolumab plus chemotherapy versus chemotherapy was observed in all randomized patients; median overall survival was 13.8 months (95% confidence interval 12.4, 14.5) versus 11.6 months (95% confidence interval 10.9, 12.5), respectively, with a

21% reduction in the risk of death versus chemotherapy (hazard ratio 0.79; 95% confidence interval 0.71, 0.88) (Fig. [1b](#)).

Fig. 1: Kaplan–Meier estimates of overall survival.

 [figure 1](#)



a, b, Overall survival with nivolumab plus chemotherapy versus chemotherapy in patients with PD-L1 CPS ≥ 5 (**a**) and in all randomized patients (**b**). Minimum follow-up, 24.0 months. **c, d,** Overall survival with nivolumab plus ipilimumab versus chemotherapy in patients with PD-L1 CPS ≥ 5 (**c**) and in all randomized patients (**d**). Minimum follow-up, 35.7 months. Chemo, chemotherapy; CI, confidence interval; HR, hazard ratio; IPI, ipilimumab; NIVO, nivolumab; OS, overall survival.

Progression-free survival (PFS) benefit was maintained after longer follow-up with nivolumab plus chemotherapy versus chemotherapy in patients with PD-L1 CPS ≥ 5 (hazard ratio 0.70; 95% confidence interval 0.60, 0.81) and in all randomized patients (hazard ratio 0.79; 95% confidence interval 0.70, 0.89); 24-month PFS rates were numerically higher in both populations (19% versus 11% and 16% versus 10%, respectively) (Extended Data Fig. [2a, b](#)). Median PFS2 (time from randomization to progression after subsequent systemic therapy, initiation of second subsequent systemic therapy or death, whichever is earlier) was numerically longer with

nivolumab plus chemotherapy versus chemotherapy (PD-L1 CPS ≥ 5 , 13.7 months (95% confidence interval 11.9, 15.0) versus 9.8 months (8.5, 10.6; hazard ratio 0.65; 95% confidence interval 0.57, 0.76); all randomized patients, 12.2 months (95% confidence interval 11.3, 13.5) versus 10.4 months (9.7, 11.2; hazard ratio 0.75; 95% confidence interval 0.67, 0.84)) (Extended Data Fig. 3).

Objective responses with nivolumab plus chemotherapy were observed in 226 (60%; 95% confidence interval 55, 65) of 378 patients with PD-L1 CPS ≥ 5 compared with 176 (45%; 95% confidence interval 40, 50) of 390 patients with chemotherapy. In all randomized patients, objective responses were observed in 350 (58%; 95% confidence interval 54, 62) of 603 patients with nivolumab plus chemotherapy versus 279 (46%; 95% confidence interval 42, 50) of 607 patients with chemotherapy (Extended Data Table 1). Additional complete responses were observed with nivolumab plus chemotherapy compared with the prespecified interim analysis at 12-month follow-up (PD-L1 CPS ≥ 5 , $n = 5$ and all randomized, $n = 6$); there were no additional complete responses with chemotherapy alone. The total number of complete responses observed with nivolumab plus chemotherapy was 49 (13%) in patients with PD-L1 CPS ≥ 5 and 65 (11%) in all randomized patients; a total of 26 (7%) and 38 (6%) patients experienced complete responses with chemotherapy, respectively. Median duration of response with nivolumab plus chemotherapy versus chemotherapy was 9.7 versus 7.0 months in patients with PD-L1 CPS ≥ 5 and 8.5 versus 6.9 months in all randomized patients, respectively (Fig. 2a,b, Extended Data Table 1). The percentage of patients with PD-L1 CPS ≥ 5 who had more than 50% tumour burden reduction was 53% with nivolumab plus chemotherapy and 44% with chemotherapy; the percentage of patients with more than 80% reduction was 27% and 18%, respectively, with consistent results in all randomized patients (Extended Data Fig. 4).

Fig. 2: Kaplan–Meier estimates of duration of response.

 **figure 2**

a, b, Duration of response per BICR with nivolumab plus chemotherapy versus chemotherapy in patients with PD-L1 CPS ≥ 5 (**a**) and in all randomized patients (**b**). **c, d**, Duration of response with nivolumab plus ipilimumab versus chemotherapy in patients with PD-L1 CPS ≥ 5 (**c**) and in all randomized patients (**d**). Number of responders (*n*) is indicated. Number of randomized patients who had target lesion measurements at baseline per BICR assessment for PD-L1 CPS ≥ 5 : NIVO + chemo, *n* = 378; chemo, *n* = 390; all randomized: NIVO + chemo, *n* = 603; chemo, *n* = 607; PD-L1 CPS ≥ 5 : NIVO + IPI, *n* = 196; chemo, *n* = 183; and all randomized: NIVO + IPI, *n* = 333; chemo, *n* = 299. BICR, blinded independent central review; DOR, duration of response.

Efficacy of nivolumab plus ipilimumab

The hierarchically tested secondary endpoint of overall survival with nivolumab plus ipilimumab versus chemotherapy in patients with PD-L1 CPS ≥ 5 did not meet the prespecified boundary for significance at 35.7-month minimum follow-up; median overall survival was 11.2 (95% confidence interval 9.2, 13.4) versus 11.6 (95% confidence interval 10.1, 12.7) months, respectively (hazard ratio 0.89; 96.5%

confidence interval 0.71, 1.10; $P = 0.2302$); 1-year overall survival rates were 47% (95% confidence interval 40, 53) and 48% (95% confidence interval 41, 54; Fig. 1c). The secondary endpoint of overall survival in all randomized patients with nivolumab plus ipilimumab versus chemotherapy was not statistically tested; median overall survival was 11.7 (95% confidence interval 9.6, 13.5) versus 11.8 (95% confidence interval 11.0, 12.7) months, respectively (hazard ratio 0.91; 96.5% confidence interval 0.77, 1.07); 1-year overall survival rates were 49% (95% confidence interval 44, 54) and 49% (95% confidence interval 44, 53; Fig. 1d). The 24-month overall survival rates with nivolumab plus ipilimumab versus chemotherapy were 25% versus 17% in patients with PD-L1 CPS ≥ 5 and 23% versus 19% in all randomized patients, respectively.

PFS and objective response rate (ORR) were not improved with nivolumab plus ipilimumab versus chemotherapy in patients with PD-L1 CPS ≥ 5 or in all randomized patients (Extended Data Fig. 2c, d, Extended Data Table 1). However, responses were more durable with nivolumab plus ipilimumab versus chemotherapy in both PD-L1 CPS ≥ 5 (median duration of response, 13.2 versus 6.9 months, respectively) and in all randomized patients (median duration of response, 13.8 versus 6.8 months; Fig. 2c, d, Extended Data Table 1).

Subgroup analyses

The hazard ratios for overall survival continued to favour nivolumab plus chemotherapy versus chemotherapy across multiple prespecified subgroups in patients with PD-L1 CPS ≥ 5 and all randomized patients with longer follow-up (Extended Data Figs. 5, 6). Overall survival benefit was enriched in patients with MSI-H tumours with nivolumab plus chemotherapy versus chemotherapy (unstratified hazard ratio 0.38; 95% confidence interval 0.17, 0.84; Extended Data Figs. 6, 7a); overall survival benefit in patients with microsatellite stable (MSS) tumours was consistent with that observed in all randomized patients (unstratified hazard ratio 0.78; 95% confidence interval 0.70, 0.88; Extended Data Figs. 6, 7b). ORR was also higher with nivolumab plus chemotherapy versus chemotherapy in patients with MSI-H tumours (55%; 95% confidence interval 32, 77 versus 39%; 95% confidence interval 17, 64, respectively) and those with MSS tumours (59%; 95% confidence interval 55, 63 versus 46%; 95% confidence interval 42, 51; Extended Data Fig. 7a, b). Similarly, nivolumab plus ipilimumab showed longer median overall survival (unstratified hazard ratio 0.28; 95% confidence interval 0.08, 0.92) and higher ORR (70%; 95% confidence interval 35, 93 versus 57%; 95% confidence interval 18, 90) compared with chemotherapy in patients with MSI-H tumours (Extended Data Fig. 7c, d).

The unstratified hazard ratios for overall survival with nivolumab plus chemotherapy in patients with PD-L1 CPS ≥ 10 , ≥ 5 and ≥ 1 were 0.66 (95% confidence interval 0.56,

0.77), 0.69 (95% confidence interval 0.60, 0.79) and 0.74 (95% confidence interval 0.66, 0.84), respectively (Fig. 3a). In patients with PD-L1 CPS < 10, <5 and <1, the unstratified hazard ratios for overall survival were 0.91 (95% confidence interval 0.78, 1.06), 0.94 (95% confidence interval 0.79, 1.11) and 0.95 (95% confidence interval 0.73, 1.24), respectively (Fig. 3a). ORR was numerically higher with nivolumab plus chemotherapy versus chemotherapy across all evaluated PD-L1 CPS subgroups (Fig. 3b). Nivolumab plus ipilimumab did not show clear improvement in overall survival or ORR by PD-L1 CPS compared with chemotherapy (Extended Data Fig. 8).

Fig. 3: Forest plot of efficacy outcomes by PD-L1 CPS with nivolumab plus chemotherapy versus chemotherapy.

 figure 3



a, Overall survival. PD-L1 CPS expression indeterminate, not evaluable or not reported for $n = 19$ patients. Data are presented as unstratified hazard ratios and 95% confidence interval. **b**, Objective response rate among randomized patients who had target lesion measurements at baseline, per blinded independent central review

assessment. PD-L1 CPS expression indeterminate, not evaluable or not reported for $n = 14$ patients; percentages may not reflect an exact difference, owing to rounding. Data are presented as unweighted ORR differences and 95% confidence interval.

Subsequent therapy

Subsequent therapy was received by 41% and 44% of randomized patients in the nivolumab-plus-chemotherapy and chemotherapy groups and by 48% and 46% of patients in the nivolumab-plus-ipilimumab and chemotherapy groups. The most common subsequent treatment was chemotherapy (36% and 39% in the nivolumab-plus-chemotherapy and chemotherapy groups and 44% and 41% in the nivolumab-plus-ipilimumab and chemotherapy groups). Subsequent immunotherapy was received by 2% and 9% of patients in the nivolumab-plus-chemotherapy and chemotherapy groups and by 3% and 12% of patients in the nivolumab-plus-ipilimumab and chemotherapy groups ([Supplementary Information](#)).

Safety

The median treatment duration was 6.8 months (range 0.1–45.0) and 4.9 months (range 0.0–44.2) with nivolumab plus chemotherapy versus chemotherapy and 1.9 months (range 0.0–24.1) and 4.9 months (range 0.1–45.5) with nivolumab plus ipilimumab versus chemotherapy ([Supplementary Information](#)). Grade 3–4 treatment-related adverse events (TRAEs) occurred in 60% and 45% of patients with nivolumab plus chemotherapy versus chemotherapy and in 38% and 46% with nivolumab plus ipilimumab versus chemotherapy (Table 1). The most common grade 3–4 TRAE was neutropaenia (15%) with nivolumab plus chemotherapy, increased lipase (7%) with nivolumab plus ipilimumab and neutropaenia (11–13%) with chemotherapy ([Supplementary Information](#)). TRAEs leading to discontinuation occurred in 38% and 25% of patients in the nivolumab-plus-chemotherapy versus chemotherapy groups, respectively, and in 22% and 26% of patients in the nivolumab-plus-ipilimumab versus chemotherapy groups (Table 1). Any-grade serious TRAEs were reported in 175 (22%) of 782 patients with nivolumab plus chemotherapy and 94 (12%) of 767 patients with chemotherapy and in 122 (30%) of 403 patients with nivolumab plus ipilimumab and 54 (14%) of 389 patients with chemotherapy. There were 16 treatment-related deaths with nivolumab plus chemotherapy, 10 with nivolumab plus ipilimumab and 5 with chemotherapy. The majority of TRAEs with a potential immunologic aetiology were grade 1 or 2; grade 3–4 events occurred in $\leq 5\%$ of patients receiving nivolumab plus chemotherapy and in $\leq 12\%$ of patients receiving nivolumab plus ipilimumab across organ categories ([Supplementary Information](#)).

Table 1 Summary of treatment-related adverse events in all treated patients

Patient-reported outcomes

Since the hierarchically tested secondary endpoint of overall survival with nivolumab plus ipilimumab versus chemotherapy in patients with PD-L1 CPS ≥ 5 was not met, the secondary endpoint of time to symptom deterioration (TTSD) in patients with PD-L1 CPS ≥ 5 and all randomized patients was not statistically tested. An improvement from baseline in the Functional Assessment of Cancer Therapy-Gastric (FACT-Ga) questionnaire total score was observed at all on-treatment assessments ([Supplementary Information](#)). The least-squares mean difference between treatment groups favoured nivolumab plus chemotherapy versus chemotherapy alone (at timepoints with ≥ 10 patients in each group); however, these differences did not reach the threshold for meaningful change (prespecified as 15.1 points; Extended Data Fig. [9a, b](#)). The proportion of patients who reported not being bothered by treatment side effects over time on the basis of the GP5 item from FACT-Ga was higher with nivolumab plus chemotherapy than with chemotherapy alone, except at baseline when patients had not received treatment (Extended Data Fig. [9c, d](#)).

Discussion

Several targeted and immuno-oncology agents have been evaluated as first-line treatment for HER2-negative gastric or GEJ cancer; however, until recently, none have significantly prolonged survival relative to chemotherapy^{[1,2,3,4,13](#)}. The positive results of CheckMate 649 reported with 12-month follow-up have established nivolumab plus chemotherapy as a standard first-line treatment for advanced gastric, GEJ or oesophageal adenocarcinoma^{[5](#)}. After 24-month follow-up, nivolumab plus chemotherapy continued to demonstrate clinically meaningful improvement in overall survival, PFS and ORR versus chemotherapy alone. Hazard ratios for overall survival were directionally improved with nivolumab plus chemotherapy versus chemotherapy relative to the 12-month follow-up^{[5](#)} (PD-L1 CPS ≥ 5 , 0.71; 98.4% confidence interval 0.59, 0.86; all randomized, 0.80; 99.3% confidence interval 0.68, 0.94), and 2-year survival rates were higher with nivolumab plus chemotherapy compared with chemotherapy. ORR was higher with nivolumab plus chemotherapy versus chemotherapy and a greater proportion of patients experienced reduction in tumour burden versus chemotherapy. Responses deepened with nivolumab plus chemotherapy with longer follow-up as evidenced by the additional complete responses compared with the 12-month follow-up.

There is considerable variation in the previously reported prevalence of PD-L1 CPS expression in gastro-oesophageal adenocarcinoma, with PD-L1 CPS ≥ 5 detected in 17–60% of patients^{[14,15,16,17](#)}. CheckMate 649 is the most robust dataset to date to report PD-L1 CPS ≥ 5 prevalence using an analytically validated assay (28–8

pharmDx) in gastric, GEJ or oesophageal adenocarcinoma. The phase 3 ORIENT-16 trial in China reported a similar PD-L1 CPS ≥ 5 prevalence of approximately 60% using the 22C3 PharmDx assay^{17,18}. In CheckMate 649, the magnitude of survival benefit continued to be enriched with nivolumab plus chemotherapy versus chemotherapy in patients with higher PD-L1 CPS, consistent with results at 12-month follow-up⁵. However, in patients with PD-L1 CPS ≥ 5 and ≥ 10 , hazard ratios for overall survival were rather close to each other, with overlapping confidence intervals, and ORR benefit was similar, suggesting no meaningful further enrichment of clinical benefit at or above PD-L1 CPS 10. Furthermore, the ORRs observed with nivolumab plus chemotherapy were higher versus chemotherapy across all evaluated PD-L1 CPS cut-offs, suggesting that clinical benefit with nivolumab plus chemotherapy is not restricted to patients with PD-L1 CPS ≥ 5 . Further analyses may help identify factors that are associated with higher magnitude of clinical benefit in patients with lower PD-L1 CPS.

Overall survival continued to favour nivolumab plus chemotherapy versus chemotherapy across multiple prespecified baseline characteristics with longer follow-up. Notably, the magnitude of survival benefit was markedly greater in the MSI-H subgroup for both patients with PD-L1 CPS ≥ 5 and all randomized patients, suggesting that benefit is independent of PD-L1 CPS. Similar results were reported with first-line pembrolizumab plus chemotherapy versus chemotherapy in patients with gastric or GEJ cancer (PD-L1 CPS ≥ 1) who had MSI-H tumours¹³. In CheckMate 649, the overall survival benefit in patients with MSS tumours was similar to that observed in all randomized patients.

The secondary endpoint of overall survival with nivolumab plus ipilimumab versus chemotherapy in CheckMate 649 did not meet the prespecified boundary for significance in patients with PD-L1 CPS ≥ 5 . The observed response rates with nivolumab plus ipilimumab were lower versus chemotherapy, and there was no enrichment with increasing PD-L1 CPS cut-offs. However, the median duration of response almost doubled with nivolumab plus ipilimumab versus chemotherapy, which is consistent with results in other solid tumours with this combination^{19,20,21,22}.

The lack of significant overall survival improvement with nivolumab plus ipilimumab is probably a result of multiple factors. There was an increase in early death rate with nivolumab plus ipilimumab versus chemotherapy; crossing of the Kaplan–Meier curves, which is a known phenomenon with immuno-oncology therapies^{13,23,24}, was observed at 12 months, and the overall survival curves remained separated thereafter in favour of nivolumab plus ipilimumab. A higher number of patients receiving subsequent immuno-oncology therapy in the chemotherapy versus nivolumab-plus-ipilimumab group (12% versus 3%, respectively) may have also contributed to these results.

Tumours in gastric, GEJ or oesophageal adenocarcinoma are composed of distinct molecular subtypes^{25,26}. Although dual checkpoint inhibition has been proven to be effective in multiple solid tumours^{19,20,21,22,27}, further research is needed to evaluate how tumour biology, molecular heterogeneity, dynamics in tumour microenvironment and other patient factors may affect the efficacy of combined PD-L1 and CTLA-4 blockade. Notably, in the small but relevant subgroup of patients with microsatellite instability, which is characterized by high tumour mutational burden and CD8-positive T-cell infiltrates and is susceptible to immune-checkpoint inhibition^{25,28,29,30}, longer overall survival and higher ORR were observed with nivolumab plus ipilimumab versus chemotherapy in CheckMate 649. These data suggest that combined immune checkpoint blockade in this patient population might be of interest to explore in future studies.

No new safety signals were identified with nivolumab plus chemotherapy in CheckMate 649 with similar frequencies of TRAEs relative to the 12-month follow-up. The safety profile of nivolumab plus ipilimumab observed in this trial was consistent with the known safety profile of this combination^{12,27}. Limitations of this study have been previously discussed⁵.

In conclusion, the long-term clinically meaningful overall survival and PFS benefit, improved and durable responses, maintained health-related quality of life, and acceptable safety profile indicate a favourable benefit–risk profile of nivolumab plus chemotherapy. These results further support the use of this regimen as a standard first-line treatment in previously untreated patients with advanced gastric, GEJ or oesophageal adenocarcinoma.

Methods

Patients

Adults with unresectable advanced or metastatic gastric, GEJ or oesophageal adenocarcinoma were enrolled, regardless of PD-L1 expression. Patients with known HER2-positive status were excluded, and prior systemic therapy for metastatic disease was not allowed. Other key inclusion criteria were an Eastern Cooperative Oncology Group performance status score of 0 or 1 and the ability to provide a fresh or archival tumour sample to determine PD-L1 status. Additional details on study criteria have been previously described⁵.

Trial design and treatments

CheckMate 649 (NCT02872116) is a randomized, open-label, multicentre, global phase 3 trial of nivolumab plus chemotherapy or ipilimumab versus chemotherapy alone, conducted at 175 hospitals and cancer centres in 29 countries across Asia, Australia, Europe, North America, and South America. Detailed study design and methods for the nivolumab-plus-chemotherapy versus chemotherapy groups have been previously described⁵. In brief, patients were initially randomized 1:1 to nivolumab plus ipilimumab or to chemotherapy from October 2016 to March 2017. The nivolumab-plus-chemotherapy group was added later, and the randomization was switched to 1:1:1 in March 2017. Enrolment to the nivolumab-plus-ipilimumab group was closed early in June 2018, and after this time, the randomization was switched to a 1:1 ratio of nivolumab plus chemotherapy versus chemotherapy to May 2019. Patients already randomized to nivolumab plus ipilimumab could continue treatment per protocol, but the data remained blinded until the pre-planned final analysis. During enrolment, the population for primary endpoints was amended to patients whose tumours expressed PD-L1 CPS ≥ 5 for the nivolumab-plus-chemotherapy versus chemotherapy groups, although patients continued to be enrolled regardless of PD-L1 expression. Additional randomization procedures and stratification by tumour cell PD-L1 status ($\geq 1\%$ versus $< 1\%$ including indeterminate), region (Asia versus United States and Canada versus rest of world), Eastern Cooperative Oncology Group performance status score (0 versus 1) and type of chemotherapy (CapeOX versus FOLFOX) have been described⁵.

Patients were administered nivolumab (360 mg every 3 weeks or 240 mg every 2 weeks) with investigator's choice of chemotherapy (CapeOX (oxaliplatin 130 mg m⁻² on day 1 and capecitabine 1,000 mg m⁻² orally twice daily on days 1–14) every 3 weeks or FOLFOX (leucovorin 400 mg m⁻² on day 1, fluorouracil 400 mg m⁻² on day 1 and 1,200 mg m⁻² on days 1–2, and oxaliplatin 85 mg m⁻² on day 1) every 2 weeks); nivolumab (1 mg kg⁻¹) with ipilimumab (3 mg kg⁻¹) every 3 weeks for 4 cycles, followed by nivolumab (240 mg every 2 weeks); or chemotherapy alone. The dosing for nivolumab 1 mg kg⁻¹ plus ipilimumab 3 mg kg⁻¹ was selected based on results of the CheckMate 032 study, where this regimen provided numerically higher ORR and longer median overall survival compared with nivolumab monotherapy or nivolumab 3 mg kg⁻¹ plus ipilimumab 1 mg kg⁻¹, along with a manageable safety profile in heavily pre-treated patients with advanced gastro-oesophageal adenocarcinoma¹². Treatment was permitted until documented disease progression, unacceptable toxicity, withdrawal of consent or trial end. Nivolumab or ipilimumab were given for a maximum of two years. Patients receiving nivolumab in combination with chemotherapy or ipilimumab were permitted to continue treatment beyond initial disease progression (per Response Evaluation Criteria in Solid Tumors (RECIST), version 1.1), based on the investigator's judgement, until subsequent progression. Dose reductions were not permitted for nivolumab and ipilimumab; dose reductions for chemotherapy were permitted per local standards. Dose delays were allowed for

both groups to manage treatment-related toxicity. Nivolumab, ipilimumab, CapeOX and FOLFOX were provided by the sponsor except in certain countries where CapeOX and FOLFOX were procured commercially if allowed by local regulations. Additional details on discontinuation criteria have been previously described⁵.

The trial was conducted according to Good Clinical Practice guidelines developed by the International Council for Harmonisation and in compliance with the trial protocol ([Supplementary Appendix](#)). The trial protocol was approved by the institutional review boards or independent ethics committees at each site (NCT02872116). All patients provided written informed consent prior to trial participation per Declaration of Helsinki principles.

Endpoints and assessments

The dual primary endpoints were overall survival (time from randomization to death) and PFS (time from randomization to the date of the first documented tumour progression (by blinded independent central review (BICR) per RECIST, version 1.1) or death) in the nivolumab-plus-chemotherapy versus chemotherapy groups⁵ in patients with PD-L1 CPS ≥ 5 . Secondary endpoints that were hierarchically tested if the primary endpoints were met were overall survival in patients with PD-L1 CPS ≥ 1 and in all randomized patients in the nivolumab-plus-chemotherapy versus chemotherapy group and overall survival and TTSD in patients with PD-L1 CPS ≥ 5 and in all randomized patients in the nivolumab-plus-ipilimumab versus chemotherapy group. Other key secondary endpoints that were not formally tested included BICR-assessed PFS and ORR evaluated at different PD-L1 CPS cut-offs and in all randomized patients. Key exploratory endpoints included BICR-assessed duration of response; landmark survival rates; PFS2 (time from randomization to progression after subsequent systemic therapy, initiation of second subsequent systemic therapy, or death, whichever is earlier); biomarkers potentially predictive of efficacy; health-related quality of life; and safety and tolerability.

Tumours were assessed using computed tomography or magnetic resonance imaging per RECIST, version 1.1, at baseline, every 6 weeks from the start of cycle 1 for 48 weeks and every 12 weeks thereafter, until disease progression per BICR assessment. Adverse events were assessed throughout the treatment period and during follow-up according to the National Cancer Institute Common Terminology Criteria for Adverse Events, version 4.0.

PRO analyses

FACT-Ga analysis was done for patients with PD-L1 CPS ≥ 5 and all randomly assigned patients who had an assessment at baseline (day 1, assessment before

administration of treatment on day of first dose) and at least one subsequent assessment while on treatment. The questionnaire completion rate, defined as the proportion of questionnaires actually received out of the expected number, was calculated and summarized at each assessment point using descriptive statistics. Mean score and mean change from baseline for the FACT-Ga scale were estimated using mixed model for repeated measures. The change from baseline was modelled as a linear function of treatment groups; trial assessment; baseline score; trial stratification factors; interaction terms between treatment group and trial assessment; interaction terms between baseline score and trial assessment; and any potential confounders. A clinically meaningful difference was defined as a 15.1 or greater change from baseline in FACT-Ga total score³¹. The *P*-value for the difference in least squares means was computed as the two-tailed probability using the t distribution. No adjustments were made for multiple comparisons. In addition, treatment burden was assessed by the individual GP5 item of the FACT-Ga. The GP5 item reads, “I am bothered by side effects of treatment.” Frequencies and percentages of the GP5 item question responses (‘not at all’, ‘a little bit’, ‘somewhat’, ‘quite a bit’ and ‘very much’) were tabulated at each assessment point with ten or more study subjects in each group.

Statistical analyses

Patients concurrently randomized to the nivolumab-plus-chemotherapy versus chemotherapy groups and the nivolumab-plus-ipilimumab versus chemotherapy groups were included in the respective final overall survival analyses. For the comparison of nivolumab plus chemotherapy and chemotherapy, patients randomized to chemotherapy before the nivolumab-plus-chemotherapy arm was introduced were not included in the analysis. For the comparison of nivolumab plus ipilimumab and chemotherapy, patients randomized to chemotherapy after the closure of nivolumab-plus-ipilimumab arm were not included in the analysis.

For nivolumab plus ipilimumab versus chemotherapy, the analysis of overall survival was pre-planned at a minimum follow-up of approximately 36 months, which corresponded with the pre-planned final analysis of overall survival for nivolumab plus chemotherapy versus chemotherapy at a 24-month minimum follow-up. Since the dual primary endpoints for nivolumab-plus-chemotherapy versus chemotherapy groups were met⁵, the secondary endpoint of overall survival in the nivolumab-plus-ipilimumab versus chemotherapy groups was hierarchically tested in patients with PD-L1 CPS ≥ 5 followed by all randomized patients. If overall survival in the nivolumab-plus-ipilimumab versus chemotherapy groups met the criteria for statistical significance, the secondary endpoint of TTSD in the nivolumab-plus-ipilimumab versus chemotherapy groups was planned to be hierarchically tested in patients with PD-L1 CPS ≥ 5 followed by all randomized patients. In the interim analysis, two-sided alpha levels of 0.02 and 0.03 (type I error) were allocated to the dual primary

endpoints of PFS and overall survival, respectively. The comparison of secondary endpoints of overall survival and TTSD for nivolumab plus ipilimumab versus chemotherapy inherited alpha independently from the two primary endpoints (fraction of α transmitted = 0.035) and was tested once after 36 months in patients with PD-L1 CPS ≥ 5 followed by all randomized patients.

The statistical power estimation for the comparison of primary endpoints for the nivolumab-plus-chemotherapy versus the chemotherapy groups has been described previously⁵. Sample size calculations of the primary endpoints were based on simulations in East software, version 6.4.1. (Cytel). The prevalence of patients with PD-L1 CPS ≥ 5 was assumed to be 35% of all randomized patients, based on limited available data^{14,24,32}, with 285 patients estimated in the nivolumab-plus-ipilimumab versus chemotherapy analysis. Based on new information from the CheckMate 649 trial, this PD-L1 CPS ≥ 5 prevalence was revised to 60% of all randomized patients, with 489 patients estimated in the nivolumab-plus-ipilimumab versus chemotherapy analysis. For overall survival, the hazard ratio was modelled as a four-piece hazard ratio with an average of 0.7. With 36-month minimum follow-up, it was expected that the 411 events would provide 93% power.

Median PFS, overall survival, and duration of response were estimated using Kaplan–Meier methods, and the corresponding two-sided 95% confidence intervals were calculated using the log–log transformation method. The stratified Cox proportional hazards regression model, with the randomization factors as the stratification factors and treatment group as a single covariate, was used to assess differences between treatment groups in overall survival and PFS. An O’Brien and Fleming α -spending function was employed to determine the hazard ratio for overall survival, using a stratified Cox proportional hazards model. Stratification factors recorded in an interactive web response system were used in the analysis.

The proportion of patients with an objective response and corresponding two-sided 95% confidence intervals were calculated using the Clopper-Pearson method.

Statistical analyses were performed using SAS software, version 9.4 (SAS Institute, Cary, NC).

Reporting summary

Further information on research design is available in the [Nature Research Reporting Summary](#) linked to this paper.

Data availability

The Bristol Myers Squibb data sharing policy (<https://www.bms.com/researchers-and-partners/independent-research/data-sharing-request-process.html>) is compliant with ICMJE guidelines. Bristol Myers Squibb will honour legitimate requests for clinical trial data from qualified researchers. Data will be shared with external researchers whose proposed use of the data has been approved. Complete de-identified patient data sets will be eligible for sharing 2 years after completion of the CheckMate 649 study. Before data are released, the researcher(s) must sign a Data Sharing Agreement, after which the de-identified and anonymized datasets can be accessed within a secured portal.

References

1. Catenacci, D. V. T. et al. Rilotumumab plus epirubicin, cisplatin, and capecitabine as first-line therapy in advanced MET-positive gastric or gastro-oesophageal junction cancer (RILOMET-1): a randomised, double-blind, placebo-controlled, phase 3 trial. *Lancet Oncol.* **18**, 1467–1482 (2017).
2. Fuchs, C. S. et al. Ramucirumab with cisplatin and fluoropyrimidine as first-line therapy in patients with metastatic gastric or junctional adenocarcinoma (RAINFALL): a double-blind, randomised, placebo-controlled, phase 3 trial. *Lancet Oncol.* **20**, 420–435 (2019).
3. Lordick, F. et al. Capecitabine and cisplatin with or without cetuximab for patients with previously untreated advanced gastric cancer (EXPAND): a randomised, open-label phase 3 trial. *Lancet Oncol.* **14**, 490–499 (2013).
4. Shah, M. A. et al. Effect of fluorouracil, leucovorin, and oxaliplatin with or without onartuzumab in HER2-negative, MET-positive gastroesophageal adenocarcinoma: the METGastric randomized clinical trial. *JAMA Oncol.* **3**, 620–627 (2017).
5. Janjigian, Y. Y. et al. First-line nivolumab plus chemotherapy versus chemotherapy alone for advanced gastric, gastro-oesophageal junction, and oesophageal adenocarcinoma (CheckMate 649): a randomised, open-label, phase 3 trial. *Lancet* **398**, 27–40 (2021).
6. *OPDIVO (Nivolumab) Injection for Intravenous Use. Prescribing Information* (Bristol Myers Squibb, 2021).
7. Das, R. et al. Combination therapy with anti-CTLA-4 and anti-PD-1 leads to distinct immunologic changes in vivo. *J. Immunol.* **194**, 950–959 (2015).

8. Brahmer, J. R. et al. Phase I study of single-agent anti-programmed death-1 (MDX-1106) in refractory solid tumors: safety, clinical activity, pharmacodynamics, and immunologic correlates. *J. Clin. Oncol.* **28**, 3167–3175 (2010).
9. Wang, C. et al. In vitro characterization of the anti-PD-1 antibody nivolumab, BMS-936558, and in vivo toxicology in non-human primates. *Cancer Immunol. Res.* **2**, 846–856 (2014).
10. Pardoll, D. M. The blockade of immune checkpoints in cancer immunotherapy. *Nat. Rev. Cancer* **12**, 252–264 (2012).
11. Wei, S. C., Duffy, C. R. & Allison, J. P. Fundamental mechanisms of immune checkpoint blockade therapy. *Cancer Discov.* **8**, 1069–1086 (2018).
12. Janjigian, Y. Y. et al. CheckMate-032 study: efficacy and safety of nivolumab and nivolumab plus ipilimumab in patients with metastatic esophagogastric cancer. *J. Clin. Oncol.* **36**, 2836–2844 (2018).
13. Shitara, K. et al. Efficacy and safety of pembrolizumab or pembrolizumab plus chemotherapy vs chemotherapy alone for patients with first-line, advanced gastric cancer: the KEYNOTE-062 phase 3 randomized clinical trial. *JAMA Oncol.* **6**, 1571–1580 (2020).
14. Lei, M. et al. Analyses of PD-L1 and inflammatory gene expression association with efficacy of nivolumab ± ipilimumab in gastric cancer/gastroesophageal junction cancer. *Clin. Cancer Res.* **27**, 3926–3935 (2021).
15. Hagi, T. et al. Multicentre biomarker cohort study on the efficacy of nivolumab treatment for gastric cancer. *Br. J. Cancer* **123**, 965–972 (2020).
16. Fassan, M. et al. PD-L1 expression in gastroesophageal dysplastic lesions. *Virchows Arch.* **477**, 151–156 (2020).
17. Xu, J. et al. LBA53—Sintilimab plus chemotherapy (chemo) versus chemo as first-line treatment for advanced gastric or gastroesophageal junction (G/GEJ) adenocarcinoma (ORIENT-16): first results of a randomized, double-blind, phase III study. *Ann. Oncol.* **32**, S1283–S1346 (2021).
18. Xu, J., Jin, Y., Liu, Y., Zhou, H. & Wang, Y. ORIENT-16: sintilimab plus XELOX vs placebo plus XELOX as 1st line treatment for unresectable advanced gastric and GEJ adenocarcinoma. *Cancer Res.* **79**, CT213 (2019).

19. Doki, Y. et al. Nivolumab combination therapy in advanced esophageal squamous-cell carcinoma. *N. Engl. J. Med.* **386**, 449–462 (2022).
20. Motzer, R. J. et al. Nivolumab plus ipilimumab versus sunitinib in advanced renal-cell carcinoma. *N. Engl. J. Med.* **378**, 1277–1290 (2018).
21. Baas, P. et al. First-line nivolumab plus ipilimumab in unresectable malignant pleural mesothelioma (CheckMate 743): a multicentre, randomised, open-label, phase 3 trial. *Lancet* **397**, 375–386 (2021).
22. Hellmann, M. D. et al. Nivolumab plus ipilimumab in advanced non-small-cell lung cancer. *N. Engl. J. Med.* **381**, 2020–2031 (2019).
23. Bang, Y. J. et al. Phase III, randomised trial of avelumab versus physician's choice of chemotherapy as third-line treatment of patients with advanced gastric or gastro-oesophageal junction cancer: primary analysis of JAVELIN Gastric 300. *Ann. Oncol.* **29**, 2052–2060 (2018).
24. Shitara, K. et al. Pembrolizumab versus paclitaxel for previously treated, advanced gastric or gastro-oesophageal junction cancer (KEYNOTE-061): a randomised, open-label, controlled, phase 3 trial. *Lancet* **392**, 123–133 (2018).
25. Bass, A. J. et al. Comprehensive molecular characterization of gastric adenocarcinoma. *Nature* **513**, 202–209 (2014).
26. Cancer Genome Atlas Research Network. Integrated genomic characterization of oesophageal carcinoma. *Nature* **541**, 169–175 (2017).
27. Wolchok, J. D. et al. Overall survival with combined nivolumab and ipilimumab in advanced melanoma. *N. Engl. J. Med.* **377**, 1345–1356 (2017).
28. Angell, H. K. et al. PD-L1 and immune infiltrates are differentially expressed in distinct subgroups of gastric cancer. *OncoImmunology* **8**, e1544442 (2019).
29. Le, D. T. et al. Mismatch repair deficiency predicts response of solid tumors to PD-1 blockade. *Science* **357**, 409–413 (2017).
30. Zhou, K. I. et al. Spatial and temporal heterogeneity of PD-L1 expression and tumor mutational burden in gastroesophageal adenocarcinoma at baseline diagnosis and after chemotherapy. *Clin. Cancer Res.* **26**, 6453–6463 (2020).
31. Garland, S. N. et al. Prospective evaluation of the reliability, validity, and minimally important difference of the functional assessment of cancer therapy-gastric (FACT-Ga) quality-of-life instrument. *Cancer* **117**, 1302–1312 (2011).

32. Kulangara, K. et al. Investigation of PD-L1 expression and response to pembrolizumab (pembro) in gastric cancer (GC) and cervical cancer (CC) using combined positive score (CPS) and tumor proportion score (TPS). *J Clin Oncol* **36**, 4065 (2018).

Acknowledgements

This study was supported by Bristol Myers Squibb and Ono Pharmaceutical Co., Ltd. We thank the patients and their families who made this study possible, the investigators and the clinical study teams at Bristol Myers Squibb and Ono Pharmaceutical Co., Ltd. for CheckMate 649 study support. Analysis of patient-reported outcomes was supported by S. Blum (Bristol Myers Squibb), and S. Hunter, E. Davenport and J. Wang (RTI Health Solutions). We thank Dako (an Agilent Technologies company) for collaborative development of the PD-L1 IHC 28-8 pharmDx assay. Professional medical writing and editorial assistance were provided by P. Dang (Parexel), funded by Bristol Myers Squibb.

Author information

Affiliations

1. National Cancer Center Hospital East, Kashiwa, Japan

Kohei Shitara

2. The University of Texas MD Anderson Cancer Center, Houston, TX, USA

Jaffer A. Ajani

3. Johannes-Gutenberg University Clinic, Mainz, Germany

Markus Moehler

4. Clinica San Carlos de Apoquindo, Pontificia Universidad Católica, Santiago, Chile

Marcelo Garrido

5. Fundación Arturo López Pérez, Providencia, Chile

Carlos Gallardo

6. Department of Gastrointestinal Oncology, Key Laboratory of Carcinogenesis and Translational Research (Ministry of Education/Beijing), Peking University Cancer Hospital and Institute, Beijing, China

Lin Shen

7. The Cancer Institute Hospital of JFCR, Tokyo, Japan

Kensei Yamaguchi

8. Klinika Onkologii i Radioterapii, Narodowy Instytut Onkologii, Warszawa, Poland

Lucjan Wyrwicz

9. II Klinika Chirurgii Ogólnej, Gastroenterologicznej i Nowotworów Układu Pokarmowego, Medical University of Lublin, Lublin, Poland

Tomasz Skoczylas

10. Fundacao Pio Xii Hospital Cancer De Barretos, Barretos, Brazil

Arinilda Campos Bragagnoli

11. Zhongshan Hospital Fudan University, Shanghai, China

Tianshu Liu

12. Oncology Center – Centre Hospitalier de l’Universite de Montreal, Montreal, Canada

Mustapha Tehfe

13. Princess Margaret Cancer Centre, Toronto, Ontario, Canada

Elena Elimova

14. Instituto Nacional de Cancerología E.S.E., Bogotá, Colombia

Ricardo Bruges

15. University of Cologne, Department of Internal Medicine, Center for Integrated Oncology Aachen Bonn Cologne Düesseldorf; Gastrointestinal Cancer Group Cologne (GCGC), Cologne, Germany

Thomas Zander

16. Hospital de Clínicas de Porto Alegre, Porto Alegre, Brazil

Sergio de Azevedo

17. Instituto Multidisciplinario de Oncologia, Clinica Viedma S.A., Viedma, Argentina

Ruben Kowalszyn

18. Hospital Universitario Miguel Servet, Zaragoza, Spain

Roberto Pazo-Cid

19. SF Nectarie Oncology Center, Craiova, Romania

Michael Schenker

20. Dana Farber Cancer Institute, Boston, MA, USA

James M. Cleary

21. Universidad de La Frontera, James Lind Cancer Research Center, Temuco, Chile

Patricio Yanez

22. St John of God Murdoch Hospital, Murdoch, Australia

Kynan Feeney

23. Laiko General Hospital of Athens, Athens, Greece

Michalis V. Karamouzis

24. Bristol Myers Squibb, Princeton, NJ, USA

Valerie Poupart, Ming Lei, Hong Xiao, Kaoru Kondo & Mingshun Li

25. Memorial Sloan Kettering Cancer Center and Weill Cornell Medical College, New York, NY, USA

Yelena Y. Janjigian

Contributions

K.S., J.A.A., M.M., M. Lei, V.P., M. Li and Y.Y.J. contributed to the conception and design of the study in collaboration with Bristol Myers Squibb. K.S., J.A.A., M.M., M.G., C.G., L.S., K.Y., L.W., T.S., A.C.B., T.L., M.T., E.E., R.B., T.Z., S.d.A., R.K., R.P.-C., M.S., J.M.C., P.Y., K.F., M.V.K. and Y.Y.J. recruited and/or treated patients and gathered clinical data on efficacy, safety and patient-reported outcomes. M. Li analysed the clinical data, M. Lei performed biomarker analyses, H.X. analysed the PRO data, and V.P. conducted statistical analyses. M. Lei, V.P., M. Li, H.X. and K.K. verified the data. All authors interpreted the data. All authors had access to all the data in the study, participated in developing or reviewing the manuscript and provided final approval to submit the manuscript for publication.

Corresponding author

Correspondence to [Yelena Y. Janjigian](#).

Ethics declarations

Competing interests

K.S. reports receiving personal fees for advisory roles from AbbVie, Boehringer Ingelheim, Bristol Myers Squibb, GlaxoSmithKline, Novartis, Pfizer, and Takeda; receiving advisory role or research funding from Astellas Pharma, Eli Lilly, Ono Pharmaceutical, Merck Pharmaceutical, and Taiho Pharmaceutical; receiving honoraria (lecture fees) from AbbVie, Novartis, and Yakult Honsha; and receiving research funding from Amgen, Chugai Pharma, Daiichi Sankyo, Dainippon Sumitomo Pharma, Medi Science, and Eisai, outside the submitted work. J.A.A. reports receiving research grants from Amgen, Astellas Pharma, Bristol Myers Squibb, Daiichi Sankyo, Delta-Fly Pharma, Gilead Sciences, Lilly/ImClone, Merck, Novartis, ProLynx, Roche/Genentech, Taiho Pharmaceutical, Takeda, and Zymeworks; serving as a consultant or in an advisory role for American Cancer Society, BeiGene, Bristol Myers Squibb, Insys Therapeutics, Merck, and Vaccinogen; receiving royalties from or holding patents and other intellectual property with Amgen, Bristol Myers Squibb, Genentech, Lilly, Medimmune, Merck, Roche, and Taiho Pharmaceutical; and receiving honoraria from Acrotech BioPharma, Aduro Biotech, Amgen, Astellas Pharma, BeiGene, Boehringer Ingelheim, Bristol Myers Squibb, Daiichi Sankyo, DAVA Pharmaceuticals, Fresenius Kabi, Gilead Sciences, Grail, Lilly, Merck, Novartis, Servier, and Zymeworks, outside the submitted work. M.M. reports receiving research grants from Amgen, Leap Therapeutics, Merck Serono, and Merck Sharp & Dohme; serving as a consultant or in an advisory role for Amgen, Bayer, Beigene, Bristol Myers Squibb, Lilly, Merck Serono, Merck Sharp & Dohme, Pfizer, Roche, Servier, and Taiho Pharmaceutical; receiving travel and accommodation

expenses from American Society of Clinical Oncology, Amgen, Bayer, European Society for Medical Oncology, German Cancer Society, Merck Serono, Merck Sharp & Dohme, and Roche; and receiving honoraria from Amgen, AstraZeneca/MedImmune, Bristol Myers Squibb, Merck Serono, Merck Sharp & Dohme Oncology, Roche/Genentech, Pierre Fabre, Sanofi, and Servier, outside the submitted work. M.G. reports receiving research grants from Bristol Myers Squibb and Novartis; receiving speakers' bureau fees from Bayer, Bristol Myers Squibb, and Merck; receiving travel and accommodations expenses from Roche; and serving as a consultant or in an advisory role for Merck Sharp & Dohme and Roche, outside the submitted work. C.G. reports receiving research grants from Bristol Myers Squibb and Merck Sharp & Dohme; receiving speakers' bureau fees from AstraZeneca, Merck Sharp & Dohme, and Novartis; receiving travel and accommodation expenses from Roche; serving as a consultant or in an advisory role for Merck Sharp & Dohme, Novartis, and Roche; and providing expert testimony for AstraZeneca, outside the submitted work. L.S. reports receiving research grants from Beijing Xiantong Biomedical Technology, Qilu Pharmaceutical, ZaiLab Pharmaceutical (Shanghai), Beihai Kangcheng (Beijing) Medical Technology, Jacobio Pharmaceuticals, and Beijing Xiantong Biomedical Technology; receiving consulting fees from Boehringer Ingelheim, Haichuang Pharmaceutical, Harbour Biomed, Merck, Merck Sharp & Dohme, and Mingji Biopharmaceutical; receiving speakers' fees from CSTONE Pharmaceutical, Hutchison Whampoa, Hengrui, and ZaiLab; and participating on a Data Safety Monitoring Board or Advisory Board for Bristol Myers Squibb, CSTONE Pharmaceutical, Rongchang Pharmaceutical, and ZaiLab, outside the submitted work. K.Y. reports receiving research grants from Boehringer Ingelheim, Bristol Myers Squibb, Chugai Pharma, Daiichi Sankyo, Eisai, Gilead Sciences, Lilly, Merck Sharp & Dohme Oncology, Ono Pharmaceutical, Sanofi, Taiho Pharmaceutical, and Yakult Honsha; receiving speakers' bureau fees from Bristol Myers Squibb Japan, Chugai Pharma, Daiichi Sankyo, Lilly, Merck, Ono Pharmaceutical, Taiho Pharmaceutical, and Takeda; and serving as a consultant or in an advisory role for Bristol Myers Squibb Japan and Daiichi Sankyo, outside the submitted work. L.W. reports receiving research grants from National Cancer Research Institute; receiving speakers' bureau fees from Amgen, Roche, Sanofi, and Servier; and serving in a consulting or advisory role for Amgen and Servier, outside the submitted work. T.S. has no competing interests to disclose. A.B. has no competing interests to disclose. T.L. has no competing interests to disclose. M.T. reports receiving research funding from Celgene; receiving honoraria from Bristol Myers Squibb, Celgene, Eisai, Merck, Pfizer, and Taiho Pharmaceutical; and serving in a consulting or advisory role for Bayer, Bristol Myers Squibb, Celgene, Eisai, Merck, Taiho Pharmaceutical, and Takeda, outside the submitted work. E.E. reports receiving research funding from Bristol Myers Squibb and Zymeworks; serving as a consultant or in an advisory role for Bristol Myers Squibb, Zymeworks, and Adaptimmune; and having an immediate family member employed by Merck, outside the submitted work. R.B. reports serving as a medical

adviser for AstraZeneca, Bristol Myers Squibb, Merck Serono, Novartis, and Pfizer; receiving clinical research funding from Bristol Myers Squibb, Merck Sharp & Dohme, Novartis, and Roche; and serving as a speaker for AstraZeneca, Bristol Myers Squibb, Merck, and Pfizer, during the conduct of the study. T.Z. reports serving as a consultant or in an advisory role for Bristol Myers Squibb, Merck Sharp & Dohme, Novartis, and Roche, outside the submitted work. S.d.A. reports receiving honoraria from AstraZeneca, Bristol Myers Squibb, Genentech, Merck Sharp & Dohme, Novartis, and Roche, outside the submitted work. R.K. reports receiving research grants from Amgen, Astellas, AstraZeneca, Athenex, Bristol Myers Squibb, Eli Lilly, Merck Sharp & Dohme, Nektar, Novartis, Pfizer, Roche, and Sanofi; receiving non-financial support from Bristol Myers Squibb, Merck Sharp & Dohme, Pfizer, and Roche; and receiving personal fees from Astellas, Bristol Myers Squibb, Gador, Merck Sharp & Dohme, Novartis, and Pfizer, outside the submitted work. R.P.-C. has no competing interests to disclose. M.S. reports receiving research funding from Abbvie, Astellas Pharma, AstraZeneca, Bristol Myers Squibb, Eli Lilly, Gilead Sciences, GlaxoSmithKline, Merck Sharp & Dohme, Novartis, Pfizer/EMD Serono, Regeneron, and Roche; and receiving travel, accommodations, and expenses from Bristol Myers Squibb, outside the submitted work. J.M.C. reports receiving research funding to his institution from Abbvie, Merus, Roche, and Bristol Myers Squibb; receiving research funding from Merck, AstraZeneca, Esperas Pharma, Bayer, and Tesaro; receiving consulting fees from Bristol Myers Squibb; receiving an honorarium for advisory board participation from Syros Pharmaceuticals; and receiving travel funding from Bristol Myers Squibb, outside the submitted work. P.Y. has no competing interests to disclose. K.F. has no competing interests to disclose. M.K. reports serving in an advisory role for Bristol Myers Squibb, Merck Sharp & Dohme, Ipsen, Roche, Sandoz, Sanofi, and Servier, outside the submitted work. V.P., M. Lei, H.X., K.K. and M. Li report being employees of Bristol Myers Squibb. Y.Y.J. reports receiving research funding from Bayer, Bristol Myers Squibb, Cycle for Survival, Department of Defense, Fred's Team, Genentech/Roche Lilly, Merck & Co, National Cancer Institute, and Rgenix; serving as a consultant or in an advisory role for Basilea Pharmaceutical, Bayer, Bristol Myers Squibb, Daiichi Sankyo, Imugene, Lilly, Merck, Merck Serono, Michael J Hennessy Associates, Paradigm Medical Communications, Pfizer, Rgenix, Seagen, and Zymeworks; receiving stock options from Rgenix; and nonfinancial relationships with Clinical Care Options, Axis Medical Education, and Research to Practice, outside the submitted work.

Peer review

Peer review information

Nature thanks Sara Lonardi, Florian Lordick and the other, anonymous, reviewers for their contribution to the peer review of this work.

Additional information

Publisher's note Springer Nature remains neutral with regard to jurisdictional claims in published maps and institutional affiliations.

Extended data figures and tables

Extended Data Fig. 1 CONSORT diagram for patient disposition.

^aIncluded death ($n = 36$), adverse events ($n = 24$), poor/noncompliance ($n = 15$), administrative reasons ($n = 5$), pregnancy ($n = 1$) and additional reasons ($n = 43$);
^bIncludes patients concurrently randomized to the nivolumab plus chemotherapy, nivolumab plus ipilimumab, and chemotherapy groups. Relevant protocol deviations were noted in 21 (1%) patients concurrently randomized to nivolumab plus chemotherapy versus chemotherapy: usage of prohibited on-treatment anti-cancer therapy ($n = 12$), baseline ECOG PS >1 ($n = 5$), incorrect cancer diagnosis ($n = 2$), prohibited prior anti-cancer therapy (at study entry) ($n = 1$) and no baseline (measurable or evaluable) disease ($n = 1$); Relevant protocol deviations were noted in 10 (1%) patients concurrently randomized to nivolumab plus ipilimumab versus chemotherapy: usage of prohibited on-treatment anti-cancer therapy ($n = 5$), incorrect cancer diagnosis ($n = 2$), no baseline PD-L1 result ($n = 2$) and baseline ECOG PS >1 ($n = 1$); ^c363 patients overlapped between the two chemotherapy groups from the 1:1:1 randomization period; ^dThe median follow-up for survival (time from concurrent randomization to last known date alive or death) was 13.1 months (range 0.1–49.5) and 11.2 months (range 0.0–47.9) in the nivolumab plus chemotherapy versus chemotherapy groups, respectively, and 11.4 months (range 0.0–52.1) and 11.5 months (range 0.0–52.8) in the nivolumab plus ipilimumab versus chemotherapy groups, respectively; ^eIncluded adverse events unrelated to study treatment ($n = 47$), maximum clinical benefit ($n = 11$), lost to follow-up ($n = 2$), patient no longer met trial criteria ($n = 1$), poor/noncompliance ($n = 1$) and other reasons ($n = 9$); ^fIncluded adverse events unrelated to study treatment ($n = 35$), maximum clinical benefit ($n = 30$), poor/noncompliance ($n = 4$), other reasons ($n = 8$), lost to follow-up ($n = 2$) and death ($n = 1$); ^gIncluded adverse events unrelated to study treatment ($n = 21$), death ($n = 3$), poor/noncompliance ($n = 1$), other reasons ($n = 6$) and not reported ($n = 5$); ^hIncluded adverse events unrelated to study treatment ($n = 15$), maximum clinical benefit ($n = 13$), lost to follow-up ($n = 2$), poor/noncompliance ($n = 2$) and other reasons ($n = 4$). ECOG PS, Eastern Cooperative Oncology Group performance status; OS, overall survival; PD-L1, programmed death ligand 1; PFS, progression-free survival.

Extended Data Fig. 2 Kaplan-Meier estimates of progression-free survival.

Progression-free survival with nivolumab plus chemotherapy versus chemotherapy in patients with PD-L1 CPS ≥ 5 (**a**) and in all randomized patients (**b**). Progression-free survival with nivolumab plus ipilimumab versus chemotherapy in patients with PD-L1 CPS ≥ 5 (**c**) and in all randomized patients (**d**). ^aPer BICR. BICR, blinded independent central review; chemo, chemotherapy; CI, confidence interval; CPS, combined positive score; HR, hazard ratio; IPI, ipilimumab; mo, months; NIVO, nivolumab; PD-L1, programmed death ligand 1; PFS, progression-free survival.

Extended Data Fig. 3 Kaplan-Meier plot of progression-free survival on subsequent therapy with nivolumab plus chemotherapy versus chemotherapy.

a, Patients with PD-L1 CPS ≥ 5 . **b**, All randomized patients. Chemo, chemotherapy; CI, confidence interval; CPS, combined positive score; HR, hazard ratio; mo, months; NIVO, nivolumab; PD-L1, programmed death ligand 1; PFS2, time from randomization to progression after subsequent systemic therapy, initiation of second subsequent systemic therapy, or death, whichever is earlier.

Extended Data Fig. 4 Waterfall plot of best percentage reduction in tumour burden with nivolumab plus chemotherapy versus chemotherapy.

a, Patients with PD-L1 CPS ≥ 5 . **b**, All randomized patients. Patients who had measurable disease at baseline per BICR and at least one on-treatment tumour assessment. Best reduction is maximum reduction in sum of diameters of target lesions. Horizontal reference line indicates the 30% reduction consistent with a RECIST v1.1 response. Asterisk symbol represents responders. Blue bars indicate nivolumab plus chemotherapy; grey bars indicate chemotherapy. BICR, blinded independent central review; chemo, chemotherapy; CPS, combined positive score; NIVO, nivolumab; PD-L1, programmed death ligand 1; RECIST, Response Evaluation Criteria in Solid Tumors.

Extended Data Fig. 5 Forest plot of overall survival in prespecified subgroups with nivolumab plus chemotherapy versus chemotherapy in patients with PD-L1 CPS ≥ 5 .

^aNot reported, $n = 28$; ^bUnknown, $n = 1$; ^cInvalid/not reported, $n = 74$. Data are presented as unstratified hazard ratios and 95% CI. CapeOX, capecitabine plus oxaliplatin; chemo, chemotherapy; CI, confidence interval; CNS, central nervous system; CPS, combined positive score; EAC, oesophageal adenocarcinoma; ECOG PS, Eastern Cooperative Oncology Group performance status; FOLFOX, 5-fluorouracil plus leucovorin plus oxaliplatin; GC, gastric cancer; GEJC, gastro-oesophageal junction cancer; HR, hazard ratio; MSI, microsatellite instability; MSI-H, microsatellite instability-high; MSS, microsatellite stable; NIVO, nivolumab; OS, overall survival; PD-L1, programmed death ligand 1.

Extended Data Fig. 6 Forest plot of overall survival in prespecified subgroups with nivolumab plus chemotherapy versus chemotherapy in all randomized patients.

^aNot reported, $n = 1$; ^bNot reported, $n = 49$; ^cUnknown, $n = 4$; ^dInvalid/not reported, $n = 159$. Data are presented as unstratified HRs and 95% CI. CapeOX, capecitabine plus oxaliplatin; chemo, chemotherapy; CI, confidence interval; CNS, central nervous system; CPS, combined positive score; EAC, oesophageal adenocarcinoma; ECOG PS, Eastern Cooperative Oncology Group performance status; FOLFOX, 5-fluorouracil plus leucovorin plus oxaliplatin; GC, gastric cancer; GEJC, gastro-oesophageal junction cancer; HR, hazard ratio; MSI, microsatellite instability; MSI-H, microsatellite instability-high; MSS, microsatellite stable; NIVO, nivolumab; OS, overall survival; PD-L1, programmed death ligand 1.

Extended Data Fig. 7 Kaplan-Meier estimates of overall survival and objective response rate by microsatellite instability status in all randomized patients.

Overall survival with nivolumab plus chemotherapy in patients with MSI-H tumours (**a**) and those with MSS tumours (**b**). Overall survival with nivolumab plus ipilimumab in patients with MSI-H tumours (**c**) and those with MSS tumours (**d**). ^aRandomized patients who had target lesion measurements at baseline per BICR assessment were **a**, NIVO + chemo, $n = 20$; Chemo, $n = 18$; **b**, NIVO + chemo, $n = 535$; Chemo, $n = 533$; **c**, Patients with MSI-H: NIVO + IPI, $n = 10$; Chemo, $n = 7$. **d**, NIVO + IPI, $n = 292$; Chemo, $n = 257$. Chemo, chemotherapy; CI, confidence interval; HR, hazard ratio; MSI-H, microsatellite instability-high; MSS, microsatellite stable; NIVO, nivolumab; ORR, objective response rate; OS, overall survival.

Extended Data Fig. 8 Forest plot of efficacy outcomes by PD-L1 CPS with nivolumab plus ipilimumab versus chemotherapy.

a, Overall survival. Data are presented as unstratified HRs and 95% CI. **b**, Objective response rate. ^aPD-L1 CPS expression indeterminate/not evaluable/not reported, $n = 15$; ^bRandomized patients who had target lesion measurements at baseline, per blinded independent central review assessment; ^cPD-L1 CPS expression indeterminate/not evaluable/not reported, $n = 10$; ^dPercentages may not reflect an exact difference due to rounding. Data are presented as unweighted ORR differences and 95% CI. Chemo, chemotherapy; CI, confidence interval; CPS, combined positive score; HR, hazard ratio; IPI, ipilimumab; NIVO, nivolumab; ORR, objective response rate; OS, overall survival; PD-L1, programmed death ligand 1.

Extended Data Fig. 9 Patient-reported outcomes.

Least squares mean (95% CI) change from baseline in FACT-Ga total score with nivolumab plus chemotherapy versus chemotherapy in patients with PD-L1 CPS ≥ 5 (nivolumab plus chemotherapy, $n = 412$; chemotherapy, $n = 386$) (**a**) and in all randomized patients (nivolumab plus chemotherapy, $n = 679$; chemotherapy, $n = 639$) (**b**). Data in panels **a** and **b** are presented as least squares mean change from baseline and 95% CI. Top and bottom dashed lines indicate minimally important difference in score. The primary meaningful change threshold is 15.1. The P -value for the difference in least squares means was computed as the two-tailed probability using the t distribution. No adjustments were made for multiple comparisons. * $P < 0.05$; in patients with PD-L1 CPS ≥ 5 , P -value was 0.022 at week 19, 0.024 at week 31, 0.002 at week 49, 0.028 at week 55, 0.015 at week 73, 0.041 at week 97, 0.039 at week 115, and 0.025 at week 121. In all randomized patients, P -value was 0.026 at week 7, 0.020 at week 19, 0.012 at week 25, 0.006 at week 31, 0.025 at week 43, <0.001 at week 49, 0.002 at week 55, 0.037 at week 67, 0.030 at week 73, 0.033 at week 85, 0.028 at week 91, 0.012 at week 97, 0.024 at week 109, 0.004 at week 115, 0.013 at week 121, and 0.039 at week 133; not formally tested. FACT-Ga GP5 (“I am bothered by side effects of treatment”) item values in patients with PD-L1 CPS ≥ 5 (**c**) and in all randomized patients (**d**). Chemo, chemotherapy; CPS, combined positive score; FACT-Ga, Functional Assessment of Cancer Therapy-Gastric; NIVO, nivolumab; PD-L1, programmed death ligand 1.

Extended Data Table 1 Response per BICR

Supplementary information

Supplementary Information

This file contains a list of sites and investigators; Supplementary Tables 1–4 and patient-reported outcomes

Reporting Summary

Rights and permissions

Open Access This article is licensed under a Creative Commons Attribution 4.0 International License, which permits use, sharing, adaptation, distribution and reproduction in any medium or format, as long as you give appropriate credit to the original author(s) and the source, provide a link to the Creative Commons license, and indicate if changes were made. The images or other third party material in this article are included in the article's Creative Commons license, unless indicated otherwise in a credit line to the material. If material is not included in the article's Creative Commons license and your intended use is not permitted by statutory regulation or exceeds the permitted use, you will need to obtain permission directly from the copyright holder. To view a copy of this license, visit <http://creativecommons.org/licenses/by/4.0/>.

Reprints and Permissions

About this article

Cite this article

Shitara, K., Ajani, J.A., Moehler, M. *et al.* Nivolumab plus chemotherapy or ipilimumab in gastro-oesophageal cancer. *Nature* **603**, 942–948 (2022).
<https://doi.org/10.1038/s41586-022-04508-4>

- Received: 22 October 2021
- Accepted: 03 February 2022
- Published: 23 March 2022
- Issue Date: 31 March 2022
- DOI: <https://doi.org/10.1038/s41586-022-04508-4>

Share this article

Anyone you share the following link with will be able to read this content:

[Get shareable link](#)

Sorry, a shareable link is not currently available for this article.

[Copy to clipboard](#)

Provided by the Springer Nature SharedIt content-sharing initiative

This article was downloaded by **calibre** from <https://www.nature.com/articles/s41586-022-04508-4>

| [Section menu](#) | [Main menu](#) |

- Article
- Open Access
- [Published: 23 March 2022](#)

Inhibition of calcium-triggered secretion by hydrocarbon-stapled peptides

- [Ying Lai](#) ¹ nAff6,
- [Giorgio Fois](#) [ORCID: orcid.org/0000-0001-5414-1149](#)²,
- [Jose R. Flores](#)³,
- [Michael J. Tuvim](#) [ORCID: orcid.org/0000-0001-8126-7716](#)³,
- [Qiangjun Zhou](#) [ORCID: orcid.org/0000-0003-1789-9588](#)¹ nAff7,
- [Kailu Yang](#) [ORCID: orcid.org/0000-0002-8234-1997](#)^{1,4},
- [Jeremy Leitz](#)¹,
- [John Peters](#) [ORCID: orcid.org/0000-0002-3192-7824](#)¹ nAff8,
- [Yunxiang Zhang](#)¹ nAff9,
- [Richard A. Pfuetzner](#)^{1,4},
- [Luis Esquivies](#)^{1,4},
- [Philip Jones](#)⁵,
- [Manfred Frick](#) [ORCID: orcid.org/0000-0002-4763-1104](#)²,
- [Burton F. Dickey](#) ³ &
- [Axel T. Brunger](#) [ORCID: orcid.org/0000-0001-5121-2036](#)^{1,4}

[Nature](#) volume 603, pages 949–956 (2022)

- 6891 Accesses
- 1 Citations
- 120 Altmetric
- [Metrics details](#)

Subjects

- [Calcium signalling](#)
- [Exocytosis](#)

- [Respiration](#)
- [Synaptic vesicle exocytosis](#)

Abstract

Membrane fusion triggered by Ca^{2+} is orchestrated by a conserved set of proteins to mediate synaptic neurotransmitter release, mucin secretion and other regulated exocytic processes^{1,2,3,4}. For neurotransmitter release, the Ca^{2+} sensitivity is introduced by interactions between the Ca^{2+} sensor synaptotagmin and the SNARE complex⁵, and sequence conservation and functional studies suggest that this mechanism is also conserved for mucin secretion⁶. Disruption of Ca^{2+} -triggered membrane fusion by a pharmacological agent would have therapeutic value for mucus hypersecretion as it is the major cause of airway obstruction in the pathophysiology of respiratory viral infection, asthma, chronic obstructive pulmonary disease and cystic fibrosis^{7,8,9,10,11}. Here we designed a hydrocarbon-stapled peptide that specifically disrupts Ca^{2+} -triggered membrane fusion by interfering with the so-called primary interface between the neuronal SNARE complex and the Ca^{2+} -binding C2B domain of synaptotagmin-1. In reconstituted systems with these neuronal synaptic proteins or with their airway homologues syntaxin-3, SNAP-23, VAMP8, synaptotagmin-2, along with Munc13-2 and Munc18-2, the stapled peptide strongly suppressed Ca^{2+} -triggered fusion at physiological Ca^{2+} concentrations. Conjugation of cell-penetrating peptides to the stapled peptide resulted in efficient delivery into cultured human airway epithelial cells and mouse airway epithelium, where it markedly and specifically reduced stimulated mucin secretion in both systems, and substantially attenuated mucus occlusion of mouse airways. Taken together, peptides that disrupt Ca^{2+} -triggered membrane fusion may enable the therapeutic modulation of mucin secretory pathways.

[Download PDF](#)

Main

Membrane fusion is an essential step for many biological processes, including enveloped virus–host cell fusion, cell–cell fusion and intracellular vesicle–membrane fusion^{12,13,14}. Fusion proteins supply the energy to overcome the high kinetic barrier to mediate lipid bilayer fusion. The underlying molecular mechanisms are highly similar for both class 1 viral fusion proteins and SNARE-mediated fusion, wherein the formation of helical bundles drives membranes together, leading to membrane fusion. However, for Ca^{2+} -triggered membrane fusion, SNARE proteins must cooperate with Ca^{2+} sensors. For example, the neuronal SNARE complex (comprising synaptobrevin-

2 (also known as VAMP2), syntaxin-1A (Stx1) and SNAP-25A) forms a specific interface with the Ca^{2+} -binding domain C2B of synaptotagmin-1 (Syt1)⁵. This primary interface is conserved in all species and across the other fast isoforms for neurotransmitter release—synaptotagmin-2 (Syt2) and synaptotagmin-9. Many of the key residues that are involved in the primary interface are located in the target-SNARE protein SNAP-25A. Residues involved in the primary interface are critical for Ca^{2+} -triggered fusion in a reconstituted system and in neuronal cultures^{5,15}. In the absence of Ca^{2+} , Syt1 interacts simultaneously with the *trans*-SNARE (through the primary interface) and the anionic plasma membrane (through the poly-basic region of Syt1 C2B), greatly enhancing the affinity of the primary complex¹⁶. After Ca^{2+} binding to Syt1, the Syt1–SNARE–membrane assembly changes^{5,16}, ultimately leading to membrane fusion.

Primary sequence conservation suggests that the primary interface also exists in other systems that use SNARE proteins and synaptotagmins⁵. In particular, mucin exocytosis in airway secretory cells is mediated by SNARE proteins, the Ca^{2+} sensor Syt2 and other factors^{1,2,11}. Syt2 is selectively expressed in airway secretory cells compared with ciliated cells, and it serves as a critical sensor for stimulated, but not baseline, mucin secretion⁶. Syntaxin-3 (Stx3) and SNAP-23 are also highly expressed in airway epithelial cells^{17,18,19}. In stimulated mucin secretion, Ca^{2+} is released from the endoplasmic reticulum through the activated inositol triphosphate receptor. Inositol triphosphate is generated by phospholipase C after binding of agonists (such as ATP or acetylcholine) to hepta-helical receptors in the plasma membrane coupled to G_q . The released Ca^{2+} in turn binds to Syt2 on the granule vesicle and then triggers SNARE-mediated fusion of the granule with the plasma membrane, leading to mucin secretion^{1,2,6}.

Both baseline and stimulated mucin secretion are impaired in *SNAP-23*-heterozygous-mutant mice¹⁸, *Vamp8*-knockout mice²⁰ and *Unc13b*-knockout (also known as *Munc13-2*) mice²¹. By contrast, stimulated mucin secretion is selectively impaired in *Munc18-2*-mutant (also known as *Stxbp2*) and Syt2-mutant mice^{6,19,22}. Stx3 binds to and colocalizes with Munc18-2 (refs. [17,19](#)) and overexpression of *Munc18-2* reduces the level of Stx3–SNAP-23 binary complex¹⁷. These findings suggested that, similar to neurotransmitter release, SNARE proteins (Stx3, SNAP-23 and VAMP8), Syt2, Munc13-2 and Munc18-2 are among the key components that drive stimulated membrane fusion between mucin-containing granules and the plasma membrane^{1,2,11}.

Syt2 deletion prevents mucus occlusion

Stimulated secretion of mucins that are highly produced in response to inflammation (together, mucus hypersecretion) is a major cause of airway obstruction in the pathophysiology of respiratory viral infection, asthma, chronic obstructive pulmonary disease and cystic fibrosis^{7,8,9,10,23}. To validate Syt2 as a target of pharmacologic inhibition, we tested whether the deletion of *Syt2* specifically in airway epithelial cells might protect against mucus occlusion. To accomplish this, we crossed mice carrying a floxed *Syt2* allele (*Syt2*^{F/F}) (ref. 24) with *Scgb1a1*^{Cre}-knockin mice^{25,26}, as *Syt2*-knockout mice die from complications of ataxia by postnatal day 24 (ref. 27), precluding the study of the pathophysiologic role of airway mucin secretion in adult *Syt2*-knockout mice. The airway-specific deletant progeny of this cross (*Syt2*^{D/D}) were born at a Mendelian ratio and appeared to be healthy, and the efficiency of deletion was essentially complete (Extended Data Fig. 1). There was no spontaneous intracellular mucin accumulation in *Syt2*^{D/D} mice that would indicate impairment of baseline mucin secretion^{1,21}. To test impairment of stimulated mucin secretion in these mice, mucous metaplasia was induced by intrapharyngeal instillation of IL-13, then secretion was stimulated with an ATP aerosol. Fractional secretion of intracellular mucin in response to ATP by wild-type (WT) and *Syt2*^{F/F} mice was 71% and 65%, respectively, whereas it was only 30% in *Syt2*^{D/D} mice (Fig. 1a, b). To test protection against airway luminal mucus occlusion, mucous metaplasia was first induced with IL-13, then mucin secretion and bronchoconstriction were stimulated by a methacholine aerosol. The scattered sites of airway mucus occlusion observed in WT and *Syt2*^{F/F} mice were reduced in *Syt2*^{D/D} mice, and the cross-sectional area of airway luminal mucus in a systematic sample of the left lung was reduced in *Syt2*^{D/D} mice by 74% compared with the WT and by 69% compared with *Syt2*^{F/F} mice (Fig. 1c, d). Together these data validated *Syt2* as a therapeutic target in muco-obstructive airway disease.

Fig. 1: Mucin secretion defects in *Syt2*-mutant mice.

 **figure 1**

a, Transverse sections of bronchial airways of mice stained with periodic acid fluorescent Schiff (PAFS) to demonstrate mucin with red fluorescence. Top, in naive mice without airway inflammation, scant intracellular mucin is visible. Treatment with IL-13 increases mucin synthesis, resulting in abundant intracellular mucin. Bottom, subsequent treatment with ATP induces mucin secretion, reducing intracellular mucin in WT C57Bl/6J mice (WT) and *Syt2*^{F/F} mice (F/F), but not in *Syt2*^{D/D} mice (D/D). Scale bar, 50 µm. **b**, Fractional mucin secretion was measured by analysing images of airways of mice treated with IL-13 alone and comparing those with those of mice treated with IL-13 followed by ATP, as shown in **a**. Individual data points and box plots are shown for two independent sets of experiments combined to give a total *n* mice (indicated below each box plot) per group (Supplementary Table 1). Comparison with the *Syt2*^{F/F} group of mice was performed using two-tailed unpaired Student's *t*-tests; ****P* = 0.00026. **c**, Transverse sections of bronchial airways of mice treated with IL-13, then with methacholine (Mch) to induce smooth muscle contraction and mucin secretion, and fixed with methacarn and stained with PAFS to demonstrate luminal mucus and residual intracellular mucin. Scale bar, 50 µm. **d**, The sum of the luminal

mucus cross-sectional area in the left lung measured at 500 μm intervals. Individual data points and box plots are shown for two independent sets of experiments combined to give a total of n mice (indicated below each box plot) per group (Supplementary Table 1). Comparison with the $\text{Syt}2^{F/F}$ group of mice was performed using two-tailed unpaired Student's t -tests; ** $P = 0.0012$.

[Source data](#)

Stapled peptide design

Helical peptides, such as a fragment of SNAP-25A involved in the primary interface (Fig. 2a and Extended Data Fig. 2), could theoretically be used to selectively interfere with this synaptotagmin–SNARE interaction and thereby disrupt the process of Ca^{2+} -triggered membrane fusion. From a therapeutic perspective, peptide-based strategies have successfully been applied to inhibit virus–host membrane fusion^{28,29,30,31,32}. However, the molecular mechanisms are quite different as viral membrane fusion inhibitors act by interfering with the formation of a six-helix bundle¹², whereas specific Ca^{2+} -triggered membrane fusion inhibitors must act in a different manner, for example, by disrupting the interaction between SNARE proteins and the Ca^{2+} sensor synaptotagmin^{5,15}. Moreover, peptide-based viral inhibitors function extracellularly whereas peptide-based secretory/synaptic vesicle inhibitors need to act intracellularly. Thus, this research addresses whether a peptide inhibitor strategy can be applied to disrupt Ca^{2+} -triggered membrane fusion.

Fig. 2: Characterization of SP9.

 **figure 2**

a, Magnified view of the primary interface between the neuronal SNARE complex (VAMP-2 (blue), Stx1 (red) and SNAP-25A (green)) and the C2B domain of Syt1 (orange) (Protein Data Bank (PDB): [5W5C](#)), indicating the region (yellow) that corresponds to the stapled peptide SP9 with staples shown as dumbbells. **b**, Schematic of the synthesis of SP9. Hydrocarbon-stapled peptides are formed by cross-linking residues at the specified positions. **c**, Sequences of peptides. S5 indicates *S* stereochemistry at the α -carbon, with 5 carbon atoms in the olefinic side chains. The superscripts denote the start and end positions of the SNAP-25A sequence. **d**, Circular dichroism (CD) spectra of 100 mM peptides measured at pH 7.4 and at 25 ± 1 °C. **e**, The percentage of α -helical content in these peptides was estimated by dividing the mean residue ellipticity $[\phi]_{222\text{obs}}$ by the reported $[\phi]_{222\text{obs}}$ for a model helical decapeptide. **f**, Interactions between Cy3-labelled SP9 or P0 and unlabelled Syt1 C2B,

the quintuple Syt1 C2B(QM) mutant and Syt2 C2B as measured by bulk fluorescence anisotropy ([Methods](#)). Data are mean \pm s.e.m. along with individual data points from $n = 3\text{--}7$ independent experiments. Hill equations were fit to estimate the dissociation constant K_d , where the Hill coefficients were constrained to 1. **g**, Peptide conformations (colours) after five independent 1 μs molecular dynamics simulations of SP9–Syt1 C2B (left) and P9–Syt1 C2B (right) superimposed onto the structure of the primary interface (grey). The simulations started from a conformation (Extended Data Fig. [2f,g](#)) that was derived from the crystal structure PDB [5W5C](#) (Supplementary Videos [1](#) and [2](#)). For one simulation of P9–Syt1 C2B, the P9 peptide dissociated around 168 ns.

[Source data](#)

Peptides typically have little secondary structure in solution when taken out of the context of the intact system. Thus, their efficacy as *in vivo* reagents may be limited by their loss of secondary structure. Considering the successful use of stapled peptides^{[33](#)} to inhibit HIV virus infection^{[34](#)} and for p53-dependent cancer therapy^{[35](#)}, we also used non-natural amino acids containing olefin-bearing groups to generate hydrocarbon-stapled peptides by a ring closing metathesis reaction using Grubbs catalyst^{[36](#)} to interfere with the primary interface. The residues that are at or near to the primary interface are identical for Syt1 and Syt2 except for V292C, and identical for SNAP-25A and SNAP-23 except for K40Q, L47I and V48T (Extended Data Fig. [2a,b](#)). As the crystal structure is known for the neuronal system, we first used it for the design of stapled peptides that disrupt this interaction, and subsequently tested the peptides in the airway epithelial system. We examined a series of stapled peptides^{[37](#)} and ultimately designed a hydrocarbon-stapled peptide consisting of a SNAP-25A fragment that included many of the key residues involved in the primary interface (named SP9; Fig. [2a–c](#) and Extended Data Fig. [2a–c](#)). It will be desirable to test other sequences and strategies in future work, including the SNAP-23 sequence itself, that might strengthen (or weaken) the interaction with Syt1 or Syt2 considering the K40Q, L47I and V48T substitutions (Extended Data Fig. [2a](#)). For SP9, four non-natural amino acids were incorporated into the sequence ([Methods](#)). Two hydrocarbon staples were made to flank three (substitution positions i and $i + 4$) amino acids within the SNAP-25A fragment (Fig. [2b,c](#)). The positions of these substitutions were chosen to be away from the primary interface (Fig. [2a](#)). As a control, we also used a non-stapled SNAP-25A fragment, named P0, that displays only 5% helicity in solution, indicating that P0 is largely a random coil (Fig. [2d,e](#)). By contrast, SP9 has substantial helical content (Fig. [2d,e](#)) and it does not aggregate, as assessed using size-exclusion chromatography (Extended Data Fig. [3a](#)). Single-molecule counting experiments with surface-immobilized SP9–Cy3 suggest that it is primarily monomeric with minor fractions of higher-order oligomers (Extended Data Fig. [3b–d](#)).

To determine whether SP9 specifically interacts with the C2B domains of Syt1 and Syt2, we labelled it with the fluorescent dye Cy3 at the C terminus. We recorded bulk fluorescence anisotropy after mixing Cy3 labelled SP9 with varying concentrations of Syt1 C2B, Syt2 C2B or a quintuple mutant of Syt1 C2B (C2B(QM)) (Fig. 2f and Extended Data Fig. 2c). SP9 binds to both Syt1 C2B and Syt2 C2B with a similar dissociation constant (K_d) of 24 μM and 35 μM , respectively, which is comparable to the K_d between Syt1 and the SNARE complex (~20 μM) (ref. 5). As a control and as expected, SP9 does not bind to the quintuple mutant of Syt1 C2B(QM) as that mutation disrupts the primary interface⁵. Moreover, we did not observe binding of the non-stapled peptide P0 to the C2B domain of either Syt1 or Syt2 in the conditions of these experiments. Taken together, SP9 binds specifically to the C2B domain of Syt1 or Syt2.

These binding experiments suggest that the stabilization of SP9 peptide by staples is important for binding. To corroborate this finding, we assessed the stability of the SP9 peptide interactions with the C2B domain of Syt1 using molecular dynamics simulations starting with a conformation derived from the crystal structure of the primary complex (Extended Data Fig. 2f,g). Four out of the five simulations of SP9 adopt binding poses at the end of the 1 μs simulations that would interfere with the formation of the primary interface (Fig. 2g (left) and Supplementary Video 1). By contrast, 1 μs simulations of this peptide without staples (referred to as P9) produced only one binding pose that would interfere with primary complex formation (Fig. 2g (right) and Supplementary Video 2). These simulations show that the interaction between SP9 and Syt1 is more dynamic at the N-terminal end of SP9, suggesting that there are opportunities for strengthening the interaction in the future.

SP9 inhibits Ca^{2+} -triggered vesicle fusion

Next, we tested whether SP9 specifically disrupts membrane fusion with reconstituted neuronal SNARE proteins and Syt1. We first tested the effect of SP9 in a single-vesicle content mixing assay with reconstituted neuronal SNARE proteins and Syt1 (Extended Data Fig. 4a). SP9 had no effect on vesicle association (Extended Data Fig. 4b), but reduced both Ca^{2+} -triggered fusion and Ca^{2+} -independent fusion (Extended Data Fig. 4c–h). As a control and to test specificity, when Syt1 was left out (that is, vesicles with VAMP2 only, referred to as VAMP2 vesicles), or replaced by the quintuple mutant of Syt1 (Syt1(QM)) that disrupts binding to the SNARE complex⁵, SP9 had little effect on either Ca^{2+} -independent or Ca^{2+} -triggered fusion using the single-vesicle content mixing assay (Extended Data Fig. 5). The specific inhibitory effect of SP9 observed in this assay is probably due to peptide binding to Syt1, in competition with the primary complex.

To test whether SP9 has a specific inhibitory effect on the process of mucin secretion, we first performed a ‘simple’ reconstitution with two types of vesicles to mimic mucin secretion: we used vesicles with reconstituted Stx3 and SNAP-23 that mimic the plasma membrane of epithelial cells (airway PM vesicles), and vesicles with reconstituted VAMP8 and Syt2 that mimic mucin-containing secretory granules (SG vesicles) ([Methods](#)) (Extended Data Figs. [6](#) and [7a](#)). Inclusion of 10 μ M of the P0 unstapled control peptide in the fusion assay had no effect on the intrinsic Ca^{2+} -independent fusion probability or Ca^{2+} -triggered cumulative fusion probability (Extended Data Fig. [7c–h](#)). By contrast, 10 μ M SP9 reduced both Ca^{2+} -triggered and, to a lesser degree, Ca^{2+} -independent fusion (Extended Data Fig. [7c–h](#)). As with the neuronal system, SP9 had no effect on vesicle association (Extended Data Fig. [7b](#)). As a control and to test specificity, when Syt2 was left out (that is, vesicles with VAMP8 only, referred to as VAMP8 vesicles), this inhibitory effect of SP9 was eliminated (Extended Data Fig. [7i–k](#)).

As Munc13 catalyses the transition of syntaxin from the syntaxin–Munc18 complex into the ternary SNARE complex^{[38,39,40](#)} and promotes proper SNARE complex formation^{[41](#)}, we next tested the effect of the SP9 stapled peptide in a more complete reconstitution that includes airway epithelial SNAREs, Syt2, the C1C2B_MUN2 fragment of Munc13-2 (referred to as Munc13-2*) (ref. [21](#)) and Munc18-2 (refs. [19,22](#)) (Fig. [3a](#)). Following previous research with neuronal proteins^{[41](#)}, to form the Stx3–Munc18-2 complex (that is, SM vesicles), we first added the ‘disassembly factors’ (NSF, α SNAP, ATP and Mg^{2+}) along with Munc18-2 to tethered airway PM vesicles. We next added Munc13-2* and SNAP-23 along with SG vesicles in the flow chamber above the tethered SM vesicles (Fig. [3b](#)).

Fig. 3: SP9 inhibits triggered fusion in a reconstituted system.

 **figure 3**

a, The domain structure of Munc13-2 and its fragment (Munc13-2*). **b**, Single-vesicle content mixing assay with complete reconstitution ([Methods](#)). Stapled peptide (10 μ M) was added together with SG vesicles and was present during all of the subsequent stages. **c**, The effect of SP9 on vesicle association. **d**, Corresponding Ca^{2+} -independent

fusion probabilities. **e**, Corresponding average probabilities of Ca^{2+} -independent fusion events per second. For comparison, the result for the SR assay (Extended Data Fig. 2) is also shown. *** $P = 0.00016$. **f**, Corresponding Ca^{2+} -triggered fusion probabilities at 500 μM and 50 μM Ca^{2+} . **g–i**, Corresponding Ca^{2+} -triggered fusion amplitudes of the first 1 s time bin after injection with 500 μM Ca^{2+} (**g**) (from left to right, *** $P = 0.0000053$, ** $P = 0.0024$, * $P = 0.0012$); the cumulative Ca^{2+} -triggered fusion probability within 1 min (**h**) (from left to right, *** $P = 0.000058$, ** $P = 0.0037$, * $P = 0.0026$); and the decay rate ($1/\tau$) of the Ca^{2+} -triggered fusion histogram (**i**). The fusion probabilities and amplitudes were normalized to the number of analysed SG-airway PM vesicle pairs (Supplementary Table 2). For comparison, the results for the SR assay (Extended Data Fig. 2) are also shown. For **c**, **e**, **g** and **h**, box plots and data points are shown for n (indicated below each box plot) independent repeat experiments (Supplementary Table 2). For **c**, **e**, **g** and **h**, statistical analysis was performed using two-tailed Student's *t*-tests. Decay constants (boxes) and error estimates (bars) in **i** were computed from the covariance matrix after fitting the corresponding histograms combining all repeats with a single exponential decay function using the Levenberg–Marquardt algorithm.

Source data

As a control, in the absence of Munc13-2*, essentially neither SG Ca^{2+} -dependent nor Ca^{2+} -independent fusion events were observed because the Stx3–Munc18-2 complex is in the closed conformation and, therefore, ternary SNARE complex formation cannot occur⁴² (Supplementary Table 2). By contrast, in the presence of Munc13-2*, robust Ca^{2+} -triggered fusion was observed at Ca^{2+} concentrations of both 50 μM and 500 μM (Fig. 3f–i). When comparing this more complete reconstituted fusion assay with the simple reconstitution (SR) assay that uses only airway SNAREs and Syt2, the Ca^{2+} -independent fusion probability is similar (Fig. 3d, e), but the 500 μM Ca^{2+} -triggered fusion amplitude and the cumulative fusion probability are significantly larger (Fig. 3g, h). Taken together, the more complete reconstitution that includes Syt2, Munc13-2*, Munc18-2, NSF and α SNAP improved Ca^{2+} -triggered fusion by an order of magnitude compared with the SR reconstitution with just epithelial airway SNARE proteins and Syt2. Moreover, the Ca^{2+} sensitivity of the more complete reconstitution is closer to the physiological range^{43,44}.

When 10 μM SP9 was added in the more complete reconstitution assay, the 50 μM and 500 μM Ca^{2+} -triggered fusion amplitude, the cumulative fusion probability and the synchronization were strongly inhibited (Fig. 3g–i). By contrast, the Ca^{2+} -independent fusion probability (Fig. 3e) was only moderately reduced compared with the Ca^{2+} -triggered amplitude and cumulative fusion probabilities. Moreover, SP9 had no effect on vesicle association (Fig. 3c). Taken together, SP9 specifically inhibits Ca^{2+} -

triggered membrane fusion in our reconstituted system that includes epithelial airway SNARE proteins, Syt2, Munc13-2*, Munc18-2, NSF and α SNAP. From a mechanistic perspective, our results further solidify the critical and active role of the conserved primary (synaptotagmin–SNARE) interface for Ca^{2+} -triggered membrane fusion.

SP9 inhibits stimulated mucin secretion in cells

We next examined whether the selected stapled peptides could also inhibit mucin secretion in primary human airway epithelial (HAE) cells. To facilitate cellular entry of the stapled peptides, we conjugated the N terminus of SP9 with cell-penetrating peptides (CPPs) (ref. [45](#)), and the C terminus with Cy3 fluorescent dye for assessing cellular entry (Fig. [4a](#)). Moreover, we conjugated SP9–Cy3 with biotin and bound it to streptavidin-conjugated bacterial toxins (non-toxic mutants of clostridial C2 toxin or diphtheria toxin (CRM197)) as a possible alternative for intracellular delivery. These toxins can deliver biotin-conjugated peptides into mammalian cells through endocytosis^{[46,47](#)}.

Fig. 4: SP9 inhibits mucin secretion from airway epithelial cells.

 **figure 4**

a, The design of synthesized SP9 with biotin or CPPs conjugated to the N terminus and Cy3 to the C terminus, respectively. Biotin–SP9–Cy3 was bound to streptavidin-conjugated C2 or CRM197. **b**, Diagram of the analysis of cumulated Cy3 intensities within individual HAE cells. **c**, Confocal collapse (projected) images of fixed HAE cells that were treated with SP9–Cy3 or SP9–Cy3 conjugated to bacterial toxins (C2, CRM197) or CPPs. Scale bar, 10 μ m. The experiment was independently repeated twice with air–liquid interface (ALI) cultures from different donors with similar

d, Quantitative analysis of intracellular Cy3 fluorescence for each peptide in MUC5AC⁺ HAE cells. Box plots and data points are shown for n cells (indicated below each box plot). Statistical analysis was performed using one-way analysis of variance (ANOVA) followed by post hoc Dunnett's test; *** $P < 0.0001$. **e**, Schematic of the peptide application and sample collection from HAE cells maintained under ALI conditions. **f**, Representative western blot immunofluorescence images for MUC5AC on an apical surface of untreated HAE cells (control), HAE cells treated with 10 μ M of SP9–Cy3, or 10 μ M of either SP9–Cy3 or P9–Cy3 conjugated to CPPs for 30 min before stimulation. Basl., MUC5AC secretion during a 30 min period before stimulation (baseline). Exp., MUC5AC secreted within a 30 min experimental period with (IL-13 + ATP) or without (IL-13) stimulation of HAE cells with 100 μ M ATP. Cells were treated with IL-13 to induce mucous metaplasia. All of the original blots are shown in Supplementary Fig. 1a. **g, h**, The ratio of baseline to reference wash secretion (fold increase in baseline secretion over reference secretion) (**g**) and the ratio of experimental to baseline (fold increase in stimulated secretion over baseline secretion) (**h**) for each condition in **f**. The numbers below the box plots indicate n for each condition, representing individual ALI cultures derived from four donors for each condition. Statistical analysis was performed using two-way ANOVA followed by post hoc Dunnett's test; * $P = 0.013$.

Source data

Confocal imaging of fixed HAE cells treated with SP9–Cy3, conjugated to either bacterial toxins or CPPs, indicated that only CPP-modified SP9–Cy3 penetrated into the cell interior (Fig. 4b–d and Extended Data Fig. 8a). Analysis of the intracellular localization in MUC5AC-positive airway secretory cells (MUC5AC⁺ cells) confirmed that CPP-modified SP9–Cy3 was delivered into the cytoplasm of secretory cells, whereas biotin–SP9–Cy3 bound to streptavidin-conjugated bacterial toxins was mainly localized to apical mucin granules (Extended Data Fig. 8b). Quantification of cumulative, intracellular Cy3 fluorescence intensities indicated that both penetratin (PEN) (ref. 48) and TAT⁴⁹ efficiently delivered SP9–Cy3 into MUC5AC⁺ cells (Fig. 4b–d). Intact epithelial morphology was observed under all of the conditions (Fig. 4c and Extended Data Fig. 8a). We therefore used SP9–Cy3 conjugated to these CPPs for all of the subsequent experiments.

To investigate the effect of CPP-conjugated SP9–Cy3 on baseline and stimulated secretion under control and mucous metaplastic conditions, we cultured HAE cells in the absence or presence of 10 ng ml⁻¹ IL-13, respectively. IL-13 treatment induces goblet cell hyperplasia and metaplasia in vitro^{50,51}, mimicking IL-13-induced mucous metaplasia in vivo^{52,53}. Consistently, MUC5AC expression was upregulated in IL-13 treated cells (Extended Data Fig. 8c). We next performed experiments under metaplastic conditions with a 30 min peptide pre-incubation at a peptide concentration

of 10 μ M (Fig. 4e). Baseline secretion was low under metaplastic conditions and was not affected by peptide treatment (Fig. 4f,g). Cell morphology also appeared normal. Short-term treatment with PEN–SP9–Cy3 and TAT–SP9–Cy3 substantially reduced stimulated (that is, IL-13 + ATP) MUC5AC secretion by 48% and 86%, respectively (Fig. 4f,h). The unconjugated SP9–Cy3 peptide had no effect on stimulated secretion. We also tested the non-stapled P9–Cy3 peptides (Fig. 4a,f,h): 10 μ M PEN–P9–Cy3 or TAT–P9–Cy3 had no effect on stimulated secretion, consistent with a specific action of the stapled SP9 on stimulated mucin secretion.

As the inhibitory effect of TAT–SP9–Cy3 was statistically significant, whereas PEN–SP9–Cy3 was just below being statistically significant, we next tested the effect of the CPP-conjugated SP9–Cy3 peptides at a higher concentration and longer duration. We incubated HAE cells with 100 μ M CPP-conjugated SP9–Cy3 for 24 h before stimulation (Extended Data Fig. 8c). Similar to the experiments at a lower peptide concentration, both PEN–SP9–Cy3 and TAT–SP9–Cy3 significantly reduced stimulated MUC5AC secretion by 73% and 83% in metaplastic HAE cells, respectively (Extended Data Fig. 8c,d). SP9–Cy3 (without CPP) and non-stapled P9–Cy3 peptides had no effect on ATP-stimulated secretion (Extended Data Fig. 8c,d). Taken together, these results suggest that CPP-conjugated SP9–Cy3 inhibits agonist-stimulated mucin secretion from secretory airway epithelial cells.

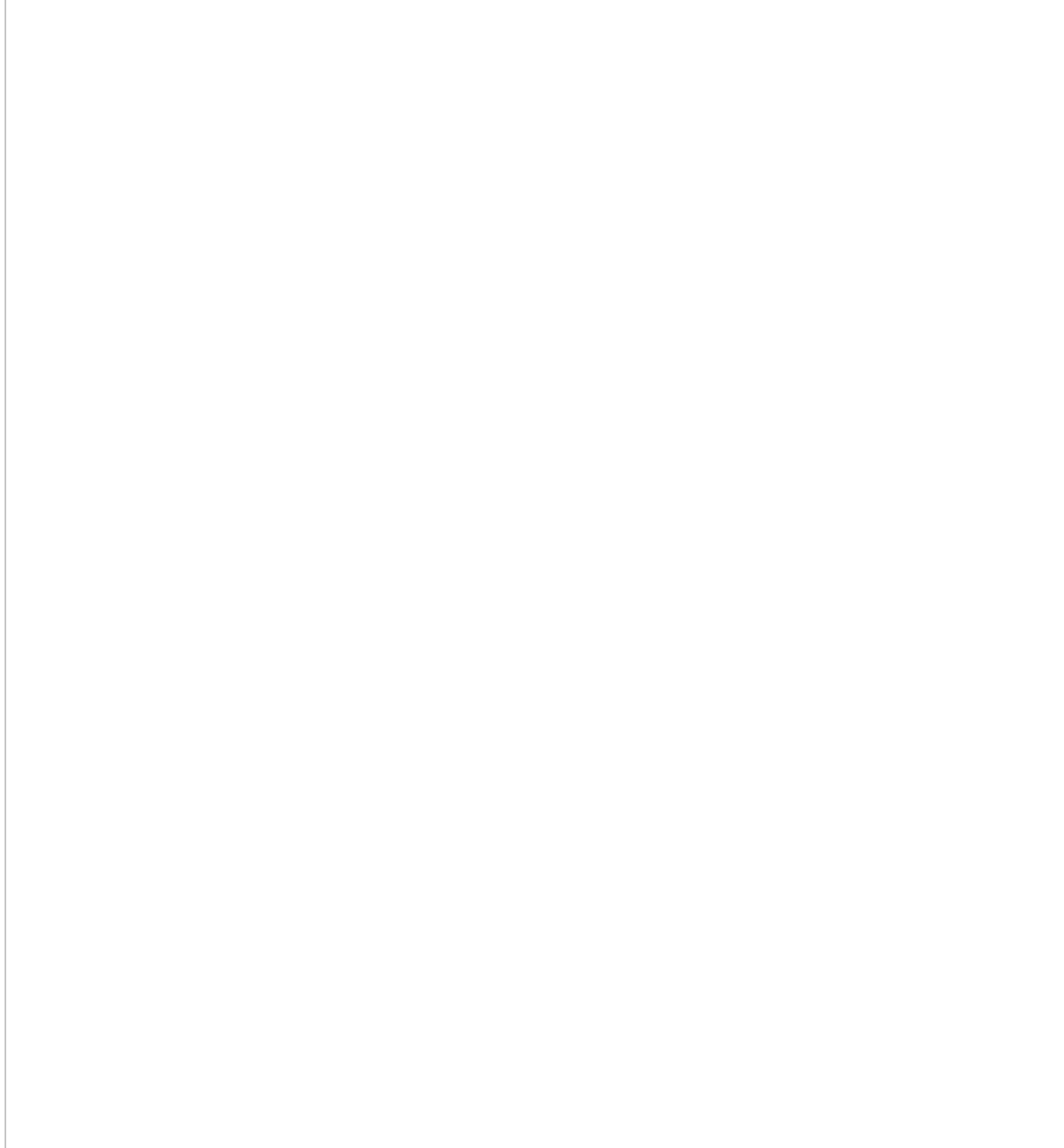
SP9 inhibits stimulated mucin secretion in mice

To investigate whether SP9 could have a therapeutic benefit *in vivo*, we introduced SP9 conjugated to CPPs and fluorophores into mouse airways using a microsprayer inserted into the distal trachea under direct visualization with a laryngoscope. Initial pilot experiments using TAT–SP9–Cy3 and PEN–SP9–Cy3 showed that the forcefully injected peptide solutions mostly bypassed the left proximal axial bronchus between lateral branches L1 and L2, although labelled peptides entered epithelial cells in the distal bronchus and alveoli (Extended Data Fig. 9a). All of the subsequent studies of airway mucin secretion were therefore performed in the distal axial bronchus. Unexpectedly, when TAT–SP9–Cy3 was introduced into the airways of mice with mucous metaplasia, serial sections showed that Cy3-labelled cells had secreted their mucin stores without stimulation by a secretagogue such as ATP or methacholine (Extended Data Fig. 9b,c). This effect was not observed with the injection of buffer alone. Thus, secretion was not induced by the shear force of the microsprayer, but it appears to be a side effect of the TAT–SP9–Cy3 compound in this system. Fortunately, PEN–SP9–Cy3 did not show this problem (Fig. 5a,b), so it was used in all of the subsequent experiments. Exploratory dose-ranging experiments showed minimal Cy3 labelling below 20 μ M PEN–SP9–Cy3, and an apparent plateau above 200 μ M, so a peptide concentration of 200 μ M in the microsprayer delivered 30 min before secretagogues was used in all subsequent experiments. Notably, labelling of ciliated

cells with PEN–SP9–Cy3 was greater than that of secretory cells (Extended Data Fig. 9d,e), perhaps reflecting the greater apical surface area of ciliated cells.

Fig. 5: SP9 inhibits mucin secretion and mucus occlusion in mice.

 figure 5



a, Transverse sections of mouse bronchial airways showing intracellular uptake of peptides (200 μ M microsprayer concentration; Cy3 is visualized in red). Nuclei fluoresce blue (DAPI), overlaid on bright-field images. Scale bar, 25 μ m. **b**, Averaged uptake fractions for two independent experiments for a total n cells (indicated below

each box plot) per group (Supplementary Table 1). Total of $n = 260$ (PEN–SP9–Cy3) and $n = 361$ (PEN–P9–Cy3) cells (6 sections from 3 mice per peptide). Statistical analysis was performed using a two-tailed unpaired Student's *t*-test, showing a non-significant difference ($P = 0.83$). ND, not detected. **c**, Fractional mucin secretion was measured by analysis of images of mouse airways treated with IL-13 to induce mucous metaplasia (top row), followed by stimulation of secretion with methacholine or PBS as control (bottom row). The sections were taken 3 mm distal to those in Fig. 1. Mice that were pretreated with PBS or PEN–P9–Cy3 show greater reductions in intracellular mucin content (PAFS stain (red)) in response to methacholine compared with mice that were pretreated with PEN–SP9–Cy3. Scale bar, 25 μm . **d**, Fractional mucin secretion measured as in **c**. Box plots and data points are shown for two independent experiments for a total n mice (indicated below each box plot) per group. Statistical analysis was performed using a two-tailed unpaired Student's *t*-test, showing a significant difference between mice that were pretreated with PEN–SP9–Cy3 compared with those that were pretreated with PBS; *** $P = 0.00000001$. **e**, Airway luminal mucus was measured by image analysis as in Fig. 1, except that the right lungs were examined instead of the left lungs. Scale bar, 25 μm . **f**, The sum of luminal mucus cross-sectional area in the caudal lobe of the right lung measured at 500 μm intervals. Box plots and data points are shown for two independent experiments combined for a total n mice (indicated below each box plot) per group. Statistical analysis was performed using a two-tailed unpaired Student's *t*-test, showing a significant difference between mice that were pretreated with PEN–SP9–Cy3 compared with those that were pretreated with PBS; * $P = 0.027$.

Source data

Aerosol administration of 200 μM (microsprayer concentration) PEN–SP9–Cy3 labelled 76% of epithelial cells in the distal left axial bronchus, whereas 200 μM of the control peptide PEN–P9–Cy3 labelled 77% of epithelial cells (Fig. 5a,b). Pretreatment with PEN–SP9–Cy3 markedly reduced the fractional secretion of intracellular mucin stimulated by methacholine (by 82.3%), whereas PEN–P9–Cy3 had no effect (Fig. 5c,d), suggesting that the effect of PEN–SP9–Cy3 is specific. Pretreatment with PEN–SP9–Cy3 also significantly reduced airway luminal mucus accumulation in the lungs (by 33.1%), whereas PEN–P9–Cy3 had no effect (Fig. 5e,f).

Discussion

The primary interface between Syt1 and the SNARE complex is essential for fast synchronous Ca^{2+} -triggered neurotransmitter release⁵. Here we designed a hydrocarbon-stapled peptide, SP9, based on a fragment of SNAP-25A that participates in the interface as observed in the crystal structure of the neuronal SNARE–Syt1 complex, and used this both to examine Syt1-dependent stimulated neurotransmitter

release and, more generally, to analyse cognate interactions of Syt isoforms with non-neuronal SNARE complexes.

The hydrocarbon staples promoted an α -helical conformation of SP9 and greatly enhanced the interaction with Syt1 (Fig. 2d, f). SP9 specifically inhibited Ca^{2+} -triggered single-vesicle fusion with reconstituted neuronal SNAREs and Syt1 (Extended Data Fig. 4). We next tested SP9 with a reconstituted simple single-vesicle fusion assay using airway SNAREs and Syt2, and found that SP9 also specifically inhibited Ca^{2+} -triggered single-vesicle fusion for the airway system (Extended Data Fig. 7). Moreover, we observed even more pronounced inhibition of Ca^{2+} -triggered vesicle fusion when both Munc13-2* and Munc18-2 were included in a more complete reconstitution with airway SNAREs and Syt2, resulting in around an eight to tenfold decrease in the Ca^{2+} -triggered fusion amplitude (Fig. 3g). By contrast, the effect of SP9 on Ca^{2+} -independent fusion was relatively modest (Fig. 3e). The observed inhibition of Ca^{2+} -triggered fusion by SP9 is probably caused by SP9 binding to Syt2 in competition with the primary interface (Fig. 2g).

We next examined whether SP9 can be delivered into HAE cells. Peptides were applied to the apical side of the reconstituted airway epithelia, mimicking intratracheal aerosol delivery *in vivo*, a significant advantage to minimize systemic off-target effects. Conjugation of SP9 with either PEN or TAT CPPs resulted in substantial peptide uptake into the cytoplasm of secretory airway cells (Fig. 4b–d). Treatment with 10 μM CPP-conjugated TAT–SP9–Cy3 or PEN–SP9–Cy3 reduced ATP-stimulated, Ca^{2+} -triggered MUC5AC secretion (Fig. 4e, f, h and Extended Data Fig. 8c, d), whereas the non-stapled CPP-conjugated P9–Cy3 peptide did not exhibit inhibitory effects at this concentration, suggesting that the inhibitory action of the SP9 compound is specific. Importantly, baseline secretion was not affected by any of the peptides in the IL-13 (metaplastic) cultures (Fig. 4g), consistent with the absence of an effect of Syt2 deletion on baseline secretion in mice⁶.

Finally, we tested the efficacy of CPP-conjugated SP9 in mice. Short-term treatment of mice with aerosolized PEN–SP9–Cy3 resulted in substantial peptide uptake into distal airway epithelial cells, and reduced methacholine-stimulated, Ca^{2+} -triggered mucin secretion and airway mucus occlusion (Fig. 5), whereas the non-stapled PEN–P9–Cy3 peptide did not exhibit an inhibitory effect, again suggesting specificity. Note that the inhibitory effects of PEN–SP9–Cy3 in mice are probably greater than its measured effects on secretion and occlusion due to peptide uptake into only 76% of epithelial cells (Fig. 5a) and preferential uptake into ciliated over secretory cells (Extended Data Fig. 9d, e). Furthermore, the higher concentration of peptides required in mice compared with in cultured cells probably reflects the brief contact of the forcefully injected aerosol in mice with airway epithelial cells (Extended Data Fig. 9a).

In summary, CPP-conjugated stapled peptides can be efficiently delivered into cultured human epithelial cells and airway epithelial cells of mice, in which they markedly and specifically reduce stimulated mucin secretion and mucus occlusion of mouse airways and they could therefore serve as a starting-point therapeutic without incurring toxicity due to reduced baseline mucin secretion. Optimization of such a therapeutic would include maximizing cellular uptake without causing transepithelial systemic delivery, improving intracellular stability and increasing potency. An optimized drug could be used both as a single-dose therapy in an acute exacerbation of airway disease (asthma, chronic obstructive pulmonary disease and cystic fibrosis), and as a drug delivered repeatedly in a patient in whom control of mucus hypersecretion is difficult to achieve with drugs directed at upstream inflammatory mediators. Therapeutic peptides derived from other host proteins have shown a very low rate of immunogenicity in clinical trials when administered systemically^{[33,54,55](#)}, as has recombinant human DNase administered repeatedly by aerosol^{[56](#)}, so this is unlikely to be a limitation of chronic therapy, although it would need to be examined. Taken together, we have shown that stimulated membrane fusion processes, such as neurotransmitter release or mucin secretion, can be manipulated pharmacologically by compounds that disrupt the interaction between the fusion proteins and Ca²⁺ sensors. In view of the broad physiological significance of calcium-regulated exocytosis in neurological, endocrine and exocrine function, our research paves the way for the development of therapeutics.

Methods

Mice

All of the experiments were approved by the Institutional Animal Care and Use Committee of MD Anderson Cancer Center. *Syt2* conditionally deleted mice with the second exon flanked by *loxP* recombination sites (floxed, *Syt2*^{F/F}) were obtained from T. C. Südhof^{[24](#)}. These were generated on a mixed 129/Sv:C57BL/6 background and backcrossed by us for ten generations onto a C57BL/6J background. To delete *Syt2* in airway epithelial cells, *Syt2*^{F/F} mice were crossed with mice in which a Cre recombinase optimized for mammalian codon usage was knocked into the secretoglobin 1A1 locus (*Scgb1a1*^{Cre}) (refs. ^{[25,26](#)}). Half of the progeny that resulted from crossing *Syt2*^{F/F} mice with *Syt2*^{F/F} mice that were also heterozygous for the *Scgb1a1*^{Cre} allele were *Syt2* deletant (*Syt2*^{D/D}) mice, and the other half were *Syt2*^{F/F} mice that served as littermate controls for the mucin-secretion experiments. Genotyping was performed by PCR using the oligonucleotide primers for *Syt2* WT and mutant alleles described in ref. ^{[24](#)}. Deletion of *Syt2* in airway epithelial cells was confirmed by immunohistochemical staining (Extended Data Fig. 1) using primary rabbit polyclonal antibodies against *Syt2* (Abcam, ab113545, 1:1,000) and secondary

donkey anti-rabbit IgG polyclonal antibodies conjugated to horseradish peroxidase (Jackson ImmunoResearch, 711-005-152, 1:5,000). Peroxidase activity was localized using a diaminobenzidine substrate kit (Vector Laboratories, SK-4100), and the slides were counterstained with haematoxylin. C57BL/6J mice were purchased from the Jackson Laboratory and used as controls to be certain the *Syt2*^{F/F} allele was not hypomorphic in airway epithelium. As *Syt2*^{F/F} mice did not differ from WT *Syt2* mice at the baseline or in the degree of mucous metaplasia and efficiency of stimulated secretion (Fig. 1), they were used as the primary comparator for *Syt2*^{D/D} mice to minimize environmental and off-target genetic differences. Mice of both sexes were used aged 6–26 weeks. The animals were housed in specific pathogen free conditions under a 12 h–12 h light–dark cycle with food and water ad libitum. Group sizes were calculated to detect between-group differences with a power of 90% and two-tailed significance of 5%, based upon effect sizes from our numerous prior studies of mucin secretion and luminal mucus accumulation. The number of animals used was the minimum that is consistent with scientific integrity and regulatory acceptability, with consideration given to the welfare of individual animals in terms of the number and extent of procedures to be carried out on each animal. Mice from the appropriate genotypes were randomly assigned to groups for all of the conditions. Investigators were blinded to the mouse group allocation during data collection and analysis. Furthermore, mouse airway images were analysed by investigators who were blinded to the genotype and treatment of the animals.

Mucin secretion and airway mucus occlusion in mice

The efficiency of stimulated mucin secretion and the extent of mucus accumulation in the airway lumen of *Syt2*-mutant mice were measured as described previously²². In brief, to increase intracellular mucin content (that is, induce mucous metaplasia), 3 µg IL-13 (BioLegend) in 40 µl PBS was instilled every other day for a total of 3 times into the posterior pharynx of mice under isoflurane anesthesia to be aspirated during inhalation. Three days after the last instillation, mucin secretion was stimulated by exposing mice for 10 min to an aerosol of 100 mM ATP in 0.9% NaCl, then the lungs were collected 20 min later. Transverse sections of bronchial airways of mice were stained with PAFS to demonstrate mucin with red fluorescence. Fractional mucin secretion was calculated as the percentage reduction in intracellular mucin content (see below for quantification) of individual mice after sequential treatment with IL-13 and ATP or methacholine compared with the group mean mucin content of mice of the same genotype treated with only IL-13. To measure intracellular airway epithelial mucin content, the lungs were inflated through the trachea with 10% neutral buffered formalin to 20 cm water pressure for 24 h at 4 °C, then embedded in paraffin. A single transverse 5 µm section was taken through the axial bronchus of the left lung between lateral branches 1 and 2, deparaffinized, rehydrated and stained with PAFS reagent.

Images were acquired using an upright microscope (Olympus BX 60) with a $\times 40$ objective lens (NA 0.75), and intracellular mucin was measured around the circumferential section of the axial bronchus using ImagePro-5.1 (Media Cybernetics). Images were analysed by investigators who were blinded to mouse genotype and treatment (Supplementary Table 1).

Quantification of mucin secretion was performed according to previous protocols^{22,57}. First, using images that were acquired in the red channel alone, the total area and fluorescence intensity of intracellular staining above the basement membrane were measured. Second, using the images captured under both red and green fluorescence, the total surface area of the epithelium and the length of the basement membrane in each field were measured. The volume density of mucin staining in the airway epithelium was then calculated stereologically as the ratio of surface area of staining to total surface area of the epithelium divided by a boundary length measurement, which is a product of the total epithelial surface area, the basement membrane length and the geometric constant $4/\pi$. As a result, data are presented as the epithelial mucin volume density, signifying the measured volume of mucin overlying a unit area of epithelial basal lamina.

To measure airway luminal mucus content in *Syt2*-mutant mice, mucous metaplasia was induced as above, then mucin secretion and bronchoconstriction were induced by exposure for 10 min to an aerosol of 150 mM methacholine. Lungs were collected and fixed by immersion for 48 h at 4 °C to avoid displacement of luminal mucus and using methanol-based Carnoy's solution (methacarn) for fixation to minimize changes in mucus volume. A single transverse 5 μm section was taken through the axial bronchus of the left lung between lateral branches 1 and 2 and stained with PAFS as above to evaluate intracellular mucin to ensure secretion had been stimulated. Then, six 5 μm sections of the paraffin blocks caudal to the initial section were taken at 500 μm intervals and stained with PAFS. Mucus in the lumens of airways was identified manually and the area summed for all twelve sections using ImagePro-5.1 (Media Cybernetics)²².

To measure the efficiency of stimulated mucin secretion and the extent of mucus accumulation in the airway lumen of WT mice treated with peptides, the same procedures as those used for analysis of *Syt2*-mutant mice were followed, except that both outcomes were measured in the same mouse because of peptide expense by fixation of the left lung through inflation with formalin to measure mucin secretion and fixation of the right lung through immersion in methacarn to measure mucus accumulation. Stimulation of mucin secretion with a single methacholine aerosol was used for both outcomes. A MicroSprayer Aerosolizer (Penn-Century) was used for intratracheal peptide delivery (50 μl) to the airways, secretion was measured in the left axial bronchus at a site 3 mm distal to the site used in the *Syt2*-mutant mice because of

greater intracellular peptide uptake in more distal airways (Extended Data Fig. 9a), and mucus accumulation was measured in the right caudal lobe taking 8–10 sections of 5 µm thickness at 500 µm intervals.

Details about experimental repeats, the number of data points n (that is, mice) and the number of images analysed for each mouse are provided in Supplementary Table 1. The experiments, involving all the experimental groups, were performed twice on two different occasions, weeks apart. Lung tissues from the mice from each of those independent experiments were processed separately.

Epithelial cell uptake of peptides in mice

To measure the uptake of SP9 and control peptides conjugated to CPP in vivo, peptides were labelled with Cy3 by conjugation at the C-terminal cystine residue, as described below. Labelled peptides (200 µM microsprayer concentration) or PBS were introduced into the airways as aerosols using a Penn-Century MicroSprayer inserted into the distal trachea under direct visualization with a laryngoscope. After 30 min, the mice were euthanized and the lungs were fixed by inflation with 10% neutral buffered formalin as described above for the measurement of mucin secretion. Transverse sections were made of the left axial bronchus, and sections were stained with DAPI to demonstrate nuclei. Fractional uptake of labelled peptides was measured as red Cy3 fluorescent staining over the number of blue DAPI-labelled nuclei in individual cells. To illustrate the relative peptide uptake by secretory and ciliated cells (Extended Data Fig. 9d), immunofluorescence staining of secretory cells was performed using primary goat polyclonal antibodies against CCSP (Millipore Sigma, ABS1673, 1:1,000), secondary donkey anti-goat IgG polyclonal antibodies conjugated to Alexa Fluor 488 (Jackson ImmunoResearch, 705-545-147, 1:1,000) and staining of nuclei with DAPI. Details about the experimental repeats, the number of data points n (that is, cells) and the number of images analysed for each mouse are provided in Supplementary Table 1.

Protein expression and purification

We used the same constructs and protocols to purify cysteine-free Stx1A, SNAP-25A, VAMP2 and Syt1 as described in ref. 41. We used the same constructs and protocols to purify NSF and αSNAP as described in ref. 58. The protein sample concentrations were measured by ultraviolet light absorption at 280 nm, and aliquots were flash-frozen in liquid nitrogen and stored at –80 °C.

Stx3

Full-length human *STX3* was expressed in *Escherichia coli* strain BL-21 (DE3) with an N-terminal, TEV-protease-cleavable hexa-histidine tag. The expression and purification protocols were mostly identical to that of Stx1A. The protein was expressed overnight at 30 °C in 8 l of autoinducing medium. Cell pellets from 8 l of culture were suspended in 1× PBS, 1 mM EDTA, 1 mM PMSF and 8 EDTA-free protease inhibitor tablets (Roche) supplemented with lysozyme and DNase I (Sigma-Aldrich). The cells were lysed using a sonicator (Thermo Fisher Scientific) and an M-110EH microfluidizer (Microfluidics). Inclusion bodies were removed by centrifugation for 30 min at 13,000 rpm in a JA-14 rotor (Beckman Coulter), and the supernatant was centrifuged at 43,000 rpm for 1.5 h in a Ti-45 rotor (Beckman Coulter) to pellet the membrane. Membranes were resuspended in 20 mM HEPES pH 7.5, 300 mM NaCl, 10% glycerol and centrifuged at 43,000 rpm for 1 h. The pellet was resuspended once more in the same buffer, dodecylmaltoside (Anatrace) was added to 2% and the sample was stirred for 1.5 h at 4 °C. The solubilized membrane was centrifuged at 40,000 rpm for 35 min, and the supernatant was loaded onto a 5 ml column of Nickel-NTA agarose (Qiagen). The column was washed with 20 mM HEPES pH 7.5, 20 mM imidazole, 300 mM NaCl, 110 mM octyl glucoside (Anatrace), 10% glycerol and the protein was eluted with wash buffer supplemented with 450 mM imidazole and 1 M NaCl. The protein fractions were pooled, digested with 110 µg TEV protease and dialysed overnight against 20 mM HEPES pH 7.5, 50 mM NaCl, 110 mM octyl glucoside (OG) (Anatrace) and 10% glycerol. The fractions were loaded onto a MonoQ 4.6/100 PE column (GE Healthcare) that had been equilibrated with dialysis buffer. The protein was eluted with a gradient of 50 mM to 1 M NaCl over 30 column volumes. Protein concentration was measured by absorption at 280 nm and aliquots were flash-frozen in liquid nitrogen and stored at –80 °C.

SNAP-23

The expression and purification protocols were mostly identical to those of SNAP-25A. Cysteine free SNAP-23, in which all cysteine residues were changed to serine, was expressed in BL21(DE3) cells using autoinducing medium from a pGEX vector as an N-terminal GST tag with a thrombin protease cleavage site to remove the tag. Cells from 4.0 l of the induced culture were resuspended in 250 ml of buffer (20 mM HEPES pH 7.5, 300 mM NaCl, 4 mM DTT, 10% glycerol) containing 1 mM PMSF and 5 EDTA-free protease inhibitor tablets. Cells were lysed by sonication. The lysate was clarified by centrifugation in a Ti45 rotor for 35 min at 40,000 rpm. The supernatant was bound to 10 ml of Glutathione Sepharose beads (GE Healthcare) for 1 h with stirring at 4 °C. The beads were collected by centrifugation, poured into a column and washed with 100 ml of buffer (20 mM HEPES pH 7.5, 300 mM NaCl, 4 mM DTT, 10% glycerol). Thrombin (10 µl of 5 mg ml⁻¹) was added to the washed beads along with 5 ml of buffer (20 mM HEPES pH 7.5, 300 mM NaCl, 4 mM DTT, 10% glycerol) and the mixture was rocked overnight at 4 °C to remove the GST tag.

The cleaved SNAP-23 sample was washed out of the column using buffer (20 mM HEPES pH 7.5, 300 mM NaCl, 4 mM DTT, 10% glycerol) and concentrated to 5 ml. The sample was injected onto a Superdex 200 (16/60) column (GE Healthcare) equilibrated in 20 mM HEPES pH 7.5, 100 mM NaCl and 10% glycerol. Protein-containing fractions were combined and concentrated to around 100 µM SNAP-23. The protein concentration was measured by absorption at 280 nm and aliquots were flash-frozen in liquid nitrogen and stored at –80 °C.

VAMP8

VAMP8 was expressed in *E. coli* strain BL-21 (DE3) with an N-terminal, TEV protease-cleavable, GST tag. The protein was expressed overnight at 25 °C in 8.0 l of autoinducing medium. Cell pellets were suspended in 20 mM HEPES pH 7.5, 300 mM NaCl, 2 mM DTT, 1 mM EDTA and 8 EDTA-free protease inhibitor tablets supplemented with lysozyme and DNase I. The cells were lysed using a sonicator (Thermo Fisher Scientific) and an M-110EH microfluidizer. Cell debris was removed by centrifugation for 30 min at 13,000 rpm in a JA-14 rotor, and the supernatant was centrifuged at 43,000 rpm for 1 h in a Ti-45 rotor to pellet the membrane. The pellet was resuspended in 20 mM HEPES pH 7.5, 300 mM NaCl, 2 mM DTT, 1 mM EDTA and 1.5% DDM and solubilized at 4 °C with stirring for 2.5 h. The solubilized membrane was centrifuged at 43,000 rpm for 35 min, the supernatant was mixed with 5 ml of Glutathione Sepharose 4B and incubated overnight at 4 °C with end-over-end mixing. The beads were washed with 20 CV of 20 mM HEPES pH 7.5, 300 mM NaCl, 2 mM DTT, 1 mM EDTA and 110 mM OG. The protein was cleaved off the column by resuspending the beads in 2 ml of wash buffer supplemented with 110 µg of TEV protease, and incubating at 4 °C for 1 h. After digestion, the column was drained and the flow through (containing cleaved VAMP8) was injected onto a Superdex 200 10/300 Increase column (GE Healthcare) equilibrated with 20 mM HEPES pH 7.5, 300 mM NaCl, 2 mM DTT and 110 mM OG. The fractions containing protein were pooled, and protein concentration was measured by absorption at 280 nm. Aliquots were flash-frozen in liquid nitrogen and stored at –80 °C.

Syt2

Syt2 was expressed in BL21(DE3) cells using autoinducing medium from a pGEX vector as an N-terminal GST tag with a thrombin protease cleavage site to remove the tag. Cells from 4 l of induced culture were resuspended in 200 ml of buffer (20 mM HEPES pH 7.5, 300 mM NaCl, 1 mM EDTA and 2 mM DTT), containing 4 EDTA-free protease inhibitor tablets. Cells were lysed by three passes through the Emulsiflex C5 homogenizer (Avestin) at 15,000 p.s.i. Unlysed cells and debris were removed by centrifugation in a JA-14 rotor for 10 min at 8,000 rpm, the supernatant was centrifuged again in the same rotor for 10 min at 8,000 rpm to remove any final debris.

The supernatant from the second centrifugation was then centrifuged in a Ti45 rotor for 1 h at 40,000 rpm to collect the membranes. Membranes were resuspended using a Dounce homogenizer in 100 ml of buffer (20 mM HEPES pH 7.5, 300 mM NaCl, 1 mM EDTA and 2 mM DTT) and *n*-dodecylmaltoside was added to a final concentration of 2% (w/v) to solubilize the membranes overnight at 4 °C with stirring. The extract was clarified by centrifugation using the Ti45 rotor at 40,000 rpm for 35 min. The extract was applied to a 5 ml bed of Glutathione Sepharose by stirring at 4 °C for 2 h. The column was washed with buffer (20 mM HEPES pH 7.5, 300 mM NaCl, 1 mM EDTA, 2 mM DTT) containing 110 mM β-octyl-glucoside and eluted with buffer (20 mM HEPES pH 7.5, 300 mM NaCl, 1 mM EDTA, 2 mM DTT) containing 110 mM β-octyl-glucoside and 20 mM reduced Glutathione. The GST tag was removed by cleavage with 10 µl of 5 mg ml⁻¹ thrombin for 2 h and the Syt2 sample was purified on a monoS column equilibrated in 20 mM HEPES pH 7.5, 100 mM NaCl, 110 mM β-octyl-glucoside and 2 mM DTT (monoS buffer). After washing the column with monoS buffer (20 mM HEPES pH 7.5, 100 mM NaCl, 110 mM β-octyl-glucoside, 2 mM DTT), the protein was eluted using a linear gradient from 100 mM to 1 M NaCl. Protein-containing fractions were combined, the protein concentration was measured by absorption at 280 nm and aliquots were flash-frozen in liquid nitrogen and stored at -80 °C.

Syt1 C2B, Syt2 C2B and Syt1 C2B(QM)

The Syt1 C2B (amino acid range 271–421), Syt2 C2B (amino acid range 272–422) domains and the Syt1 C2B(QM) (amino acid range 271–421, R281A, E295A, Y338W, R398A, R399A) mutant were expressed as GST-tagged fusion proteins in *E. coli* BL21 (DE3) cells at 30 °C overnight. After collecting the cells by centrifugation, the sample was resuspended in lysis buffer containing 50 mM HEPES-Na pH 7.5, 300 mM NaCl, 2 mM DTT and EDTA-free protease inhibitor cocktail, and then sonicated and centrifuged. The supernatant was incubated with Glutathione Sepharose beads. The resin was extensively washed with 50 ml of wash buffer I containing 50 mM HEPES-Na pH 7.5, 300 mM NaCl and 1 mM DDT, followed by 50 ml of wash buffer II containing 50 mM HEPES-Na pH 7.5, 300 mM NaCl, 1 mM DTT and 50 mM CaCl₂. The GST tag was cleaved overnight at 4 °C with PreScission protease (GE Healthcare) in cleavage buffer containing 50 mM HEPES-Na pH 7.5, 300 mM NaCl, 1 mM DTT and 2 mM EDTA. The cleaved proteins were purified by monoS column and gel filtration on Superdex 75 (GE Healthcare). The protein concentration was measured by absorption at 280 nm and aliquots were flash-frozen in liquid nitrogen and stored at -80 °C.

Munc13-2*

The Munc13-2* fragment of Munc13-2 (amino acid range 451–1407, that is, including the C1, C2B and the C-terminally truncated MUN domains, but excluding residues 1326–1343) was cloned into a pFastBac HTB vector with a GST tag and a PreScission cleavage site. The deletion of residues 1326–1343 in this construct prevents aggregation^{39,59}, and the C-terminal truncation improves solubility. Cells from 8 l of SF9 cell culture were resuspended in 200 ml resuspension buffer (RB) (50 mM Tris, pH 8.0, 500 mM NaCl, 1 mM EDTA, 0.5 mM TCEP, 10% glycerol) containing 6 EDTA-free protease inhibitor tablets. The cells were lysed by three passes through the Avestin C5 homogenizer at 15,000 p.s.i. The lysate was clarified by centrifugation for 35 min at 40,000 rpm in a Ti45 rotor. The supernatant was mixed with 15 ml Glutathione Sepharose beads at 4 °C with stirring for 2 h. The beads were washed using the Akta Prime system (GE Healthcare) with 20 ml RB, 90 ml RB + 1% Triton X-100, then eluted with RB + 50 mM reduced Glutathione. Peak fractions were pooled and then 100 µl of 10 mg ml⁻¹ PreScission protease was added and incubated overnight. The cleaved proteins were purified by gel filtration on the Superdex 200 column. The protein concentration was measured by absorption at 280 nm and aliquots were flash-frozen in liquid nitrogen and stored at –80 °C.

Munc18-2

Munc18-2 (amino acid range 1–594) was cloned into a pFastBac HTB vector with an N-terminal hexa-histidine tag and a TEV-cleavage site. Cells from 4.0 l of a SF9 cell culture were resuspended in 100 ml resuspension buffer (RB) (20 mM sodium phosphate, pH 8.0, 300 mM NaCl, 2 mM DTT, 10% glycerol with 1 mM PMSF) containing 6 EDTA-free protease inhibitor tablets. The cells were lysed via 3 passes through the Avestin C5 homogenizer at 15,000 p.s.i. The lysate was clarified by centrifugation for 35 min at 40,000 rpm in a Ti45 rotor. The supernatant was mixed with 3 ml Ni-NTA beads at 4 °C stirring for 1 h. The beads were washed using an Akta Prime system with 20 ml each of RB, then eluted with RB + 300 mM imidazole. Peak fractions were pooled and then 100 µl of 11 mg ml⁻¹ TEV protease was added. The mixture was dialysed overnight against 1 l of 500 ml of 20 mM HEPES pH 7.5, 300 mM NaCl, 2 mM DTT, 10% glycerol. The TEV cleaved protein was injected on a Superdex 200 column. Peak fractions were combined and the protein concentration was measured by ultraviolet light absorption at 280 nm. Aliquots of 100 µl were flash-frozen in liquid N₂ and stored at –80 °C.

Peptide synthesis

The stapled peptide SP9 and the non-stapled peptide P0 (Fig. 2c), as well as peptide chimeras with conjugated CPPs or biotin at the N terminus, and/or conjugated fluorescent dye Cy3 labels at the C terminus (SP9–Cy3, biotin–SP9–Cy3, PEN–SP9–Cy3, PEN–P9–Cy3, TAT–SP9–Cy3 and TAT–P9–Cy3 (Fig. 4a); P0–Cy3 (Fig. 2f)) were synthesized and purified by Vivitide (formerly New England Peptide). Peptide synthesis was carried out using solid-phase peptide synthesis and Fmoc chemistry. The peptides were cleaved using trifluoroacetic acid and standard scavengers. The peptides were purified using reverse-phase high-pressure liquid chromatography (RP-HPLC). For the stapled peptides, α,α -disubstituted non-natural amino acids of olefinic side chains were synthesized (*S*5–*S* stereochemistry, bridging 5 amino acids).

The hydrocarbon-staple was made using Grubbs catalyst³⁶. For all stapled peptides, the N termini were acetylated and the C termini were amidated. For example, SP9 was synthesized at a 0.2 mmol scale using Rink amide resin on a Liberty Blue instrument (CEM). Standard protecting groups were used for all amino acids. All amino acids were coupled using 5 equivalents of amino acid/HBTU/DIEA relative to resin loading; amino acids after *S*5 were triple coupled using the same molar excess. Fmoc deprotection was performed with 20% piperidine in dimethylformamide (DMF). After final Fmoc deprotection, the N terminus was acetylated using 0.8 M acetic anhydride and 0.43 M *N*-methyl-2-pyrrolidone in DMF. Ring-closing metathesis was performed using first-generation Grubbs catalyst in dichloroethane (DCE); the reaction was allowed to proceed overnight protected from light. The resin was then rinsed with DCE, followed by 1% sodium diethyldithiocarbamate trihydrate in DMF (4 × 30 min). The resin was then rinsed with DMF and dichloromethane. The peptide was cleaved and deprotected using trifluoroacetic acid:H₂O:ethane-1,2-dithiol:thioanisole/ethylmethylsulfide (84:4:4:4) for 3 h, precipitated in ether and centrifuged to pellet. The pellet was resuspended in ether and centrifuged, after which the solvent was decanted. The pellet was dissolved in 1:1 acetonitrile:H₂O and lyophilized. The crude peptide was purified by RP-HPLC using a C18 column (10 µm, 120 Å, 25 × 250 mm), and a

gradient of 42–58% buffer B (0.1% trifluoroacetic acid in acetonitrile) for 140 min.

The biotin-labelled stapled peptide, biotin–SP9–Cy3, was biotinylated at the N terminus by cross-linking biotin through the carbon spacer 6-aminohexaonic.

For the specified peptides, the C-terminal cystine residue was conjugated to Cy3 fluorescent dyes through maleimide reaction chemistry at pH 7.4 and a 1–2 molar ratio of dye to peptide, and after conjugation the Cy3-labelled peptides were purified again. For example, purified SP9 was dissolved in PBS:acetonitrile:DMSO (2:1:1). Cy3-maleimide (1 equivalent) was dissolved in DMSO and added to the peptide solution; the reaction was allowed to proceed for 1 h in the dark. The conjugated peptide was purified by RP-HPLC using a C18 column (10 µm, 120 Å, 25 × 250 mm), and a gradient of 46–66% buffer B for 140 min.

All of the peptides were purified to >90–95% and quality control was performed by liquid chromatography coupled with mass spectrometry (LC–MS) by the manufacturer (HPLC chromatograms and LC–MS data for SP9, TAT–SP9–Cy3, PEN–SP9–Cy3, PEN–P9–Cy3, TAT–P9–Cy3, SP9–Cy3 and P0 are provided in Supplementary Figs. 2–8, respectively).

Subsequently, the peptides were lyophilized and shipped. The LC–MS quality-control data indicate that the peptides have the predicted molecular mass according to their chemical composition. Moreover, 1H 1D and 2D HSQC, HMBC, ROESY NMR experiments of 5 mg SP9 dissolved in DMSO (Supplementary Fig. 9) show that the staple (*S*5)-residues are at the expected positions in the peptide sequence and are connected with the neighbouring residues. Although there is some spectral overlap for some of the resonances, the data are that are consistent with formation of two *S*5–*S*5 pairs. Taken together, the data show that SP9 has the expected sequence and chemical configuration.

For each group of experiments, aliquots of peptide powder were directly dissolved in the specified buffers at ~1 mM concentration using a vortexer, and then diluted to the specified peptide concentrations. For example, to prepare a stock solution of SP9, 2 mg SP9 peptide powder was weighed out. Considering the molecular mass of 2222 g mol^{−1} of SP9 (Supplementary

Fig. 2), this corresponds to 9×10^{-7} mol. For the desired concentration of 1 mM SP9, we added 9×10^{-7} mol $l^{-1} \times 10^{-3}$ mol $l^{-1} = 0.9$ ml buffer. The concentration of the stock solution was confirmed by absorption measurement at 205 nm using a Nanodrop instrument (Thermo Fisher Scientific).

CD spectroscopy

CD spectra were measured using the AVIV stop-flow CD spectropolarimeter at 190–250 nm using a cell with a 1 mm path length. The sample containing 100 μ M of synthesized peptides in PBS buffer (137 mM NaCl, 2.7 mM KCl, 10 mM Na₂HPO₄ and 2 mM KH₂PO₄, pH 7.4) was measured at 20 °C. For the correction of the baseline error, the signal from a blank run with PBS buffer was subtracted from all the experimental spectra. The α -helical content of each peptide was calculated by dividing the mean residue ellipticity $[\phi]_{222\text{obs}}$ by the reported $[\phi]_{222\text{obs}}$ for a model helical decapeptide⁶⁰.

Cryo-electron microscopy

PM and SG vesicles were separately vitrified on lacey carbon grids using the Vitrobot (Thermo Fisher Scientific), and imaged using the FEI Tecnai F20 transmission cryo-electron microscope with a field emission gun (FEI) operated at 200 kV. Images were recorded on a Gatan K2 Summit electron-counting direct detection camera (Gatan) in electron-counting mode⁶¹. Nominal magnifications of $\times 5,000$ and $\times 9,600$ (corresponding to pixel sizes of 7.4 Å and 3.8 Å) were used for airway PM and SG vesicles, respectively (Extended Data Fig. 6a). The diameters of the vesicles (Extended Data Fig. 6b) were measured using EMAN2 (ref. ⁶²).

Bulk fluorescence anisotropy measurements

In the bulk fluorescence anisotropy experiments, P0 and SP9 were labelled with the fluorescent dye Cy3 at the C terminus. The fluorescence anisotropy was measured using the Tecan Infinite M1000/PRO fluorimeter using an excitation wavelength of 530 ± 5 nm and emission wavelength of 580 ± 5

nm at 27.2 °C. The fluorescent-dye-labelled samples were diluted to 10 nM concentration in TBS (20 mM Tris, pH 7.5, 150 mM NaCl, 0.5 mM TCEP) for optimal read out.

Molecular dynamics simulations

The starting point for all of the molecular dynamics simulations was the crystal structure of the SNARE–Syt-1–complexin-1 complex at 1.85 Å resolution (PDB: [5W5C](#))¹⁵. Before the simulations, the Syt1 C2A domain, the crystallographic water molecules, Mg²⁺ and glycerol molecules were deleted from the crystal structure. Specifically, the following residues were included in the simulations of the primary interface: Syt1 C2B (amino acid range 270–419), synaptobrevin-2 (amino acid range 29–66), Stx1A (amino acid range 191–244), SNAP-25A (amino acid ranges 10–74 and 141–194). Complexin-1 was not included in the simulations. For the primary interface (SNARE–Syt1 C2B) simulations, the Syt1 C2B molecule that produces the primary interface was used.

For the simulations of Syt1 C2B–P9, Syt1 C2B (amino acid range 270–419) and residues 37–53 of SNAP-25 were used (corresponding to the P9 sequence: EESKDAGIRTLVMLDEQ). For the simulations of Syt1 C2B–SP9, the Syt1 C2B–P9 complex was used as a starting point and the staples for SP9 were created by using CHARMM topology and parameter files for S5 and the covalent bond between S5 residues⁶³. Initial coordinates for the S5 residues were generated by mutating the native residues into Lys using PyMol v.2.5.1 (Schrödinger), and then using the VMD mutate command⁶⁴ to change Lys into S5. The SP9 and P9 peptides were simulated with an acetylated N terminus, and an amidated C terminus. For all of the simulations, the NAMD program was used⁶⁵.

As a control, five 1 μs molecular dynamics simulations of the primary interface were performed in a solvated environment (Extended Data Fig. [2d, e](#)). For these simulations, the starting models were placed in a 113 × 125 × 116 Å periodic boundary condition box. The empty space in the box was filled with 50,420 water molecules using the VMD solvate plugin. The system has a total of 157,833 atoms. The system was charge-neutralized and ionized by addition of 155 potassium and 138 chloride ions,

corresponding to a salt concentration of ~145 mM using the VMD autoionize plugin.

For the simulations with P9 and SP9, the starting models were placed in a $80 \times 80 \times 80$ Å periodic boundary condition box. The empty space in the box was filled with ~15,200 water molecules using the VMD solvate plugin. The system has a total of 48,486 atoms. The system was charge-neutralized and ionized by the addition of 42 potassium and 44 chloride ions, corresponding to a salt concentration of ~145 mM using the VMD autoionize plugin.

The CHARMM22 (P9–Syt1 C2B and SP9–Syt1 C2B simulations) or CHARMM36 (primary interface simulations) all-hydrogen force fields and parameters⁶⁶ were used with a non-bonded cut-off of 11 Å. A constant-pressure method was used by adjusting the size of the box. The particle mesh Ewald method was used to accelerate the calculation of long-range electrostatic non-bonded energy terms. Langevin dynamics (with a friction term and a random force term) was used to maintain the temperature of the simulation. All hydrogen-heavy-atom bonds were kept rigid using the Rattle method as implemented in NAMD.

For the simulations with stapled peptides, in the relaxation step, dihedral angle restraints were added to restrain the S5–S5 CE–CE double bond in the *cis* conformation, the S5 olefinic side chains in the *trans* conformation, and all α -helices in the α -helical conformation (using the ssrestraints plugin for VMD). In all of the subsequent steps (heating steps and production runs), all these dihedral angle restraints were turned off. For all of the other simulations with peptides without staples, in the relaxation step, α -helical (secondary structure) restraints were added for all α -helices (using the ssrestraints plugin for VMD). In all of the subsequent steps (heating steps and production runs), all these dihedral angle restraints were turned off. The system was equilibrated by the following procedure: (1) relaxation step, ramping up the temperature from 0 to 50 K for 50 ps with a 1 fs time step; (2) first heating step, ramping up the temperature from 50 to 100 K for 50 ps with a 1 fs time step; (3) second heating step, ramping up the temperature from 100 to 250 K for 150 ps with a 1 fs time step. For all simulations, 1 ns chunks were run at a temperature of 300 K with a time step of 1 fs. Five

independent 1 μ s simulations were performed for each system (primary interface, SP9–Syt1 C2B, P9–Syt1 C2B) by using different initial random number seeds. As expected, the primary interface is stable in these simulations.

One simulation of P9–Syt1 C2B resulted in a dissociation event (Fig. 2g (green, right)). Interestingly, the dissociated peptide P9 is highly dynamic, revealing a variety of distorted, partially helical conformations. Presumably, the increased dynamics of the non-stapled P9 peptide resulted in the destabilization of the interactions with Syt1 C2B, producing the rather different binding poses of P9 (Fig. 2g).

All of the simulations were performed on the Stanford Sherlock Cluster using 4 nodes, each node consisting of dual ten-core CPU 2.4 Ghz Intel processors, that is, a total of 80 CPUs were used for each simulation. The MPI-parallel NAMD2 2.14b1 executable was used. To visualize the results, only protein components are shown, and all of the structures were fitted to each other, and displayed using PyMOL v.2.5.1.

Vesicle reconstitution

For the ensemble lipid mixing assay, the lipid composition of the SV vesicles was phosphatidylcholine (PC) (46%), phosphatidylethanolamine (PE) (20%), phosphatidylserine (PS) (12%), cholesterol (20%) and 1,1'-dioctadecyl-3,3,3',3'-tetramethylindodicarbocyanine perchlorate (DiD) (Invitrogen) (2%); for the both neuronal and airway PM vesicles, the lipid composition was brain total lipid extract supplemented 3.5 mol% PIP2, 0.1 mol% biotinylated PE and 2 mol% 1,1'-dioctadecyl-3,3,3',3'-tetramethylindocarbocyanine perchlorate (DiI) (Invitrogen). All the lipids are from Avanti Polar Lipids.

For single-vesicle content mixing assay, the lipid composition of the SV, SG, VAMP2, or VAMP8 vesicles was PC (48%), PE (20%), PS (12%) and cholesterol (20%); for both the neuronal and airway PM vesicles, the lipid composition was brain total lipid extract supplemented 3.5 mol% PIP2 and 0.1 mol% biotinylated PE.

The reconstitution method for neuronal PM and SV vesicles is described in detail in refs. [41](#),[67](#),[68](#). The same methods were used for airway PM, SG, VAMP2 and VAMP8 vesicles. Dried lipid films were dissolved in 110 mM OG buffer containing purified proteins at protein-to-lipid ratios of 1:200 for VAMP2 and Stx1A for SV and neuronal PM vesicles, respectively (or 1:200 for VAMP8 and Stx3 for SG and airway PM vesicles, respectively), and 1:800 for Syt1 for SV vesicles (or 1:1,200 for Syt2 for SG vesicles).

A three to fivefold excess of SNAP-25A or SNAP-23 (with respect to Stx1A or Stx3) was added to the protein–lipid mixture for neuronal or airway PM vesicles. Detergent-free buffer (20 mM HEPES pH 7.4, 90 mM NaCl and 0.1% 2-mercaptoethanol) was added to the protein–lipid mixture until the detergent concentration was at (but not lower than) the critical micelle concentration of 24.4 mM, that is, vesicles did not yet form. For the preparation of SV, SG, VAMP2, or VAMP8 vesicles for the single-vesicle content mixing assay, 50 mM sulforhodamine B (Thermo Fisher Scientific) was added to the protein–lipid mixture. The vesicles subsequently formed during size-exclusion chromatography using a Sepharose CL-4B column, packed under near constant pressure by gravity with a peristaltic pump (GE Healthcare) in a 5.5 ml column with a ~5 ml bed volume that was equilibrated with buffer V (20 mM HEPES pH 7.4 and 90 mM NaCl) supplemented with 20 µM EGTA and 0.1% 2-mercaptoethanol. The eluent was dialysed into 2 l of detergent-free buffer V supplemented with 20 µM EGTA, 0.1% 2-mercaptoethanol, 5 g of Bio-beads SM2 (Bio-Rad) and 0.8 g l⁻¹ Chelex 100 resin (Bio-Rad). After 4 h, the buffer was exchanged with 2 l of fresh buffer V supplemented with 20 µM EGTA, 0.1% 2-mercaptoethanol and Bio-beads, and the dialysis was continued overnight for another 12 h. We note that the chromatography equilibration and elution buffers did not contain sulforhodamine, so the effective sulforhodamine concentration inside SV, SG, VAMP2 or VAMP8 vesicles is considerably (up to tenfold) lower than 50 mM. For the ensemble lipid mixing assay, the reconstitution method is the same as that for the single-vesicle content mixing assay, except that 50 mM sulforhodamine B was omitted for all the steps.

As described previously^{[67](#)}, the presence and purity of reconstituted proteins in the airway system was confirmed by SDS–PAGE of the vesicle

preparations and the directionality of the membrane proteins (facing outward) was assessed by chymotrypsin digestion followed by SDS–PAGE gel electrophoresis. The size distributions of the airway PM and SG vesicles were analysed by cryo-electron microscopy (Extended Data Fig. [6a, b](#)) as described previously^{[69](#)}.

Single-molecule counting experiments with SP9–Cy3

PEG-coated flow chambers were prepared using the same protocol as for the single-vesicle content mixing experiments. Freshly synthesized SP9–Cy3 powder was first dissolved in an imaging buffer (20 mM HEPES pH 7.4, 90 mM NaCl and 0.5 mM TCEP) at a concentration of 50 µM, then centrifuged at around 16,000 g for 10 min to remove potential insoluble materials. The sample’s concentration was remeasured by absorption by Cy3 at 550 nm before serial dilution to concentrations of 100 nM, 10 nM, 1 nM and 0.5 nM. Diluted sample (5 µl) was injected into a flow chamber on the quartz slides followed by an immediate (~500 µl) wash with imaging buffer. There is some degree of non-specific binding of SP9–Cy3 to the imaging surface, enabling the counting of molecules in fluorescent spots by observing single-molecule photobleaching events^{[70](#)}. After quickly focusing, the sample stage was moved to a fresh location within the same sample chamber distant from prior illumination and the recording was started before exciting SP9–Cy3 by green (532 nm) laser light at an excitation power of ~8 mW. Multiple recordings were performed at fresh locations within the same chamber.

The number of SP9–Cy3 molecules in a fluorescent spot was counted by observing sequential stepwise photobleaching events. Fluorescent spots were automatically detected by smCamera and time traces for each spot generated. The time traces were automatically analysed by Hidden Markov modelling^{[71,72](#)} using a script written for MATLAB. We applied constraint-based clustering to initiate the Hidden Markov model (HMM) and calculated the probability matrices of transition and emission iteratively. The most probable state sequences were then reconstructed with a standard Viterbi algorithm. The time traces and automatic HMM fits were manually inspected. For many traces, there were distinct stepwise decreases in fluorescence intensity where the stepwise decreases were approximately as

recognized by HMM (Extended Data Fig. 3c). Traces were selected that showed distinct stepwise fluorescence intensity decreases and that had undergone complete photo-bleaching at the end of the observation period. Histograms of the number of photo-bleaching steps (also known as the number of SP9–Cy3 molecules per fluorescent spot) were then generated (Extended Data Fig. 3d).

Single-vesicle content mixing experiments

All single-vesicle fusion experiments were performed on a prism-type total internal reflection fluorescence microscope using 532 nm (green) laser (CrystaLaser) and 637 nm (red) laser (OBIS) excitation. Two observation channels were created by a 640 nm single-edge dichroic beamsplitter (FF640-FDi01-25x36, Semrock): one channel was used for the fluorescence emission intensity of the content dyes and the other channel for that of the Cy5 dye that is part of the injected Ca^{2+} solution. The two channels were recorded on two adjacent rectangular areas ($45 \times 90 \mu\text{m}^2$) of a charge-coupled device camera (iXon+ DV 897E, Andor Technology). The imaging data were recorded and analysed using the smCamera program⁷³ developed by K. Suk Lee and T. Ha. Fluorescent peaks were automatically detected using smCamera and time traces were saved in smCamera format as well as in plain text (scripts to convert the smCamera files to tiff and text files were provided by M. Hyn Jo). Candidates for fusion events in the time traces were detected using a script written for MATLAB and then confirmed by manual inspection.

Flow chambers were assembled by creating a ‘sandwich’ consisting of a quartz slide and a glass coverslip that were both coated with polyethylene glycol (PEG) molecules, including 0.1% (w/v) biotinylated-PEG except when stated otherwise, and using double-sided tape to create up to five flow chambers. Coating the surface with PEG molecules alleviates non-specific binding of vesicles. The same protocol and quality controls (surface coverage and non-specific binding) were used as described previously^{67,74} except that PEG-SVA (Laysan Bio) instead of mPEG-SCM (Laysan Bio) was used as it has a longer half-life. The flow chambers were incubated with neutravidin for 30 min (0.1 mg ml⁻¹).

For the single-vesicle fusion experiments described in Fig. 3 and Extended Data Figs. 4, 5 and 7, biotinylated neuronal or airway PM vesicles (100 \times dilution) were tethered to the imaging surface by incubation at room temperature (25 °C) for 30 min followed by three rounds of washing with 120 μ l buffer V to remove unbound neuronal or airway PM vesicles; each buffer wash effectively replaces the 3 μ l flow chamber volume more than 100 times.

For the complete reconstitution (Fig. 3), to form airway SM vesicles with reconstituted Stx3–Munc18-2 complex, we added the ‘disassembly factors’ (1 μ M Munc18-2, 0.5 μ M NSF, 5 μ M α SNAP, 3 mM ATP and 3 mM Mg²⁺) to tethered airway PM vesicles (Fig. 3b), according to previous work with neuronal proteins⁴¹. This procedure results in tethered SM vesicles. Next, the flow chamber with the tethered SM vesicles was washed with buffer V along with 0.5 μ M Munc-13-2* and 2 μ M SNAP-23.

For all of the reconstitution experiments, after the start of illumination and recording of the fluorescence from a particular field of view of the flow chamber, SV, SG, VAMP2 or VAMP8 vesicles (diluted 100 to 1,000 times; including peptides at the specified concentration, 0.5 μ M Munc-13-2* and 2 μ M SNAP-23, if applicable) were loaded into the flow chamber to directly monitor vesicle association of SG, SV, VAMP2 or VAMP8 vesicles to neuronal or airway PM vesicles for 1 min. When peptide was included in a particular experiment, it was mixed with the SV, SG, VAMP2 or VAMP8 vesicles before loading into the flow chamber. Thus, the peptide would have a chance to bind to Syt1 or Syt2 in the SV or SG vesicles before loading them into the flow chamber. While continuing the recording, the flow chamber was washed three times with 120 μ l of buffer V (including peptides at the specified concentration, 0.5 μ M Munc-13-2* and 2 μ M SNAP-23, if applicable) to remove unbound vesicles.

For the complete reconstitution (Fig. 3), note that Munc13-2* will catalyse the transfer of Stx3 from the Stx3–Munc18-2 complex into the ternary SNARE complex with SNAP-23 and VAMP8; we therefore call the tethered vesicles again as PM vesicles after this transfer (Fig. 3b).

Subsequently, we continued recording for another minute to monitor spontaneous fusion events. To initiate Ca^{2+} -triggered fusion events within the same field of view, a solution consisting of buffer V, 500 μM Ca^{2+} or 50 μM Ca^{2+} , 500 pM Cy5 dye molecules (used as an indicator for the arrival of Ca^{2+} in the evanescent field) and, if applicable, peptide was injected into the flow chamber. The injection was performed at a speed of 66 $\mu\text{l s}^{-1}$ by a motorized syringe pump (Harvard Apparatus) using a withdrawal method similar to the one described previously⁷⁴.

Multiple acquisition rounds and repeats for the single-vesicle content mixing experiments

To increase the throughput of the assay and make better use of the vesicle samples, after intensive washing ($3 \times 120 \mu\text{l}$) with buffer V (which includes 20 μM EGTA to remove Ca^{2+} from the sample chamber), we repeated the entire acquisition sequence (SV, SG, VAMP2 or VAMP8 vesicle loading, counting the number of freshly associated vesicle-vesicle pairs, monitoring of Ca^{2+} -independent fusion, Ca^{2+} -injection and monitoring of Ca^{2+} -triggered fusion) in a different imaging area within the same flow chamber. Five such acquisition rounds were performed with the same sample chamber. SV, SG, VAMP2 or VAMP8 vesicles were diluted $1,000\times$ for the first and second acquisition rounds, $200\times$ for the third and fourth acquisition rounds, and $100\times$ for the fifth acquisition round to offset the slightly increasing saturation of the surface with SG, SV, VAMP2 or VAMP8 vesicles. The entire experiment (each with five acquisition rounds) was then repeated several times (Supplementary Table 2) (referred to as repeat experiment). Among the specified number of repeats, there are at least three different protein preparations and vesicle reconstitutions, so the variations observed in the bar charts reflect sample variations as well as variations among different flow chambers. At least two independent reconstitutions were performed for each condition, and multiple technical repeats were performed using different imaging areas, so the number n refers to the number of repeats combining at least two independent reconstitutions for each condition; all of the repeats were successful, and the number of repeats was deemed to be sufficient to reach significance between different conditions.

Cell culture

Primary HAE cells from several donors were obtained from Promocell at passage 2 or isolated from fresh tissues that were obtained during tumour resections or lung transplantation with fully consent of patients (Ethics approval: ethics committee Medical School Hannover, project no. 2701-2015). Cells were isolated according to the protocol by ref. [57](#), aliquots were maintained in liquid nitrogen until use. HAE cells from individual donors were thawed and expanded in a T75 flask (Sarstedt) in Airway Epithelial Cell Basal Medium supplemented with Airway Epithelial Cell Growth Medium Supplement Pack (both Promocell) and with 5 µg ml⁻¹ Plasmocin prophylactic, 100 µg ml⁻¹ Primocin and 10 µg ml⁻¹ Fungin (all from InvivoGen). Growth medium was replaced every two days. After reaching 90% confluence, HAE cells were detached using DetachKIT (Promocell) and seeded into 6.5 mm Transwell filters with a 0.4 µm pore size (3470, Corning Costar). The filters were precoated with collagen solution (StemCell Technologies) overnight and irradiated with ultraviolet light for 30 min before cell seeding for collagen cross-linking and sterilization. Cells (3.5×10^4) in 200 µl growth medium were added to the apical side of each filter, and an additional 600 µl of growth medium was added basolaterally. The apical medium was replaced after 48 h. After 72–96 h, when cells reached confluence, the apical medium was removed and basolateral medium was switched to differentiation medium ± 10 ng ml⁻¹ IL-13 (IL012; Merck Millipore). Differentiation medium consisted of a 50:50 mixture of DMEM-H and LHC Basal (Thermo Fisher Scientific) supplemented with Airway Epithelial Cell Growth Medium SupplementPack as previously described [75](#) and was replaced every 2 days. Air lifting (removal of apical medium) defined day 0 of ALI culture, and cells were grown at ALI conditions until experiments were performed at day 25 to 28. To avoid mucus accumulation on the apical side, HAE cell cultures were washed apically with Dulbecco's phosphate buffered solution (DPBS) for 30 min every 3 days from day 14 onwards.

Mucin-secretion assay in HAE cells

Mucin-secretion experiments under static, that is, non-perfused, conditions were conducted as described previously^{51,52,76} with modifications for the peptide treatments. In brief, for the 24 h peptide treatment, 20 μ l of DMEM \pm 100 μ M peptides was added to the apical surface 24 h before stimulation. On the day of the assay, cells were washed five times with 100 μ l DMEM for 1 h for each wash on the apical side. Apical supernatants were collected after every wash (wash 1–5), then 100 μ l of DMEM \pm 100 μ M peptides was added to the apical surface and HAE cells incubated for 15 min before collecting the supernatant (baseline wash). HAE cells were then incubated for an additional 15 min with 100 μ l DMEM \pm 100 μ M ATP (Sigma-Aldrich) before collecting the supernatants (experimental washes) (Fig. 4e). After sample collection, cells were lysed in 100 μ l of lysis buffer (lysate) containing 50 mM Tris-HCl pH 7.2, 1 mM EDTA, 1 mM EGTA, 1% Triton-X (Sigma-Aldrich), protease inhibitor cOmplete mini EDTA-free and phosphatase inhibitor PhosSTOP (Roche). The protocol was adapted for 30 min peptide treatment as follows. After wash 5, 100 μ l of DMEM \pm 10 μ M or 100 μ M of peptides (Fig. 4e) was added to the apical surface and HAE cells incubated for 30 min (baseline wash). HAE cells were then incubated for 30 min with 100 μ l DMEM \pm 100 μ M ATP to collect experimental washes.

All of the samples were diluted 1:10 in PBS (washes and cell lysates) and 50 μ l of each sample was vacuum-aspirated onto a 0.45 μ m pore nitrocellulose membrane using the Bio-Dot MicrofiltrationApparatus (Bio-Rad). Subsequently, membranes were incubated with Intercept blocking buffer (Li-Cor) for 1 h before probing with anti-MUC5AC (MA1–21907, Invitrogen) added at 1:250 in Intercept blocking buffer for 1 h. Membranes were then washed four times for 10 min in PBS-Tween-20 (PBST) before incubation with the IRDye secondary antibodies (926–33212 or 926–68072; Li-Cor) diluted at 1:10,000 in Intercept blocking for 1 h. All of the steps were performed at room temperature. Fluorescent signals were acquired using the Odyssey Fc Imaging System (Li-Cor) and quantified using ImageJ (v.2.0.0; NIH). Equal volumes of samples were loaded on the gels for control and peptide treatments (all of the raw gels are provided in Supplementary Fig. 1). Differences in total MUC5AC signal result from differences in IL-13 induced metaplasia between individual filters.

Stimulated secretion was therefore normalized to baseline secretion within individual filters to account for filter-to-filter heterogeneities.

To account for donor heterogeneity, all of the relevant experiments were performed in HAE cell ALI cultures generated from at least four individual donors. Complete sets of control and experimental conditions were conducted in ALI cultures from the same donor. Donors were selected randomly from our depository. Individual ALI cultures from the same donor were then randomly allocated to a control treatment groups. Thus, covariates including sex, age and clinical history were identical in all of the conditions. No blinding was performed. Donor numbers are indicated in the respective figure legends. Donor participant sex, age and smoking status is listed in Supplementary Table 3.

Immunofluorescence staining in HAE cells for CPP uptake experiments

HAE cells grown on Transwell filters were incubated with 20 µl of DMEM ± 100 µM specified peptides (Fig. 4a) on day 28 of establishing ALI. Then, 24 h later, cells were fixed for 20 min in 2% paraformaldehyde in DPBS. Cells were then permeabilized for 10 min with 0.2% saponin and 10% FBS (Thermo Fisher Scientific) in DPBS. Cells were washed twice with DPBS and stained with anti-MUC5AC (45M1, MA1-21907, Thermo Fisher Scientific) antibodies diluted 1:100 in DPBS, 0.2% saponin and 10% FBS overnight at 4 °C. Subsequently, cells were washed twice with DPBS and incubated for 1 h at room temperature in DPBS, 0.2% saponin and 10% FBS containing AlexaFluor-488-labelled anti-mouse secondary antibodies (1:500; Thermo Fisher Scientific) and DAPI (1:5,000; Thermo Fisher Scientific). Images were taken on an inverted confocal microscope (Leica TCS SP5) using a ×40 lens (Leica HC PL APO CS2 40x1.30 OIL). Images for the blue (DAPI), green (AlexaFluor 488) and red (Cy3) channels were taken in sequential mode using appropriate excitation and emission settings.

Image analysis for analysis of CPP uptake in HAE cells

Serial sections of images along the basolateral to apical cell axis (*z* axis) were acquired with a 0.28 µm distance between individual *z*-sections to

analyse the distribution of intracellular Cy3 fluorescence (Extended Data Fig. 8). Fluorescence intensity profiles along the z axis in individual cells were calculated for all of the channels using the Lecia LAS X software (Leica). In brief, fluorescence intensities of DAPI, AlexaFluor 488 (MUC5AC) and Cy3 were analysed within individual cells at each z -section, normalized and fluorescence intensity traces were calculated along the basolateral to apical cell axis. Traces were exported to GraphPad Prism 7 for graph plotting. For quantitative analysis of intracellular Cy3 fluorescence intensities, maximum projections of all z -sections were calculated using the Leica LAS X software and average fluorescence intensities were analysed for individual MUC5AC $^+$ cells. Experiments to analyse peptide uptake were performed in HAE cell ALI cultures from two individual donors and complete sets of experimental conditions were conducted in ALI cultures from both donors.

For binding of biotin–SP9–Cy3 to bacterial toxins, C2 and CRM197 were conjugated to streptavidin. Biotin–SP9–Cy3 and streptavidin-conjugated toxins were mixed at a 10:1 ratio at 30 °C for 30 min before adding to cells.

Quantification and statistical analysis

Origin, MATLAB and Prism were used to generate all curves and graphs. The fusion experiments were conducted at least three times with different protein preparations and vesicle reconstitutions, and properties were calculated as the mean \pm s.e.m. Two-tailed Student's t -tests were used to test statistical significance in Figs. 1, 3 and 5 and Extended Data Figs. 4, 5 and 7 with respect to the specified reference experiment. Statistical significance in Fig. 4 and Extended Data Fig. 8 was assessed using ANOVA followed by post hoc Dunnett's test or by two-tailed Student's t -tests, where appropriate.

Box plots are defined as follows: the whiskers show the minimum and maximum values (excluding outliers), the box limits show the 25% and 75% percentiles, the square point denotes the mean, and the centre line denotes the median.

Software and code

The HAE cell data collection was performed using the Leica LAS X v3.1.5.16308, Li-Cor Odyssey Fc Imaging System v.5.2. The data for the single-vesicle fusion experiments and single molecule counting experiments were collected by the smCamera program developed by T. Ha.

Data analysis was performed for the HAE cell experiments using MS Excel for Mac v.16.36, GraphPad Prism v.7 and NIH ImageJ v.2.0.0-rc69. For the mouse experiments, ImagePro-5.1 (Media Cybernetics) was used. For the single-vesicle fusion experiments, single-molecule counting experiments, fluorescence anisotropy experiments and circular dichroism experiments, OriginPro 8 and MATLAB-2021b were used. EMAN2-2.91 was used to analyse the Cryo-EM images in Extended Data Fig. [6a](#). NAMD2 v.2.14b1 was used for the molecular dynamics simulations. Pymol v.2.5.1 was used for modelling mutations and visualization.

Animal statement

All the mouse work was conducted in accordance with the UT MD Anderson Cancer Center IACUC guidelines, and under the IACUC supervision; protocol no. 00001214-RN02.

Reporting summary

Further information on research design is available in the [Nature Research Reporting Summary](#) linked to this paper.

Data availability

The imaging data for the single-vesicle fusion experiments, the studies of primary HAE cells, the mucin-secretion and airway mucus occlusion studies in mice, and the NAMD input files and trajectories of the molecular dynamics simulations are available in the Dryad repository <https://doi.org/10.5061/dryad.dz08kprz7>. Full versions of the blots are provided in Supplementary Fig. [1](#). [Source data](#) are provided with this paper.

Code availability

MATLAB analysis scripts for the single-vesicle fusion, single-molecule counting experiments and smCamera file conversions are available in the Zenodo repository <https://doi.org/10.5281/zenodo.6370585>.

References

1. Jaramillo, A. M., Azzegagh, Z., Tuvim, M. J. & Dickey, B. F. Airway mucin secretion. *Ann. Am. Thorac. Soc.* **15**, S164–S170 (2018).
2. Davis, C. W. & Dickey, B. F. Regulated airway goblet cell mucin secretion. *Annu. Rev. Physiol.* **70**, 487–512 (2008).
3. Südhof, T. C. Neurotransmitter release: the last millisecond in the life of a synaptic vesicle. *Neuron* **80**, 675–690 (2013).
4. Thorn, P., Zorec, R., Rettig, J. & Keating, D. J. Exocytosis in non-neuronal cells. *J. Neurochem.* **137**, 849–859 (2016).
5. Zhou, Q. et al. Architecture of the synaptotagmin–SNARE machinery for neuronal exocytosis. *Nature* **525**, 62–67 (2015).
6. Tuvim, M. J. et al. Synaptotagmin 2 couples mucin granule exocytosis to Ca^{2+} signaling from endoplasmic reticulum. *J. Biol. Chem.* **284**, 9781–9787 (2009).
7. Goldblatt, D. L. et al. Inducible epithelial resistance against acute Sendai virus infection prevents chronic asthma-like lung disease in mice. *Br. J. Pharmacol.* **177**, 2256–2273 (2020).
8. Evans, C. M. et al. The polymeric mucin Muc5ac is required for allergic airway hyperreactivity. *Nat. Commun.* **6**, 6281 (2015).
9. Bossé, Y., Riesenfeld, E. P., Paré, P. D. & Irvin, C. G. It's not all smooth muscle: non-smooth-muscle elements in control of resistance to airflow. *Annu. Rev. Physiol.* **72**, 437–462 (2010).
10. Hays, S. R. & Fahy, J. V. The role of mucus in fatal asthma. *Am. J. Med.* **115**, 68–69 (2003).

11. Fahy, J. V. & Dickey, B. F. Airway mucus function and dysfunction. *N. Engl. J. Med.* **363**, 2233–2247 (2010).
12. Harrison, S. C. Viral membrane fusion. *Virology* **479–480**, 498–507 (2015).
13. Brunger, A. T., Choi, U. B., Lai, Y., Leitz, J. & Zhou, Q. Molecular mechanisms of fast neurotransmitter release. *Annu. Rev. Biophys.* **47**, 469–497 (2018).
14. Podbilewicz, B. Virus and cell fusion mechanisms. *Annu. Rev. Cell Dev. Biol.* **30**, 111–139 (2014).
15. Zhou, Q. et al. The primed SNARE–complexin–synaptotagmin complex for neuronal exocytosis. *Nature* **548**, 420–425 (2017).
16. Voleti, R., Jaczynska, K. & Rizo, J. Ca²⁺-dependent release of synaptotagmin-1 from the SNARE complex on phosphatidylinositol 4,5-bisphosphate-containing membranes. *eLife* **9**, e57154 (2020).
17. Riento, K. et al. Interaction of Munc-18-2 with syntaxin 3 controls the association of apical SNARES in epithelial cells. *J. Cell Sci.* **111**, 2681–2688 (1998).
18. Ren, B. et al. SNAP23 is selectively expressed in airway secretory cells and mediates baseline and stimulated mucin secretion. *Biosci. Rep.* **35**, e00220 (2015).
19. Kim, K. et al. Munc18b is an essential gene in mice whose expression is limiting for secretion by airway epithelial and mast cells. *Biochem. J.* **446**, 383–394 (2012).
20. Jones, L. C. C. et al. VAMP8 is a vesicle SNARE that regulates mucin secretion in airway goblet cells. *J. Physiol.* **590**, 545–561 (2012).
21. Zhu, Y. et al. *Munc13-2*^{−/−} baseline secretion defect reveals source of oligomeric mucins in mouse airways. *J. Physiol.* **586**, 1977–1992 (2008).

22. Jaramillo, A. M. et al. Different Munc18 proteins mediate baseline and stimulated airway mucin secretion. *JCI Insight* **4**, e124815 (2019).
23. Boucher, R. C. Muco-obstructive lung diseases. *N. Engl. J. Med.* **380**, 1941–1953 (2019).
24. Luo, F. & Südhof, T. C. Synaptotagmin-7-mediated asynchronous release boosts high-fidelity synchronous transmission at a central synapse. *Neuron* **94**, 826–839 (2017).
25. Liu, J. et al. ErbB2 pathway activation upon Smad4 loss promotes lung tumor growth and metastasis. *Cell Rep.* **10**, 1599–1613 (2015).
26. Li, H. et al. Cre-mediated recombination in mouse Clara cells. *Genesis* **46**, 300–307 (2008).
27. Pang, Z. P. et al. Synaptotagmin-2 is essential for survival and contributes to Ca^{2+} triggering of neurotransmitter release in central and neuromuscular synapses. *J. Neurosci.* **26**, 13493–13504 (2006).
28. Xia, S. et al. Fusion mechanism of 2019-nCoV and fusion inhibitors targeting HR1 domain in spike protein. *Cell. Mol. Immunol.* **17**, 765–767 (2020).
29. Kilby, J. M. et al. Potent suppression of HIV-1 replication in humans by T-20, a peptide inhibitor of gp41-mediated virus entry. *Nat. Med.* **4**, 1302–1307 (1998).
30. Russell, C. J., Jardetzky, T. S. & Lamb, R. A. Membrane fusion machines of paramyxoviruses: capture of intermediates of fusion. *EMBO J.* **20**, 4024–4034 (2001).
31. Watanabe, S. et al. Functional importance of the coiled-coil of the ebola virus glycoprotein. *J. Virol.* **74**, 10194–10201 (2000).
32. Lu, L. et al. Structure-based discovery of Middle East respiratory syndrome coronavirus fusion inhibitor. *Nat. Commun.* **5**, 3067 (2014).

33. Moiola, M., Memeo, M. G. & Quadrelli, P. Stapled peptides—a useful improvement for peptide-based drugs. *Molecules* **24**, 3654 (2019).
34. Bird, G. H. et al. Hydrocarbon double-stapling remedies the proteolytic instability of a lengthy peptide therapeutic. *Proc. Natl Acad. Sci. USA* **107**, 14093–14098 (2010).
35. Chang, Y. S. et al. Stapled α -helical peptide drug development: a potent dual inhibitor of MDM2 and MDMX for p53-dependent cancer therapy. *Proc. Natl Acad. Sci. USA* **110**, E3445–E3454 (2013).
36. Schafmeister, C. E., Po, J. & Verdine, G. L. An all-hydrocarbon cross-linking system for enhancing the helicity and metabolic stability of peptides. *J. Am. Chem. Soc.* **122**, 5891–5892 (2000).
37. Lai, Y. et al. Screening of hydrocarbon-stapled peptides for inhibition of calcium-triggered exocytosis. Preprint at *bioRxiv* <https://doi.org/10.1101/2022.03.21.484632> (2022).
38. Basu, J. et al. A minimal domain responsible for Munc13 activity. *Nat. Struct. Mol. Biol.* **12**, 1017–1018 (2005).
39. Ma, C., Su, L., Seven, A. B., Xu, Y. & Rizo, J. Reconstitution of the vital functions of Munc18 and Munc13 in neurotransmitter release. *Science* **339**, 421–425 (2013).
40. Yang, X. et al. Syntaxin opening by the MUN domain underlies the function of Munc13 in synaptic-vesicle priming. *Nat. Struct. Mol. Biol.* **22**, 547–554 (2015).
41. Lai, Y. et al. Molecular mechanisms of synaptic vesicle priming by Munc13 and Munc18. *Neuron* **95**, 591–607 (2017).
42. Ma, C., Li, W., Xu, Y. & Rizo, J. Munc13 mediates the transition from the closed syntaxin-Munc18 complex to the SNARE complex. *Nat. Struct. Mol. Biol.* **18**, 542–549 (2011).

43. Evans, J. H. & Sanderson, M. J. Intracellular calcium oscillations induced by ATP in airway epithelial cells. *Am. J. Physiol.* **277**, L30–L41 (1999).
44. Kim, T. D., Eddlestone, G. T., Mahmoud, S. F., Kuchtey, J. & Fewtrell, C. Correlating Ca^{2+} responses and secretion in individual RBL-2H3 mucosal mast cells. *J. Biol. Chem.* **272**, 31225–31229 (1997).
45. Guidotti, G., Brambilla, L. & Rossi, D. Cell-penetrating peptides: from basic research to clinics. *Trends Pharmacol. Sci.* **38**, 406–424 (2017).
46. Fellermann, M. et al. Super-resolution microscopy unveils transmembrane domain-mediated internalization of cross-reacting material 197 into diphtheria toxin-resistant mouse J774A.1 cells and primary rat fibroblasts in vitro. *Arch. Toxicol.* **94**, 1753–1761 (2020).
47. Fahrer, J. et al. C2-streptavidin mediates the delivery of biotin-conjugated tumor suppressor protein P53 into tumor cells. *Bioconjug. Chem.* **24**, 595–603 (2013).
48. Derossi, D., Joliot, A. H., Chassaing, G. & Prochiantz, A. The third helix of the Antennapedia homeodomain translocates through biological membranes. *J. Biol. Chem.* **269**, 10444–10450 (1994).
49. Vivès, E., Brodin, P. & Lebleu, B. A truncated HIV-1 Tat protein basic domain rapidly translocates through the plasma membrane and accumulates in the cell nucleus. *J. Biol. Chem.* **272**, 16010–16017 (1997).
50. Turner, J. et al. Goblet cells are derived from a FOXJ1-expressing progenitor in a human airway epithelium. *Am. J. Respir. Cell Mol. Biol.* **44**, 276–284 (2011).
51. Winkelmann, V. E. et al. Inflammation-induced upregulation of P2X 4 expression augments mucin secretion in airway epithelia. *Am. J. Physiol. Lung Cell. Mol. Physiol.* **316**, L58–L70 (2019).

52. Zhu, Y. et al. Baseline goblet cell mucin secretion in the airways exceeds stimulated secretion over extended time periods, and is sensitive to shear stress and intracellular mucin stores. *PLoS ONE* **10**, e0127267 (2015).
53. Wills-Karp, M. et al. Interleukin-13: central mediator of allergic asthma. *Science* **282**, 2258–2261 (1998).
54. Ali, A. M., Atmaj, J., Van Oosterwijk, N., Groves, M. R. & Dömling, A. Stapled peptides inhibitors: a new window for target drug discovery. *Comput. Struct. Biotechnol. J.* **17**, 263–281 (2019).
55. Lau, J. L. & Dunn, M. K. Therapeutic peptides: historical perspectives, current development trends, and future directions. *Bioorg. Med. Chem.* **26**, 2700–2707 (2018).
56. Yang, C. & Montgomery, M. Dornase alfa for cystic fibrosis. *Cochrane Database Syst. Rev.* **3**, CD001127 (2021).
57. Evans, C. M. et al. Mucin is produced by Clara cells in the proximal airways of antigen-challenged mice. *Am. J. Respir. Cell Mol. Biol.* **31**, 382–394 (2004).
58. Choi, U. B. et al. NSF-mediated disassembly of on- and off-pathway SNARE complexes and inhibition by complexin. *eLife* **7**, e36497 (2018).
59. Li, W. et al. The crystal structure of a Munc13 C-terminal module exhibits a remarkable similarity to vesicle tethering factors. *Structure* **19**, 1443–1455 (2011).
60. Yang, J. T., Wu, C.-S. C. & Martinez, H. M. Calculation of protein conformation from circular dichroism. *Methods Enzymol.* **130**, 208–269 (1986).
61. Li, X. et al. Electron counting and beam-induced motion correction enable near-atomic-resolution single-particle cryo-EM. *Nat. Methods* **10**, 584–590 (2013).

62. Tang, G. et al. EMAN2: an extensible image processing suite for electron microscopy. *J. Struct. Biol.* **157**, 38–46 (2007).
63. Speltz, T. E. et al. Stapled peptides with γ -methylated hydrocarbon chains for the estrogen receptor/coactivator interaction. *Angew. Chem. Int. Ed.* **55**, 4252–4255 (2016).
64. Humphrey, W., Dalke, A. & Schulten, K. VMD: visual molecular dynamics. *J. Mol. Graph.* **14**, 33–38 (1996).
65. Phillips, J. C. et al. Scalable molecular dynamics on CPU and GPU architectures with NAMD. *J. Chem. Phys.* **153**, 044130 (2020).
66. Brooks, B. R. et al. CHARMM: the biomolecular simulation program. *J. Comput. Chem.* **30**, 1545–1614 (2009).
67. Kyoung, M. et al. In vitro system capable of differentiating fast Ca^{2+} -triggered content mixing from lipid exchange for mechanistic studies of neurotransmitter release. *Proc. Natl Acad. Sci. USA* **108**, E304–E313 (2011).
68. Lai, Y. et al. Complexin inhibits spontaneous release and synchronizes Ca^{2+} -triggered synaptic vesicle fusion by distinct mechanisms. *eLife* **3**, e03756 (2014).
69. Diao, J. et al. A single-vesicle content mixing assay for SNARE-mediated membrane fusion. *Nat. Commun.* **1**, 54 (2010).
70. Dresser, L. et al. Amyloid- β oligomerization monitored by single-molecule stepwise photobleaching. *Methods* **193**, 80–95 (2021).
71. Messina, T. C., Kim, H., Giurleo, J. T. & Talaga, D. S. Hidden Markov model analysis of multichromophore photobleaching. *J. Phys. Chem. B* **110**, 16366–16376 (2006).
72. Blanco, M. R., Johnson-Buck, A. E. & Walter, N. G. in *Encyclopedia of Biophysics* (ed. Roberts, G. C. K.) 971–975 (Springer, 2013).

73. Lee, K. S., Balci, H., Jia, H., Lohman, T. M. & Ha, T. Direct imaging of single UvrD helicase dynamics on long single-stranded DNA. *Nat. Commun.* **4**, 1878 (2013).
74. Kyoung, M., Zhang, Y., Diao, J., Chu, S. & Brunger, A. T. Studying calcium-triggered vesicle fusion in a single vesicle-vesicle content and lipid-mixing system. *Nat. Protoc.* **8**, 1–16 (2013).
75. Schmidt, et al. IL-13 impairs tight junctions in airway epithelia. *Int. J. Mol. Sci.* **20**, 3222 (2019).
76. Abdullah, L. H., Wolber, C., Kesimer, M., Sheehan, J. K. & Davis, C. W. Studying mucin secretion from human bronchial epithelial cell primary cultures. *Methods Mol. Biol.* **842**, 259–277 (2012).

Acknowledgements

We thank R. Adachi, M. Singh, T. Südhof, T. Velkov and C. Wang for discussions; T. Südhof for providing the *Syt2* conditional knockout mice; Z. Azzegagh and V. Oren for technical assistance with mucin secretion in mice; H. Barth and M. Fellermann for providing bacterial toxins (C2 and CRM197); P. Braubach for providing donor tissue; C. Schilpp for isolation of HAE cells; S. Lynch for performing the NMR experiments for SP9; H. Chong and colleagues at Vivitide for their expertise in peptide synthesis and collaborative efforts; K. Marcus for providing script files for the molecular dynamics simulations; and C. Mayne for providing parameters for the molecular dynamics simulations. We acknowledge the Deutsche Forschungsgemeinschaft (DFG, German Research Foundation) (251293561 (SFB1149) and 175083951, to M.F.), the National Institutes of Health (NIH) (R37MH63105 to A.T.B.; R01 HL129795 and R21 AI137319 to B.F.D.) and the Cystic Fibrosis Foundation (DICKEY18G0 and DICKEY19P0) for support. The contents of this publication are solely the responsibility of the authors and do not necessarily represent the official views of NIGMS or NIH.

Author information

Author notes

1. Ying Lai

Present address: National Clinical Research Center for Geriatrics, West China Hospital, State Key Laboratory of Biotherapy and Collaborative Innovation Center of Biotherapy, Sichuan University, Chengdu, China

2. Qiangjun Zhou

Present address: Department of Cell & Developmental Biology, Vanderbilt Brain Institute, Center for Structural Biology, Vanderbilt University, TN, USA

3. John Peters

Present address: Department of Biological Chemistry and Molecular Pharmacology, Harvard Medical School, Boston, MA, USA

4. Yunxiang Zhang

Present address: Department of Chemistry, Fudan University, Shanghai, China

Affiliations

1. Department of Molecular and Cellular Physiology, Stanford University, Stanford, CA, USA

Ying Lai, Qiangjun Zhou, Kailu Yang, Jeremy Leitz, John Peters, Yunxiang Zhang, Richard A. Pfuetzner, Luis Esquivies & Axel T. Brunger

2. Institute of General Physiology, Ulm University, Ulm, Germany

Giorgio Fois & Manfred Frick

3. Department of Pulmonary Medicine, University of Texas MD Anderson Cancer Center, Houston, TX, USA

Jose R. Flores, Michael J. Tuvim & Burton F. Dickey

4. Howard Hughes Medical Institute, Stanford University, Stanford, CA,
USA

Kailu Yang, Richard A. Pfuetzner, Luis Esquivies & Axel T. Brunger

5. Institute for Applied Cancer Science, University of Texas MD
Anderson Cancer Center, Houston, TX, USA

Philip Jones

Contributions

Y.L., G.F., M.F., M.J.T., B.F.D. and A.T.B. designed experiments. Y.L. performed fusion, binding and CD experiments. J.L. and J.P. wrote MATLAB scripts to analyse the fusion experiments. G.F. and M.F. performed HAE cell experiments. Y.L., M.J.T., P.J. and Q.Z. performed inhibitor design. K.Y. performed EM experiments. K.Y. and J.L. performed single-molecule counting experiments, and Y.L. and Y.Z. analysed these data. R.A.P. and L.E. assisted with protein purification. M.J.T. performed mouse *Syt2* knockout experiments. J.R.F. performed mouse experiments and analyses. Y.L., G.F., M.F., B.F.D. and A.T.B. wrote the manuscript.

Corresponding authors

Correspondence to [Ying Lai](#), [Manfred Frick](#), [Burton F. Dickey](#) or [Axel T. Brunger](#).

Ethics declarations

Competing interests

The authors declare no competing interests.

Peer review

Peer review information

Nature thanks Bazbek Davletov, Andrew Jamieson and the other, anonymous, reviewer(s) for their contribution to the peer review of this work. Peer review reports are available.

Additional information

Publisher's note Springer Nature remains neutral with regard to jurisdictional claims in published maps and institutional affiliations.

Extended data figures and tables

Extended Data Fig. 1 Related to Figure 1. Efficiency of Syt2 deletion in airway secretory cells.

Bronchial airways of Syt2^{WT} and Syt2^{D/D} mice were stained with antibodies to Syt2 and secondary antibodies conjugated to horseradish peroxidase (brown colour, see Methods). Secretory cells in Syt2 WT mice (left panel) have a domed appearance with their apical poles staining intensely for Syt2 (filled triangle). There was less intense linear staining of tufted ciliated cells in the region of ciliary basal bodies (open triangle), which often stain non-specifically. Secretory cells in Syt2^{D/D} mice did not stain for Syt2 (filled triangle), but linear staining of ciliated cells was similar to that in Syt2^{WT}. We enumerated secretory cells in 3 mice of each genotype and found 46% in Syt2^{WT} and 48% in Syt2^{D/D}, ±4%, which did not differ significantly, indicating there was no loss of viability of secretory cells in Syt2^{D/D} mice. In Syt2^{WT} mice, 91% of secretory cells stained for Syt2, whereas in Syt2^{D/D} mice, only 7% stained for Syt2, indicating a deletion efficiency ~92%. Results for Syt2^{F/F} mice were indistinguishable from those for Syt2^{WT}. Scale bar, 50 μm. Experiments were repeated twice with similar results.

Extended Data Fig. 2 Related to Figure 2. The conservation of the primary interface.

a, Primary sequence alignments between neuronal and airway systems (Stx1A vs. Stx3, SNAP-25A vs. SNAP-23, and Syt1 vs. Syt2). White: absolutely conserved, grey: similar, black: not conserved. Red boxes indicate residues involved in salt bridges and hydrogen bonds, orange boxes indicate residues involved in hydrophobic interactions in the primary interface. The yellow line indicates the residues of SP9 shown as the yellow region in panel **b** and **c**. **b**, Close-up view of the primary interface (PDB ID

5W5C) with grey colour and labels indicating the locations of sequence differences in the primary interface between the neuronal and airway epithelial systems (SNAP-25A vs. SNAP-23, Syt1 vs. Syt2); the corresponding labels indicate the sequence differences. Yellow: region that corresponds to SP9 with staples shown as dumbbells. **c**, Close-up view of the primary interface with residues shown as sticks that are important for the primary interface, including R281, E295, Y338, R398, R399 in Syt1 C2B (also corresponding to residues mutated in Syt1(QM)) and K40, D51, E52, E55, Q56, D166 in SNAP-25A and D231, E234, E238 in Stx1A. Yellow: region that corresponds to SP9 with staples shown as dumbbells. **d**, Starting point of the molecular dynamics simulations of the primary interface. **e**, End points of five independent 1- μ sec simulations (colours) of the primary interface. **f**, Starting point of the SP9–Syt1-C2B simulations. **g**, Starting point of the P9–Syt1-C2B simulations. All starting points were derived from the crystal structure with PDB ID 5W5C.

Extended Data Fig. 3 Related to Figure 2. Characterization of the oligomeric state of SP9.

a, Size exclusion chromatography (SEC) profiles of peptides. Each peptide was filtered with a 0.2 micrometer filter and then loaded on a Superdex 75 column in buffer V (20 mM HEPES, pH 7.4, 90 mM NaCl). The dashed line indicates the border of the void volume at ~8 ml. The difference in retention times for P0 and SP9 may be related to the conformations of the peptides. **b**, Representative TIRF images of immobilized SP9-Cy3 at specified concentrations. Scale bar, 410 μ m. **c**, Representative time traces showing single-molecule stepwise photobleaching events of SP9-Cy3. Black lines correspond to the fluorescence intensity of SP9-Cy3 and red lines correspond to the idealized trajectory obtained by Hidden Markov Model analysis (HMM) (Methods). **d**, Distribution of multiple SP9-Cy3 molecules in (diffraction limited) fluorescent spots at specified concentrations. Fluorescent spots were automatically selected by smCamera. The number of SP9-Cy3 molecules per fluorescent spot was determined from the observed fluorescence intensity time traces by HMM and verified by manual inspection (Methods). Bar graphs were calculated from 167, 675, 937, and 520 selected traces at concentrations of 0.5, 1, 10, and 100 nM SP9-Cy3, respectively.

[Source data](#)

Extended Data Fig. 4 Related to Figure 3. SP9 inhibits both Ca²⁺-independent and Ca²⁺-triggered vesicle fusion with reconstituted neuronal SNAREs and Syt1.

a, Schematic of the single vesicle content mixing assay. Neuronal PM: plasma membrane mimic vesicles with reconstituted Stx1A and SNAP-25A; SV: synaptic vesicle mimic with reconstituted VAMP2 and Syt1. After SV - neuronal PM vesicle association, vesicle pairs either undergo Ca²⁺-independent fusion or remain associated until fusion is triggered by Ca²⁺ addition. 10 μM of P0 or SP9 was added together with SV vesicles and was present in all subsequent stages. **b**, Effect P0 and SP9 on vesicle association. **c**, Corresponding Ca²⁺-independent fusion probabilities. **d**, Corresponding average probabilities of Ca²⁺-independent fusion events per second (** p = 0.00022). **e**, Corresponding Ca²⁺-triggered fusion probabilities. (**f-h**) Corresponding Ca²⁺-triggered fusion amplitudes of the first 1-sec time bin upon 500 μM Ca²⁺-injection (**f**) (* p = 0.017), the cumulative Ca²⁺-triggered fusion probability within 1 min (**g**) (* p = 0.039), and the decay rate (1/τ) of the Ca²⁺-triggered fusion histogram (**h**). The fusion probabilities and amplitudes were normalized to the number of analysed neuronal SV - neuronal PM vesicle pairs (Supplementary Table 2). Panels **b**, **d**, **f**, **g** show box plots and data points for n (indicated below each box plot) independent repeat experiments (Supplementary Table 2). Two-tailed Student's t-tests were used for SP9 vs. No SP. Decay constants (boxes) and error estimates (bars) in panels **h** computed from the covariance matrix upon fitting the corresponding histograms combining all repeats with a single exponential decay function using the Levenberg-Marquardt algorithm.

[Source data](#)

Extended Data Fig. 5 Related to Figure 3. SP9 has no effect on vesicle fusion mediated by neuronal SNAREs alone, or by Syt1(QM).

a–c, SP9 has no effect on vesicle fusion mediated by neuronal SNAREs alone. **a**, Effects of 10 μ M of P0 or SP9 on vesicle association. **b**, Corresponding Ca^{2+} -independent fusion probabilities. **c**, Corresponding average probabilities of Ca^{2+} -independent fusion events per second. **d–j**, the quintuple Syt1(QM) mutant alleviates the inhibitory effect of SP9 on neuronal synaptic vesicle fusion. **d**, Effect of 10 μ M of SP9 on vesicle association (* $p = 0.01629$). **e**, Corresponding Ca^{2+} -independent fusion probabilities. **f**, Corresponding average probabilities of Ca^{2+} -independent fusion events per second. **g**, Corresponding Ca^{2+} -triggered fusion probabilities. **(h–j)** Corresponding Ca^{2+} -triggered fusion amplitude of the first 1-sec time bin upon 500 μ M Ca^{2+} -injection (**h**), the cumulative Ca^{2+} -triggered fusion probability within 1 min (**i**), and the decay rate ($1/\tau$) of the Ca^{2+} -triggered fusion histogram (**j**). The fusion probabilities and amplitudes were normalized to the number of analysed neuronal SV - neuronal PM vesicle pairs (Supplementary Table 2). Panels **a**, **c**, **d**, **f**, **h**, **i** show box plots and data points for n (indicated below each box plot) independent repeat experiments (Supplementary Table 2). Two-tailed Student's t-tests were used for SP9 vs. No SP. Decay constants (boxes) and error estimates (bars) in panels **j** computed from the covariance matrix upon fitting the corresponding histograms combining all repeats with a single exponential decay function using the Levenberg-Marquardt algorithm.

[Source data](#)

Extended Data Fig. 6 Related to Figure 3. Airway PM and SG vesicle preparation.

a, Cryo-EM images of airway PM and SG vesicles as defined in Methods. Scale bar, 100 nm. **b**, Diameter distributions for airway PM and SG vesicles.

[Source data](#)

Extended Data Fig. 7 Related to Figure 3. SP9 inhibits Ca^{2+} -triggered vesicle fusion with reconstituted airway epithelial SNAREs and Syt2.

a, Schematic of the single vesicle content mixing assay. Airway PM: plasma membrane mimic vesicles with reconstituted airway Stx3 and SNAP-23; SG: secretory granule mimics with reconstituted VAMP8 and Syt2. After SG - airway PM vesicle association, vesicle pairs either undergo Ca^{2+} -independent fusion or remain associated until fusion is triggered by Ca^{2+} addition. 10 μM of P0 or SP9 was added together with SG vesicles and was present during all subsequent stages. **b**, Effects of P0 or SP9 on vesicle association. **c**, Corresponding Ca^{2+} -independent fusion probabilities. **d**, Corresponding average probabilities of Ca^{2+} -independent fusion events per second (* $p = 0.014$). **e**, Corresponding Ca^{2+} -triggered fusion probabilities. **f–h**) Corresponding Ca^{2+} -triggered fusion amplitudes of the first 1-sec time bin upon 500 μM Ca^{2+} -injection (**f**) (* $p = 0.012$), the cumulative Ca^{2+} -triggered fusion probability within 1 min (**g**) (** $p = 0.0018$), and the decay rate ($1/\tau$) of the Ca^{2+} -triggered fusion histogram (**h**). **i–k**, SP9 has no effect on vesicle fusion mediated by airway SNAREs alone. **i**, Effects of 10 μM of P0 or SP9 on vesicle association using the assay described above. **j**, Corresponding Ca^{2+} -independent fusion probabilities. **k**, Corresponding average probabilities of Ca^{2+} -independent fusion events per second. Panels **b**, **d**, **f**, **g**, **i**, **k** show box plots and data points for n (indicated below each box plot) independent repeat experiments (Supplementary Table 2). Two-tailed Student's t-tests were used for SP9 vs. No SP. Decay constants (boxes) and error estimates (bars) in panel **h** computed from the covariance matrix upon fitting the corresponding histograms combining all repeats with a single exponential decay function using the Levenberg-Marquardt algorithm.

[Source data](#)

[**Extended Data Fig. 8 Related to Figure 4. SP9 penetrates epithelial cells when conjugated to CPPs and inhibit mucin secretion from airway epithelium cells.**](#)

a, Representative confocal images (z-sections) of fixed HAE cells treated with SP9-Cy3 or SP9-Cy3 conjugated to CPPs or biotin. Biotin-SP9-Cy3 was bound to streptavidin-conjugated C2 or CRM197. The experiment was repeated twice with ALI cultures from different donors with similar results.

Scale bar, 10 µm. **b**, The diagram illustrates the analysis of intracellular localization of MUC5AC, Cy3, and DAPI in airway secretory cells. Fluorescence intensities of DAPI, AlexaFluor 488 (MUC5AC) and Cy3 were analysed within individual MUC5AC⁺ cells at each z-section, normalized and fluorescence intensity traces calculated along the basolateral to apical cell axis. **c**, Representative western blot immunofluorescence images for MUC5AC on apical surface of untreated HAE cells (control 1 and 2) or HAE cells treated with 100 µM SP9-Cy3, PEN-SP9-Cy3, TAT-SP9-Cy3, PEN-P9-Cy3, or TAT-P9-Cy3 for 24 h before stimulation. *Wash* represents MUC5AC accumulated during culture and before start of experiment. *Baseline* represents unstimulated MUC5AC secretion during a 15 min period after removal of accumulated MUC5AC and *experimental* represents MUC5AC secreted within 15 min of stimulation with (ATP) or without (no ATP) 100 µM ATP. *Lysate* represents MUC5AC within HAE cells at the end of the experiment. Cells were treated with IL-13 to induce mucous metaplasia. All original blots are shown in Supplementary Fig 1b. **d**, Box plots and data points show the ratio of experimental / baseline secretion (fold increase of stimulated secretion over baseline secretion) following 24 h preincubation with 100 µM of the respective peptides. Numbers below box-plots indicate n for each condition, representing individual ALI cultures derived from 4 donors for each condition. * p = 0.046 for HAE cells treated with 100 µM PEN-SP9-Cy3, and p = 0.016 for HAE cells treated with 100 µM TAT-SP9-Cy3, assessed by two-way ANOVA followed by post-hoc Dunnett's test.

[Source data](#)

[**Extended Data Fig. 9 Related to Figure 5. Uptake of labelled SP9 conjugated to CPP into mouse airway epithelial cells.**](#)

a, Predominant delivery of 100 µM TAT-SP9-Cy3 to distal airways of mice using a microsprayer. The left panel shows a lack of uptake of the labelled peptide in the proximal axial bronchus, sectioned 1 mm below our usual site of transverse section between lateral branches 1 and 2, though uptake in alveoli surrounding the airway can be seen. The middle panel shows a section through the periphery of the lung, with extensive uptake of the labelled peptide in alveolar epithelial cells. The right panel shows patchy

uptake of the labelled peptide in the distal axial bronchus, sectioned 3 mm below lateral branches 1 and 2. Scale bar, 50 μ m. **b**, Two serial transverse sections of the left axial bronchus of a mouse with mucous metaplasia induced by prior instillation of IL-13, then treated with 300 μ M aerosolized TAT-SP9-Cy3. The left panel is stained with PAFS (red) to demonstrate intracellular mucin, and shows some cells with high mucin content (open arrowheads) and other cells with low mucin content (closed arrowheads), presumably due to induced mucin secretion. The right panel shows blue fluorescent staining of nuclei with DAPI and red fluorescent staining of epithelial cells that have internalized TAT-SP9-Cy3. The same cells indicated in the left panel are also indicated in the right panel, showing that cells that internalize TAT-SP9-Cy3 tend to have low intracellular mucin content, possibly due to the cell-penetrating peptide conjugate allowing calcium entry into the cytoplasm to induce secretion. Scale bar, 20 μ m. **c**, Sections of the left axial bronchus of mice with mucous metaplasia induced by prior instillation of IL-13, and not further treated (left panel), or subsequently treated with aerosolized 100 mM ATP (middle panel) or 1 mM TAT-SP9-Cy3 (right panel). These show high intracellular mucin content (red: PAFS stain) in the mice not treated with an aerosolized drug, extensive secretion of intracellular mucin in the mice treated with ATP, and extensive apocrine mucin secretion in the mice treated with TAT-SP9-Cy3, possibly due to disruption of mucin granule membrane integrity causing intracellular mucin swelling at this high peptide concentration. Scale bar, 50 μ m. **d**, Transverse section of the left axial bronchus of a mouse taken 30 min after treatment with aerosolized 20 μ M PEN-SP9-Cy3. Immunofluorescent staining for CCSP shows green secretory cells (arrowheads), red PEN-SP9-Cy3 fluorescence, and blue nuclei stained with DAPI. Green secretory cells are observed to not visibly take up PEN-SP9-Cy3, in contrast to ciliated cells, the other major airway epithelial cell type that is not labelled here with a lineage marker, but avidly internalize red PEN-SP9-Cy3 fluorescence. Scale bar, 50 μ m. **e**, Section of the left axial bronchus of a mouse treated as in “c” (with PEN-SP9-Cy3), showing red fluorescent staining of ciliated cells with ciliary tufts clearly visible by differential interference microscopy (arrowheads), but no staining of intervening secretory cells. Scale bar, 20 μ m. Similar results were obtained multiple times.

Supplementary information

Supplementary Information

Supplementary Figs 1–9.

Reporting Summary

Peer Review File

Supplementary Table 1

Data summary table for the mouse airway mucin secretion and mucus occlusion experiments.

Supplementary Table 2

Data summary table for the single-vesicle fusion experiments.

Supplementary Table 3

Donor participant sex, age and smoking status for HAE cell experiments.

Supplementary Video 1

Video showing rocking views of the end points of five independent 1 μ s simulations of SP9–Syt1 C2B. The corresponding coordinates are available in the source data.

Supplementary Video 2

Video showing rocking views of the end points of five independent 1 μ s simulations of P9–Syt1 C2B. The corresponding coordinates are available in the source data.

Source data

[Source Data Fig. 1](#)

[Source Data Fig. 2](#)

[Source Data Fig. 3](#)

[Source Data Fig. 4](#)

[Source Data Fig. 5](#)

[Source Data Extended Data Fig. 3](#)

[Source Data Extended Data Fig. 4](#)

[Source Data Extended Data Fig. 5](#)

[Source Data Extended Data Fig. 6](#)

[Source Data Extended Data Fig. 7](#)

[Source Data Extended Data Fig. 8](#)

Rights and permissions

Open Access This article is licensed under a Creative Commons Attribution 4.0 International License, which permits use, sharing, adaptation, distribution and reproduction in any medium or format, as long as you give appropriate credit to the original author(s) and the source, provide a link to the Creative Commons license, and indicate if changes were made. The images or other third party material in this article are included in the article's Creative Commons license, unless indicated otherwise in a credit line to the material. If material is not included in the

article's Creative Commons license and your intended use is not permitted by statutory regulation or exceeds the permitted use, you will need to obtain permission directly from the copyright holder. To view a copy of this license, visit <http://creativecommons.org/licenses/by/4.0/>.

Reprints and Permissions

About this article

Cite this article

Lai, Y., Fois, G., Flores, J.R. *et al.* Inhibition of calcium-triggered secretion by hydrocarbon-stapled peptides. *Nature* **603**, 949–956 (2022).
<https://doi.org/10.1038/s41586-022-04543-1>

- Received: 05 July 2021
- Accepted: 11 February 2022
- Published: 23 March 2022
- Issue Date: 31 March 2022
- DOI: <https://doi.org/10.1038/s41586-022-04543-1>

Share this article

Anyone you share the following link with will be able to read this content:

[Get shareable link](#)

Sorry, a shareable link is not currently available for this article.

[Copy to clipboard](#)

Provided by the Springer Nature SharedIt content-sharing initiative

Further reading

- **Mucus secretion blocked at its source in the lungs**

- Irina Gitlin
- John V. Fahy

Nature (2022)

Mucus secretion blocked at its source in the lungs

- Irina Gitlin
- John V. Fahy

News & Views 23 Mar 2022

This article was downloaded by **calibre** from <https://www.nature.com/articles/s41586-022-04543-1>

| [Section menu](#) | [Main menu](#) |

Amendments & Corrections

- [**Author Correction: Programmable interactions and emergent geometry in an array of atom clouds**](#) [11 March 2022]
Author Correction •
- [**Author Correction: The challenges and opportunities of battery-powered flight**](#) [15 March 2022]
Author Correction •
- [**Author Correction: Late Quaternary dynamics of Arctic biota from ancient environmental genomics**](#) [16 March 2022]
Author Correction •
- [**Author Correction: A highly distorted ultraelastic chemically complex Elinvar alloy**](#) [17 March 2022]
Author Correction •
- [**Publisher Correction: Activation mechanism of PINK1**](#) [15 March 2022]
Publisher Correction •
- [**Publisher Correction: Burning plasma achieved in inertial fusion**](#) [16 March 2022]
Publisher Correction •
- [**Publisher Correction: Gut microbiota modulates weight gain in mice after discontinued smoke exposure**](#) [15 March 2022]
Publisher Correction •

- Author Correction
- [Published: 11 March 2022](#)

Author Correction: Programmable interactions and emergent geometry in an array of atom clouds

- [Avikar Periwal](#) ORCID: [orcid.org/0000-0001-7601-0932^{1 na1}](https://orcid.org/0000-0001-7601-0932),
- [Eric S. Cooper^{1 na1}](#),
- [Philipp Kunkel](#) ORCID: [orcid.org/0000-0002-8145-9184^{1,2 na1}](https://orcid.org/0000-0002-8145-9184),
- [Julian F. Wienand](#) ORCID: [orcid.org/0000-0001-9347-0850^{1,3}](https://orcid.org/0000-0001-9347-0850),
- [Emily J. Davis¹](#) &
- [Monika Schleier-Smith](#) ORCID: [orcid.org/0000-0002-4686-3528^{1,2}](https://orcid.org/0000-0002-4686-3528)

Nature volume **603**, page E29 (2022)

- 348 Accesses
- 3 Altmetric
- [Metrics details](#)

Subjects

- [Quantum optics](#)
- [Quantum simulation](#)
- [Ultracold gases](#)

The [Original Article](#) was published on 22 December 2021

[Download PDF](#)

Correction to: *Nature* <https://doi.org/10.1038/s41586-021-04156-0>

Published online 22 December 2021

In the version of this article initially published, there was an error in Fig. 4a. Due to an error during the composition process, the top-left graph in Fig. 4a displayed an incorrect drive waveform for the Archimedean geometry, which inadvertently duplicated the lower waveform. The schematic of the drive waveform has been corrected in the HTML and PDF versions of the article

Author information

Author notes

1. These authors contributed equally: Avikar Periwal, Eric S. Cooper, Philipp Kunkel

Affiliations

1. Department of Physics, Stanford University, Stanford, CA, USA

Avikar Periwal, Eric S. Cooper, Philipp Kunkel, Julian F. Wienand, Emily J. Davis & Monika Schleier-Smith

2. SLAC National Accelerator Laboratory, Menlo Park, CA, USA

Philipp Kunkel & Monika Schleier-Smith

3. Fakultät für Physik, Ludwig-Maximilians-Universität, Munich, Germany

Julian F. Wienand

Corresponding author

Correspondence to [Monika Schleier-Smith](#).

Rights and permissions

[Reprints and Permissions](#)

About this article

Cite this article

Periwal, A., Cooper, E.S., Kunkel, P. *et al.* Author Correction: Programmable interactions and emergent geometry in an array of atom clouds. *Nature* **603**, E29 (2022). <https://doi.org/10.1038/s41586-022-04610-7>

- Published: 11 March 2022
- Issue Date: 31 March 2022
- DOI: <https://doi.org/10.1038/s41586-022-04610-7>

Share this article

Anyone you share the following link with will be able to read this content:

[Get shareable link](#)

Sorry, a shareable link is not currently available for this article.

[Copy to clipboard](#)

Provided by the Springer Nature SharedIt content-sharing initiative

| [Section menu](#) | [Main menu](#) |

- Author Correction
- [Published: 15 March 2022](#)

Author Correction: The challenges and opportunities of battery-powered flight

- [Venkatasubramanian Viswanathan](#) ORCID: orcid.org/0000-0003-1060-5495¹,
- [Alan H. Epstein](#) ORCID: orcid.org/0000-0002-2850-5831²,
- [Yet-Ming Chiang](#) ORCID: orcid.org/0000-0002-0833-7674³,
- [Esther Takeuchi](#)^{4,5},
- [Marty Bradley](#)⁶,
- [John Langford](#)⁷ &
- [Michael Winter](#)⁸

[Nature](#) volume 603, page E30 (2022)

- 403 Accesses
- 3 Altmetric
- [Metrics details](#)

Subjects

- [Aerospace engineering](#)
- [Batteries](#)

The [Original Article](#) was published on 26 January 2022

[Download PDF](#)

Correction to: *Nature* <https://doi.org/10.1038/s41586-021-04139-1>

Published online 26 January 2022

In the version of this Perspective initially published, there was a typographical error in the Abstract. In the text now reading “We conclude that battery packs suitable for flight with specific energy approaching 600 watt hours per kilogram may be achievable in the next decade given sufficient investment targeted at aeronautical applications,” “kilowatt hours” initially appeared in place of “watt hours.” The error has been corrected in the HTML and PDF versions of the article

Author information

Affiliations

1. Department of Mechanical Engineering, Carnegie Mellon University, Pittsburgh, PA, USA

Venkatasubramanian Viswanathan

2. Department of Aeronautics and Astronautics, Massachusetts Institute of Technology, Cambridge, MA, USA

Alan H. Epstein

3. Department of Materials Science and Engineering, Massachusetts Institute of Technology, Cambridge, MA, USA

Yet-Ming Chiang

4. Department of Materials Science and Chemical Engineering, Stony Brook University, Stony Brook, NY, USA

Esther Takeuchi

5. Interdisciplinary Science Department, Brookhaven National Laboratory, Upton, NY, USA

Esther Takeuchi

6. Department of Aerospace and Mechanical Engineering, University of Southern California, Los Angeles, CA, USA

Marty Bradley

7. Electra.aero, Falls Church, VA, USA

John Langford

8. Pratt & Whitney, Hartford, CT, USA

Michael Winter

Corresponding authors

Correspondence to [Venkatasubramanian Viswanathan](#) or [Alan H. Epstein](#).

Rights and permissions

[Reprints and Permissions](#)

About this article

Cite this article

Viswanathan, V., Epstein, A.H., Chiang, YM. *et al.* Author Correction: The challenges and opportunities of battery-powered flight. *Nature* **603**, E30 (2022). <https://doi.org/10.1038/s41586-022-04612-5>

- Published: 15 March 2022
- Issue Date: 31 March 2022

- DOI: <https://doi.org/10.1038/s41586-022-04612-5>

Share this article

Anyone you share the following link with will be able to read this content:

[Get shareable link](#)

Sorry, a shareable link is not currently available for this article.

[Copy to clipboard](#)

Provided by the Springer Nature SharedIt content-sharing initiative

This article was downloaded by **calibre** from <https://www.nature.com/articles/s41586-022-04612-5>

| [Section menu](#) | [Main menu](#) |

- Author Correction
- Open Access
- [Published: 16 March 2022](#)

Author Correction: Late Quaternary dynamics of Arctic biota from ancient environmental genomics

- [Yucheng Wang](#) ORCID: [orcid.org/0000-0002-7838-226X^{1,2 na1}](https://orcid.org/0000-0002-7838-226X),
- [Mikkel Winther Pedersen](#) ORCID: [orcid.org/0000-0002-7291-8887^{2 na1}](https://orcid.org/0000-0002-7291-8887),
- [Inger Greve Alsos](#) ORCID: [orcid.org/0000-0002-8610-1085^{3 na1}](https://orcid.org/0000-0002-8610-1085),
- [Bianca De Sanctis^{1,4}](#),
- [Fernando Racimo²](#),
- [Ana Prohaska](#) ORCID: [orcid.org/0000-0001-5459-6186¹](https://orcid.org/0000-0001-5459-6186),
- [Eric Coissac^{3,5}](#),
- [Hannah Lois Owens⁶](#),
- [Marie Kristine Føreid Merkel³](#),
- [Antonio Fernandez-Guerra²](#),
- [Alexandra Rouillard](#) ORCID: [orcid.org/0000-0001-5778-6620^{2,7}](https://orcid.org/0000-0001-5778-6620),
- [Youri Lammers³](#),
- [Adriana Alberti](#) ORCID: [orcid.org/0000-0003-3372-9423^{8,9}](https://orcid.org/0000-0003-3372-9423),
- [France Denoeud](#) ORCID: [orcid.org/0000-0001-8819-7634⁹](https://orcid.org/0000-0001-8819-7634),
- [Daniel Money](#) ORCID: [orcid.org/0000-0001-5151-3648¹](https://orcid.org/0000-0001-5151-3648),
- [Anthony H. Ruter²](#),
- [Hugh McColl](#) ORCID: [orcid.org/0000-0002-7568-4270²](https://orcid.org/0000-0002-7568-4270),
- [Nicolaj Krog Larsen²](#),
- [Anna A. Cherezova](#) ORCID: [orcid.org/0000-0002-6199-8164^{10,11}](https://orcid.org/0000-0002-6199-8164),

- [Mary E. Edwards](#)^{12,13},
- [Grigory B. Fedorov](#)^{10,11},
- [James Haile](#) ORCID: orcid.org/0000-0002-8521-8337²,
- [Ludovic Orlando](#) ORCID: orcid.org/0000-0003-3936-1850¹⁴,
- [Lasse Vinner](#)²,
- [Thorfinn Sand Korneliussen](#)^{2,15},
- [David W. Beilman](#) ORCID: orcid.org/0000-0002-2625-6747¹⁶,
- [Anders A. Bjørk](#)¹⁷,
- [Jialu Cao](#)²,
- [Christoph Dockter](#) ORCID: orcid.org/0000-0001-5923-3667¹⁸,
- [Julie Esdale](#)¹⁹,
- [Galina Gusarova](#)^{3,20},
- [Kristian K. Kjeldsen](#) ORCID: orcid.org/0000-0002-8557-5131²¹,
- [Jan Mangerud](#) ORCID: orcid.org/0000-0003-4793-7557^{22,23},
- [Jeffrey T. Rasic](#) ORCID: orcid.org/0000-0002-3549-6590²⁴,
- [Birgitte Skadhauge](#) ORCID: orcid.org/0000-0001-7317-4376¹⁸,
- [John Inge Svendsen](#)^{22,23},
- [Alexei Tikhonov](#)²⁵,
- [Patrick Wincker](#) ORCID: orcid.org/0000-0001-7562-3454⁹,
- [Yingchun Xing](#)²⁶,
- [Yubin Zhang](#) ORCID: orcid.org/0000-0003-4920-3100²⁷,
- [Duane G. Froese](#) ORCID: orcid.org/0000-0003-1032-5944²⁸,
- [Carsten Rahbek](#)^{6,29},
- [David Nogues Bravo](#)⁶,
- [Philip B. Holden](#) ORCID: orcid.org/0000-0002-2369-0062³⁰,
- [Neil R. Edwards](#) ORCID: orcid.org/0000-0001-6045-8804³⁰,
- [Richard Durbin](#) ORCID: orcid.org/0000-0002-9130-1006⁴,
- [David J. Meltzer](#) ORCID: orcid.org/0000-0001-8084-9802^{2,31},
- [Kurt H. Kjær](#)²,
- [Per Möller](#)³² &
- [Eske Willerslev](#) ORCID: orcid.org/0000-0002-7081-6748^{1,2,33,34}

Nature volume **603**, page E31 (2022)

- 451 Accesses

- 1 Altmetric
- [Metrics details](#)

Subjects

- [Climate-change ecology](#)
- [Ecological networks](#)
- [Metagenomics](#)
- [Next-generation sequencing](#)
- [Palaeoecology](#)

The [Original Article](#) was published on 20 October 2021

[Download PDF](#)

Correction to: *Nature* <https://doi.org/10.1038/s41586-021-04016-x>

Published online 20 October 2021

In the version of this article initially published, David Nogues Bravo's name appeared incorrectly (David Bravo Nogues). Ref. 61 has also been updated to read "Wang, Y. et al. Supporting data for: Late Quaternary dynamics of Arctic biota from ancient environmental genomics.

<https://doi.org/10.18710/3CVQAG>, DataverseNO, V1 (2021)". The changes have been made to the HTML and PDF versions of the article

Author information

Author notes

1. These authors contributed equally: Yucheng Wang, Mikkel Winther Pedersen, Inger Greve Alsos

Affiliations

1. Department of Zoology, University of Cambridge, Cambridge, UK

Yucheng Wang, Bianca De Sanctis, Ana Prohaska, Daniel Money & Eske Willerslev

2. Lundbeck Foundation GeoGenetics Centre, GLOBE Institute, University of Copenhagen, Copenhagen, Denmark

Yucheng Wang, Mikkel Winther Pedersen, Fernando Racimo, Antonio Fernandez-Guerra, Alexandra Rouillard, Anthony H. Ruter, Hugh McColl, Nicolaj Krog Larsen, James Haile, Lasse Vinner, Thorfinn Sand Korneliussen, Jialu Cao, David J. Meltzer, Kurt H. Kjær & Eske Willerslev

3. The Arctic University Museum of Norway, UiT—The Arctic University of Norway, Tromsø, Norway

Inger Greve Alsos, Eric Coissac, Marie Kristine Føreid Merkel, Youri Lammers & Galina Gusarova

4. Department of Genetics, University of Cambridge, Cambridge, UK

Bianca De Sanctis & Richard Durbin

5. Université Grenoble Alpes, Université Savoie Mont Blanc, CNRS, LECA, Grenoble, France

Eric Coissac

6. Center for Macroecology, Evolution and Climate, GLOBE Institute, University of Copenhagen, Copenhagen, Denmark

Hannah Lois Owens, Carsten Rahbek & David Nogues Bravo

7. Department of Geosciences, UiT—The Arctic University of Norway, Tromsø, Norway

Alexandra Rouillard

8. Université Paris-Saclay, CEA, CNRS, Institute for Integrative Biology of the Cell (I2BC), Gif-sur-Yvette, France

Adriana Alberti

9. Génomique Métabolique, Genoscope, Institut François Jacob, CEA, CNRS, Université Evry, Université Paris-Saclay, Evry, France

Adriana Alberti, France Denoeud & Patrick Wincker

10. Institute of Earth Sciences, St Petersburg State University, St Petersburg, Russia

Anna A. Cherezova & Grigory B. Fedorov

11. Arctic and Antarctic Research Institute, St Petersburg, Russia

Anna A. Cherezova & Grigory B. Fedorov

12. School of Geography and Environmental Science, University of Southampton, Southampton, UK

Mary E. Edwards

13. Alaska Quaternary Center, University of Alaska Fairbanks, Fairbanks, AK, USA

Mary E. Edwards

14. Centre d'Anthropobiologie et de Génomique de Toulouse, Université Paul Sabatier, Faculté de Médecine Purpan, Toulouse, France

Ludovic Orlando

15. National Research University, Higher School of Economics, Moscow, Russia

Thorfinn Sand Korneliussen

16. Department of Geography and Environment, University of Hawaii,
Honolulu, HI, USA

David W. Beilman

17. Department of Geosciences and Natural Resource Management,
University of Copenhagen, Copenhagen, Denmark

Anders A. Bjørk

18. Carlsberg Research Laboratory, Copenhagen, Denmark

Christoph Dockter & Birgitte Skadhauge

19. Center for Environmental Management of Military Lands, Colorado
State University, Fort Collins, CO, USA

Julie Esdale

20. Faculty of Biology, St Petersburg State University, St Petersburg,
Russia

Galina Gusarova

21. Department of Glaciology and Climate, Geological Survey of
Denmark and Greenland, Copenhagen, Denmark

Kristian K. Kjeldsen

22. Department of Earth Science, University of Bergen, Bergen, Norway

Jan Mangerud & John Inge Svendsen

23. Bjerknes Centre for Climate Research, Bergen, Norway

Jan Mangerud & John Inge Svendsen

24. US National Park Service, Gates of the Arctic National Park and
Preserve, Fairbanks, AK, USA

Jeffrey T. Rasic

25. Zoological Institute, , Russian Academy of Sciences, St Petersburg,
Russia

Alexei Tikhonov

26. Resource and Environmental Research Center, Chinese Academy of
Fishery Sciences, Beijing, China

Yingchun Xing

27. College of Plant Science, Jilin University, Changchun, China

Yubin Zhang

28. Department of Earth and Atmospheric Sciences, University of Alberta,
Edmonton, Alberta, Canada

Duane G. Froese

29. Center for Global Mountain Biodiversity, GLOBE Institute, University
of Copenhagen, Copenhagen, Denmark

Carsten Rahbek

30. School of Environment, Earth and Ecosystem Sciences, The Open
University, Milton Keynes, UK

Philip B. Holden & Neil R. Edwards

31. Department of Anthropology, Southern Methodist University, Dallas,
TX, USA

David J. Meltzer

32. Department of Geology, Quaternary Sciences, Lund University, Lund,
Sweden

Per Möller

33. Wellcome Trust Sanger Institute, Wellcome Genome Campus,
Cambridge, UK

Eske Willerslev

34. MARUM, University of Bremen, Bremen, Germany

Eske Willerslev

Corresponding author

Correspondence to [Eske Willerslev](#).

Rights and permissions

Open Access This article is licensed under a Creative Commons Attribution 4.0 International License, which permits use, sharing, adaptation, distribution and reproduction in any medium or format, as long as you give appropriate credit to the original author(s) and the source, provide a link to the Creative Commons license, and indicate if changes were made. The images or other third party material in this article are included in the article's Creative Commons license, unless indicated otherwise in a credit line to the material. If material is not included in the article's Creative Commons license and your intended use is not permitted by statutory regulation or exceeds the permitted use, you will need to obtain permission directly from the copyright holder. To view a copy of this license, visit <http://creativecommons.org/licenses/by/4.0/>.

[Reprints and Permissions](#)

About this article

Cite this article

Wang, Y., Pedersen, M.W., Alsos, I.G. *et al.* Author Correction: Late Quaternary dynamics of Arctic biota from ancient environmental genomics. *Nature* **603**, E31 (2022). <https://doi.org/10.1038/s41586-022-04628-x>

- Published: 16 March 2022
- Issue Date: 31 March 2022
- DOI: <https://doi.org/10.1038/s41586-022-04628-x>

Share this article

Anyone you share the following link with will be able to read this content:

[Get shareable link](#)

Sorry, a shareable link is not currently available for this article.

[Copy to clipboard](#)

Provided by the Springer Nature SharedIt content-sharing initiative

This article was downloaded by **calibre** from <https://www.nature.com/articles/s41586-022-04628-x>

- Author Correction
- [Published: 17 March 2022](#)

Author Correction: A highly distorted ultraelastic chemically complex Elinvar alloy

- [Q. F. He](#) ORCID: [orcid.org/0000-0002-1728-8579^{1 na1}](https://orcid.org/0000-0002-1728-8579),
- [J. G. Wang^{1,2 na1}](#),
- [H. A. Chen](#) ORCID: [orcid.org/0000-0002-0728-2165^{3 na1}](https://orcid.org/0000-0002-0728-2165),
- [Z. Y. Ding¹](#),
- [Z. Q. Zhou¹](#),
- [L. H. Xiong⁴](#),
- [J. H. Luan⁵](#),
- [J. M. Pelletier⁶](#),
- [J. C. Qiao^{1,6,7}](#),
- [Q. Wang⁸](#),
- [L. L. Fan⁹](#),
- [Y. Ren](#) ORCID: [orcid.org/0000-0001-9831-6035^{4,10}](https://orcid.org/0000-0001-9831-6035),
- [Q. S. Zeng](#) ORCID: [orcid.org/0000-0001-5960-1378^{11,12}](https://orcid.org/0000-0001-5960-1378),
- [C. T. Liu](#) ORCID: [orcid.org/0000-0001-7888-9725^{1,5}](https://orcid.org/0000-0001-7888-9725),
- [C. W. Pao](#) ORCID: [orcid.org/0000-0003-0821-7856¹³](https://orcid.org/0000-0003-0821-7856),
- [D. J. Srolovitz](#) ORCID: [orcid.org/0000-0001-6038-020X^{14,15}](https://orcid.org/0000-0001-6038-020X) &
- [Y. Yang](#) ORCID: [orcid.org/0000-0002-0491-8295^{1,5}](https://orcid.org/0000-0002-0491-8295)

[Nature](#) volume 603, page E32 (2022)

- 438 Accesses
- 1 Altmetric

- [Metrics details](#)

Subjects

- [Mechanical properties](#)
- [Metals and alloys](#)

The [Original Article](#) was published on 09 February 2022

[Download PDF](#)

Correction to: *Nature* <https://doi.org/10.1038/s41586-021-04309-1>

Published online 9 February 2022

In the version of this article initially published, the affiliation listed for H. A. Chen was in error. The correct affiliation, Institute of Materials Science and Engineering, National Taipei University of Technology, Taipei, Taiwan, has been amended in the HTML and PDF versions of this article

Author information

Author notes

1. These authors contributed equally: Q. F. He, J. G. Wang, H. A. Chen

Affiliations

1. Department of Mechanical Engineering, City University of Hong Kong, Kowloon, Hong Kong, China

Q. F. He, J. G. Wang, Z. Y. Ding, Z. Q. Zhou, J. C. Qiao, C. T. Liu & Y. Yang

2. College of Mechanical Engineering, Dongguan University of Technology, Dongguan, China

J. G. Wang

3. Institute of Materials Science and Engineering, National Taipei University of Technology, Taipei, Taiwan

H. A. Chen

4. X-ray Science Division, Argonne National Laboratory, Lemont, IL, USA

L. H. Xiong & Y. Ren

5. Department of Materials Science and Engineering, Hong Kong Institute for Advanced Study, City University of Hong Kong, Kowloon, Hong Kong, China

J. H. Luan, C. T. Liu & Y. Yang

6. MATEIS, Université de Lyon, UMR CNRS5510, INSA-Lyon, Villeurbanne, France

J. M. Pelletier & J. C. Qiao

7. School of Mechanics, Civil Engineering and Architecture, Northwestern Polytechnical University, Xi'an, China

J. C. Qiao

8. Laboratory for Structures, Institute of Materials, Shanghai University, Shanghai, China

Q. Wang

9. College of Physics and Materials Science, Tianjin Normal University, Tianjin, China

L. L. Fan

10. Department of Physics, City University of Hong Kong, Kowloon, Hong Kong, China
Y. Ren
11. Center for High Pressure Science and Technology Advanced Research, Shanghai, China
Q. S. Zeng
12. Jiangsu Key Laboratory of Advanced Metallic Materials, School of Materials Science and Engineering, Southeast University, Nanjing, China
Q. S. Zeng
13. Research Center for Applied Sciences, Academia Sinica, Taipei, Taiwan
C. W. Pao
14. Department of Mechanical Engineering, The University of Hong Kong, Hong Kong, China
D. J. Srolovitz
15. International Digital Economy Academy (IDEA), Shenzhen, China
D. J. Srolovitz

Corresponding authors

Correspondence to [C. W. Pao](#), [D. J. Srolovitz](#) or [Y. Yang](#).

Rights and permissions

[Reprints and Permissions](#)

About this article

Cite this article

He, Q.F., Wang, J.G., Chen, H.A. *et al.* Author Correction: A highly distorted ultraelastic chemically complex Elinvar alloy. *Nature* **603**, E32 (2022). <https://doi.org/10.1038/s41586-022-04626-z>

- Published: 17 March 2022
- Issue Date: 31 March 2022
- DOI: <https://doi.org/10.1038/s41586-022-04626-z>

Share this article

Anyone you share the following link with will be able to read this content:

[Get shareable link](#)

Sorry, a shareable link is not currently available for this article.

[Copy to clipboard](#)

Provided by the Springer Nature SharedIt content-sharing initiative

This article was downloaded by **calibre** from <https://www.nature.com/articles/s41586-022-04626-z>

- Publisher Correction
- [Published: 15 March 2022](#)

Publisher Correction: Activation mechanism of PINK1

- [Zhong Yan Gan](#) [ORCID: orcid.org/0000-0001-5755-7780](#)^{1,2},
- [Sylvie Callegari](#) [ORCID: orcid.org/0000-0002-4402-945X](#)^{1,2},
- [Simon A. Cobbold](#) [ORCID: orcid.org/0000-0002-9927-8998](#)^{1,2},
- [Thomas R. Cotton](#) [ORCID: orcid.org/0000-0001-6709-9218](#)^{1,2},
- [Michael J. Mlodzianoski](#) [ORCID: orcid.org/0000-0002-3510-9167](#)^{1,2},
- [Alexander F. Schubert](#) [ORCID: orcid.org/0000-0002-1834-3787](#)³,
- [Niall D. Geoghegan](#) [ORCID: orcid.org/0000-0001-9884-0769](#)^{1,2},
- [Kelly L. Rogers](#) [ORCID: orcid.org/0000-0002-6755-0221](#)^{1,2},
- [Andrew Leis](#)^{1,2},
- [Grant Dewson](#) [ORCID: orcid.org/0000-0003-4251-8898](#)^{1,2},
- [Alisa Glukhova](#) [ORCID: orcid.org/0000-0003-4146-965X](#)^{1,2,4,5} &
- [David Komander](#) [ORCID: orcid.org/0000-0002-8092-4320](#)^{1,2}

[Nature](#) volume 603, page E33 (2022)

- 436 Accesses
- 2 Altmetric
- [Metrics details](#)

Subjects

- [Autophagy](#)
- [Cryoelectron microscopy](#)
- [Enzyme mechanisms](#)

- [Kinases](#)
- [X-ray crystallography](#)

The [Original Article](#) was published on 21 December 2021

[Download PDF](#)

Correction to: *Nature* <https://doi.org/10.1038/s41586-021-04340-2>
Published online 21 December 2021

This article was originally published on 21 December 2021 with Open Access under a Creative Commons Attribution (CC BY) 4.0 International License. After publication the author(s) decided to cancel the Open Access. Therefore, the copyright of the article has been changed to a standard Springer Nature licence (© The Author(s), under exclusive licence to Springer Nature Limited). The original article has been corrected online

Author information

Affiliations

1. Walter and Eliza Hall Institute of Medical Research, Parkville, Victoria, Australia

Zhong Yan Gan, Sylvie Callegari, Simon A. Cobbold, Thomas R. Cotton, Michael J. Mlodzianoski, Niall D. Geoghegan, Kelly L. Rogers, Andrew Leis, Grant Dewson, Alisa Glukhova & David Komander

2. Department of Medical Biology, University of Melbourne, Melbourne, Victoria, Australia

Zhong Yan Gan, Sylvie Callegari, Simon A. Cobbold, Thomas R. Cotton, Michael J. Mlodzianoski, Niall D. Geoghegan, Kelly L. Rogers, Andrew Leis, Grant Dewson, Alisa Glukhova & David Komander

3. Medical Research Council Laboratory of Molecular Biology,
Cambridge, UK

Alexander F. Schubert

4. Drug Discovery Biology, Monash Faculty of Pharmacy and
Pharmaceutical Sciences, Monash University, Parkville, Victoria,
Australia

Alisa Glukhova

5. Department of Biochemistry and Pharmacology, University of
Melbourne, Melbourne, Victoria, Australia

Alisa Glukhova

Corresponding author

Correspondence to [David Komander](#).

Rights and permissions

[Reprints and Permissions](#)

About this article

Cite this article

Gan, Z.Y., Callegari, S., Cobbold, S.A. *et al.* Publisher Correction:
Activation mechanism of PINK1. *Nature* **603**, E33 (2022).

<https://doi.org/10.1038/s41586-022-04591-7>

- Published: 15 March 2022
- Issue Date: 31 March 2022
- DOI: <https://doi.org/10.1038/s41586-022-04591-7>

Share this article

Anyone you share the following link with will be able to read this content:

[Get shareable link](#)

Sorry, a shareable link is not currently available for this article.

[Copy to clipboard](#)

Provided by the Springer Nature SharedIt content-sharing initiative

This article was downloaded by **calibre** from <https://www.nature.com/articles/s41586-022-04591-7>

| [Section menu](#) | [Main menu](#) |

- Publisher Correction
- Open Access
- [Published: 16 March 2022](#)

Publisher Correction: Burning plasma achieved in inertial fusion

- [A. B. Zylstra](#) [ORCID: orcid.org/0000-0003-0489-7479¹](#),
- [O. A. Hurricane](#) [ORCID: orcid.org/0000-0002-8600-5448¹](#),
- [D. A. Callahan¹](#),
- [A. L. Kritchler](#) [ORCID: orcid.org/0000-0002-9694-1088¹](#),
- [J. E. Ralph¹](#),
- [H. F. Robey²](#),
- [J. S. Ross¹](#),
- [C. V. Young](#) [ORCID: orcid.org/0000-0002-8075-7550¹](#),
- [K. L. Baker¹](#),
- [D. T. Casey](#) [ORCID: orcid.org/0000-0003-2125-677X¹](#),
- [T. Döppner](#) [ORCID: orcid.org/0000-0002-5703-7125¹](#),
- [L. Divol¹](#),
- [M. Hohenberger](#) [ORCID: orcid.org/0000-0002-5887-9711¹](#),
- [S. Le Pape³](#),
- [A. Pak¹](#),
- [P. K. Patel¹](#),
- [R. Tommasini](#) [ORCID: orcid.org/0000-0002-1070-3565¹](#),
- [S. J. Ali](#) [ORCID: orcid.org/0000-0003-1823-3788¹](#),
- [P. A. Amendt¹](#),
- [L. J. Atherton¹](#),
- [B. Bachmann](#) [ORCID: orcid.org/0000-0001-7992-0018¹](#),
- [D. Bailey¹](#),
- [L. R. Benedetti¹](#),
- [L. Berzak Hopkins¹](#),

- [R. Betti](#)⁴,
- [S. D. Bhandarkar](#)¹,
- [J. Biener](#) ORCID: orcid.org/0000-0002-3722-3924¹,
- [R. M. Bionta](#)¹,
- [N. W. Birge](#)²,
- [E. J. Bond](#)¹,
- [D. K. Bradley](#)¹,
- [T. Braun](#) ORCID: orcid.org/0000-0002-4633-5311¹,
- [T. M. Briggs](#)¹,
- [M. W. Bruhn](#)¹,
- [P. M. Celliers](#)¹,
- [B. Chang](#)¹,
- [T. Chapman](#)¹,
- [H. Chen](#) ORCID: orcid.org/0000-0002-0181-1695¹,
- [C. Choate](#)¹,
- [A. R. Christopherson](#)¹,
- [D. S. Clark](#)¹,
- [J. W. Crippen](#)⁵,
- [E. L. Dewald](#)¹,
- [T. R. Dittrich](#)¹,
- [M. J. Edwards](#)¹,
- [W. A. Farmer](#) ORCID: orcid.org/0000-0001-6758-220X¹,
- [J. E. Field](#)¹,
- [D. Fittinghoff](#) ORCID: orcid.org/0000-0002-6089-8911¹,
- [J. Frenje](#)⁶,
- [J. Gaffney](#) ORCID: orcid.org/0000-0002-2408-0047¹,
- [M. Gatun Johnson](#) ORCID: orcid.org/0000-0002-2383-1275⁶,
- [S. H. Glenzer](#) ORCID: orcid.org/0000-0001-9112-0558⁷,
- [G. P. Grim](#) ORCID: orcid.org/0000-0002-9648-3427¹,
- [S. Haan](#)¹,
- [K. D. Hahn](#)¹,
- [G. N. Hall](#)¹,
- [B. A. Hammel](#)¹,
- [J. Harte](#)¹,

- [E. Hartouni](#)¹,
- [J. E. Heebner](#)¹,
- [V. J. Hernandez](#)¹,
- [H. Herrmann](#) [ORCID: orcid.org/0000-0002-5092-5373](#)²,
- [M. C. Herrmann](#)¹,
- [D. E. Hinkel](#)¹,
- [D. D. Ho](#)¹,
- [J. P. Holder](#) [ORCID: orcid.org/0000-0003-1833-4001](#)¹,
- [W. W. Hsing](#)¹,
- [H. Huang](#)⁵,
- [K. D. Humbird](#)¹,
- [N. Izumi](#) [ORCID: orcid.org/0000-0003-1114-597X](#)¹,
- [L. C. Jarrott](#)¹,
- [J. Jeet](#) [ORCID: orcid.org/0000-0002-9109-1563](#)¹,
- [O. Jones](#)¹,
- [G. D. Kerbel](#)¹,
- [S. M. Kerr](#) [ORCID: orcid.org/0000-0003-4822-564X](#)¹,
- [S. F. Khan](#)¹,
- [J. Kilkenny](#)⁵,
- [Y. Kim](#)²,
- [H. Geppert Kleinrath](#)²,
- [V. Geppert Kleinrath](#) [ORCID: orcid.org/0000-0002-6869-5772](#)²,
- [C. Kong](#)⁵,
- [J. M. Koning](#) [ORCID: orcid.org/0000-0002-8713-7741](#)¹,
- [J. J. Kroll](#)¹,
- [M. K. G. Kruse](#)¹,
- [B. Kustowski](#) [ORCID: orcid.org/0000-0003-2085-3206](#)¹,
- [O. L. Landen](#) [ORCID: orcid.org/0000-0002-1499-8217](#)¹,
- [S. Langer](#)¹,
- [D. Larson](#)¹,
- [N. C. Lemos](#)¹,
- [J. D. Lindl](#)¹,
- [T. Ma](#) [ORCID: orcid.org/0000-0002-6657-9604](#)¹,
- [M. J. MacDonald](#) [ORCID: orcid.org/0000-0002-6295-6978](#)¹,

- [B. J. MacGowan](#) [ORCID: orcid.org/0000-0003-1040-1900¹](#),
- [A. J. Mackinnon¹](#),
- [S. A. MacLaren¹](#),
- [A. G. MacPhee¹](#),
- [M. M. Marinak¹](#),
- [D. A. Mariscal¹](#),
- [E. V. Marley¹](#),
- [L. Masse¹](#),
- [K. Meaney²](#),
- [N. B. Meezan](#) [ORCID: orcid.org/0000-0002-7671-2886¹](#),
- [P. A. Michel¹](#),
- [M. Millot](#) [ORCID: orcid.org/0000-0003-4414-3532¹](#),
- [J. L. Milovich](#) [ORCID: orcid.org/0000-0002-9762-3591¹](#),
- [J. D. Moody¹](#),
- [A. S. Moore¹](#),
- [J. W. Morton⁸](#),
- [T. Murphy](#) [ORCID: orcid.org/0000-0002-6137-9873²](#),
- [K. Newman¹](#),
- [J.-M. G. Di Nicola¹](#),
- [A. Nikroo¹](#),
- [R. Nora¹](#),
- [M. V. Patel¹](#),
- [L. J. Pelz¹](#),
- [J. L. Peterson](#) [ORCID: orcid.org/0000-0002-5167-5708¹](#),
- [Y. Ping](#) [ORCID: orcid.org/0000-0002-4879-9072¹](#),
- [B. B. Pollock¹](#),
- [M. Ratledge⁵](#),
- [N. G. Rice⁵](#),
- [H. Rinderknecht](#) [ORCID: orcid.org/0000-0003-4969-5571⁴](#),
- [M. Rosen¹](#),
- [M. S. Rubery⁸](#),
- [J. D. Salmonson¹](#),
- [J. Sater¹](#),
- [S. Schiaffino¹](#),

- [D. J. Schlossberg](#) [ORCID: orcid.org/0000-0002-8713-9448¹](#),
- [M. B. Schneider¹](#),
- [C. R. Schroeder¹](#),
- [H. A. Scott¹](#),
- [S. M. Sepke¹](#),
- [K. Sequoia⁵](#),
- [M. W. Sherlock¹](#),
- [S. Shin¹](#),
- [V. A. Smalyuk¹](#),
- [B. K. Spears](#) [ORCID: orcid.org/0000-0001-6946-8996¹](#),
- [P. T. Springer¹](#),
- [M. Stadermann¹](#),
- [S. Stoupin¹](#),
- [D. J. Strozzi](#) [ORCID: orcid.org/0000-0001-8814-3791¹](#),
- [L. J. Suter¹](#),
- [C. A. Thomas⁴](#),
- [R. P. J. Town¹](#),
- [E. R. Tubman¹](#),
- [C. Trosseille¹](#),
- [P. L. Volegov](#) [ORCID: orcid.org/0000-0003-0361-7500²](#),
- [C. R. Weber¹](#),
- [K. Widmann](#) [ORCID: orcid.org/0000-0001-5623-6619¹](#),
- [C. Wild⁹](#),
- [C. H. Wilde²](#),
- [B. M. Van Wonterghem¹](#),
- [D. T. Woods¹](#),
- [B. N. Woodworth¹](#),
- [M. Yamaguchi⁵](#),
- [S. T. Yang¹](#) &
- [G. B. Zimmerman¹](#)

Nature volume **603**, page E34 (2022)

- 451 Accesses

- 1 Altmetric
- [Metrics details](#)

Subjects

- [Laser-produced plasmas](#)
- [Nuclear fusion and fission](#)

The [Original Article](#) was published on 26 January 2022

[Download PDF](#)

Correction to: *Nature* <https://doi.org/10.1038/s41586-021-04281-w>
Published online 26 January 2022

In the version of this article initially published, an author's name was omitted from the list. C. Trosseille (Lawrence Livermore National Laboratory, Livermore, CA, USA) was missing from the author list, and their contribution to the X-ray framing camera was also not shown. The amendments have been made to the html and PDF versions of the article

Author information

Author notes

1. These authors contributed equally: A. B. Zylstra, O. A. Hurricane

Affiliations

1. Lawrence Livermore National Laboratory, Livermore, CA, USA
A. B. Zylstra, O. A. Hurricane, D. A. Callahan, A. L. Kritch, J. E. Ralph, J. S. Ross, C. V. Young, K. L. Baker, D. T. Casey, T. Döppner, L. Divol, M. Hohenberger, A. Pak, P. K. Patel, R. Tommasini, S. J. Ali, P. A. Amendt, L. J. Atherton, B. Bachmann, D.

Bailey, L. R. Benedetti, L. Berzak Hopkins, S. D. Bhandarkar, J. Biener, R. M. Bionta, E. J. Bond, D. K. Bradley, T. Braun, T. M. Briggs, M. W. Bruhn, P. M. Celliers, B. Chang, T. Chapman, H. Chen, C. Choate, A. R. Christopherson, D. S. Clark, E. L. Dewald, T. R. Dittrich, M. J. Edwards, W. A. Farmer, J. E. Field, D. Fittinghoff, J. Gaffney, G. P. Grim, S. Haan, K. D. Hahn, G. N. Hall, B. A. Hammel, J. Harte, E. Hartouni, J. E. Heebner, V. J. Hernandez, M. C. Herrmann, D. E. Hinkel, D. D. Ho, J. P. Holder, W. W. Hsing, K. D. Humbird, N. Izumi, L. C. Jarrott, J. Jeet, O. Jones, G. D. Kerbel, S. M. Kerr, S. F. Khan, J. M. Koning, J. J. Kroll, M. K. G. Kruse, B. Kustowski, O. L. Landen, S. Langer, D. Larson, N. C. Lemos, J. D. Lindl, T. Ma, M. J. MacDonald, B. J. MacGowan, A. J. Mackinnon, S. A. McLaren, A. G. MacPhee, M. M. Marinak, D. A. Mariscal, E. V. Marley, L. Masse, N. B. Meezan, P. A. Michel, M. Millot, J. L. Milovich, J. D. Moody, A. S. Moore, K. Newman, J.-M. G. Di Nicola, A. Nikroo, R. Nora, M. V. Patel, L. J. Pelz, J. L. Peterson, Y. Ping, B. B. Pollock, M. Rosen, J. D. Salmonson, J. Sater, S. Schiaffino, D. J. Schlossberg, M. B. Schneider, C. R. Schroeder, H. A. Scott, S. M. Sepke, M. W. Sherlock, S. Shin, V. A. Smalyuk, B. K. Spears, P. T. Springer, M. Stadermann, S. Stoupin, D. J. Strozzi, L. J. Suter, R. P. J. Town, E. R. Tubman, C. Trosseille, C. R. Weber, K. Widmann, B. M. Van Wonterghem, D. T. Woods, B. N. Woodworth, S. T. Yang & G. B. Zimmerman

2. Los Alamos National Laboratory, Los Alamos, NM, USA

H. F. Robey, N. W. Birge, H. Herrmann, Y. Kim, H. Geppert Kleinrath, V. Geppert Kleinrath, K. Meaney, T. Murphy, P. L. Volegov & C. H. Wilde

3. Laboratoire pour l'utilisation des Lasers Intenses chez École Polytechnique, Palaiseau, France

S. Le Pape

4. Laboratory for Laser Energetics, University of Rochester, Rochester, NY, USA

R. Betti, H. Rinderknecht & C. A. Thomas

5. General Atomics, San Diego, CA, USA

J. W. Crippen, H. Huang, J. Kilkenny, C. Kong, M. Ratledge, N. G. Rice, K. Sequoia & M. Yamaguchi

6. Massachusetts Institute of Technology, Cambridge, MA, USA

J. Frenje & M. Gatu Johnson

7. SLAC National Accelerator Laboratory, Menlo Park, CA, USA

S. H. Glenzer

8. Atomic Weapons Establishment, Aldermaston, UK

J. W. Morton & M. S. Rubery

9. Diamond Materials, Freiburg, Germany

C. Wild

Corresponding authors

Correspondence to [A. B. Zylstra](#) or [O. A. Hurricane](#).

Additional information

Rights and permissions

Open Access This article is licensed under a Creative Commons Attribution 4.0 International License, which permits use, sharing, adaptation, distribution and reproduction in any medium or format, as long as you give appropriate credit to the original author(s) and the source, provide a link to the Creative Commons license, and indicate if changes were made. The images or other third party material in this article are

included in the article's Creative Commons license, unless indicated otherwise in a credit line to the material. If material is not included in the article's Creative Commons license and your intended use is not permitted by statutory regulation or exceeds the permitted use, you will need to obtain permission directly from the copyright holder. To view a copy of this license, visit <http://creativecommons.org/licenses/by/4.0/>.

[Reprints and Permissions](#)

About this article

Cite this article

Zylstra, A.B., Hurricane, O.A., Callahan, D.A. *et al.* Publisher Correction: Burning plasma achieved in inertial fusion. *Nature* **603**, E34 (2022).
<https://doi.org/10.1038/s41586-022-04607-2>

- Published: 16 March 2022
- Issue Date: 31 March 2022
- DOI: <https://doi.org/10.1038/s41586-022-04607-2>

Share this article

Anyone you share the following link with will be able to read this content:

[Get shareable link](#)

Sorry, a shareable link is not currently available for this article.

[Copy to clipboard](#)

Provided by the Springer Nature SharedIt content-sharing initiative

| [Section menu](#) | [Main menu](#) |

- Publisher Correction
- [Published: 15 March 2022](#)

Publisher Correction: Gut microbiota modulates weight gain in mice after discontinued smoke exposure

- [Leviel Fluhr](#)¹ na1,
- [Uria Mor](#) [ORCID: orcid.org/0000-0002-2918-6406](#)¹ na1,
- [Aleksandra A. Kolodziejczyk](#)¹,
- [Mally Dori-Bachash](#)¹,
- [Avner Leshem](#) [ORCID: orcid.org/0000-0003-4082-2036](#)^{1,2},
- [Shlomik Itav](#)¹,
- [Yotam Cohen](#)¹,
- [Jotham Suez](#) [ORCID: orcid.org/0000-0003-3836-972X](#)¹,
- [Niv Zmora](#)^{1,3,4},
- [Claudia Moresi](#)¹,
- [Shahar Molina](#)¹,
- [Niv Ayalon](#)¹,
- [Rafael Valdés-Mas](#)¹,
- [Shanni Hornstein](#)¹,
- [Hodaya Karbi](#)¹,
- [Denise Kviatcovsky](#) [ORCID: orcid.org/0000-0002-9697-0380](#)¹,
- [Adi Livne](#)¹,
- [Aurelie Bukimer](#)¹,
- [Shimrit Eliyahu-Miller](#)¹,
- [Alona Metz](#)¹,
- [Alexander Brandis](#)⁵,

- [Tevie Mehlman⁵](#),
- [Yael Kuperman](#) [ORCID: orcid.org/0000-0003-3830-1856⁶](#),
- [Michael Tsoory⁶](#),
- [Noa Stettner⁶](#),
- [Alon Harmelin⁶](#),
- [Hagit Shapiro](#) ^{1 na2} &
- [Eran Elinav](#) [ORCID: orcid.org/0000-0002-5775-2110^{1,7 na2}](#)

[*Nature*](#) volume **603**, page E35 (2022)

- 498 Accesses
- 2 Altmetric
- [Metrics details](#)

Subjects

- [Metabolic disorders](#)
- [Microbiome](#)

The [Original Article](#) was published on 08 December 2021

[Download PDF](#)

Correction to: *Nature* <https://doi.org/10.1038/s41586-021-04194-8>
Published online 8 December 2021

In the version of this article initially published, there was an error in Fig. 4a. In the original version, breaks in the straddle line to indicate which columns pertain to the top-most labels “No Abx” and “Abx” were missing, while “Abx” was centered over the last two columns, rather than the last three columns (resp., “None,” “PBS” and “DMG.”). The errors have been corrected in the HTML and PDF versions of the article

Author information

Author notes

1. These authors contributed equally: Leviel Fluhr, Uria Mor
2. These authors jointly supervised this work: Hagit Shapiro, Eran Elinav

Affiliations

1. Immunology Department, Weizmann Institute of Science, Rehovot, Israel

Leviel Fluhr, Uria Mor, Aleksandra A. Kolodziejczyk, Mally Dori-Bachash, Avner Leshem, Shlomik Itav, Yotam Cohen, Jotham Suez, Niv Zmora, Claudia Moresi, Shahar Molina, Niv Ayalon, Rafael Valdés-Mas, Shanni Hornstein, Hodaya Karbi, Denise Kviatcovsky, Adi Livne, Aurelie Bukimer, Shimrit Eliyahu-Miller, Alona Metz, Hagit Shapiro & Eran Elinav

2. Department of Surgery, Tel Aviv Sourasky Medical Center, Tel Aviv, Israel

Avner Leshem

3. Research Center for Digestive Tract and Liver Diseases, Tel Aviv Sourasky Medical Center, Sackler Faculty of Medicine, Tel Aviv University, Tel Aviv, Israel

Niv Zmora

4. Internal Medicine Department, Tel Aviv Sourasky Medical Center, Tel Aviv, Israel

Niv Zmora

5. Department of Biological Services, Weizmann Institute of Science, Rehovot, Israel

Alexander Brandis & Tevie Mehlman

6. Department of Veterinary Resources, Weizmann Institute of Science,
Rehovot, Israel

Yael Kuperman, Michael Tsoory, Noa Stettner & Alon Harmelin

7. Division of Cancer-Microbiome Research, DKFZ, Heidelberg,
Germany

Eran Elinav

Corresponding authors

Correspondence to [Hagit Shapiro](#) or [Eran Elinav](#).

Rights and permissions

[Reprints and Permissions](#)

About this article

Cite this article

Fluhr, L., Mor, U., Kolodziejczyk, A.A. *et al.* Publisher Correction: Gut microbiota modulates weight gain in mice after discontinued smoke exposure. *Nature* **603**, E35 (2022). <https://doi.org/10.1038/s41586-022-04611-6>

- Published: 15 March 2022
- Issue Date: 31 March 2022
- DOI: <https://doi.org/10.1038/s41586-022-04611-6>

Share this article

Anyone you share the following link with will be able to read this content:

[Get shareable link](#)

Sorry, a shareable link is not currently available for this article.

[Copy to clipboard](#)

Provided by the Springer Nature SharedIt content-sharing initiative

This article was downloaded by **calibre** from <https://www.nature.com/articles/s41586-022-04611-6>

| [Section menu](#) | [Main menu](#) |

Nature Outlook